UNIVERSITY OF SOUTHAMPTON

FACULTY OF ENGINEERING AND THE ENVIRONMENT

Civil, Maritime & Environmental Engineering and Sciences Unit

Experimental & Computational Structural Analysis of Masonry Panels Subject to Long Duration Blast Loading

by

Richard A. Keys

Thesis for the degree of Doctor of Philosophy
March 2016

UNIVERSITY OF SOUTHAMPTON

ABSTRACT

FACULTY OF ENGINEERING AND THE ENVIRONMENT

Civil, Maritime & Environmental Engineering Science Unit

Thesis for the degree of Doctor of Philosophy

EXPERIMENTAL & COMPUTATIONAL STRUCTURAL ANALYSIS OF MASONRY PANELS SUBJECT TO LONG DURATION BLAST LOADING

by Richard A. Keys

Even in simple, quasi-static cases, blast and its interaction with structures is a complex phenomenon. Long duration blast, defined for the purposes of this research as a blast event with a positive phase duration in excess of 100ms, increases this complexity due to not only the persistent effects of the static blast overpressure, but also the dynamic pressure associated with drag wind trailing the shock front. Brittle materials such as concrete and masonry produce large numbers of initial fragments, which when caught in the drag wind produce substantial debris distributions, presenting a number of potential hazards ranging from infrastructure obstruction to personal injury.

This research investigates the effects of long duration blast loading of masonry structures, using a modular 'Base Panel' approach to descirbe structures as a composition of simple panels. Five experimental blast trials were conducted, testing a total of 22 masonry structures against varying blast parameters. The results showed correlations between both the breakage and debris distributions with respect to panel geometry. Computational Fluid Dynamics and the Applied Element Method were used to model the experimental trials, with the results showing good agreement offering a promising modelling platform for future work. The results, both experimental and computational, deomonstrate the 'Base Panel' approach to be an effective tool for the prediction of masonry debris distribution.

Contents

Declaration of Authorship

I, Richard A. Keys declare that the report entitled

Experimental & Computational Structural Analysis of Masonry Panels Subject to Long Duration Blast Loading

and the work presented in the report is both my own and have been generated by me as a result of my own original research. I confirm that:

- this work was done wholly or mainly while in candidature for a research degree at this University;
- where any part of this report has previously been submitted for a degree or any other qualification at this University or any other institution, this has been clearly stated;
- where I have consulted the published work of others, this is always clearly attributed;
- where I have quoted from the work of others, the source is always given. With the exception of such quotations, this report is entirely my own work;
- I have acknowledged all main sources of help;
- where the report is based on work done by myself jointly with others, I have made clear exactly what was done by others and what I have contributed myself

Signed: .....

Date: .....

Acknowledgements

Firstly, the author would like to thank Dr Simon Clubley for his oversight and support throughout the course of this research project. The author would also like to express gratitude to the UK Ministry of Defence for providing the use of testing facilities at MoD Shoeburryness. All data hereby obtained through the use of such facilities remains the property of the UK MoD. The assistance of the Spurpark Ltd. trials division is gratefully acknowledged with respect to experimental planning, instrumentation and implementation. Finally, the author would also like to thank Dr. T. Rose for his assistance with CFD modelling in Air3D.

List of Figures

List of Tables

List of Symbols

Blast

b	Waveform Decay Constant	(-)
c_0	Velocity of Sound in Air	(ms$^-$1)
c_p	Specific Heat at Constant Pressure	(KJkg^{-1}K^{-1})
c_V	Specific Heat at Constant Volume	(KJkg^{-1}K^{-1})
d	Diameter	(m)
I	Impulse	(kPa.ms)
I_{pi^+}	Positive Phase Incident Impulse	(kPa.ms)
I_{pi^-}	Negative Phase Incident Impulse	(kPa.ms)
I_{pr^+}	Positive Phase Reflected Impulse	(kPa.ms)
I_{pr^-}	Negative Phase Reflected Impulse	(kPa.ms)
I_q	Dynamic Associated Impulse	(kPa.ms)
L_w^+	Positive Phase Blast Wavelength	(m)
L_W^-	Negative Phase Blast Wavelength	(m)
l	Length of Shock Wave	(m)
M_s	Mach Number	(-)
m	Mass	(kg)
p	Pressure	(kPa)
p_0	Ambiant Pressure	(kPa)
p_i	Peak Static Overpressure	(kPa)
p_i^+	Positive Phase Static Overpressure	(kPa)
p_i^-	Negative Phase Static Overpressure	(kPa)
p_r	Reflected Pressure	(kPa)
p_r^+	Positive Phase Reflected Pressure	(kPa)
p_r^-	Negative Phase Reflected Pressure	(kPa)

q	Dynamic Pressure	(kPa)
r	Radial Distance	(m)
R	Distance from Charge of Mass W_1	(m)
t	Time / Duration	(s)
t_0	Arrival Time	(ms)
t^+	Positive Phase Duration	(ms)
t^-	Negative Phase Duration	(ms)
U	Shock / Blast Wave Velocity	(ms^{-1})
u	Particle Velocity	(ms^{-1})
W	Charge Mass	(kg)
x	Distance	(m)
Z	Distance from Charge of Mass W	(m)
Γ	Vortex Circulation	(-)
γ	Ratio of Specific Heats	(-)
θ	Angle of Blast Wave Clearing	($^\circ$)
λ	Scaling Ratio	(-)
ρ	Density	(kgm^{-3})
ρ_0	Ambiant / Initial Density	(kgm^{-3})
$\vec{\omega}$	Vorticity vector	(-)

Fluid Dynamics

a	Acceleration	(ms^{-2})
e	Total Internal Energy per Unit Mass	(Jkg^{-1})
E_i	Internal Energy	(J)
F	Flux Term	(-)
f	Directional Force	(N)
F_b	Body Force	(N)
F_s	Surface Force	(N)
G	Flux Term	(-)
H	Flux Term	(-)
i	Unit Vector in x	(-)
J	Flux Term	(-)
j	Unit Vector in y	(-)
k	Unit Vector in z	(-)
k	Thermal Conductivity	$(\mathrm{Wm}^{-1}\mathrm{K}^{-1})$
L	Dimension of Interaction	(m)
m	Mass	(kg)
$\vec{n}$	Unit Vector in S	(-)
p	Pressure	(kPa)
$\dot{q}$	Rate of Volumetric Heat Addition per Unit Mass	$(\mathrm{Jkg}^{-1}\mathrm{s}^{-1})$
Q_c	Heating of Element by Thermal Conduction	(J)
Q_v	Volumetric Element Heating	(J)
Re	Reynolds Number	(-)
S	Contour surface	(-)
T	Temperature	(K)
t	Time	(s)
U	Flux Vector	(-)

u	Velocity Component in x	(ms^{-1})
v	Velocity Component in y	(ms^{-1})
$\vec{V}$	Velocity	(ms^{-1})
V_n	Velocity in $\vec{n}$	(ms^{-1})
W	Work Done	(J)
w	Velocity Component in z	(ms^{-1})
W_b	Work Done due to Body Forces	(J)
W_s	Work Done due to Surface Forces	(J)
x	Distance (Cartesian)	(m)
y	Distance (Cartesian)	(m)
z	Distance (Cartesian)	(m)
λ	Viscosity Coefficient	$(\mathrm{kgm}^{-1}\mathrm{s}^{-1})$
μ	Molecular Viscosity Coefficient	$(\mathrm{kgm}^{-1}\mathrm{s}^{-1})$
ν	Volume Element	(m^3)
ρ	Density	(kgm^{-3})
τ	Directional Fluid Stress	(Pa)
ϕ_t	Net Flux of Heat	(Js^{-1})

Debris Distribution

A_P	Average Presented Area	(m^2)
C_D	Drag Coefficient	(-)
F_D	Drag Force	(N)
I	Impulse	(kPa.ms)
I_b	Impulse Required for Breakage	(kPa.ms)
I_t	Impulse Remaining after Breakage	(kPa.ms)
g	Acceleration due to Gravity	(ms^{-2})
L	Projectile Length	(m)
m	Mass	(kg)
m_{mas}	Mass of Masonry	(kg)
N	Total Number of Projectiles	(-)
n	Source Function	(-)
P	Momentum	(Ns)
S_N	Shape Number	(-)
U	Projectile Velocity	(kg)
$\vec{V}$	Velocity Vector	(ms^{-1})
v	Velocity	(ms^{-1})
V_b	Brick Volume	(m^3)
V_i	Pre-Impact Velocity	(ms^{-1})
V_f	Post-Impact Velocity	(ms^{-1})
V_m	Mortar Volume	(m^3)
x	Distance (Cartesian)	(m)
y	Distance (Cartesian)	(m)
z	Distance (Cartesian)	(m)
α	Projectile Launch Angle	(°)
β	Azimuthal Angle	(°)
δ	Kronecker Delta Function	(-)

θ_i	Pre-Impact Angle	$(^\circ)$
θ_f	Post-Impact Angle	$(^\circ)$
ρ	Density	(kgm^{-3})
ρ_b	Brick Density	(kgm^{-3})
ρ_m	Mortar Density	(kgm^{-3})

Numerical Methods

a	Velocity of Sound (AUSM)	(ms^{-1})
a	Cell Height (AEM)	(m)
b	Element Length	(m)
d	Displacement	(m)
E	Young's Modulus (AEM)	(-)
E	Specific Total Energy (AUSM)	(J)
e	Total Internal Energy per Unit Mass	(Jkg^{-1})
E_c	Young's Modulus of Concrete	(-)
E_s	Young's Modulus of Steel	(-)
F	Force / Loading Vector (AEM)	(N)
F	Flux Term (AUSM)	(-)
G	Shear Modulus (AEM)	(Nm^{-2})
H	Enthalpy	(J)
i	Spring Number (AEM)	(-)
k_g	Global Stiffness Matrix	(-)
k_g	Local Stiffness Matrix	(-)
k_n	Normal Spring	(-)
k_r	Rotational Stiffness	(Nm^{-1})
k_s	Shear Spring	(-)
L	Cell Left Boundary (AUSM)	(-)
L	Spring Location (AEM)	(-)
M	Mach Number (AUSM)	(-)
M	Transmitted Moment (AEM)	(Ns)
m	Mass	(kg)
n	Number of Springs (AEM)	(-)
p	Pressure	(kPa)
R	Cell Right Boundary (AUSM)	(-)

R	Rotational Velocity (AEM)	(ms^{-1})
T	Element Thickness (AEM)	(m)
t	Time	(s)
U	Flux Vector	(-)
u	Velocity Component in x	(ms^{-1})
v	Velocity Component in y	(ms^{-1})
V	Velocity	(ms^{-1})
w	Velocity Component in z	(ms^{-1})
x	Distance (Cartesian)	(m)
y	Distance (Cartesian)	(m)
z	Distance (Cartesian)	(m)
α	Element Angle	$(^\circ)$
Δ	Displacement Vector	(m)
ϵ	Spring Element Displacements	(m)
ϵ_a	Spring Element Strains	(Pa)
θ	Element Angle	$(^\circ)$
ν	Poisson's Ratio	(-)
ρ	Density	(kgm^{-3})
σ	Element Stresses	(Pa)
$+$	Directional Identifier	(-)
$-$	Directional Identifier	(-)

Chapter 1

Introduction

The works presented in the following thesis are divided into a total of Seven chapters, including the following introduction. A literature review was conducted to assess previous works in the relevant fields, highlighting important contributions and identifying potential gaps in the literature. The experimental methodology outlines the research methodology and offers a detailed description of the experimental trial design. The experimental results provide an in depth review of the data obtained from all aspects of the experimental trials. The development of the computational modelling routine is discussed in detail, providing an explanation of the techniques used to build upon the experimental data. The experimental analysis delivers comparative analysis of the various experimental trials, highlighting observed effects of parametric variance. Finally, the research is summarised and the conclusions outlined, with a brief discussion of potential further development of the research.

1.1 Research Motivation

Even in simple, quasi-static cases, blast and its interaction with structures is a complex phenomenon. Blast waves propagate as a high pressure, high density, high velocity shock

discontinuity followed by high velocity particle winds, a rarefaction wave and another smaller shock wave. The interaction of blast waves and structures involves both the clearing of the blast wave over the structure, creating vortices and reflections followed by multi-stage dynamic loading of the structure from all directions. Much research has been conducted into standard, high explosive (*HE*) blast and its interaction with structures. This research distinguishes itself by investigating the effects of *long duration* blast loading, defined for the purposes of this research as a blast wave with a positive phase duration in excess of 100ms. Long duration blast and its interaction with structures offers an added complexity, due to the increased impulses associated with the high pressure shock front and the persistent effects of the drag wind and its associated dynamic pressure.

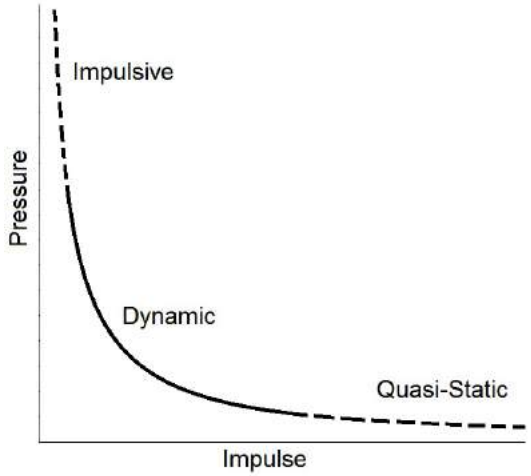

Figure 1.1: Illustration of a $P - I$ diagram

Damage predictions of structures subject to blast loading are often made using pressure-impulse ($P - I$) curves, illustrated in Figure 1.1, in which the curve represents a pre-determined level of damage, most commonly structural failure. Whilst such curves offer insight into whether or not the structure has failed, no information is given about the condition of the structure above the curve. Long duration blast loads are characterised by both high pressures and impulses, placing them in the dynamic region well beyond the failure curve. Within this region, once structural failure has occurred, large impulses are continuously transmitted to the structure which can cause significant debris distributions, especially in the case of concrete or masonry structures. Whilst airborne, blast induced

debris poses multiple hazards, including secondary damage effects to surrounding buildings and the risk of potentially lethal injuries; furthermore, following the initial airborne threat, the debris pile itself can cause major obstructions to localised infrastructure and significantly hinder emergency services and rescue operations.

High pressure, long duration blast loads are produced by the detonation of large quantities of explosives, typically with a minimum TNT equivalence of approximately 40T. The nature of such detonations leads to the failure of multiple structures and wide spread debris distribution, which can cause large scale obstructions to infrastructure at radial distances of hundreds of metres. Such large scale explosions have been caused by accidental explosions in chemical processing and storage facilities such as the 1988 'PEPCON disaster' [1], fireworks factories such as the 2004 'Seest fireworks disaster' [2] and arms storage depots, the largest examples of which can be seen on Table 7 of the 'Unplanned Explosions at Munitions Sites' handbook [3].

The motivation for this research is to acquire new information pertaining the long duration blast effects on masonry structures, which can aid in the assessment, rescue efforts and clean-up operations resulting from damage caused by large scale detonations in, or near urban environments and propose guidelines for minimum safe distances between such facilities and residential buildings. Specifically, this research aims to conduct a series of experimental blast trials on masonry structures to identify the effect of structural geometry, blast overpressure and blast impulse on both the breakage mechanism and subsequent debris distribution of masonry structures. This research will also attempt to establish a predictive model to describe the debris field produced by a given masonry structure subject to long duration blast loading.

1.2 Aims & Objectives

To achieve the goals of this research project, the primary aims can be outlined as:

1. Investigate the effects of structural geometry on the breakage of masonry structures subject to long duration blast

2. Investigate the effects of structural geometry on the debris distribution of masonry structures subject to long duration blast

3. Investigate the effects of pressure and impulse on the breakage of masonry structures subject to long duration blast

4. Investigate the effects of pressure and impulse on the debris distribution of masonry structures subject to long duration blast

Each of the four aims require experimental blast trials to obtain new data with a primary focus on the described variables; structural geometry, blast over pressure and blast impulse. A single blast trial can implement multiple structures with varying geometries, however multiple blast trials are required to vary the blast pressure and impulse. Blast impulse is obtained by integrating the pressure over the duration of the blast, therefore both pressure and duration describe the blast impulse. To separately vary the pressure and impulse, both long and short duration trials are required to investigate the effects of duration and hence impulse. Due to their cost and exclusivity, data obtained from experimental blast trials is an invaluable commodity, meaning each trial will be have scientific importance in isolation, as well as part of the larger programme. By using the experimental data to benchmark a computational modelling routine, results can be extended, providing a detailed examination of the effects of the structural geometry and blast parameters on both the breakage and debris distribution of masonry. These objectives can be outlined as:

1. Conduct a series of experimental blast trials, varying the structural geometry, blast overpressure and blast impulse.

2. Analyse the experimental data and use it to benchmark a computational modelling routine to accurately model breakage and debris distribution.

3. Use both experimental and computational data to describe characteristics of masonry breakage and debris dispersion.

Figure 1.2 illustrates the progression of the research project, highlighting the design and execution of the long and short duration trials and the supporting computational developments. Due to the added complexity of long duration blast trials, they will be preceded by the short duration HE trials, to provide data to begin the computational benchmarking process. Once the models reliably predict short duration blast, they can be adapted to model long duration blast.

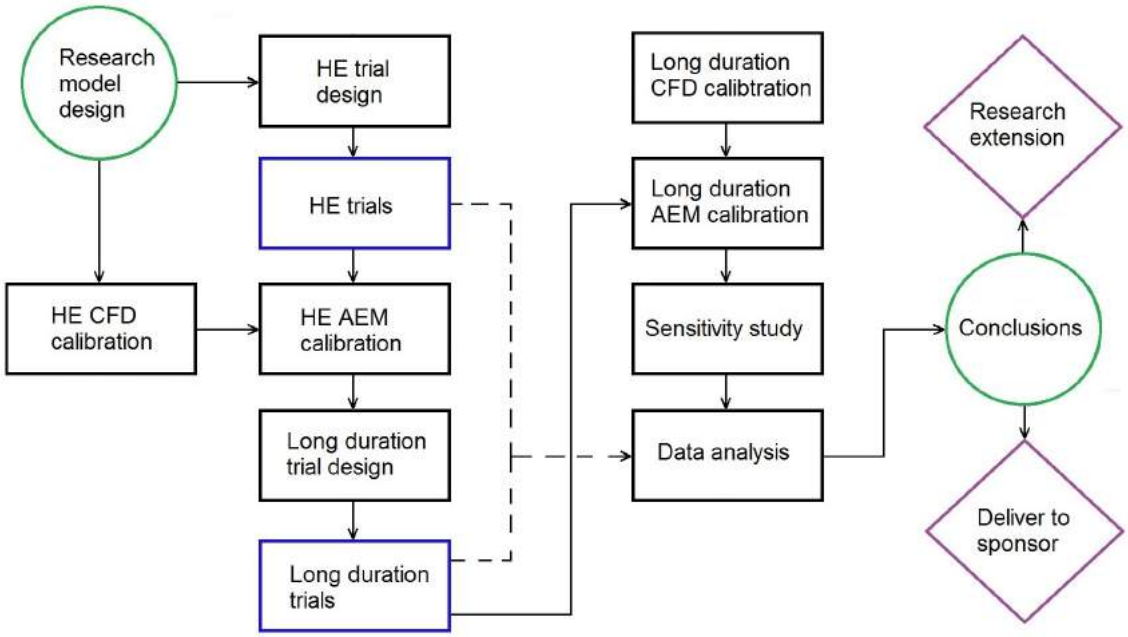

Figure 1.2: Flow chart illustrating research project progression

1.3 Summary

The hazards presented by masonry structures when subject to long duration blast loads primarily result from the dispersion of debris, which can lead to personal injury, secondary damage and infrastructure blockage. This research aims to develop a predictive model to describe the debris field produced by a give masonry structure when subjected to varying blast loads. To achieve these goals, this research study will employ a combination of short and long duration experimental blast trials and use the data to benchmark a computational modelling routine.

Chapter 2

Literature Review

The following literature review is presented as two sections. The theoretical background explores the important concepts upon which this research is based, with an in depth discussion and deravation of the key parameters vital to understanding physical processes and interactions present in this research. A discussion of the relevent seminal works is presented in section 2.2, exploring previous research efforts examining the breakage mechanisms of masonry, the response of masonry to blast loads, fragmentation and debris modelling and applications of the Applied Element Method.

2.1 Theoretical Background

The following sections provide a summary of the physical concepts and ideas behind the key fields relating to this research project. Firstly, an in-depth view of blast physics including general blast evolution and propagation, a specific look at the cause and effects of long duration blast loads and general blast structure interaction illustrates the specific parameters which affect this research project. Following the investigation on blast physics, a summary of the governing equations of fluid dynamics and flow regimes em-

phasises the nature of blast propagation from first principles and offers insight into the assumptions commonly made with blast structure interaction and numerical modelling. Finally the relevant numerical methods, Computational Fluid Dynamics (CFD) and the Applied Element Method (AEM), are assessed from first principles and gauged in terms of appropriateness and performance.

2.1.1 Blast

The blast waves produced from an explosive device will differ dramatically depending on the type of explosion and hence explosive device. In the case of explosive materials which decompose at a rate much below the speed of sound in the material, the combustion process is known as *deflagration* [4]. The resulting pressure wave will also propagate much slower than the speed of sound with a much longer duration. Conventional and high explosive (*HE*) devices are classified as *detonating* explosives, as the rate of reaction, again mostly combustion, for detonation is extremely high. The resulting explosion from detonation produces shock waves that travel many times the speed of sound in a given medium [4].

Explosions caused by detonation can subsequently be split into either chemical or physical explosions. This is determined depending on the composition of the explosive material or type of explosion. A physical blast has no thermal component and results from, for example, a bursting pipe containing compressed gas. As the pipe bursts the densely packed gas will expand at a high velocity, forming a blast wave. As there was no combustion or chemical reaction to produce the aforementioned blast wave, there is no thermal component [5]. All industrial and military explosives use chemical blasts generated by detonating various chemical compounds which provides both thermal and blast effects.

2.1.1.1 Blast Wave Evolution

The formation and propagation of a blast wave is characterised primarily in terms of pressure. The high temperature and high pressure gaseous bi-products from an explosion

will expand rapidly in every direction away from the source. The air surrounding the explosion is compressed as the various gases rapidly expand, creating a high pressure, high velocity blast wave [4].

The blast wave pressure is called *overpressure* or *static overpressure*, denoted by p_i and is quantified as the pressure difference above (or below) the ambient pressure of the specific medium, p_0. The time in which $p_i > p_0$ is known as the positive phase duration, t^+, similarly the time in which $p_i < p_0$ is known as the negative phase duration. Integrating p_i over $t = t^+$ and $t = t^-$ give the positive and negative specific impulses ${I_{p_i}}^+$ and ${I_{p_i}}^-$ respectively, in which total impulse $I = {I_{p_i}}^+ + {I_{p_i}}^-$. The *peak static overpressure*, $p_{i(max)}$, is the maximum overpressure of the wave front at a specific point in space; the value of which decreases as the blast propagates away from the source. Each of these parameters are illustrated by the Friedlander curve, shown in Figure 2.1, which is obtained by gauging the overpressure at a fixed point in space for the duration of the blast and is characterised by the Friedlander equation

$$p_i(t) = p_i(max)\left(1 - \frac{t}{t^+}\right)e^{-\frac{bt}{t^+}} \tag{2.1}$$

in which b is the waveform decay constant.

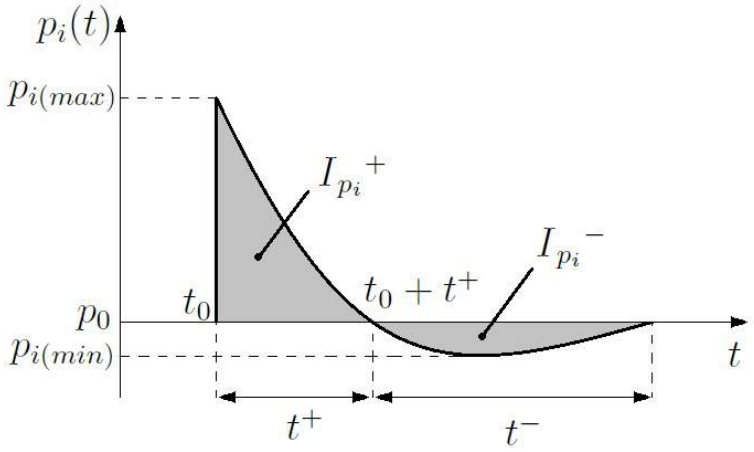

Figure 2.1: A Typical Friedlander Curve

A blast wave is most commonly divided into two phases, the positive phase and the negative phase. The positive phase is the wave front resulting from the detonation and is characterised by both a high peak pressure and large impulse. The high velocity of

the travelling blast wave creates a partial vacuum in its wake, which is responsible for the negative or suction phase. Following the negative phase, or rarefaction wave, is small positive shock wave known as the second shock. The cause of the second shock is widely debated; however it is believed to be caused by the expansion of the detonation products. The effects of the second shock are small by comparison to the initial positive phase and even the negative phase. The Unified Facilities Criteria (UFC 3-340-02) [6] states that the effects of the negative phase are usually less important than those of the positive phase when considering structural design. The effects of the second shock are even smaller than those of the negative phase and thus for the purposes of this research the second shock will be neglected.

Once the wave front has travelled far enough from the source, the partial vacuum causes a suction effect reversing the effective direction of the overpressure at any fixed point within this region. For a free air burst, i.e. detonation above a certain altitude, the blast wave will propagate freely without interference. This is known as the regular region. For a surface or low altitude burst, the blast wave will reflect off of the Earth's surface. This reflected blast wave then interacts and superposes with the initial incident blast wave. As described by Glasstone and Dolan [7], at any region above the surface two shocks will be felt, the first due to the incident blast wave and the second due to the reflected wave which arrives a short time later. This is illustrated in Figure 2.2, at time t_3 the incident wave front has reached point B, whereas the reflected wave does not reach point B until time t_4. The overpressure of the reflected wave will be considerably less than that of the incident wave as more of the energy has been dissipated through the ground.

As the incident wave propagates it heats and compresses the air (or relevant medium). This allows for the reflected wave to propagate at a higher velocity in the wake of the incident blast wave. Eventually, shown in Figure 2.2 at time t_n, the reflected wave will catch the incident wave. This superposed wave is known as the Mach stem.

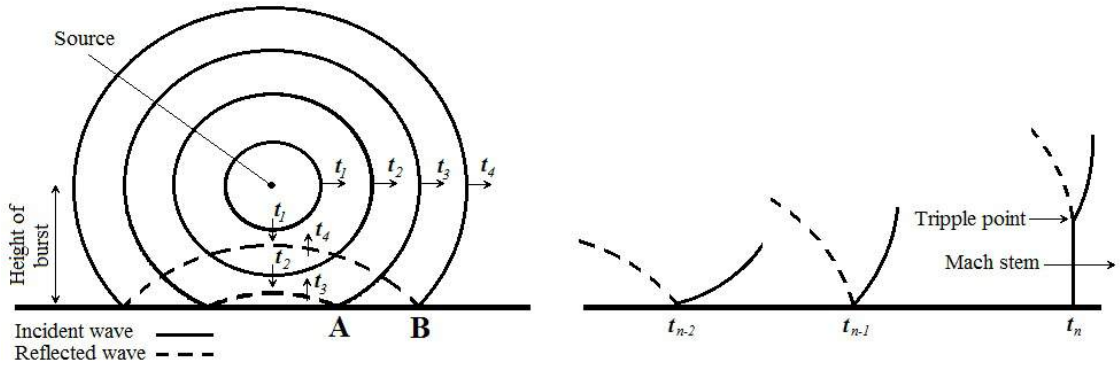

Figure 2.2: Blast surface reflections, interactions and Mach stem formation

2.1.1.2 Blast Wave Parameters

The first calculations for the conditions across a blast wave front were given by Rankine and Hugoniot in 1870 [8], from these calculations all conserved quantities across a shock wave can be derived. The equations for overpressure, dynamic pressure, density and velocity across a wave front can be found in a number of sources including Glasstone and Dolan [7] and Smith and Mays [4]. The velocity of a shock or blast wave can be expressed by

$$U = c_0\sqrt{1 + \frac{\gamma + 1}{2\gamma}\left(\frac{p_i}{p_0}\right)} \tag{2.2}$$

where U is the velocity of the shock front, c_p and c_v are the specific heats at constant pressure and volume respectively with $\gamma = \frac{c_p}{c_V}$, p_0 is the ambient pressure ahead of the shock front, p_i is the peak static overpressure behind the shock front and c_0 is the ambient speed of sound given by

$$c_0 = \sqrt{\frac{\gamma p_0}{\rho_0}} \tag{2.3}$$

where ρ_0 is the ambient density ahead of the shock front. The specific heat capacities of air at standard atmospheric temperature (300K) are

$$c_{p(air)} = 1.01\text{kJ/kgK} \tag{2.4}$$

$$c_{V(air)} = 0.718\text{kJ/kgK} \tag{2.5}$$

therefore

$$\gamma_{(air)} = \frac{1.01}{0.718} = 1.40 \tag{2.6}$$

Approximating γ as $\frac{7}{5}$, the expression for the blast wave parameters can be simplified and re-written for air. Applying this to equation 2.2 the shock velocity it is reduced to

$$U_{(\text{air})} = c_0\sqrt{\frac{6p_i + 7p_0}{7p_0}} \tag{2.7}$$

The particle velocity, u (also known as the drag wind), behind the shock front is given by

$$u = \frac{c_0 p_i}{\gamma p_0\sqrt{1 + \frac{\gamma+1}{2\gamma}\left(\frac{p_i}{p_0}\right)}} \tag{2.8}$$

which when substituting equation 2.2 becomes

$$u = \frac{{c_0}^2 p_i}{U\gamma p_0} \tag{2.9}$$

so that for air

$$u_{(air)} = \frac{5c_0 p_i}{7p_0\sqrt{1 + \frac{6p_i}{7p_0}}} \tag{2.10}$$

or

$$u_{(air)} = \left(\frac{5}{7}\right)\frac{{c_0}^2 p_i}{U p_0} \tag{2.11}$$

The particle velocity is normally expressed in terms of the dynamic pressure, q, which

is related to the particle velocity by

$$q = \frac{1}{2}\rho u^2 \tag{2.12}$$

where ρ is the density behind the shock front. It is clear from this relation that q is the kinetic energy per unit volume of the drag wind and is known as the dynamic pressure as it has the same dimensions of pressure. Before it is possible to quantify the dynamic pressure, an expression is needed for the density behind the shock front. By rearranging the Rankine-Hugoniot relations, the pressure behind the shock front can be related to the ambient pressure by

$$\rho = \left(\frac{2\gamma p_0 + (\gamma+1)p_i}{2\gamma p_0 + (\gamma-1)p_i}\right)\rho_0 \tag{2.13}$$

which in air reduces to

$$\left(\frac{\rho}{\rho_0}\right)_{(air)} = \frac{7 + \frac{6p_i}{p_0}}{7 + \frac{p_i}{p_0}} \tag{2.14}$$

Recalling equation 2.3 for c_0 and substituting equations 2.8 and 2.13 into equation 2.12 and rearranging, the dynamic pressure can be expressed as

$$q = \frac{{p_i}^2}{2\gamma p_0 + (\gamma-1)p_i} \tag{2.15}$$

Note that the dynamic pressure can be expressed purely as a function of ambient pressure and peak static overpressure. For large blasts and hence large overpressures, it can be seen that for $p_i >> p_0$, $q \propto p_i$. Once again when substituting $\gamma = \frac{7}{5}$ for air

$$q_{(air)} = \left(\frac{5}{2}\right)\frac{{p_i}^2}{7p_0 + p_i} \tag{2.16}$$

meaning for a large blast in air

$$q_{(air)} \rightarrow \left(\frac{5}{2}\right)p_i \tag{2.17}$$

Note for large blasts in which $p_i >> p_0$, as approximated in equation 2.17, the dynamic pressure can become an incredibly destructive force. The final blast pressure parameter,

reflected pressure, p_r, occurs when a blast wave strikes a surface normal to the direction of propagation of the blast wave. Reflected pressure is given by

$$p_r = 2p_i + (\gamma + 1)q \tag{2.18}$$

or, when substituting for equation 2.15

$$p_r = 2p_i + \frac{(\gamma + 1){p_i}^2}{2\gamma p_0 + (\gamma - 1)p_i} = 2p_i \left(\frac{4\gamma p_0 + (3\gamma - 1)p_i}{4\gamma p_0 + 2(\gamma - 1)p_i} \right) \tag{2.19}$$

and in air, this is reduced to

$$p_{r(air)} = 2p_i \left(\frac{7p_0 + 4p_i}{7p_0 + p_i} \right) \tag{2.20}$$

It can be seen from equation 2.20 that if $p_i >> p_0$, i.e. for a large blast then $p_r \rightarrow 8p_i$, and for a weak blast in which $p_i << p_0$ then $p_r \rightarrow 2p_i$. This substantial increase in reflected overpressure for a high incident overpressure can be explained by equation 2.17, showing the high dynamic pressures produced by high incident overpressures.

When modelling blast effects and blast interactions, it is essential to know the overpressure at any distance of any mass of charge. The use of scaled blast parameters gives efficient representations of blast wave data for a wide range of charges up to around the Megaton range [9]. The most widely used approach for blast wave scaling is the Hopkinson-Cranz cube root scaling [10], which relates the diameters d_1 and d_2 of two charges to their TNT mass equivalent by

$$\lambda = \left(\frac{d_1}{d_2} \right) = \left(\frac{W}{W_1} \right)^{\frac{1}{3}} \tag{2.21}$$

where λ is the scaling ratio. The ratios of impulse, positive phase duration and range at which a particular overpressure is developed will also be λ. The Hopkinson-Cranz law is most commonly expressed as

$$\lambda = \left(\frac{Z}{R} \right) = \left(\frac{W}{W_1} \right)^{\frac{1}{3}} \tag{2.22}$$

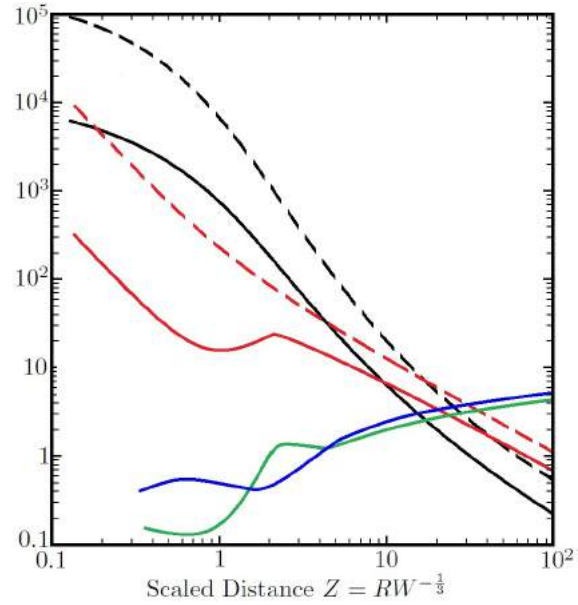

(a) Positive phase spherical

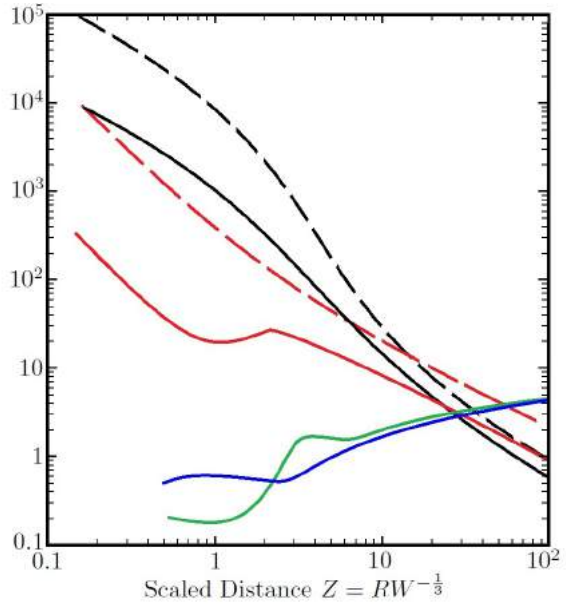

(b) Positive phase hemispherical

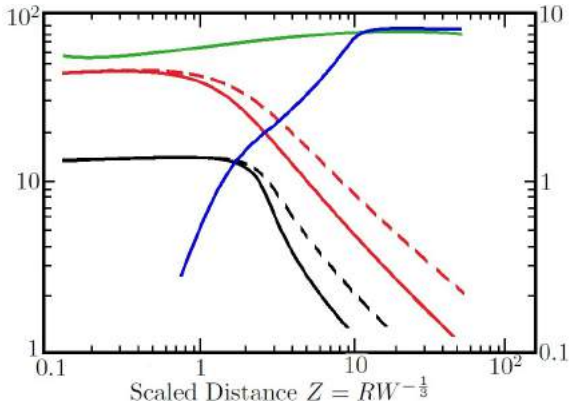

(c) Negative phase spherical

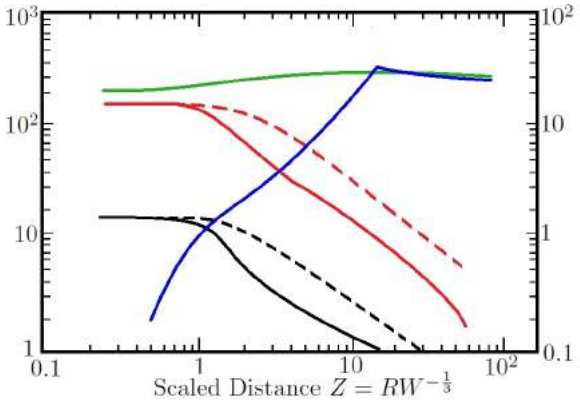

(d) Negative phase hemispherical

(e) Legend

Figure 2.3: Incident and reflected scaled blast parameters from a detonation of TNT at sea level.

where Z is the distance from a charge of mass W at which an overpressure p_i is experienced and R is the distance from a charge of mass W_1 which experiences the same overpressure p_i. By normalising W_1 as a standard reference charge of 1kT equation 2.21

reduces to

$$Z = RW^{\frac{1}{3}} \tag{2.23}$$

reducing the scaling ratio to $\lambda = W^{\frac{1}{3}}$ [7, 9]. Scaled distance is used as a standard by which to compare different blast parameters for different detonations and charge masses. Figure 2.3 illustrates the relationships of static overpressure p_i, reflected pressure p_r, static impulse I_i, reflected impulse I_r, phase duration t_0 and blast wavelength L_w with respect to scaled distance Z, for both the positive and negative phases for detonations of both spherical and hemispherical charges at sea level. It should be noted that in Figures 2.3c and 2.3d, L_w and t_0 are plotted on the second (right) Y-axis.

2.1.1.3 Blast Structure Interaction

This section will summarise the effects of structures and other obstructions to the flow of a blast wave. Any natural or man-made structure, or even non-uniform terrains will have some effect on the natural flow of a blast wave. As outlined by Needham, the overpressure manifests as a crushing force on all exposed sides of the structure, whilst the dynamic pressure acts to accelerate drag sensitive objects [11]. Structures with large incident surface areas and little depth can be considered drag targets, as the overpressure quickly equalises over the structure, thus the majority of the loading is as a result of the drag winds and associated dynamic pressures. Conversely, structures with a smaller surface area and increased depth experience a longer net pressure whilst the blast wave travels the length of the structure. Needham also suggests as a general rule, the dimensions of the disturbance of the blast wave are approximated as 4-5 times the dimensions of the structure in the direction perpendicular to the flow; however for a dynamic pressure dominated blast, it can potentially be up to 40 structure dimensions before the blast wave returns to undisturbed flow [11].

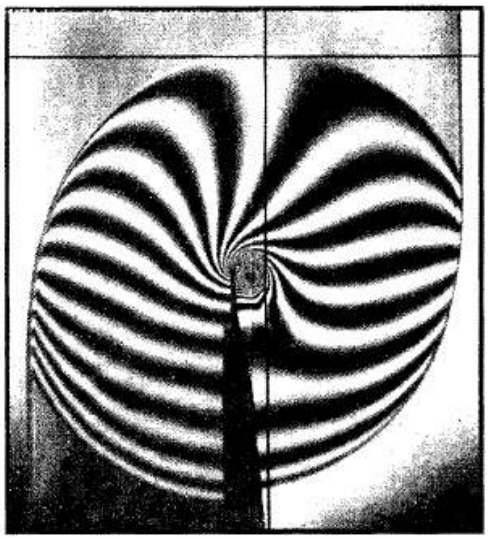

Figure 2.4: Interferogram of the non-uniform flow region around a thin vertical wall [12]

The simplest case of blast wave interaction is the propagation over a thin vertical wall [12]. Figure 2.4 shows such an interaction in which the formation of a vortex can be seen around the edge of the wall which is visible as a black spike. The angle of the body over which the blast wave propagates has a significant impact on the vortex produced as well as the wave velocity [13]. This can be expressed as

$$\frac{\Gamma}{t} = f(M_s, \theta) \tag{2.24}$$

where Γ is the vortex circulation, $\frac{\Gamma}{t}$ is the rate of change of vortex circulation, M_s is the Mach number and θ is the angle of the rigid body over which the blast wave propagates. The rate of change of vortex circulation is most commonly expressed as

$$\frac{\Gamma}{t} = \frac{1}{2}{U_1}^2 + \frac{1}{2}{U_2}^2 \tag{2.25}$$

where U_1 and U_2 are the shock velocities either side of the vortex boundary. The vorticity transport equation, which is derived from the Navier-Stokes equations of fluid flow, governs the movement of individual particles in an inviscid vortex flow for a vorticity

$\overline{\omega}$ and is given by

$$\frac{d\overline{\omega}}{dt} = -\overline{\omega}\,(\nabla.\overline{v}) - \frac{\nabla p \times \nabla \rho}{\rho^2} \tag{2.26}$$

where the vorticity vector $\overline{\omega}$ is the curl of the field velocity vector $\overline{v}$, that is ($\overline{\omega} = \nabla \times \overline{v}$), p is the local pressure and ρ is the local density [14]. The effects of blast wave clearing and vortex interaction can be easily viewed by iterating equation 2.26 with a high resolution Euler solver. Figure 2.5 shows a plan cross-section of the vortex, V_1, pressure contours created by the blast wave at a time just before the arrival of the second shock, S_2, in which the blast is moving in the positive x direction. The rotational energy of the vortex eventually degrades and returns to normal flow, which as seen from equations 2.24 and 2.25 is a function of the rotational velocity of the vortex and hence of the incident blast wave.

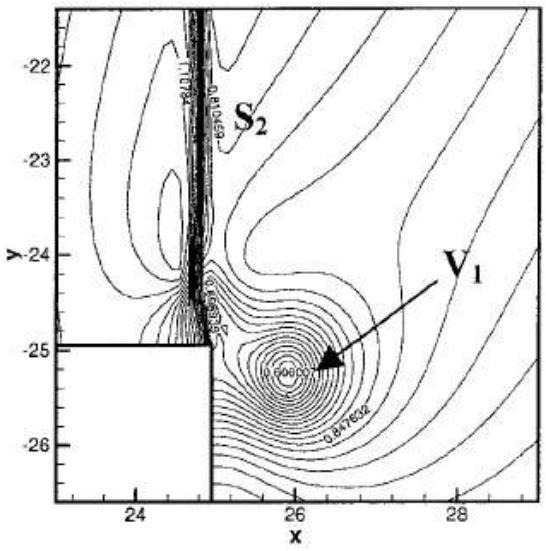

Figure 2.5: Numerical model of blast wave clearing around a perpendicular wall [13]

2.1.2 Fluid Dynamics

The concepts discussed in Section 2.1.1 describe blast waves as the propagation of a discontinuity of compressed air through a specific medium. The effects and interactions of the compressed air in the wave front and the particle flow which follow it are described

by the governing equations of fluid dynamics. Understanding the flow and interaction of the high pressure discontinuity and drag winds enables the development of a suitable experimental program and more realistic computational models.

2.1.2.1 Governing Equations

The governing equations of fluid dynamics are based on the continuity, momentum and energy equations which are derived here using the approach outlined by J. D. Anderson Jr. [15]. The general form of the governing equations are derived for viscous flow from one of the two methods shown in Figure 2.6.

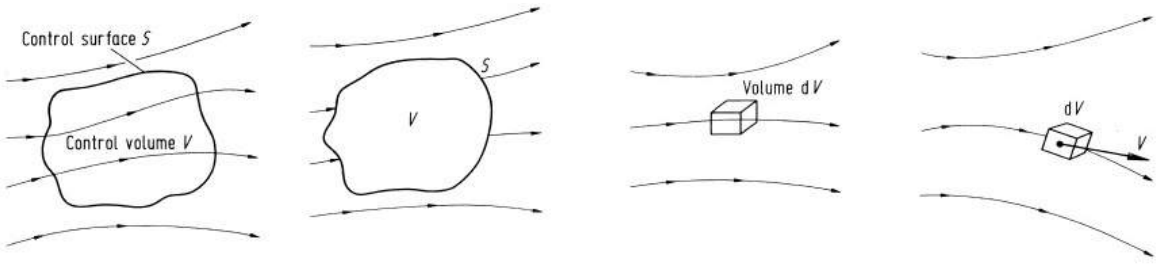

(a) Finite control volume (b) Infinitesimal fluid element

Figure 2.6: Methods for deriving the governing equations of fluid dynamics [15]

The approach shown in Figure 2.6a considers a finite control volume with a finite control surface, whilst the approach shown in Figure 2.6b considers an infinitesimal fluid element. In either case the governing equations can be derived by considering the volume or element fixed in space and examining the fluid flow through this region, which will give the conservation form of the governing equations. Alternatively, the volume or element can be considered to be moving with the fluid, which will lead to the non-conservation form of the governing equations.

To derive the non-conservation form of the continuity equation using the finite control volume, it can be considered to have a fixed mass m at all times; however as it moves through the fluid, its volume and density change. Considering an infinitesimal element dS on the surface of the control volume moving with local velocity $\vec{V}$ such that

$$\vec{V} = u\vec{i} + v\vec{j} + w\vec{k} \tag{2.27}$$

where $\vec{i}$, $\vec{j}$ and $\vec{k}$ are the unit vectors moving along the x, y and z axes and u, v and w are the x, y and z components of the velocity. The change in the control volume $\Delta\nu$ due to the movement of dS is given as

$$\Delta\nu = \left[\left(\vec{V}\Delta t\right)\cdot\vec{n}\right] dS \tag{2.28}$$

where $\vec{n}$ is the unit vector in the direction of dS. The surface integral across the whole volume is then

$$\frac{d\nu}{dt} = \oiint_S \vec{V}\cdot\vec{n}dS \tag{2.29}$$

Using the divergence theorem

$$\iiint_v (\nabla\cdot\vec{V})dv = \oiint_S \vec{V}\cdot\vec{n}dS \tag{2.30}$$

and inspecting the volume element $dv = d(\delta\nu)$, equation 2.29 yields

$$\nabla\cdot\vec{V} = \frac{1}{\delta\nu}\frac{d(\delta\nu)}{dt} \tag{2.31}$$

The mass δm of the element $\delta\nu$ remains fixed, such that

$$\frac{d(\rho\delta\nu)}{dt} = \delta\nu\frac{d\rho}{dt} + \rho\frac{d(\delta\nu)}{dt} = 0 \tag{2.32}$$

Combining equations 2.31 and 2.32 gives

$$\frac{d\rho}{dt} + \rho\nabla\cdot\vec{V} = 0 \tag{2.33}$$

Equation 2.33 is the continuity equation in non-conservation form. To obtain the conservation form of the continuity equation, the finite control volume is assumed to be fixed in space as the fluid flows through it. The net flow of mass out of the control volume, Δm, must be equal to the negative rate of change of mass inside the volume, $-\frac{dm}{dt}$. The

elemental mass flow across the area dS is

$$\rho V_n dS = \rho \vec{V} \cdot \vec{n} \vec{dS} \tag{2.34}$$

where V_n is the velocity component in the direction of $\vec{n}$. The net mass flow out of the control volume is the surface integral equation 2.34, which is

$$\Delta m = \oiint_S \rho \vec{V} \cdot \vec{dS} \tag{2.35}$$

If the mass contained within the volume $d\nu$, the mass within the volume is $\rho d\nu$ and the total mass is

$$m = \iiint_\nu \rho d\nu \tag{2.36}$$

and the rate of mass decrease is thus

$$-\frac{dm}{dt} = -\frac{\partial}{\partial t} \iiint_\nu \rho d\nu \tag{2.37}$$

therefore

$$\frac{\partial}{\partial t} \iiint_\nu \rho d\nu + \oiint_S \rho \vec{V} \cdot \vec{dS} = 0 \tag{2.38}$$

Applying divergence theorem to the surface integral, equation 2.38 becomes

$$\iiint_\nu \frac{\partial \rho}{\partial t} d\nu + \iiint_\nu \nabla \cdot (\rho \vec{V}) d\nu = 0 \tag{2.39}$$

which can be expressed as

$$\iiint_\nu \left(\frac{\partial \rho}{\partial t} + \nabla \cdot (\rho \vec{V}) \right) d\nu = 0 \tag{2.40}$$

The integral can only be equal to zero if the integrand is zero at every point in space,

which reduces equation 2.40 to

$$\frac{\partial \rho}{\partial t} + \nabla \cdot (\rho \vec{V}) = 0 \tag{2.41}$$

Equation 2.41 is the conservation form of the continuity equation. The next of the governing equations is the momentum equation, which again has both conservation and non-conservation forms. Applying Newton's second law $F = ma$ to an infinitesimal moving volume of fluid, the forces acting on the fluid can be attributed to body forces and surfaces forces. Body forces act directly on the volume (gravity, electromagnetic etc.) whereas surface forces act directly on the surface of the volume (pressure, shear stress and normal stress). The body force F_b acting in the x direction on a volume with dimensions dx, dy and dz can be expressed as

$$F_{bx} = \rho f_x (dxdydz) \tag{2.42}$$

The force due to pressure acting on the rear face of the fluid element in the x direction is simply $pdydz$; however there is also a force due to pressure acting on the front face of the element pressing in the opposing direction. The total surface force due to pressure alone acting in the x direction is then

$$F_{px} = \left[p - \left(p - \frac{\partial p}{\partial x} dx \right) \right] dydz \tag{2.43}$$

The normal stress acting on the fluid element is often neglected as its effect is negligible compared to that of the shear stress; however with shock waves and blast waves which have high velocities, the normal stress has a large effect on the propagation of the fluid. The normal stress in the x direction τ_{xx} act opposing the pressure with the front of the element being caught in the suction of the stream and the rear end being dragged along behind it. The shear stresses act in the same way as the normal stress with the front end being caught in the suction of the flow. In the x direction, the contributing shear stresses are then τ_{yx} and τ_{zx}. Summing all of these surface forces along with the body force, the

total force acting on the element can be expressed as

$$\begin{aligned} F_x = & \left[p - \left(p - \frac{\partial p}{\partial x}dx\right)\right] dydz \\ & + \left[\left(\tau_{xx} - \frac{\partial \tau_{xx}}{\partial x}dx\right) - \tau_{xx}\right] dydz \\ & + \left[\left(\tau_{yx} - \frac{\partial \tau_{yx}}{\partial y}dy\right) - \tau_{yx}\right] dydz \\ & + \left[\left(\tau_{zx} - \frac{\partial \tau_{zx}}{\partial z}dz\right) - \tau_{zx}\right] dydz + \rho f(dxdydz) \end{aligned} \tag{2.44}$$

Given that

$$m = \rho(dxdydz) \tag{2.45}$$

and

$$a_x = \frac{du}{dt} \tag{2.46}$$

Combining equations 2.44, 2.45 and 2.46 gives

$$\rho\frac{du}{dt} = -\frac{\partial p}{\partial x} + \frac{\partial \tau_{xx}}{\partial x} + \frac{\partial \tau_{yx}}{\partial y} + \frac{\partial \tau_{zx}}{\partial z} + \rho f_x \tag{2.47}$$

and

$$\rho\frac{dv}{dt} = -\frac{\partial p}{\partial y} + \frac{\partial \tau_{xy}}{\partial x} + \frac{\partial \tau_{yy}}{\partial y} + \frac{\partial \tau_{zy}}{\partial z} + \rho f_y \tag{2.48}$$

$$\rho\frac{dw}{dt} = -\frac{\partial p}{\partial z} + \frac{\partial \tau_{xz}}{\partial x} + \frac{\partial \tau_{yz}}{\partial y} + \frac{\partial \tau_{zz}}{\partial z} + \rho f_z \tag{2.49}$$

for the y and z directions. Equations 2.47, 2.48 and 2.49 are the x, y and z components of the momentum equation for viscous flow and the non-conservation form of the Navier-Stokes equations. Combining the relationships

$$\rho\frac{du}{dt} = \rho\frac{\partial u}{\partial t} + \rho\vec{V}\cdot\nabla u \tag{2.50}$$

$$\rho\frac{\partial u}{\partial t} = \frac{\partial(\rho u)}{\partial t} - u\frac{\partial \rho}{\partial t} \tag{2.51}$$

and

$$\rho\vec{V}\cdot\nabla u = \nabla\cdot(\rho u\vec{V}) - u\nabla\cdot(\rho\vec{V}) \tag{2.52}$$

gives

$$\rho\frac{du}{dt} = \frac{\partial(\rho u)}{\partial t} - u\left[\frac{\partial \rho}{\partial t} + \nabla\cdot(\rho\vec{V})\right] + \nabla\cdot(\rho u\vec{V}) \tag{2.53}$$

The term in brackets is the continuity equation which is equal to zero. By substituting equation 2.53 and the y and z equivalents into the Navier-Stokes equations gives the conservation form of the Navier-Stokes equations:

$$\frac{\partial(\rho u)}{\partial t} + \nabla\cdot(\rho u\vec{V}) = -\frac{\partial p}{\partial x} + \frac{\partial \tau_{xx}}{\partial x} + \frac{\partial \tau_{yx}}{\partial y} + \frac{\partial \tau_{zx}}{\partial z} + \rho f_x \tag{2.54}$$

$$\frac{\partial(\rho v)}{\partial t} + \nabla\cdot(\rho v\vec{V}) = -\frac{\partial p}{\partial y} + \frac{\partial \tau_{xy}}{\partial x} + \frac{\partial \tau_{yy}}{\partial y} + \frac{\partial \tau_{zy}}{\partial z} + \rho f_y \tag{2.55}$$

$$\frac{\partial(\rho w)}{\partial t} + \nabla\cdot(\rho w\vec{V}) = -\frac{\partial p}{\partial z} + \frac{\partial \tau_{xz}}{\partial x} + \frac{\partial \tau_{yz}}{\partial y} + \frac{\partial \tau_{zz}}{\partial z} + \rho f_z \tag{2.56}$$

For Newtonian fluids, the normal and shear stresses are given as

$$\tau_{xx} = \lambda\nabla\cdot\vec{V} + 2\mu\frac{\partial u}{\partial x} \tag{2.57}$$

$$\tau_{yy} = \lambda\nabla\cdot\vec{V} + 2\mu\frac{\partial v}{\partial y} \tag{2.58}$$

$$\tau_{zz} = \lambda\nabla\cdot\vec{V} + 2\mu\frac{\partial w}{\partial z} \tag{2.59}$$

$$\tau_{xy} = \tau_{yx} = \mu\left(\frac{\partial v}{\partial x} + \frac{\partial u}{\partial y}\right) \tag{2.60}$$

$$\tau_{xz} = \tau_{zx} = \mu\left(\frac{\partial w}{\partial x} + \frac{\partial u}{\partial z}\right) \tag{2.61}$$

$$\tau_{yz} = \tau_{zy} = \mu\left(\frac{\partial w}{\partial y} + \frac{\partial v}{\partial z}\right) \tag{2.62}$$

where μ is the molecular or dynamic viscosity and λ is the viscosity coefficient. Substituting these equations into equations 2.54, 2.55 and 2.56 obtains the full Navier-Stokes (momentum) equations in conservation form.

$$\begin{aligned}\frac{\partial(\rho u)}{\partial t} + \frac{\partial(\rho u^2)}{\partial x} + \frac{\partial(\rho uv)}{\partial y} + \frac{\partial(\rho uw)}{\partial z} = \\ -\frac{\partial p}{\partial x} + \frac{\partial}{\partial x}\left(\lambda\nabla\cdot\vec{V} + 2\mu\frac{\partial u}{\partial x}\right) + \frac{\partial}{\partial y}\left[\mu\left(\frac{\partial v}{\partial x} + \frac{\partial u}{\partial y}\right)\right] \\ + \frac{\partial}{\partial z}\left[\mu\left(\frac{\partial u}{\partial z} + \frac{\partial w}{\partial x}\right)\right] + \rho f_x\end{aligned} \tag{2.63}$$

$$\begin{aligned}\frac{\partial(\rho v)}{\partial t} + \frac{\partial(\rho uv)}{\partial x} + \frac{\partial(\rho v^2)}{\partial y} + \frac{\partial(\rho vw)}{\partial z} = \\ -\frac{\partial p}{\partial y} + \frac{\partial}{\partial x}\left[\mu\left(\frac{\partial v}{\partial x} + \frac{\partial u}{\partial y}\right)\right] + \frac{\partial}{\partial y}\left(\lambda\nabla\cdot\vec{V} + 2\mu\frac{\partial v}{\partial y}\right) \\ + \frac{\partial}{\partial z}\left[\mu\left(\frac{\partial w}{\partial y} + \frac{\partial v}{\partial z}\right)\right] + \rho f_y\end{aligned} \tag{2.64}$$

$$\begin{aligned}\frac{\partial(\rho w)}{\partial t} + \frac{\partial(\rho uw)}{\partial x} + \frac{\partial(\rho vw)}{\partial y} + \frac{\partial(\rho w^2)}{\partial z} = \\ -\frac{\partial p}{\partial z} + \frac{\partial}{\partial x}\left[\mu\left(\frac{\partial u}{\partial z} + \frac{\partial w}{\partial x}\right)\right] + \frac{\partial}{\partial y}\left[\mu\left(\frac{\partial w}{\partial y} + \frac{\partial v}{\partial z}\right)\right] \\ + \frac{\partial}{\partial z}\left(\lambda\nabla\cdot\vec{V} + 2\mu\frac{\partial w}{\partial y}\right) + \rho f_z\end{aligned} \tag{2.65}$$

The final governing equation, the energy equation, is derived using the first law of thermodynamics - energy conservation, which for an infinitesimal fluid element can be

expressed as

$$\frac{dE_i}{dt} = \phi_t + W \tag{2.66}$$

where $\frac{dE_i}{dt}$ is the rate of change of energy inside the fluid element, ϕ_t is the net flux of heat into the element and W is the rate of work done on the element due to body and surface forces. The rate of work done due to body forces is given as

$$W_b = \rho \vec{f} \cdot \vec{v}(dxdydz) \tag{2.67}$$

The work done due to surface forces can be obtained by considering the pressure and the shear and normal stresses on the fluid element. For the x direction, this is

$$W_s = \left[-\frac{\partial(up)}{\partial x} + \frac{\partial(u\tau_{xx})}{\partial x} + \frac{\partial(u\tau_{yx})}{\partial y} + \frac{\partial(u\tau_{zx})}{\partial z} \right] dxdydz \tag{2.68}$$

Thus, the total work done due to body and surface forces in x, y and z is

$$\begin{aligned} W = \Bigg[& -\left(\frac{\partial(up)}{\partial x} + \frac{\partial(vp)}{\partial y} + \frac{\partial(wp)}{\partial z} \right) + \frac{\partial(u\tau_{xx})}{\partial x} + \frac{\partial(u\tau_{yx})}{\partial y} \\ & + \frac{\partial(u\tau_{zx})}{\partial z} + \frac{\partial(v\tau_{xy})}{\partial x} + \frac{\partial(v\tau_{yy})}{\partial y} + \frac{\partial(v\tau_{zy})}{\partial z} + \frac{\partial(w\tau_{xz})}{\partial x} \\ & + \frac{\partial(w\tau_{yz})}{\partial y} + \frac{\partial(w\tau_{zz})}{\partial z} \Bigg] dxdydz + \rho \vec{f} \cdot \vec{V} dxdydz \end{aligned} \tag{2.69}$$

The net heat flux, ϕ_t of the fluid element is expressed as a sum of the volumetric heating of the element Q_v and the heating of the element by thermal conduction Q_c. If $\dot{q}$ is the rate of volumetric heat addition per unit mass, then the volumetric heating of the element is

$$Q_v = p\dot{q}dxdydz \tag{2.70}$$

and the heating due to thermal conduction in the x direction is

$$Q_c = -\frac{\partial \dot{q}_x}{\partial x} dxdydz \tag{2.71}$$

Heat transfer by thermal conduction is proportional to the local temperature gradient such that

$$\dot{q}_x = -k\frac{\partial T}{\partial x} \tag{2.72}$$

where k is the thermal conductivity. Hence the total net flux of heat into the element is

$$\phi_t = \left[p\dot{q} + \frac{\partial}{\partial x}\left(k\frac{\partial T}{\partial x}\right) + \frac{\partial}{\partial y}\left(k\frac{\partial T}{\partial y}\right) + \frac{\partial}{\partial z}\left(k\frac{\partial T}{\partial z}\right)\right] dxdydz \tag{2.73}$$

The rate of change of energy of the fluid can be expressed as the sum of its internal energy per unit mass, e, and its kinetic energy $V^2/2$ over time for the volume of the fluid element as

$$\frac{dE_i}{dt} = \rho\frac{d}{dt}\left(e + \frac{V^2}{2}\right) dxdydz \tag{2.74}$$

Substituting equations 2.69, 2.72 and 2.73 into equation 2.66 gives

$$\begin{aligned}\rho\frac{d}{dt}\left(e + \frac{V^2}{2}\right) = \rho\dot{q} &+ \frac{\partial}{\partial x}\left(k\frac{\partial T}{\partial x}\right) + \frac{\partial}{\partial y}\left(k\frac{\partial T}{\partial y}\right) + \frac{\partial}{\partial z}\left(k\frac{\partial T}{\partial z}\right) \\ &+ \frac{\partial(up)}{\partial x} + \frac{\partial(vp)}{\partial y} + \frac{\partial(wp)}{\partial z} + \frac{\partial(u\tau_{xx})}{\partial x} + \frac{\partial(u\tau_{yx})}{\partial y} \\ &+ \frac{\partial(u\tau_{zx})}{\partial z} + \frac{\partial(v\tau_{xy})}{\partial x} + \frac{\partial(v\tau_{yy})}{\partial y} + \frac{\partial(v\tau_{zy})}{\partial z} + \frac{\partial(w\tau_{xz})}{\partial x} \\ &+ \frac{\partial(w\tau_{yz})}{\partial y} + \frac{\partial(w\tau_{zz})}{\partial z} + \rho\vec{f}\cdot\vec{V}\end{aligned} \tag{2.75}$$

Adding equations 2.47, 2.48 and 2.49 and subtracting from equation 2.75 and substituting the viscosity coefficients from equations 2.57, 2.58, 2.59, 2.60, 2.61 and 2.62 gives

the full non-conservation form of the energy equation.

$$\begin{aligned}\rho\frac{de}{dt} &= \rho\dot{q} + \frac{\partial}{\partial x}\left(k\frac{\partial T}{\partial x}\right) + \frac{\partial}{\partial y}\left(k\frac{\partial T}{\partial y}\right) + \frac{\partial}{\partial z}\left(k\frac{\partial T}{\partial z}\right) \\ &\quad - p\left(\frac{\partial u}{\partial x} + \frac{\partial v}{\partial y} + \frac{\partial w}{\partial z}\right) + \lambda\left(\frac{\partial u}{\partial x} + \frac{\partial v}{\partial y} + \frac{\partial w}{\partial z}\right)^2 \\ &\quad + \mu\left[2\left(\frac{\partial u}{\partial x}\right)^2 + 2\left(\frac{\partial v}{\partial y}\right)^2 + 2\left(\frac{\partial w}{\partial z}\right)^2 + \left(\frac{\partial u}{\partial y} + \frac{\partial v}{\partial x}\right)^2\right. \\ &\quad \left. + \left(\frac{\partial u}{\partial z} + \frac{\partial w}{\partial x}\right)^2 + \left(\frac{\partial v}{\partial z} + \frac{\partial w}{\partial y}\right)^2\right]\end{aligned} \tag{2.76}$$

Using the relation

$$\begin{aligned}\rho\frac{de}{dt} &= \rho\frac{\partial e}{\partial t} + \rho\vec{V}\cdot\nabla e \\ &= \frac{\partial(\rho e)}{\partial t} - e\frac{\partial \rho}{\partial t} + \rho\vec{V}\cdot\nabla e \\ &= \frac{\partial(\rho e)}{\partial t} - e\left[\frac{\partial \rho}{\partial t} + \nabla\cdot(\rho\vec{V})\right] + \nabla\cdot(\rho e\vec{V})\end{aligned} \tag{2.77}$$

Substituting equation 2.77 into equation 2.76 with the continuity equation being equal to zero gives the full conservation form of the energy equation

$$\begin{aligned}\frac{\partial(\rho e)}{\partial t} + \nabla\cdot(\rho e\vec{V}) &= \rho\dot{q} + \frac{\partial}{\partial x}\left(k\frac{\partial T}{\partial x}\right) + \frac{\partial}{\partial y}\left(k\frac{\partial T}{\partial y}\right) + \frac{\partial}{\partial z}\left(k\frac{\partial T}{\partial z}\right) \\ &\quad - p\left(\frac{\partial u}{\partial x} + \frac{\partial v}{\partial y} + \frac{\partial w}{\partial z}\right) + \lambda\left(\frac{\partial u}{\partial x} + \frac{\partial v}{\partial y} + \frac{\partial w}{\partial z}\right)^2 \\ &\quad + \mu\left[2\left(\frac{\partial u}{\partial x}\right)^2 + 2\left(\frac{\partial v}{\partial y}\right)^2 + 2\left(\frac{\partial w}{\partial z}\right)^2 + \left(\frac{\partial u}{\partial y} + \frac{\partial v}{\partial x}\right)^2\right. \\ &\quad \left. + \left(\frac{\partial u}{\partial z} + \frac{\partial w}{\partial x}\right)^2 + \left(\frac{\partial v}{\partial z} + \frac{\partial w}{\partial y}\right)^2\right]\end{aligned} \tag{2.78}$$

All of the governing equations of fluid dynamics have the same generic form

$$\frac{\partial U}{\partial t} + \frac{\partial F}{\partial x} + \frac{\partial G}{\partial y} + \frac{\partial H}{\partial z} = J \tag{2.79}$$

thus, grouping all of the x, y, z and t components of the governing equations into the column vectors F, G, H and U respectively allows the entire system to be described by

equation 2.79.

2.1.2.2 Reynolds Number & Inviscid Flow

The Reynolds number is a ratio of the effects of internal to viscous forces acting on a fluid to determine whether the fluid flow is laminar or turbulent, represented in Figures 2.7a and 2.7b respectively.

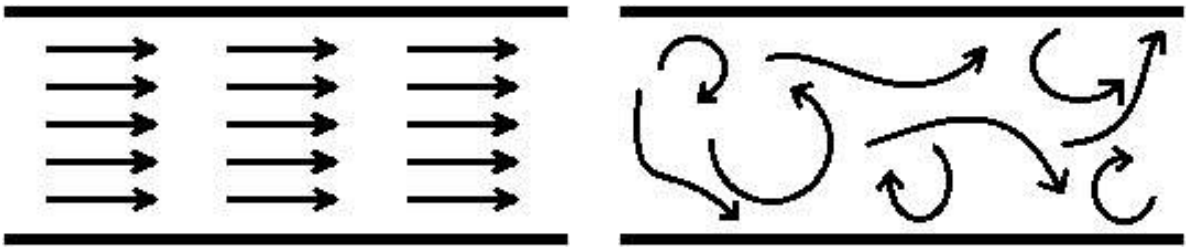

(a) Laminar flow (b) Turbulent flow

Figure 2.7: Representation of laminar and turbulent fluid flow through a tube

The Reynolds number is given as

$$Re = \frac{\rho V L}{\mu} \tag{2.80}$$

where ρ is the fluid density, V is the relative velocity, L the dimension of interaction (length or diameter) and μ is the dynamic viscosity. A Reynolds number of $Re < 2000$ is considered to be laminar flow and $Re > 4000$ is considered to be turbulent flow, with $4000 > Re > 2000$ being the transitional phase. From equation 2.80, higher velocities are associated with turbulent flow, whilst high viscosity associated with laminar flow. Assuming a wave velocity of 400ms^{-1} and a minimum positive phase duration of 100ms, the blast wavelength would be approximately 40m. The dynamic viscosity of air at 25° is approximately 1.86×10^{-4} and would thus have an approximate Reynolds number with an order of magnitude of 10^8, well within the region of turbulent flow.

The large ratio of internal to viscous forces suggests that the blast could be considered as inviscid turbulent flow. The inviscid form of the governing equations negates the effects of viscosity, mass diffusion and thermal conductivity. The inviscid form of the governing equations are hence much simpler. Both the conservation and non-conservation forms

of the continuity equation remain the same; however the x, y and z components of the non-conservation form of the momentum equation become [15]

$$\rho\frac{du}{dt} = -\frac{\partial p}{\partial x} + \rho f_x \tag{2.81}$$

$$\rho\frac{dv}{dt} = -\frac{\partial p}{\partial y} + \rho f_y \tag{2.82}$$

$$\rho\frac{dw}{dt} = -\frac{\partial p}{\partial z} + \rho f_z \tag{2.83}$$

respectively and the conservation form becomes

$$\frac{\partial(\rho u)}{\partial t} + \nabla\cdot(\rho u\vec{V}) = -\frac{\partial p}{\partial x} + \rho f_x \tag{2.84}$$

$$\frac{\partial(\rho v)}{\partial t} + \nabla\cdot(\rho v\vec{V}) = -\frac{\partial p}{\partial y} + \rho f_y \tag{2.85}$$

$$\frac{\partial(\rho w)}{\partial t} + \nabla\cdot(\rho w\vec{V}) = -\frac{\partial p}{\partial z} + \rho f_z \tag{2.86}$$

in x, y and z respectively. The non-conservation form of the energy equation is reduced to

$$\rho\frac{d}{dt}\left(e + \frac{V^2}{2}\right) = p\dot{q} - \frac{\partial(up)}{\partial x} - \frac{\partial(vp)}{\partial y} - \frac{\partial(wp)}{\partial z} + \rho\vec{f}\cdot\vec{V} \tag{2.87}$$

and the conservation form becomes

$$\frac{\partial}{\partial t}\left[\rho\left(e + \frac{V^2}{2}\right)\right] + \nabla\cdot\left[\rho\left(e + \frac{V^2}{2}\right)\vec{V}\right] = \rho\dot{q} - \frac{\partial(up)}{\partial x} - \frac{\partial(vp)}{\partial y} - \frac{\partial(wp)}{\partial z} + \rho\vec{f}\cdot\vec{V} \tag{2.88}$$

Compared to the full viscous forms, the inviscid forms of the governing are much simpler. The use of the inviscid form of the governing equations for propagating blast is

an acceptable practice when studying the isolated propagation of a blast wave; however this does not consider blast structure interactions in which boundary layer effects between the flow and the structure can have a large effect and should not necessarily be neglected.

2.1.3 Numerical Methods

Numerical methods are the driving force behind engineering models and computational structural analysis tools. The ability to assess the response of a structure over a period of time under the application of a wide variety of forces across the entire structure at high resolution is an invaluable asset in research. This research project investigates the response of masonry subjected to blast loads, a problem that can be addressed in two separate stages; the first stage being the application of load to a structure from the blast wave and the second being the effect of the loading to the structure itself.

Understanding the propagation of a blast wave and its interaction with structures is important, but the ability to quantify not only the pressures applied across the surface of the structure, but the associated time profile is paramount to predicting the breakage of the structure. Computational Fluid Dynamics (*CFD*) is vital to this stage of the assessment.

With a full understanding of the loading regimes across the surface of the structure, the next stage is to analyse its response. This process requires the structure to be modelled as a discritised continuum of small elements, the internal connections of which depend on the particular approach and solver. There are various numerical methods and engineering tools which model this type of interaction; the Applied Element Method (*AEM*) is one such tool which has an additional focus to discretised breakage and brittle materials and is discussed further in this section.

2.1.3.1 Computational Fluid Dynamics (*CFD*)

Computational Fluid Dynamics is a numerical method which uses the physical equations of fluid dynamics to simulate the propagation of fluid flow through a domain and around objects or structures. Both shock and blast waves are characterised by a wave of

compressed air travelling through a given medium and can thus be modelled using CFD.

Advection Upstream Splitting Method (*AUSM*)

Computational fluid dynamics models the domain through which fluid flows as a number of cells in which each cell contains physical values obtained by solving the governing equations. All bar the most basic CFD simulations involve reflections and fluid flow traveling in multiple directions. This leads to particles traveling in a number of directions through a single cell; hence a method is needed to model the interactions between individual cells describing the direction of the flux [16]. The current, most widely accepted scheme of flux splitting is the Advection Upstream Splitting Method (*AUSM*) developed by Liou and Steffen [17] and its successors AUSM+ [18], AUSMD and AUSMV leading to AUSMDV [19].

AUSM can be described by considering a one dimensional system for an ideal gas in which the Euler is given by

$$\frac{\partial U}{\partial t} + \frac{\partial F}{\partial x} = 0 \tag{2.89}$$

where the flux vectors U and F are given by

$$U = \begin{pmatrix} \rho \\ \rho u \\ \rho v \\ \rho E \end{pmatrix} \tag{2.90}$$

$$F = \begin{pmatrix} \rho v \\ \rho u^2 + p \\ \rho uv \\ \rho uH \end{pmatrix} \tag{2.91}$$

where the specific total energy $E = e + V^2/2 = e + (u^2 + v^2)/2$ and the enthalpy $H = E + p/\rho$. The flux vector F can be expressed as a sum of the convective and

pressure terms

$$F = \begin{pmatrix} \rho \\ \rho u \\ \rho v \\ \rho H \end{pmatrix} u + \begin{pmatrix} 0 \\ p \\ 0 \\ 0 \end{pmatrix} = F^{(c)} + \begin{pmatrix} 0 \\ p \\ 0 \\ 0 \end{pmatrix} \tag{2.92}$$

The convective terms can be treated as scalar quantities convected by a suitably defined velocity, u, at the cell interface whereas the pressure terms are governed by the acoustic wave speeds. These terms are thus treated separately. Considering a cell interface $\frac{1}{2}$ joining cells L and R such that $L < \frac{1}{2} < R$, the convective terms can be rewritten as

$$F^{(c)}_{1/2} = u_{1/2} \begin{pmatrix} \rho \\ \rho u \\ \rho v \\ \rho H \end{pmatrix}_{L/R} = M_{1/2} a \begin{pmatrix} \rho \\ \rho u \\ \rho v \\ \rho H \end{pmatrix}_{L/R} \tag{2.93}$$

where the suffix $1/2$ denotes the value at the L/R cell boundary, a is the speed of sound and M is the Mach number such that

$$u = Ma \tag{2.94}$$

and

$$(\ldots)_{L/R} = \begin{cases} (\ldots)_L & \text{if } M_{1/2} \geq 0 \\ (\ldots)_R & \text{otherwise} \end{cases} \tag{2.95}$$

The Mach number at the interface $M_{1/2}$ can be expressed as a combination of the wave speeds $(M \pm 1)$ traveling towards the interface $\frac{1}{2}$ from both cells L and R as

$$M_{1/2} = M^+_L + M^-_R \tag{2.96}$$

For supersonic flow, the Mach number is given as the full scalar Mach number in

the downwind direction and zero in the upwind direction; however for subsonic flow, the Mach number is approximated by a second order polynomial according to the van Leer splitting [16], hence the Mach number is given by

$$M^{\pm} = \begin{cases} \pm\frac{1}{4}(M \pm 1)^2 & \text{if } M_{1/2} \geq 0 \\ \frac{1}{2}(M \pm |M|) & \text{otherwise} \end{cases} \tag{2.97}$$

The pressure at the $\frac{1}{2}$ interface can also be expressed as

$$p_{1/2} = p_L^+ + p_R^- \tag{2.98}$$

Similarly to the Mach number, pressure splitting can also be expressed in terms of first order $(1 \pm M)$ or second order $(M \mp 1)^2$ polynomials as

$$p_1 : p^{\pm} = \begin{cases} \frac{p}{2}(1 \pm M) & \text{if } |M| \leq 1 \\ \frac{p}{2}(M \pm |M|)/M & \text{otherwise} \end{cases} \tag{2.99}$$

and

$$p_2 : p^{\pm} = \begin{cases} \frac{p}{4}(M \pm 1)^2(2 \mp M) & \text{if } |M| \leq 1 \\ \frac{p}{2}(M \pm |M|)/M & \text{otherwise} \end{cases} \tag{2.100}$$

$F_{1/2}$ can now be expressed as

$$\begin{aligned} F_{1/2} = \begin{pmatrix} \rho u \\ \rho u^2 + p \\ \rho uv \\ \rho uH \end{pmatrix}_{L/R} &= M_{1/2}\frac{a}{2}\left[\begin{pmatrix} \rho \\ \rho u \\ \rho v \\ \rho H \end{pmatrix}_L + \begin{pmatrix} \rho \\ \rho u \\ \rho v \\ \rho H \end{pmatrix}_R\right] \\ &\quad - |M_{1/2}|\frac{a}{2}\left[\begin{pmatrix} \rho \\ \rho u \\ \rho v \\ \rho H \end{pmatrix}_R - \begin{pmatrix} \rho \\ \rho u \\ \rho v \\ \rho H \end{pmatrix}_L\right] + \begin{pmatrix} 0 \\ p_L^+ + p_R^- \\ 0 \\ 0 \end{pmatrix} \end{aligned} \tag{2.101}$$

The first term on the RHS of equation 2.101 is now a Mach number weighted average and the second term on the RHS is the numerical dissipation rendering the flux formula upwinding with a scalar coefficient $|M_{1/2}|$. Equation 2.101 now describes the entire flux in terms of its split components in both the upstream and downstream x directions. Similar equations for $G_{1/2}$ and $H_{1/2}$ also describe the flux splitting in the y and z directions respectively.

Modified Upwind Scheme for Conservation Laws (*MUSCL*)

The MUSCL-Hancock scheme, when combined with a flux splitting scheme, is a method of achieving second order accuracy in CFD models [20]. From the 1D Euler Equation for a perfect gas

$$\frac{\partial U}{\partial t} + \frac{\partial F}{\partial x} = 0 \tag{2.102}$$

for cell number i, the left and right interface values for U_i^L and U_i^R are calculated using the Total Variation Diminishing (TVD) scheme conditions

$$U_{i+1/2} = U_i + \frac{1}{2}m_i \tag{2.103}$$

and

$$U_{i-1/2} = U_i - \frac{1}{2} m_i \tag{2.104}$$

where m_i is the slope joining the neighbouring cells. The half time-step variables are contained within each cell and evolved according to

$$\bar{U}_i^L = U_i^L + \frac{1}{2}\frac{\Delta t}{\Delta x}\left[F(U_i^L) - F(U_i^R)\right] \tag{2.105}$$

$$\bar{U}_i^R = U_i^R + \frac{1}{2}\frac{\Delta t}{\Delta x}\left[F(U_i^L) - F(U_i^R)\right] \tag{2.106}$$

and the fluxes $F(U)_i^L$ and $F(U)_i^R$ are calculated from the Euler Equation (2.102). The numerical fluxes $F^*_{i\pm1/2}$ are calculated using a splitting scheme such as AUSM. Finally, the full time-step conserved variables are calculated using

$$U_i^{(n+1)} = U_i^n - \frac{\Delta t}{\Delta x}\left(F^*_{i+1/2} - F^*_{i-1/2}\right) \tag{2.107}$$

Air3D

Air3D is a CFD software developed by T. Rose [20] for evaluating the propagation of blast waves through air and around structures. Air3D solves the inviscid forms of the Euler equations in 1D, 2D and 3D using the MUSCL-Hancock method and the AUSMDV flux splitting scheme for both spherical and hemispherical blast waves (height of burst). Air3D also provides the ability to create complex geometries for infinite, semi-infinite or finite structures with infinitely rigid or semi-rigid surfaces. The scope of the solver is limited only by computational requirements and the semi-empirical nature of some of its governing equations. In terms of computational limitations, the CPU clock speed determines the speed of the solution; however, the number of cells that can be used in a particular model is limited by the RAM. Each cell contains 11 variables and so requires 44 bytes, thus the number of cells is limited by the amount of RAM.

In terms of limitations, the models required for this research project should not exceed

the available computational limits. Extreme scaled distances are not suitable for models developed with Air3D; however the requirements for this research project lie well within this range. As a pure CFD solver, Air3D does not account for the structural response to blast waves, thus an infinitely rigid surface would be used to assess the flow interaction with the structure. When subjected to blast loads in the region of hundreds of kilopascals, initial masonry breakage and displacement is observed within the 10→20ms period; therefore, the CFD models will have to be carefully benchmarked against experimental data.

2.1.3.2 Applied Element Method (*AEM*)

The Applied Element Method (*AEM*) is one of a large variety of numerical methods designed for computational structural analysis. Almost all such numerical methods work on the same basic principal, which involves dividing the structure into a discritised continuum. The formation of elements is determined based on material properties and can be implemented as a quadrangular or triangular mesh of variable density.

The first two element based numerical methods tailored to structural analysis of concrete were known as the Smeared Crack Approach [21], and the Discrete Crack Approach [22]. As the names suggest, both methods were designed to attempt to quantify the formation of cracks in concrete structures. The Discrete Crack Approach introduces a physical discontinuity between the elements and appears as an actual crack in the structure propagating along the element boundaries. With the Smeared Crack Approach, cracks manifest themselves numerically as an orthotropic elasticity relation which replaces the isotropic stress-strain relations at the integration point [23]. Such numerical methods are categorised as continuous or discrete based on the method of mesh generation and the subsequent solver.

Continuous methods such as the Finite Element Method (*FEM*), model the structure as a continuous surface or volume, with nodes situated on the element vertices and boundaries. Field quantities of elements (stress, strain, displacement etc.) are approximated using piecewise polynomial interpolation over the nodes and by further connecting ele-

ments, the field quantities can be interpolated over the entire structure [24]. Continuous methods have many advantages and are widely used for a large variety of applications; however, the fundamental principal of a continuous surface does not permit such methods to model progressive collapse but simply identify the point of failure. To assess the potential failure modes and progressive collapse of structures, especially those constructed from brittle materials such as concrete, masonry or glass, a different approach is required.

AEM is a discrete method which uses face connecting normal springs, x-z shear springs and y-z shear springs to model the interactions between elements. Figure 2.8 illustrates the connecting normal and shear springs on a two dimensional element face [25].

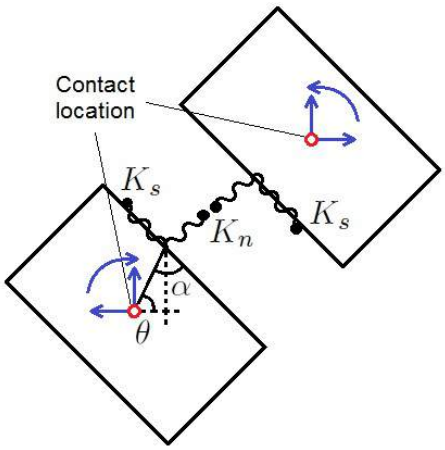

Figure 2.8: Element shape, contact location and degrees of freedom

K_n and K_s are the normal and shear springs respectively and are determined by

$$K_n = \frac{EdT}{a} \tag{2.108}$$

and

$$K_s = \frac{GdT}{a} \tag{2.109}$$

where d is the distance between springs, T is the thickness of the element, a is the length of the representative area, E is the Young's modulus and G is the shear modulus. This simple 2D problem has only 2 types of spring, normal and planar shear with the area of effect joining the central axis of each element. In this simplistic 2D case, each element

has 3 degrees of freedom and the effect of Poisson's ratio is neglected. The local stiffness matrix for the pair of contact springs in this problem, $[K_L]$, can be assessed using simple geometry and is given in equation 2.110

$$\begin{pmatrix} \sin^2(\theta+\alpha)K_n & -K_n\sin(\theta+\alpha)\cos(\theta+\alpha) & \cos(\theta+\alpha)K_sL\sin(\alpha) \\ +\cos^2(\theta+\alpha)K_s & +K_s\sin(\theta+\alpha)\cos(\theta+\alpha) & -\sin(\theta+\alpha)K_L\cos(\alpha) \\ \\ -K_n\sin(\theta+\alpha)\cos(\theta+\alpha) & \sin^2(\theta+\alpha)K_s & \cos(\theta+\alpha)K_nL\cos(\alpha) \\ +K_s\sin(\theta+\alpha)\cos(\theta+\alpha) & +\cos^2(\theta+\alpha)K_n & +\sin(\theta+\alpha)K_sL\sin(\alpha) \\ \\ \cos(\theta+\alpha)K_sL\sin(\alpha) & \cos(\theta+\alpha)K_nL\cos(\alpha) & L^2\cos^2(\alpha)K_n \\ -\sin(\theta+\alpha)K_nL\cos(\alpha) & +\sin(\theta+\alpha)K_sL\sin(\alpha) & +L^2\sin^2(\alpha)K_s \end{pmatrix} \tag{2.110}$$

The global stiffness matrix, $[K_G]$, for an element is obtained by summing all the local stiffness matrices for each set of contact springs around the element. The governing equation for the element is then

$$[K_G][\Delta] = [F] \tag{2.111}$$

where $[\Delta]$ is the displacement vector and $[F]$ is the loading vector.

With any given AEM model, the number of connecting springs and the element size and number will have an effect on the accuracy of the model. During the development of AEM, Meguro and Tagel-Din [25] conducted various sensitivity studies including the effect of the number of springs and elements size on the stiffness and its calculated error. The number of springs was found to have no effect on the translational degrees of freedom; however element rotation, which depends on the theoretical rotational stiffness K_r, is resisted by the number of normal springs.

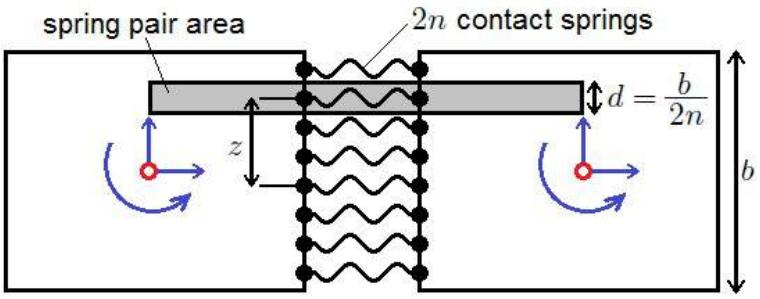

Figure 2.9: Effect of number of contact springs on rotational stiffness

Considering the 2D problem shown in Figure 2.9, the number of springs can be considered as $2n$ and the theoretical rotational stiffness for a normal spring is

$$K_r = \int_{y=-b/2}^{y=b/2} \frac{ET}{b} z^2 dz = \frac{ETb^2}{12} \tag{2.112}$$

and

$$K_r = \frac{ETb^2}{4n^3} \sum_{i=1}^{n} (i - 0.5)^2 \tag{2.113}$$

where T is the element thickness, E is the Young's modulus, b is the element height and i is the spring number. Equation 2.113 clearly shows that the theoretical rotational stiffness is a function of the number of springs. Table 2.1 shows the relation between the number of connecting springs and the calculated error in rotational stiffness. It is clear from Table 2.1 that a small increase in the number of springs per element face has a large effect on the calculated error.

Table 2.1: The effect of the number of springs on the calculated error in rotational stiffness

$2n$	2	4	6	8	10	20
Error Ratio (%) $[100\,(K_r^n/K_r^t - 1)]$	25	6.3	2.8	1.6	1.0	0.3

The elements shown in Figure 2.9 are square with an area of b^2 with $2n$ springs connecting each face; by reducing the base element size from 1 to 2 such that 4 elements of area $\frac{1}{4}b^2$ occupy the same space, keeping the same number of spring pairs per element face will increase the number of spring pairs across the original boundary to $4n$. To

achieve the same level of accuracy as the original model, the model only requires half the number of springs per element. The sensitivity study conducted by Meguro and Tagel-Din [25] uses a laterally loaded cantilever shown in Figure 2.10a in which the number of base elements is varied and the test is run for 10 spring pairs and 20 spring pairs.

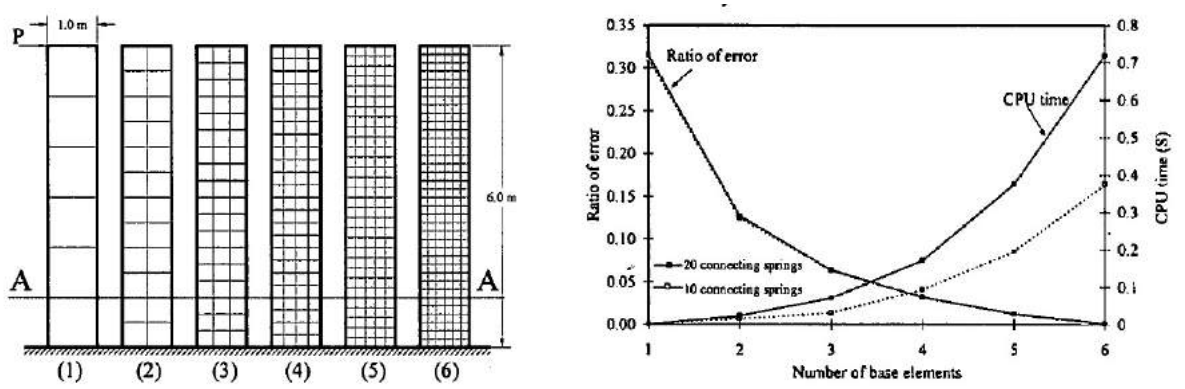

(a) Dimensions and element arrangements of laterally loaded cantilever models

(b) Relations between the number of base elements, ratio of error and CPU time

Figure 2.10: AEM base element number and spring pair sensitivity study [25]

It is clear from Figure 2.10b that the base element size has a greater effect on ratio of error whilst the spring number merely increases the CPU time. Consulting table 2.1 shows the error ratio for 20 springs is, however, not much lower than for 10 springs. It is therefore a reasonable assumption that the base element size should be scaled against the number of springs to achieve the most efficient model.

As previously mentioned, these simplistic 2D models do not take into account the Poisson's ratio effect. A simple way to take this effect into account is to add two more degrees of freedom to each element; these being both the horizontal and vertical compressions. This technique would require extra CPU time in assembling the stiffness matrix; hence AEM adopts a different method to deal with the Poisson's ratio effect. Within the original degrees of freedom of the element assembly, AEM detects which element boundaries are connected to other elements both statically in the original model and dynamically as springs break and cracks are formed. Each edge of the element is given a value of 0 or 1 depending on whether it is connected to an adjacent element.

For the element i, the transmitted force F_i is given by

$$F_i = \frac{\nu E_i T_i}{4(1-\nu^2)} \tag{2.114}$$

and the transmitted moment M_i is given by

$$M_i = \frac{\nu E_i T_i}{4(1-\nu^2)} \cdot \frac{a}{4} \tag{2.115}$$

where ν is Poisson's ratio, E is the Young's modulus, T is the element thickness and a is the element size. The global stiffness matrix for each element is updated for each time step by adjusting the values for each degree of freedom: the horizontal velocity u, the vertical velocity v and the rotational velocity R, using the binary value of the edge connectivity to determine which can transmit force and moments.

In the case where Poisson's ratios not equal to zero, after the global stiffness matrices the values of strain can be calculated from the displacements of the spring ends ϵ_x and ϵ_y as

$$\epsilon_x = \frac{d_x}{a} \tag{2.116}$$

and

$$\epsilon_y = \frac{d_y}{a} \tag{2.117}$$

where d_x and d_y are the relative displacements of the spring ends in x and y. Note, equations 2.116 and 2.117 have no dependence on Poisson's ratio. Next the average strains for each element ϵ_{xa} and ϵ_{ya} are calculated such that the stresses, σ_x and σ_y, for each for each spring can be calculated. For concrete, the stresses are calculated as

$$\sigma_x = E_c \frac{\epsilon_x + \nu \epsilon_{ya}}{1-\nu^2} \tag{2.118}$$

and

$$\sigma_y = E_c \frac{\epsilon_y + \nu \epsilon_{xa}}{1 - \nu^2} \tag{2.119}$$

where E_c is the Young's modulus for concrete. For steel the stresses are simply

$$\sigma_x = E_s \epsilon_x \tag{2.120}$$

$$\sigma_y = E_s \epsilon_y \tag{2.121}$$

where E_s is the Young's modulus for steel.

Debris distribution is a key factor in this research project, thus an AEM driven software package is ideal, due to its high solver efficiency compared to other numerical methods. Extreme Loading for Structures (*ELS*) is an AEM based software package created by Applied Science International and the developers of AEM and was chosen as it is specifically tailored to modelling progressive collapse and discretised breakage.

2.2 Seminal Works

The following sections offer a discussion of previous works in the fields relevant to this research project. Topics including masonry failure and the common types of collapase, the response of masonry to various types of blast loading, previous research into long duration blast loading and its interaction with structures, blast induced fragmentation of brittle materials and debris distribution models. The discussion outlines the seminal works and their contributions to the field as well as highlighting gaps in the literature.

2.2.1 Masonry Failure

As with all construction materials, much research and analysis has been conducted to investigate various material properties and failure modes of masonry. Many examples of research into masonry response to axial, shear and lateral loads offer insight into the common failure modes of masonry. Lishak et al. [26], present a range of common

masonry failure modes when subjected to various axial loads and shear stresses, illustrated in Figure 2.11.These failure modes also present themselves various other experimental research studies, such as the series of experiments conducted by Dhanasekar and Page [27, 28]. The research investigated the axial compressive strength of masonry through application of both uniaxial and biaxial loads to masonry panels, whilst varying the relative loading angle. The uniaxial tests showed failure by cracking along the bedding joins in differing positions depending on the loading angle, similar to the those outlined in Figures 2.11a, 2.11b and 2.11d, whilst biaxial loading resulted in splitting of the masonry parallel to the face of the structure, as depicted in Figure 2.11c.

Alecci et al. [29], compared the shear strength of masonry walls with lime, cement-lime and cement mortar, with the results showing similar diagonal cracking patterns along the bedding planes with varying load-displacement profiles. Whilst the aim of these experiments were to compare shear testing techniques, the results highlight the effects of masonry subject to shear stresses, agreeing with the illustration in Figure 2.11g. Recent studies by Costigan et al. [30] investigate the behaviour of masonry under compression with different lime-based mortars, showing higher compressive strengths and better stress strain characteristics. Compression tests have also been conducted on rubble stone masonry walls by Milosevic et al. [31]. Two different types of lime based mortar were used showing both partial and total collapse. Before rupturing, both structures showed cracking between the brick, or in this case rubble and mortar joints, again presenting further evidence of this particular type of masonry failure when subject to axial loading.

Several studies have also investigated the failure modes of masonry subject to static or incremental lateral loads. Earlier research conducted by Alessandri and Brebbia [32], static loads to the side of a 4m heigh windowed masonry structure using hydraulic jacks and a steel i-beam to achieve a relatively uniform pressure distribution. The structure was loading until cracks began to form around the windows near to the loading point. The wall was repaired and restrengthened with cement injections and an additional load was applied to both sides of the structure at once, inducing a series of cracks to form around the other window with agreement from the accompanying numerical models.

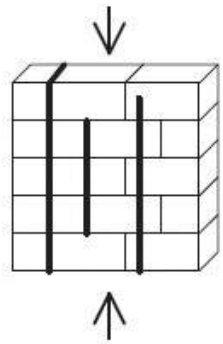

(a) Partition into columns

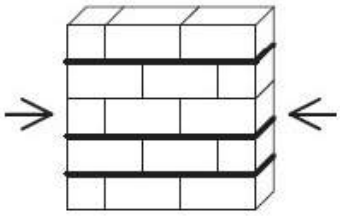

(b) Partition into one or multiple layers

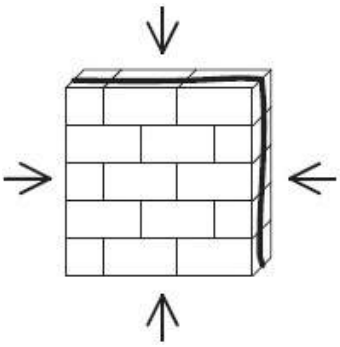

(c) Splitting parallel to the external surface

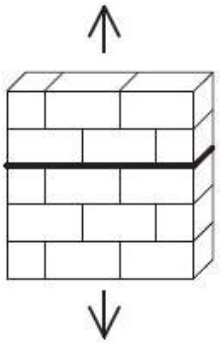

(d) Break along a bed joint

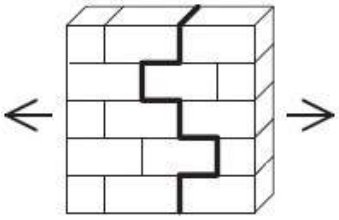

(e) Break along a tooting crack

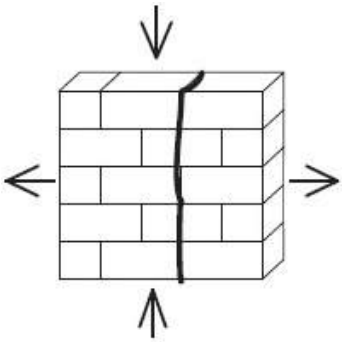

(f) Vertical break through masonry elements

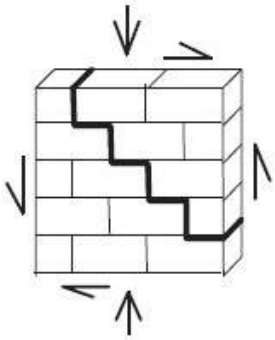

(g) Splitting along a stepped crack

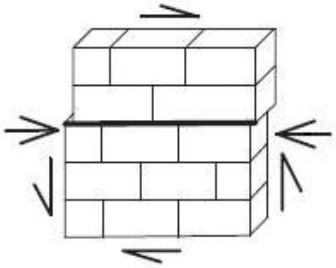

(h) Shear along the bed

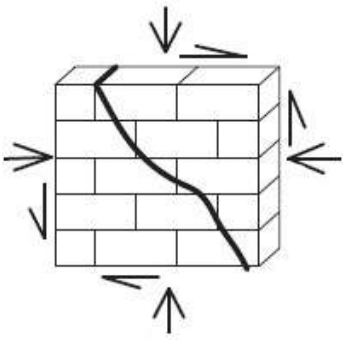

(i) Splitting along an inclined crack

Figure 2.11: The main forms of masonry failure in plane stress state [26]

Herbert et al. [33] placed $1/6^{th}$ scaled masonry walls into a centrifuge to achieve correct stress profiles throughout the structure. Lateral loads were the applied using air-bags to simulate uniform wind lateral loads, with the results showing horizontal cracks forming along the bedding planes at mid height, for each of the test specimens. Further cracks formed on each of the structures spanning from the central crack line to top and bottom of the structures, not adhering to the bedding planes. The experiments conducted by Liu and Manesh [34] offer further examples of static lateral loading of masonry walls. Steel frames, enclosing masonry in-fill walls with aspect ratios of 1:1.3 were subjected to both axial and lateral loads simultaneously. The experiments showed structures with windowed openings or structures subjected to combined loads developed diagonal cracking patterns prior to ultimate failure.

The failure and collapse of masonry subject to seismic activity has also been extensively researched, offering further insight into masonry failure mechanisms. Yuan et al. [35] provide a number of examples of masonry and reinforced concrete walls subject to earthquakes, each displaying a different response based on the boundary conditions and magnitude of the earthquake. The responses include cracking, partial failure and complete collapse. Research conducted by Mauro et al. [36], highlights the relative strength masonry structures to earthquake loading and the response of each of the structural sections or ground acceleration and vibrational loading, with case studies showing detachment of the façade from the main structure. Preciado [37] investigated the vulnerability of masonry towers to earthquakes, giving examples of observed damage showing crack formation around windows and above arches, as well as vertical spanning cracks running the length of the tower around a corner joint. Finite Element Models showed the lateral and vertical forces differ based on the type of roof. Similar research into the failure modes of masonry subject to cyclic loading has also been investigated, such as the experiments conducted by Penna et al. [38]. Both reinforced and unreinforced masonry walls were subjected to a series of axial cyclic loads of 300kN and 450kN, with the results showing large numbers of cracks for across the face of the structure without adhering to the bedding planes.

The failure of masonry, for most types of brick / stone and mortar as presented in the literature, show favourable breakage along the bedding joints; including horizontal, vertical and diagonal cracks. Cracking of the bricks themselves are not uncommon; however, they occur as a result of crack lines running between two bedding joints through the centre of the brick. Some loading scenarios, biaxial for example, result in splitting through the structure, parallel to the face.

2.2.2 Blast Loading of Masonry

Several research studies have focussed on the effects of near field blast structure interaction and the response of various materials to extremely high impulsive loads, such as the 2GPa measured by Drotleff et al. [39]. Early research outlines the destructive crushing force of near field detonations with experimental and computational work showing rupture and spalling of materials [40, 41, 42]. Recent research efforts use both experimental trials and high fidelity numerical models to analyse effects of near field loading, such as the efforts of Yan et al. [43] to investigate the near field effects of blast on reinforced concrete beams. The research highlights large crack formation propagating away from the blast, combined with spallation and exfoliation of the concrete. Most examples in the literature of near-field blast loading of brittle materials such as concrete of masonry conclude the key failures to be rupture and spallation, such as the research conducted by Dörr et al. [44, 45], showing high levels of localised fragmentation for masonry subject to 250g and 1000g PETN surface charges.

Research has also been conducted to investigate the response of concrete structures to blast loading, providing additional insight into the response of brittle materials. Reinforced and fibre reinforced concrete panels were subjected to blast loads with a scaled distance between $0.41\text{mkg}^{-1/3}$ and $0.57\text{mkg}^{-1/3}$ in tests conducted by Pantelides et al. [46], with results showing extensive cracking and spalling in simple RC panels with reduced damage to FRC panels. Many additional studies have investigated the effects of reinforcement of concrete, such as the tests conducted by Razaqpur et al. [47], assessing the performance of glass fibre reinforced polymer retrofits when subject to 22.4kg

and 33.4kg of ANFO at 3m, with thre results again showing improved resistance when reinforced.

Much less research appears to have been conducted directly investigating the effects of blast loading on masonry walls. Mayrhofer [48] for example conducts extensive research on the effects of reinforced masonry walls subject to blast loading. The specimens were loaded using a shock tube to apply loads of approximately 150kPa for 40ms with the results showing arching of the masonry between the bedding planes, held together by the reinforcement. Urgessa and Maji [49] also subject concrete masonry walls with varying levels of fibre reinforcement to blast loads, in particular 0.45kg charges achieving incident overpressures of approximately 100kPa, leading to peak displacements between of 15-20mm based on the level or reinforcement.

Fischer et al. [50] subjected a "blast proof" masonry wall system with a window to car bomb like yeild at a stand-off distance of 15m, yielding an incident overpressure of approximately 150kPa for 15ms. The structure was reinforced resulting in roughly symmetrical arching about the vertical supports. The reinforcement webbing also restricted any debris infill resulting in the large blocks collapsing outwards, the blocks themselves mostly undamaged as the breakage was along the bedding joints.

A study by Moradi et al. [51, 52] showed unreinforced concrete masonry walls pinned at the top exhibit inwards arching about horizontal crack lines which form at approximately mid-height. Similar experiments by Abou-Zeid et al. [53] also subjected unreinforced concrete masonry walls to explosive loading, in 14 tests utilising 15kg-250kg of ANFO at stand-off distances varying from 15m-20m. The walls were fixed top and bottom, resulting in central cracking along the bedding planes and inwards rotation of the upper and lower halves about the crack. The results were plotted on pressure-impulse iso-damage curves to illustrate the level of damage from "minor" to "demolition," based on the severity of the cracking.

Research investigating the blast effects on brick masonry walls is very sparse, with a study by Wei and Stewart [54], building on experiments conducted by Varma et al. [55], currently offering the best results available. The tests subjected unreinforced brick

masonry walls to a range of scaled distances between 1.01mkg$^{-1/3}$ and 2.48mkg$^{-1/3}$ with charges between 20kg and 50kg. The walls themselves were constructed using clay bricks with a compressive strength of 12.24MPa with wall thicknesses of 230mm and 355mm and a height and width of 3m×3m. The experimental results showed the 230mm thickness walls collapsed when subjected to charges between 40kg-50kg at stand-off distances of 7m and under; the 355mm walls however only collapse when subject to 50kg charges below 4m stand-off distance. Blast scenarios with higher scaled distances caused almost no damage, with lower scaled distances causing extensive cracking. Numerical models benchmarked on the experimental trials revealed the maximum deflection of walls varied slightly based on the class of mortar used, but was insignificant when subject to larger blast loads. The boundary conditions and wall thicknesses had a large influence on the maximum deflections and rotations of the walls, with 355mm thick walls fixed at all 4 sides showing the lowest deflections.

The primary focus of blast testing on brittle construction materials appears to be concrete, specifically testing the effectiveness of fibre, glass fibre and polymer reinforcements. The literature highlights cracking, bending and arching to be the primary failure modes, with high levels of damage such as spalling caused by near field detonations, resulting from extremely high pressures. Furthermore, the blast trials which have been conducted to investigate masonry primarily focus on concrete masonry, with very few studies investigating brick masonry. The results show the primary breakage mechanisms appear to be along the brick mortar bedding planes; however proximity and hence higher pressure increase the probability of damage to the bricks themselves.

2.2.3 Fragmentation & Debris Distribution

Several research studies have investigated methods to predict the fragmentation of various materials subject to blast, with a particular focus on the fragmentation of rock on behalf of the mining industry. Fragmentation models with a focus on rock and mining generally assume embedded charges, with the radius and depth of the borehole presenting key variables. Empirical methods such as the Kuz-Ram model [56] predict the percentage of

mass with a specific fragment size. Additional studies, such as the research conducted by Morin and Ficarazzo [57], build upon the Kuz-Ram model, in this case using Monte-Carlo simulation to predict fragmentation.

The distribution of debris is described by three stages, the launch following fragmentation, the in-flight kinematics and finally the ground impact. A small number of research studies have investigated debris mechanics, attempting to describe various features of the resulting rubble pile, mostly the size and location of fragments. A model proposed by Weng et al. [58] was developed through a series of AUTODYN models using blast with a scaled distance of $2\text{mkg}^{-1/3}$ and $3\text{mkg}^{-1/3}$. The models showed cracks propagating from the centre of the walls to the edges, yielding large numbers of initial fragments, with a velocity gradient increasing towards the centre. Analysis of the models revealed few fragments to be below 0.025m, with the majority of fragments between 0.05m-0.1m in size, following a smooth exponential decay towards the largest fragments of size 0.3m. The results are then compared to the Weibull distribution [59] with good agreement. The research concludes that for a scaled distance of $2\text{mkg}^{-1/3}$, 70% of the fragments are located between 5m-10m and for a scaled distance of $3\text{mkg}^{-1/3}$, over 70% of the fragments were located less than 5m away. It should be noted that scaled distance does not account for blast duration or impulse, only pressure.

A study by Lu and Xu [60] investigate the debris launch velocity of internal blast on vented concrete structures. The research proposes a theoretical-empirical method of relating the ratio of vent opening size to internal surface area of the structure with the initial debris launch velocity. The method was also used to derive a linear relationship between the internal loading density of the structure and the initial fragment velocity. In both cases the predictions show good agreement with previous experimental trials conducted by Dörr et al. [61]. Additional research published by Xu and Lu [62] uses the same empirical model to relate the strain rate to the normalised concrete strength and is compared to experimental results from four different research studies, again showing good agreement.

Another statistical model, developed by van der Voort and Weerheijm [63], describes

the debris dispersion produced from internal detonations of reinforced concrete structures. The theory defines a probabilistic source function to determine a range in which the final debris can be located; the source function is described in terms of the launch conditions of the debris, including the spherical launch angle in co-ordinates, the projectile length and projectile velocity. The model was validated against a series of experimental trials, plotting the range at which debris was located against the number density of projectiles in varying size categories. The experimental results offered data from explosives with a TNT equivalence of 6.9kg, 20kg, 80kg, 110kg and 120kg, with the data showing the number of fragments decreasing with distance for all projectile categories. The empirical formula showed relatively good agreement with the experimental trials, offering better agreement for smaller charge masses.

Knock et al. [64] conducted a study to investigate the bounce and roll of masonry debris. The research used a high velocity gas cannon to fire cubic and spherical chunks of masonry debris between 50-150ms^{-1} at impact angles between 5-25°. Linear correlations were observed between the impact angle and the change in angle, along with the impact angle and the ratio of initial and final impact velocities. Upon reducing the hardness of the ground, both correlations were altered, with increase impact angle showing a lower ratio of velocities and a higher change in angles. The research concludes that there was little to no difference between spherical or cubic debris and the behaviour differed depending on the impact surface, which could be categorised as deformable or rigid.

There are few examples in the literature describing explosively produced debris from brittle structures and even fewer examples discussing masonry. The focus of previous research is primarily focused on using statistical models to describe the dispersion of debris. As debris distribution is such a complex problem, involving many variables including the type, mass and stand-off of the explosive, the subsequent break-up of the structure, the launch conditions of the debris and parameters such as the in-flight drag, previous models attempt to describe the resulting debris in terms of projectile density at a given range.

2.2.4 Long Duration Blast

For the purposes of this research, long duration blast has been defined as a blast load with a positive phase duration in excess of 100ms. The duration of the blast wave is dependent on the volume of air in the shock front (cross sectional length) and velocity. As blast waves expand, the volume of air in the shock front increases; hence long duration waves occur in the later stage of propagation. For a blast wave to reach this stage of propagation with enough energy to cause significant structural response requires a large scale explosive event. Such explosive events include 1981 'Mill Race Event' in which 544T of ANFO were detonated [65], the 1983 'Direct Course Experiment' in which 600T of ANFO were detonated [66] and other extreme examples including the notable 1945 'Project Trinity' with an estimated TNT equivalence of 19kT [67] and the 'Easy' shot from the 1951 'Operation Greenhouse' with an estimated TNT equivalence of 47kT [68].

These are all examples of controlled experimental detonations; however, large scale accidental detonations can also lead to long duration blast loading, most commonly as a result of hydrocarbon vapour cloud detonation due to the large quantities in which they are stored. These are the most common forms of long duration blast structure interaction. Notable examples of large scale hydrocarbon detonations include the 2005 'Buncefield Disaster' which had an estimated TNT equivalence of 250T [69] and the more recent 2013 'Texas Fertilizer Explosion' in which a fire led to the detonation of 30T of ammonium nitrate, amongst other combustible materials stored within the facility [70].

The shock propagation of deflagration is much slower and hence the positive phase duration is much longer; however, the associated incident overpressure of deflagration is not high enough to be included here as a long duration blast load. Certain types of hydrocarbon, ammonium nitrate for example, undergo deflagration or detonation depending on a number of parameters including storage conditions and phase state [71]. Large quantities of ammonium nitrate stored in confinement provide an increased risk of deflagration to detonation transitions and can thus produce high pressure, long duration blast waves.

Typically, blast waves generated by hydrocarbon and vapour cloud detonation have a

slower rise to reach the peak overpressure compared to the sharp rise of a standard blast wave. Several recent research studies have investigated the deflagration to detonation transition of vapour cloud explosions, using both experimental and numerical techniques. Hansen and Johnson [72] investigate the far-field blast predictions from fast deflagration and vapour cloud explosions, using experimental results from a scaled Buncefield type event. The pressure time histories showed that in the near-field, 2m from the ignition point, the rise was incredibly slow, taking 20ms to reach peak pressure - on third of the total positive phase duration. At 5m the rise was reduced to 10ms, at 8m the rise was less than 5ms and by 11m the rise could be considered instantaneous. Johnson, Tomlin and Walker [73] as present similar results, using a 45m long testing rig to simulate vapour cloud explosions. The results showed similar levels of damage to the test items as observed near the Buncefield explosion. The pressure time histories showed a slow rise to a low peak pressure at 12m from ignition, but a sharp rise to a high peak pressure at 21m. Similar tests conducted by Pekalski et al. [74] highlight the increase in flame speed further from the ignition point, with 0-500ms^{-1} observed between the first 5m, with speeds recorded up to 3000ms^{-1} between 5-12m.

Very few experimental long duration blast trials have been conducted for research purposes and the literature offers little to no discussion of the effects of long duration blast loads. The primary cause of long duration blast in the modern world is highlighted as accidental explosions and processing facilities including hydrocarbon vapour cloud detonation. Although vapour cloud detonation is known for offering a different pressure profile, recent studies have shown that at medium to long range, the pressure profile behaves as a typical blast wave, travelling as a sharp shock discontinuity.

2.2.5 Applied Element Method

The Applied Element Method (AEM) has been used in a number of research studies for a range of buildings, materials and loading conditions, presenting encouraging results, particularly where progressive collapse and large displacements are concerned. An investigation into the cause of the I-35W bridge in Minnesota by Salem and Helmy [75]

used AEM to model the bridges' failure and progressive collapse. In this particular case, AEM was chosen based on its advantages over FEM when modelling collapse and large deformations. A detailed model of the entire bridge was constructed and the load was applied using lumped masses to correctly model the inertia of vehicles and increased until failure occurred. The failure was attributed to the buckling of a gusset plate, matching the observed results, with the subsequent collapse also showing excellent agreement with the field observations. An additional investigation by Salem [76] used AEM to model the collapse of the Utatsu Ohashi Bridge in Japan, this time resulting from a tsunami. Loading resulting from a tsunami is not dissimilar from blast loading, with pressure time profiles showing a sharp rise followed by decay; however the velocity is much lower, density is much higher and drag forces much greater. Comparison of the AEM results and observed bridge collapse showed good agreement, with both the failure mechanism and displacement of the large structural bridge members.

Helmy et al. [77] conducted study of progressive collapse of multistory reinforced concrete structures using AEM, with a particular focus on the contribution of masonry infill walls. A detailed model of a 10 story building was constructed following UFC 2009 [78], with explicitly modelled concrete masonry infill walls. The progressive collapse of the structure was modelled by removing various structural elements, with and without the added support of masonry walls at various positions. The AEM models showed the expected collapse mechanism and offered a detailed analysis of the effects of various structural members. The masonry model and masonry collapse mechanism performed well, highlighting the increased resistance to collapse offered by using masonry walls in the lower sections of the structure. AEM has also been used to model blast loading, Coffield and Adeli [79] investigated the failure of irregular steel buildings when subject to blast loads. Multiple iterations of a large 10-story building were modelled using AEM, each model consisting of a different bracing arrangement, whilst the blast loads were kept consistent. The analysis highlighted the bracing arrangement which provided the most resistance and the effect of blast loading was reduced when placed near re-entrant corners. The analysis highlighted

Kernicky et al. [80] conducted an experiment in which 0.45kg (1lb) of PETN was placed in a blast chamber, 3.43m from a concrete masonry wall and modelled the experiment using AEM. The model was constructed using explicitly modelled masonry blocks, mortar, grout and attached steel components, with the blast loading applied directly using the software. A timestep of 1μs was used initially during the loading, then reduced down to 10μs for a further 0.5s, following a further reduction to 100μs until the response decayed. Small networks of cracks were observed over the surface of the structure, with the most notable damage was due to displacement of a masonry block connected to one of the steel supports, matching the observed damage in the experimental trial. The natural frequencies of the wall were measured experimentally and computationally pre and post blast, with AEM again showing good agreement with the experimental results.

2.3 Summary

The background and theory behind blast, fluid dynamics and numerical methods were discussed, highlighting key concepts and parameters required to understand the this research project. The production, characterisation, propagation, evolution and structural interaction of blast waves were investigated, outlining the relation between incident, reflected and dynamic pressures and the type and severity of damage inflicted by each. A derivation of the governing equations of fluid dynamics was given, with a comparison between the various flow regimes and application of these concepts to the relevant long duration blast parameters. The mathematical techniques used in CFD and AEM were also discussed, outlining the method with which numerical results will be developed for this research.

A number of excellent research studies have investigated many aspects of masonry failure mechanisms, blast loading, long duration blast loading and debris distribution. A number of quasi-static loading tests on masonry have revealed a variety of failure mechanisms, the majority of in-plane and out of plane loading scenarios result in breakage of the masonry between the brick and mortar bonds. Particularly lateral, out of plane loading results in horizontal cracking of the masonry followed by arching. Blast testing

of masonry has also revealed similar results, with horizontal breakage occurring along the bedding planes; however, the majority of blast tests have investigated concrete masonry and some form of reinforcement, with limited results directly related to brick masonry. Blast research with a specific focus on brick masonry appears to be focussed on near-field detonations which lead to a completely different failure mechanism due to the extremely high pressures.

Few research studies have been conducted to investigate the distribution of debris, with little to no focus on masonry. The dispersion of debris is modelled using a probabilistic approach, categorising the types of fragments located within certain regions of the debris pile. Given the complexity of blast induced debris, characterising the resulting ruble pile in terms of regions of high density and large fragments offers a good estimation of the regions in which personal injury or infrastructure blockage would be the highest. The causes of long duration blast have been identified as primarily accidental explosions in processing facilities with vapour cloud detonations presenting the most risk. The blast profiles of vapour cloud explosions are representative of traditional blast waves in the near to far field, which is the region in which the positive phase duration is at its highest.

Upon reviewing the literature, it is clear that there are gaps in terms of long duration blast loading, debris distribution of masonry and blast loading of masonry. Whilst blast loading of concrete masonry and some brick masonry have been researched, there are few experimental results. No research has investigated the effects of from long duration blast loading on masonry structures, or the distribution of debris resulting from long duration blast. Based on the literature, this research aims to distinguish itself by investigating the effects of long duration blast loading of masonry structures, with a focus on the debris distribution of masonry subject to long positive phase durations and high dynamic pressures.

Chapter 3

Experimental Methodology

3.1 Research Methodology

Thus far, little research has been conducted into long duration blast loading and even less regarding its effects on masonry structures. As a result, this research must start from the most simple scenarios, which, in terms of masonry are unreinforced walls constructed from single leaf, running bonds. Whilst almost all real-world masonry structures are built using insulated cavity walls reinforced by timber or steel frames, this simplistic model offers both a first step in the development of such damage predictions; furthermore, the inherently weak nature of such structures should provide a 'worst-case' damage assessment.

For the purposes of experimentation, even simplistic, single leaf masonry walls present a large number of variable parameters, in terms of both the structural and material parameters, coupled with the a number of parameters associated with the blast wave itself. Certain parameters must remain fixed throughout the experiments for any comparisons to be made. As the masonry bonds remain fixed for each trial, the masonry itself will also be kept constant; hence the material parameters for both the brick and mortar will

remain constant. The key remaining parameter in terms of masonry construction is the structural geometry. This can be altered in terms of height, width, depth, number of corners, floors, roof type and internal load bearing walls. A series of trials conducted by AWE using the Large Blast / Thermal Simulator (*LB/TS*) [81] at White Sands Missile Range, New Mexico, named the Discrete Orion series [82], subjected a full scale masonry structure to a long duration blast load. Figure 3.1 shows the masonry breakage and debris entrainment of the Discrete Orion trial.

Figure 3.1: Discrete Orion Series [82]

It can be clearly seen from the images shown in Figure 3.1 that both the interior, load bearing walls and floors show little to no response. The exact nature of the blast wave used for the Discrete Orion series and its parameters are unknown; however the operating envelope of the LB/TS is between 1-600kT [83], the associated pressures and impulses of which are much higher than those investigated in this research. Based on this, the masonry structures investigated for this research will be single story and will not use

internal, load bearing walls. Whilst these structural components may not be affected by incident blast loads, they may offer added structural resistance to exterior walls; however, to incorporate interior walls and the multiple stories required to implement upper floors, the minimum size of the structure increases drastically, which is not necessarily possible to implement in the experimental trials. Furthermore, as previously mentioned, this research is an initial step in the development of predictive algorithms for real-world masonry buildings, thus, maintaining a simplistic masonry structure is acceptable whilst obtaining initial results.

With these assumptions taken into account, the main remaining structural parameters are dimensional and the geometry can be varied in terms of height, width, depth and number of corners. By fixing the height of the structure, the variable dimensions can be limited to its 2D plan geometry, which can be simplified and sectioned into full or simplistic 'base panels,' as illustrated in Figures 3.2 and 3.3 respectively.

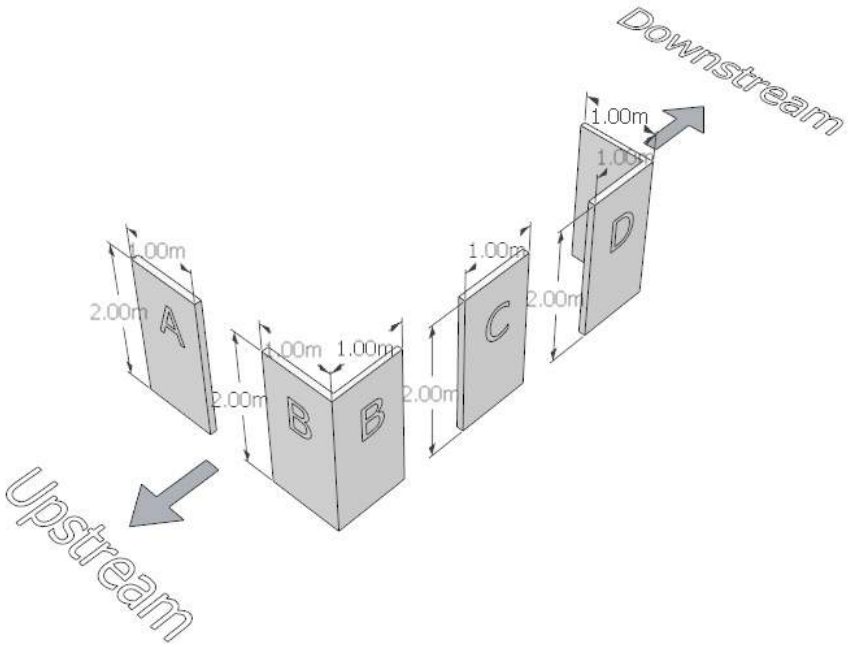

Figure 3.2: Base panel model for small masonry structures

Firstly, it is clear from both Figures 3.2 and 3.3, that for both models all walls are assumed to be either normal or parallel to the incident blast wave. Whilst angled walls are part of masonry construction, incorporating these into the base panel model would

require a further, full assessment into the effects of oblique angles of incidence.

The panels shown in Figure 3.2 highlight the sections of a simple rectangular masonry structure which experience the blast loading in different ways. The simplest of the base panels is designated the '**A**' panel, which in isolation experiences a blast normal interaction. The '**C**' panel is a 90° rotation of the **A** panel which lies parallel to the blast. The '**B**' and '**D**' panels are both combinations of the **A** and **C** panels to form front and rear corner joints respectively. The height of the base panels is fixed at 2m and the unit width and unit length are both fixed at 1m; these base measurements allow for added simplicity when investigating dimensional ratios, i.e. a free standing wall normal to the blast, constructed from n **A** panels, can be implemented in integer height to width ratios starting with 2:1 for the case of $n = 1$. In this particular model, the corner joints are assumed to have different behaviour and are thus labelled as independent panels.

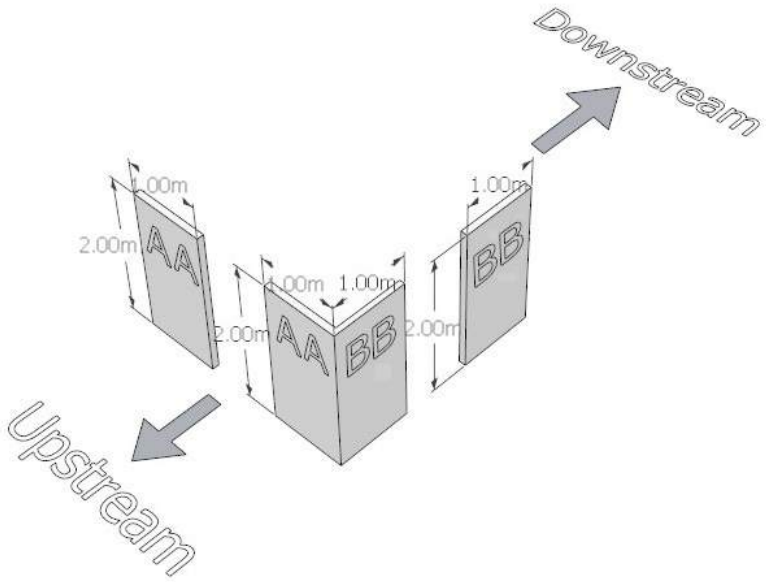

Figure 3.3: Simplified base panel model for small masonry structures

The further simplified model consists of two base panels, **AA** and **BB**, illustrated in Figure 3.3. The differences between the breakage mechanisms and subsequent debris distribution of two connected **AA** panels, or two connected **BB** panels are expected to be linearly proportional. For example, linear relationships are expected to relate

the maximum debris throw and surface area covered by one base panel to the maximum debris throw and surface area covered by n base panels of the same type, subject the same blast conditions; however, the effects on the debris distribution of a panel constructed from an **AA** panel and a **BB** panel would differ drastically compared to its individual constituents, due to the increased dimensionality and subsequent strengthening of the panel. For this reason, the full base panel model, shown in Figure 3.2, which treats corner joints as independent base panels will be implemented. The hypothesis being that the potentially standardised breakage and debris distribution of any individual base panel will require simple, linear, proportional modifications to estimate the resulting breakage and debris distribution when combined with one or more base panels; thus allowing for an approximation of the effects on a large quantity of simple masonry structures. The simplest, enclosed structure is displayed in Figure 3.4.

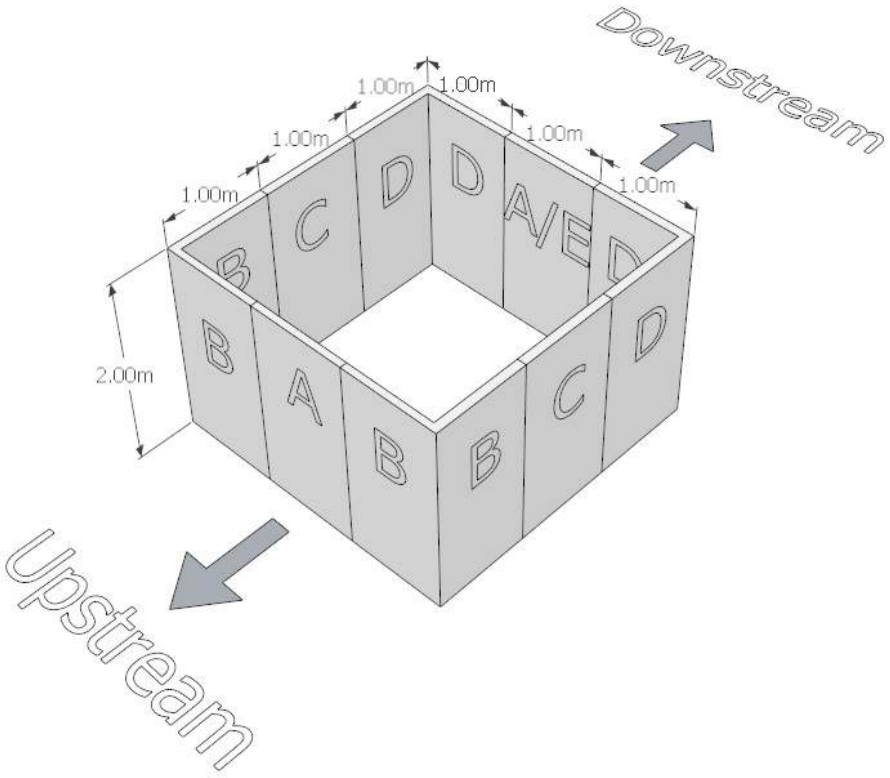

Figure 3.4: Simple masonry construction using the base panel model

This structure utilises each of the base panels at least once to form a simple, square masonry building with dimensions 3m×3m×2m. In this particular example the central,

rear panel displayed in Figure 3.4, is labelled as **A/E**. Whilst this is in fact a simple **A** panel, the shielding effects from the front face of the structure have an effect on the mechanism by which it is loaded. In the absence of vertical restrictions to blast in-fill effects, the **A/E** panel will experience reduced pressure, turbulent blast loading to its interior, upstream face. In the presence of vertical in-fill restrictions such as a roof, the interior, upstream face of the **A/E** panel will only experience the blast as a result of failure from the front wall, thus allowing the blast wave to enter the structure. In both cases, the rear, downstream face of the **A/E** panel will experience loading from the downstream direction resulting from the wrap around pressures of the blast wave. The panel is not explicitly labelled as an **E** panel as it cannot be tested experimentally in isolation. The **D** panel is given an explicit label as it can be used on the front face of masonry structures as a facing corner and thus can be tested in isolation.

Assessing the breakage patterns and debris distribution of each panel in isolation and in a variety of combinations, both experimentally and computationally will provide a robust data set on which to being development of a set of predictive algorithms.

3.2 High Explosives Trials

The experimental trials form the basis for the entire research project, offering new results pertaining breakage mechanisms and debris distribution of masonry structures subjected to varying blast loads. First hand experimental data is not only a powerful resource in isolation, but when used to benchmark a computational modelling routine it provides the potential to develop a well calibrated model. Due to the obvious safety precautions and restricted access to explosive materials, blast trials are an unique commodity and conducted almost exclusively in the UK by the Ministry of Defence (MoD). The experimental trials conducted for this research project make use of testing facilities operated and owned by the UK MoD and the Atomic Weapons Establishment (AWE); with an estimated cost of approximately £125,000 per test, it is vital that the experimental programme is designed not only to maximise the quantity of obtainable data, but to obtain comparable data sets which can be easily extended and further developed. As discussed in

Section 3.1, this research project adopts the 'Base Panel' model with a view to predicting the breakage and debris distribution of a variety of masonry geometries.

The interaction of long duration blast and structures is a more complex system than typical short duration blast. The computational tools used to assess long duration blast loading were primarily designed for use with typical HE blast loading. Firstly, to ensure the computational tools are appropriate for use with long duration blast loads, they must be benchmarked against conventional HE blast loads.

The HE trials were conducted at the Windrush Arena, located at MoD Shoeburyness, Foulness Island and is displayed in Figure 3.5.

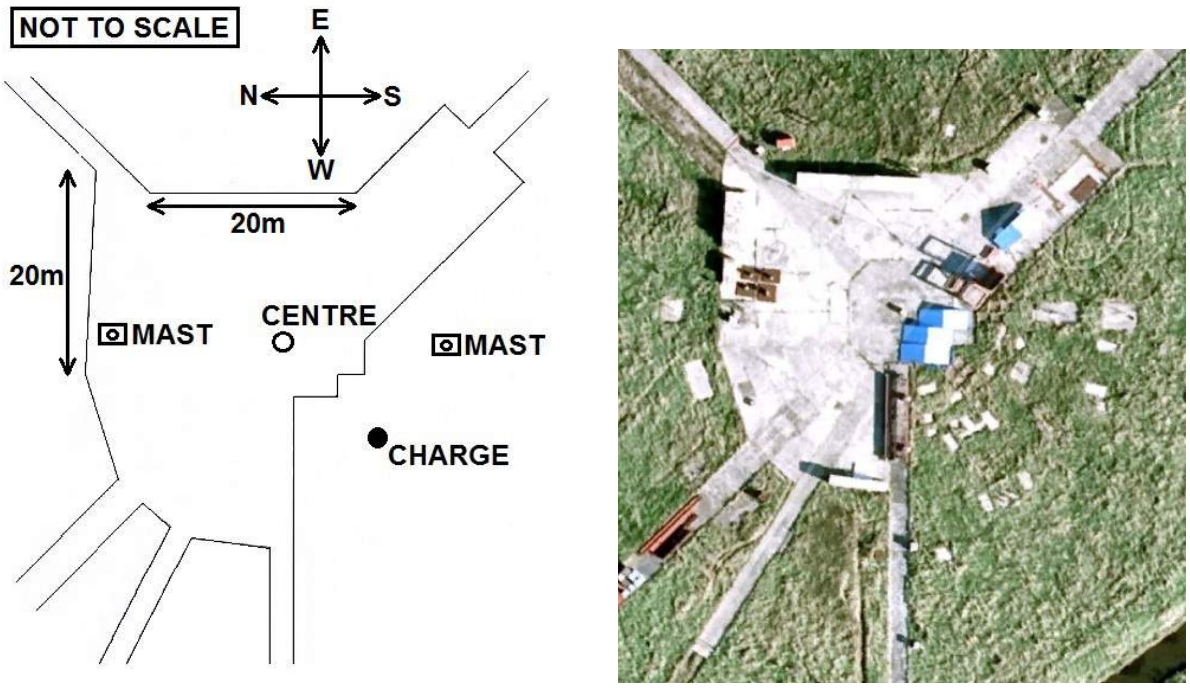

(a) Outline Sketch (b) Satellite View

Figure 3.5: The Windrush Arena

The Windrush Arena was designed for HE charges up to 500kg TNT equivalence, with the geometry incorporating five radial spokes, all of which intersect the central point which is marked in Figure 3.5a between the two instrumentation masts; however, the charge location is marked off of the right hand side of the arena. The HE trials conducted for this research project were part of a collaborative effort between two other researchers, which resulted in the arena being heavily instrumented. The outer, Eastern side of the arena was occupied by two steel ISO containers with annealed glass mounted on

the blast normal face as part of an investigation into low pressure blast effects on glazing breakage, conducted by Robert Johns; the area closest to the charge was occupied by hardened steel boxes as part of an investigation into synergistic thermal and blast effects on steel, conducted by Laurence Clough. To ensure that each test item, for all three of the simultaneous experiments, achieved the appropriate blast parameters, without interference from other structures, the charge location was altered to satisfy the required criteria for all experiments. Further details of the HE trial parameters are discussed in Section 3.5 and were presented at the 15th International Symposium for the Interaction of the Effects of Munitions with Structures [84].

3.3 Long Duration Trials

The nature by which long duration blast waves are produced requires large amounts of explosives, in excess of 30T TNT equivalence, which is both highly impractical and expensive. The Air Blast Tunnel (ABT), located at MoD Shoeburyness, Foulness Island, is a ≈200m long shock tube designed to replicate long duration blast events and is displayed in Figure 3.6. The ABT is the UK's nuclear blast simulator and has been used for a variety of roles since 1964, including nuclear blast hardening testing, fire-blast interaction, structural response and debris generation studies [85]. The ABT generates long duration blast waves by detonating PETN detcord, located in the narrow, 1.8m section of the tunnel as illustrated in Figure 3.6c, which is wound using a special former to produce a specific blast with non-uniform reflections. The tunnel is designed as a large shock tube with pre-calculated radial expansions, which in combination with the initial blast reflections increases the blast wavelength and hence duration, whilst maintaining high overpressures. The current maximum operating threshold of the ABT utilises 100m of PETN detcord with a net explosive quantity (NEQ) of 4kg TNT equivalence, generating near field overpressures in the region of 3MPa. Within the two instrumentation sections, displayed in Figure 3.6c, the maximum blast parameters can be attributed to approximately 450T TNT equivalence at a stand-off distance of 240m and 200T TNT equivalence at a stand-off distance of 250m in the 4.9m and 10.2m sections respectively.

These approximations were calculated using the Kingery and Bulmash polynomials [86]. At the mouth of the ABT is a Rarefaction Wave Eliminater (RWE), shown in Figure 3.6c, which consists of two rows of staggered scaffold poles, allowing the ABT to vent the blast wave whilst restricting reflections back into the tunnel and minimising the effects of the negative phase. To ensure the ABT can properly vent the blast wave, neither section can be instrumented such that it restricts more than 33% of the cross sectional area of that particular section, which is approximately 13.6m^2 and 5.7m^2 for the 10.2m and 4.9m sections respectively.

(a) Illustrating the RWE, viewing West

(b) Satellite view

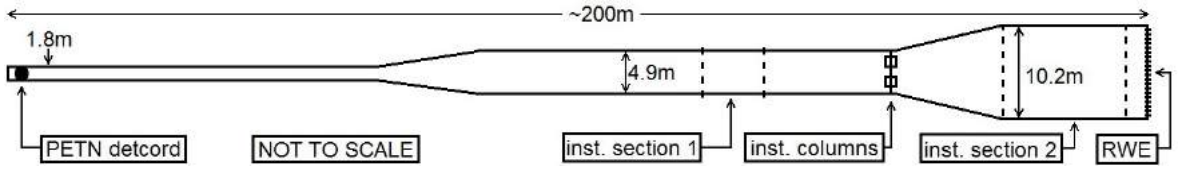

(c) Outline sketch

Figure 3.6: The Air Blast Tunnel

3.4 'MW' Series

The first set of trials, designated the 'MW Series,' were conducted at the very beginning of the research project, the results of which were presented at the 16th International Symposium on the Interactions and Effects of Munitions and Structures [87]. The first

trial, MW1, subjected an unmortared brick wall to a long duration blast load in the 4.9m section of the ABT, with a target overpressure and positive phase duration of approximately 110kPa and 200ms respectively. This trial was designed before the beginning of the research project and so its construction does not meet all the parameters of the base panel model; however, it's (x,y,z) dimensions 0.1m×1m×2m, match those of the standard **A** panel of the base panel model. The trial was initially designed to investigate brick velocities in the absence of any bonding agent; furthermore, this trial provides valuable insight into the subsequent debris distribution of unrestrained bricks. The wall was constructed from unmortared Class B engineering bricks, each with dimensions 10mm×210mm×65mm, a mass of ≈3.2kg and a maximum compressive strength of approximately 9.5Nmm^{-2}. The bricks were stacked in alternating rows of 5 whole bricks followed by 4 whole bricks and two half bricks for 31 rows, totalling 140 whole bricks and 30 half bricks, with an estimated mass of ≈511kg. Figures 3.7a and 3.7b show the MW1 structure pre-shot, from the upstream and downstream perspectives respectively. The wooden frame was used for construction and support purposes and was removed before the time of firing.

(a) Upstream perspective (b) Downstream perspective

Figure 3.7: Pre-shot images of structure 'MW1'

The trial was instrumented using two high speed phantom cameras recording at

5,000fps, one located upstream from the wall, shown in Figure 3.8a and one at an off-set, side on position, shown in Figure 3.8b. The cameras were mounted in hardened steel containers to both shield the cameras from the blast wave and reduce vibrations. The static, dynamic and reflected pressure time histories were recorded using Endveco-8510, Kulite-20D and Kulite-LQ125 pressure transducers, displayed in Figures 3.9a, 3.9b and 3.9c respectively. The phantom cameras, lighting arrays, pressure transducers and detonator were all connected to a sequencer to ensure all data was properly recorded at the correct time interval. Radial 1m intervals were marked in the longitudinal, x direction, along the ABT's main axis to aid in the post-shot debris collection. Finally, the upstream face of the wall was painted white to increase the contrast of the high speed photography and each brick was given a unique number, relating to its original position within the structure. Figure 3.10 displays the full MW1 trial schematic from both a plan (x,y) and cross sectional (z,y) perspective, indicating the relative positions of the full instrumentation array. For all experimental trials, each individual structure is assigned a unique structure ID (SID), as the MW1 trial tested only one structure, it was assigned the SID MW1.

(a) Side-on position (b) Upstream position

Figure 3.8: Phantom camera & lighting array for the MW series

(a) Endveco-8510 (static) pressure transducer (b) Kulite-20D (dynamic) pressure transducer (c) Kulite-LQ125 (reflective) pressure transducer at base

Figure 3.9: Pressure transducers instrumented for the MW series

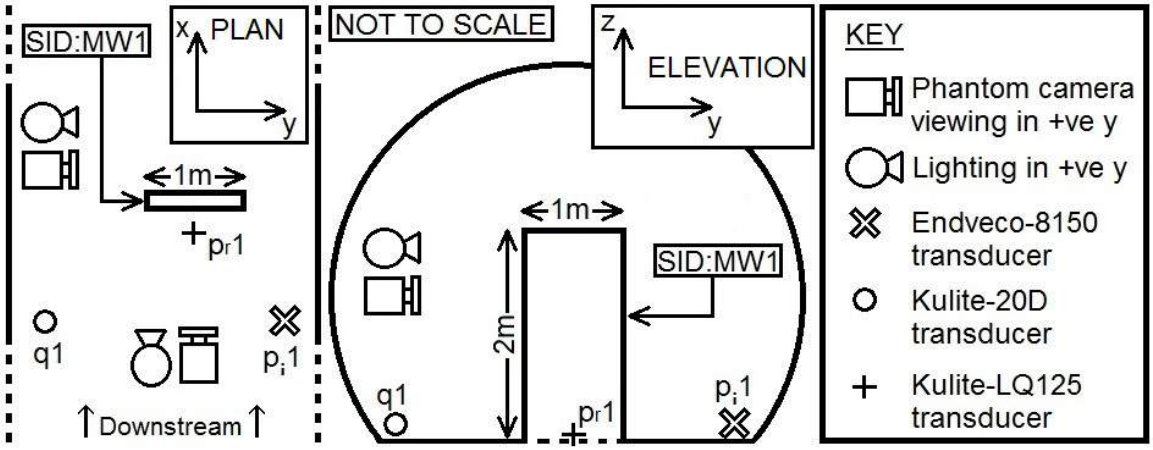

Figure 3.10: Plan and cross sectional views of trial 'MW1.' Full schematic indicating positions of pressure transducers and phantom cameras

The second trial in the MW series, MW2, was designed and instrumented directly after the MW1 trial to investigate the effects of mortar on brick velocities and debris distribution. MW2 shares the same geometry as MW1 with (x,y,z) dimensions of 0.1m×1m×2m. The structure was built from frogged, facing London bricks with dimensions 10mm×210mm×65mm, a mass of ≈2.1kg and a maximum compressive strength of 40-60Nmm^{-2}, joined by a class (ii) mortar in accordance with BS:5628-1:2005 [88], with a tested compressive strength of 8-10Nmm^{-2}, joined in a 10mm bedding. Each row of

bricks consisted of 4 whole bricks and 1 half brick, with 27 rows of bricks and a total of 108 whole bricks and 27 half bricks. The total mass of the bricks was therefore ≈268kg, the total mass of the mortar cannot be estimated to the same degree, due to the its non uniform application density, resulting from the different fill fractions of each frog. As with MW1, 1m radial markers were placed in the longitudinal, x, direction along the ABT's main axis. The upstream face of the wall was painted for higher contrast imaging and each brick was given a unique number relating to its original position within the structure. The MW2 structure is shown pre-shot from the upstream and downstream perspectives in Figures 3.11a and 3.11b respectively.

(a) Upstream perspective (b) Downstream perspective

Figure 3.11: Preshot images of structure 'MW2'

The instrumentation array for MW2 remained unchanged to that of MW1 with the exception of the lighting. Although the position and angle of the lighting remained the same, the lamps themselves were changed, providing slightly more luminosity. The full schematic for trial MW2 is displayed in Figure 3.12, detailing the position of the full instrumentation array from both the plan (x,y) and cross-sectional (z,y) perspectives. Table 3.1 highlights the key experimental parameters for both the MW1 and MW2 trials.

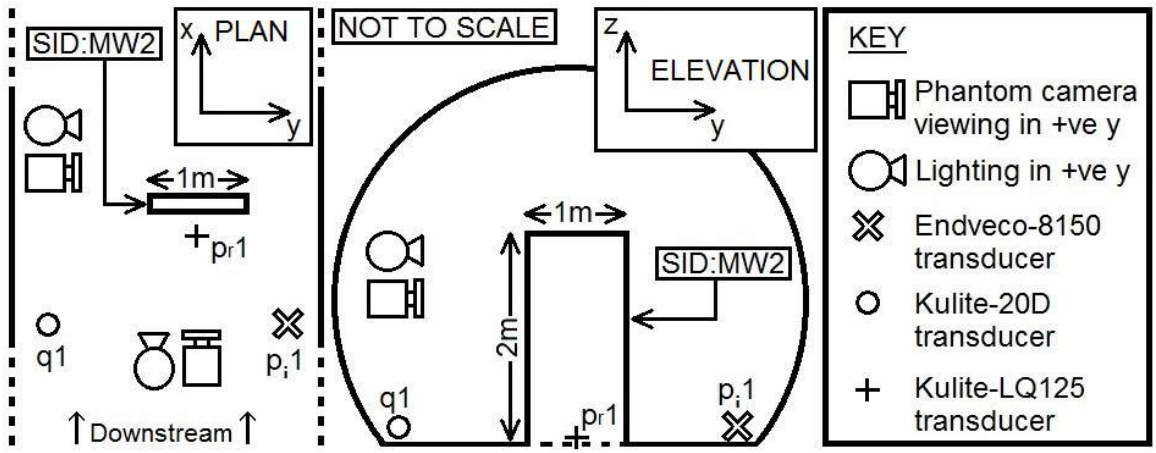

Figure 3.12: Plan and cross sectional views of trial 'MW2.' Full schematic indicating positions of pressure transducers and phantom cameras

Table 3.1: Summary parameters for the MW series

SID	Type	Mortared	m_{brick}	Sampling	Target		Cameras	
					p_i	t^+	Upstream	Side
MW1	-	×	≈3.2kg	p_i, p_r, q	110kPa	200ms	✓	✓
MW2	**A**	✓	≈2.1kg	p_i, p_r, q	110kPa	200ms	✓	✓

3.5 Windrush Arena Series

The second series of trials conducted for this research project, designated the 'Windrush Arena Series,' consisted of two HE trials using the historically named Windrush Arena. Following the MW series, the base panel model was designed to maximise the application of data from all future trials. Whilst the development of the base panel model was independent of the MW series, the dimensions of structure MW2 were implemented as the dimensions of the **A** panel. As discussed in Section 1, the (y,z) dimensions 1m×2m of the **A** panel allow for implementation of integer height to width ratios; furthermore, assigning the dimensions of MW2 to the **A** panel increases the value of the pre-existing data within the new model. The base panel model also assumes that the material parameters are to remain constant across each individual panel; therefore the material parameters of the MW2 trial were defined as the fixed parameters for all future trials.

The Windrush Arena Series was originally commissioned to provide first hand exper-

imental results on which to benchmark the computational modelling routine; the trial design was tailored to achieve direct comparissons between long and short duration blast loads. Each of the Windrush Arena trials instrumented five masonry panels from the base panel model. The charge size and stand-off distance of the individual panels was designed to achieve a range of pre-calculated overpressures. Both trials utilised 39kg of TNT-Flake, initiated by 2×1kg PE-4 booster charges, equating to a total NEQ (net explosive quantity) and TNT equivalence of 41kg. The first HE trial, designated 'WR1,' instrumented five **A** panels at varying stand-off distance to investigate the ability of the computational routine to model breakage. The stand-off distances were fixed at 10.6m, 13m, 15m, 19.5m and 36m to achieve peak static overpressures of 110kPa, 72kPa, 55kPa, 35kPa and 14kPa respectively, which were determined to match specific parameters. 110kPa and 55kPa match the current maximum operating envelope of the ABT in the 4.9m and 10.2m sections respectively; thus providing a direct comparison of the effects of the high impulses and drags winds associated with large positive phase durations. The 13m radial, corresponding to a peak static overpressure of 72kPa, offers a clear midpoint between the 10.6m and 15m radials. The 19.5m radial, corresponding to 35kPa is around the breakage limit of masonry and thus tests the ability of the computational routine to model the boundary case scenario. At the 36m radial, corresponding to 14kPa, the blast load is not high enough to cause any breakage, even to an inherently weak structure such as the basic **A** panel; thus providing a no-break scenario to model.

(a) WR1A (b) WR1B (c) WR1C (d) WR1D (e) WR1E

Figure 3.13: Preshot images of all structures from trial 'WR1'

A 500mm×500mm grid was painted around each structure to aid in the debris collection process and each brick was given a unique number relating to its original position within the structure. Figures 3.13a, 3.13b, 3.13c, 3.13d and 3.13e show pre-shot images of structures with SID: WR1A, WR1B, WR1C, WR1D and WR1E respectively from trial WR1. The support straps were removed before firing.

For short duration HE blast loading, the effect of drag wind and its associated dynamic pressure is low, hence no dynamic pressure gauges were instrumented for either of the Windrush Arena trials; furthermore, no reflective pressure gauges were available. Two radial spokes of Endveco-8510 static pressure transducers were instrumented to gauge the blast propagation across different sections of the arena; the radial spokes were separated by a relative angle of 45°. The pressure transducers were protected using metallic disks with one pressure gauge at each radial point of interest, that is 10.6m, 13m, 15m, 19.5m and 36m. The radial spokes were denoted p_i1 and p_i2 and can be seen in Figures 3.14a and 3.14b respectively, each gauge was given a unique gauge ID (GID) based on it's position.

(a) p_i1 radial. Showing GID: p_i1(A-E)

(b) p_i2 radial. Showing GID: p_i2(A-D)

Figure 3.14: Endveco-8510 pressure transducer radial spokes for the Windrush Arena Series

(a) Downstream position (b) Side on / off-set position

Figure 3.15: Phantom camera instrumentation for the Windrush Arena Series

As the Windrush Arena trials were a collaborative effort, only two phantom cameras were available, both cameras were mounted in hardened steel containers for blast shielding and recording at 2,000fps. The first camera, shown in Figure 3.15a, viewed structure WR1A from the downstream perspective. The other camera, shown in Figure 3.15b, captures an off-set perspective of all structures except WR1C. Figure 3.16 displays a full plan schematic of trial WR1 indicating the relative position of each structure and their unique SID's and the relative positions the full instrumentation array. Table 3.2 displays the relevant instrumentation information for each individual structure implemented for trial WR1.

Table 3.2: Instrumentation for Windrush Arena trial 'WR1'

SID	Type	r	$\theta_{relative}$	Target p_i	Gauge ID	Cameras	
						Downstream	Offset
WR1A	**A**	10.6m	0°	110kPa	p_i1A, p_i2A	✓	✓
WR1B	**A**	13m	333°	72kPa	p_i1B, p_i2B	×	✓
WR1C	**A**	15m	313°	55kPa	p_i1C, p_i2C	×	×
WR1D	**A**	19.5m	19°	35kPa	p_i1D, p_i2D	×	✓
WR1E	**A**	36m	296°	14kPa	p_i1E, p_i2E	×	✓

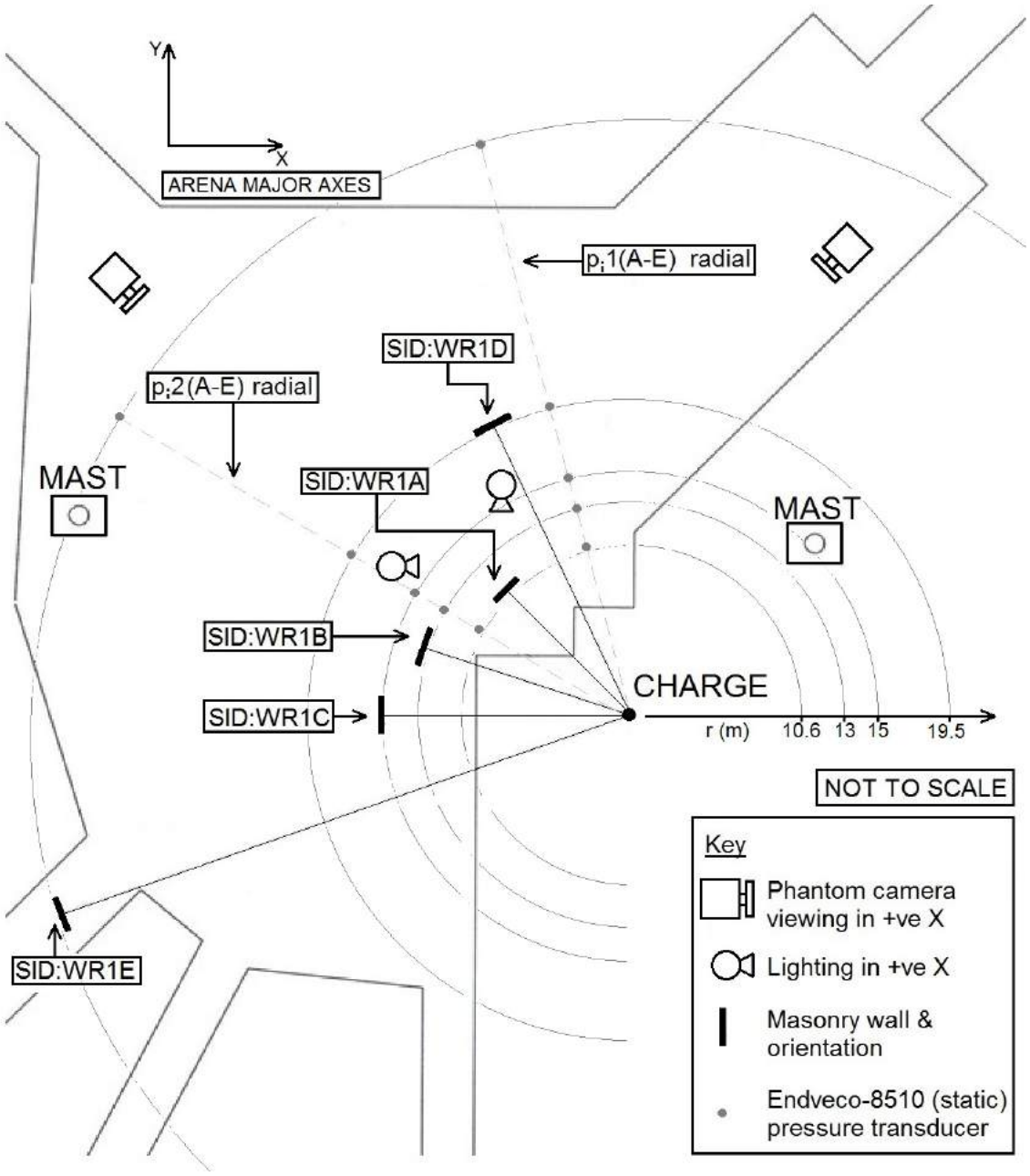

Figure 3.16: Plan view of Windrush Arena trial 'WR1.' Full schematic indicating the position and orientation of each test item, pressure transducers and phantom cameras.

The aim of the second HE trial, designated 'WR2,' was to increase the standard short duration blast data set, for application to both computational benchmarking, investigating geometrical effects on structural failure and later comparison to long duration blast data. To achieve this, WR2 utilised the same explosive charge which consisted of 39kg TNT-Flake boosted by 2×1kg PE-4 charges with a NEQ and TNT equivalence of 41kg. Keeping the radial stand-off distances constant whilst varying the base panels and hence

geometry, offered direct comparative data between the two HE trials and provided an increased set of HE data, for use with both computational benchmarking and comparison to long duration blast.

From the WR1 trial, the 19.5m and 36m radials, which corresponded to peak static overpressures of 35kPa and 14kPa respectively, were designed as the boundary and non-responding cases. It was not necessary to retest non-responding scenarios; thus in the absence of the two low pressure radials, additional structures were implemented at the higher pressure radials. Firstly, the structure WR1C had to be rebuilt one week before the firing of the WR1 trial, resulting in a decreased compressive strength in the mortar. This structure was a vital element as it was the short duration test of the **A** panel at an equivalent pressure to the 10.2m section of the ABT at 55kPa. This structure was retested in the WR2 trial with SID WR2C, which additionally offered first hand data comparing the effects of the compressive strength of mortar to structural failure. Whilst the **C** panel could be tested in isolation, the results would not necessarily offer useful data and was discarded for the HE tests. The **B** panel is a vital structural element and understanding how corner panels affect the breakage of structures is a key aspect in the model development. Three **B** panels were tested; WR2A, WR2D and WR2E, at the 10.6m, 13m and 15m radials corresponding to 110kPa, 72kPa and 55kPa respectively. Finally, a **D** panel, with SID WR2B, was tested on the 10.6m radial; this offered first hand data on the **D** panel subject to short duration blast, comparable to the pressure regime of the 4.9m section of the ABT; furthermore, as a rotation of the **B** panel, the data offers insight into the failure modes of the corner panels.

The instrumentation array for the WR2 trial remained unchanged from the WR1 trial. The two radial spokes, p_i1 and p_i2, remained fixed in place between both trials; however with test items placed only on the 10.6m, 13m and 15m radials, only gauges p_i1(A-C) and p_i2(A-C) recorded relevant pressure data. The camera positions and frame rates remained unchanged; however the relative positions of the test items were changed such that WR2B was recorded from the downstream position and the offset camera captured structures WR2A, WR2B, WR2C and WR2E. 500mm$\times$500mm grids were marked around

each structure for debris collection purposes and each structure was painted for easy identification. Originally, each 1m panel of the corner structures was to be painted a different colour; however the structures were painted shortly before firing and the colour scheme was misinterpreted. Each brick was given a unique number relating to its original position in the wall, thus despite an incorrect colour scheme, the distribution of each 1m panel can still be examined.

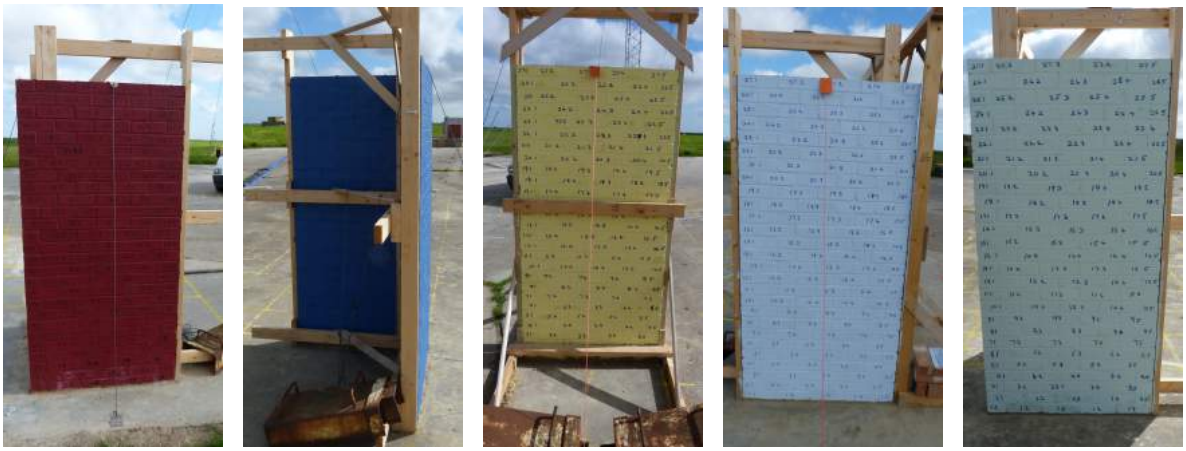

(a) WR2A (b) WR2B (c) WR2C (d) WR2D (e) WR2E

Figure 3.17: Preshot images of all structures from trial 'WR2,' taken from the upstream perspective

(a) WR2A (b) WR2B (c) WR2C (d) WR2D (e) WR2E

Figure 3.18: Preshot images of all structures from trial 'WR2,' taken from the downstream perspective

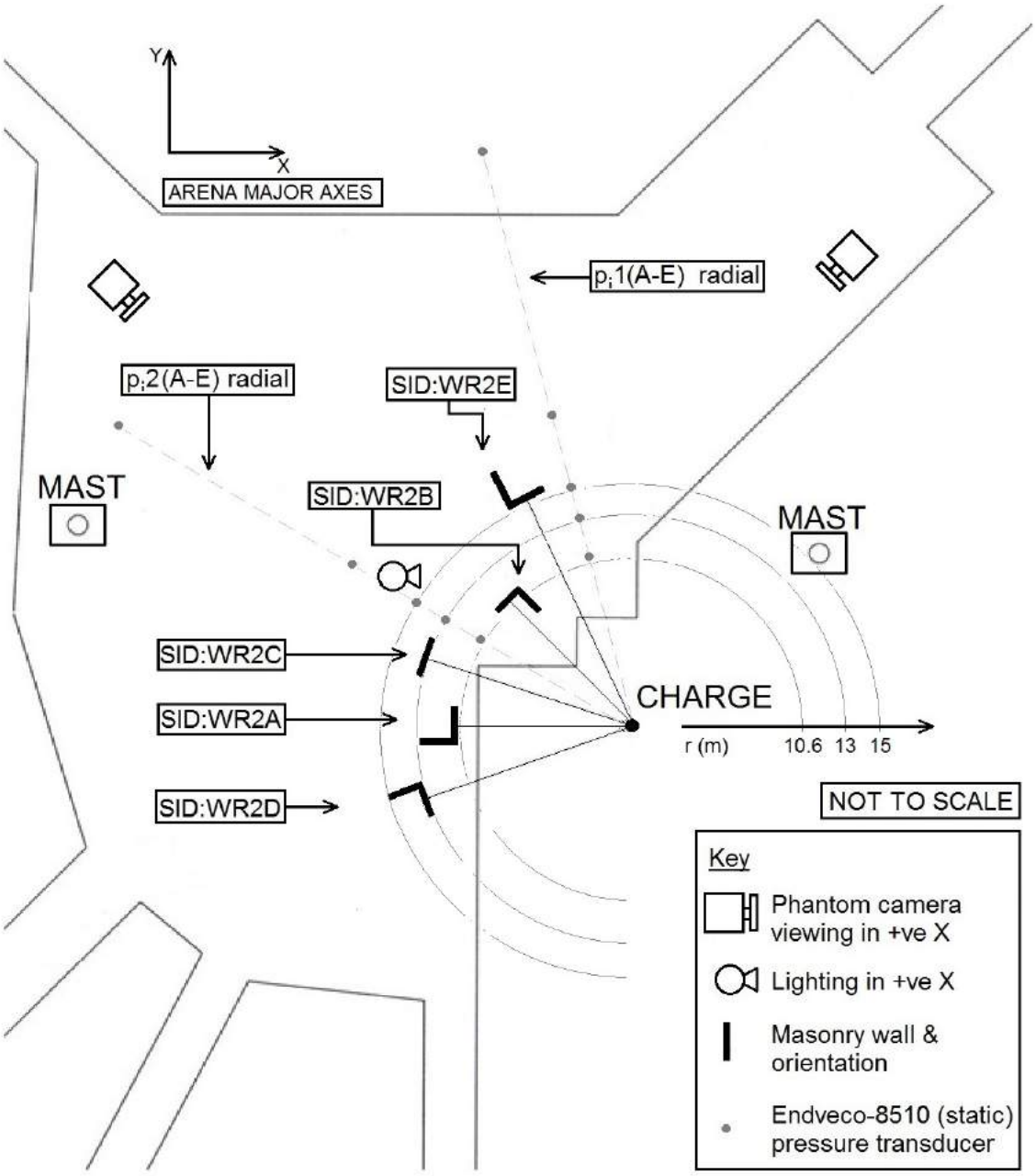

Figure 3.19: Plan view of Windrush Arena trial 'WR2.' Full schematic indicating the position and orientation of each test item, pressure transducer and phantom cameras.

Table 3.3: Instrumentation for Windrush Arena trial 'WR2'

SID	Type	r	$\theta_{relative}$	Target p_i	Gauge ID	Cameras	
						Downstream	Offset
WR2A	**B**	10.6m	0°	110kPa	p_i1A, p_i2A	×	✓
WR2B	**D**	10.6m	315°	110kPa	p_i1A, p_i2A	✓	✓
WR2C	**A**	15m	334°	55kPa	p_i1C, p_i2C	×	×
WR2D	**B**	13m	298°	72kPa	p_i1B, p_i2B	×	✓
WR2E	**B**	15m	20°	55kPa	p_i1C, p_i2C	×	✓

Pre-shot photos from all structures in the WR2 trial are shown from the upstream and downstream perspectives in Figures 3.17 and 3.18 respectively. Table 3.3 highlights the key instrumentation parameters for all structures from the WR2 trials and Figure 3.19 shows a full plan schematic of trial WR2, detailing the relevant structural positions and orientations and the position of the full instrumentation array. Finally, Table 3.4 presents a summary of the target blast parameters for all structures in the Windrush Arena Series, in which r is the radial distance, Z is the scaled distance, p_i is the peak static overpressure, p_r is the peak reflective pressure, I_i is the static impulse, I_r is the reflective impulse, t_a is the shock arrival time, t^+ is the positive phase duration and U is the blast wave velocity.

Table 3.4: Windrush Arena series: Summary target parameters

	SID:(WR)									
	1A	**2A**	**3A**	**4A**	**5A**	**1B**	**2B**	**2C**	**2D**	**2E**
Panel type	**A**	**A**	**A**	**A**	**A**	**B**	**D**	**A**	**B**	**B**
r (m)	10.6	13	15	19.5	36	10.6	10.6	15	13	15
Z (m)	3.07	3.77	4.35	5.66	10.44	3.07	3.07	4.35	3.77	4.35
p_i (kPa)	110	72	55	35	14	110	110	55	72	55
p_r (kPa)	310	186	134	79	29	310	310	134	186	134
I_i (kPa.ms)	313	262	231	183	103	313	313	231	262	231
I_r (kPa.ms)	752	595	506	378	196	752	752	506	595	506
t_a (ms)	12.8	18.1	22.9	34.2	78.9	12.8	12.8	22.9	18.1	22.9
t^+ (ms)	10.0	11.4	12.3	13.7	16.7	10.0	10.0	12.3	11.4	12.3
U (ms^{-1})	470	430	410	390	360	470	470	410	430	410

3.6 'BWL' Series

The 'BWL' trial series was the largest and most important series of trials conducted for this research project. Three trials, designated BWL1, BWL2 and BWL3, were designed to complement the results achieved from both the MW and WR series whilst acquiring as much data as possible to further develop the base panel model. Each of the BWL trials were instrumented in the ABT and utilised 100m of wound PETN detcord, with a NEQ of 4kg, to achieve the maximum obtainable overpressures. Both sections of the ABT were instrumented to maximise the data obtained from each firing. The target pressure of 110kPa and positive phase duration of 200ms in the 4.9m section of the tunnel corresponds to approximately 450T TNT equivalence at a stand-off distance of

240m and the target overpressure of 55kPa and positive phase duration of 150ms in the 10.2m section correspond to approximately 250T TNT equivalence at a stand-off distance of 200m [86].

To achieve enough varied data to develop the base panel model, experimental data investigating the results of both individual base panels and composite structures subjected to long duration blast were required. The most basic and important panels were the **A** and **B** panels and it was imperative that these panels were instrumented in both the 10.2m and 4.9m sections. The **D** panel was implemented in the WR2 trial as WR2B, which was subjected to a short duration overpressure of 110kPa. Instrumenting a **D** panel in the 4.9m section of the ABT provided the opportunity to directly compare results. Testing structures comprised of multiple base panels not only provides valuable data allowing predictions to be made for larger structures, but it demonstrates the different behaviour of each individual panel when connected to any other panel. Using small composite base panels provides important data to understanding the direct effects of basic structural geometry on both breakage and debris distribution.

Larger structures utilise more base panels and hence provide more data; however with limited space in the ABT, only one large structure could be tested in each BWL trial. In the absence of a roof, rectangular structures experience blast in-fil from above; this has a significant effect on the breakage of the structure, as the side and rear walls are loaded from the inside. The BWL trials were required to test large enclosed structures, in the absence of blast in-fill, but without an attached roof. The original solution was to mount a steel cover on support columns over the top of the structure to stop blast in-fill. Within the confines of the ABT and subject to the extreme conditions which it creates, this initially proved a challenging obstacle. A simple solution would be to secure a steel roof in place over the structure, mounted on support columns such that no contact with the top of the masonry wall is made. Considering the dimensions of the smallest square structure utilising each individual base panel would be 3m×3m, the minimum required area of the steel column would be 4m×4m, to ensure there is minimal interference with structural response. Under turbulent, long duration blast loading, such a cover would

oscillate dramatically, applying hammer effects to the top of the structure, illustrated by Figure 3.20; thus interfering with the response.

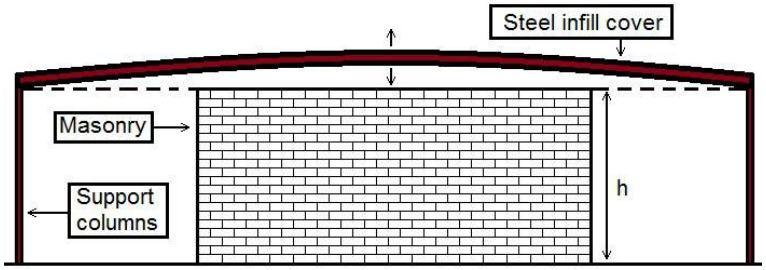

Figure 3.20: Illustration of blast induced hammer effects (viewing along axis of blast propagation)

The solution was to implement the rectangular structures with half symmetry along the ABTs main longitudinal axis, i.e. in the blast direction. Half symmetric rectangular structures have an exposed side which is vulnerable to blast in-fill; however, blocking this with a large steel structure designed to support the roof, both reduces hammer effects and blast in-fill from above and from the side.

A steel enclosure was designed, with plan (x,y) dimensions of 4m×4m, to cover one structure per trial with plan dimensions ranging from 3m×1.5 to 4m×2m. The main support section was constructed from 20mm steel plates, bolted to the ground and spanning 1m laterally and the entire 4m length longitudinally. The support section was hollow and used to mount four phantom cameras, two recording the breakage inside the enclosed structure and two recording the other structure(s) in the 10.2m section. The hollow interior, shown in Figure 3.21b, provided excellent blast shielding for the phantom cameras and allowed access to the interior of the masonry structures once they had been built. Apertures were also cut into the roof of the structure, displayed in Figure 3.21c, to allow the lighting array to cover all areas of the interior. The roof of the steel enclosure was constructed from a single 4m×4m sheet of 20mm steel, secured to three scaffold poles, spaced at 2m intervals and bolted in place by three I-beams from above to resist the blast wave. The corners of the roof were further secured to the ground by steel cables; Figure 3.21a displays the steel enclosure securely fixed in place.

(a) Downstream perspective

(b) Interior

(c) Upstream perspective & appetures

Figure 3.21: Steel enclosure for the large masonry structures instrumented in the BWL series

Each of the BWL trials was instrumented with seven fixed phantom cameras, each recording at 2,000fps; additional cameras were used in each trial with positions and perspectives varying between each trial. As with the MW series, two cameras were fixed in the 4.9m section, both mounted in hardened steel boxes, one positioned upstream from the structure, recording in the downstream direction, shown in Figure 3.22c and one positioned side-on from the structure, recording in the side-on direction, shown in Figure 3.22d.

As previously mentioned, the hollow interior of the support section of the steel enclosure was used to mount 4 phantom cameras, displayed in Figure 3.22b; two of which were used to record the interior of the large, enclosed structure from the side-on perspective. As the structural dimensions ranged from 3m×1.5m to 4m×2m, one camera was not enough to record the entire interior of the structure. To cover a large range over a short distance, both of these cameras used wide angle, 14mm lenses. The other two cameras located in the interior of the steel enclosure, recorded the other structure(s) in the 10.2m section from the side-on perspective; this allowed a larger range of in-flight debris to be recorded. Finally, two phantom cameras, mounted in hardened steel boxes, were positioned in the 10.2m section, upstream from the large enclosed structure and other structure(s), viewing in the downstream direction and are displayed in Figure 3.22a.

As with all previous trials, each phantom camera was accompanied by one or more lights. The 10.2m section instrumented a total of eleven lighting arrays; four mounted on the roof of the steel enclosure, lighting through apertures in the roof, two lighting

(a) 10.2m (upstream)

(b) 10.2m (enclosure interior, capturing side-on)

(c) 4.9m (upstream)

(d) 4.9m (side-on)

Figure 3.22: Fixed phantom cameras capturing all three trials from the BWL series, indicating ABT section and recording perspective

(a) Above the steel enclosure, lighting inside

(b) 10.2m section rear lighting

(c) 10.2m section front lighting

Figure 3.23: Sample set of the fixed lighting array for the BWL series

(a) p_i1 & q1 (b) p_i3, p_i4 & p_i5 (c) p_r1

Figure 3.24: Sample set of the fixed static, dynamic and reflected pressure gauges used for the BWL series

the front, most upstream faces of each structure, two lighting the rear of the enclosed structure and three lighting the rear of the other structure(s). As with the MW series, the 4.9m section instrumented two lighting arrays, one positioned upstream from the structure lighting the front (blast normal) face, and one positioned side on. Selections from the lighting array are displayed in Figure 3.23.

A total of six Endveco-8510 pressure transducers, four Kulite-20D pressure transducers and two Kulite-LQ125 pressure transducers were instrumented to record the static, dynamic and reflective pressures respectively and assigned unique gauge GID's p_i(1-6), q(1-4) and p_r(1-2). In the 4.9m section, a single set of static and dynamic pressure transducers were placed in-line with the front, most upstream face of the structure, accompanied by a reflective pressure gauge mounted on a steel plate, bolted to the ground. In the 10.2m section, three static pressure transducers were placed at 1m intervals along the central, longitudinal axis of the ABT, displayed in Figure 3.24b, to gauge the static pressure along the centre of the ABT. A single dynamic pressure gauge was also instrumented along the central axis, accompanied by a reflective pressure transducer mounted on the front face of the steel enclosure, shown in Figure 3.24c. Finally, both edges of the

10.2m section were instrumented with a set of static and dynamic pressure gauges, positioned in-line with the front, most upstream face of the respective structures to gauge the various pressures as close to the structures as possible; one such set displayed in Figure 3.24a.

The first trial in the BWL series, designated BWL1, instrumented three structures with unique SID's BWL1A, BWL1B and BWL1C. The first of these structures, BWL1A, was an effective repeat of the MW2 trial; that is, an **A** panel with (x,y,z) dimensions of 0.1m×1m×2m was positioned in the 4.9m section of the ABT. As the number of available experimental trials was limited, repeating specific trials to obtain variance would sacrifice the required data set. BWL1A was the only repeated long duration blast trial and was conducted to observe experimental variance between two schematically identical trials, to determine an acceptable level of accuracy within the computational models. The structure was painted with each brick given a unique number relating to its original position within the structure and the pre-existing 1m radial, longitudinal markers were used for debris collection purposes.

Structure BWL1B, was a composite **AB** panel, with max (x,y,z) dimensions of 1m×2m×2m, placed in the 10.2m section of the ABT. This geometry is constructed by the two most important base panels and provided crucial information relating to the effects of basic geometric alterations on both breakage and debris distribution. Each 1m (x,y) section of the structure was painted a different colour, each brick was assigned a unique number relating to its original position within the structure and 500mm×500mm grids were painted around the structure for assistance with the debris collection.

The final test item, BWL1C which utilised the large steel enclosure, was a 4m×1.5m×2m half rectangular structure. This geometry was designed to investigate the effects of greater depth than width, which as discussed in Section 2 experiences delayed equalisation of the reflective pressure. The structure was aligned against the edge of the steel enclosure without any physical attachments to interfere with the breakage. The top of the structure was approximately 10mm lower than the roof of the steel enclosure; to ensure there would be no blast in-fill and minimal hammer effect, without physically fixing the wall

to the enclosure, vinyl strips were placed on top of the structure and the gap was sealed using expanding foam. The front and rear faces of the structure, being 1.5m wide, were painted a single colour, with each 1m section of the side wall painted a different colour. Each brick was given a unique number relating to its original position in the wall and a 500mm×500mm grid was painted around the structure for debris collection purposes.

Structures BWL1A, BWL1B and BWL1C are displayed, before firing, in Figures 3.25, 3.26 and 3.27 respectively. Figure 3.28 illustrates the full BWL1 trial schematic including the relevant positions of each structure, tagged with its SID and the full instrumentation array.

Figure 3.25: Structure BWL1A pre-shot: downstream perspective

(a) Upstream perspective (b) Downstream perspective

Figure 3.26: Structure BWL1B pre-shot

(a) **(1)** - Interior, downstream perspective

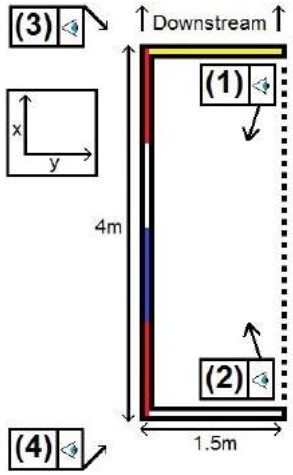

(b) Positions & perspectives

(c) **(2)** - Interior, upstream perspective

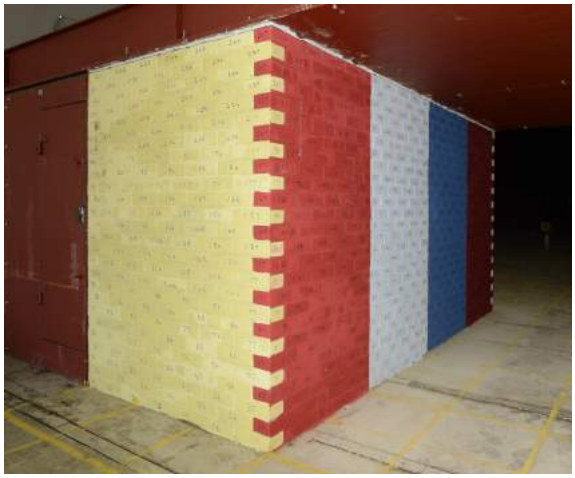

(d) **(3)** - Exterior, downstream perspective

(e) **(4)**- Exterior, upstream perspective

Figure 3.27: Pre-shot photographs of structure BWL1C, accompanied by a diagram indicating camera positions and perspectives

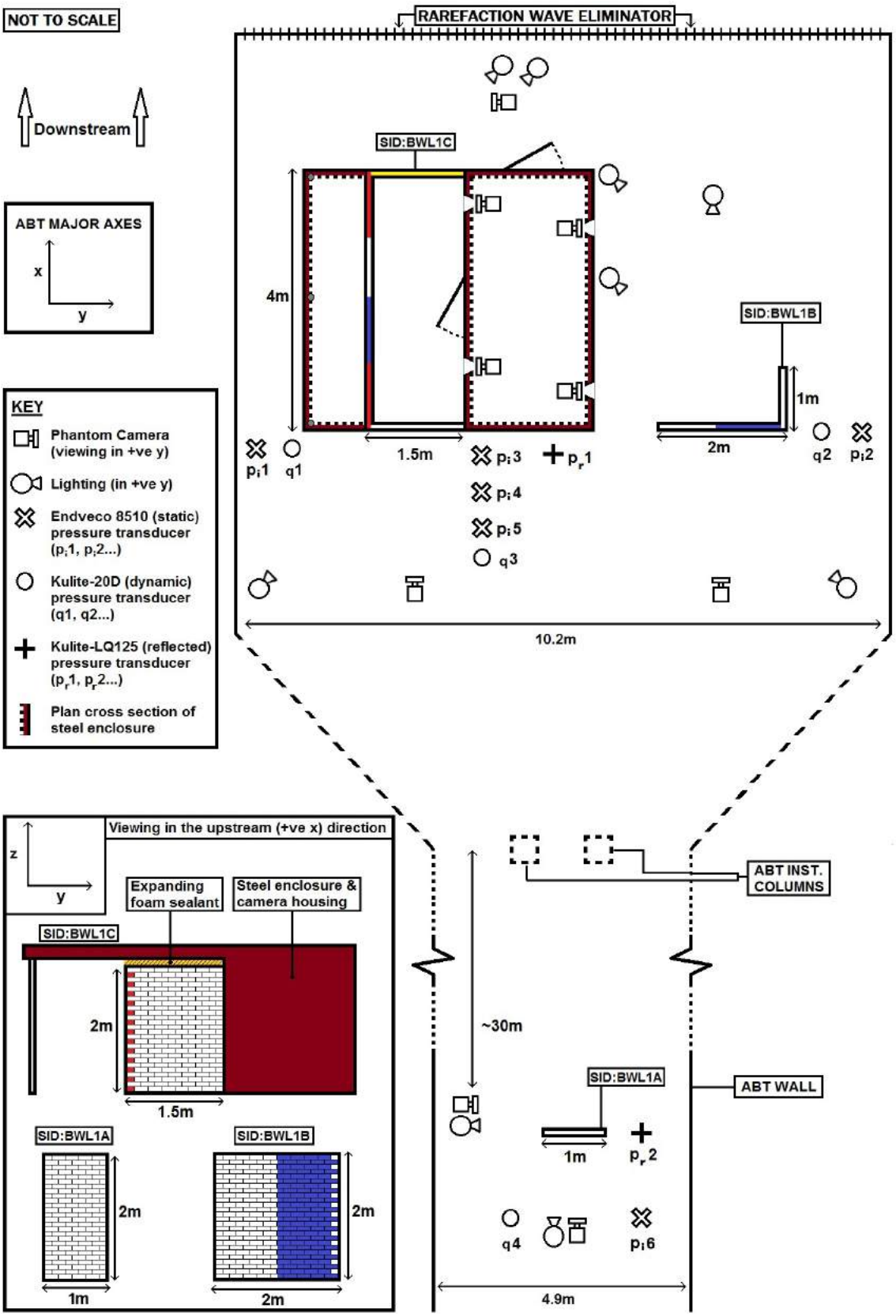

Figure 3.28: Full plan schematic of ABT trial 'BWL1,' indicating the relative positions of each individual structure, static, dynamic and reflective pressure transducers, phantom cameras and lighting.

The second trial, BWL2, tested four structures with SID's BWL2A, BWL2B, BWL2C and BWL2D. The first structure, BWL2A, was a **B** panel, that is a blast normal corner panel with (x,y,z) dimensions of 1m×1m×2m, located in the 4.9m section of the ABT. As well as providing key data to the development of the base panel model, this particular structure offered direct comparisons to BWL1A, an **A** panel in the 4.9m section of the tunnel and WR2A, a **B** panel subjected to a short duration blast load with a matching overpressure of 110kPa.

Two base panels and a large enclosed structure were tested in the 10.2m section of the ABT; the base panels, BWL2B and BWL2C were **B** and **A** panels respectively. With the addition of these results, both the **A** panel and **B** panel would have been tested for both long and short duration blasts at 55kPa and 110kPa and as a composite **AB** panel at 55kPa.

Finally, the large enclosed structure, BWL2D, had (x,y,z) dimensions 3m×2m×2m. This particular geometry was chosen as a half symmetric 90° rotation of the full rectangular geometry of structure BWL1C. In combination, these two structures provide data relating the structural response of large blast normal surfaces compared to greater depth. As with BWL1C, vinyl strips were placed on top surface of the walls and covered with expanding foam to seal the gap between the structure and the enclosure.

The additional rear phantom camera was moved and rotated at a $\approx 45°$ angle such that it recorded both the side and rear walls. For all structures each 1m (x,y) section of the wall was painted a different colour and each brick was given a unique number relating to its original position within the structure. 500mm×500mm grids were painted around each structure in the 10.2m section and radial 1m bins were marked down the major, longitudinal axis in the 4.9m section for debris collection purposes.

Structures BWL2A, BWL2B, BWL2C and BWL2D are displayed from various perspectives before firing in Figures 3.29, 3.30, 3.31 and 3.32 respectively; Figure 3.33 illustrates the full plan schematic for trial BWL2, indicating the relative positions of each structure, static, dynamic and reflective pressure transducers, the phantom cameras and accompanying lighting arrays.

(a) Upstream perspective (b) Side perspective (c) Downstream perspective

Figure 3.29: Structure BWL2A pre-shot

(a) Upstream perspective (b) Side perspective (c) Downstream perspective

Figure 3.30: Structure BWL2B pre-shot

(a) Upstream perspective

(b) Downstream perspective

Figure 3.31: Structure BWL2C pre-shot

(a) **(1)** - Interior, downstream perspective

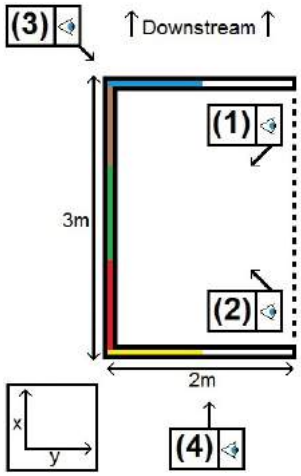

(b) Positions & perspectives

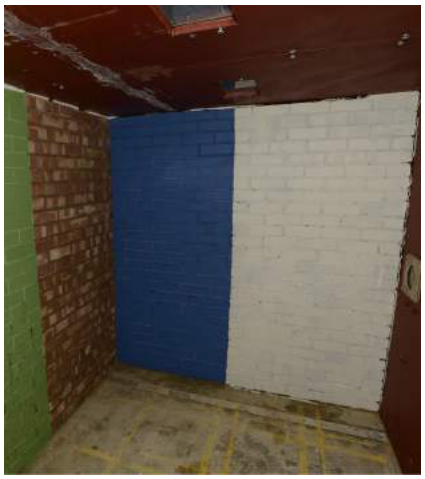

(c) **(2)** - Interior, upstream perspective

(d) **(3)** - Exterior, downstream perspective

(e) **(4)**- Exterior, upstream perspective

Figure 3.32: Pre-shot photographs of structure BWL2D, accompanied by a diagram indicating camera positions and perspectives

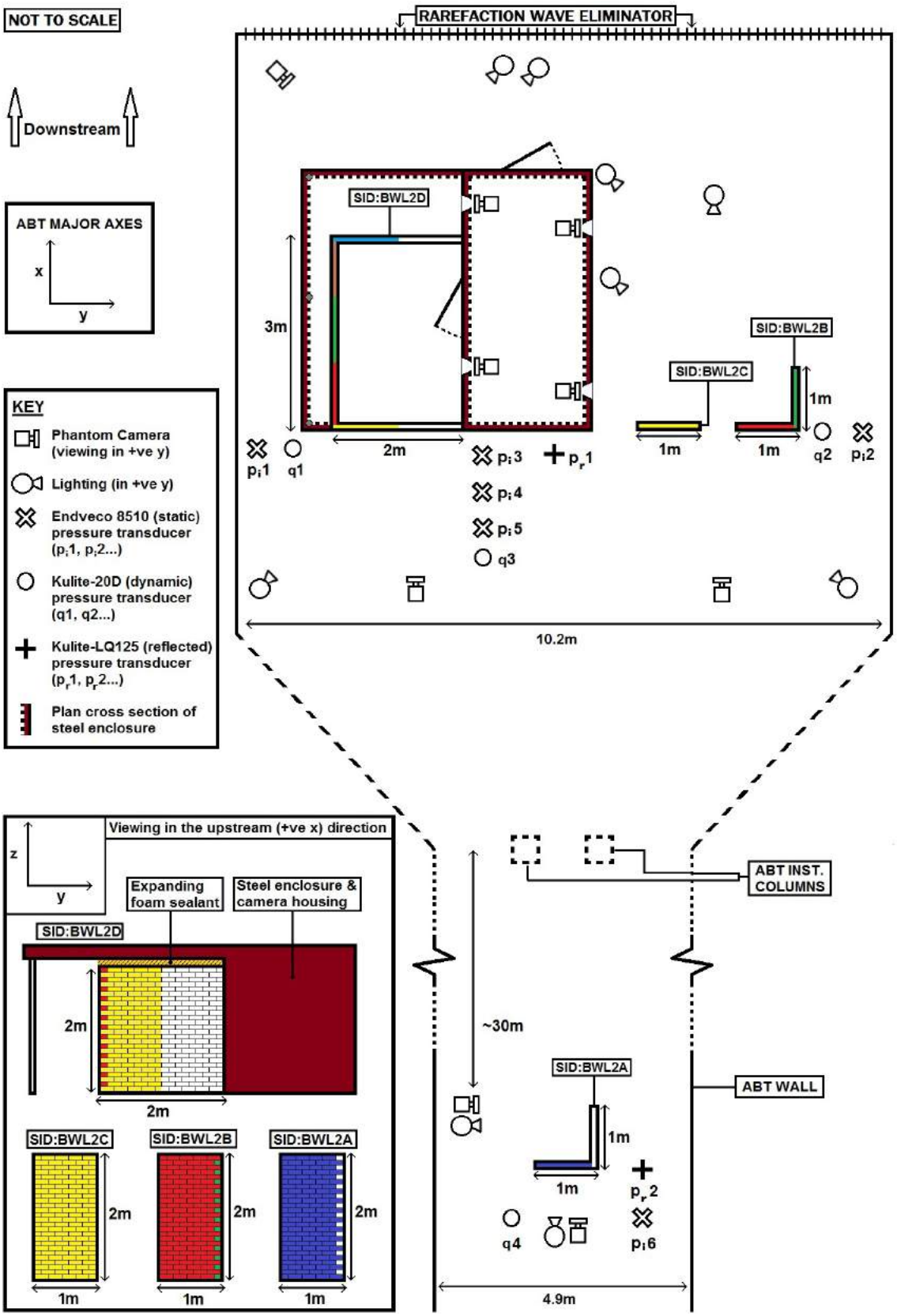

Figure 3.33: Full plan schematic of ABT trial 'BWL2,' indicating the relative positions of each individual structure, static, dynamic and reflective pressure transducers, phantom cameras and lighting.

The final trial of the BWL series, BWL3 tested three structures with SID's BWL3A, BWL3B and BWL3C. The first structure, BWL3A was a **D** panel, that is a 1m×1m×2m corner panel with the blast normal face at the rear of the structure, located in the 4.9m section of the ABT. The **D** panel was chosen as the final structure subjected to a long duration blast wave with overpressures of 110kPa, as it was the final base panel that could be tested in isolation and was directly comparable to structure WR2B, a **D** panel subjected to a short duration blast wave with an overpressure of 110kPa.

The smaller structure tested in the 10.2m section, BWL3B, was an **AA** panel, that is structure with (x,y,z) dimensions 0.1m×2m×2m, comprising two **A** panels joined together. This particular geometry was chosen as it varies the aspect ratio of the flat base panel; furthermore, this structure provides a direct experimental link between all small geometries tested, allowing an in-depth analysis of the effects of basic geometry on both breakage and debris distribution.

The large enclosed structure, BWL3C, was a 3m×1.5m×2m half square geometry. Of the other two large structures tested, this structure applies the two smaller x,y dimensions from both structures. Ideally if a fourth test was available, the larger half square geometry of 4m×2m×2m would also have been tested. The smaller geometry was chosen as the 3m×3m x,y square represents the smallest possible structure which can be created using each of the base panels at least once.

The rear phantom camera from the previous trial remained in place, recording both the rear and side walls from a $\approx 45^{\circ}$ angle; however an additional phantom camera was available and was positioned to record the side wall from the exterior perspective. As with BWL1C, the front and rear 1.5m walls of BWL3C were painted a single colour; BWL3A, BWL3B and the rest of BWL3C were painted such that each 1m (x,y) section were different colours and each brick given a unique number relating to its original position in the wall. 500mm×500mm grids were painted around each structure in the 10.2m section and 1m radial markers were painted along the major, longitudinal axis in the 4.9m section for debris collection purposes.

Structures BWL3A, BWL3B and BWL3C are displayed from various perspectives

before firing in Figures 3.34, 3.35 and 3.36 respectively. Figure 3.37 illustrates the full plan schematic for trial BWL2, indicating the relative positions of each structure, static, dynamic and reflective pressure transducers, the phantom cameras and accompanying lighting arrays; Table 3.5 highlights the key instrumentation parameters for each structure tested in the BWL series, including base panel composition, dimensions, number of whole and half bricks and the approximate brick mass, closest gauges and number of phantom cameras.

(a) Upstream perspective (b) Side perspective (c) Downstream perspective

Figure 3.34: Structure BWL3A pre-shot

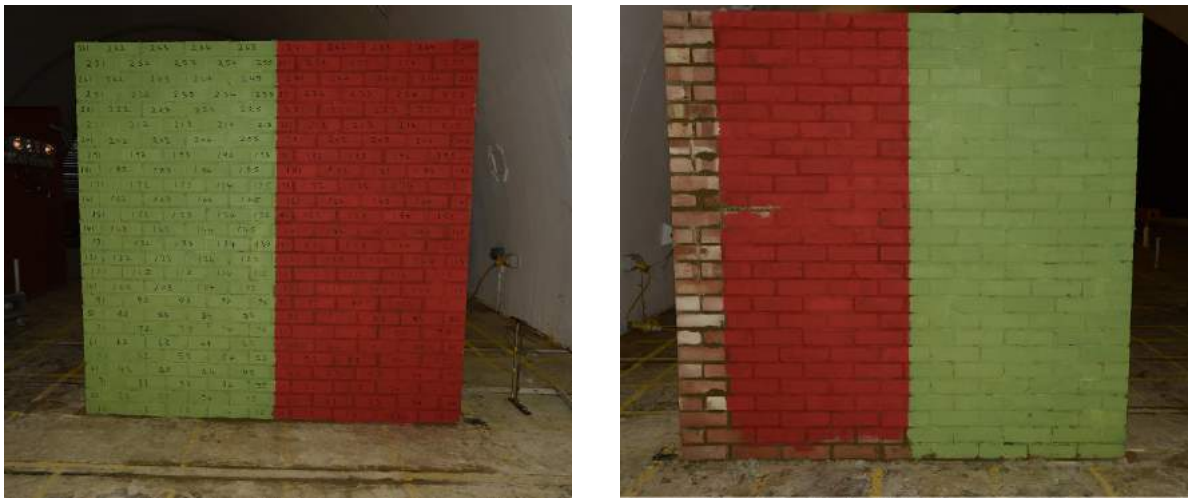

(a) Upstream perspective (b) Downstream perspective

Figure 3.35: Structure BWL3B pre-shot

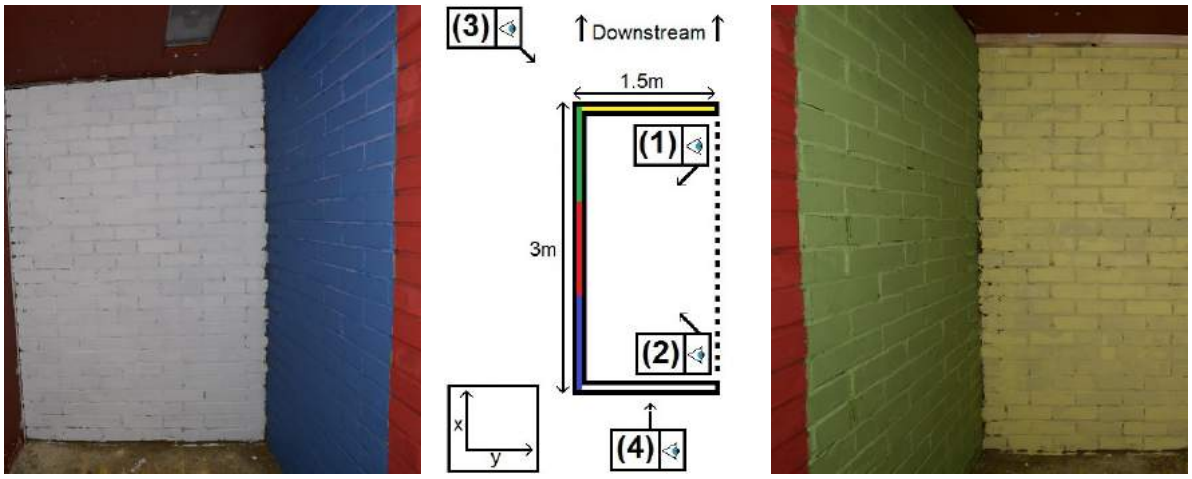

(a) **(1)** - Interior, downstream perspective (b) Positions & perspectives (c) **(2)** - Interior, upstream perspective

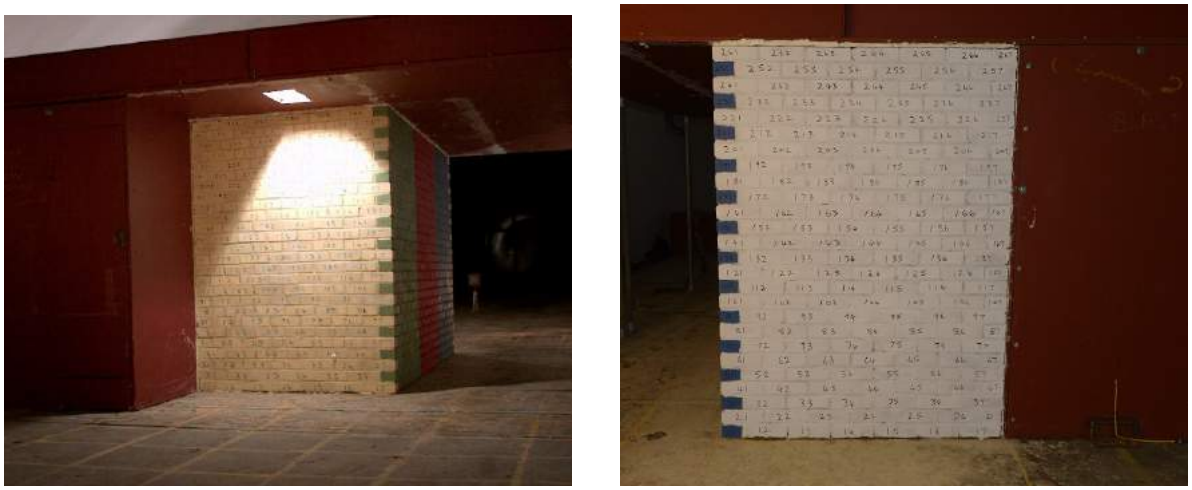

(d) **(3)** - Exterior, downstream perspective (e) **(4)**- Exterior, upstream perspective

Figure 3.36: Pre-shot photographs of structure BWL3C, accompanied by a diagram indicating camera positions and perspectives

Table 3.5: Summary instrumentation parameters for the 'BWL' series

SID	Type / Composite	Dimensions (x,y,z) (m)	Brick Stats 1	$\frac{1}{2}$	Σm (kg)	Closest GID p_i	q	p_r	Cameras
BWL1A	**A**	0.1×1×2	104	26	246	6	4	2	2
BWL1B	**AB**	1×2×2	325	26	710	2	2	1	3
BWL1C	$\frac{\mathbf{A}}{\mathbf{2}}$**BCCD**$\frac{\mathbf{E}}{\mathbf{2}}$	4×1.5×2	754	26	1611	1,3	1	1	4
BWL2A	**B**	1×1×2	208	26	465	6	4	2	2
BWL2B	**B**	1×1×2	208	26	465	2	2	1	3
BWL2C	**A**	0.1×1×2	104	26	246	3	2	1	3
BWL2D	**ABCDE**	3×2×2	780	26	1665	1,3	1	1	4
BWL3A	**D**	1×1×2	208	26	465	6	4	2	2
BWL3B	**AA**	0.1×2×2	221	26	491	2	2	1	3
BWL3C	$\frac{\mathbf{A}}{\mathbf{2}}$**BCD**$\frac{\mathbf{E}}{\mathbf{2}}$	3×1.5×2	650	26	1392	1,3	1	1	5

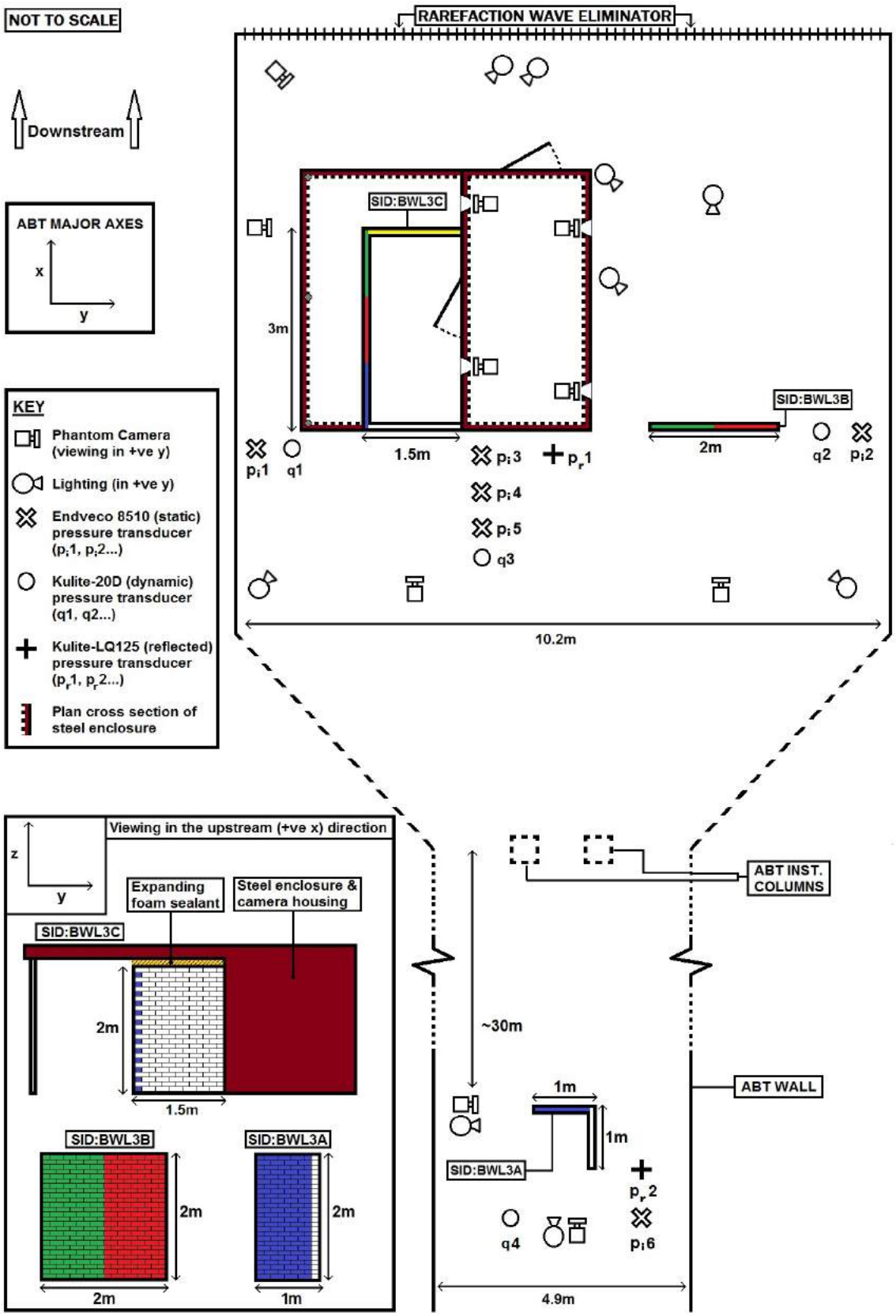

Figure 3.37: Full plan schematic of ABT trial 'BWL3,' indicating the relative positions of each individual structure, static, dynamic and reflective pressure transducers, phantom cameras and lighting.

3.7 Summary

The research methodology proposes the method of decomposing structures into simple panels of 1m in length, the "base panel" model. By considering a structure as a collection of smaller substructures, explosively produced debris from such a structure may be described as a combination of the debris fields of each of its individual panels.

To validate the base panel model, a series of high explosive short duration trials and shock tube long duration trials were proposed. The purpose of the short duration trials was to provide direct comparisons to the long duration trials, with target overpressures and structural geometries selected to match the long duration trials. The short duration trials were also used to assist in the calibration of the numerical methods, using a simple blast scenario without large impulses or drag winds. The long duration trials were designed to investigate a wide array of simple and composite panel geometries at incident overpressures of 110kPa and 55kPa. The long duration trials will provide the key data from this research project, offering new data on masonry breakage and debris distribution.

Chapter 4

Experimental Results

The results of the experimental trials, outlined in Chapter 3, provide new insight into the behaviour of masonry subject to blast loads, both long and short duration. This chapter compares target and achieved blast parameters from each test and highlights the results from each structure tested; including the breakage patterns and the longitudinal, lateral, (x,y,m) and number distributions of debris for each individual test item.

4.1 'MW' Series

The 'MW' series, detailed in Section 3.4 consisted of two trials, MW1 and MW2, which subjected two masonry panels to a long duration blast wave in the 4.9m section of the ABT, with an approximate TNT equivalence of 450T at a stand-off distance of 240m.

4.1.1 MW1

The first trial, MW1, tested an unmortared masonry wall constructed from class B engineering bricks. The static, dynamic and reflective pressure histories recorded for trial MW1 and their associated, cumulative impulses are displayed in Figure 4.1.

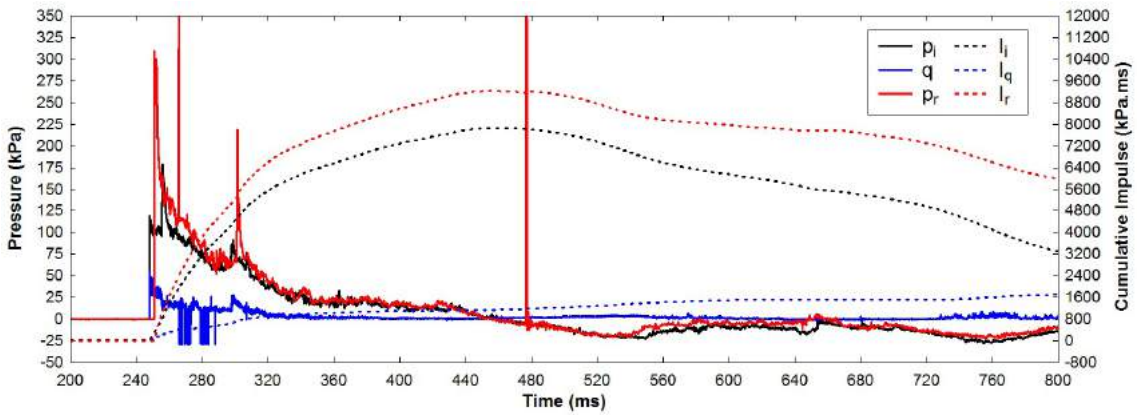

Figure 4.1: Recorded static, dynamic and reflective pressure time histories and integrated impulses from trial MW1

The static pressure, p_i, recorded a value of 119.2kPa at the peak of the shock discontinuity at 248.3ms. A second, higher peak of 179.8kPa was recorded at 255.8ms; however, this was due to the blast reflection off of the upstream face of the structure and was therefore not the peak static overpressure. Integrating the static pressure gives a peak value of 7866.2kPa.ms at time 460.2ms, corresponding to the end of the positive phase which was therefore 204.4ms. At 800ms, the cumulative impulse drops to 3341.9kPa.ms, implying the total impulse of the negative phase was equivalent to -4524.3kPa.ms; as stated in Chapter 2, the effects of negative phase are often neglected when dealing with blast structure interactions and as negative phase associated impulse has little effect on debris distribution, it is also neglected throughout this research.

Due to reflections, the gauge integrated value for impulse over predicts the actual transferred impulse. The impulse transmitted through the reflection spike in isolation can be estimated at approximately 200kPa.ms, therefore it is likely that the impulse calculated from integrating the gauge data overpredicts by a value in the region of 500kPa.ms. The reflective pressure, p_r, recorded a peak value of 309.1kPa at 251.0ms, an arrival time of 1.7ms later than the static pressure as the reflective pressure gauge was placed slightly further downstream, attached to the face of the structure. Three large peaks were observed at 265.6ms, 300.8ms and 476.6ms; however these spikes results from gauge noise and all have durations of $\leq$1ms and thus do not interfere with the impulse estimation. The peak value of the cumulative impulse was 9231.7kPa.ms, recorded at 477ms; whilst

this would imply the positive phase duration for reflective pressure was 226ms, the gauge was attached to the structure, which did not remain in the same position. The value of the reflective impulse at 460.2ms, corresponding to the end of the positive phase as recorded by the static pressure gauge, was 9180.2kPa.ms, implying a potential additional 51.5kPa.ms was transmitted through movement of the pressure gauge, which corresponds to 0.56% of the total recorded impulse. The dynamic pressure, q, recorded a peak value of 55.7kPa at 248.4ms and a peak impulse of 1706.2kPa.ms at 800ms.

As dynamic pressure is a measure of the kinetic energy transferred from the blast wind, it does not have a negative phase and the positive phase persists for much longer; therefore the cumulative impulse increases continuously until the gauge is switched off. At 330ms the cumulative impulse of the dynamic pressure reached 1027.1kPa.ms, contributing 60% of the total associated impulse in 81.6ms. Between 330ms and 800ms the dynamic pressure fluctuates continuously between 1-3kPa which is too low to have any significant impact on debris distribution, yet the impulse increases by 679.1kPa.ms.

Figures 4.2 and 4.3 show the breakage and displacements of the structure at 0ms, 20ms, 50ms, 100ms, 150ms and 200ms from the upstream and side perspectives respectively. At 20ms, the first signs of structural response were observed in the form of lateral, y separation between the individual bricks. By 50ms this separation became more pronounced, particularly along the structures central, vertical z axis. The brick layers alternated between 5 whole bricks and 3 whole bricks and two half bricks; this particular arrangement is symmetrical about the central z axis of the structure, which in combination with the lateral separation of bricks along this axis began to divide the structure into two large pseudo-fragments.

At 100ms, the bricks located in the upper, outer edges of the structure began to completely detach from the rest of the structure, as displayed in Figure 4.2d. Between 100-200ms, larger numbers of bricks continued to detach from the main body of the structure at the outer edges, the vertical separation along the central z axis became larger as the blast wind flowed through the gap. Inspecting the high speed photograph from the side perspective, displayed in Figure 4.3, shows the structure beginning to

tilt about its base, with a clear displacement by 50ms. After 50ms, the tilting motion combined with a translational motion in the longitudinal, positive x direction. The tilting motion of the structure was caused by increased frictional forces towards the base of the structure, which results in an apparent velocity gradient spanning the vertical height of the structure. As the structure was unmortared, bricks located in the top layers of the structure become quickly unrestrained and entrained in the blast wave.

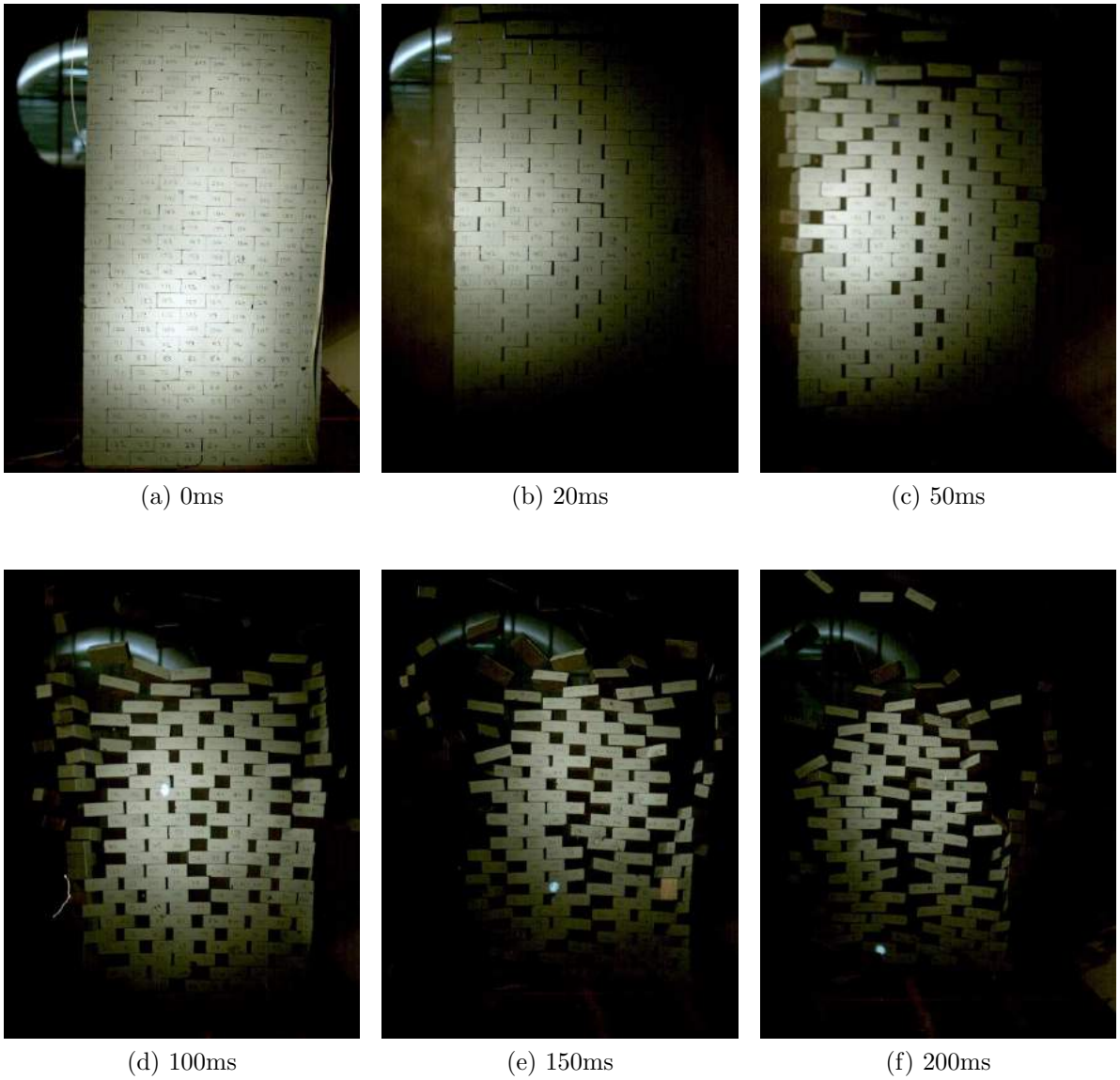

(a) 0ms (b) 20ms (c) 50ms

(d) 100ms (e) 150ms (f) 200ms

Figure 4.2: High speed photography (from the upstream perspective) of the breakage of structure MW1

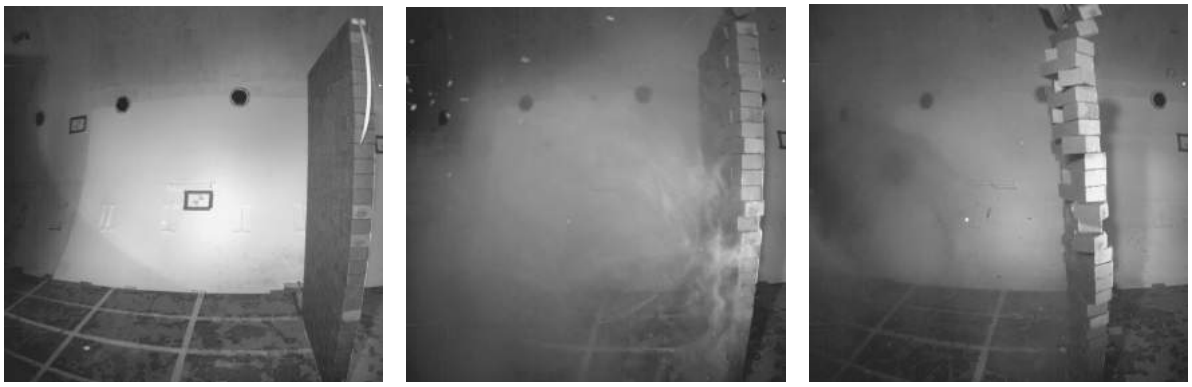

(a) 0ms (b) 20ms (c) 50ms

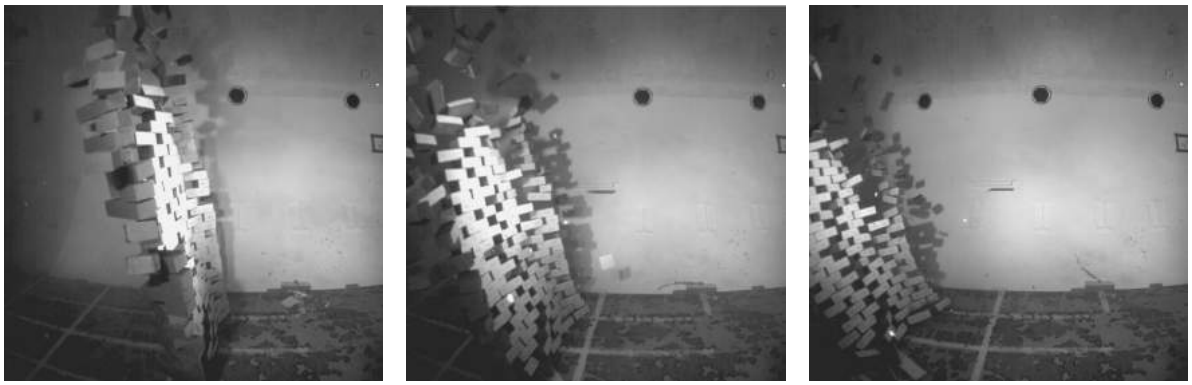

(d) 100ms (e) 150ms (f) 200ms

Figure 4.3: High speed photography (from the side perspective) of the breakage of structure MW1

Using the images captured by the high speed photography, measurements were made for displacement by determining the number of pixels between two fixed points of known dimensions within the image. This provided a distance calibration scale, which, combined with the 200μs frame interval allowed measurements to be taken for distance and time, thus allowing calculations to be made for velocity and acceleration. Due to the camera parallax, the scale differs slightly at different points across the image, which gives an associated parallax error. To reduce the parallax error, different calibration scales were used at different points across the image; however in the absence of accurate scales, the parallax error for these measurements can be challenging to quantify.

With a limited resolution of 600x600, there is also an associated pixel error with any displacement measurements. The size of the bricks and the displacements over which they are measured significantly reduces pixel error. Combination of these two errors cannot

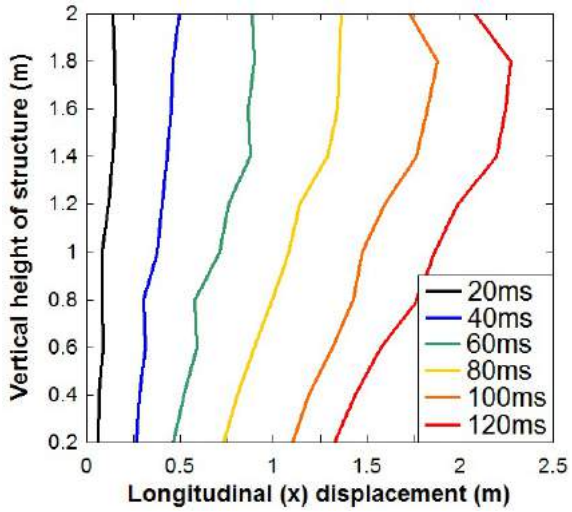

(a) Displacement relative to structural position

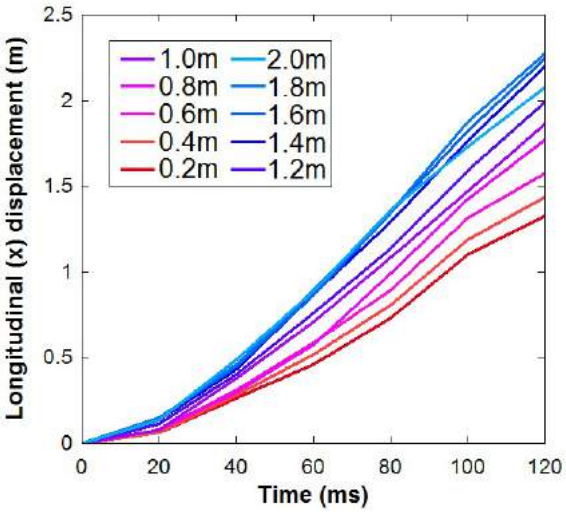

(b) Absolute displacement

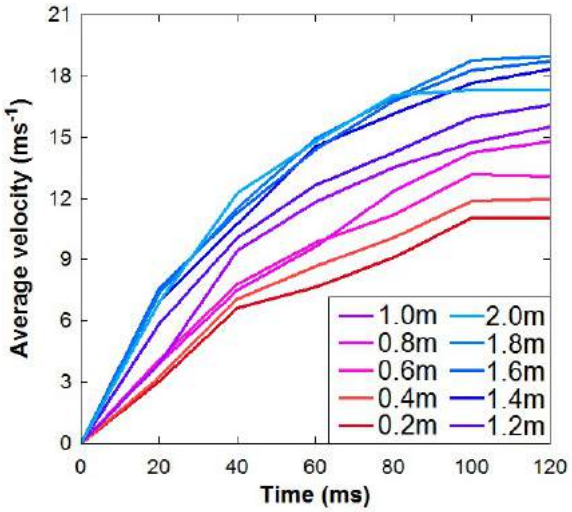

(c) Average velocity

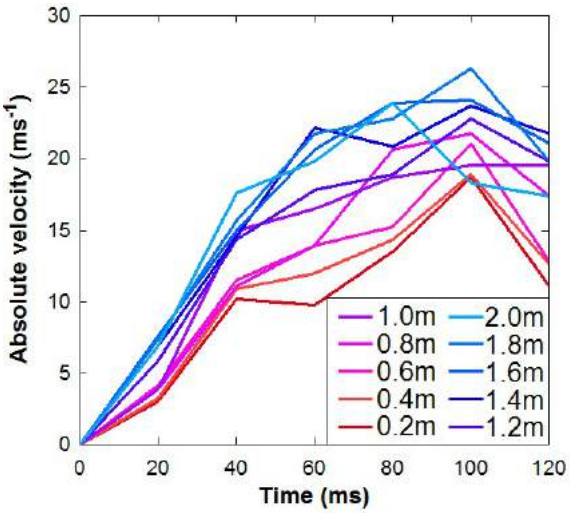

(d) Absolute velocity

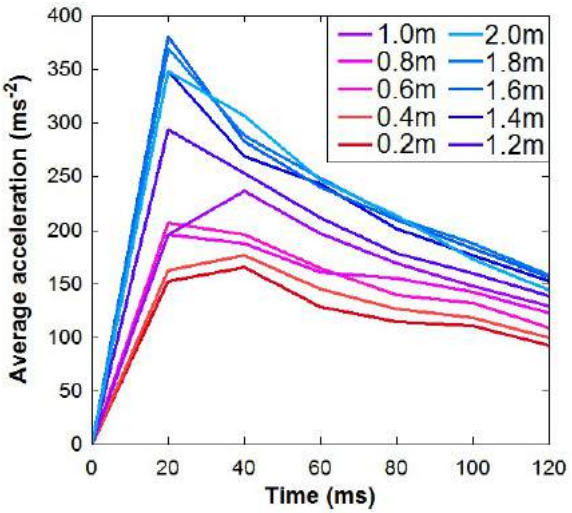

(e) Average acceleration

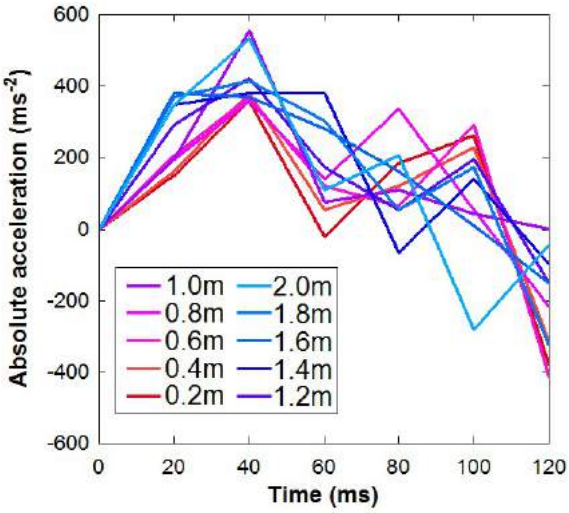

(f) Absolute acceleration

Figure 4.4: MW1 displacement, velocity and acceleration time plots relative to the verical height within the structure

be accurately determined; therefore, error is negated in all measurements taken using the high speed photography. Whilst the values extracted are not necessarily exact, they provide suitable approximations and offer realistic displacement time trends.

Figure 4.4a shows the longitudinal x displacement of structure MW1 at 0.2m intervals along the structures vertical axis at 20ms intervals between 20ms and 120ms, beyond which the furthest fragments from the upper section of the structure were out of measurement range. The distance between each curve represents the actual displacement over a 20ms interval and the combined tilting and translation motion of the structure in the downstream, positive x direction is illustrated by the increasing relative distance between the curves with each time step.

This motion can be observed upon inspection of Figure 4.4b, which shows the absolute longitudinal displacement with respect to time for each 0.2m section of the structure. Figure 4.4c, displays the average velocity of each of the vertical monitoring points with respect to time. The difference in velocity between each of the monitoring points increases with time, representing an increasing velocity gradient from the bottom to the top of the structure. Referring back to Figure 4.4a, the displacement of the top 0.2m of the structure between 100-200ms was overtaken by the section directly below it.

This is also displayed in the average velocity graph as the curve labelled '2.0m' drops below the 1.8m, 1.6m and 1.4m points. At this point, the upper fragments became completely entrained in the blast wave; inspection of the high speed video showed an increasing velocity in the z direction, potentially due to increased rotational motion of the fragments and the associated varying drag forces. The absolute velocity, displayed in Figure 4.4d, shows the velocity of each vertical monitoring point between each 20ms time step, which increased until 100ms, where it began to drop rapidly.

Inspection of Figure 4.1, shows this corresponds to a drop in the dynamic pressure; the dynamic pressure still persisted beyond this point, but at a low magnitude, reducing the kinetic energy transferred to the fragments; furthermore, referring to Figure 4.2d, the observable brick separation in the structures y,z plane became significantly large at 100ms, such that the upstream blast normal face of the structure presented gaps through

which the blast could vent; resulting in less transferred force.

Figure 4.4e shows the change in average acceleration with respect to time and Figure 4.4f shows the absolute acceleration between each 20ms time step. The absolute acceleration increased over the first 40ms. After 40ms the acceleration decreases, yet remains positive until 80-100ms, depending the vertical position within the structure, after which all monitored fragments begin to decelerate.

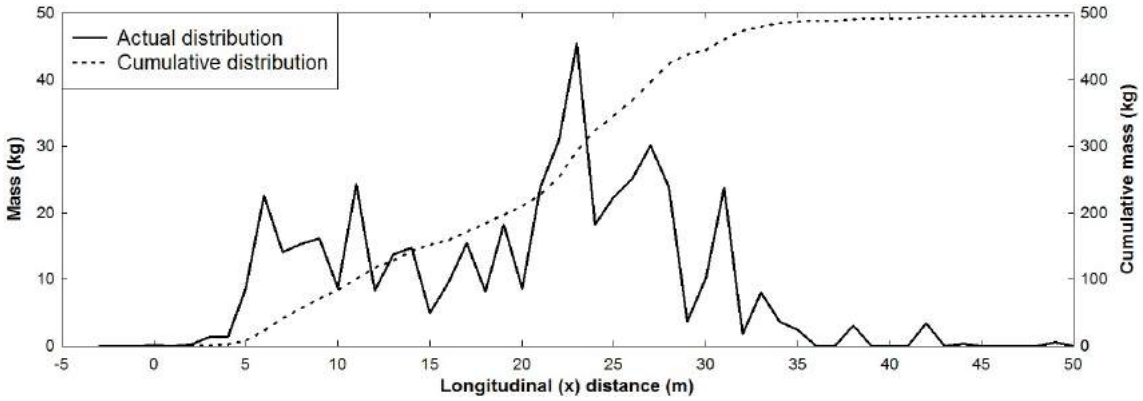

Figure 4.5: MW1 longitudinal and cumulative longitudinal mass distributions

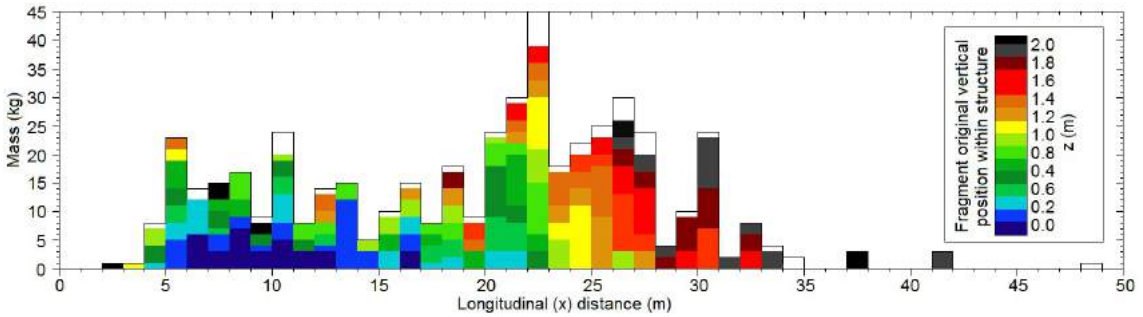

Figure 4.6: MW1 longitudinal (x) mass distribution indicating (z) origin of debris

The longitudinal debris distribution of structure MW1, displayed in Figure 4.5, shows a peak displacement of 49m. The majority of the debris, 226.4kg, was located between 20m$< x <$29m, corresponding to approximately 45.6% of the overall recorded mass of 496.5kg, which was 14.5kg less than the prediction made of the total mass of the structure pre-firing of 511kg. Within the region 20m$< x <$29m, the peak bin mass of 45.5kg was recorded at 23m, followed by the second highest bin mass of 30kg recorded at 27m. Outside of this range, three smaller peaks were recorded at 6m, 11m, and 31m with

masses of 22.6kg, 24.3kg and 23.8kg respectively. The peak at 31m was due to debris colliding with the instrumentation columns, located at the 31m marker. In the absence of these columns, the distribution between 30m$< x <$50m is expected to be more evenly distributed.

Figure 4.6 shows the longitudinal debris distribution indicating the original vertical fragment position and was plotted using the unique numbers assigned to each individual brick; the key illustrates the relation between the plotted colour and the original vertical height of the fragments within the structure, the absence of colour, white, represents unidentifiable fragments. The region 5m$< x <$15m contained most of the debris from the lower 0.6m of the structure, with fragments originally located vertically between 0.6m and 1.2m evenly distributed between 5m$< x <$25m and the upper section on the structure was mostly distributed beyond x=25m. Based on the initial trajectories observed from the high speed photography, displayed in Figure 4.3, this distribution follows the expected pattern, with a higher original z position corresponding to a further longitudinal x distribution.

4.1.2 MW2

MW2 was the trial upon which the base panel model was developed, with structure MW2 defined as the **A** panel. As with MW1, MW2 was instrumented in the 4.9m section of the ABT and subjected to a full power shot with a target peak static overpressure of 110kPa and positive phase duration of 200ms. The static, dynamic and reflective pressures recorded in the MW2 trial and their associated cumulative impulses are displayed in Figures 4.7.

The static pressure, p_i, recorded a peak value of 108.9kPa at the arrival of the shock discontinuity at time 207.6ms. Similarly to MW1, a reflection was recorded from the blast normal face of the wall with a magnitude of 160.2kPa at 214.9ms. Integrating the gauge data presented a value of 7457.1kPa.ms, recorded at 417.6ms corresponding to the end of the positive phase duration which was thus 210ms. The impulse of the reflected peak can be approximated to 90kPa.ms, less than half of the approximated impulse of the

reflected peak from the MW1 trial, suggesting the static impulse obtained by integrating the gauge data is more accurate for trial MW2.

The reflected pressure recorded a peak value of 311.7kPa at time 226.4ms, with a peak recorded impulse of 9616.6kPa at time 404.6ms, suggesting a positive phase duration of 178.2ms, 31.8ms less than the recorded positive phase duration of the static pressure. The peak recorded value for dynamic pressure was 98.8kPa, recorded at 226.4ms, was due to gauge noise, whilst the peak value recorded at the arrival of the shock discontinuity was 40.5kPa at 207.8ms. The peak associated dynamic impulse was 1651.6kPa.ms, recorded at 750ms; however, after approximately 285ms, the dynamic pressure dropped below 3kPa. At 285ms, the associated dynamic impulse was recorded as 1033.1kPa.ms, 62.6% of the peak value. As mentioned in the case of MW1, the effects of dynamic pressure were negligible beyond this point.

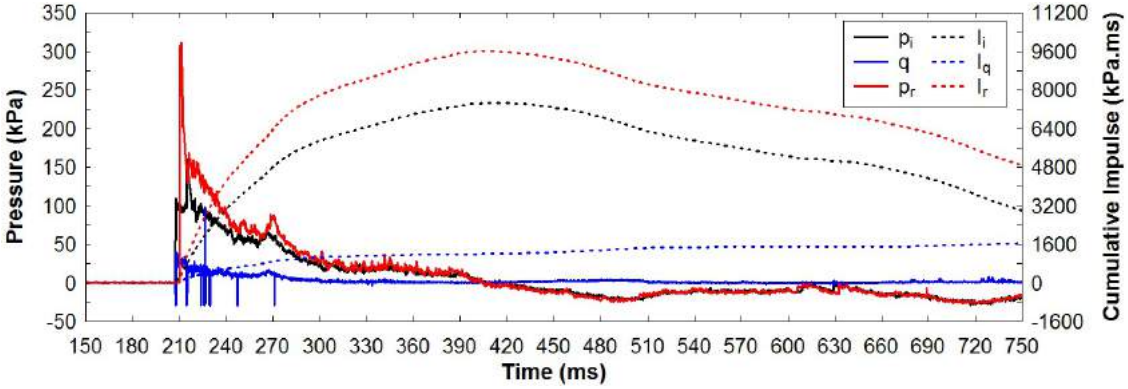

Figure 4.7: Recorded static, dynamic and reflective pressure time histories and cumulative impulses from trial MW2

Figures 4.8 and 4.9 show the breakage and displacements of structure MW2 at 0ms, 20ms, 50ms, 100ms, 150ms and 200ms from the upstream and side perspectives respectively. The first signs of breakage were observed at 8ms in the form of small cracks along the mortar bedding planes in the upper 3 layers of brick, corresponding to the top 0.25m section of the structure. By 20ms, an initial stepped crack, shown in Figure 4.8b, was clearly visible and had extended, running along the bedding plane between the 22nd and 23rd layers.

Between 20-50ms, the structure began to tilt about its base in the positive x direction,

causing another separation along the bedding plane between the 11th and 12th layers, approximately 0.85m above the base. Another stepped crack formed at the bottom of the structure, from the outer edge of the 4th layer, 0.3m above the base, down to the centre of the base of the structure, which led to a crack forming between the 4th and 5th layers. Cracks continued to form in the upper section creating 4 larger fragments, clearly visible in Figure 4.8c. At approximately 70ms, another crack began to form between the 7th and 8th layers at 0.55m above the base, becoming clearly visible at 100ms.

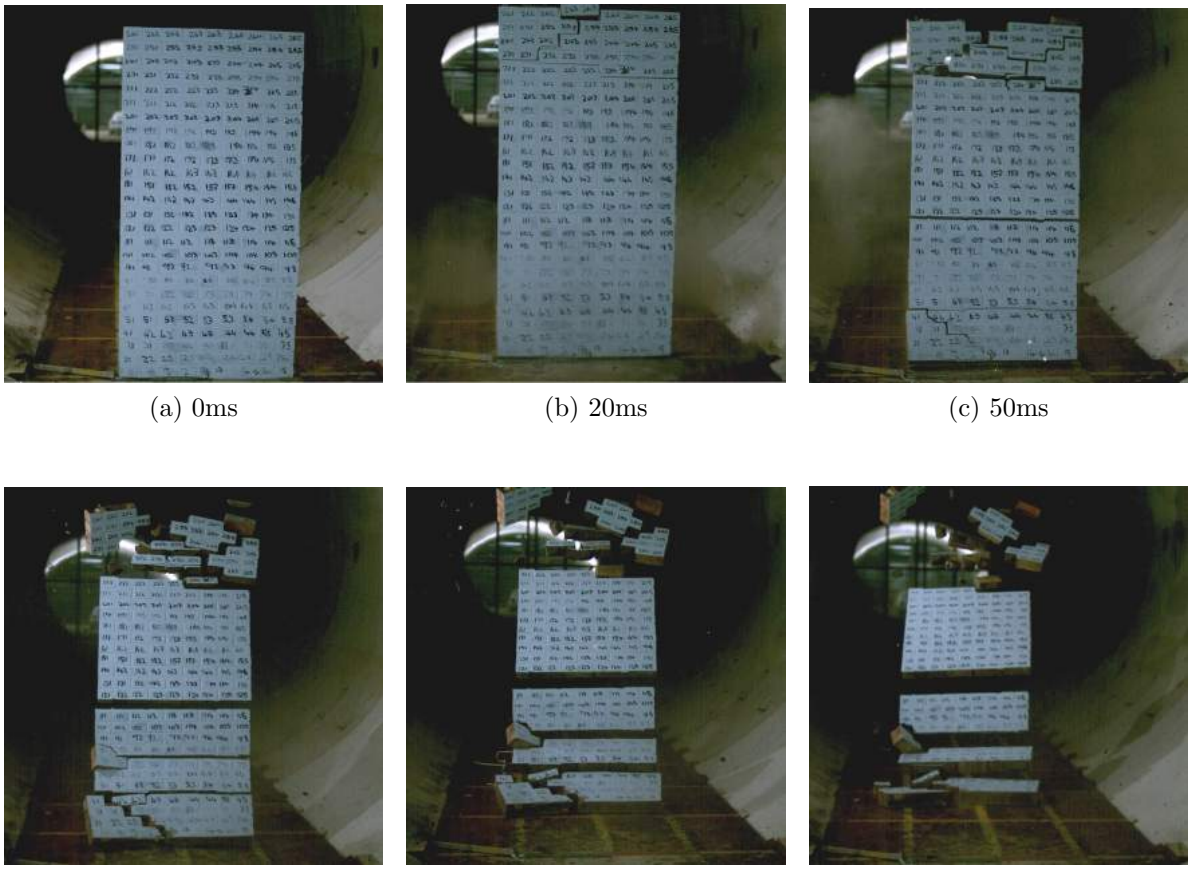

(a) 0ms (b) 20ms (c) 50ms

(d) 100ms (e) 150ms (f) 200ms

Figure 4.8: High speed photography (from the upstream perspective) of the breakage of structure MW2

Between 100-200ms, little additional breakage and fragmentation was observed; during this time, the individual fragments became unrestrained and were free to move without the resisting, frictional forces created by the structure. After 100ms, both the static and reflected pressures dropped below 30kPa and were too low to cause any additional fragmentation. The initial tilting of the structure about its base, which occurred between

20-50ms, combined with a translational motion in the positive x direction, once the mortar bond to the ground was overcome. Figures 4.9d, 4.9e and 4.9f show an apparent velocity gradient across the vertical axis of the structure; this is due to the increasing frictional forces towards the base of the structure in combination with the tilting effect, similar to MW1. The breakage produced four initial large fragments (10+ bricks) and six medium sized fragments (4+ bricks), accounting for upwards of 90% of the total mass.

(a) 0ms (b) 20ms (c) 50ms

(d) 100ms (e) 150ms (f) 200ms

Figure 4.9: High speed photography (from the side perspective) of the breakage of structure MW2

In conjunction with MW1, measurements were taken from the high speed video using fixed points with known separations to calibrate displacement. Errors were typically small and although approximations, all measurements show realistic trends, representative of the actual response of the structure. Displacement time histories were measured at 20ms intervals between 0-120ms, beyond which the upper sections of the structure were out of viewing range.

Figure 4.10a shows the displacements of the structure at 20ms intervals between 20ms and 120ms with respect to vertical height of the strcuture, in which the distance between curves represents the absolute displacement between successive measurements. The gradient of the curves increases most rapidly at 0.6m, 0.8m and 1.8m, which correspond to the lateral breakage lines observed in the Figures 4.8 and 4.9. Between these points, each curve displays a relatively smooth gradient, representing the individual large fragments which tilt in the positive x direction.

The absolute displacements, illustrated in Figure 4.10b, show the longitudinal displacement increasing towards the top of the structure; however, similarly to MW1, the top 0.2m of the structure falls behind its expected position. This was the first section of the structure to respond to the blast wave, with a lateral crack forming at 1.75m resulting in the top section of the structure becoming unstrained by 20ms. In the absesne of direct contact with the rest of the structure, this top section did not receive any frictional forces causing an additional, prolonged tilting motion.

Figure 4.10c shows the average velocity at each measured time, demonstrating observed velocity gradient across all vertical monitoring points, which increases with time; the same trend of logarithmically increasing velocity with respect to time, was observed across all monitoring points. Figure 4.10d displays the absolute velocity between each 20ms time step, illustrating an increase in fragment velocity across all monitoring points until approximately 100ms. At this point, the large fragments had rotated significantly in the positive x direction, reducing the drag coefficient; as the dynamic pressure was also below 3kPa at this time, the drag forces were reduced even further.

Figure 4.10e displays the average acceleration at each measured 20ms interval and Figure 4.10f shows the absolute acceleration between each 20ms interval. For all monitoring points, the acceleration rapidly increased for the first 20ms and continues to increase, at a lower rate, until 40ms. After 40ms, the fragments continued to accelerate; however at an even lower rate, until approximately 60ms for fragments from the lower sections of the structure and 80ms for fragments from the upper section of the structure. Referring to Figure 4.7, the dynamic pressure drops to 3kPa at approximately 60ms after its ar-

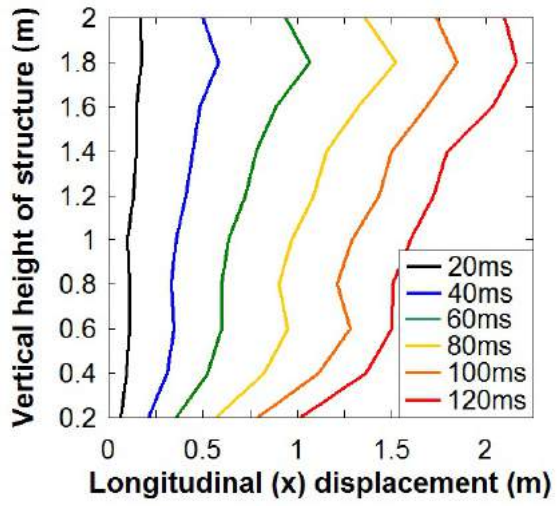

(a) Displacement relative to structural position

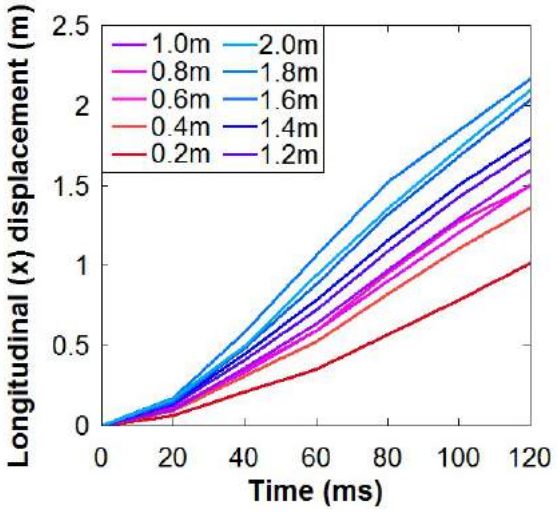

(b) Absolute displacement

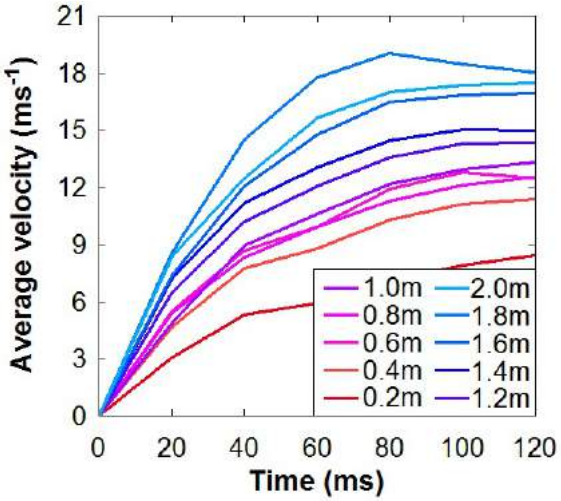

(c) Average velocity

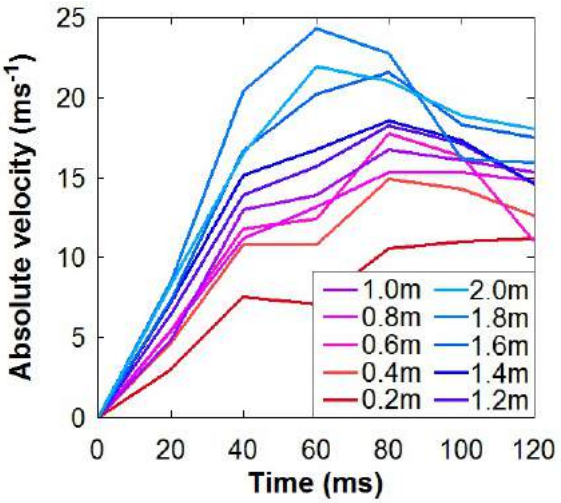

(d) Absolute velocity

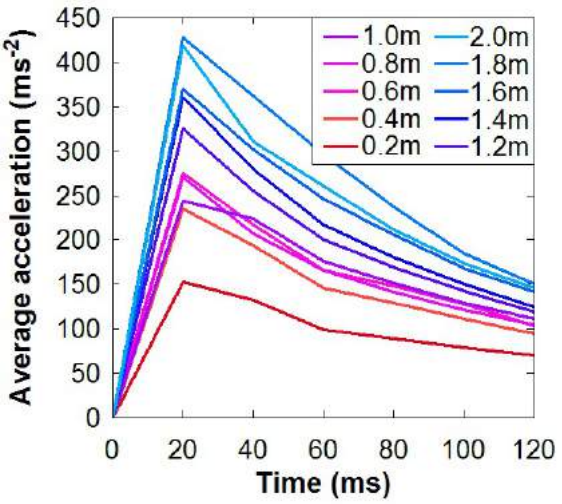

(e) Average acceleration

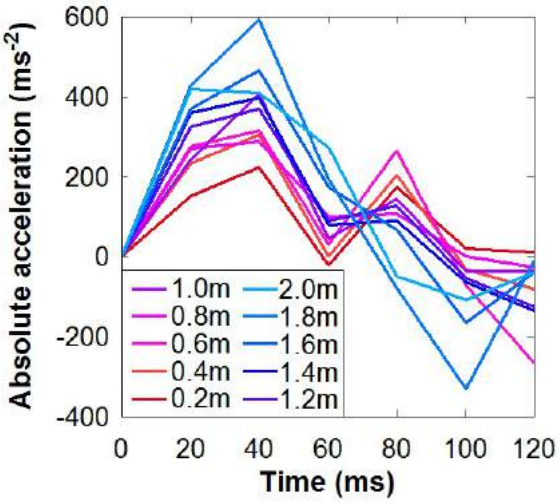

(f) Absolute acceleration

Figure 4.10: MW2 displacement, velocity and acceleration time plots relative to the verical height within the structure

rival, which in combination with the decreasing drag coefficients of the large fragments, resulting from rotation into the blast stream, caused the structure decelerate beyond 80ms.

The longitudinal debris distribution of stucture MW2 is displayed in Figure 4.11, which shows the individual distributions of each fragment type, i.e. brick, mortar and composite brick and mortar. The maximum throw distance was 44m, a composite fragment of brick and mortar located from the top of the structure. The majority of the debris was located between 20m< x <30m, with the highest bin density at 25m, with a mass of 40.9kg. As with MW1, a smaller peak was located at 31m due to the instrumentation columns with a bin mass of 15.0kg. A similar peak was located at 11m, which contained the largest individual fragment with a mass of 12.0kg, consisting of four bricks mortared together, originating from the edge of the 2nd and 3rd rows.

Comparing the individual fragment distributions, within the first 20m the majority of the debris consisted of composite fragments of brick and mortar; between 20m< x <25m, the total mass from individual bricks is roughly equal to that of the composite fragments and finally between 25m< x¡30m, the majority of the mass was composed of individual bricks. Consulting Figure 4.12, which displays the longitudinal mass distribution in terms of the original vertical position of the fragments, the debris located between 25m< x <30m originated from the top 0.5m of the structure. Upon impact with the ground, the fragments located from increased vertical positions were subject to high impact forces, resulting in further fragmentation; furthermore, fragments originating from the upper section of the structure were already smaller (2-5 bricks), thus, upon impact with the ground a much higher percentage of bricks were separated from the mortar.

Figure 4.12 also indicates the majority of the debris located between 20m< x <30m originated from the central vertical region between 0.5m-1.5m; referring to the phantom analysis, this region corresponds to the largest initial fragment, which spanned 10 rows of brick with an approximate height of 0.75m. The distribution between 5m< x <15m consisted primarily of debris originating from the lower 0.5m section of the structure; from this vertical position, the impact force of the debris was much lower and the majority

of fragments located between 5m< x <15m were composite brick and mortar. Finally, further comparison of Figures 4.11 and 4.12 shows that the distribution of loose mortar fragments is approximately equal to the additional, unknown mass outlined in white in Figure 4.12.

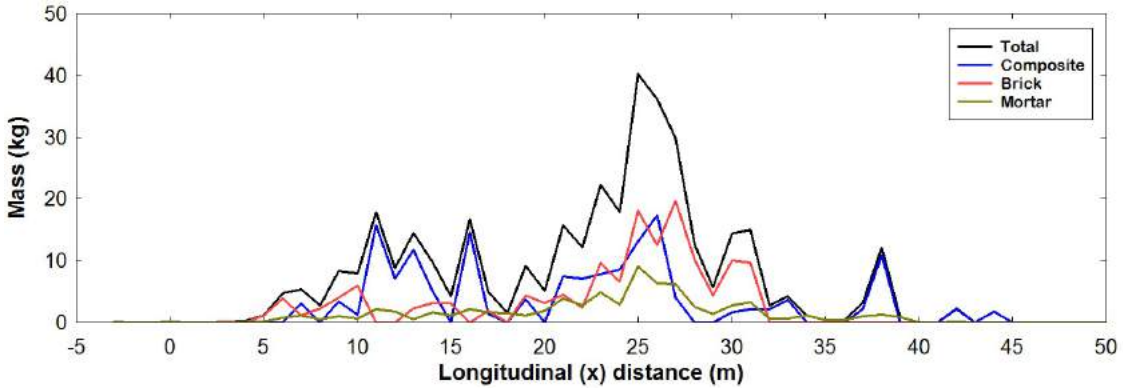

Figure 4.11: MW2 longitudinal (x) debris mass distribution

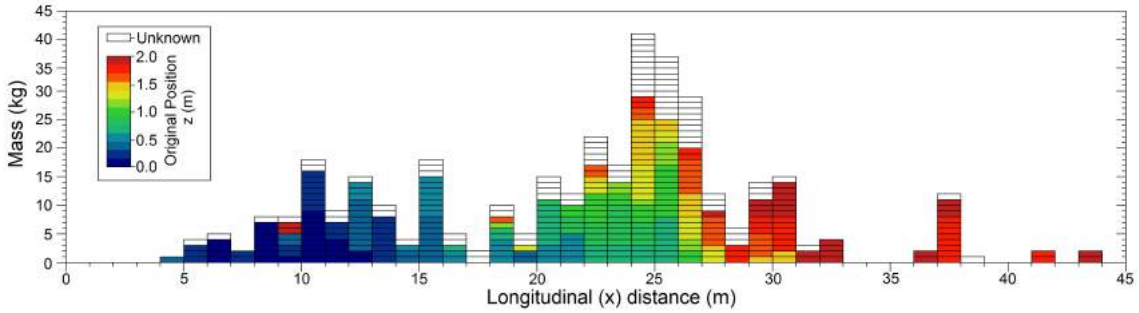

Figure 4.12: MW2 longitudinal (x) mass distribution indicating (z) origin of debris

4.2 'Windrush' Series

The 'Windrush' series, detailed in Section 3.5, consisted of two HE trials, WR1 and WR2, each of which instrumented five masonry structures subject to a 41kg TNT equivalent charge at varying stand-off distances. Figure 4.13 shows images of the fireball created by the WR1 detonation, in which the wall test panels are visible in the foreground.

(a) 5ms (b) 75ms (c) 350ms

Figure 4.13: Trial WR1 detonation

4.2.1 WR1

For each of the Windrush arena trials two radial spokes, p_iA and p_iB, illustrated in Figure 3.16, of five Endveco-8510 piezo-resistive pressure transducers were instrumented to gauge the static pressure time histories at radial stand-off distances matching those of the test items. Figure 4.14 displays the pressure time histories and integrated, cumulative impulse histories of all static pressure gauges instrumented in the WR1 trial.

Unlike gauge data obtained from ABT trials, the gauge data from the arena trials all exhibit marked noticeable second shocks as a proximity consequence to the detonation by-products. Whilst the second shock did not interfere directly with the gauge data, the integrated gauge data, presented in Figures 4.14b and 4.14d show a small increase in impulse upon the arrival of the second shock. Although the magnitude of this increase is almost negligible, the positive phase duration could not be exactly quantified by examining the time at which the peak impulse was observed; therefore, the positive phase durations were manually extracted by examining the point at which the pressure reduces below 0kPa.

The 10.6m radial, corresponding to a target peak static pressure of 110kPa, recorded peak a pressure of 115.2kPa at 33.9ms and a positive phase duration of 7.6ms from gauge p_i1A and a peak pressure of 99.0kPa at a time 33.8ms and a positive phase duration of 7.2ms from gauge p_i2A. The pressure recorded on the p_i1 radial was 16.2kPa higher than that of the p_i2 radial and the positive phase duration was also 0.4ms longer, giving an average recorded peak static overpressure of 107.1kPa. The target positive phase duration

for the 10.6m radial was 10.0ms, putting the achieved results between 34-38% below the target.

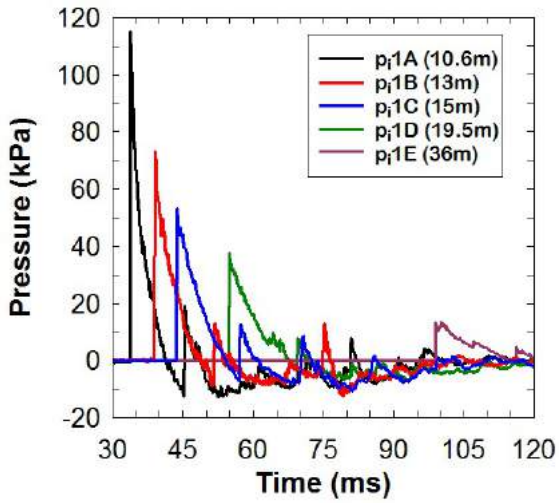

(a) Pressure (p_i1 radial)

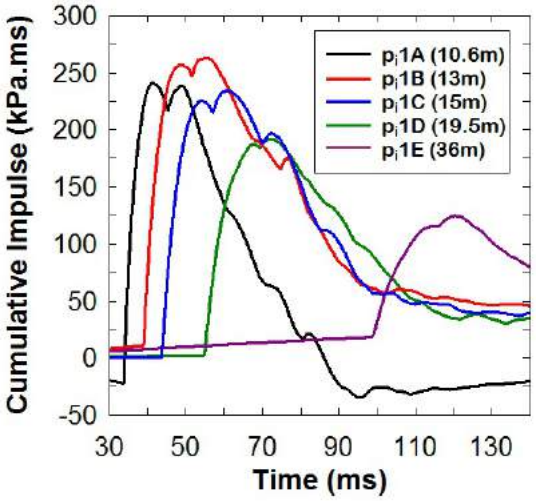

(b) Cumulative Impulse (p_i1 radial)

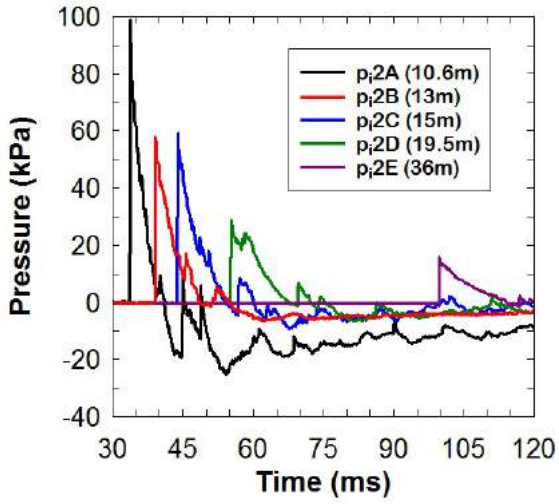

(c) Pressure (p_i2 radial)

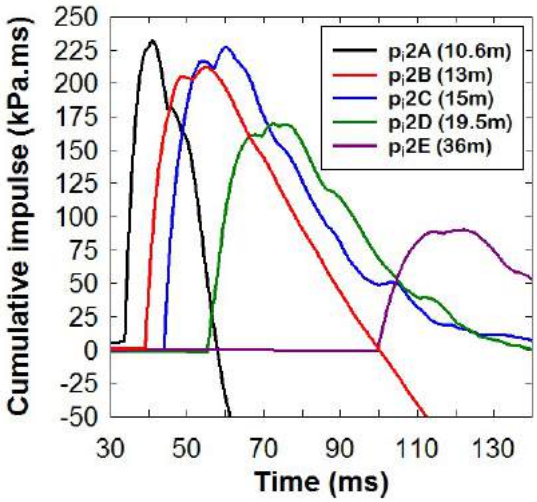

(d) Cumulative Impulse (p_i2 radial)

Figure 4.14: Static pressure time histories from trial WR1

The peak impulse recorded by p_i1A was 240.8kPa.ms at 41.4ms and the peak impulse recorded by p_i2A was 232.2kPa.ms at 41.0ms, both peaks correspond with the end of the positive phase duration. The target impulse at the 10.6m radial was 313kPa.ms; although the pressure recorded by p_i2A was 11kPa below the target value, p_i1A recorded 5.2kPa above the target value, yet both gauges recorded 23-25% below the target impulse, clearly resulting from the decreased positive phase duration. Gauges p_i1B and p_i2B, located at the 13m radial, recorded peak static overpressures of 73.1kPa at 39ms and 58.2kPa at

39.1ms respectively, with positive phase durations of 9.8ms and 9.4ms respectively.

The target overpressure at the 13m radial was 72kPa, with gauges p_i1B and p_i2B measuring 1.1kPa, 1.5%, above the target and 13.8kPa, 19%, below the target respectively giving a mean recorded pressure of 65.5kPa, 9% below the target. The target positive phase duration was 11.4ms, with the recorded values being 14-18% below the target value, an improvement of 20% over the 10.6m radial. The peak recorded impulses from gauges p_i1B and p_i2B were 212.3kPa.ms at 55.1ms and 263.1kPa.ms at 55.2ms respectively, both values correspond to the contribution of impulse from the second shock. Disregarding the second shock, the peak recorded impulses from gauges p_i1B and p_i2B were 204.9kPa.ms at 48.4ms and 256.8kPa at 48.9ms, indicating increases of 7.4kPa.ms and 6.3kPa.ms to the transmitted impulse by the second shock.

At 13m, the target impulse was 262kPa.ms, putting the recorded data between 19% below and 0.4% above the target in the presence of the second shock and between 2-22% below the target in the absence of the second shock. At the 15m radial, corresponding to a target peak static overpressure of 55kPa, gauges p_i1C and p_i2C recorded peak values of 53.1kPa at 43.7ms and 59.5kPa at 43.9ms respectively, with positive phase durations of 10.5ms and 10.7ms respectively. Firstly, the pressure recorded by p_i2C was higher than the pressure recorded by p_i2B, suggesting that there was an error in the p_i2B recording.

The mean recorded peak static overpressure was 56.3kPa, 1.3kPa above the target, with a range of 5.4kPa. The target positive phase duration was 12.3ms, putting the recorded values between 13-15% below the target value. The peak impulses recorded by p_i1C and p_i2C were 234.4kPa.ms at 61.2ms and 227.1kPa.ms at 60ms respectively, both corresponding to the contribution of transmitted impulse from the second shock. In the absence of the second shock, the impulses recorded by p_i1C and p_i2C were 225.3kPa.ms at 54.2ms and 216.9kPa.ms at 54.2ms respectively. The target impulse at 15m was 231kPa.ms, meaning with the contribution of the second shock, the recorded impulses were between 2% below and 1% above the target value. Neglecting the second shock, the recorded values were between 2-6% below the target impulse.

At the 19.5m radial, corresponding to a target peak static overpressure of 35kPa,

gauges p_i1D and p_i2D recorded peak values of 37.4kPa at 54.9ms and 29.1kPa at 55.3ms respectively, with positive phase durations of 11.5ms and 12.3ms respectively. The recorded pressures were between 17% below and 6% above the target pressure, with a range of 8.3kPa and a mean recorded pressure of 33.3kPa, 1.7kPa below the target. The target positive phase duration was 13.7ms, putting the values between 10-16% below the target value. The peak values of impulse recorded by gauges p_i1D and p_i2D were 191.9kPa.ms at 71.8ms and 169.6kPa.ms at 72.6ms respectively, both values correspond to the contribution of impulse transmitted by the second shock; neglecting the second shock gave values of 187.2kPa at 67.7ms and 161.3kPa at 67.7ms respectively. The target impulse at 19.5m was 183kPa.ms, putting the recorded values between 7% below and 5% above with the contribution of the second shock and between 12% below and 3% in the absesne of the second shock.

At the final pressure radial, 36m, corresponding to a target pressure of 14kPa, gauges p_i1E and p_i2E recorded peak values of 13.6kPa at 100.2ms and 15.7kPa at 99.8ms respectively, with positive phase durations of 15.1ms and 14.4ms respectively. The recorded pressures were between 3% below and 11% above the target pressure, with a range of 2.1kPa and a mean recorded pressure of 14.7kPa, 0.7kPa below the target. The target positive phase duration was 16.7ms, putting the values between 10-14% below the target value. The peak values of impulse recorded by gauges p_i1E and p_i2E were 124.6kPa.ms at 120.4ms and 90.0kPa.ms at 122.1ms respectively, both values correspond to the contribution of impulse transmitted by the second shock; neglecting the second shock gives values of 115.6kPa at 115.1ms and 88.8kPa at 114.2ms respectively. The target impulse at 36m was 103kPa.ms, putting the recorded values between 13% below and 20% above with the contribution of the second shock and between 13% below and 12% neglecting the second shock.

Comparing the expected arrival time of the blast at each gauge location, the charge was determined to have detonated at 21ms. In general, the target blast overpressures were achieved within a good degree of accuracy. Between the two radial spokes, p_i1 provided results closer to the expected parameters than p_i2. There are discrepancies

with some particular results provided by p_i2, especially from p_i2B, which recorded a lower pressure than p_i2C; however, having two comparable sets of pressure readings allows for a clear determination as to what the actual overpressures were at each radial distance. The positive phase duration was, on average, 18% below the expected value, resulting in impulse predictions also being less than the expected value. The purpose of these HE trials was to compare short duration blast loading to long duration blast loading at predetermined overpressures. Whilst the values for positive phase duration and impulse were lower than expected, the important parameter, overpressure, was achieved within a good degree of accuracy.

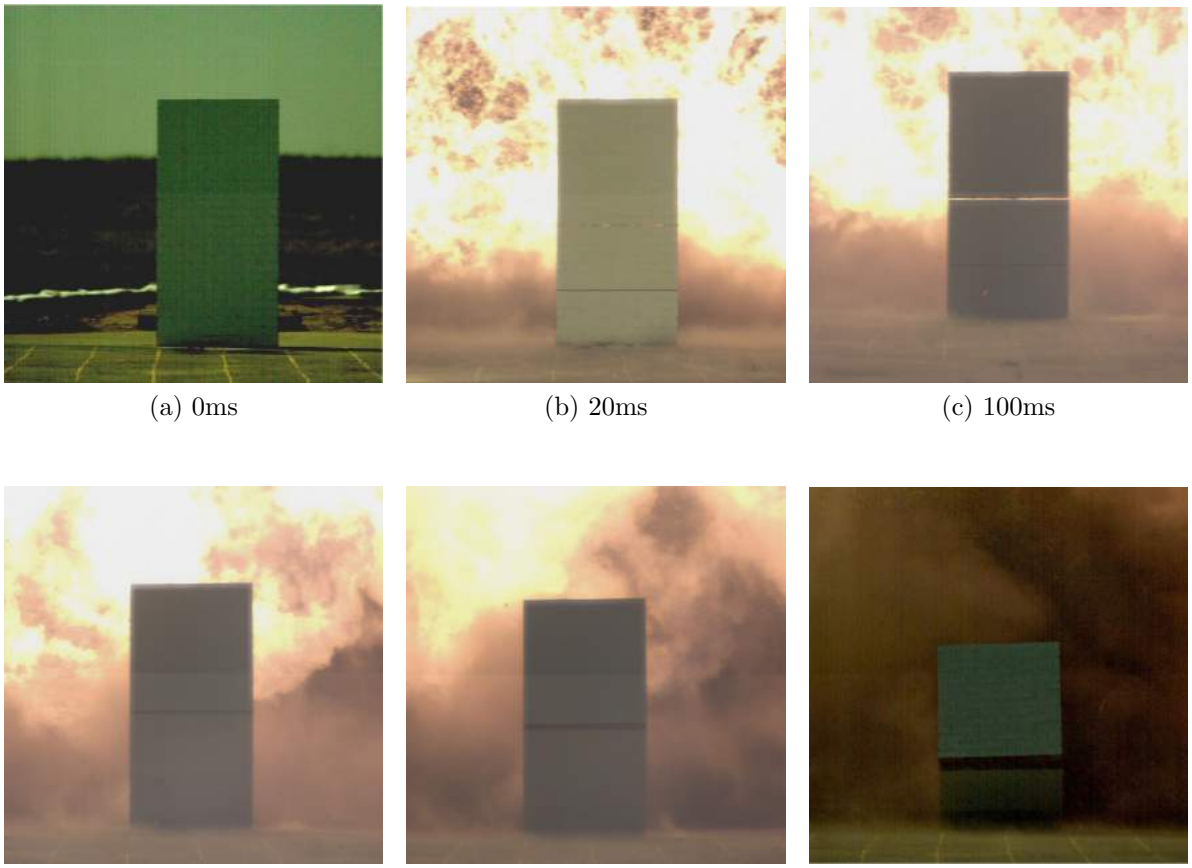

(a) 0ms (b) 20ms (c) 100ms

(d) 200ms (e) 300ms (f) 500ms

Figure 4.15: High speed photography (from the downstream perspective) of the breakage of structure WR1A

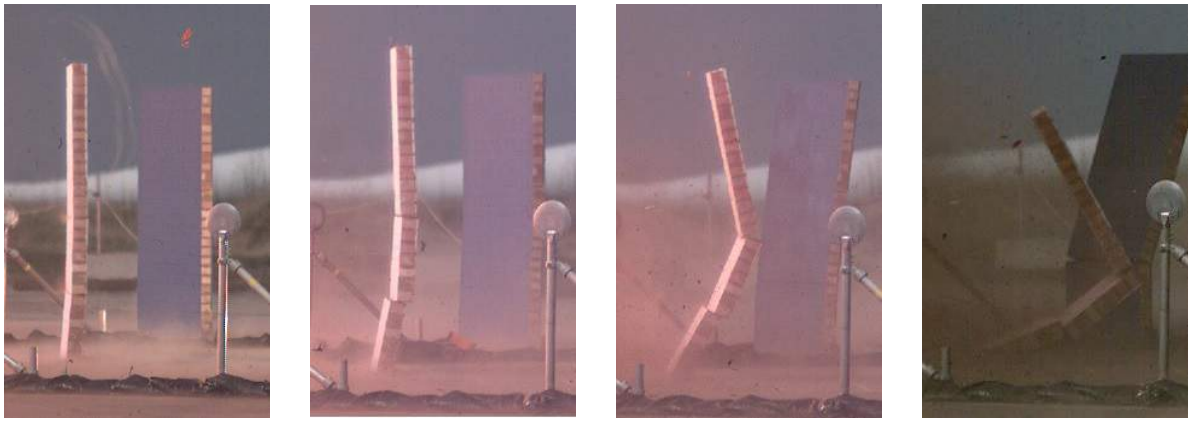

(a) 20ms (b) 100ms (c) 300ms (d) 500ms

Figure 4.16: High speed photography (from the side perspective) of the breakage of structure WR1A

Figures 4.15 and 4.16 show the breakage of structure WR1A from the downstream and side perspectives respectively. The first signs of breakage were observed at approximately 5ms after the arrival of the blast, in the form of a crack along the masonry bedding plane between the 6^{th} and 7^{th} layers of brick, 0.5m above the base of the structure. By 20ms, the crack became larger and more defined, an additional crack began to form at half the height of the structure, between the 13^{th} and 14^{th} layers of brick.

By 100ms, the upper crack became more pronounced and the structure had broken into three, distinct large fragments. The lower fragment began to tilt in the downstream, positive x direction about its base and the second, middle fragment also began to tilt, with the tilting moment also about base of the structure. The top fragment however began to tilt in the opposite direction about the upper crack line. The positive phase cleared the structure by 7.6ms and the second shock had passed by 11ms; the second crack was barely visible at 20ms, meaning no more impulse was transferred to the structure once the crack lines had formed and no additional force acted on the structure in the upstream direction. In the absence of force, the structure slowly collapsed, tilting about the base and upper crack-line.

The longitudinal debris distribution, displayed in Figure 4.17a, shows 57% of the debris fell within -0.5m$< x <$0.5m and the majority of the debris, 82% of the overall mass, fell within -1m$< x <$1m. Figure 4.17c, which shows the longitudinal debris distribution

with respect to the original z position of the debris, indicates that the majority of the debris which fell within -0.5m< x <0.5m, originated from the top and bottom of the structure. Referring to Figure 4.16, this was due to the rotation of the upper and lower halves about the crack-line at half height; thus, the middle section of the wall fell further downstream and the top and bottom sections landed around the origin.

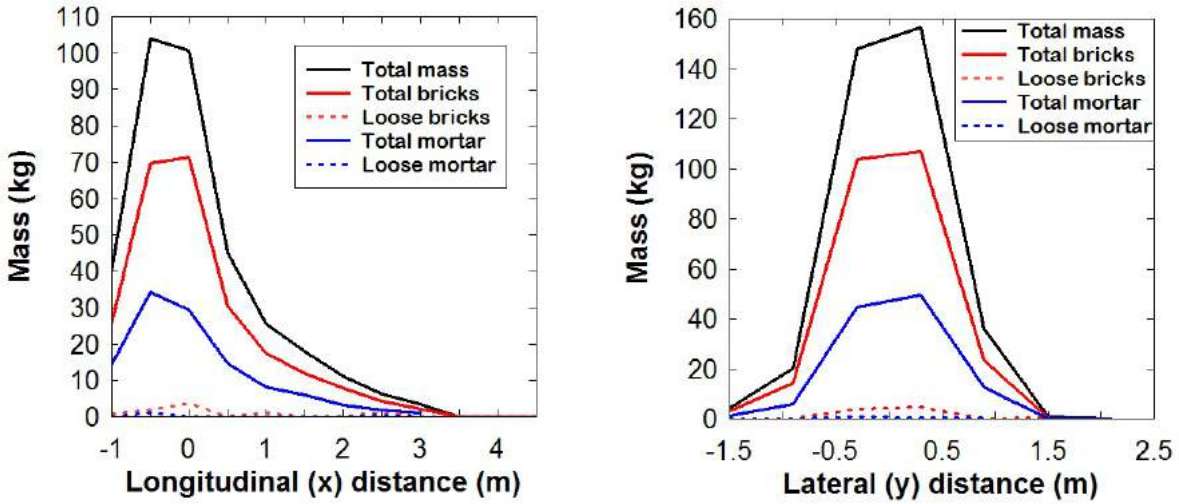

(a) Longitudinal distribution (b) Lateral distribution

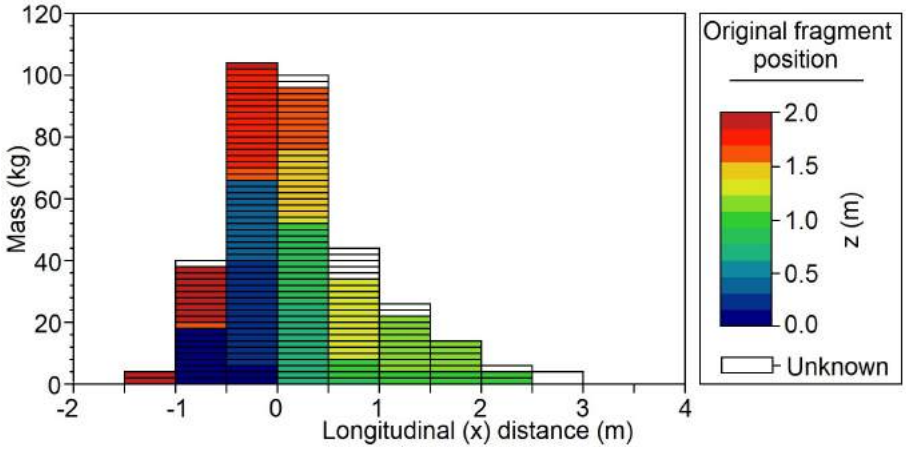

(c) Longitudinal distribution indicating original z position of fragments

Figure 4.17: Longitudinal and lateral debris distribution plots of structure WR1A

Figure 4.17b displays the lateral debris distribution and shows a symmetric distribution around the central y=0 axis of both brick and mortar and hence the overall distribution. The majority of the debris, just over 83% of the overall mass, was located within -0.5m< y <0.5m and 99% the overall debris was located between -1m< y <1m. From both Figures 4.17a and 4.17b, the individual composition of fragments shows that

less than 3% of the debris mass consisted of loose bricks and less than 0.5% of loose mortar, suggesting that impact force was not high enough to separate the bricks and mortar.

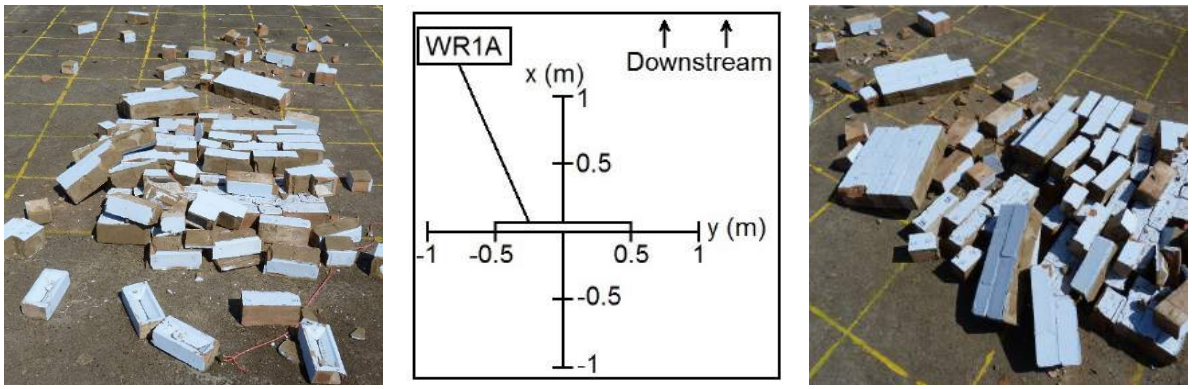

(a) Postshot photograph (perspective: upstream)

(b) Positional information

(c) Postshot photograph (perspective: side)

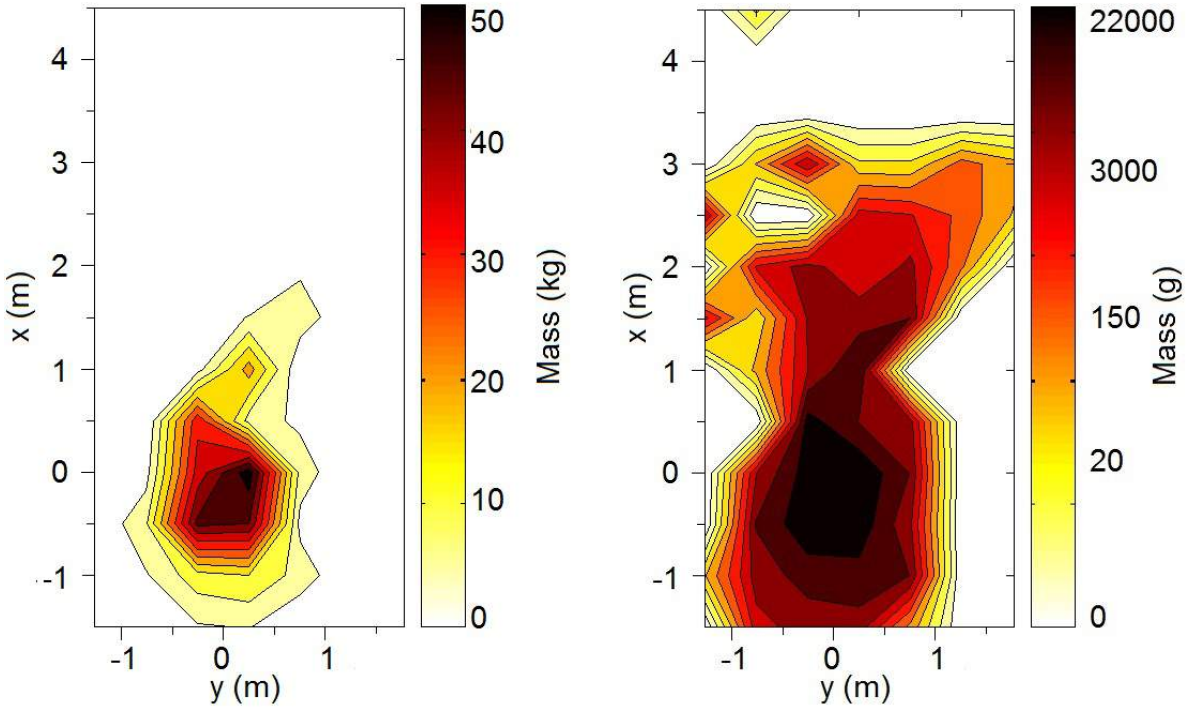

(d) (x, y) mass distribution (absolute)

(e) (x, y) mass distribution (logarithmic)

Figure 4.18: Debris mass distribution of structure WR1A

The x,y mass distribution is displayed in Figures 4.18d and 4.18e plotted on absolute and logarithmic scales respectively, in which Figure 4.18b indicates the original position of the structure. The absolute scale shows the majority of the debris, located in a 1m^2 area centred around the origin. The logarithmic scale shows three areas of medium density,

with masses of approximately 3kg between 1m< x <3m, corresponding to single fragments consisting of a single brick attached to varying amounts of mortar. Figures 4.18a and 4.18c show post-shot photographs of the debris from the upstream and side perspectives respectively; the largest fragment is visible in the top left of Figure 4.18c and consisted of 8 whole bricks and 4 half bricks with a total mass of 30.5kg, originating from approximately 1.5m from the base of the structure on the outer edge and was located in bin (0.5,-0.5).

Structure WR1B was the only structure, other than WR1A, in which the breakage was recorded and is displayed in Figure 4.19. The first signs of breakage occurred at approximately 180ms in the form of a horizontal crack along the bedding plane between the 8^{th} and 9^{th} layers, corresponding to 0.6m above the base of the structure. The positive phase duration recorded at the 13m radial was 9.8ms and 16.2ms including the second shock, meaning a delay of over 160ms before any observable response. The upper section of the structure began to tilt about the crack-line in the downstream direction, with a noticeable displacement by 400ms, shown in Figure 4.19b.

(a) 0ms (b) 400ms (c) 800ms

Figure 4.19: Breakage of structure WR1B

Once the upper section had tilted far enough at approximately 500ms, the opposing force exerted onto the lower section caused it to tilt in the opposing direction about its base. At approximately 800ms, the upper section developed a second horizontal crack line between the 13^{th} and 14^{th} layers, corresponding to 1m above the base of the structure; this additional cracking resulted from the moment created by the tilting motion, causing

the blast weakened bonds to break at the weakest point. The second crack line can be clearly observed at 900ms and is shown in Figure 4.19c.

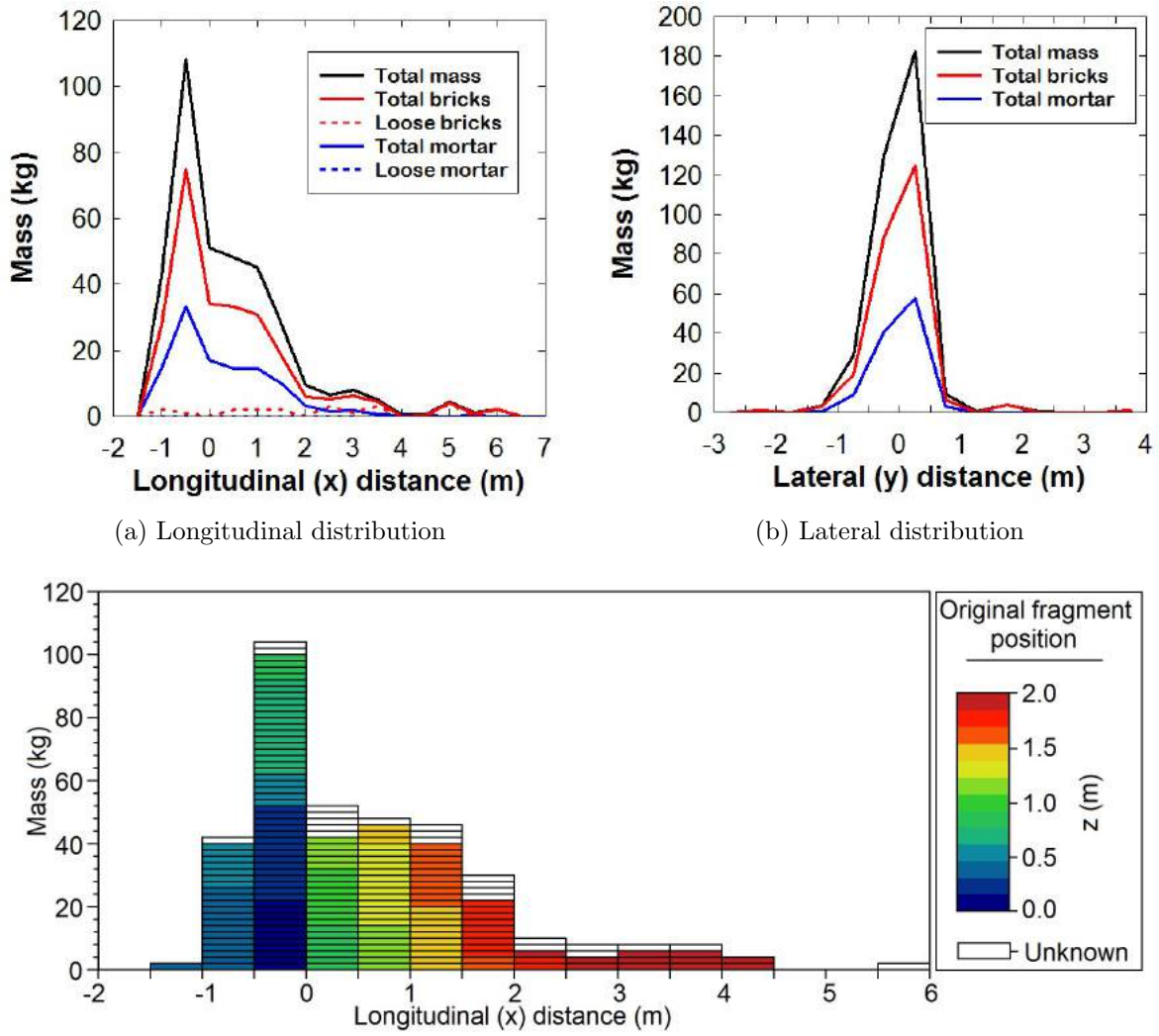

(a) Longitudinal distribution

(b) Lateral distribution

(c) Longitudinal distribution indicating original z position of fragments

Figure 4.20: Longitudinal and lateral debris distribution plots of structure WR1B

The longitudinal debris distribution of structure WR1B, displayed in Figure 4.20a, shows 42% of the overall mass, 360.7kg, fell between -1.5m< x <0m. The longitudinal distribution indicating the original vertical fragment position, presented in Figure 4.20c, shows that this mass originated from the bottom 0.85m of the structure. referring to Figure 4.19c this corresponds to the bottom fragment which tilted in the upstream direction and the middle fragment which tilted in the downstream direction about the base of the crack-line, which moved in the upstream direction as the bottom fragment tilted. Between 0m< x <1m, the fragments originated from between 1m and 1.5m above the

base of the structure, contributing 27% of the structures overall mass. Beyond x=1m, the debris is evenly distributed from the top 0.5m section of the structure.

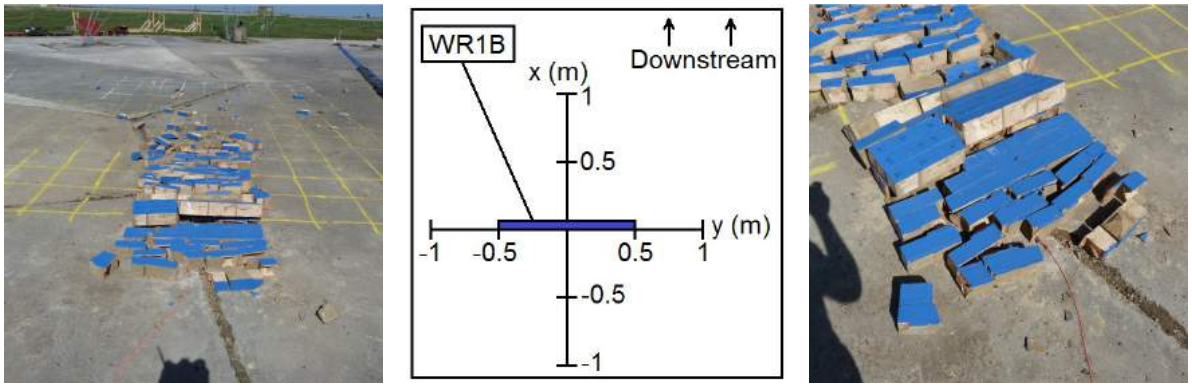

(a) Postshot photograph (perspective: upstream) (b) Positional information (c) Postshot photograph (perspective: side)

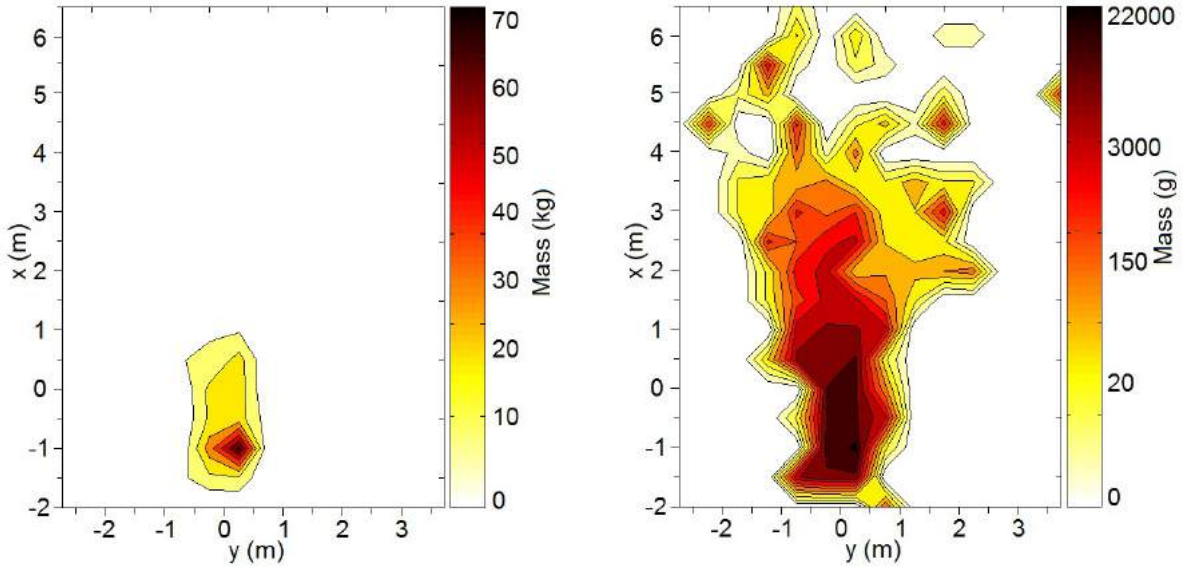

(d) (x, y) mass distribution (absolute) (e) (x, y) mass distribution (logarithmic)

Figure 4.21: Debris mass distribution of structure WR1B

As with WR1A, the majority of the debris consisted of composite brick and mortar fragments due to low impact forces. The lateral distribution, displayed in Figures 4.20b, shows a larger portion of the debris landed in the positive x direction, with 53.3kg more debris located in the y=0m bin compared to the y=-0.5m bin. Inspection of Figures 4.21a and 4.21c which show post-shot photographs of the debris, suggest that the distribution is symmetrical about y=0; however, the large, lower sections of the wall cracked upon impact with the ground, presenting an approximate ratio of 2:3 about the y=0 axis. Although the actual debris distribution was almost symmetrical, the larger fragments

slightly overlapped both bins, but were logged in the y=0m bin which contained over 60% of their total mass, resulting in a skewed lateral debris plot. A total of 89% of the overall mass was located within -0.5m< y <0.5m and the majority of debris, comprising 97% of the overall mass was located within -1m< y¡1m.

Figures 4.21d and 4.21e show the absolute and logarithmic x,y mass distributions of structure WR1B respectively, with Figure 4.21b indicating the relative, original position of the structure. The absolute scale shows the majority of the mass located in the region -1.5m< x <1m and -0.5m< y <0.5m with 72.1kg, 20% of the overall mass, located in a single bin (-0.5,0.5). The logarithmic scale shows the total area covered by the debris and positions of the farthest, outlying bricks which spread up to x=6m. The largest fragment, with a mass of 32.5kg comprising 10 whole bricks and 3 half bricks, originating from the outer edge of the middle fragment, and was located in the high density bin at (-0.5,0.5).

The exact breakage mechanism of structure WR1C is unknown as it was not in view of any of the high speed cameras; however examination of the debris distribution provides insight into the position of crack formations and tilting moments. Figure 4.22a, which displays the longitudinal debris distribution of structure WR1C, shows that the majority of the debris fell between -1.5m< x <1m, which presents a similar longitudinal distribution to WR1A, suggesting a similar tilting motion about a horizontal crack line.

Figure 4.22c, which displays the longitudinal distribution indicating original vertical fragment position, shows the first 2 layers of brick located in the x=-0.5m bin, the 3rd to 7th layers of brick located in the x=-1m bin and the 8th to 12th layers of brick distributed between -3m< x <-1m. The remainder of the x=-0.5m bin was populated by bricks from the 13th to 15th layers. This suggests that a crack formed somewhere between the 6th and 9th layers, between 0.4m and 0.7m above the base of the structure, with the lower fragment tilting in the upstream, negative x direction about its base and the upper fragment tilting about the moving crack-line, in the downstream, positive x direction.

Beyond the x=0 mark, the distribution follows the expected pattern for a structure tilting in the positive x direction, with fragments from higher original z positions located further downstream. The longitudinal distribution of loose bricks, plotted in Figure 4.22a,

increases significantly between 0m< x <1m, suggesting higher impact forces at within this range; if the large, upper fragment tilted as one single mass, the lower section of this fragment would impact the ground first causing deceleration of its upper section and hence reduced impact forces.

The decrease of loose bricks located beyond the x=1m bin agrees with this prediction. It should be noted that structure WR1C had to be rebuilt 1 week before firing, meaning the compressive strength of the mortar was considerably lower than any other structure tested for this research project. It is therefore likely that a much higher number of cracks manifested on the mortar bedding planes; however the lower blast pressures and impulses, 56.3kPa and 221.1kPa.ms (mean recorded values) were potentially too low to cause multiple cracks. In the absence of high speed photography, the true breakage pattern cannot be resolved.

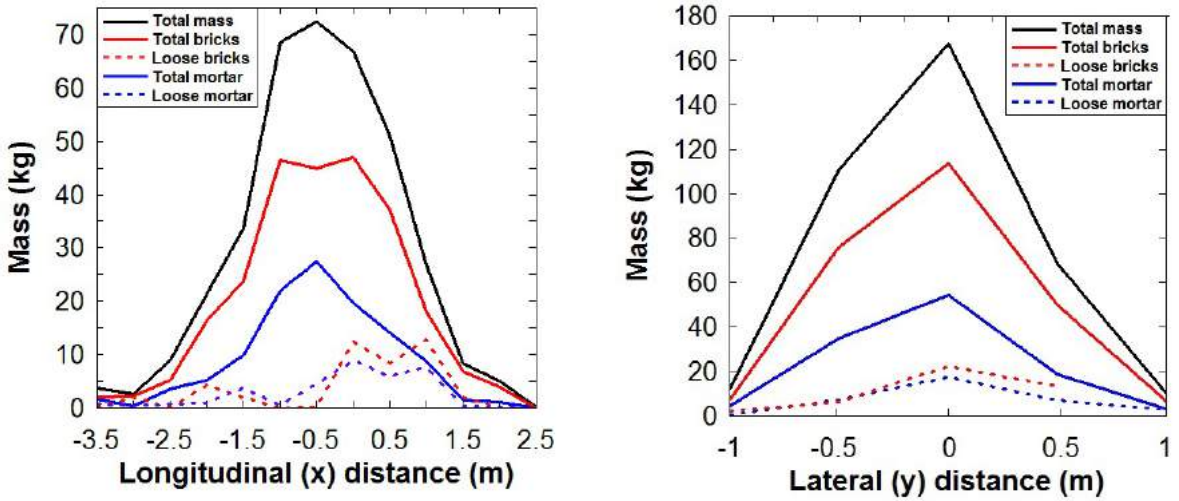

(a) Longitudinal distribution

(b) Lateral distribution

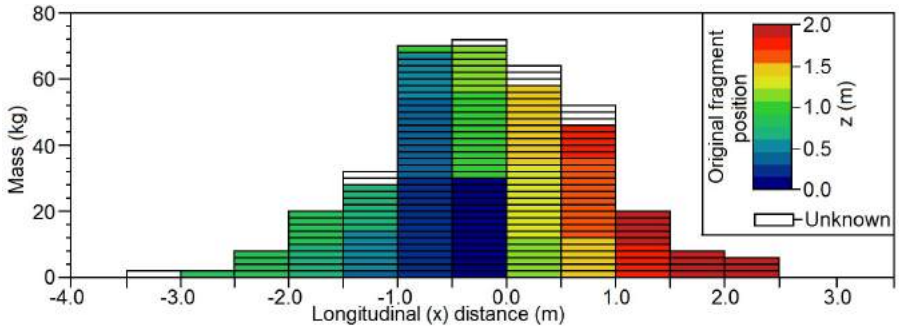

(c) Longitudinal distribution indicating original z position of fragments

Figure 4.22: Longitudinal and lateral debris distribution plots of structure WR1C

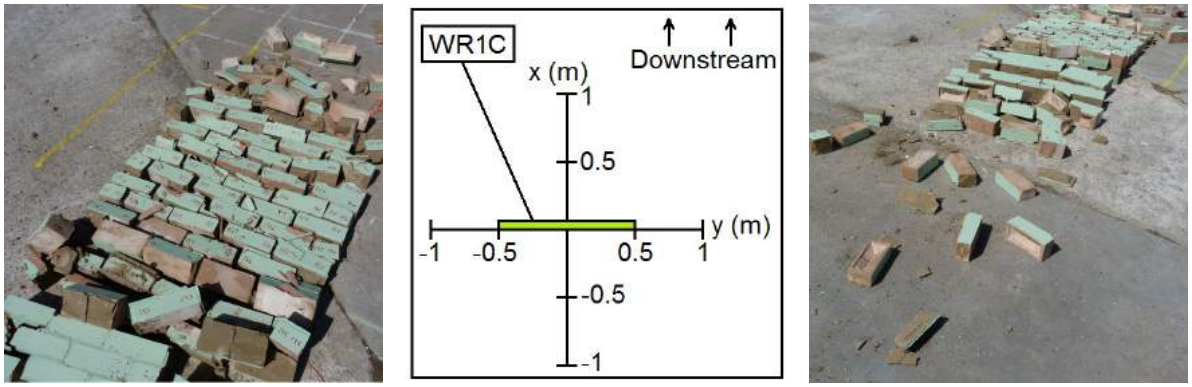

(a) Postshot photograph (perspective: upstream) (b) Positional information (c) Postshot photograph (perspective: downstream)

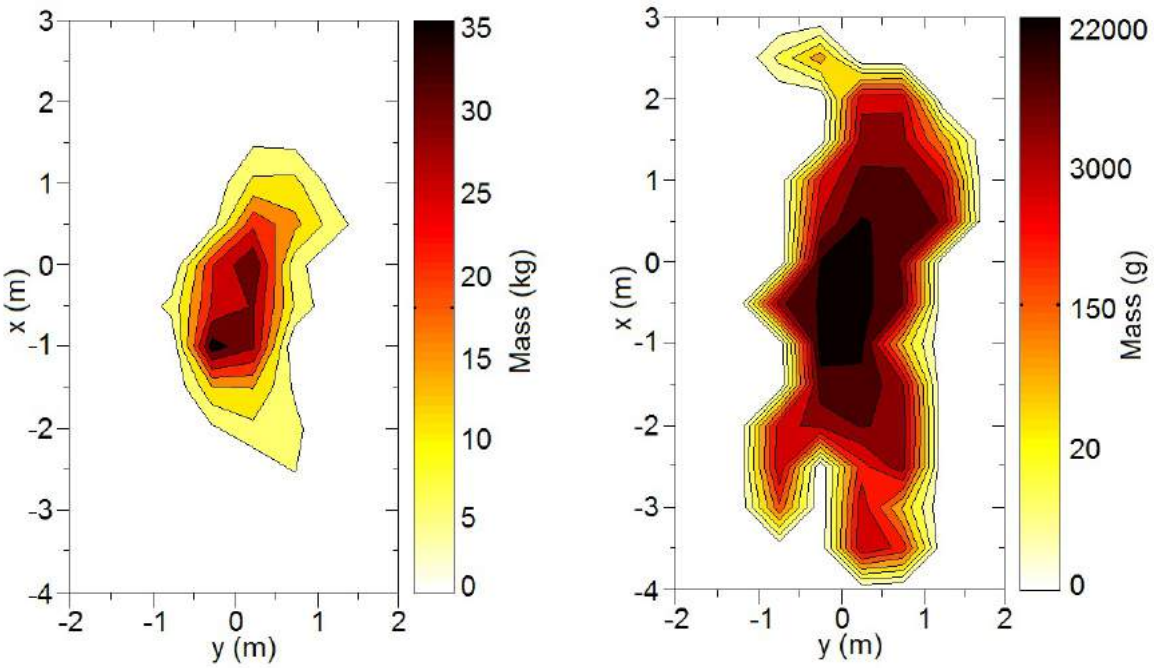

(d) (x, y) mass distribution (absolute) (e) (x, y) mass distribution (logarithmic)

Figure 4.23: Debris mass distribution of structure WR1C

The lateral distribution, displayed in Figure 4.22b, shows the entire mass located within -1m< y <1m, with 75%, 278kg, of which were located within -0.5m< y <0.5m. Similarly to WR1B, the distribution is weighted slightly in the negative y direction; in its original state, 13 bricks sat symmetrically along the central vertical axis, these bricks were all logged in the bin which contained the higher percentage of mass, which for each of these bricks was ≈60% in the y=-0.5m bin.

By sampling all composite fragments and subtracting the brick mass, the average mass of mortar per composite fragment was calculated as 850g, giving the average mass

of composite fragments containing a single brick to be 3kg; therefore, the mass of the 13 central brick was ≈39kg. Subtracting this value from the mass difference between the y=-0.5m and y=0m bins reduces the mass difference to 18kg, 6% of the mass located within -0.5m< y <0.5m.

Figures 4.23a and 4.23c show post-shot photographs of the debris distribution of WR1C, showing larger fragments located in the y=-0.5m bin. Figures 4.23d and 4.23e show the absolute and logarithmic x,y mass distributions of structure WR1C respectively, illustrating the central high density area and overall distributions respectively.

Structure WR1D was located on the 19.5m radial and experience a mean recorded peak static overpressure of 33.3kPa. This was originally planned as the boundary case scenario in which the target overpressure, 35kPa was approximately the breakage limit of masonry. No observable response was identified, with the structure remaining in its original position, without any cracking or noticeable damage. Structure WR1E, located at 36m and experiencing a mean recorded peak static overpressure of 14.7kPa was designed as the non-responding case. As expected, the structure remained undamaged with no observable signs of response. Post shot photographs of structures WR1D and WR1E are displayed in Figures 4.24a and 4.24b respectively.

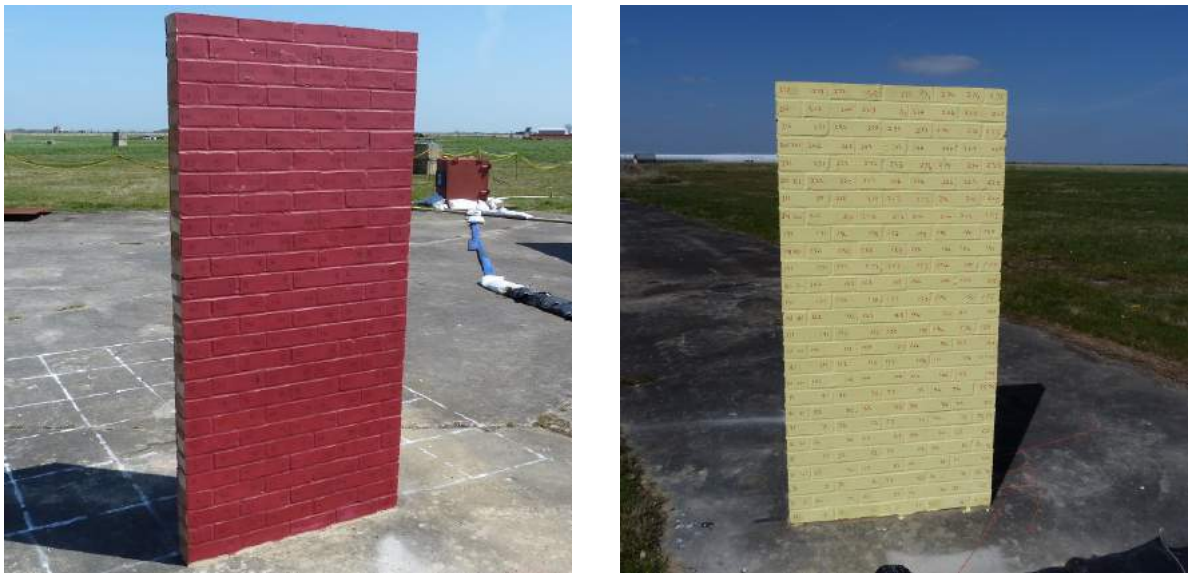

(a) WR1D (b) WR1E

Figure 4.24: Post shot photographs of the non-responding structures from trial WR1

4.2.2 WR2

The second HE trial, WR2, instrumented five masonry structures at varying radial stand-off distances from a charge of 41kg TNT equivalence. Three structures utilised the **B** panel corner geometry from the base panel model, one utilised the **D** panel corner geometry, with the final structure being a repeat of trial WR1C with the compressive strength of the mortar falling within the desired range of 8-10Nmm^{-2}.

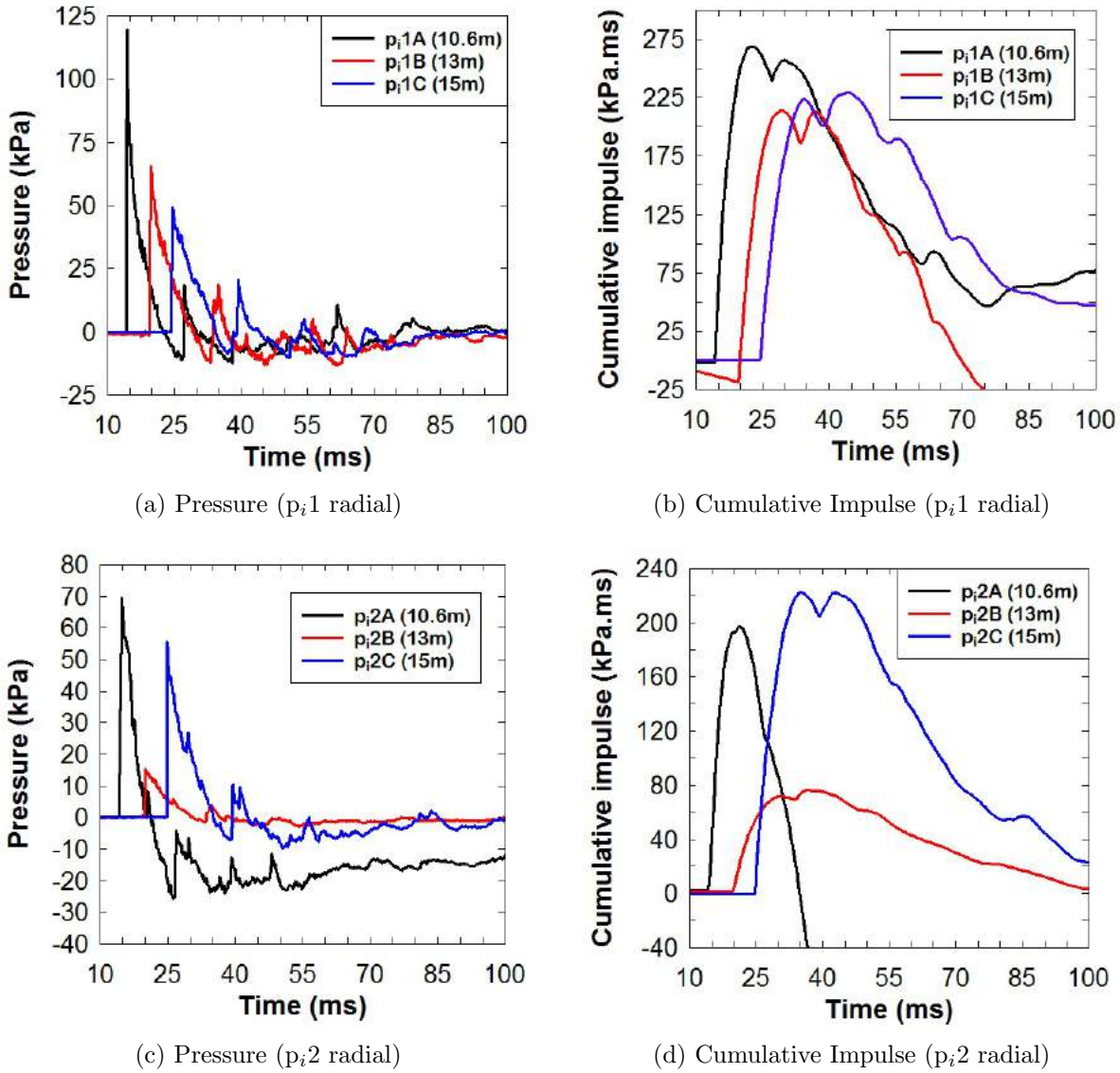

(a) Pressure (p_i1 radial)

(b) Cumulative Impulse (p_i1 radial)

(c) Pressure (p_i2 radial)

(d) Cumulative Impulse (p_i2 radial)

Figure 4.25: Static pressure time histories from trial WR2

As structures WR1D and WR1E did not respond, the five structures were instrumented at the 10.6m, 13m and 15m radials, where the static pressure time histories were

monitored by six Endveco-8510 piezo-resistive pressure transducers positioned in two radial spokes, labelled p_i1(A-C) and p_i2(A-C). The pressure time histories recorded by the p_i1 and p_i2 radials are displayed in Figures 4.25a and 4.25c respectively and the integrated gauge data representing cumulative impulse recorded by radials p_i1 and p_i2 are displayed in Figures 4.25b and 4.25d respectively.

The gauges at the 10.6m radial, p_i1A and p_i2A, recorded peak static overpressures of 119.6kPa at 14.4ms and 69.7kPa at 14.7ms respectively, with positive phase durations of 8.2ms and 6.5ms respectively. As with trial WR1, the recorded positive phase durations were considerably below the target values, in this case between 18-38%. The peak static overpressure recorded by p_i1A was 9.6kPa, 9%, above the target, which, considering the duration of the peak was <1ms, is within an acceptable range; p_i2 however recorded 40.3kPa, 37.7%, below the target pressure.

Inspecting the pressure time history of p_i2A, displayed in Figure 4.25c, shows unusual behaviour after 21.2ms when the negative phase began. The negative pressure dropped to -25.6kPa, which was 15.2kPa and 233% lower than p_i1A; furthermore, the second shock, which was seen to arrive at the end of the negative phase did not ever rise above 0kPa. This suggests that the gauge either malfunctioned or was not properly calibrated and highlights the importance of instrumenting multiple gauges at each monitoring point. Disregarding the recorded data from p_i2A, the peak recorded impulse from p_i1A was 268.6kPa.ms, 44kPa.ms and 16% lower than the target value of 313kPa.ms.

At the 13m radial, gauges p_i1B and p_i2B recorded peak static overpressures of 65.5kPa at 19.7ms and 15.3kPa at 20ms respectively with positive phase durations of 9.8ms and 10.5ms respectively. Firstly, the value recorded by p_i2B was significantly below the target overpressure of 72kPa; however, the positive phase duration was within 0.7ms of the value recorded by p_i1B, suggesting the gauge was either incorrectly calibrated or obstructed, thus recording lower pressures. The peak pressure recorded by p_i1B was 6.5kPa, 9% lower than the target value and the peak recorded value for impulse was 214.1kPa.ms, 47.9kPa.ms and 18% below the target value of 262kPa.ms.

The peak value recorded by p_i1B was 4.28× higher than the recorded value of p_i2B;

multiplying the p_i2B gauge data by 4.28 and integrating gives a peak impulse of 306.5kPa.ms, suggesting that not only was the magnitude of the recorded pressure incorrect, but also the waveform decay constant. The target positive phase duration at 13m was 11.4ms, putting the recorded values between 8-14% below the target.

At the outer, 15m radial, gauges p_i1C and p_i2C recorded peak static overpressure of 49.1kPa at 24.6ms and 55.6kPa at 24.8ms respectively and positive phase durations of 9.7ms and 10.3ms respectively. Both gauges showed good agreement with a range of 6.5kPa and values falling between 10% below and 1% above the target overpressure of 55kPa and a mean recorded pressure of 52.4kPa. The positive phase durations were between 16-21% below the target value of 12.3ms. The recorded impulses from gauges p_i1C and p_i2C were 223.4kPa.ms and 222.2kPa.ms respectively, showing good agreement with a range of 1.2kPa.ms and a mean value of 222.8kPa.ms. The target impulse at the 15m radial was 231kPa.ms, putting the recorded values between 3-4% below the target value.

Comparing the arrival times for each of the pressure time histories with their expected arival times, shows the p_i1 radial predicting the detonation to occur at 1.6ms and the p_i2 radial predicting 1.9ms, in which the 0.3ms difference is a sequencing delay between the two radials. Although they do not offer any directly useful results, inspection of gauges p_i2D and p_i2E recorded values approximately matching those of p_i1D and p_i1E and their target pressures respectively. As the recorded data from p_i2C also matches p_i1C, it is suspected that there was a fault in the instrumentation of the first two gauges in the p_i2 radial.

As with WR1, the recorded positive phase durations and impulses were all lower than the expected values; however, once again, the key parameters from the HE trials were the overpressures. To summarise the blast parameters of the Windrush series, the target parameters were met to within an acceptable degree of accuracy. All of the target parameters were predictions made using the Kingery and Bulmash polynomials [86], which are semi-empirical in nature and do not offer exact values. These equations were simply used to approximate the radial distances required to achieve certain overpressures,

with no predetermined requirement for specific durations or impulses.

Similarly to structure WR1C, the breakage of the majority of structures in the WR2 trial was not recorded by high speed photography; although the corner geometries of the **B** and **D** panels are more complex than those of the simple **A** panel, the debris distributions provided some insight into the breakage mechanisms of these structures.

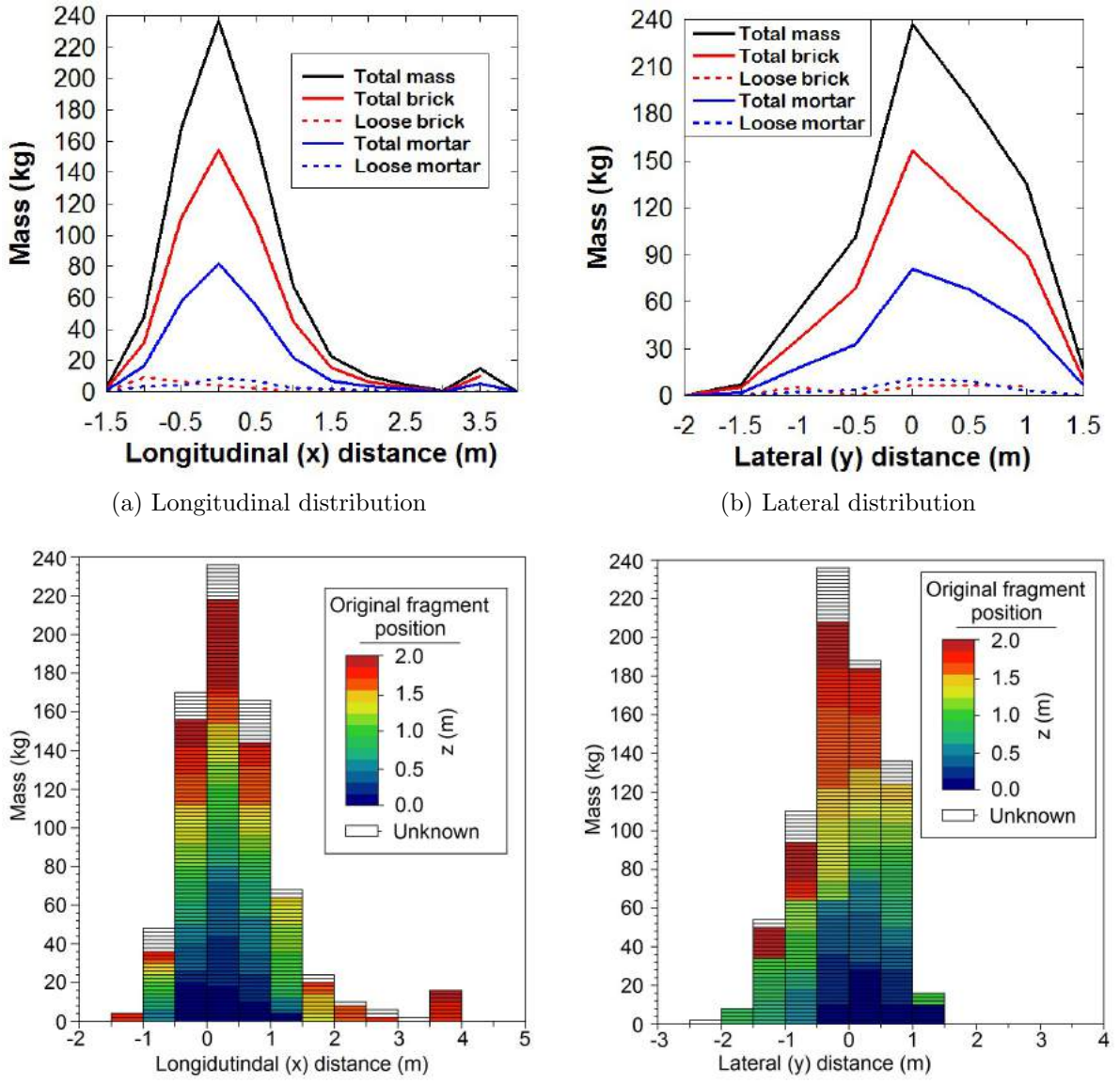

(a) Longitudinal distribution

(b) Lateral distribution

(c) Longitudinal distribution indicating original z position of fragments

(d) Lateral distribution indicating original z position of fragments

Figure 4.26: Longitudinal and lateral debris distribution plots of structure WR2A

The longitudinal debris distribution of structure WR2A, displayed in Figure 4.26a, shows the peak distribution in the x=0m bin, with a mass of 236.8kg. Within the region -0.5m< x <1m, the distribution was almost symmetrical, with 169.0kg and 163.3kg

located in the x=-0.5m and x=0.5m bins respectively. Figure 4.26c also shows an almost symmetrical distribution of debris in terms of original position within this region.

As illustrated by Figure 4.27b, the side panel of the structure was positioned between 0m< x <1m, at y=-0.5m, with the front panel placed along x=0m between -0.5m< y <0.5m. This suggests that the side panel rotated about the corner joint and collapsed inwards as a result of the pressure on its outside face, a prediction supported by the even longitudinal distribution of debris with respect to original vertical position within the x=0m and x=0.5m bins; if the side panel rotated and toppled about its base at y=-0.5m, the distribution would be in the lateral direction, meaning no longitudinal bias towards original vertical position.

The high density distribution in the x=-0.5m bin had a recorded mass of 169.0kg, which corresponds to approximately half the mass of an **A** panel, or one quarter of the mass of a **B** panel. The debris within this longitudinal bin shows no vertical bias, suggesting it originated from both the front and side panels. Beyond the x=1m mark, the distribution shows a large mass of approximately 65kg originating vertically between 1m and 1.5m, followed by a small distribution of fragments originating from the upper vertical positions. These fragments originated from the front wall, resulting from the incident pressure forcing the wall to collapse in the positive x direction.

The lateral distributions, shown in Figures 4.26b and 4.26d, show the majority of the debris, 426.6kg or 58% of the overall mass, was located between -0.5m< y <0.5m,, corresponding to the original position of the front panel. The distribution of debris within this region shows no vertical bias, suggesting the majority of the front panel was located within this region; however, the lateral distribution outside of this region provides some insight into the breakage of the side panel.

The y=0.5m bin contained a large portion of the mass originated from between 0.75m and 1.5m above the base of the structure, suggesting a tilting of the side panel in the positive y direction. As previously mentioned, this is a result of the incident blast pressure on the outer face of the side panel; however, in the -1.5m< y <-0.5m region a large portion of mass corresponded to the upper 0.5m vertical section of the structure, suggesting that

a horizontal crack formed on the upper section of the side panel.

Post-shot photographs of the debris from the upstream and downstream perspectives, shown in Figures 4.27a and 4.27c respectively, illustrate the high density distribution, centred around the (0.5,0) mark corresponding to the point at which the central axes of both panels intersect. Figures 4.27d and 4.27e show the absolute and logarithmic x,y mass distributions respectively; the logarithmic scale shows the total area covered by the debris was approximately 13m^2, with the outer extents populated by single, large fragments.

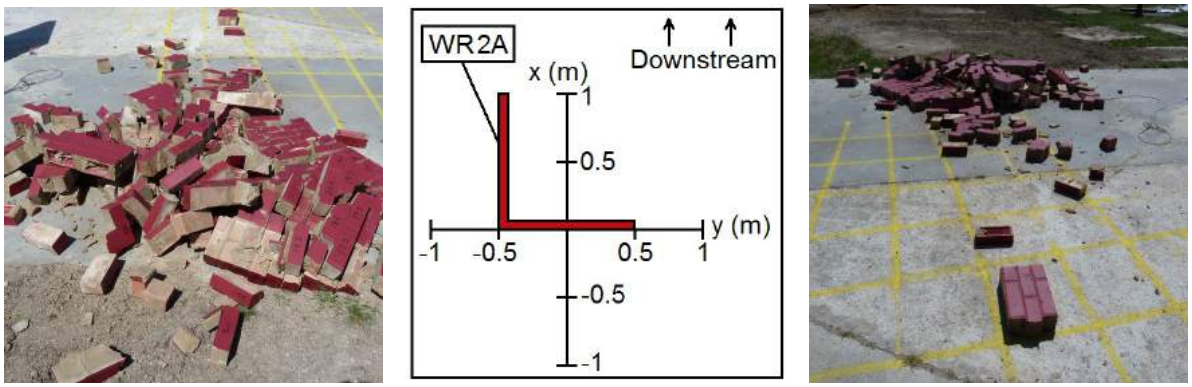

(a) Postshot photograph (perspective: upstream)

(b) Positional information

(c) Postshot photograph (perspective: downstream)

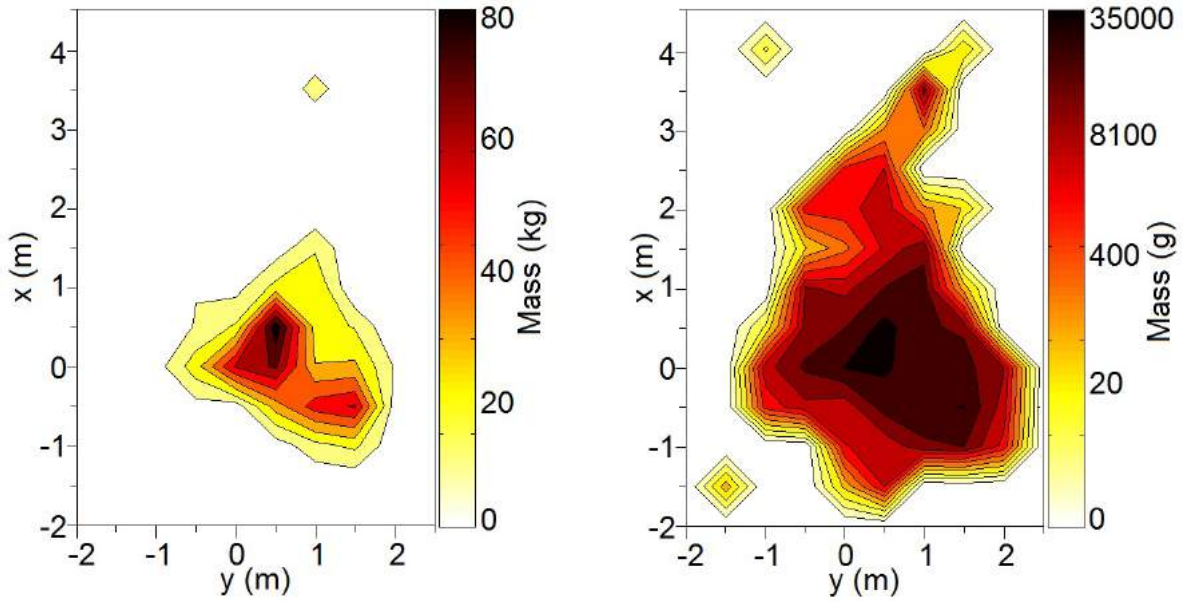

(d) (x, y) mass distribution (absolute)

(e) (x, y) mass distribution (logarithmic)

Figure 4.27: Debris mass distribution of structure WR2A

The absolute scale illustrates the central, high density area in which the majority

of the mass was located; several large fragments were recorded within this region, the largest of which had masses of 20.5kg, 19.1kg and 17.2kg located in the (0.5,0.5), (1,1) and (0.5,0.5) bins respectively; the three large fragments consisted of 6.5, 6, and 5.5 bricks mortared together, all originating from the side panel at approximate heights of 1.9m, 1.5m and 1.2m respectively. The total recorded mass of the structure was 741kg, with 487.9kg of brick and 253.1kg of mortar, corresponding to 66% and 34% of the overall mass respectively.

Structure WR2B was a **D** panel, oriented such that the most upstream face of the blast normal panel was positoned at the 10.6m radial, illustrated by Figure 4.29b; note, the positioning of this structure is essentially a 180° rotation of WR2A about (0.05,0), where 0.05m is half the depth of a brick.

The longitudinal distributions, displayed in Figures 4.28a and 4.28c, show the majority of the debris located in the region -1m$< x <$0m, corresponding to the original position of the side panel; within this region, a total of 436.3kg of debris, 60% of the overall mass was recorded, consisting almost entirely of composite brick and mortar fragments. Figure 4.28c shows that the entire lower section of the wall, up to 0.7m above the base, was located within this region.

The post-shot photographs, displayed in Figure 4.29a and 4.29c, clearly show that this lower section remained in its original position. The distribution of mass between 0m$< x <$1m, shows large quantities of debris originating from the middle, vertical position of the stucture. This mass is resulted from loading of the upstream face of the rear, blast normal panel, causing a tilting motion about the horizontal cracks which formed above the lower section between the 7^{th}, 8^{th} and 9^{th} layers of brick.

The distribution of fragments originating from the top section of the structure, located beyond x=0, was lower than expected if the entire rear, blast normal panel tilted in the upstream direction about the lower, horizontal crack line; this suggests an additional horizontal crack formed higher up, causing counter tilting of the top section.

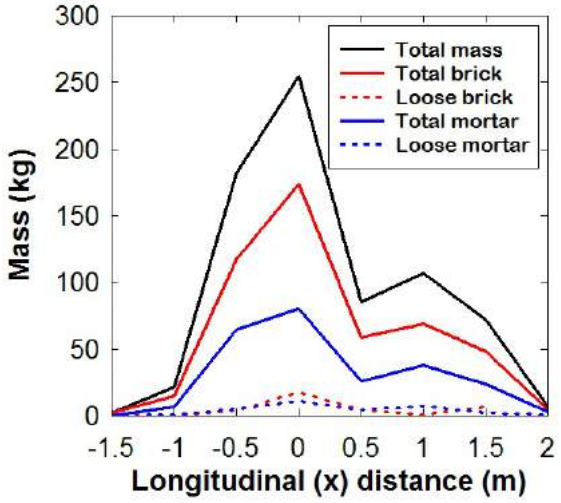

(a) Longitudinal distribution

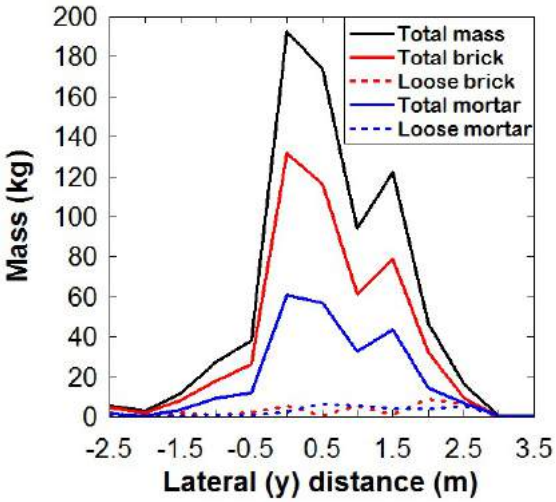

(b) Lateral distribution

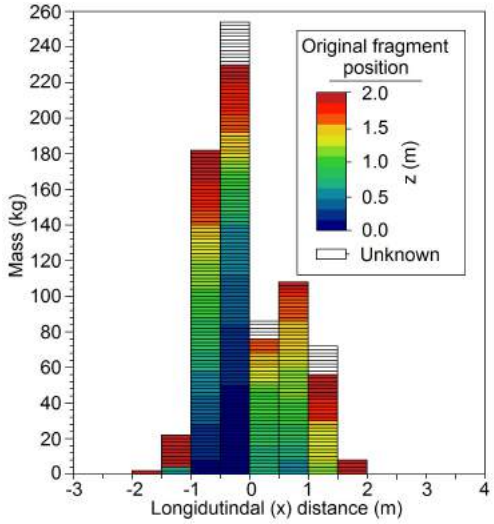

(c) Longitudinal distribution indicating original z position of fragments

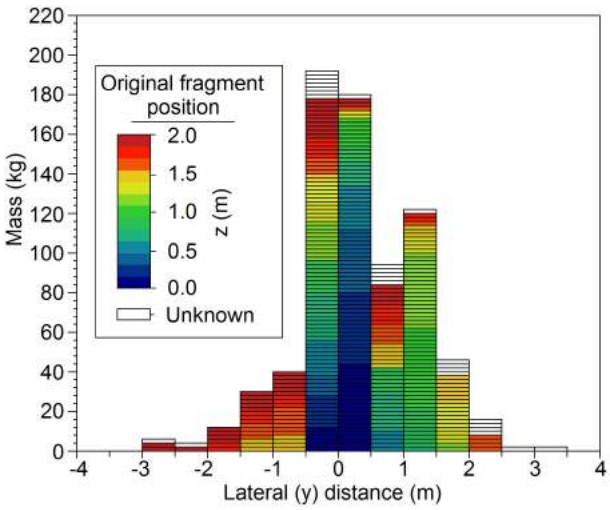

(d) Lateral distribution indicating original z position of fragments

Figure 4.28: Longitudinal and lateral debris distribution plots of structure WR2B

The lateral distribution, displayed in Figure 4.28b, shows 50% of the debris, 366.1kg of the overall mass, located within the region -0.5m< y <0.5m, corresponding to the original position of the rear, blast normal panel. As with the longitudinal distributions, Figure 4.28d shows the entire lower section of the structure located within this region. Beyond this region, lateral distributions show approximately 200kg of mass originating from the central, vertical position distributed between 0.5m< y <2m; as with the rear, blast normal panel, the side panel most likely developed horizontal crack-lines between the 7^{th}, 8^{th} and 9^{th} layers of brick, causing a tilting in the positive y direction.

As the **D** panel is oriented such that the 'interior' is exposed directly to the blast, this allows the blast wave to reflect between the two panels, resulting in a net load applied to the interior face of the side panel, thus resulting in a tilting motion in the positive y direction. In the region $y < -0.5$m, all of the recorded fragments originated from the upper 0.5m section of the structure, specifically the side panel. This suggests that an additional horizontal crack formed higher up on the side panel, causing a counter tilting motion of the upper section in the negative y direction.

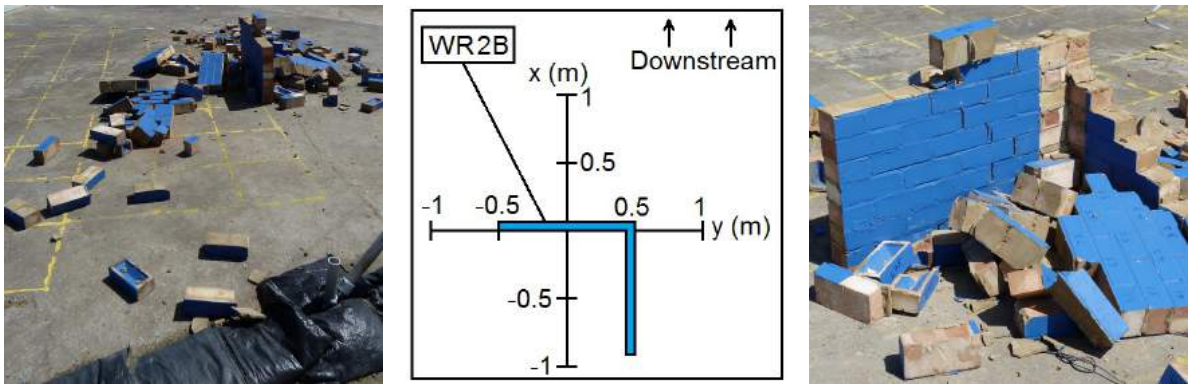

(a) Postshot photograph (perspective: side)

(b) Positional information

(c) Postshot photograph (perspective: upstream, close-up)

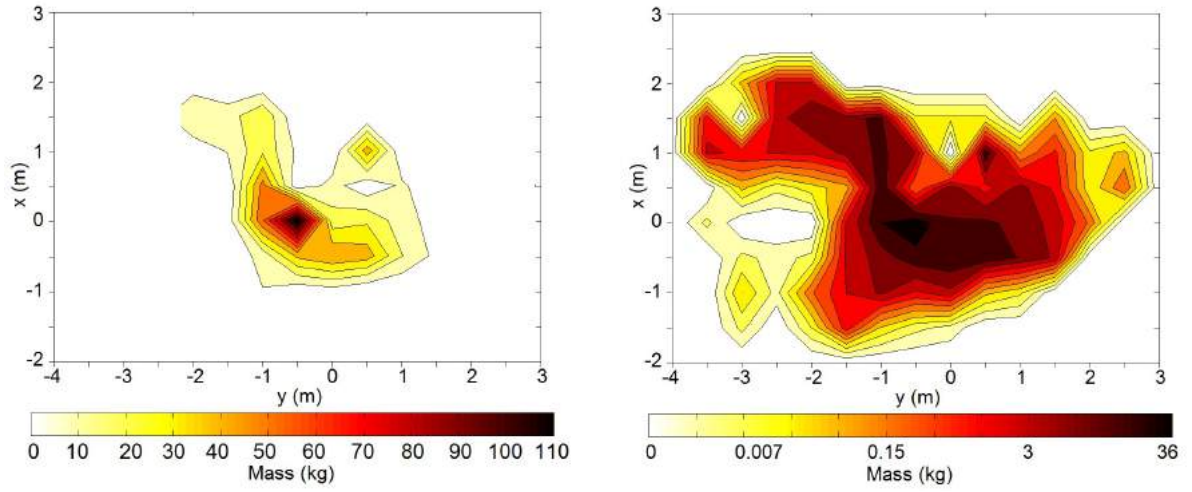

(d) (x, y) mass distribution (absolute)

(e) (x, y) mass distribution (logarithmic)

Figure 4.29: Debris mass distribution of structure WR2B

The x,y mass distributions of structure WR2B are displayed in Figures 4.29d and 4.29e plotted on absolute and logarithmic scales respectively. The logarithmic distribution shows the debris distribution covering an approximate area of 17m.5^2, with the maximum x,y extents covering an area of 26m^2. The absolute x,y mass distribution shows the

highest density are of the debris distribution located between 0.5m< x <0.5m and -1m< y <0m, in which the two largest recorded fragments were located. The masses of these fragments were 87.8kg and 45.1kg and formed the undistributed base of the structure, separated into two separate fragments by a crack along the central axis of the rear, blast normal face; their combined mass was approximately 18% of the overall mass of the structure.

The largest two recorded fragments which did not remain in their original positions were located in bins (-1,0) and (1,1), with masses of 34.3kg and 31kg respectively; the larger consisting of 10 whole bricks and 3 half bricks mortared together, originating from the edge of the side panel at 0.5m above the base and the smaller fragment consisting of 8 whole bricks and 4 half bricks mortared together, originating from the rear, blast normal face at 1.2m above the base. The total recorded mass was 731.3kg, consisting of 488.8kg of brick and 242.6kg of mortar. It should be noted that the overall mass was 10kg less than that of WR2A, 9.1kg of which was logged as mortar.

Structure WR2C, an **A** panel located at the 15m radial position, was an effective repeat of trial WR1C, such that the compressive strength of the mortar was within the same range as the rest of the trials in the Windrush series. The longitudinal debris distributions of structure WR2C, displayed in Figures 4.30a and 4.30b, show the peak distribution was recorded in the x=-0.5m bin with a steadily decreasing distribution in the downstream, positive x direction.

The lower 0.3m section of the structure was located in the x=-0.5m bin, with the next 0.3m section located in the x=-1m bin, suggesting that the lower section of the structure tilted in the upstream direction about its base. The next 0.3m section, that is between 0.6-0.9m, was located in the x=-0.5m bin, suggesting a horizontal crack formed at approximately 0.5m, causing a counter tilting of the upper section of the wall in the downstream direction. Further in the downstream direction, beyond x=0m, the original vertical position of the fragments increased with longitudinal distance; the amount of debris logged within each successive bin in this region decreases steadily with longitudinal distance.

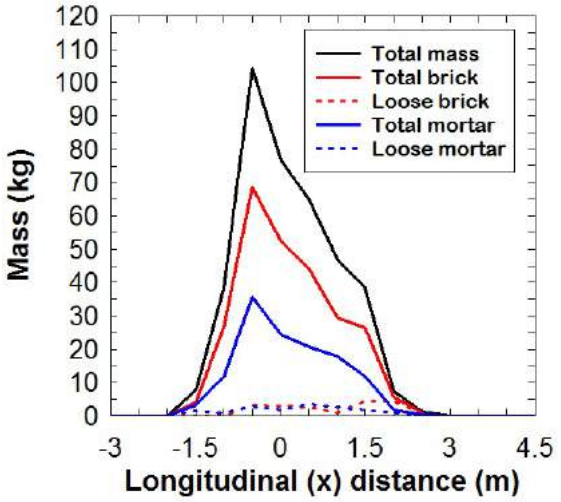

(a) Longitudinal distribution

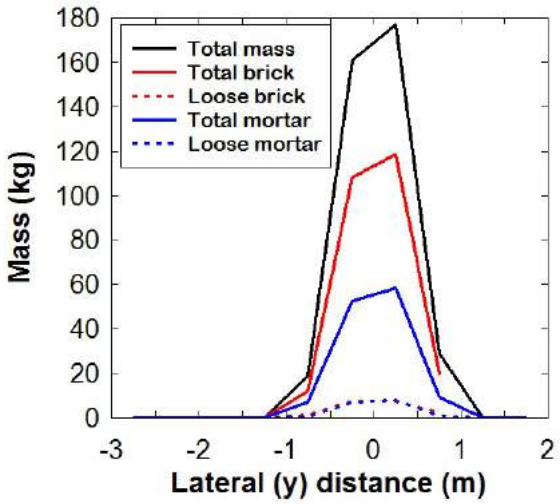

(b) Lateral distribution

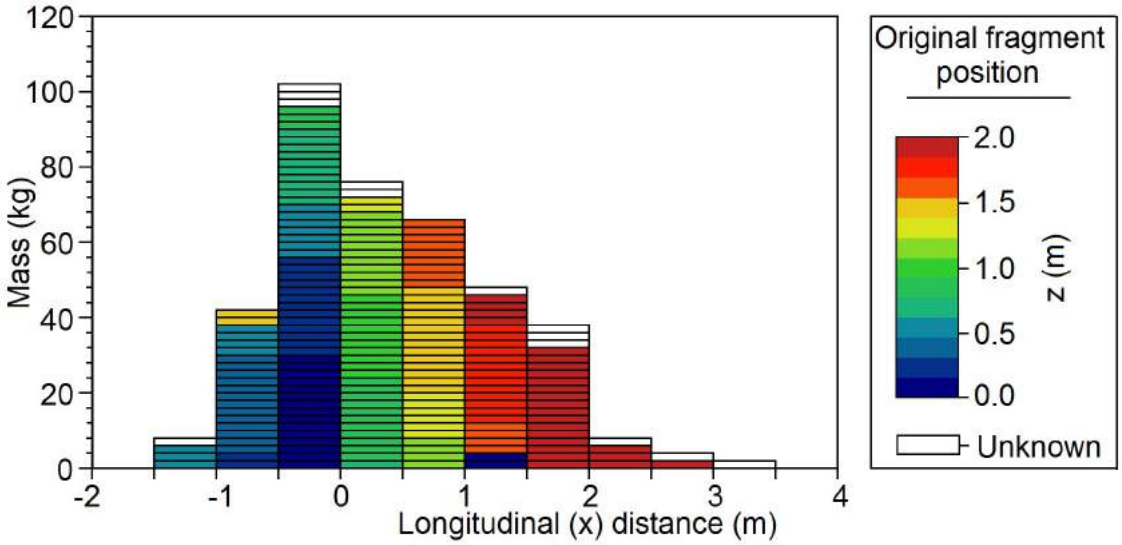

(c) Longitudinal distribution indicating original z position of fragments

Figure 4.30: Longitudinal and lateral debris distribution plots of structure WR2C

As the large fragment tilted towards the ground, the impact force increased with respect to original vertical position; a certain force is required to overcome the brick to mortar bonds, at higher vertical positions a larger amount of energy is transferred to each fragment once the bonds were overcome, leading to an excess in kinetic energy. This results in the slowly increasing vertical distance of the fragments located higher within the structure. Further evidence to this can be deduced upon inspection of the longitudinal distribution of loose brick, shown in Figure 4.30a, which increases beyond the x=1m bin, resulting from higher impact forces increasing the brick to mortar separation.

The lateral distribution, displayed in Figure 4.30b, shows a symmetrical distribution

about y=0m, slightly weighted in the positive y direction, with 160.9kg located in the y=-0.5m bin and 176.7kg located in the y=0m bin, which constitute 88% of the overall mass of the structure. Within the -1m< y <1m region, 99.9% of the overall mass was recorded, presenting a slightly increased weighted distribution about y=0m, with 46.6% of the debris located within -1m< y <0m and 53.3% of the debris located within 0m< y <1m, corresponding to 26.1kg.

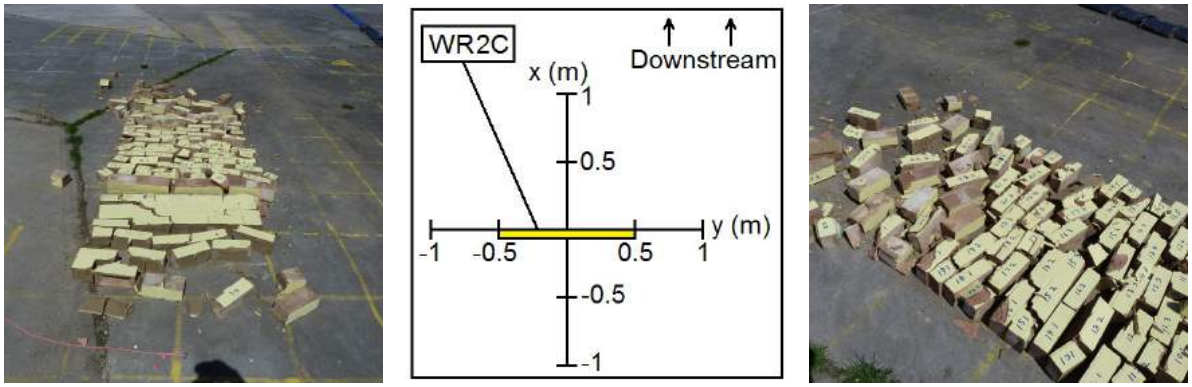

(a) Postshot photograph (perspective: upstream)

(b) Positional information

(c) Postshot photograph (perspective: side)

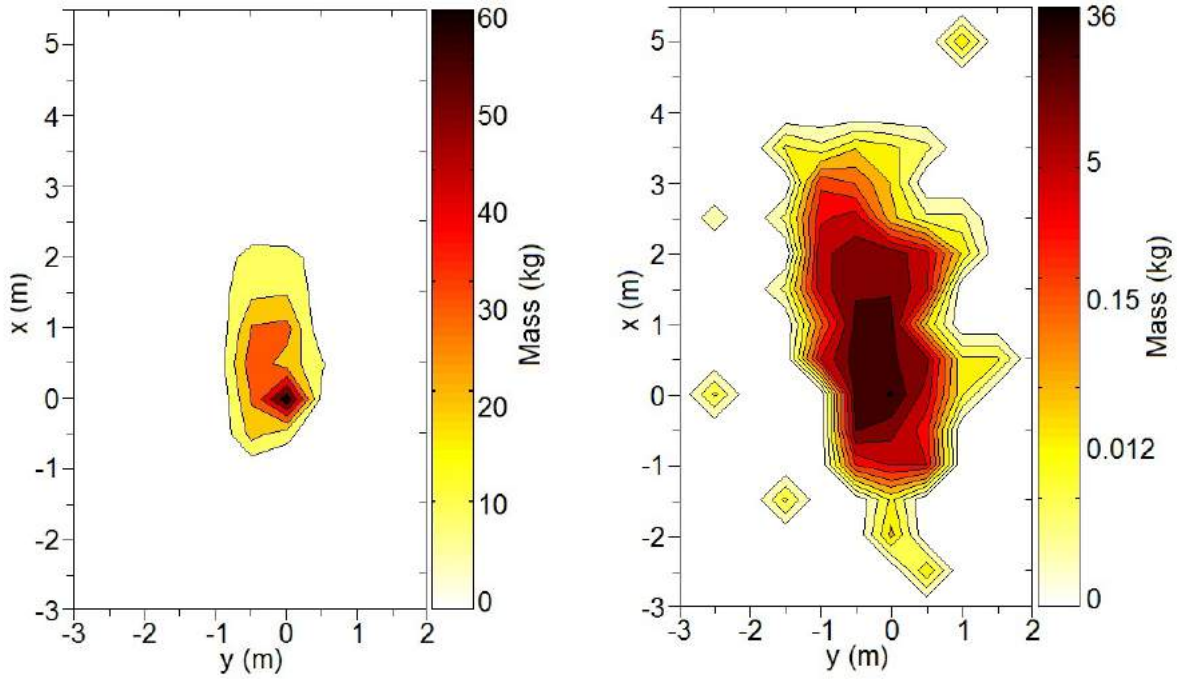

(d) (x, y) mass distribution (absolute)

(e) (x, y) mass distribution (logarithmic)

Figure 4.31: Debris mass distribution of structure WR2C

The post-shot photographs, displayed in Figures 4.31a and 4.31c, show a relatively even lateral distribution, with the total mass of the wall constrained within its original

1m width, indicating that the weighted distribution is potentially due to a larger number of fragments located along the central axis being logged in the y=0m bin; however, if a single fragment is located in multiple bins, it is logged in the bin which contains the majority of its mass, meaning that the lateral distribution should still be slightly weighted. The individual fragment distribution showed a total of 80 composite fragments consisting of one, whole undamaged brick attached to mortar, corresponding to 77% of the total number of whole bricks in the structure.

A total of ten composite fragments were recorded containing more than one whole brick, the largest of which had a mass of 18.0kg, consisting of 6 whole bricks mortared together, originating from the centre of the base of the structure, located at (-0.5,0.5). The x,y mass distributions of structure WR2C are displayed in Figures 4.31d and 4.31e, plotted on an absolute and logarithmic scale respectively. The absolute scale shows the highest density region corresponds to the location of the largest fragment at (-0.5,0.5). The distribution density steadily decreases laterally, whilst weighted in the positive x direction. The logarithmic scale shows the total debris field covering an approximate area of 12.75m^2, with the x,y extents of the debris field covering a maximum, rectangular area of 36m^2.

Structure WR2D, a **B** panel located at the 13m radial, displayed a boundary case response, showing high levels of breakage and structural damage and no debris distribution. A horizontal crack, visible in Figure 4.32a, formed between the 17$^{\text{th}}$ and 18$^{\text{th}}$ layers of brick, approximately 1.3m from the base of the structure, on the side panel, spanning its entire width; the crack continued through the corner joint, forming a stepped crack along the mortar joints up to the top row of bricks, visible in Figure 4.32b.

The crack propagated uniformly between the layers of brick with the exception of the 20$^{\text{th}}$ layer, in which the crack formed along the centre of the brick. On the outer edge of the top layer of bricks on the front, blast normal panel, the stepped crack expanded between three individual bricks, separating them from the rest of the structure. The large fragment created by the stepped crack, became completely unattached from the remainder of the structure, resting in its original position. On the front, blast normal

panel, another, small horizontal crack formed between the 16^{th} and 17^{th} layers of brick, joining the upper, stepped crack at the corner joint. There was almost no displacement of bricks around this crack, making it difficult to see but, is slightly visible in Figures 4.32a and 4.32c. It is unclear as to whether this crack causes complete separation of the two layers in the absence of observable displacement.

At the intersection point of the three aforementioned cracks, approximately 1.2m above the base of the structure on the corner joint, a crack ran vertically down the side face of the corner panel, shown in Figures 4.32a and 4.32c running through alternating mortar joints and brick centres. The vertical crack extended to the connection between the 6^{th} and 7^{th} layers of brick, approximately 0.75m in height, where it propagated onto the front, blast normal face of the structure. The vertical crack also continued for an additional 3 layers of brick where it formed a stepped crack on the side panel, down to its base, giving the vertical crack a total height of approximately 0.9m.

The horizontal crack forming along the front, blast normal face, dispalyed in Figures 4.32b and 4.32d, ran the width of the structure between the 6^{th} and 7^{th} layers, approximately 0.45m above the base of the structure. In combination with the vertical crack, this created a large, unattached fragment spanning the width of the front face, approximately 0.5m in height, or larger if the upper, smaller horizontal crack on the front face caused separation. The lower horizontal crack also intersected a stepped crack, running from the outer edge of the front, blast normal face uniformly along the brick and mortar joints to intersect between the 6^{th} and 7^{th} layers at the corner joint.

Another stepped crack ran from this point on the side panel, down to its base, creating a stepped corner base fragment. In total, the crack systems formed between 5-6 large initial fragments and 3 small fragments, each consisting of one brick. The predicted masses of the large fragments were 193kg for the upper fragment, 253kg for the fragment in the centre of the blast normal face, with 147kg and 106kg above and below the small crack-line respectively, 234kg for the fragment on the lower section of the side wall and 52kg for the base fragment. **B** panels are inherently stronger and more stable than **A** panels as they are constructed in an additional, relative dimension. Whilst the incident

overpressure was strong enough to form the crack pattern, the impulse was not enough to move any of the large fragments, especially due to the large frictional forces between them. All of the cracks observed across the structure intersect at varying positions, meaning the cracking pattern can be attributed to the formation and propagation of one single crack; however the exact origin and direction of propagation of the crack cannot be quantified in the absence of high speed photography.

(a) Side perspective (b) Upstream perspective (c) Side perspective (d) Downstream perspective

Figure 4.32: Post-shot photographs of structure WR2D

The final structure from the WR2 trial, WR2E, was a **B** panel located at the 15m radial. WR2E showed a small debris distribution, displayed in Figure 4.33a, in which a total of 9 bricks from the outer edge of the top 3 layers of the front, blast normal face became detached, falling in the downstream direction. Four bricks were located within the $1m^2$ area covered by the structure, two were located in bin (0.5,0.5), one in (1,0.5) and one in (1,1.5), such that (0,0) corresponds to the centre of the front, blast normal panel.

Five small crack-lines were observed across both faces of the structure; the first small crack is displayed in Figure 4.33c, a stepped crack running from the centre of the base of the side panel up to the corner joint between the 6^{th} and 7^{th} layers, approximately 0.45m above the base of the structure, where it intersects with the second and third cracks. The second crack followed the same pattern, forming from the centre of the base of the front,

blast normal panel between the brick and mortar bonds and intersects the first crack at 0.45m above the base of the corner joint.

The third crack, again intersecting the same point and shown in Figure 4.33b, ran horizontally across the front, blast normal panel; another horizontal crack ran between the 16th and 17th layers of brick, corresponding to approximately 1.2m above the base of the structure. These two horizontal cracks were joined by a vertical crack, with a height of 0.75m, at approximately 0.4m from the corner joint. The crack pattern shows similarity to that of WR2D; however less severe due to the lower incident overpressure. In both cases, horizontal cracks formed between the 6th and 7th layers and the 16th and 17th layers, with a pair of stepped cracks connecting the centre of the base of both panels to the corner joint, between the 6th and 7th layers.

(a) Upstream perspective (b) Downstream perspective (c) Upstream perspective: close-up

Figure 4.33: Post-shot photographs of structure WR2E

4.3 'BWL' Series

The BWL series consisted of three long duration trials conducted in the ABT, each of which subjected masonry structures with varying geometries to target peak static overpressures 110kPa for approximately 200ms and 55kPa for approximately 150ms in the 4.9m and 10.2m sections respectively. Each of the three BWL trials utilised both

sections of the ABT to increase the overall productivity of each firing and increase the amount of obtainable data.

4.3.1 BWL1

The pressure time histories and their respective integrated, associated impulses, from both the 4.9m and 10.2m sections of the ABT, instrumented in trial BWL1 are displayed in Figure 4.34, the relative positions of which are illustrated in Figure 3.28. The 4.9m section was monitored by gauges p_i6, p_r4 and q4, with their pressure time histories and integrated cumulative impulses displayed in Figures 4.34a and 4.34b respectively.

The static overpressure in the 4.9m section, monitored by gauge p_i6, recorded a peak value of 179.5kPa at 318.7ms; however similarly to the gauge data from the MW series, this peak value corresponds to a reflection of the blast wave from the upstream face of the structure. The peak static overpressure at the arrival of the shock discontinuity was 99.9kPa at 311.8ms, 9% below the target pressure of 110kPa. The peak associated impulse was recorded as 7251.6kPa.ms at 525.2ms, providing a positive phase duration of 213.4ms and the estimated impulse from the pressure spike at 318.7ms, due to structural reflections, is approximately 300kPa.ms, 4% of the total recorded impulse.

The peak reflected impulse in the 4.9m section was 290.2kPa at 314.2ms, recorded by gauge p_r2, which is within the expected region for a static pressure of 110kPa. At 417.1ms, the reflected pressure increased instantaneously to 113kPa, where it fluctuated between 108.6kPa and 118.4kPa for the remainder of the recording period. Beyond 417.1ms, the reflective pressure data was therefore lost due to an unknown fault with the pressure gauge, meaning the cumulative impulse can only be recorded up to 417.1ms, 102.9ms after the peak reflective pressure was recorded.

The positive phase duration recorded by the static overpressure was 213.4ms, meaning the peak reflective impulse would be expected at 527.6ms, 110.5ms after the gauge fault occurred. The reflective impulse recorded at 417.0ms was 7264.2kPa.ms; however, assuming the reflective pressure follows a uniform decay between 417.0ms and 526.7ms, the additional impulse would be slightly below 1000kPa.ms, suggesting the overall reflective

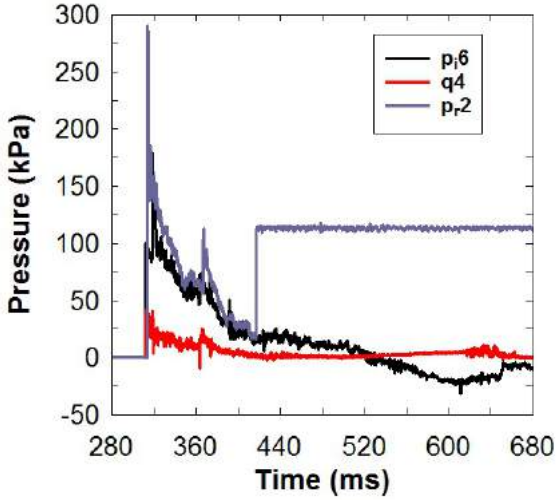

(a) Pressures: 4.9m section

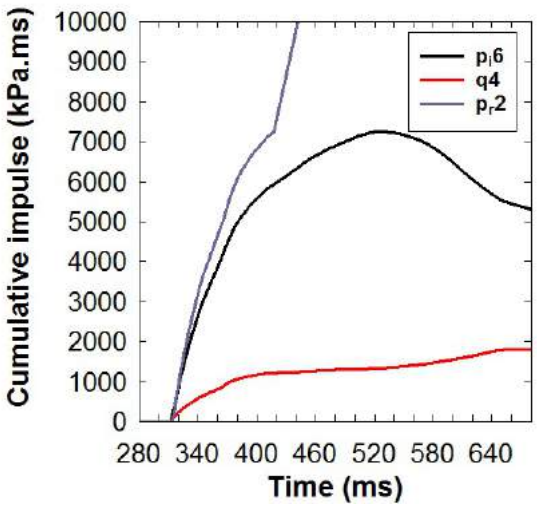

(b) Impulses: 4.9m section

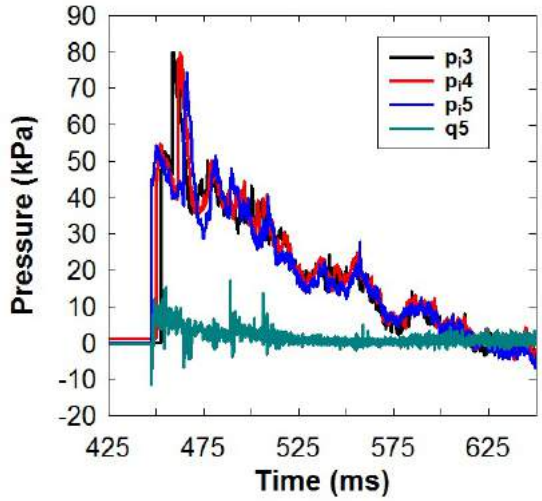

(c) Pressures: 10.2m section (central)

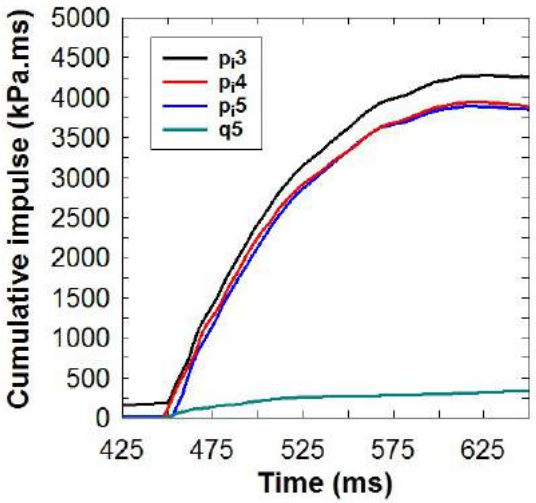

(d) Impulses: 10.2m section (central)

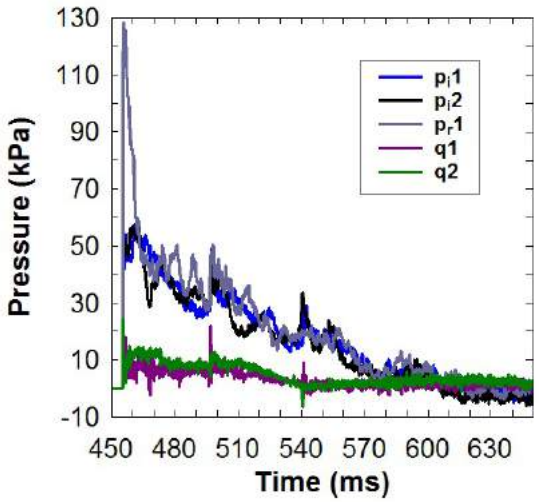

(e) Pressures: 10.2m section (edges)

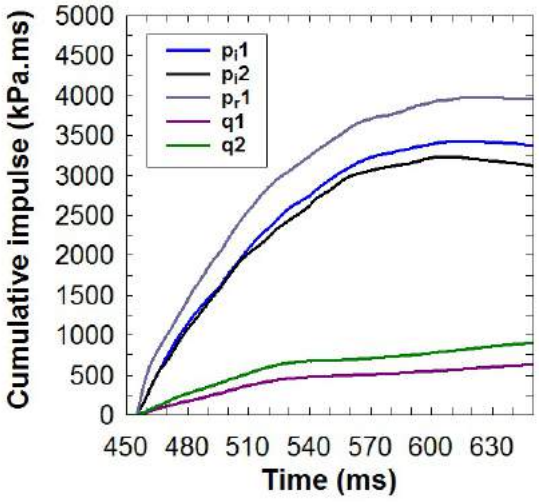

(f) Impulses: 10.2m section (edges)

Figure 4.34: Pressure time histories and integrated impulses from trial BWL1

impulse was approximately 8250kPa.ms.

The peak dynamic pressure in the 4.9m section, recorded by gauge q4, was 42.3kPa at 312.6ms. At approximately 405ms, the dynamic pressure reduces to below 3kPa, where it fluctuates by ±2kPa continuously as the dynamic pressure does not have a negative phase. During these small positive fluctuations, the pressure is too low to have any noticeable effect on structural response, or more importantly during this time period, debris distribution. The peak associated impulse was 1816.9kPa.ms at 667.2ms; however, the associated impulse at 405ms, which roughly corresponds to the end of its effective phase, was 1191.8kPa, 66% of the peak associated impulse.

Gauges p_i3, p_i4, p_i5 and q3 were located in the 10.2m section of the ABT, positioned along its central axis, spaced by 1m intervals, illustrated by Figure 3.28; the pressure time histories and integrated cumulative impulse time histories of which are displayed in Figures 4.34c and 4.34d. The peak static overpressure recorded by gauges p_i3, p_i4 and p_i5 were 79.8kPa at 458.5ms, 79.9kPa at 462.4ms and 74.6kPa at 462.3ms respectively. These gauges were all placed along the central axis of the ABT and thus each gauge recorded a reflection from the upstream face of the large steel enclosure.

Ignoring reflections, the peak static overpressure recorded at the arrival of the shock discontinuity from gauges p_i3, p_i4 and p_i5 were 52.7kPa at 454.4ms, 54.8kPa at 452.3ms and 54.3kPa at 449.8ms respectively. The mean peak pressure recorded along the central axis was therefore 53.9kPa, 2% below the target pressure, with a range of 2.1kPa. The peak cumulative impulse calculated from gauges p_i3, p_i4 and p_i5 were 4280.4kPa.ms at 625.3ms, 3946.2kPa.ms at 623.6ms and 3897.1kPa.ms at 616.2ms respectively, giving a mean impulse of 4041.2kPa.ms and a range of 383.3kPa, 9% of the mean.

The additional impulse transmitted through the reflection spikes were calculated as approximately 200kPa.ms, 250kPa.ms and 150kPa.ms for gauges p_i3, p_i4 and p_i5 respectively, reducing the overall impulses to approximately 4080kPa.ms, 3700kPa.ms and 37500kPa.ms respectively. Using the time at which the peak impulse was recorded, the positive phase durations recorded gauges p_i3, p_i4 and p_i5 were 170.9ms, 171.3ms and 166.4ms, providing a mean recorded positive phase duration of 169.5ms along the central

axis of the 10.2m section of the ABT.

The peak dynamic pressure recorded by gauge q3 was 17.4kPa at 489.3ms; however, this value corresponds to a spike, most likely due to gauge noise. At the arrival of the shock discontinuity, q3 did not record a definitive peak pressure; furthermore, at the time of arrival, 447.6ms, the dynamic pressure was recorded as -11.2kPa.ms. Dynamic pressure cannot be less than zero, meaning this value can be attributed to a gauge fault. The peak value for dynamic pressure recorded in the first 5ms after the time of arrival was 12.2kPa at 449.2ms. The peak recorded dynamic impulse was 381.0kPa.ms at 779.8ms; however at approximately, 510ms the pressure drops below 3kPa and fluctuates between 1-3kPa, at which time the impulse was recorded as 235.5kPa.ms. Whilst there was no explicit target for dynamic pressure, both the peak pressure and associated dynamic impulse recorded by q3, were much lower than expected.

A reflective pressure gauge, p_r1, was placed on the upstream face of the steel enclosure to monitor the reflective pressure in-line with the structure. A group of static and dynamic pressure gauges were placed at the edge of the tunnel to monitor pressures near the ABT wall; the pressure time histories and integrated cumulative impulse time histories are displayed in Figures 4.34e and 4.34f respectively.

The peak static overpressures recorded by p_i1 and p_i2 were 57.7kPa at 461ms and 59.0kPa at 462.5ms respectively. These values were both recorded approximately 10ms after the arrival of the shock discontinuity. For both static gauges, nothing was located directly downstream to reflect the blast wave, meaning these peak readings are most likely caused by reflections off of the edge of the ABT. The peak pressures recorded by p_i1 and p_i2 at the arrival of the shock discontinuity were 54.8kPa at 455.1ms and 51.6kPa at 455.1ms, giving a mean recorded peak pressure of 53.2kPa, 3% below the target pressure of 55kPa, with a range of 3.2kPa.

Both static pressure time histories recorded at the edge of the 10.2m section show continuous fluctuations at 10ms intervals, indicating that the blast flow around the edge of the ABT was more turbulent than the centre. The peak static cumulative impulses were 3427.5kPa.ms at 619.5ms and 3234.6kPa.ms at 606.2ms, recorded by gauges p_i1 and

p_i2 respectively, giving a mean impulse of 3331.1kPa.ms, with a range of 192.9kPa.ms. For both of these static pressure gauges, the continuous fluctuations in pressure means that any corrections to approximate the overall impulse would cary a large associated uncertainty. Comparing the mean recorded impulses from the central and outer edges of the 10.2m section show the impulse on the edges to be 18% lower.

Comparing the mean impulse from the edge of the 10.2m section to the mean of the approximately corrected impulses in the centre of the 10.2m section shows that the impulse on the edge was 7% lower than the centre. The positive phase durations recorded by gauges p_i1 and p_i2 were 164.4ms and 151.1ms respectively, presenting a range of 13.3ms in the positive phase duration across the ABT, with a mean value of 157.8ms, which was 7% lower than the positive phase duration recorded along the centre of the ABT.

The peak dynamic pressures, recorded by q1 and q2, were 23.9kPa at 455.1ms and 24.3kPa at 455.1ms respectively, with total recorded associated impulses of 979.1kPa.ms at 862.3ms and 693.4kPa.ms at 772ms respectively. The peak recorded pressures from both q1 and q2 were over twice as high as the value used for q3, suggesting either the dynamic pressure on the edges of the ABT was higher, or the recorded values were higher due to turbulence.

At approximately 530ms, the dynamic pressure recorded from both q1 and q2 dropped below the 3kPa region, at which point their recorded cumulative impulses were 645.9kPa.ms and 454.5kPa.ms respectively, corresponding to 65% and 75% of the total recorded impulses respectively. The reflective pressure gauge p_r1, recorded a peak value of 128.2kPa at 455.7ms, which is within the expected range of reflective pressure, corresponding to a static pressure of 110kPa. The peak impulse was recorded as 3978.4kPa.ms at 618.1ms, giving a positive phase duration of 162.4ms.

The structure located in the 4.9m section of the ABT for trial BWL1 was structure BWL1A, an **A** panel and effective repeat of structure MW2. The breakage of structure BWL1A at 0ms, 20ms, 50ms, 100ms, 150ms and 200ms is displayed in Figures 4.35 and 4.36 from the upstream and side perspectives respectively.

(a) 0ms (b) 20ms (c) 50ms

(d) 100ms (e) 150ms (f) 200ms

Figure 4.35: High speed photography (from the upstream perspective) of the breakage of structure BWL1A

The first visible signs of breakage occur at 10ms in the form of a horizontal crack line between the 21st and 22nd layers of brick, approximately 0.3m from the top of the structure and became clearly visible by 20ms, shown in Figure 4.35b. At 30ms, the crack began to spread into the 22nd layer of brick, separating each of the individual bricks. The structure began to tilt about its base, causing additional cracking to form in the bottom quadrant of the structure.

By 50ms, small crack patterns were visible in the bottom 0.3m of the structure, with a clear horizontal crack line separating the 7th and 8th layers of brick, corresponding to 0.75m above the base of the structure, causing the upper section of the structure to tilt about the new crack-line at 0.75m. Between 50-100ms, another clear horizontal crack line formed at approximately 1.5m above the base of the structure, between the 14th and 15th layers of brick.

(a) 0ms (b) 20ms (c) 50ms

(d) 100ms (e) 150ms (f) 200ms

Figure 4.36: High speed photography (from the side perspective) of the breakage of structure BWL1A

Additional breakage was observed in both the top and bottom sections of the structure, including a clear observable translation of the structure in the downstream, positive x direction. The tilting motion of the structure in combination with the translation created a velocity gradient across the vertical height of the structure due to the increase in frictional forces towards the base. Between 100-200ms, a slight increase in breakage was observed in the lower section of the structure, with the rest of the fragments sustaining no additional damage.

Using the high speed photography, measurements were taken for the displacement of each 0.2m, vertical section of the structure at 20ms intervals between 0-120ms, at which time the upper sections of the structure were out of viewing range. Pixel error was neglected due to the low resolution in combination with relatively large monitoring intervals, with slight adjustments made to the calibration scale at varying positions to

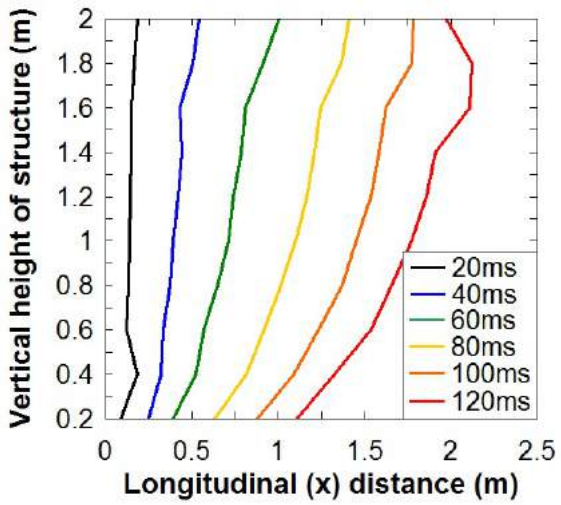

(a) Displacement relative to structural position

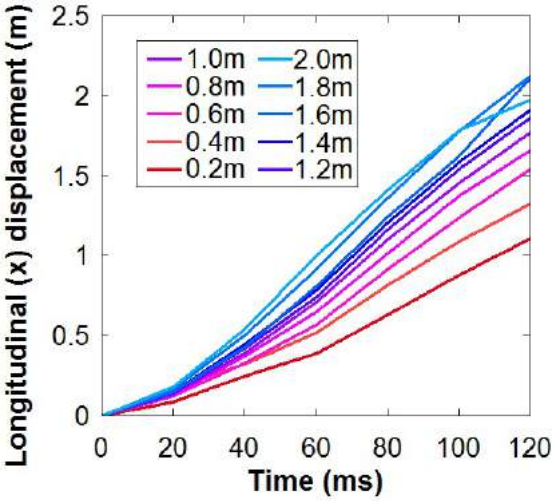

(b) Absolute displacement

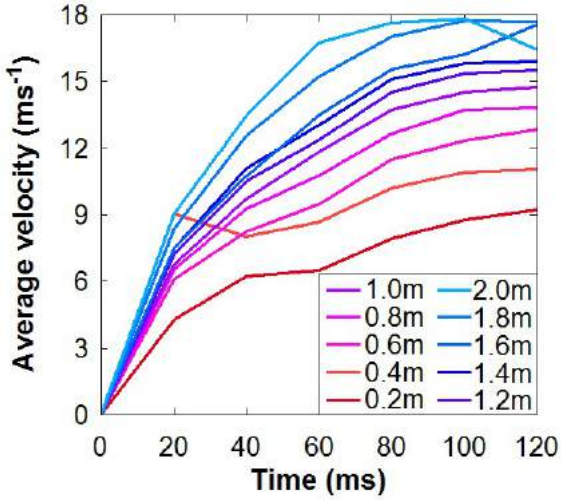

(c) Average velocity

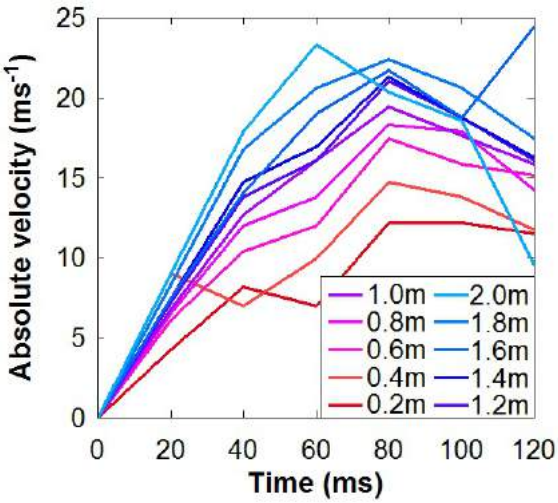

(d) Absolute velocity

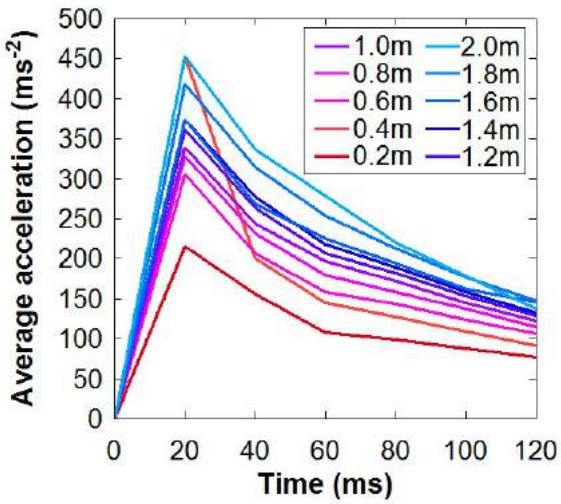

(e) Average acceleration

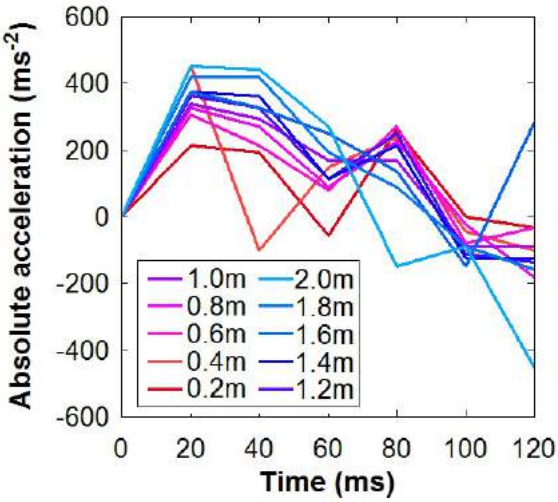

(f) Absolute acceleration

Figure 4.37: BWL1A displacement, velocity and acceleration time plots relative to the verical height within the structure

account for parallax. Figure 4.37a, which displays the vertical height of the structure with respect to absolute displacement at 20ms intervals, illustrates the combined tilting and translational motions of the structure. This relationship is also shown in Figure 4.37b, represented by the increasing difference in displacement between the curves with respect to time.

The average velocity, which is calculated as the total displacement over total time, is displayed in Figure 4.37c and showing a logarithmic trend, with a sharp rise in the velocity over the first 20ms, which begins to steadily plateau towards 120ms. The absolute velocity, displayed in Figure 4.37d, represents the velocity between each monitored time interval and shows a similar logarithmic trend across the majority of curves; however, the curves representing the top section of the structure at 1.8m and 2.0m, display a large increase and decrease in velocity respectively between 100-120ms.

The fragment originating from the 1.8m position consisted of 12 whole bricks and 3 half bricks and was completely unrestrained and entrained in the blast wave, giving it a significantly higher momentum; the fragments originating from 2.0m however, were individual bricks entrained in the blast wave. With a lower momentum combined with the blast wind flowing underneath the fragments, a significant percentage of the velocity was in the positive z direction.

The average and absolute accelerations, displayed in Figure 4.37e and 4.37f, both show a significant increase in the acceleration over the first 20ms. The absolute acceleration shows, excluding the top and bottom sections of the structure, that although the acceleration decreases, the fragments continue to accelerate until approximately 100ms, after which the accelerations drop below 0ms^{-2} and the fragments begin to decelerate. This corresponds to the point at which there is no significant dynamic pressure to transmit additional energy to the fragments.

The longitudinal debris distribution, displayed in Figure 4.38, shows the peak debris distribution located between 20m$< x <$35m, with a maximum longitudinal distance of 48m. The peak distribution of 47.3kg was located at 31m, corresponding to the position of the ABT's instrumentation columns. In the absesnce of the columns, this debris is

expected to be distributed more evenly between 30m< x <40m, with a slightly higher maximum distribution range. A series of peaks were observed at 19m, 22m and 27m, each of which correspond to one of the larger initial fragments formed at the time of breakage.

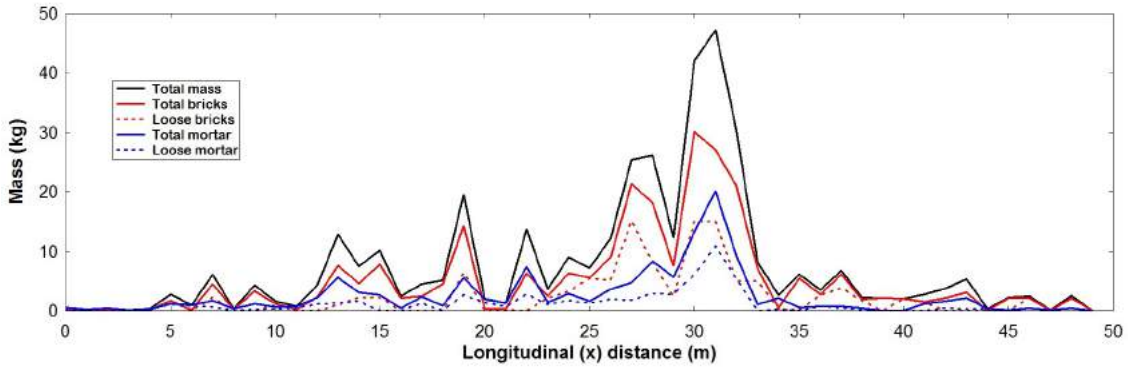

Figure 4.38: BWL1A longitudinal mass distributions

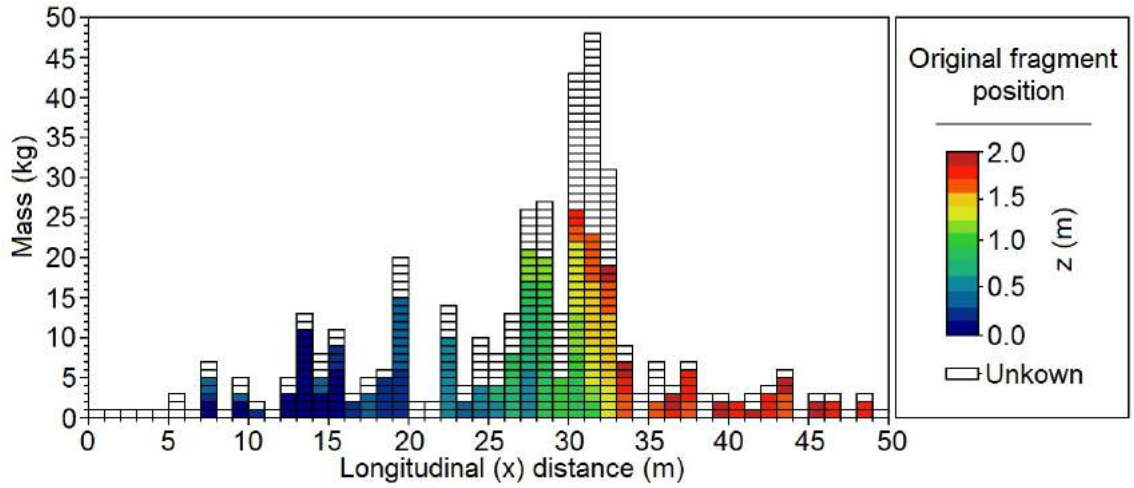

Figure 4.39: BWL1A longitudinal (x) mass distribution indicating (z) origin of debris

The distribution of loose brick fragments was approximately 45% of the total brick mass, which is significantly higher than any of the HE trials, due to the high impact forces with the ground. Figure 4.39, displays the longitudinal distribution indicating the original vertical fragment position within the structure; which, based on the combined tilting and translational motion of the structure, shows the expected distribution in which a higher initial z position corresponds to a larger x distribution.

The breakage of structue BWL1B, a composite **AB** panel, from the upstream and side perspectives are displayed in Figures 4.40 and 4.41 respectively, at 0ms, 20ms, 50ms,

100ms, 150ms and 200ms. The first visible signs of breakage occurred at approximately 15ms; however, unlike the smaller geometries, the cracking was not clearly visible until approximately 30ms. Figure 4.40c, which displays the breakage from the upstream perspective at 50ms, shows vertical separation forming between the front and side panels which spanned the entire vertical height of the structure.

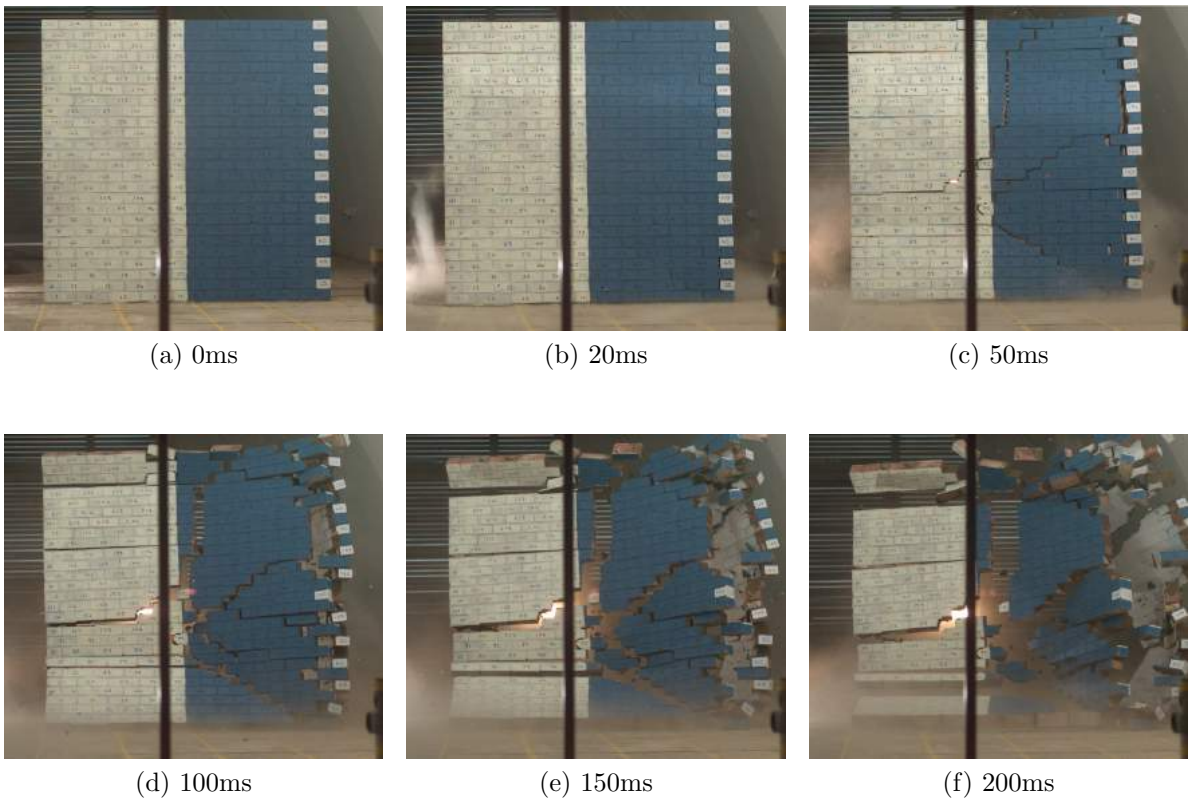

(a) 0ms (b) 20ms (c) 50ms

(d) 100ms (e) 150ms (f) 200ms

Figure 4.40: High speed photography (from the upstream perspective) of the breakage of structure BWL1B

Another vertical crack, ran slightly to the right (photo perspective) of the central axis of the front face of the structure to the mortar joint between the 10^{th} and 11^{th} layers of brick, approximately 0.75m above the base, where it ran horizontally to the edge of the structure, creating a large unrestrained fragment. A stepped crack ran from the corner joint between the 15^{th} and 16^{th} layers of brick, approximately 1.1m above the base, to the 9^{th} layer of brick at the centre of the structure, where it ran back to the corner joint at the base of the structure.

By 100ms, the large initial fragments created by the initial crack lines became clearly

separated with additional cracks forming, creating a much larger number of initial fragments. The two front panels began to tilt in the downstream direction about the base of the structure, whilst rotating about the corner joint. This created an effective two dimensional velocity gradient about both the corner joint and the base of the structure, giving a rotational motion to all of the unrestrained fragments.

The initial crack pattern of the side wall was difficult to determine, as the translational motion of the front panels obscured the camera view; however, a clear rotational motion about the corner joint was visible, with two clear horizontal cracks forming at approximately 30% and 60% of the height of the structure. The combined rotational motion of the side panel with the clearing effect of the blast on its interior face, caused a tilting motion about its base and the lower horizontal crack line.

(a) 0ms (b) 20ms (c) 50ms

(d) 100ms (e) 150ms (f) 200ms

Figure 4.41: High speed photography (from the side perspective) of the breakage of structure BWL1B

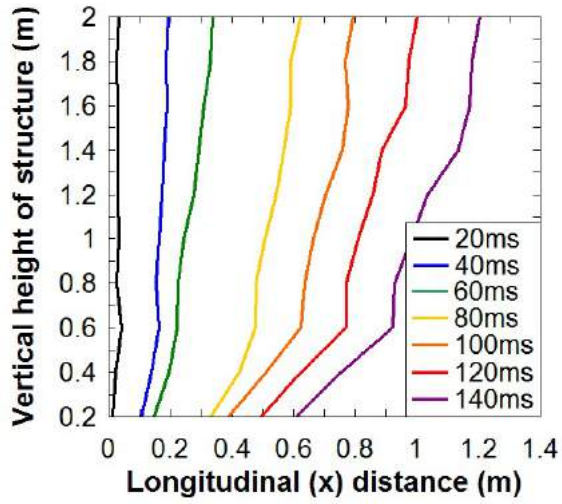

(a) Displacement relative to structural position

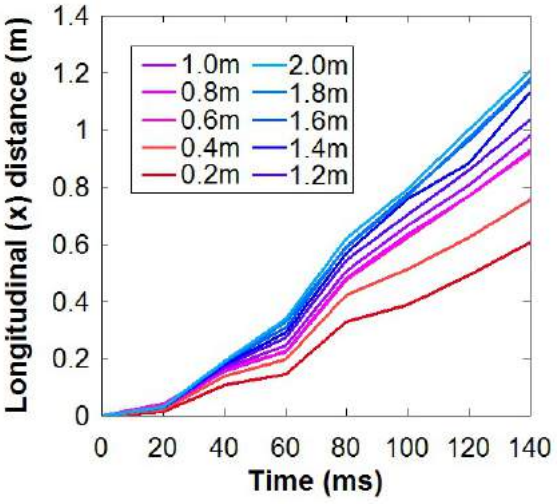

(b) Absolute displacement

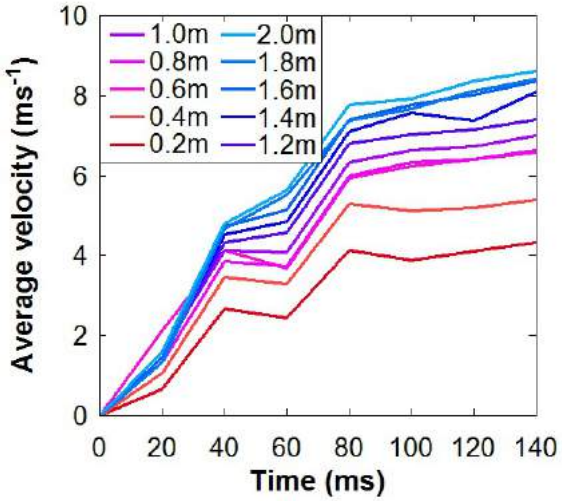

(c) Average velocity

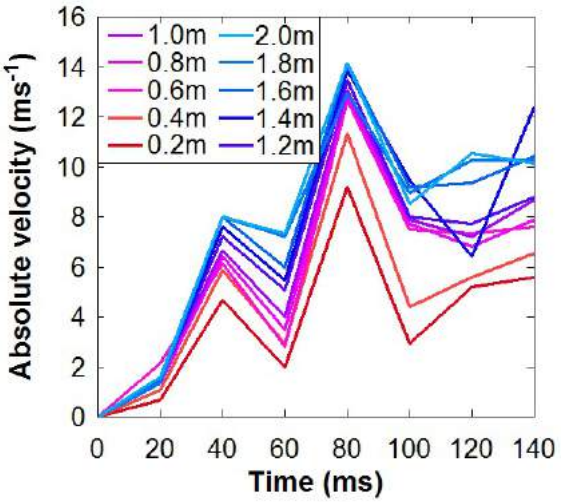

(d) Absolute velocity

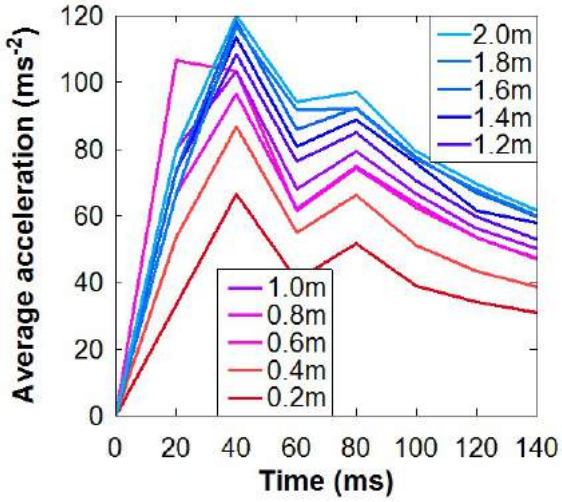

(e) Average acceleration

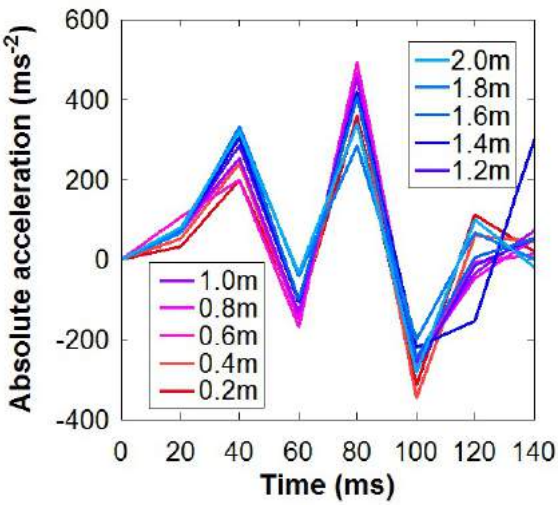

(f) Absolute acceleration

Figure 4.42: BWL1B displacement, velocity and acceleration time plots relative to the verical height within the structure

Figure 4.42a displays the absolute longitudinal displacement of the outside, white **A** panel of the composite **AB** structure BWL1B with respect to original vertical position in the structure for 20ms intervals between 0-140ms, providing a visual representation of the combined tilting and translational motion of the structure. The absolute displacement, displayed in Figure 4.42b, shows a relatively linear increase in displacement with respect to time, the gradient of which increases towards the top of the structure. The average velocity gradient, displayed in Figure 4.42c, shows a logarithmic increase in velocity over the 140ms monitoring period, with an unexpected drop in velocity between 40-60ms.

This reduction in velocity is visible in Figure 4.42d, which displays the absolute velocity. Another unexpected drop in velocity occurred at 100ms, after which the velocity once again increased, both of which result from an error in the measurements taken from the high speed photography. Whilst two phantom cameras recorded the side perspective of the structure, the camera located further downstream recorded later stage fragmentation; thus initial displacement time information could only be extracted from one camera.

The shaking of the camera also caused considerable blurring of the images as the camera was protected behind a hardened plastic aperture, making any corrections due to camera shaking a non-trivial task. Neglecting the 60ms and 100ms points for both velocity time histories presents a similar set of logarithmically increasing curves as discussed in previous trials, with peak velocities ranging from 8-14ms^{-1} from the base to the top of the structure.

Similarly, neglecting the 60ms and 100ms data points for the average and absolute accelerations, displayed in Figures 4.42e and 4.42f respectively, shows similar trends to previously discussed trials. The average acceleration increased until 40ms at which point it started to gradually decrease; the absolute acceleration however shows an increase in acceleration until 80ms, after which the acceleration decreased, although remained positive until 120ms, at which points the fragments began to decelerate.

The original position of structure BWL1B was centred about (0,0), as represented by Figure 4.44b, with the side panel located along y=1m, extending between 0m$< x <$1m. The longitudinal debris distribution of structure BWL1B, displayed in Figure 4.43a, shows

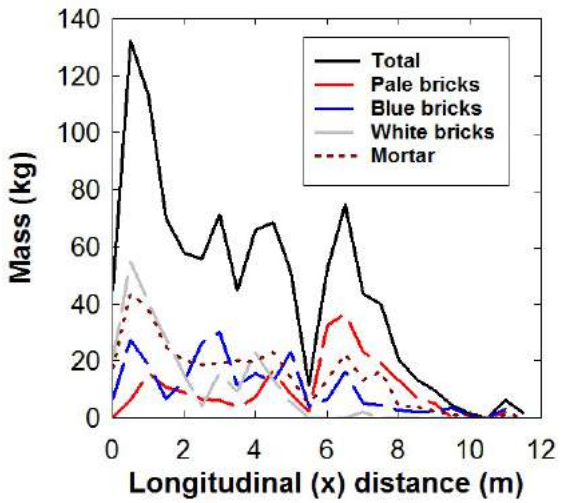

(a) Longitudinal distribution

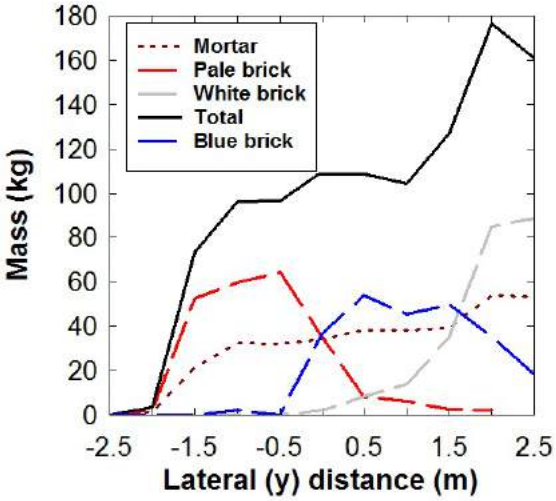

(b) Lateral distribution

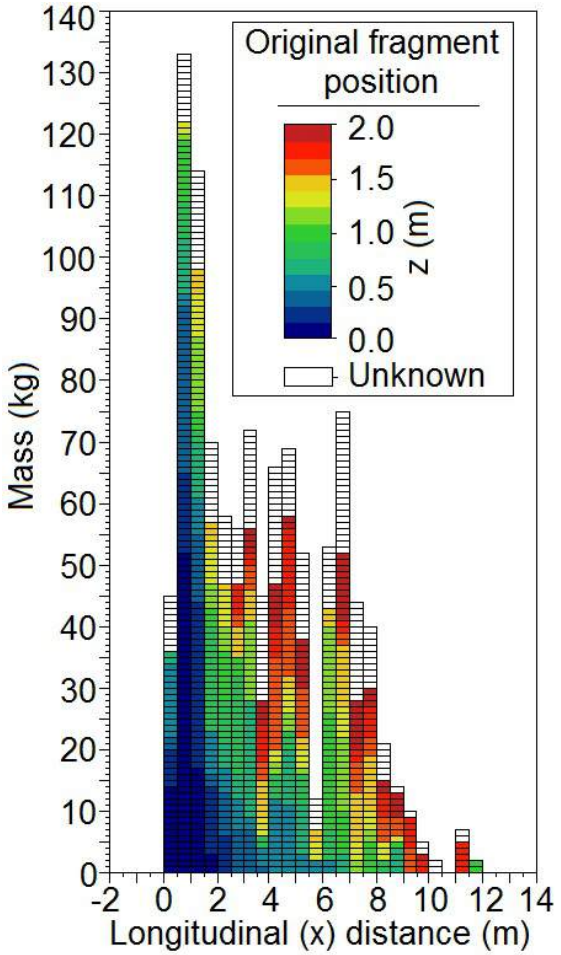

(c) Longitudinal distribution indicating original z position of fragments

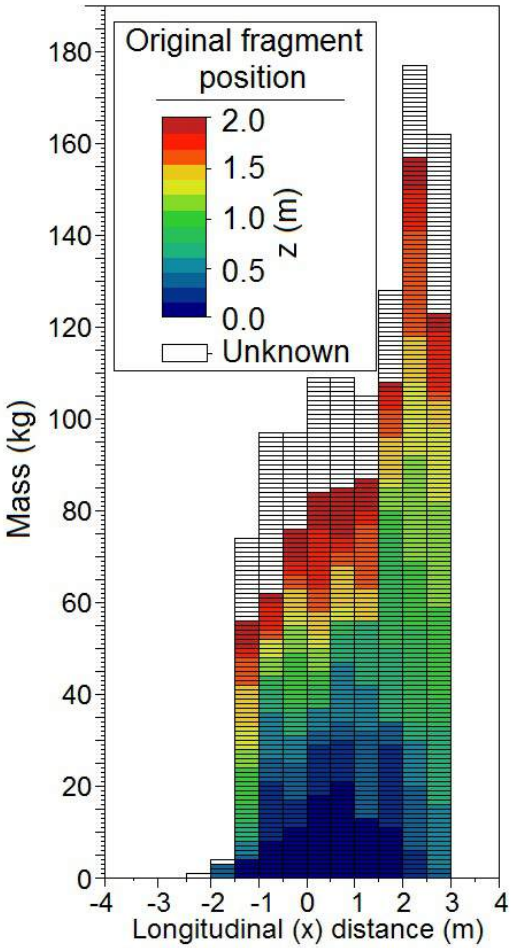

(d) Lateral distribution indicating original z position of fragments

Figure 4.43: Longitudinal and lateral debris distribution plots of structure BWL1B

the highest density distribution to be within the first 2m, with a peak distribution of 132.5kg located in the x=0.5m bin, resulting from the collision of the side panel with the wall of the ABT.

The distribution drops to approximately 70kg between 1.5m< x <4.5m, where it reduces significantly to 11.4kg at x=5.5m. The distribution then increases to a mass of 75kg at x=6.5m, after which it slowly reduces until x=11.5m, at which point the furtherst fragment was located. The distribution of brick from the individual panels is represented by the grey, blue and red lines, corresponding to the side, central blast normal and outer blast normal panels respectively. The distribution of the side panel extends to x=5.5m, with the majority located within the first 2m, resulting in the high density distribution within this region.

The central, blast normal panel followed a relatively uniform distribution compared to the overall mass; whilst the outer, blast normal panel showed a peak at x=6.5m, resulting in the sudden high density peak. Comparison to Figure 4.43c, which illustrates the longitudinal debris distribution in terms of original vertical fragment position, shows the first area of high density consists of fragments originating from the lower 0.5m of the structure, with additional fragments from the side panel located between 0.5m and 1.2m above the base.

Between 2m< x <8m, the distribution is relatively even between fragments in the top half of the structure; beyond x=8m, the fragments originate only from the top 0.5m section of the structure. The even distribution between 2m< x <8m is a result of the apparent 2 dimensional velocity gradient across the structure, giving the outer and central blast normal panels slightly staggered distributions.

The lateral debris distribution, displayed in Figure 4.43b, shows the peak distribution of 177.8kg occurred at y=2m. The individual panel distributions show this region to be mostly populated by bricks originating from the side panel, with both blast normal panels displaying a relatively symmetrical distribution about their respective central axes. Figure 4.43d, which displays the lateral distribution indicating the original vertical fragment position, shows a symmetrical distribution of fragments originating from the

bottom 0.5m section of the structure.

The distribution was symmetrical about y=0.5m, as opposed to the central axis of the structure, resulting from the additional mass from the side wall, originating from the y=1m position. The distribution shows almost instantaneous drops to zero at both extents, in the positive y direction this results from impact of the fragments with the wall of the ABT.

(a) Postshot photograph (perspective: upstream)

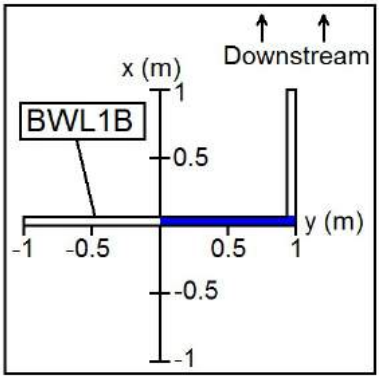

(b) Positional information

(c) Postshot photograph (perspective: downstream)

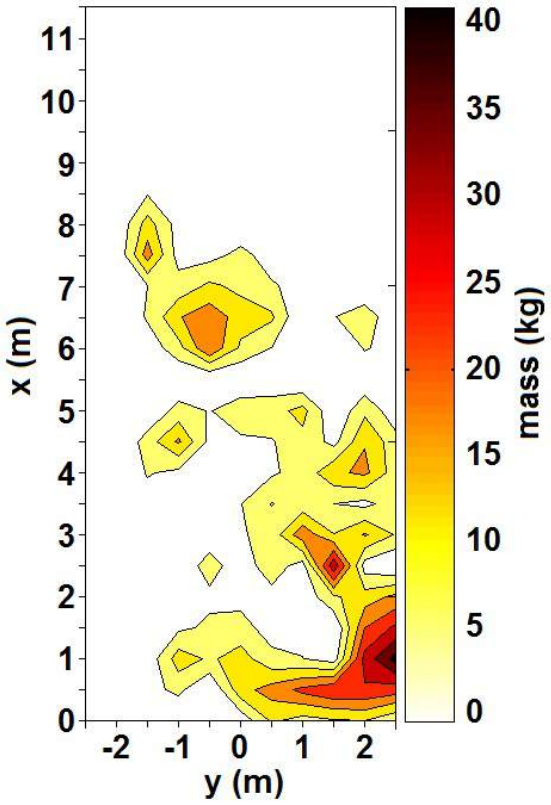

(d) (x, y) mass distribution (absolute)

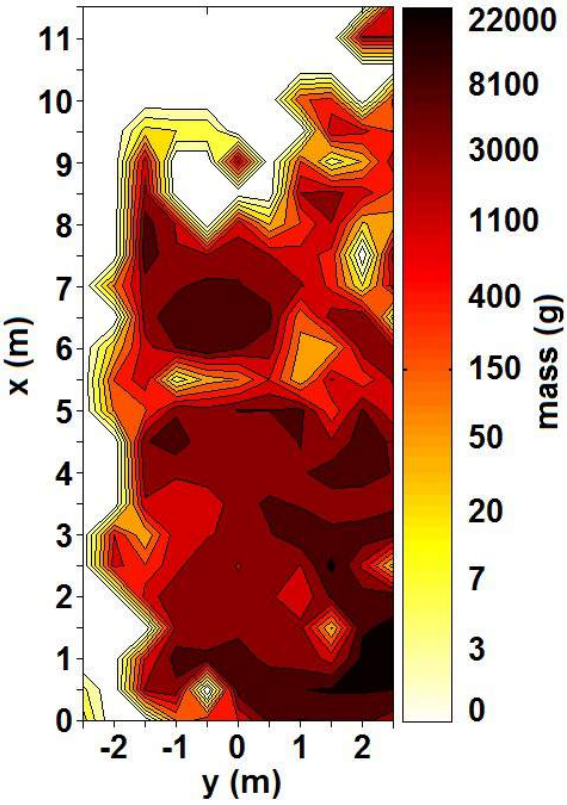

(e) (x, y) mass distribution (logarithmic)

Figure 4.44: Debris mass distribution of structure BWL1B

The post-shot photographs of structure BWL1B, displayed from the upstream and downstream perspectives in Figures 4.44a and 4.44c respectively, show the debris distribution to cover the ground with an almost uniform height of 100mm, with varying density regions. The logarithmic x,y mass distribution, displayed in Figure 4.44e, illustrates the extents of the obstruction caused by the debris distribution, with an approximated area of 44.75m^2, covering a total rectangular area of 66m^2.

The absolute distribution, displayed in Figure 4.44d, shows the highest density area located around (1,2.5), resulting from the impact of the side wall with the ABT, in which the largest fragment was located, with a mass of 16.8kg, originating from the centre of the side panel. General high density regions were also observed around (4.5,2) and (-1,6), corresponding to the inner and outer blast normal panels respectively, illustrating their staggered distributions.

The breakage of structure BWL1C, a half rectangular enclosed structure with maximum x,y dimensions of 4m×1.5m, with base panel structure $\frac{\mathbf{A}}{\mathbf{2}}\mathbf{BCCD}\frac{\mathbf{E}}{\mathbf{2}}$, is displayed in Figures 4.45 and 4.46 from the upstream and inside, side-on perspectives respectively, at 0ms, 20ms, 50ms, 100ms, 150ms and 200ms. The structural response was also recorded inside the structure from a further downstream perspective and from the side perspective downstream from the structure; however these views do not capture much additional information providing insight into the breakage mechanism of the structure.

The first signs of breakage were observed on the front face of the structure at approximately 15ms in the form of a vertical crack forming along the connection with front face and the corner joint; by 20ms, clear brick separation was observed along these cracklines, along with a slight indentation of the wall at around 0.75m above the base of the structure, 1m from the corner joint. At 50ms, the point of indentation along the front face developed into a triple crack system running vertically to the top of the structure and horizontally to the outer edge of the structure with a stepped crack running to the base of the structure at the corner joint, creating three large fragments.

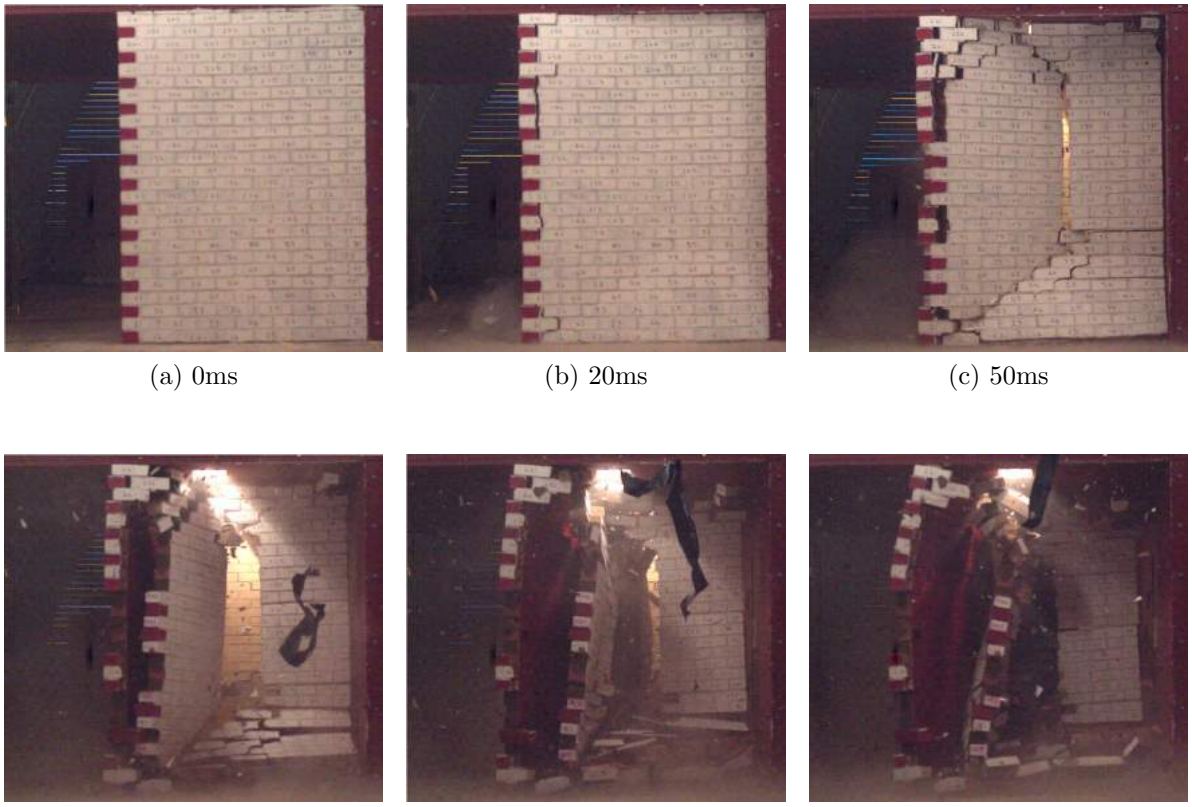

(a) 0ms (b) 20ms (c) 50ms

(d) 100ms (e) 150ms (f) 200ms

Figure 4.45: High speed photography (from the upstream perspective) of the breakage of structure BWL1C

The inner fragment connected to the side panel began to rotate and translate about the corner joint, whilst the lower fragment rotated about its base and the upper, outer fragment translated in the downstream direction with a slight tilting motion about the horizontal crack at its base. The side panels also began to respond at 50ms, primarily the more upstream panels as the transmitted impulse at this time was slightly higher. A vertical crack began to form at approximately 1m from the most upstream face of the structure, joining a less pronounced horizontal crack between the 7^{th} and 8^{th} layers of brick, approximately 0.5m above the base of the structure and spanning, at this time, for approximately 1m horizontally, corresponding to the width of the second side panel.

By 100ms, the lower fragment on the front, blast normal face had undergone further fragmentation with each brick on its inner edge completely separated. The outer fragment continued to translate with little to no titling motion and the inner fragment, originally connected to the side wall continued to rotate about the corner joint with little to no

translational motion; however it began to tilt laterally away from the side panel. The inside view at 100ms shows the horizontal cracking extend towards the rear face of the structure, where it divided into two separate stepped cracks propagating towards the rear corner joint at both its base and approximately 1m above the base.

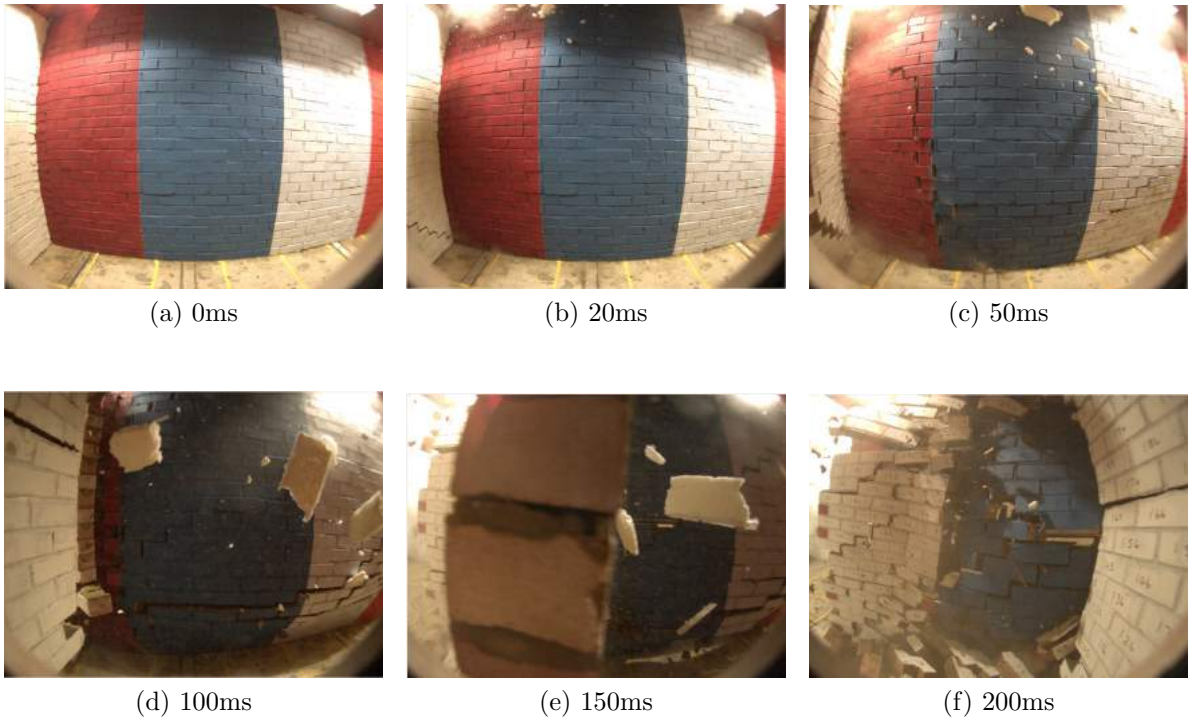

(a) 0ms (b) 20ms (c) 50ms

(d) 100ms (e) 150ms (f) 200ms

Figure 4.46: High speed photography (from the inside, side-on perspective) of the breakage of structure BWL1C

The three most downstream faces of the side wall began to simultaneously tilt and translate inwards, whilst the most upstream face of the side begins to simultaneously tilt outwards about its base whilst rotating about the corner joint. Each of these respective motions continued unchanged until collision with either the steel enclosure, or with the ground. Small stepped crack patterns formed at various places along the rear wall from approximately 50ms; however the wrap around pressures of the blast wave were not high enough to cause substantial breakage.

The rotation of the most downstream side panel caused increased separation of the cracks in the rear wall. The rear wall itself did not collapse The inward rotational motion about the corner joint in combination with the negative phase caused the rear panel

to become wedged between the roof of the steel enclosure and the ground. The upper translating fragment from the front, blast normal face of the structure collided with the inner, upstream face of the rear wall at approximately 400ms, causing additional cracking over the rear wall and two small fragments to become detached from the outer edge of the rear wall, at approximately 1m above the base.

(a) Perspective (upstream, close-up)

(b) Perspective (downstream, offset)

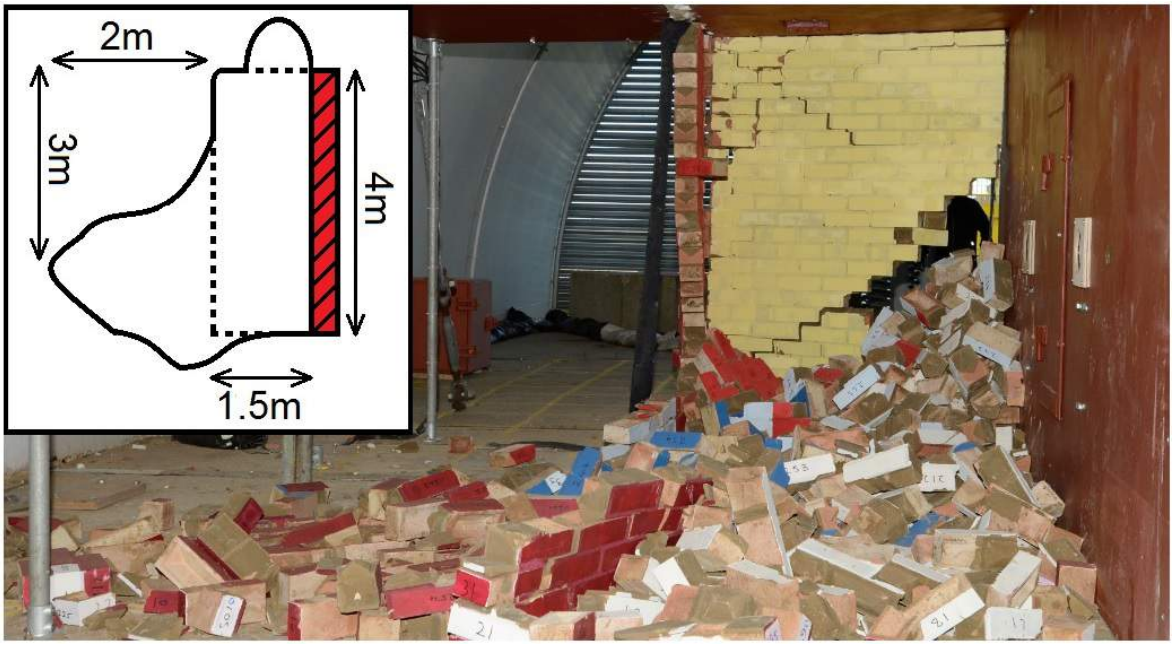

(c) Perspective (upstream), including outline sketch of debris

Figure 4.47: Post-shot photographs of the debris distribution of structure BWL1C

Due to the positions of the phantom cameras, no accurate measurements could be made of the displacement, velocity and acceleration time histories for any of the panels of structure BWL1C. The debris distribution of structure BWL1C, displayed in Figure 4.47,

fell largely within the outline area of the structure, resulting in a distribution of an estimated 2.5×10^3kg of debris within a small area. With such high density area of debris, the previous method of collecting each individual fragment and logging its x,y position, mass and composition would create a large recording error, difficulty in determining fragment locations; furthermore, the partially collapsed rear wall, presented a large potential hazard making manual debris collection a safety risk. To gain quantitative data relating to the debris distribution, a series of x,y,z readings were taken at 200mm square intervals across the surface of the debris pile using a laser theodolite. The data was discovered to be subsequently corrupt after the rubble was cleared and no measurements of the debris were retrievable with an acceptable accuracy.

Visual analysis of the photographs show the peak height of the distribution to be approximately 1m, located at the rear of the interior of the structure, bordering the rear wall and the steel enclosure. The peak region is displayed in Figure 4.47c, which also illustrates an outline sketch of the area covered by the debris, which was approximately 10m^2. Figure 4.47c also shows the top of the debris pile, close to the steel enclosure is populated by white bricks which originated from the front, blast normal face of the structure. Figure 4.47a shows the top of the outer section of the debris pile is populated by red bricks, originated from the most upstream side panel, the only side panel to rotate and tilt outwards.

Finally, Figure 4.47b shows rear and rear side panels which remained wedged between the ground and the roof of the steel enclosure. Vertical cracking can be seen along the corner joint connecting the two panels, with a series of stepped cracks running along the rear panel. A gap in the rear panel was created as two fragments were forced outwards, in the downstream direction, resulting from the large translating fragment from the front panel. This point also corresponds to the peak height of distribution, which decreased uniformly in both x and y towards to extents of the distribution.

4.3.2 BWL2

The pressure time histories and their respective integrated, associated impulses, from both the 4.9m and 10.2m sections of the ABT, instrumented in trial BWL2 are displayed in Figure 4.48. The 4.9m section was monitored by gauges p_i6, p_r4 and q4, with their pressure time histories and integrated cumulative impulses displayed in Figures 4.48a and 4.48b respectively.

The static overpressure in the 4.9m section, monitored by gauge p_i6, recorded a peak value of 181.7kPa at 218.5ms, which as with previous trials corresponds to a reflection off of the most upstream face of the structure instrumented in the 4.9m section. In the absence of this reflection, the peak recorded static overpressure was 104.2kPa at 211.5ms, 5% below the target pressure. The maximum static impulse recorded was 7198.1kPa at 426.5ms, giving a positive phase duration of 215ms. The estimated impulse due to the reflection was approximately 400kPa.ms, reducing the recorded impulse to a maximum value of approximately 6800kPa.ms.

The peak reflected pressure recorded by gauge p_r2, was 291.4kPa at 214.1ms, with a maximum recorded reflected impulse of 8444.1kPa.ms. Finally, the dynamic pressure in the 4.9m section of the ABT recorded by gauge q4, presented a peak value of 55.9kPa at 211.6ms. At approximately 290ms, the dynamic pressure dropped below 3kPa, at which point the associated dynamic impulse was 1155.7kPa.ms. The peak associated dynamic impulse was recorded as 2213.9kPa.ms at 900ms. The total impulse transmitted before 290ms, the point at which the associated dynamic impulse became too low to have any noticeable effect on the debris, was approximately 52% of the overall associated dynamic impulse.

Gauges p_i3, p_i4, p_i5 and q3 were located along the central axis of the ABT in the 10.2m section, each separated by 1m, the pressure time histories and cumulative impulse time histories of which are displayed in Figures 4.48c and 4.48d respectively. Each of the three static pressure gauges recorded peak values resulting from reflections from the most upstream face of the steel enclosure, which for gauges p_i3, p_i4 and p_i5 were 78.0kPa at 366.9ms, 80.5kPa at 363.1ms and 79.8kPa at 359.3ms respectively.

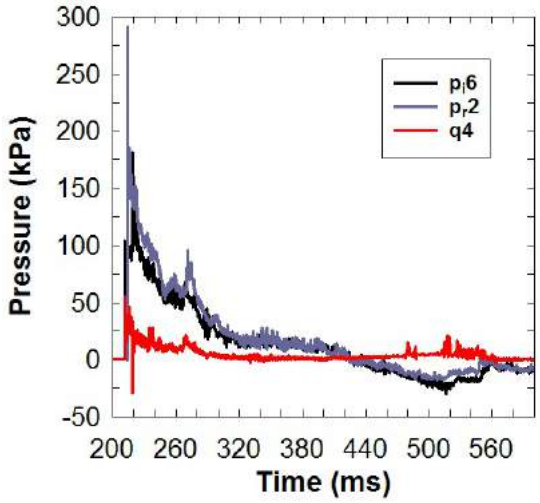

(a) Pressures: 4.9m section

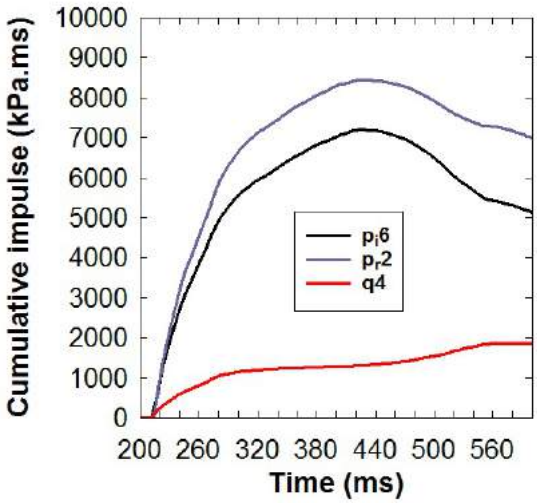

(b) Impulses: 4.9m section

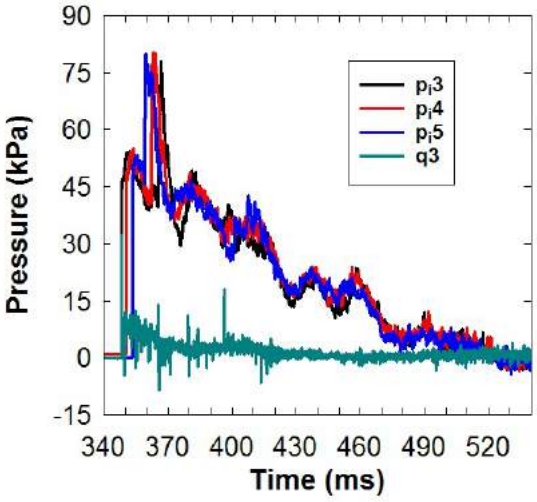

(c) Pressures: 10.2m section (central)

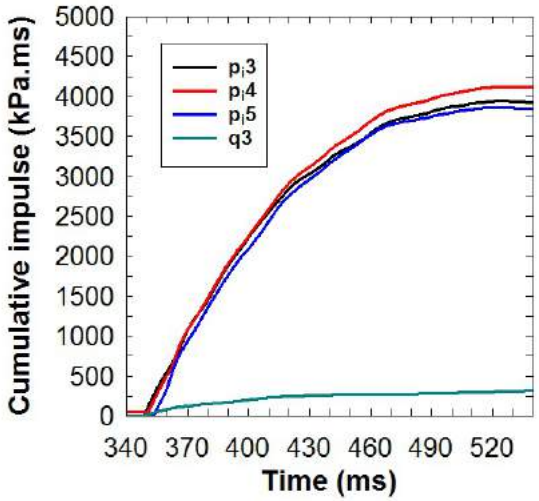

(d) Impulses: 10.2m section (central)

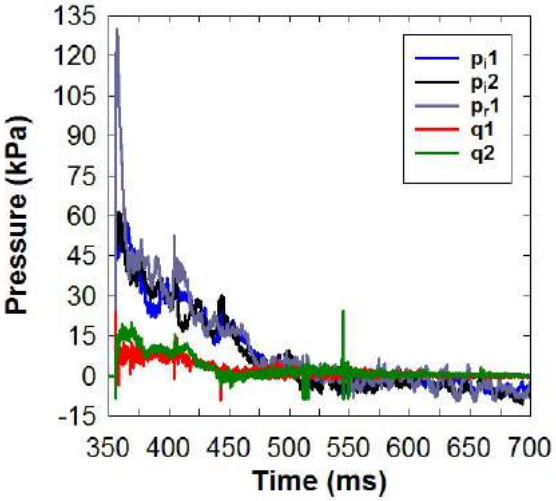

(e) Pressures: 10.2m section (edges)

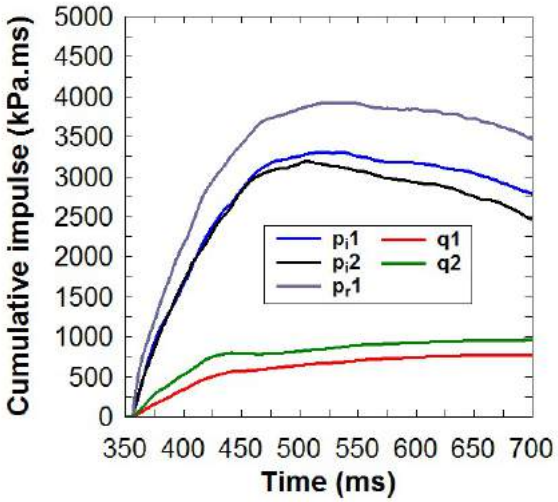

(f) Impulses: 10.2m section (edges)

Figure 4.48: Pressure time histories and integrated impulses from trial BWL2

Neglecting these reflections, these gauges recorded peak values at the arrival of the shock discontinuity of 54.4kPa.ms at 352ms, 55.1kPa at 353.8ms and 53.3kPa at 355.9ms respectively, providing a range of 1.8kPa and a mean value of 54.3kPa, 1% below the target value. The peak recorded impulses from gauges p_i3, p_i4 and p_i5 were 3946.6kPa at 524.5ms, 4125.3kPa at 527.2ms and 3863.0kPa at 523.1ms respectively, giving positive phase durations of 157.5ms, 164.1ms and 163.8ms, with a range of 6.6ms and a mean value of 161.8ms. The range in recorded static impulses along the central axis was 262.3kPa, with a mean value of 3978.3kPa.

The estimated impulse recorded by the reflections was, for each gauge, approximately 120kPa, which would reduce the mean recorded impulse by 120kPa, giving a maximum mean transmitted static impulse of 3858.3kPa in the centre of the 10.2m section of the ABT. The peak recorded dynamic pressure by gauge q4 was 32.2kPa at 348.3ms which reduced to below 3kPa by approximately 420ms, at which time it fluctuated between 1-3kPa. The total transmitted associated dynamic impulse recorded by q4 was 370.4kPa.ms at 694.3ms and 245.5kPa.ms at 420ms, corresponding to 66% of the peak value.

The front, blast normal, most upstream face of all structures in the 10.2m section of the ABT were placed in-line, with a pair of static and dynamic pressure gauges placed at each edge of the ABT, in combination with a reflective pressure gauge mounted on the front, most upstream face of the steel enclosure; the pressure and cumulative impulse time histories of which are displayed in Figures 4.48e and 4.48f respectively.

The static pressure gauges, p_i1 and p_i2 recorded peak pressures of 57.4kPa at 365.4ms and 61.6kPa at 358ms respectively, giving a mean value of 59.5kPa, 8% above the target pressure, with a range of 4.2kPa. The mean peak static pressure recorded on the outer edges of the tunnel was therefore 5.1kPa, 9% higher than the pressure in the centre of the 10.2m section. The peak cumulative impulses recorded by gauges p_i1 and p_i2 were 3303.6kPa at 536.8ms and 3187.9kPa.ms at 504.4ms respectively, giving a range of 115.7kPa.ms and a mean value of 3245.8kPa.ms, 612.6kPa.ms lower than the impulse measured in the centre of the 10.2m section. The positive phase durations were recorded as 171.4ms and 146.4ms by gauges p_i1 and p_i2 respectively; the longer duration recorded

by p_i1 resulted in the larger reading of impulse, despite the lower pressure.

The peak dynamic pressures recorded by gauges q1 and q2 were 23.9kPa at 355.9ms and 24.5kPa at 544.9ms respectively. However, the reading from q2 corresponds to an isolated peak, most likely due to gauge noise. The peak value at the arrival of the shock discontinuity from gauge q2 was 19.4kPa at 361.6ms, giving a range of 5.1kPa and a mean value of 22kPa, 10.2kPa lower than the dynamic pressure recorded by q3 in the centre of the 10.2m section.

The total recorded dynamic associated impulses from gauges q1 and q2 were 762.7kPa.ms at 660.7ms and 963.9kPa.ms at 770.6ms respectively. At 440ms, corresponding to the point where the pressure recorded by both gauges dropped below 3kPa, the recorded dynamic associated impulses were 537.8kPa.ms and 797.8kPa.ms respectively, corresponding to 71% and 82% of the total recorded values. The peak reflective pressure measured by gauge p_r1 was 130.1kPa at 356.5ms, with a recorded impulse of 3924.9kPa.ms at 527.8ms.

The breakage of sructure BWL2A, a **B** panel located in the 4.9m section of the ABT is displayed from the upstream and side-on perspectives in Figures 4.49 and 4.50 respectively at times 0ms, 20ms, 50ms, 100ms, 150ms and 200ms. The first signs of breakage occurred at 10ms in the form of a vertical crack running along the front, blast normal panel at the corner joint. By 20ms, considerable brick separation was observed with both panels almost completely unrestrained from one another.

An additional horizontal crack began to form between the 21st and 22nd layers of brick, approximately 0.3m from the top of the blast normal face; the side on perspective also shows the front panel beginning to tilt about its base. A vertical crack began to form down the centre of the blast normal face at approximately 25ms, by 50ms, this crack had completely split the front panel in half, with additional horizontal cracks forming 0.3m from the base of the structure and 0.75m from the top of the structure.

The blast normal panel retained its tilting motion for all fragments; however, the outer fragment created by the central separation displayed a large translational motion in combination with the tilting, as seen with previously tested **A** panels, whilst the inner fragment began to rotate about the corner joint. Three horizontal cracks formed along

the side panel at approximately 0.25m, 1.2m and 1.5m from the base of the structure, with the panel displaying an inwards rotation about the corner joint.

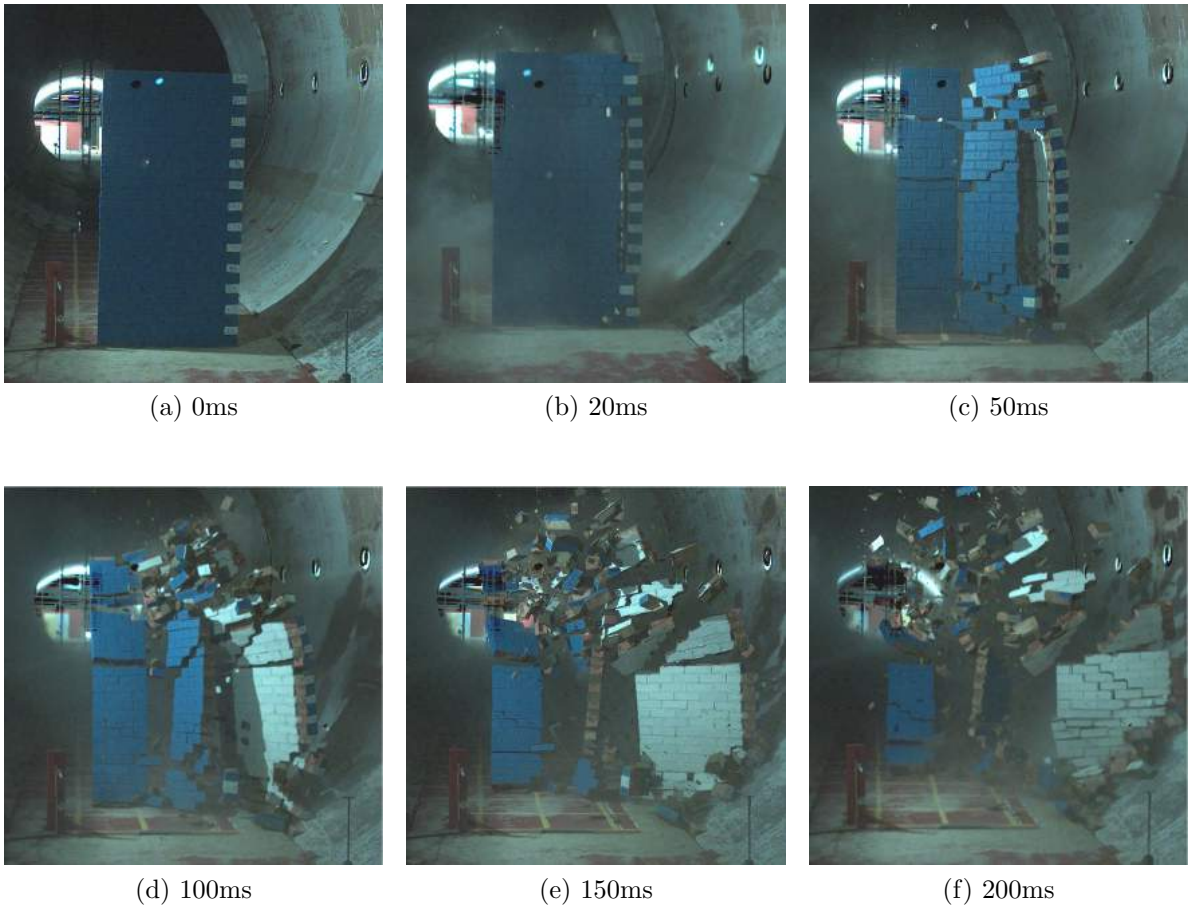

(a) 0ms (b) 20ms (c) 50ms

(d) 100ms (e) 150ms (f) 200ms

Figure 4.49: High speed photography (from the upstream perspective) of the breakage of structure BWL2A

At approximately 75ms, the upper, inner fragments formed on both the blast normal and side panels collided due to the counter rotational motions about the corner joint, causing further fragmentation of both panels, creating a large number of small fragments by 100ms. The large lower fragments from the side panel and the inner fragment of the blast normal panel continue lose a considerable amount of momentum from the impact, causing the side panel to topple and rotate, whilst the lower inner fragment of the blast normal panel translated in the downstream direction.

The outer fragments of the blast normal face continue to translate in the downstream direction without any collisions or interference with any other fragments, thus maintaining their momentum. By 200ms, the side panel began to impact with the lower section of the

wall of the ABT, with a downwards rotating motion, suggesting that in its absence there would not be significant lateral distribution, compared with the longitudinal distribution. A large number of small fragments each consisting of a mass less than or approximately equal to the mass of a single brick, created by the impact of the front and side panels, travelled downstream with considerably less velocity than the larger fragments which avoided the initial panel collision.

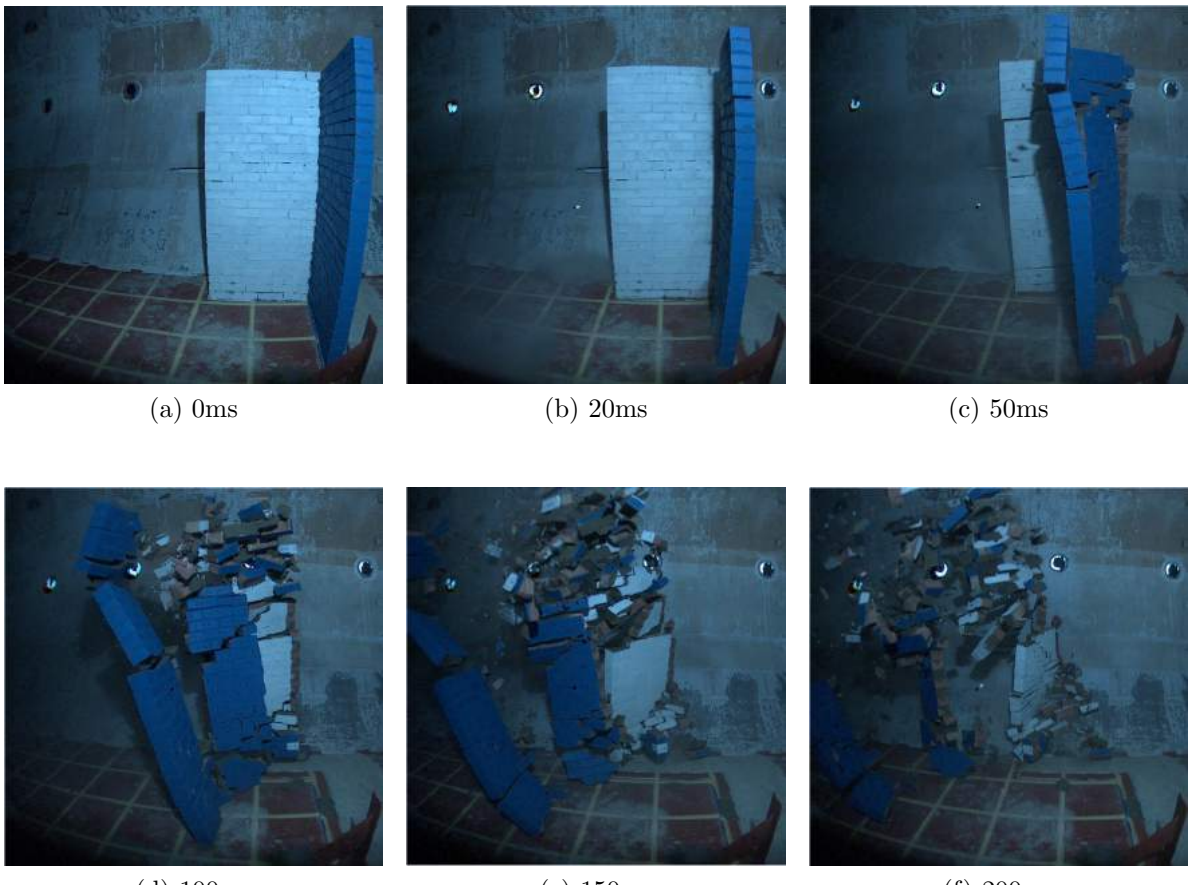

(a) 0ms (b) 20ms (c) 50ms

(d) 100ms (e) 150ms (f) 200ms

Figure 4.50: High speed photography (from the side perspective) of the breakage of structure BWL2A

The displacement, velocity and acceleration time histories of structure BWL2A, obtained from measurements of the high speed photography are displayed in Figure 4.51, in which all measurements were taken of the unrestrained outer fragment which exhibited both tilting and translational motion. The longitudinal displacement with respect to the vertical height of the structure is displayed in Figure 4.51a at 20ms intervals between 0-120ms and illustrates a much smaller tilting motion that observed with previous

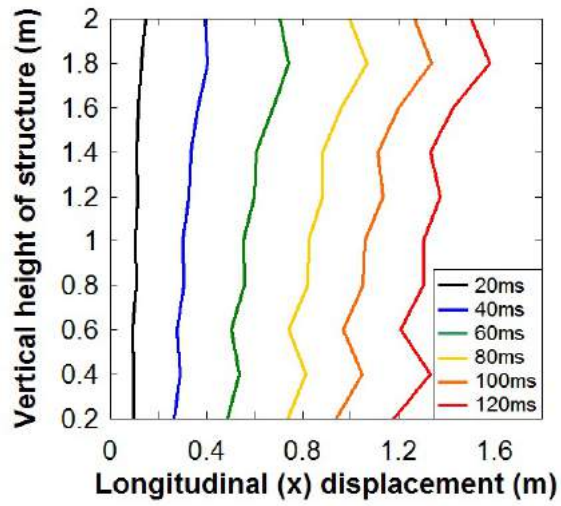

(a) Displacement relative to structural position

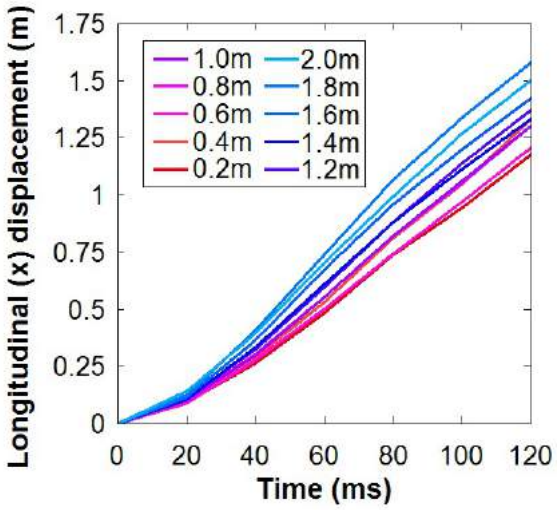

(b) Absolute displacement

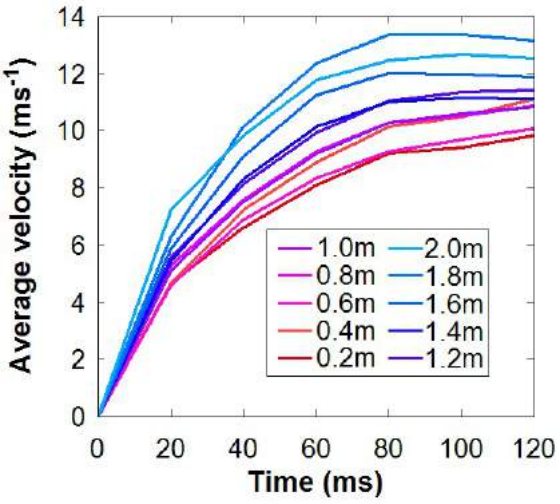

(c) Average velocity

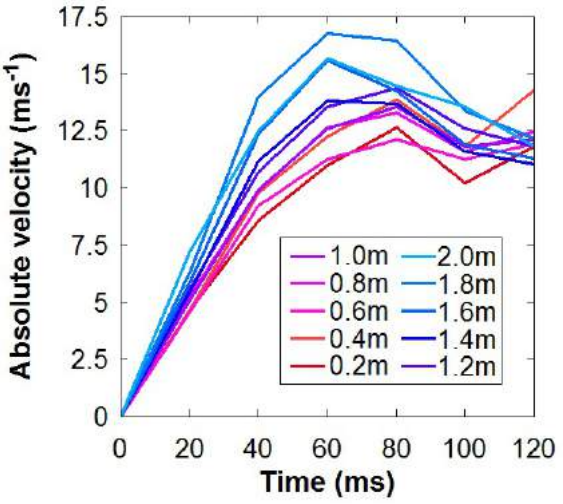

(d) Absolute velocity

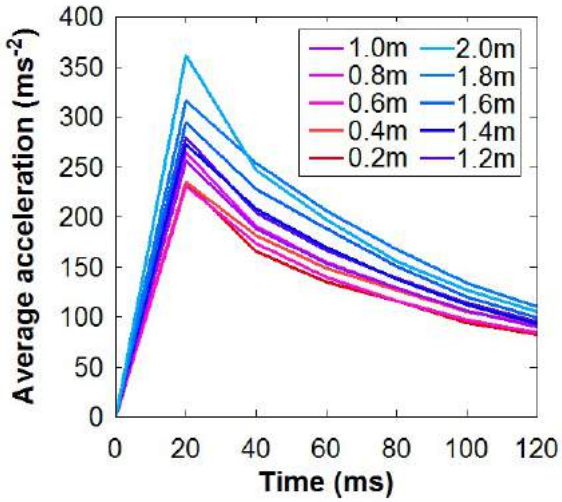

(e) Average acceleration

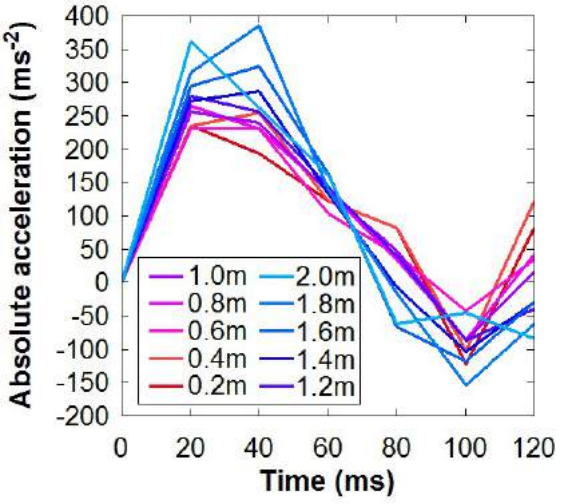

(f) Absolute acceleration

Figure 4.51: BWL2A displacement, velocity and acceleration time plots relative to the verical height within the structure

structures.

The lower 0.4m showed the most pronounced tilting, with a counter tilting motion displayed from the fragment between located between 0.4m and 0.6m vertically. Between 0.6m and 1.6m vertically, the fragments translated with almost no tilting, with the top section of the structure showing a similar counter tilting motion to the bottom. A slight velocity gradient was observed across the vertical height of the structure and is illustrated by the difference in gradient of the displacement time histories displayed in Figure 4.51b.

The absolute and average velocity time histories, presented in Figures 4.51d and 4.51c, show a similar logarithmic increase in velocity as observed in previous trials. The average velocities show a consistent plateau for each monitoring points between 60-120ms; however the absolute velocities, which represent the actual recorded change in velocity between each 20ms monitoring point, show a drop in velocity across all but the lowest fragments after 100ms. The sudden increase in velocity displayed by the lowest fragments is most likely due to an error associated with camera shaking or an unquantifiable parallax error.

The average acceleration time histories, displayed in Figure 4.51e, show a similar trend to all previously measured structures, with high accelerations over the first 20ms which slowly decay, but remain positive. The absolute acceleration, which measures the change in velocity between each 20ms monitoring point, again shows a similar pattern to previous trials, with an increase in acceleration over the first 20-40ms, followed by a decrease in acceleration, although still positive, until 60ms, at which point the fragments begin to decelerate. The sudden increase in acceleration of all vertical monitoring points between 100-120ms further demonstrates the possibility of an error in the final measurements, as the fragments did not receive any additional energy transfer that would explain and increase in acceleration.

The longitudinal debris distribution of structure BWL2A, displayed in Figure 4.52, shows the majority of the mass located within the first 15m, with the peak distribution located at x=2m, with a total bin mass of 74.4kg, 45.5kg of which originated were white bricks originating from the side panel. Within the x=2m bin, the two largest fragments

were located, with masses of 14.2kg and 12.6kg, both originating from the centre of the white, side panel.

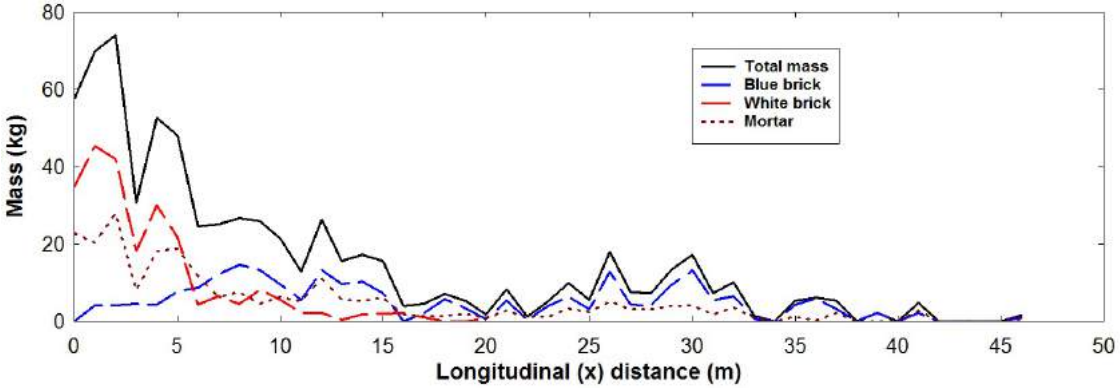

Figure 4.52: BWL2A longitudinal mass distributions

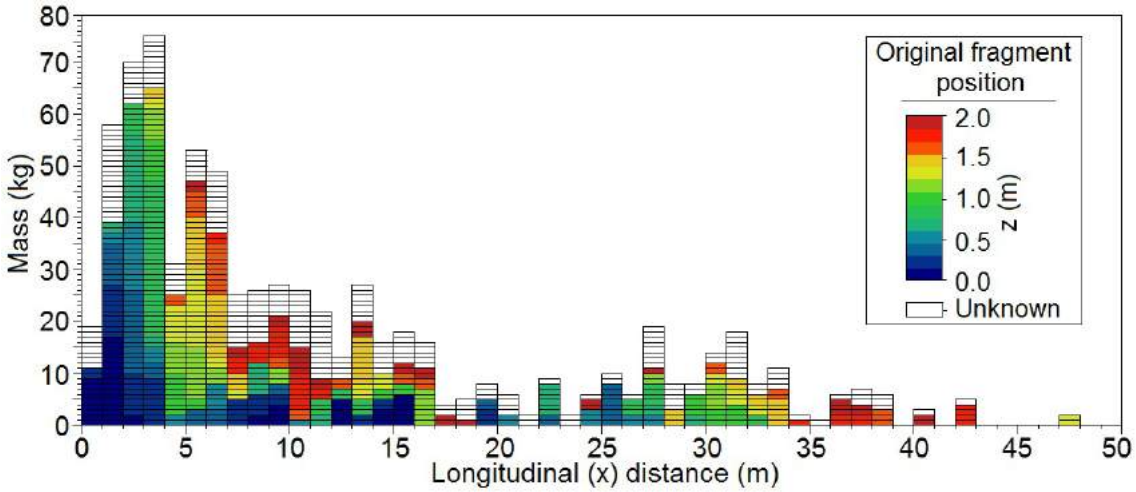

Figure 4.53: BWL2A longitudinal (x) mass distribution indicating (z) origin of debris

The majority of the debris originating from the side panel, 83%, was located within the first 6m, with the furthest fragment located at x=20m. The distribution of blue bricks from the front, blast normal panels was relatively uniformly distributed between 0m¡x¡35m, with a slight reduction in the distribution between 15m< x <20m. The longitudinal distribution indicating original vertical position of the fragments, presented in Figure 4.53, shows that the original vertical position of fragments increased with x between 25m< x¡40m, suggesting this debris originated from the outer unrestrained fragment of which the displacement time histories were previously measured. The distribu-

tion of the other vertical half of the front, blast normal panel was distributed between 5m< x <15m. The bricks located in the first 5m all originated from the lower half of the side panel and its upper half, which underwent additional fragmentation upon impact with the inner half of the front panel, is distributed between 5m< x <10m.

The breakage of structure BWL2B, a **B** panel located in the 10.2m section of the ABT, is displayed in Figure 4.54 from the upstream perspective. Although the breakage of BWL2B was recorded from the side perspective, the most upstream of these cameras, monitoring breakage, malfunctioned, providing no useable data. This was the same camera responsible for the distorted displacement time measurements taken for BWL1B and was replaced after the BWL2 trial.

The camera further downstream only recorded late stage debris distribution and the view was partially obstructed by structure BWL2C. The first visible signs of breakage occurred at 10ms in the form of a vertical crack on the front, blast normal face of the structure along the corner joint. At 20ms, the vertical crack extended into a stepped crack between the 4^{th} and 5^{th} layers, 0.3m above the base, running to the centre of the base of the front blast normal panel. As with the previous **B** panel, BWL2A, between 20-50ms both the front and side panels began to rotate towards eachother about the corner joint, causing increased cracking across both faces.

At 50ms, a stepped crack running from the 19^{th} layer of brick at the corner joint to the upper outer edge of the blast normal panel formed. Between 50-100ms, the rotation of both panels caused increased cracking and brick separation creating five large fragments on each panel. A slight tilting motion of the both faces in combination with the rotation about the corner joint led to a small collision between the side panel and the upper inner fragment of the blast normal panel. This collision only caused minor additional fragmentation as the momentum and energy was significantly lower than that observed in the 4.9m section of the ABT.

Each panel continued to collapse without any significant translational motion, leading the side panel to rotate and topple outwards, eventually colliding with the wall of the ABT at 400ms, whilst each fragment of the front panel tilted about its base and rotated

about the corner joint until impacting with the ground between 1m< x <3m, depending on the height of the fragment.

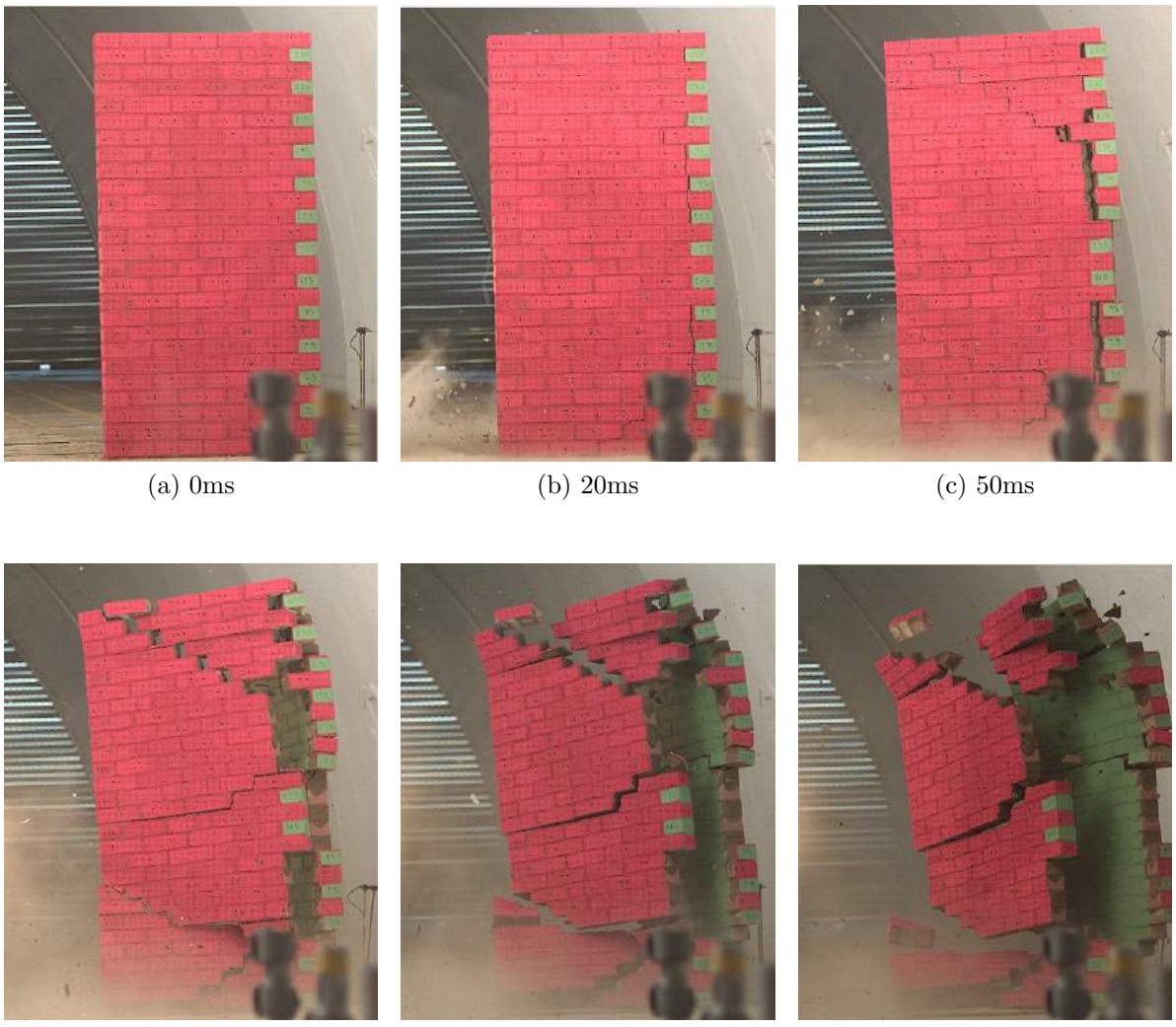

(a) 0ms (b) 20ms (c) 50ms

(d) 100ms (e) 150ms (f) 200ms

Figure 4.54: High speed photography (from the upstream perspective) of the breakage of structure BWL2B

The longitudinal debris distribution of structure BWL2B, displayed in Figure 4.55a, shows a peak distribution of 139.3kg located in the x=1.5m bin, in which the largest fragment of mass 26.8kg was located, originating from the base of the corner joint. A total of 99% of the total mass of the side panel was located within the first 2.5m, with only one additional fragment located at x=4m.

The distribution of red bricks from the front, blast normal panel showed a steadily increasing distribution between 0m< x <3.5m, where it peaked with a total mass of

40.7kg, and then steadily decreased to 0kg between 3.5m< x <11m. Figure 4.55c, which illustrates the longitudinal distribution indicating the original vertical position of fragments shows the distribution between 2.5m< x¡11m consisting of bricks primarily from the central, vertical region of the structure. As the green bricks from the side panel were all located within the first 2.5m, this indicates that the distribution from both the top and bottom of the front, red, blast normal panel was also contained within the first 2.5m.

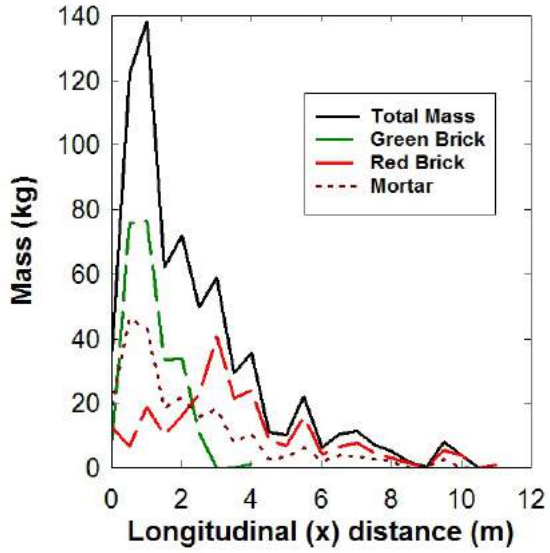

(a) Longitudinal distribution

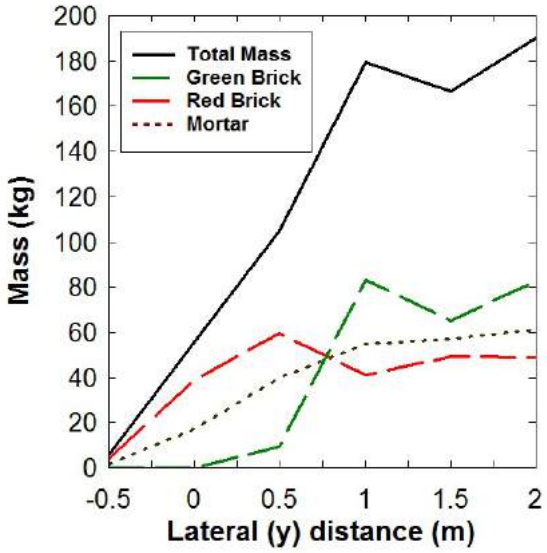

(b) Lateral distribution

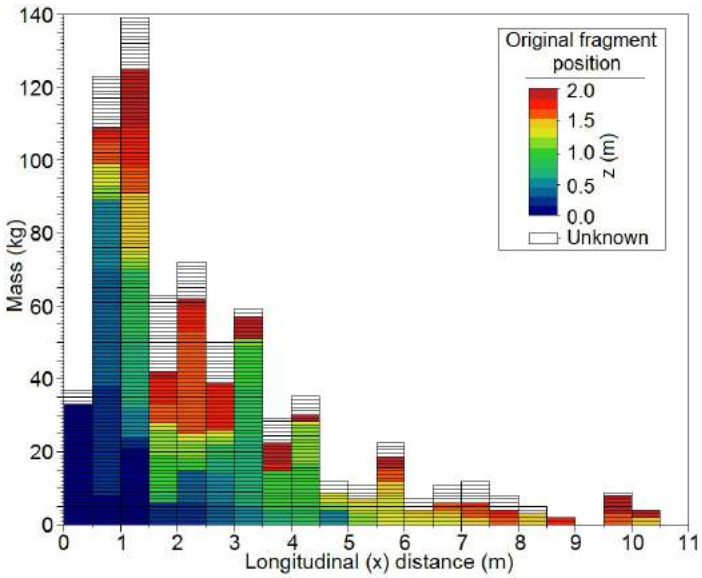

(c) Longitudinal distribution indicating original z position of fragments

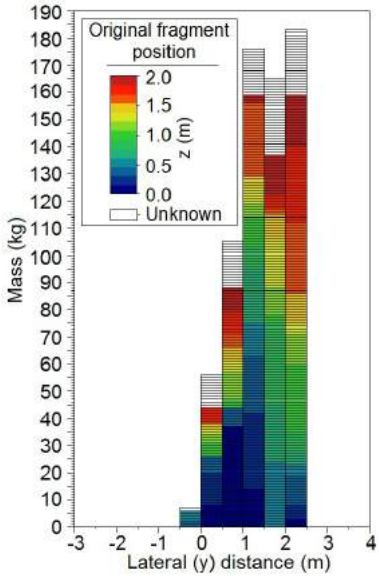

(d) Lateral distribution indicating original z position of fragments

Figure 4.55: Longitudinal and lateral debris distribution plots of structure BWL2B

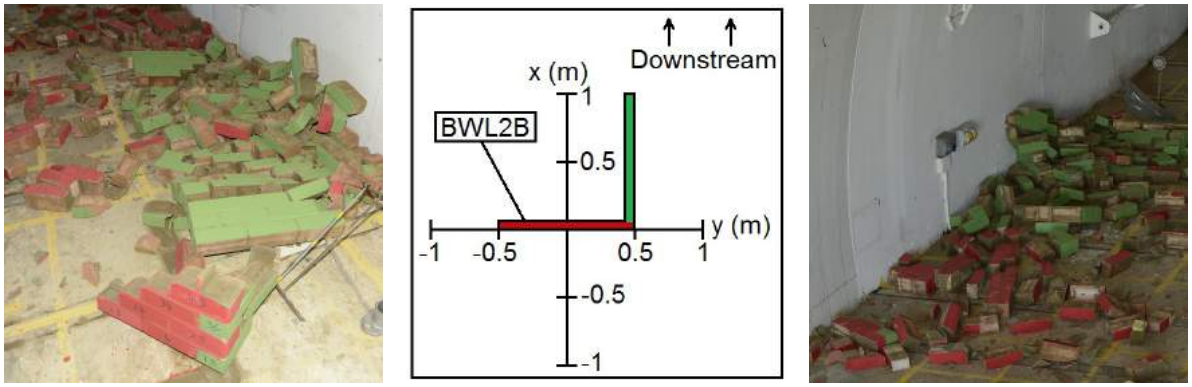

(a) Postshot photograph (perspective: upstream)

(b) Positional information

(c) Postshot photograph (perspective: downstream)

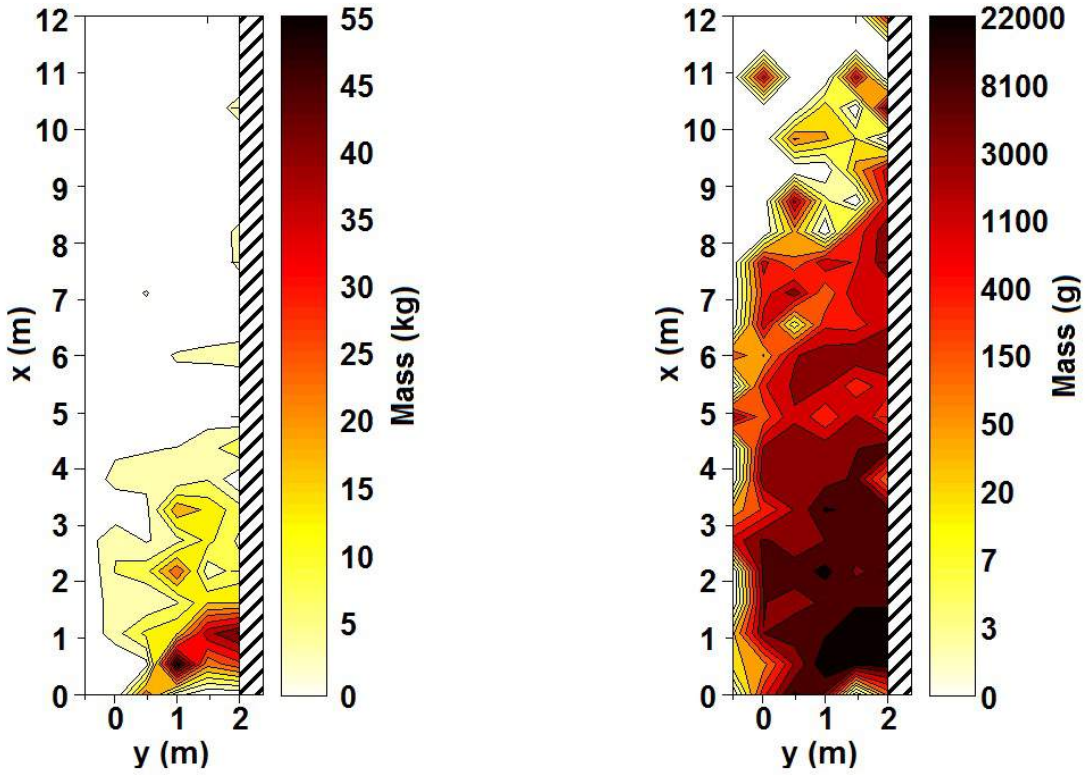

(d) (x, y) mass distribution (absolute)

(e) (x, y) mass distribution (logarithmic)

Figure 4.56: Debris mass distribution of structure BWL2B

The lateral distribution, displayed in Figure 4.55b, shows a steadily increasing distribution from -0.5m< y <1m. The structure was positioned with the blast normal face centred about y=0m, illustrated by Figure 4.56b, with the side panel located along y=0.5m. The front, blast normal panel was relatively evenly distributed between 0m< y <2m, whilst the side panel was almost entirely distributed between 1m< y <2m.

The lateral distribution indicating original vertical fragment position, presented in Figure 4.55d, shows fragments originating from the base of the structure were primarily

located between 0m< y¡1.5m, with the central and upper sections distributed between 1m< y <2m. This was the expected distribution considering the outwards, rotational motion of the side panel in combination with the downstream tilting and lateral rotational motion of the blast normal panel.

The logarithmic x,y mass distribution, displayed in Figure 4.56e, illustrates the area covered by the debris distribution, which is approximately 24m^2, obstructing a total rectangular area of 34.5m^2. The absolute x,y mass distribution, displayed in Figure 4.56d shows the highest density region was located between 0m< x <1m and 1m< y <2m, in which the two peak densities were located at (0.5,1) and (1,2). These two high density regions can be observed in the post-shot photographs displayed in Figures 4.56a and 4.56c, showing the large fragment responsible for the high density at (0.5,1) and the piling against the wall of the ABT at (1,2) respectively.

As with structure BWL2B, the breakage of structure BWL2C, an **A** panel located in the 10.2m section of the ABT, was not recorded from the side perspective due to a malfunction with relevant phantom camera. The later stage debris distribution was recorded by another phantom camera further downstream; however initial fragment displacement, velocity and acceleration time histories could not be taken. The breakage of BWL2C from the upstream perspective is displayed in Figure 4.57 at 20ms, 50ms, 100ms, 150ms and 200ms.

The first visual signs of breakage occurred at approximately 30ms in the form of a horizontal crack forming between the 17th and 18th layers of brick, approximately 1.25m above the base of the structure; however at 20ms, small fragments of both brick and mortar between 2-3mm in width were observed peeling from the lower section of the structure. A second horizontal crack formed at approximately 40ms between the 7th and 8th layers of brick, 0.45m above the base, on the left hand side of the structure which stepped vertically up two layers and propagated to the right hand side between the 9th and 10th layers of brick.

(a) 0ms (b) 20ms (c) 50ms

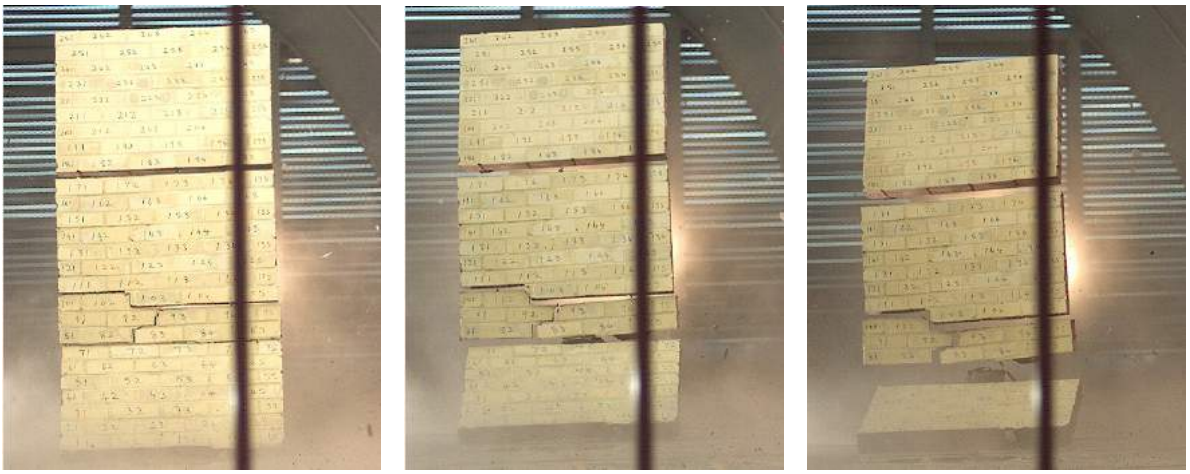

(d) 100ms (e) 150ms (f) 200ms

Figure 4.57: High speed photography (from the upstream perspective) of the breakage of structure BWL2C

The separation of these horizontal crack lines increased by 50ms, at which time the structure displayed noticeable tilting about its base in the downstream direction. At approximately 80ms, the horizontal stepped crack extended and completely separated the 7^{th} and 8^{th} layers of brick. The upper section of the same crack pattern also extended by an additional brick between the 9^{th} and 10^{th} layers, raising above the 10^{th} layer before extending to the edge of the structure. No additional fragmentation or cracking occurred beyond this point.

The full formation of the crack between the 7^{th} and 8^{th} layers of brick caused the lowest fragment to become completely unrestrained from the rest of the structure, which

reduced the tilting motion of the upper section of the structure. The lowest fragment continued to tilt about its base, whilst the rest of the structure translated with little momentum in the positive x direction until impacting with the ground.

The longitudinal debris distribution of structure BWL2C is displayed in Figure 4.58a, which shows a maximum fragment distribution of 13m. Besides small flakes of both brick and mortar with masses of the order of 0.01kg, there was no debris distributed between 0m$< x <$2m. The peak distribution was located at 6.5m with a bin mass of 67.5kg, resulting from collision with the debris and the lighting array.

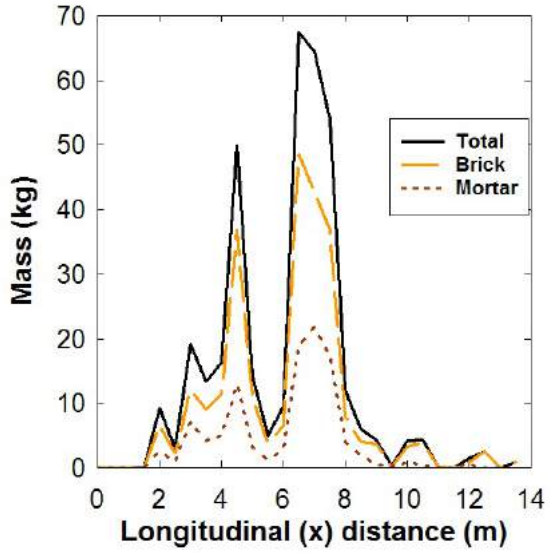

(a) Longitudinal distribution

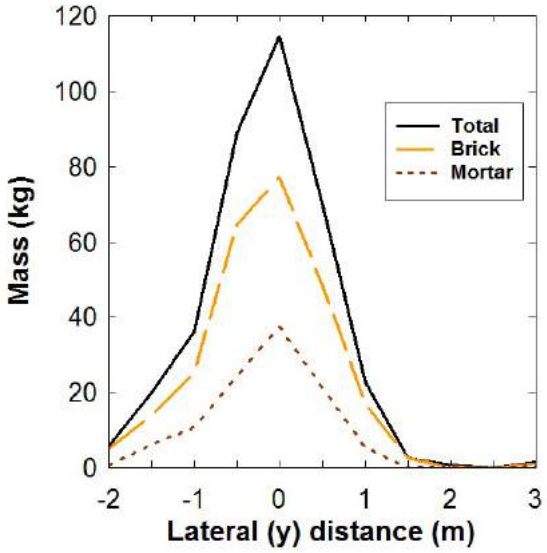

(b) Lateral distribution

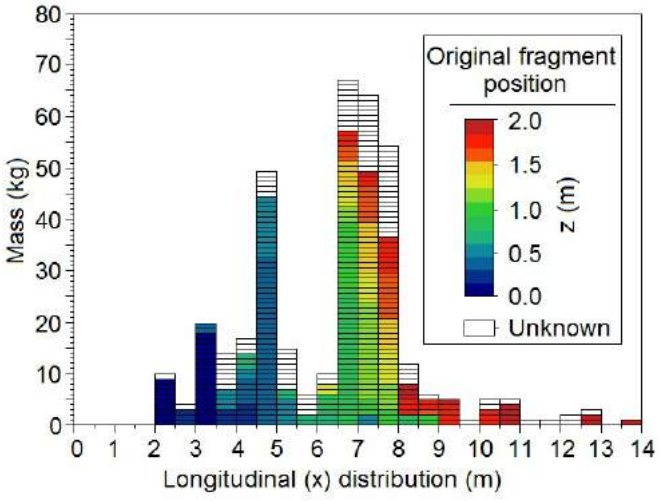

(c) Longitudinal distribution indicating original z position of fragments

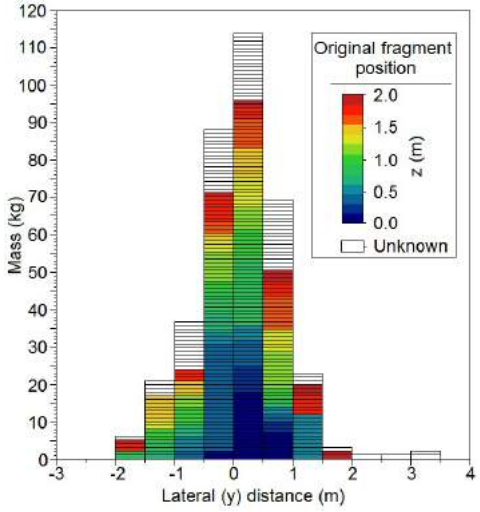

(d) Lateral distribution indicating original z position of fragments

Figure 4.58: Longitudinal and lateral debris distribution plots of structure BWL2C

(a) Postshot photograph (perspective: upstream)

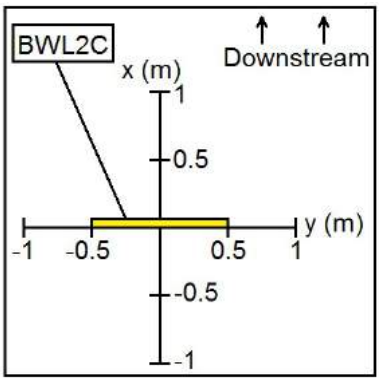

(b) Positional information

(c) Postshot photograph (perspective: downstream)

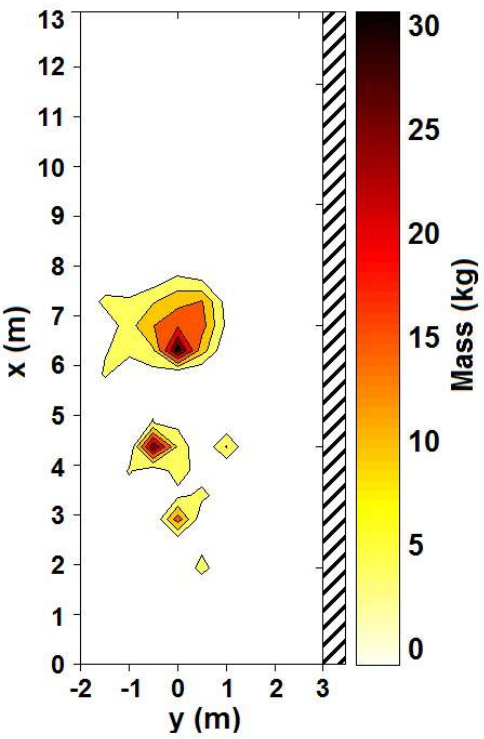

(d) (x, y) mass distribution (absolute)

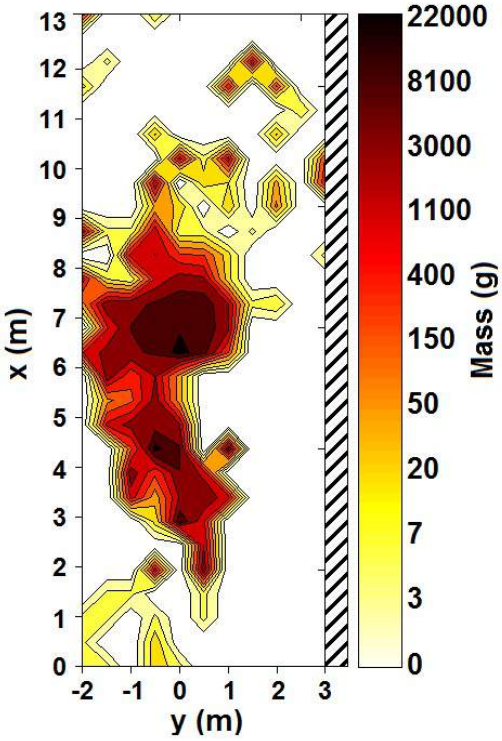

(e) (x, y) mass distribution (logarithmic)

Figure 4.59: Debris mass distribution of structure BWL2C

High speed photography showed all fragments of debris impacting the ground before the x=7m, suggesting that in the absence of the lighting obstruction, the debris would have been distributed slightly more evenly between 6.5m$< x \lesssim$12m, with an increased maximum throw distance. Another, smaller peak was located at x=4.5m, with a mass of 49.8kg in which the largest fagment with a mass of 26.0kg was located, originating from the botom quadrant of the structure. The distinctive double peak results from the reduced initial fragmentation, which caused the debris to be distributed to small areas in

large quantities.

The longitudinal distribution indicating original vertical fragment position, displayed in Figure 4.58c, shows the expected vertical distribution of fragments for a structure with a combined tilting and translational motion, that is, a higher initial z position resulted in a larger x distribution. As previously noted, the large mass located at x=4.5m originates from the bottom quadrant of the wall, whilst the distribution around the lighting array was composed of the majority of the upper section of the structure.

The lateral distributions, displayed in Figures 4.58b and 4.58d show a relatively symmetrical distribution, with a slight bias in the positive y direction which contained 58% of the debris. With a larger lateral distribution than those observed in the HE trials, the bias was not due to fragments overlapping bin boundaries, rather slight rotations of the initial fragments caused by the asymmetric cracking patterns. As a result, the large fragments collided with the ground at an angle, causing a slightly offset lateral distribution. The lateral distribution indicating original vertical fragment position shows the lower sections of the structure located closer to the y=0 position, with a slight increase in lateral distribution, in both directions, for fragments originating for higher up in the structure.

Post-shot photographs, displayed in Figures 4.59a and 4.59c, show the location of the largest single fragment and the large debris piling around the lighting array. The positional identifier displayed in Figure 4.59b, shows the structure centred about (0.05,0) for reference to the x,y debris distributions presented in Figures 4.59d and 4.59e, plotted on absolute and logarithmic scales respectively. The logarithmic scale illustrates the total area covered by the debris, approximated as 27.25m^2, obstructing a maximum rectangular area of 77m^2, whilst the absolute scale indicates the areas of high density at (-0.5,4.5) and (0,6.5).

The large enclosed structure in the 10.2m section of trial BWL2 was BWL2D, with maximum x,y dimensions of 3m×4m, constructed from base panels **ABCDE**. The breakage of BWL2D is displayed from the upstream and inside, side-on perspectives in Figures 4.60 and 4.61 respectively, at 0ms, 20ms, 50ms, 100ms, 150ms and 200ms. The

structure was also recorded from the downstream perspective, displayed in Figure 4.62; however, the resolution was too low to see any detailed breakage patterns. Furthermore, beyond 50ms the dust build up from the blast clearing completely obstructed the view of the structure. Although recordings from this particular camera do not directly assist in breakage analysis, the excessive dust clearly illustrates vortex formation as a result of blast clearing.

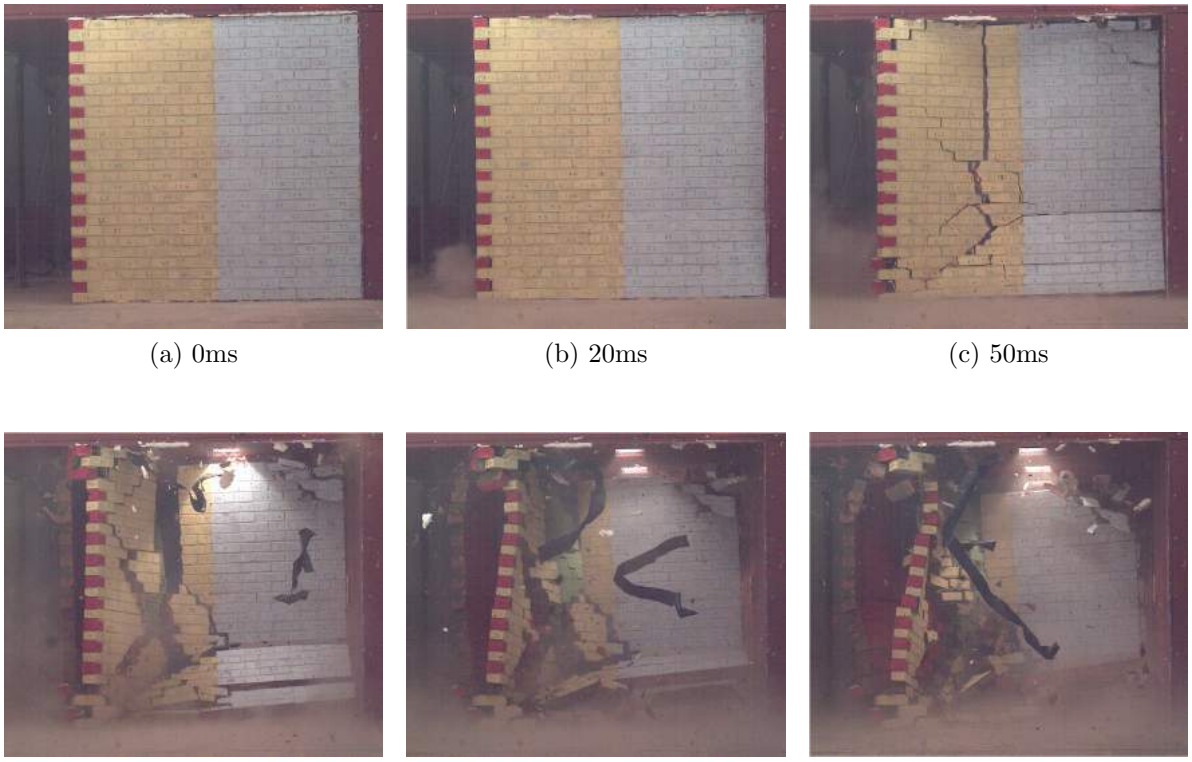

(a) 0ms (b) 20ms (c) 50ms

(d) 100ms (e) 150ms (f) 200ms

Figure 4.60: High speed photography (from the upstream perspective) of the breakage of structure BWL2D

First signs of structural response were observed at 10ms in the form of a stepped crack running from the base of the corner joint on the front, blast normal panel, to approximately 0.6m above the base of the structure and 0.5m from the corner joint. At 20ms, this crack pattern was barely visible from the upstream perspective; however the inside, side-on perspective shows the crack forming from the inside of the front face, alongside some noticeable inwards motion of the front panels; Furthermore, at 20ms, a cracking pattern began to form on the side panels, with a vertical crack running from the

top of the side panel, approximately 0.75m from the upstream corner joint, connected to the base of the upstream corner joint by a stepped crack 0.4m above the base.

Between 20-50ms, the crack pattern on the side panels extended in the downstream direction, with a series of stepped cracks which met at approximately 1m from the downstream corner joint and 1m above the base. A stepped crack ran from this intersection point to the base of the downstream corner joint and another to the top of the downstream corner joint, with a final stepped crack connecting the two crack patterns. All of the fragments created by the crack patterns began to tilt inwards.

Meanwhile on the front, blast normal face, the stepped crack is joined by a horizontal crack at 0.6m, running from the outer edge of the structure to approximately 0.75m from the corner joint. A further, vertical crack connected this intersection point to the base of the structure, with small additional cracks forming around the intersection point. Similarly to the previous enclosed structure, BWL1C, the lower fragment created by the horizontal crack tilted about its base, the larger upper, outer fragment translated with a slight tilt about the horizontal crack line and the inner fragment connected to the side panels rotates inwards around the corner joint.

Between 50-200ms, additional fragmentation occurred over the front blast normal panel through extra cracks propagating from the initial crack pattern. The motion of the large initial fragments remained unchanged, with the lower fragment continuing to tilt about its base, the upper, outer fragment translated downstream towards the rear of the structure and the inner fragment continued to rotate about the corner joint. Additional fragments were formed around the crack pattern on the side panels and the inward tilting motion also remained unchanged; the most upstream of the side panels however began to tilt outwards about its base.

Although rotation about the corner joint had been observed in the side panels of corner geometries, the influence of the additional side panels counteracted this rotation, causing the most upstream of the side panels to rotate about the vertical crack which formed 0.75m downstream of the corner joint. At approximately 100ms, cracks began to form over the rear panel. In common with the previous larger enclosed structure, the rear

panel became wedged between the ground and the roof of the steel enclosure, stopping any tilting, rotational or translational motion.

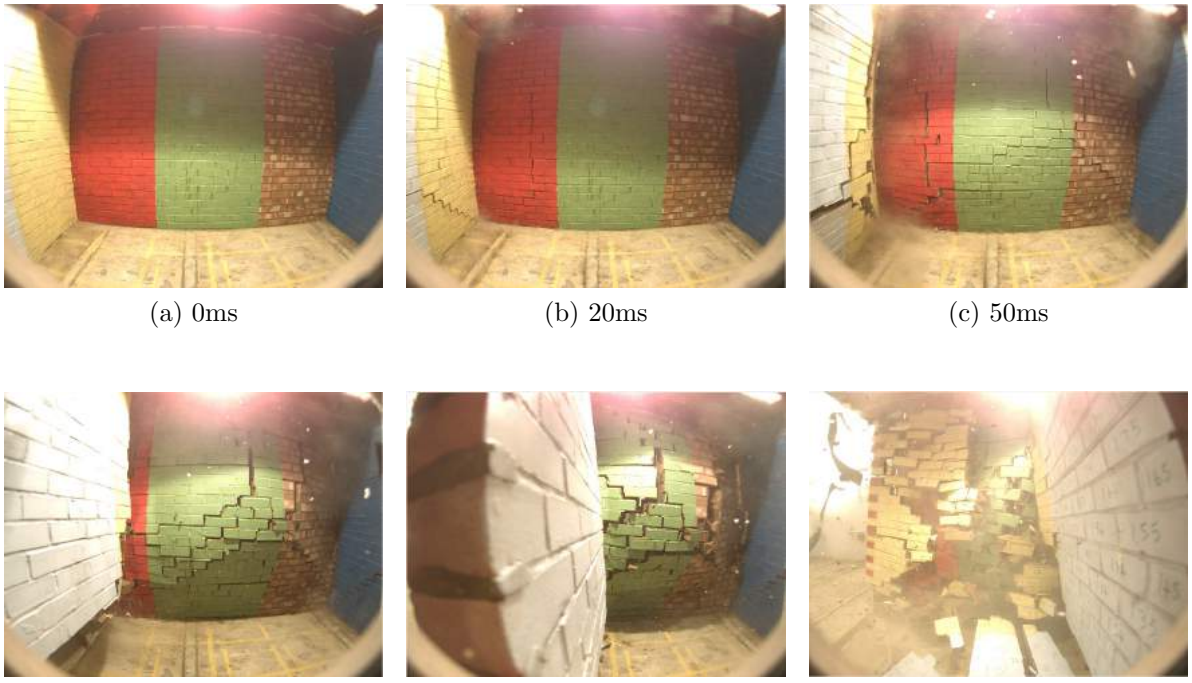

(a) 0ms (b) 20ms (c) 50ms

(d) 100ms (e) 150ms (f) 200ms

Figure 4.61: High speed photography (from the inside, side-on perspective) of the breakage of structure BWL2D

(a) 0ms (b) 20ms (c) 50ms

Figure 4.62: High speed photography (from the rear perspective) of the blast clearing around structure BWL2D and vortex production

Similarly to structure BWL1C, the downstream panel of structure BWL2D became wedged between the ground and the roof of the steel enclosure, which in combination with the high density debris distribution, made manual debris collection both impractical

and unsafe. The outline debris distribution, alongside a post-shot photo taken from the upstream perspective, is displayed in Figure 4.47c, illustrating an approximate area of 6.25m^2 covered by the debris, obstructing a maximum rectangular area of 11.25m^2.

(a) Perspective (downstream)

(b) Perspective (side)

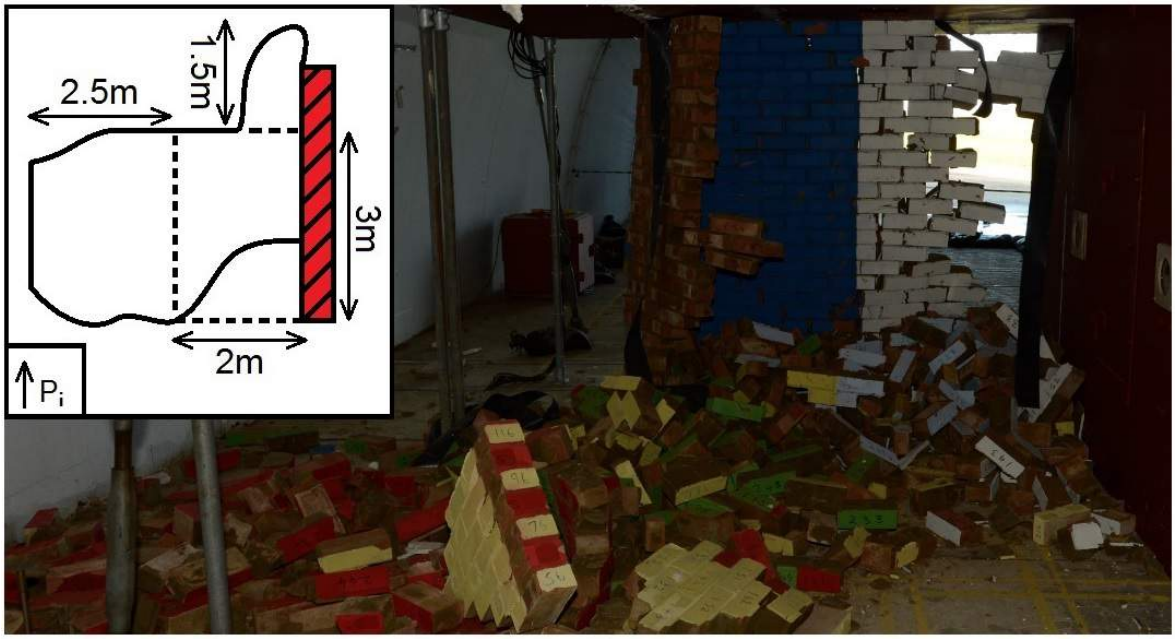

(c) Perspective (upstream), including outline sketch of debris

Figure 4.63: Post-shot photographs of the debris distribution of structure BWL2D

The rear and most downstream side panel, constrained between the floor and the roof of the steel enclosure, were more delicately held in place than in structure BWL1C. A large number of loose fragments were balanced on the edges of the structure and required little

force to remove. The peak distribution with an approximate height of 0.6m was located against the rear panel and the steel enclosure, again similaraly to BWL1C. The larger blast normal surface area of the structure allowed more blast in-fill once the front panel was breached, which in combination with the impact from the high momentum of the large fragment, caused additional damage to the rear panel, illustrated in Figure 4.63a. The most downstream side panel was also constrained between the floor and the roof of the rear structure, after having both rotated about the most downstream corner joint whilst tilting inwards about the base.

4.3.3 BWL3

The pressure time histories and their respective integrated, associated impulses, from both the 4.9m and 10.2m sections of the ABT, instrumented in trial BWL3 are displayed in Figure 4.64. The 4.9m section was monitored by gauges p_i6, p_r4 and q4, with their pressure time histories and integrated cumulative impulses displayed in Figures 4.64a and 4.64b respectively. The static overpressure in the 4.9m section, monitored by gauge p_i6, recorded a peak value of 130.0kPa at 223.9ms resulting from a reflection from the upstream face of the structure.

At the arrival of the shock discontinuity, the peak pressure recorded by p_i6 was 97.7kPa at 211.5ms, 11% below the target pressure and a peak impulse of 7036.4kPa.ms at 427.6ms, giving a positive phase duration of 216.1ms. The additional impulse recorded as a result of the blast reflection was, in this case, too small to cause any noticeable change to the overall recorded impulse. Gauge p_r2 did not record any data until 290.0ms, with a peak value of 256.8kPa; although this was within the expected range of reflective pressure, little to no decay was measured, resulting in a peak recorded impulse of 131,117.3kPa.ms at 900ms, almost 10× higher than the expected reflected impulse over an infinite surface.

The reflected pressure readings in the 4.9m section for trial BWL3 were therefore discarded as the data was subject to some form of gauge fault. The dynamic pressure in the 4.9m section recorded a peak value of 42.7kPa at 213.8ms, which dropped below 3kPa at approximately 290ms, which through no obvious correlation, corresponds to the

point at which the reflected pressure readings began. The associated dynamic impulse at 290ms was 1120.9kPa.ms, 49% of the total impulse which was recorded as 2289.5kPa.ms at 900ms.

The static pressure along the central axis of the 10.2m section of the ABT was monitored by gauges p_i3, p_i4 and p_i5, each spaced by 1m intervals. For each gauge, the peak recorded pressures resulted from reflections from the most upstream blast normal face of the steel enclosure which were 79.8kPa at 359.2ms, 80.5kPa at 363.0ms and 72.1kPa at 365.8ms respectively. At the arrival of the shock discontinuity, the peak pressures measured by gauges p_i3, p_i4 and p_i5 were 52.7kPa at 354.3ms, 52.7kPa at 354.4ms and 56.3kPa at 350.4ms, giving a range of 3.6kPa and a mean value of 53.9kPa, 2% below the target pressure.

The peak recorded impulses were 3805.1kPa.ms at 521.7ms, 3877.7kPa.ms at 522.1ms and 3881.0kPa at 519.8ms respectively, giving a range of 75.0kPa.ms and a mean value of 3854.6kPa.ms. Using the peak impulse times to calculate the positive phase durations gave 167.4ms, 167.7ms and 169.4ms for gauges p_i3, p_i4 and p_i5 respectively, with a mean value of 168.2ms and a range of 2ms.

The dynamic pressure in the centre of the 10.2m section of the ABT was monitored by gauge g3, which recorded peak value of 15.4kPa at 365.4ms, corresponding to excessive gauge noise; the value at the arrival of the shock discontinuity at 351.5ms was 13.9kPa. The dynamic associated impulse at 425ms, corresponding to the time at which the dynamic pressure reduced below 3kPa was 247.0kPa.ms, 65% of the total associated impulse of 379.8kPa at 698.3ms.

The static pressures monitored in-line with the most upstream face of each structure were recorded by gauges p_i1 and p_i2, reading peak values of 55.0kPa at 356.4ms and 57.4kPa at 358ms respectively, giving a range of 2.4kPa and a mean pressure of 56.2kPa, 2% above the target pressure. These results show good consistency with the readings from the centre of the ABT, with the mean value at the edges being 2.3kPa, or 4% higher than the centre of the ABT.

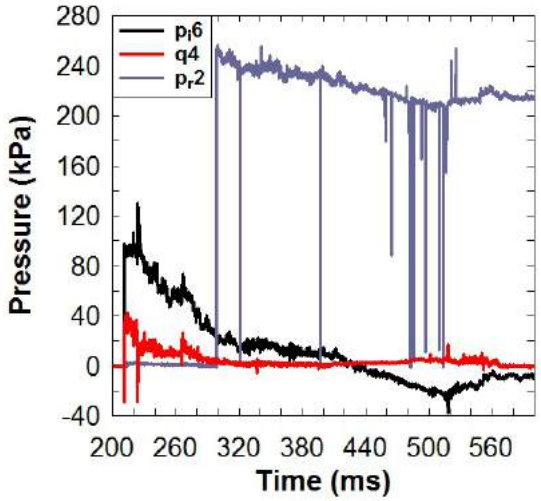

(a) Pressures: 4.9m section

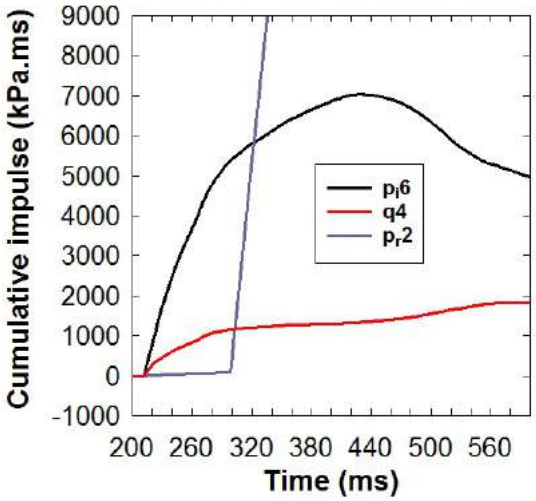

(b) Impulses: 4.9m section

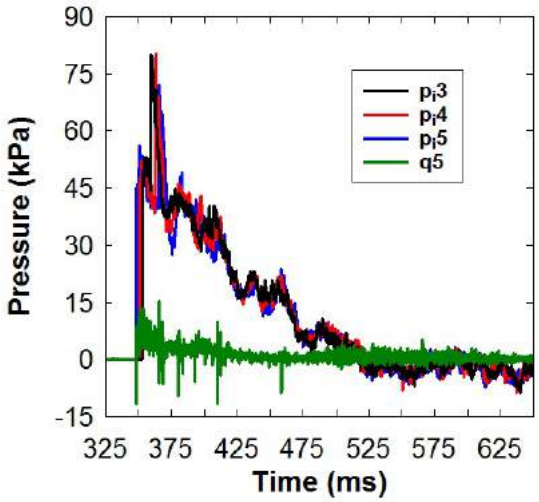

(c) Pressures: 10.2m section (central)

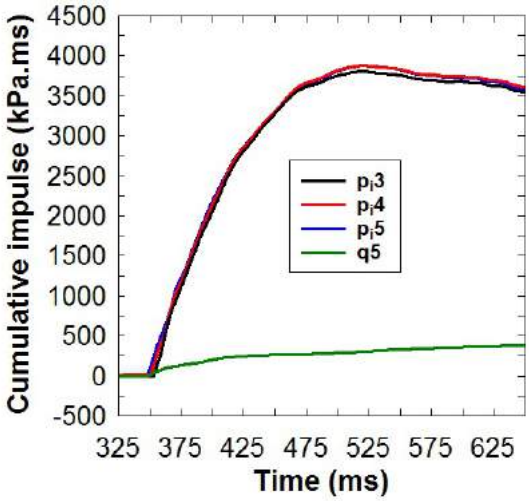

(d) Impulses: 10.2m section (central)

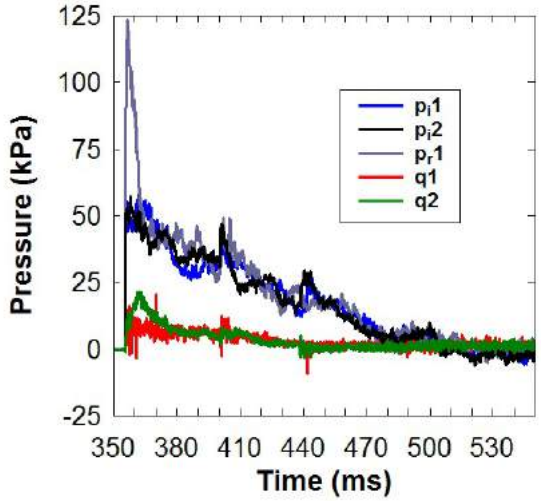

(e) Pressures: 10.2m section (edges)

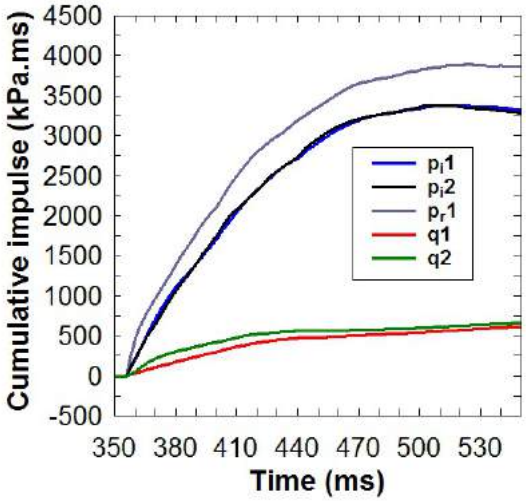

(f) Impulses: 10.2m section (edges)

Figure 4.64: Pressure time histories and integrated impulses from trial BWL3

The total transferred impulse recorded by gauges p_i1 and p_i2 were 3377.5kPa.ms at 504.7ms and 3382.0lkPa.ms at 518.8ms respectively, giving a mean value of 3379.8kPa.ms and a range of 4.5kPa.ms, again showing good consistency with the centre of the 10.2m section with a difference of 474.8kPa.ms, or 12%. The positive phase durations were calculated as 148.3ms and 160.8ms respectively, giving a range of 12.5ms and a mean value of 154.5ms, 13.6ms or 8% lower than the centre of the 10.2m section; although the static pressures differ by only 2%, the 8% increase in duration in the centre of the ABT increased the difference in mean recorded impulses.

The reflective pressure gauge, p_r1, which was mounted on the front, blast normal face of the steel enclosure recorded a peak value of 123.4kPa at 356.7ms and a peak impulse of 3888.9kPa at 523.9ms. The dynamic pressure, monitored by gauges q1 and q2 recorded peak values of 20.6kPa at 370.2ms and 21.4kPa at 363.0ms respectively. The associated dynamic impulses at 430ms, corresponding to the approximate time at which the pressure drops below 3kPa, were 488.3kPa.ms and 568.7kPa.ms respectively, compared to the maximum recorded values of 684.7kPa.ms at 685.3ms and 727.3kPa.ms at 715.3ms respectively.

The breakage of structure BWL3A, a **D** panel in the 4.9m section of the ABT is displayed in Figures 4.65 and 4.66 from the upstream and side perspectives respectively at times 0ms, 20ms, 50ms, 100ms, 150ms and 200ms.

First observable signs of breakage occurred at 10ms in the form of a vertical crack running along the corner joint, separating the side and rear, blast normal panels. By 20ms, the crack became more pronounced, forcing several individual bricks from the side panel loose, at which point the front and sie panels were completely unrestrained. An additional vertical crack began to appear approximately 0.3m from the corner joint on the rear, blast normal panel and by 30ms, this vertical crack was more pronounced, with three horizontal cracks forming over the rear, blast normal panel.

The lowest horizontal crack formed at approximately 0.5m above the base between the 7^{th} and 8^{th} layers of brick, with another forming at approximately 1.2m above the base between the 16^{th} and 17^{th} layers of brick and the final horizontal crack formed between

the 21st and 22nd layers of brick, approximately 1.6m above the base of the structure. The front panel was split by the three horizontal cracks and the vertical crack into eight initial fragments, with the upper fragments subject to further fragmentation resulting from the turbulent blast clearing.

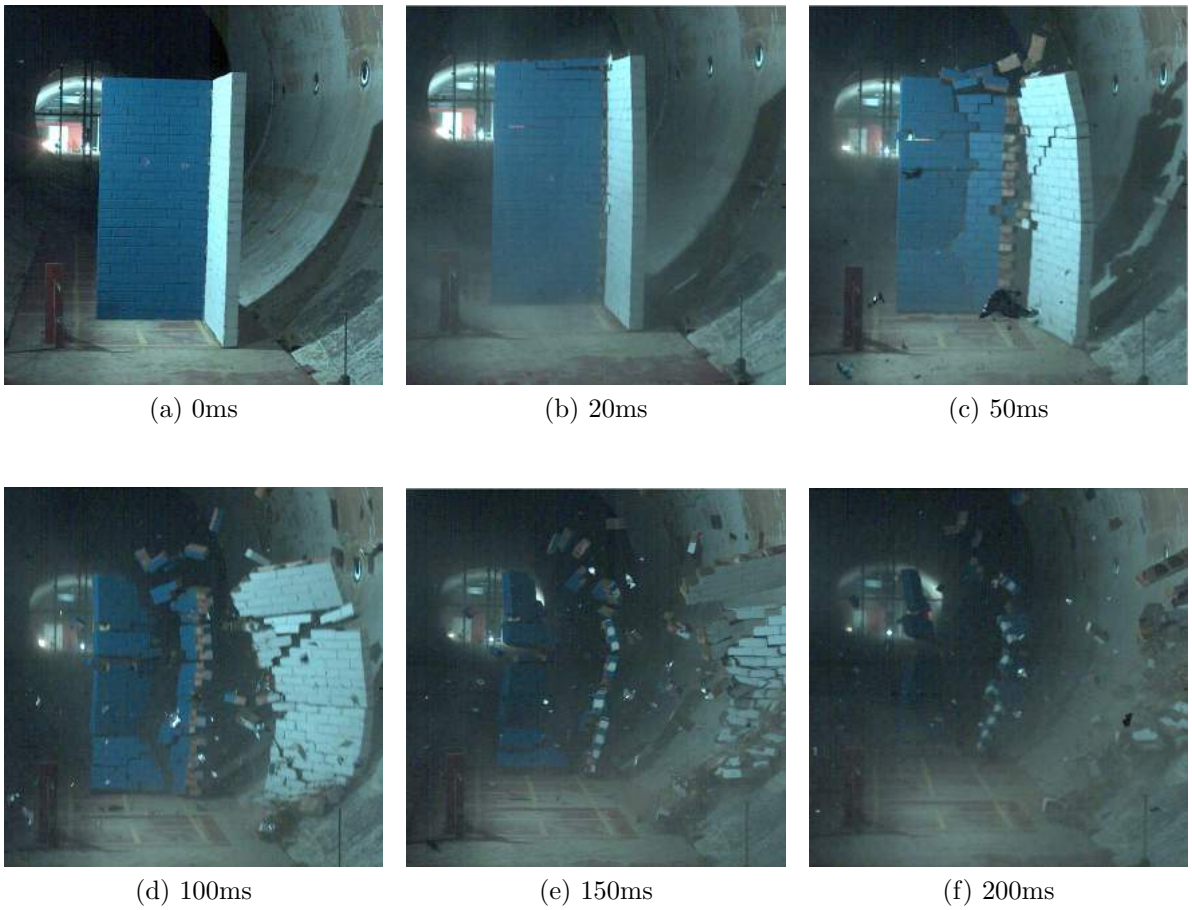

(a) 0ms (b) 20ms (c) 50ms

(d) 100ms (e) 150ms (f) 200ms

Figure 4.65: High speed photography (from the upstream perspective) of the breakage of structure BWL3A

A stepped crack formed on the side wall from 1.2m above the base at the corner joint and followed a uniform stepped pattern to approximately 1.6m above the base on the outer edge and a further horizontal crack formed on the side panel between the 12th and 13th layers, corresponding to approximately 0.9m above the base of the structure. Similarly to BWL2A, the outer fragments from the blast normal panel displayed mostly translational motion in the downstream direction, with the lower fragments exhibiting tilting about the base; however, as a result of blast clearing through the central vertical crack, the outer fragments also exhibited an outwards rotational motion. The inner

fragments from the rear blast normal panel exhibited a counter rotational motion, which in both cases was clearly visibly by 100ms.

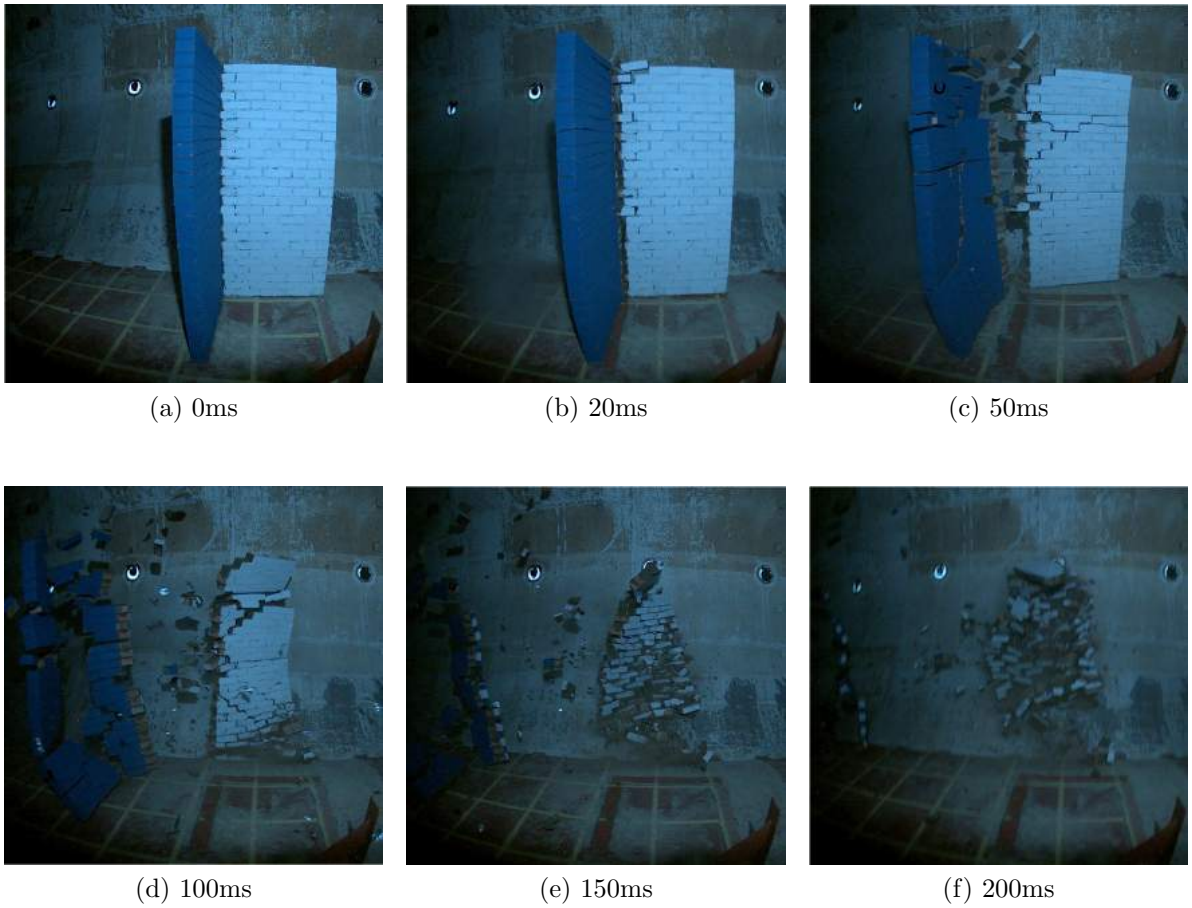

(a) 0ms (b) 20ms (c) 50ms

(d) 100ms (e) 150ms (f) 200ms

Figure 4.66: High speed photography (from the side perspective) of the breakage of structure BWL3A

The side panel displayed an outwards rotation about the corner joint across all fragments, with the lower fragments also tilting laterally outwards about the base and the upper fragments tilting laterally inwards about the horizontal crack which formed approximately half the height of the structure. The side panel also displayed a considerable lateral translational motion by comparison to structure BWL2B and by 100ms, the lower section of the side panel began to collide with the wall of the ABT, with considerable momentum remaining in the upper fragments.

At 150ms, the side panel had almost completely collided with the wall of the ABT causing significant further fragmentation, with only the uppermost fragment still entirely airborne. The inner fragments from the rear blast normal panel had rotated a little

over 90° about the corner joint, with all but the lowest of the outer fragments from the blast normal panel continuing to rotate outwards. The various motions of each fragment continued unchanged until impact with the ground, with little to no further fragmentation from any of the airborne debris.

Measurements of the initial longitudinal displacement, velocity and acceleration times histories for structure BWL3A could only be taken for the outer fragment which exhibited significant translational motion and are presented in Figure 4.67 between 0-100ms.

As previously discussed, the lower section of this particular fragment displayed a slight tilting moment about its base, whereas the rest of the structure rotated outwards about its outer edge. Figure 4.67a, which shows the longitudinal displacement over 0.2m intervals of the vertical height of the structure between 0-100ms, illustrates the motion of the monitoring points, which were on the outside edge and thus showed no relative rotation, to be almost entirely translational, with little to no tilting in the positive x direction. The small tilting motion can also be observed from Figure 4.67b, which displays the longitudinal displacement with respect to time for each vertical monitoring point, with the distance between the 0.2m curve and the 2m curve at 100ms is approximately 110mm, 10% of the total displacement at this time.

Similarly to all previous trials, the average velocities, displayed in Figure 4.67c, follow a typically logarithmic increase, with a large increase in velocity over the first 20ms, continuing to increase at a lower rate until 60ms, after which the velocity plateaus; the absolute velocity however, displayed in Figure 4.67d, shows a steady increase in velocity over the first 60ms, reaching peak values of between 14.6ms^{-1} and 12.3ms^{-1} for the top and bottom sections of the structure respectively.

After 60ms, the velocity of each fragment began to decrease as the dynamic pressure became too low to have any significant effect on the fragments. Between 80-100ms, the curve corresponding to the 1.6m monitoring point increased by 3.3ms^{-1}, which resulted from rotation of the fragment whilst in-flight, causing this particular monitoring point to have an apparent increase in velocity, whereas the effective velocity of the whole fragment still decreased. This effect was also observed, to a lesser extent, in the 0.2m and 0.4m

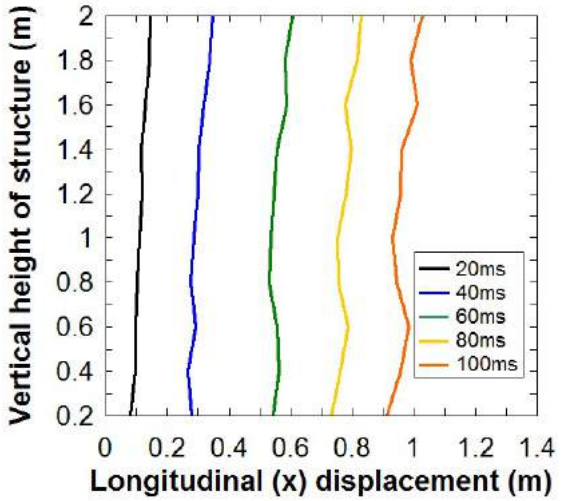

(a) Displacement relative to structural position

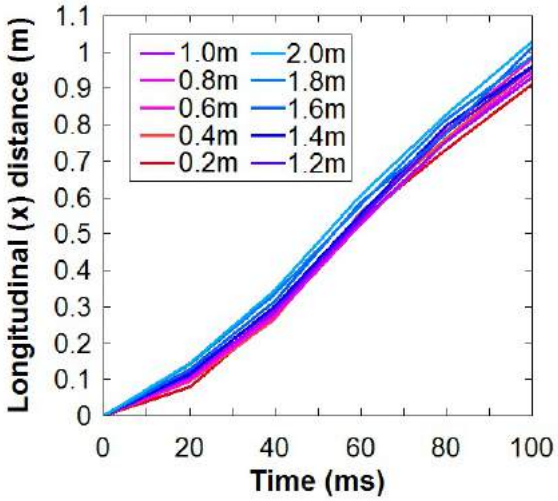

(b) Absolute displacement

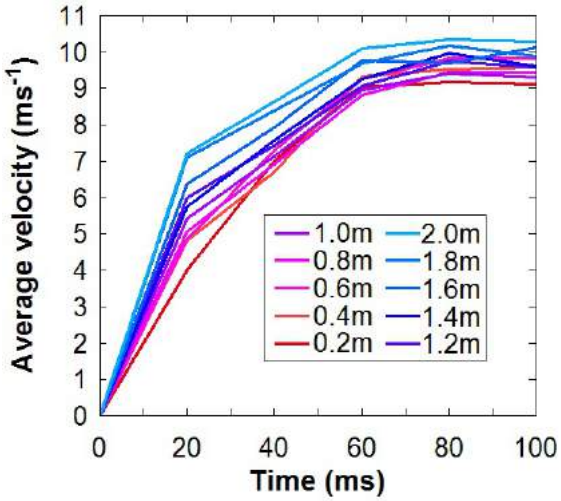

(c) Average velocity

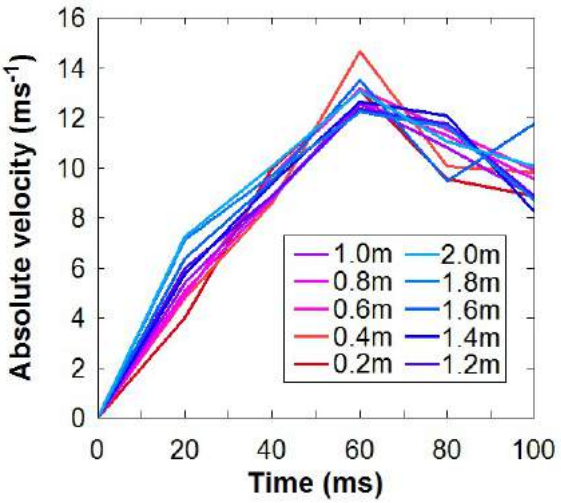

(d) Absolute velocity

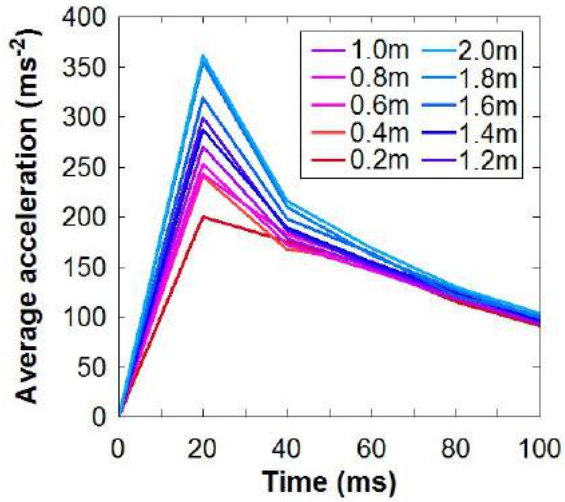

(e) Average acceleration

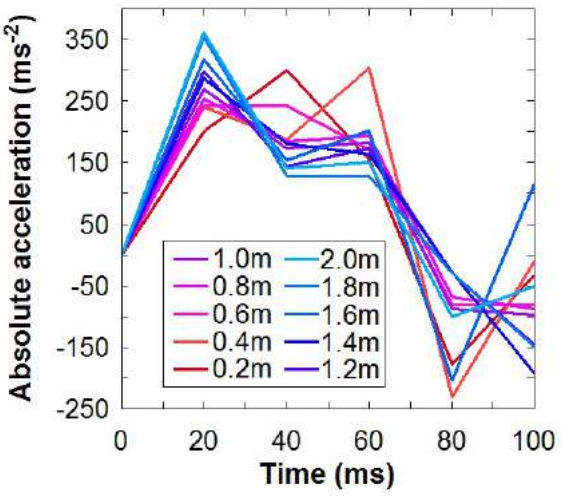

(f) Absolute acceleration

Figure 4.67: BWL3A displacement, velocity and acceleration time plots relative to the verical height within the structure

fragments as well as at 1.6m, with an unexpected increase in absolute acceleration, or rather decrease in deceleration between 80-100ms, shown in Figure 4.67f.

The general shape of the absolute accelerations was similar to previous structures, with a high initial acceleration, followed by a decreasing yet positive acceleration to approximately 80ms, after which the fragments began to decelerate. The average acceleration, displayed in Figure 4.67e also showed a similar trend of rapidly increasing acceleration, followed by a gentle decline over the measured time period.

The longitudinal debris distribution of structure BWL3A, presented in Figure 4.68, displayed similar patterns to both BWL1A and BWL2A. As previous structures in the 4.9m section of the ABT were measured with the most upstream point of the structure defined as x=0m, the same principle was applied to BWL3A, such the most upstream point of the side wall corresponds to x=0m, meaning the side wall itself ran from x=0m to x=1m and is therefore directly comparable to structure BWL2A.

As with BWL2A, the majority of the mass of the side wall was located between 0m$< x <$10m, containing the peak distributions of 76.5kg and 74.6kg located at x=2m and x=3m respectively resulted from the impact of the side panel with the wall of the ABT. The rear, blast normal panel followed a distribution similar to that of BWL1A, with the majority of the debris, 58.3kg, located at x=31m, corresponding to the position of the instrumentation columns.

Whilst both BWL2A and BWL3A were corner panels with an effective 180° rotation, the interaction of the blast with the structure differs drastically, with the clearing effects of the blast forcing the panels outwards as opposed to inwards. The longitudinal distribution indicating initial vertical fragment position, displayed in Figure 4.69, shows the distribution between 20m$< x <$45m contained bricks from all heights of the structure, increasing in z with x. These fragments correspond to the large set of outer fragments of which the initial displacement time measurements were taken.

The distribution of white bricks from the side wall, located between 0m$< x <$10m, shows fragments originating from the lower sections were located between 1m$< x <$4m, with the central vertical section of the structure distributed evenly between 3m$< x <$10m

and fragments from the top section of the side panel were evenly distributed across the entire region. This illustrates the rotation of the side panel in the downstream direction giving, creating an offset of vertical position in the downstream direction at the time of impact with the wall of the ABT. The relatively even distribution of fragments originating from the upper section of the side panel results from the entrainment effect of the dynamic pressure.

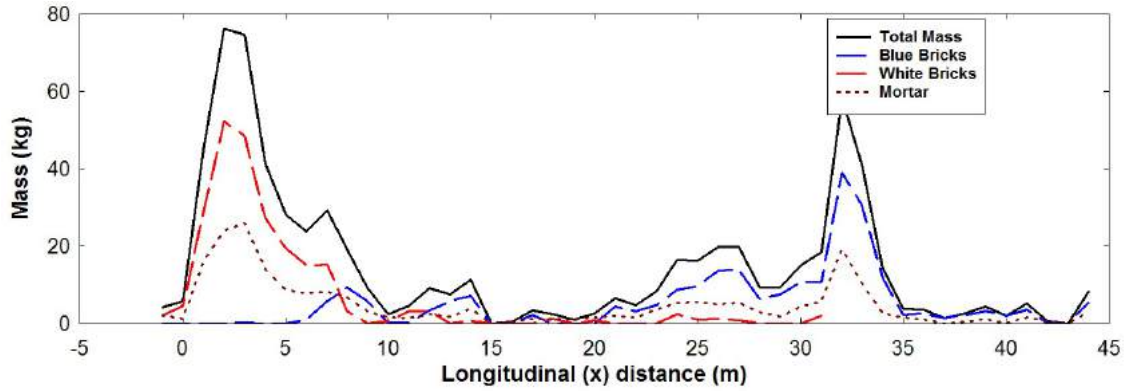

Figure 4.68: BWL3A longitudinal mass distributions

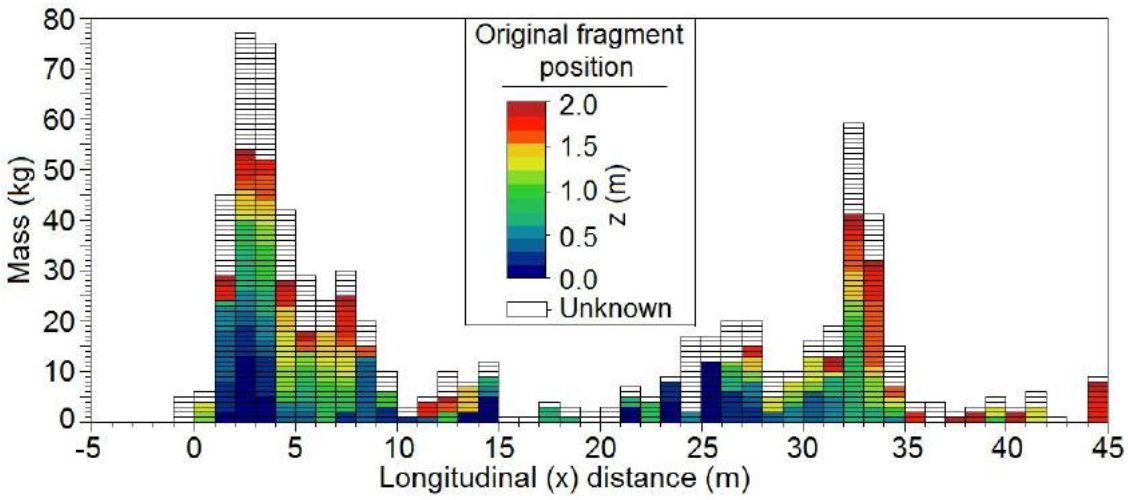

Figure 4.69: BWL3A longitudinal (x) mass distribution indicating (z) origin of debris

The breakage of structure BWL3B, a composite **AA** panel located in the 10.2m section of the ABT, is displayed from the upstream and side perspectives in Figures 4.70 and 4.71 respectively at times 0ms, 20ms, 50ms, 100ms, 150ms and 200ms.

First visual signs of structural response were observed at approximately 20ms in the

form of a horizontal crack line between the 10^{th} and 11^{th} rows of brick, approximately 0.75m above the base of the structure. The crack manifests on the rear of the structure and is visible in Figure 4.71b, in combination with a slight tilting of the lower section of the structure about its base.

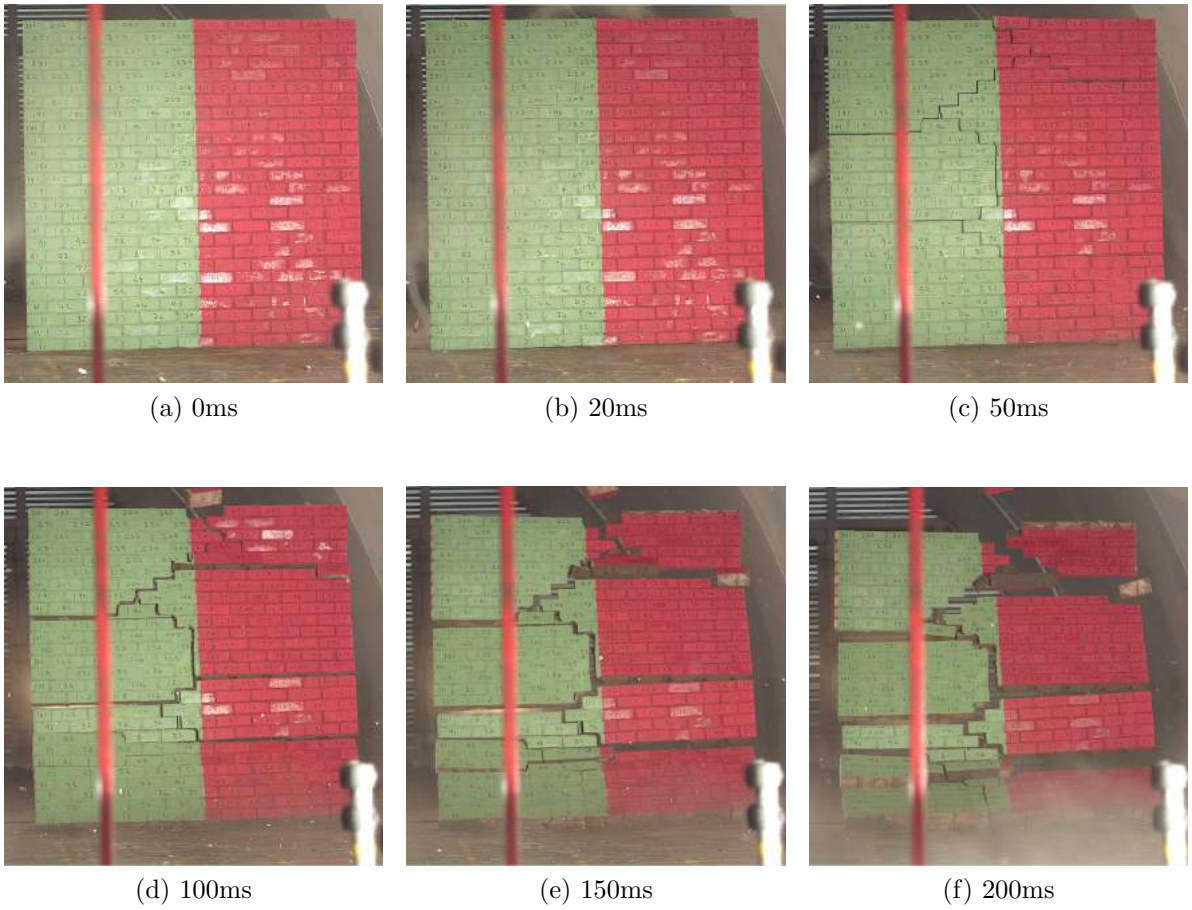

(a) 0ms (b) 20ms (c) 50ms

(d) 100ms (e) 150ms (f) 200ms

Figure 4.70: High speed photography (from the upstream perspective) of the breakage of structure BWL3B

By 30ms, multiple cracks began to form across the front, most upstream face of the structure and were clearly visible by 50ms. A horizontal crack formed on the upper section of each of the 1m panels, running approximately 0.5m from the edges of the structure. On the left, green panel a crack formed between the 17^{th} and 18^{th} layers of brick, approximately 1.3m above the base of the structure joined to the upper horizontal crack on the right, red panel, which formed at approximately 1.6m, by a uniform stepped crack.

The initial horizontal crack which formed at 0.75m above the base of the structure

on the left, green panel, ran to the centre of the structure where it joined a pair of horizontal cracks forming on the right, red panel at approximately 0.55m and 0.9m. A small vertical crack running down the central, vertical axis of the structure joined the two crack patterns, dividing the structure into six distinct fragments.

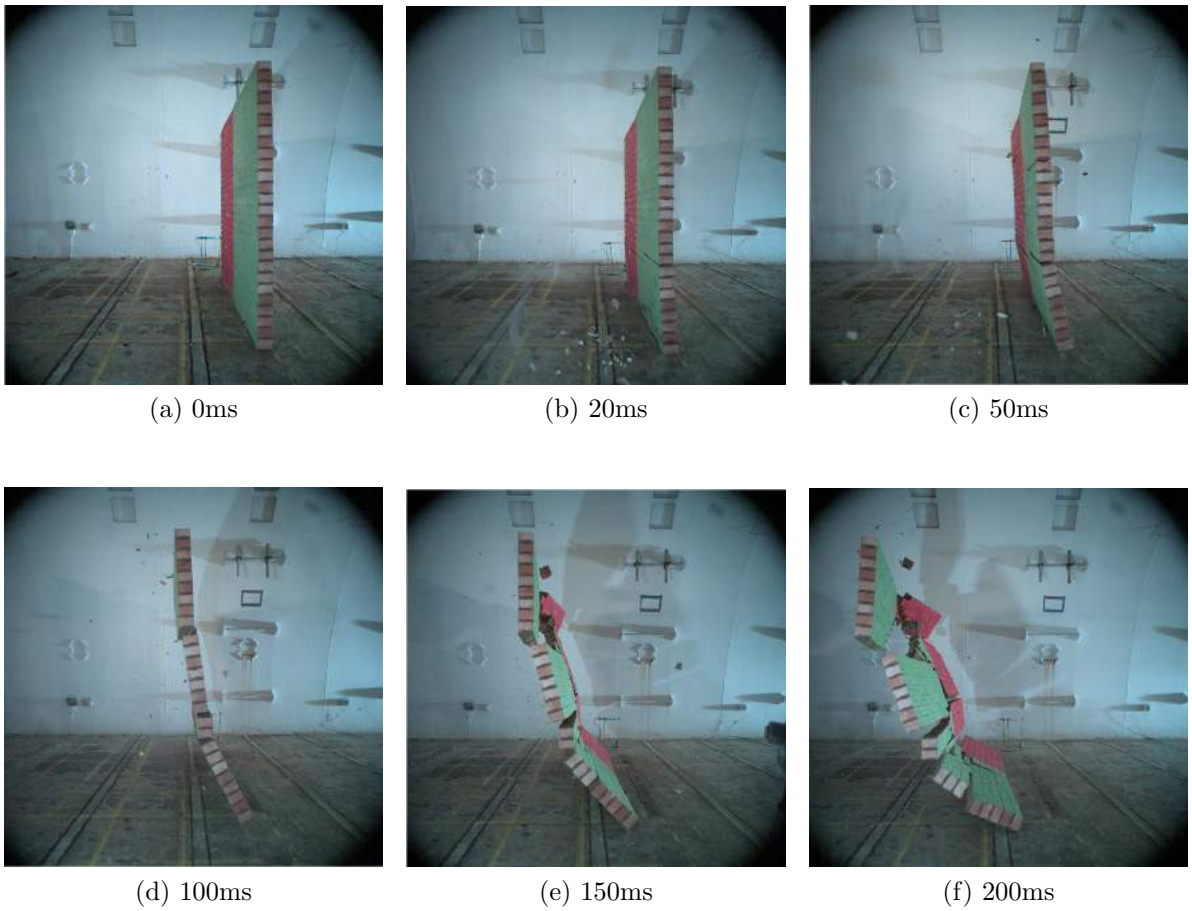

(a) 0ms (b) 20ms (c) 50ms

(d) 100ms (e) 150ms (f) 200ms

Figure 4.71: High speed photography (from the side perspective) of the breakage of structure BWL3B

The tilting motion of the lower fragment about its base continued, with the upper fragments displaying only slight tilting about the top of the lower fragment in combination with a translational motion in the downstream direction. By 100ms, the respective motions of the structure became more pronounced, with a more noticeable tilt of the central section of the structure about the top of the lower fragment.

On the left, green panel of the lower fragment, two additional horizontal cracks began to form at approximately 0.4m and 0.7m, with the brick separation of the upper fragments significantly increasing such that each fragment became completely unrestrained.

Between 100-200ms, no additional fragmentation was observed, with the separation between the pre-existing fragments slowly increasing. By 200ms, a noticeable velocity gradient was observed across the vertical height of the structure, resulting from the tilting motion. The lowest fragment had tilted by approximately 90°, whilst the uppermost fragment continued to display solely translational motion, with a slight rotation in the upstream direction caused by blast clearing beneath the fragment.

The phantom camera recording the breakage of structure BWL3B was replaced between trials BWL2 and BWL3 and was fitted with a lower angled lens, such that the initial downstream motion of the structure could be captured for a longer duration. The initial longitudinal displacement, velocity and acceleration time histories of structure BWL3B are displayed in Figure 4.72f between 0-220ms, with measurements taken at 20ms intervals.

The longitudinal displacement with respect to vertical position, displayed in Figure 4.72a, illustrates the combined tilting and translational motion of the structure about its base. The translational motion increases towards the top of the structure, whilst the tilting motion decreases, with no positive tilting from the uppermost fragments, which as discussed previously, began to exhibit counter tilting due to blast clearing effects. This was also observed in the displacement time history displayed in Figure 4.72b, as the curves representing the upper 0.5m of the structure are almost identical.

The average velocity, displayed in Figure 4.72c shows a logarithmic increase in velocity across all monitoring points, as with previous structures. There are significant velocity gradients across the vertical height of the structure. The absolute velocities, shown in Figure 4.72d, indicated a maximum velocity of 9.2m^{-1} at the top of the structure compared to 2.1m^{-1} at the base of the structure. Small fluctuations in the absolute velocity are observed across all monitoring points.

The velocity of the fragments do not continuously increase and decrease, each of the fragments contained 2-3 monitoring points, causing apparent fluctuations in velocity as the fragments rotate or tilt. The velocity of the entire fragment more closely resembles the average velocity. The same effect is more pronounced when inspecting the absolute

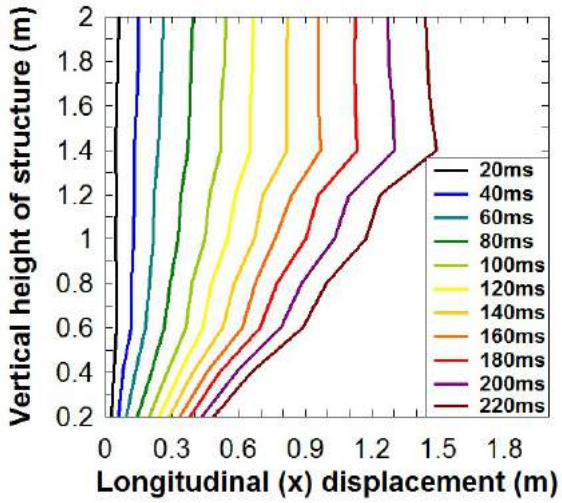

(a) Displacement relative to structural position

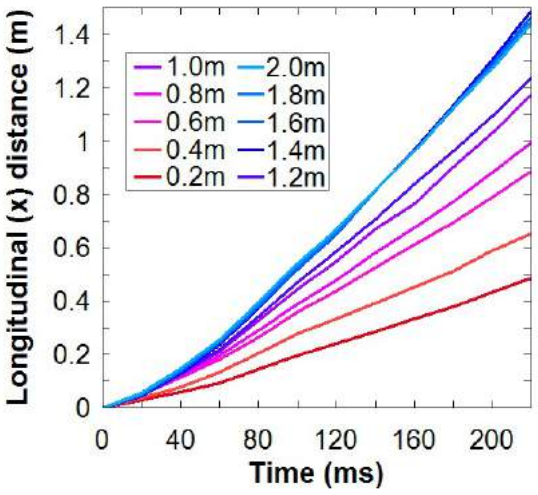

(b) Absolute displacement

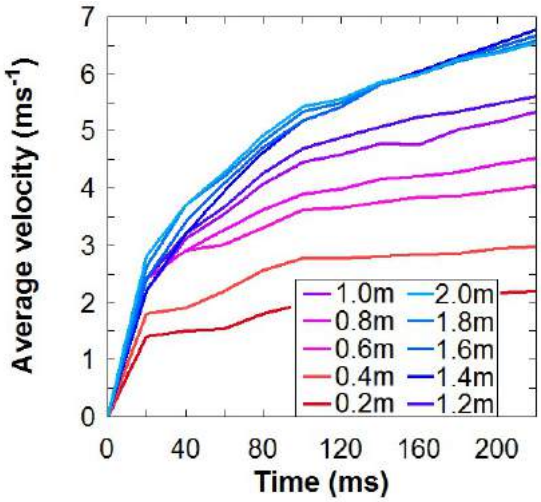

(c) Average velocity

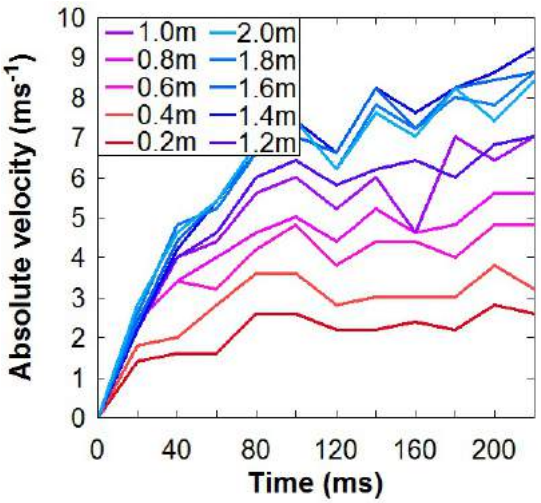

(d) Absolute velocity

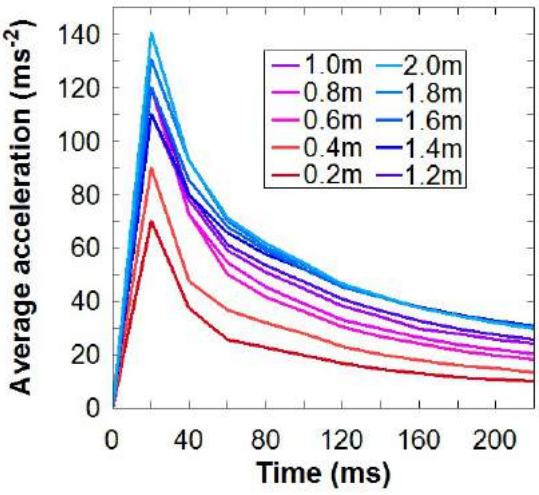

(e) Average acceleration

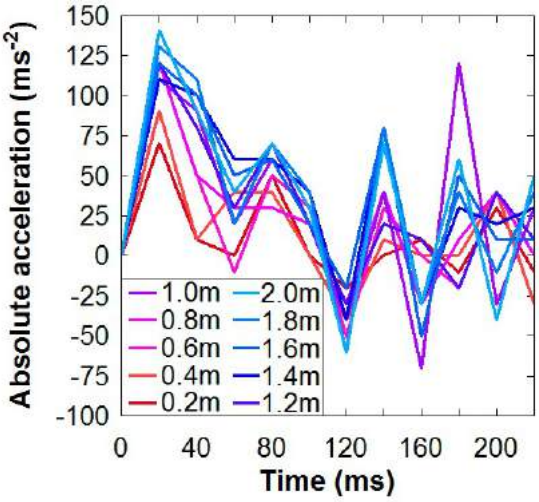

(f) Absolute acceleration

Figure 4.72: BWL3B displacement, velocity and acceleration time plots relative to the verical height within the structure

acceleration, displayed in Figure 4.72f, as the fluctuations are increased by a factor of 20, based on the 20ms time intervals. Unlike the average velocity, the average acceleration, displayed in Figure 4.72e, does not represent the actual accelerations of each fragment, as it always shows positive acceleration. Whilst the shape of the curve is representative of actual acceleration, it should be noted that beyond approximately 100ms, the fragments began to decelerate.

The longitudinal debris distribution of BWL3B, displayed in Figure 4.73a, shows three distinctive peaks at x=1m, x=4m and x=7m of masses 94.5kg, 59.7kg and 92.2kg respectively. The first peak corresponds to the lower fragment, which tilted about its base with a relatively low translational velocity, which is confirmed by the longitudinal distribution indicating initial vertical fragment position, displayed in Figure 4.73c.

The peak at x=4m was composed of debris originating from approximately 0.7m above the base of the structure, corresponding to another large fragment. The final peak at 7m however, results from a collision of the debris with the lighting array. The longitudinal distribution shows that a higher percentage of this debris originated from the left, green panel, which was directly upstream from the lighting array. Overall distribution shows an expected increase in longitudinal displacement for fragments originating from higher vertical positions.

Between 10m$< x <$14.5m, the distribution was populated almost entirely by red bricks originating from the top section of the structure. The maximum distribution of x=14.5m was limited by collision with the debris and the RWE at the rear end of the ABT. In the absence of this obstruction, the maximum distribution is expected to have increased by between 2-5m. The overall lateral debris distribution, displayed in Figure 4.73b is roughly symmetrical about y=0; however the distribution is limited in the positive y direction by the side wall of the ABT, located at y=2m.

The distribution of the individual panels are also relatively symmetric about their individual central axes; the slightly higher peak distribution of the left, green panel was also due to the collision with the lighting array. The lateral distribution indicating original vertical position, displayed in Figure 4.73d, shows fragments from higher original positions

to have a slightly increased lateral displacement, due to the increasing fragment separation with longitudinal displacement and the correlation between longitudinal displacement and original vertical position. The lateral distribution of fragments from the uppermost section of the right, red panel was larger due to their unrestricted flight path, as opposed to the uppermost fragments from the left, green panel colliding with the lighting array and being constrained primarily within the region -1m< y <0m.

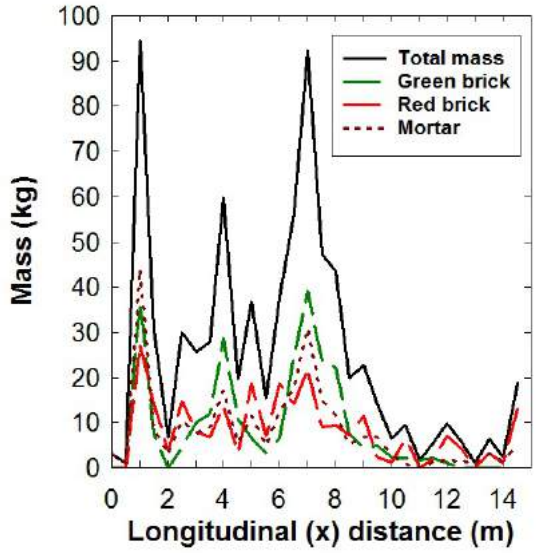

(a) Longitudinal distribution

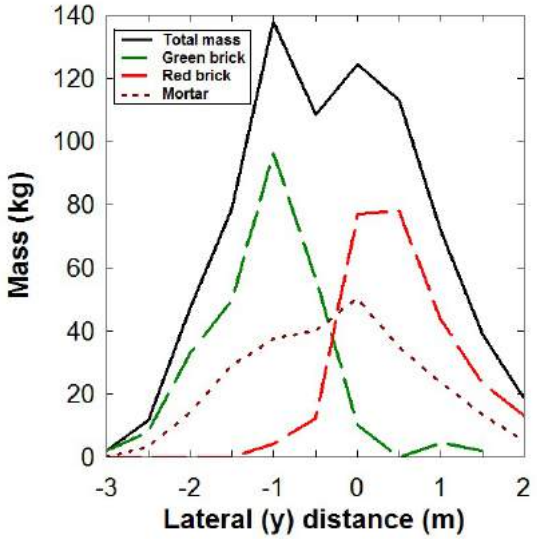

(b) Lateral distribution

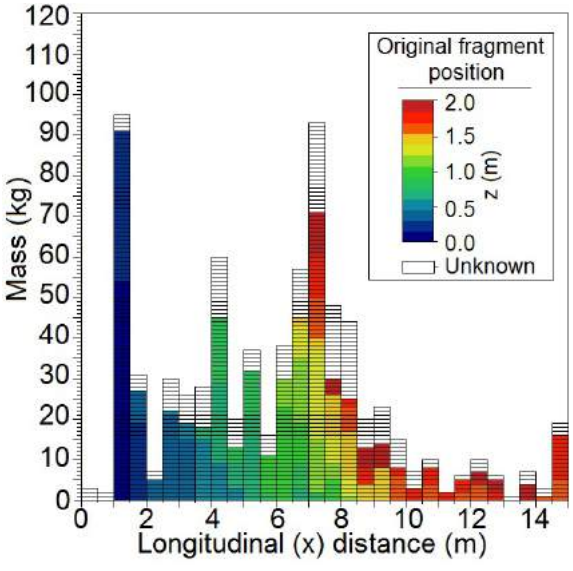

(c) Longitudinal distribution indicating original z position of fragments

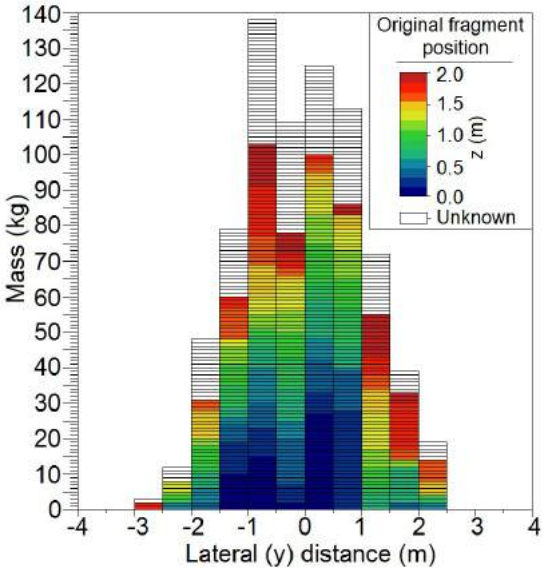

(d) Lateral distribution indicating original z position of fragments

Figure 4.73: Longitudinal and lateral debris distribution plots of structure BWL3B

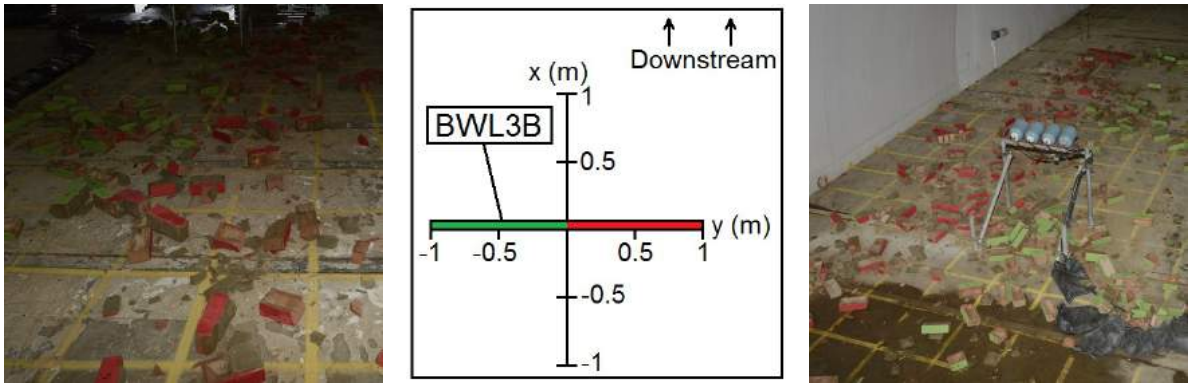

(a) Postshot photograph (perspective: upstream)

(b) Positional information

(c) Postshot photograph (perspective: downstream)

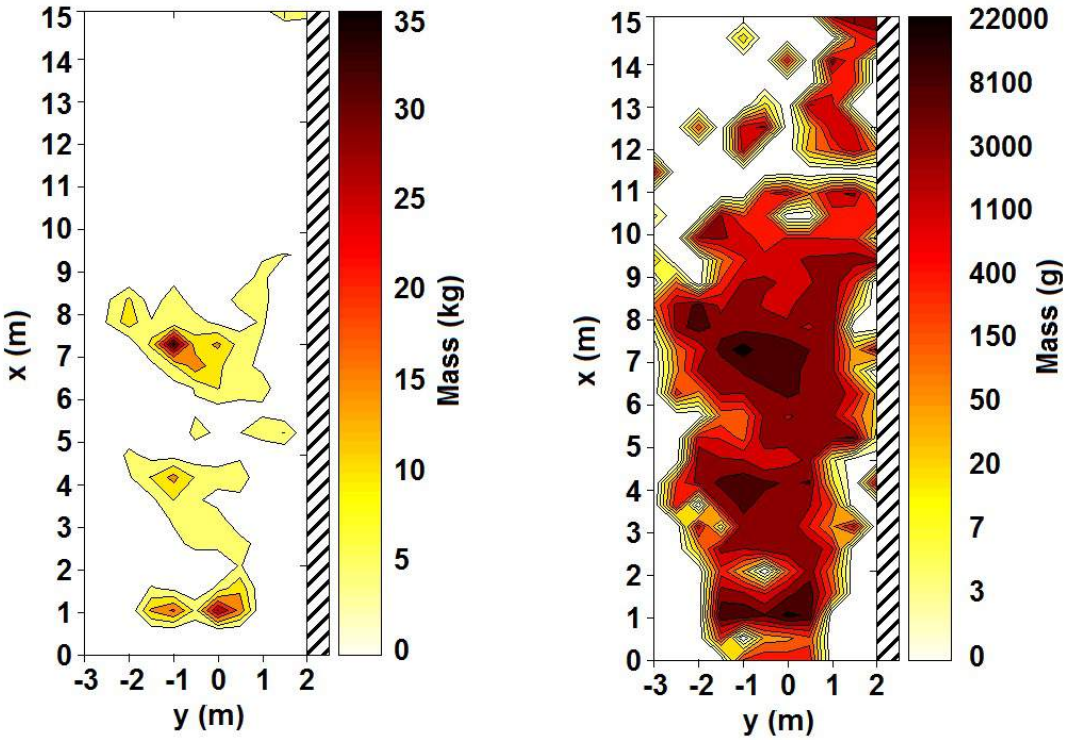

(d) (x, y) mass distribution (absolute)

(e) (x, y) mass distribution (logarithmic)

Figure 4.74: Debris mass distribution of structure BWL3B

The three largest fragments, with masses of 27.4kg, 17.8kg and 14.7kg were all located in the x=1m bin, originating from the lowest initial fragment, from the centre, outer right (red) and outer left (green) sides respectively and were responsible for the high density region located between 1m< x <1.5m and -1.5m< y <1m, displayed in the absolute x,y mass distribution in Figure 4.74d.

Fragments originating from higher vertical positions within the structure impacted the ground with increased energy, causing additional fragmentation and resulting in a large

number of smaller fragments, illustrated by the post-shot photographs taken from the upstream and downstream perspectives, displayed in Figures 4.74a and 4.74a respectively. The x,y mass distribution, plotted on the logarithmic scale in Figure 4.74e, illustrates the area covered by the debris distribution, which was approximately 48m^2, obstructing a maximum rectangular area of 82.5m^2.

The final structure tested was the large enclosed structure BWL3C in the 10.2m section of the ABT, with maximum x,y dimensions of 3m×1.5m and a base panel geometry of $\mathbf{\frac{A}{2}BCD\frac{E}{2}}$. The breakage of structure BWL3C from the upstream, inside side-on and downstream perspectives are displayed in Figures 4.75, 4.76 and 4.77 respectively, at times 0ms, 20ms, 50ms, 10ms, 150ms and 200ms.

(a) 0ms (b) 20ms (c) 50ms

(d) 100ms (e) 150ms (f) 200ms

Figure 4.75: High speed photography (from the upstream perspective) of the breakage of structure BWL3C

At 20ms, vertical cracks began to form along both the front and rear faces of the structure along the corner joint, alongside a stepped crack from the base of the corner

joint on the front, upstream face to approximately 0.6m above the base of the structure and 1m from the corner joint. By 50ms, the vertical crack on the rear face of the structure widened, with noticeable brick separation across the entire height of the crack. The rear face began to arch inwards with no additional cracking; however, the front and side panels were subjected to extensive crack formation.

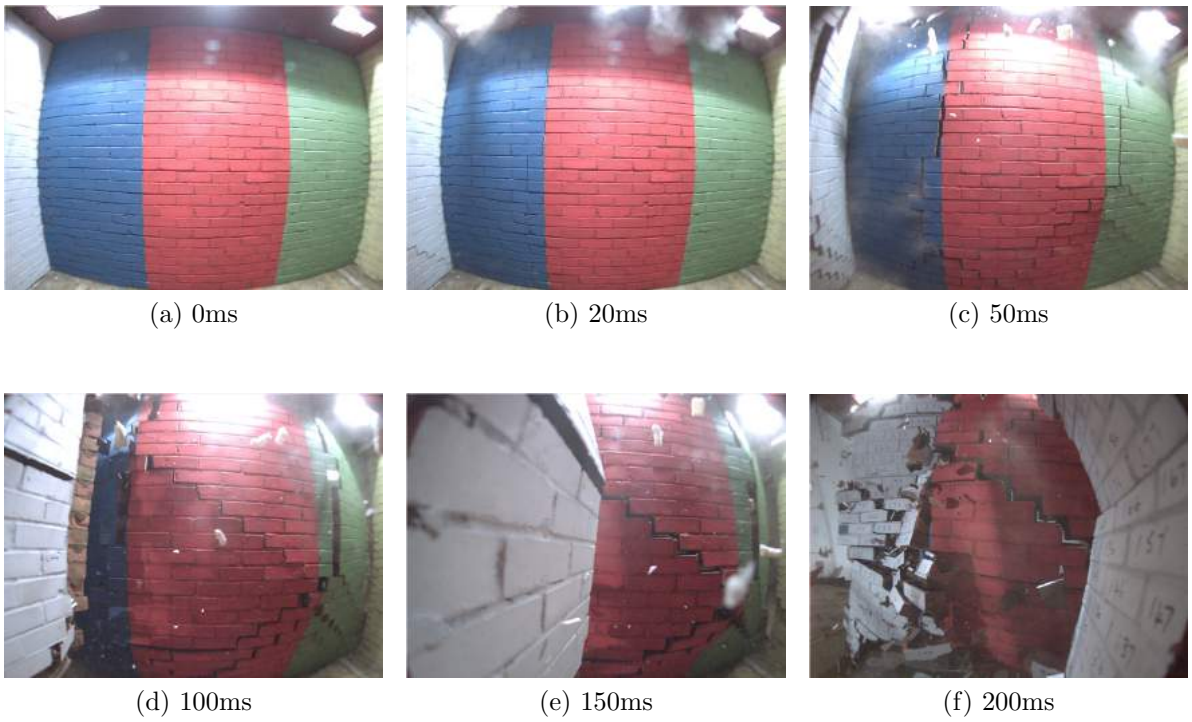

(a) 0ms (b) 20ms (c) 50ms

(d) 100ms (e) 150ms (f) 200ms

Figure 4.76: High speed photography (from the side perspective) of the breakage of structure BWL3C

The stepped crack along the front face of the structure propagated into two horizontal cracks at approximately 0.6m and 0.8m, running to the edge of the structure. A secondary horizontal crack formed from the top of the stepped crack, running to the top of the structure. Combined with the initial vertical crack along the corner joint, the cracking pattern on the front panels created three large initial fragments and one smaller fragment.

Similarly to both previous enclosed structures, the lower fragment began to tilt about its base, the upper, outer fragment began to translate in the downstream direction and the fragment originally connected to the corner joint began to rotate about the corner joint. Two vertical cracks formed from the top of the side panels at approximately 1m

from the front and rear faces, effectively separating the side wall into its individual 1m panels.

A series of stepped cracks formed along the base of the side wall, connecting the base of the corner joints to the vertical crack lines at approximately 0.3m above the base of the structure and 0.9m above the base of the structure for the upstream and downstream vertical cracks respectively. The side panels also began to display inwards arching, which was significantly more well defined by 100ms; the most upstream of the side panels however exhibited an additional inwards rotation about the corner joint.

(a) 0ms (b) 20ms (c) 50ms

(d) 100ms (e) 150ms (f) 200ms

Figure 4.77: High speed photography (from the downstream perspective) of the breakage of structure BWL3C

At 100ms, the original fragment trajectories across the front face of the structure remained unchanged; however extensive further crack formation and fragmentation occurred, resulting from the blast clearing of the fragments within the confined space through which it flowed. The rear panel began to rotate inwards about the corner joint,

which in combination with the inwards arching caused a series of stepped cracks to form from the top and bottom of the corner joint, running the width of the rear panel.

Between 100-200ms, the motion of the rear panel remained largely unchanged, with no additional fragmentation. The side panels continued to arch inwards, with the exception of the most upstream of the side panels, which in combination with its outwards rotation about the corner joint, began to collapse outwards. The lowest of the fragments from the front face collided with the ground, causing additional fragmentation, whilst the fragment originally connected to the corner joint begins to collide with bricks from the side panels, also causing additional fragmentation. The outermost panel continued to translate in the downstream direction towards the rear panel, unobstructed by other fragments, until colliding with the rear face at approximately 350ms.

By 200ms, the infill of the blast wave begins to act on the rear panel in the downstream direction, reversing its initial arching motion. Shortly thereafter, at 350ms, fragments from the front panel collide with the rear panel, causing the rotational motion about the rear corner joint to change direction. The impact also resulted in considerable fragmentation of the rear panel, causing the lower sections to collapse in the downstream direction, whilst the top section of the structure tilted inwards about the point of impact. By approximately 1,000ms, the middle side panel collided with the ground and the wall of the steel enclosure, whilst the most upstream of the side panels impacted the ground after collapsing outwards. Finally at approximately 1,500ms, the debris from the upper section of the rear panel impacted the ground.

Similarly to the previous large enclosed structures, the rear section of the structure became constrained between the roof of the steel enclosure and the ground, in this case, the most downstream of the side panels. The high density debris distribution in combination with the delicately balanced large rear fragment, made manual collection of the debris both impractical and unsafe.

Post-shot photographs of the debris distribution of structure BWL3C are displayed in Figure 4.78, including an approximated outline sketch of the debris field. Figure 4.78a shows a close-up photograph of the large constrained fragment, illustrating the two bricks

from the highest vertical position within the structure forced against the roof of the steel enclosure. Figure 4.78b, shows the debris field from the downstream perspective, indicating the longitudinal extents of the debris reaching slightly further than the rear of the steel enclosure at x=4m. The debris consisted of white bricks from the most upstream panel, covered by yellow bricks originating from the rear panel.

(a) Perspective (side, close-up)

(b) Perspective (downstream)

(c) Perspective (upstream), including outline sketch of debris

Figure 4.78: Post-shot photographs of the debris distribution of structure BWL3C

The downstream perspective, presented in Figure 4.78c, shows the blue bricks from the most upstream of the side walls created the majority of the lateral distribution. Within

the original extents of the structure, white bricks from the front panel covered the first third, followed by red bricks from the middle side panel covering the second third and white bricks from the front panel covered by yellow bricks from the rear panel occupying the final third. The outline sketch of the debris distribution, presented in Figure 4.78c, indicates an approximate area of 16.25m^2 was covered by the debris field, obstructing a maximum rectangular area of 20m^2.

4.4 Summary

The experimental results present data obtained from the blast pressure time histories, breakage patterns, fragment ballistics and debris dispertion. The pressure time histories showed reliable and consistent incident overpressure, dynamic pressure and reflected pressure recordings from both sections of the ABT. Some gauge faults lead to corrupt data; however enough data was recorded across all trials to ensure consistent blast parameters, to within $\pm 5\%$ of all parameters.

Analysis of the phantom footage showed velocity gradients develop over all structurs, with higher initial velocities in the upper section of the structures. The 4.9m section of the ABT showed peak fragment velocities between 20-25ms^{-1}, for **A** panels and 10-15ms^{-1} for **B** and **D** panels, whilst the 10.2m section of the ABT showed peak velocities of 10-15ms^{-1}. The breakage of **A** panels in the HE trials showed 1-2 horizontal breakage lines forming in each of the failure scenarios. The **A** panels in the ABT showed 3 horizontal breakage lines form at 55kPa; at 110kPa, breakage was initiated by 2-3 horizontal breakage lines but continued to develop into a more widespread network of cracks. The **B** panels in the ABT again showed breakage on the blast normal face, vertical cracking along the corner joint and inwards rotation of the side face. At 110kPa the initial fragmentation was more severe, but the overall breakage pattern was the same. Similar patterns were also observed in composite structures, with the individual structural components exhibiting behaviour representative of their corresponding base panels. The breakage patterns of the large enclosed structures also presented similarities, in terms of the cracking pattern along the front face of the structures, collapse of the side walls and vertical restriction of

the rear panel.

The debris distributions of structures in the 4.9m section of the ABT reached maximum throw distances of 40-50m, with clusters of debris forming around the instrumentation columns and as a result of larger fragments. The **B** and **D** panels presented high density distributions within the first 5m resulting for the collapse of the side panels. The corner panels, **B** and **AB**, in the 10.2m section also showed high density distributions resulting from the collapse of the side panels; however the high density region was constrained to the first 2m, due to the reduced impulse. The distribution of all blast normal panels in the 10.2m section of the ABT was relatively similar, again presenting high density regions due to impact with obstructions and large inital fragments.

Overall, the data obtained from the experimental trials offers results pertaining breakage patterns, initial fragmentation and debris distribution for a range of pressures, impulses and structural geometries.

Chapter 5

Computational Modelling

Computational modelling is a powerful tool which assists in both understanding and predicting structural behaviour. The ability to accurately model both blast structure interaction and structural response enables the experimental results to be extended, offering the potential to investigate the effects of a large number of parameters on both breakage and debris distribution.

With the key variable parameter in the experimental trials being structural geometry, a computational modelling routine benchmarked against experimental trials can be used to extend the results and investigate the response of a larger number of geometries. The computational modelling routine used for this research is divided into three stages; blast propagation, blast structure interaction and structural response. The first two stages are conducted using Computational Fluid Dynamics and the final stage is conducted using the Applied Element Method. This section details the initial development of the computational modelling routine, for all three of the aforementioned stages.

5.1 High Explosive Modelling

The computational modelling routine was initially benchmarked against the Windrush arena trials, as both the loading scenario and structural response mechanisms are much less extreme than in the long duration case.

5.1.1 Computational Fluid Dynamics

The blast propagation and structural interactions were assessed using the CFD solver Air3D [20]. Various factors can affect the accuracy of a CFD model, including the blast input parameters, assessment domain and mesh cell size. For conventional HE blast loads, the stand-off distance of the structure is small compared with long duration blast loads, meaning the domain through which the blast wave propagates is relatively small. Within a smaller domain, the problem cell size can be reduced without increasing the problem size and computational requirements.

The highest resolution results which can be produced from a CFD model are static pressure time histories from a 1D model with a high cell density. Figure 5.1 shows the pressure time histories of a 1D Air3D model of the Windrush arena trials, that is a 41kg TNT equivalent detonation with monitoring points at the relevant distances, compared with the experimental gauge data, specifically radial p_i1 from trial WR1; the target pressures from the Windrush trials, the peak recorded pressures and the peak pressures of the CFD model are displayed in Table 5.1 and also shows the percentage differences between the respective values.

The CFD curves in Figure 5.1 were all translated in the x direction such that the arrival times of each CFD curve matched the equivalent experimental curve, allowing for simpler comparisons to be made. Arrival time is automatically set to 0ms for all loads during the structural response modelling; hence this simple translation does not affect the results. The static pressure histories of each of the CFD curves shows very good agreement with the experimental results in the positive phase. The shape of the CFD curves show good agreement with the experimental curves, with the waveform decay constants matching both the peak overpressure and positive phase durations.

The peak pressures, displayed in Table 5.1, show the values calculated by the CFD model to be between $7.9 - 18.7\%$ above the values recorded by the trial and between $11.9 - 16.9\%$ above the predicted target values. After the positive phase, the CFD models consistently show the second shock arriving later than the experimental results; however as neither the second shock or negative phase are relevant for the purposes of this research, only the accuracy of the positive phase is taken into account.

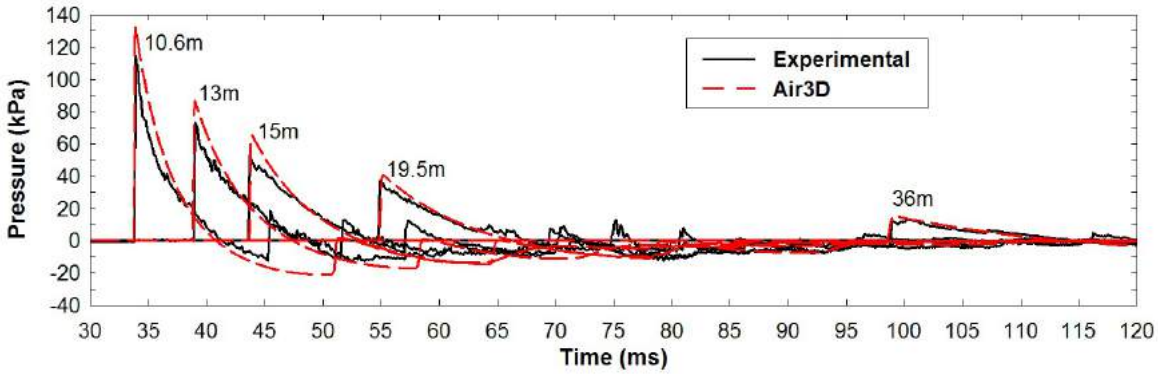

Figure 5.1: 1D Air3D static pressure compared to recorded values from the HE Windrush arena trials

Table 5.1: 1D Air3D peak overpressure predictions of the Windrush HE trials

$p_i(max)$ (kPa)			Differences ($\times 100\%$)			
Target (a)	Trial (b)	Air3D (c)	$\left(\frac{b}{a}-1\right)$	$\left(\frac{c}{a}-1\right)$	$\left(\frac{c}{a}-\frac{b}{a}\right)$	$\left(\frac{c}{b}-1\right)$
110	115.1	132.4	+4.4	+16.9	+12.5	+13.1
72	73.1	86.5	+1.5	+16.8	+15.3	+15.5
55	53.2	65.4	−3.4	+15.9	+19.3	+18.7
35	37.4	40.6	+6.4	+13.8	+7.4	+7.9
14	13.6	15.9	−2.9	+11.9	+14.8	+14.5

The cumulative impulse time histories for both the 1D Air3D model and the experimental gauge data from the Windrush arena trials are displayed in Figure 5.2; the peak predicted impulse, experimentally measured impulse and CFD calculated impulses are highlighted in Table 5.1 which also displays the percentage differences between the respective values. The impulse calculated through CFD was much closer to the predicted or target impulse with values between $1.5 - 4.3\%$ above the target impulse; compared

to the recorded values however, the CFD results were between 16.1% below and 21.6% above the experimental results.

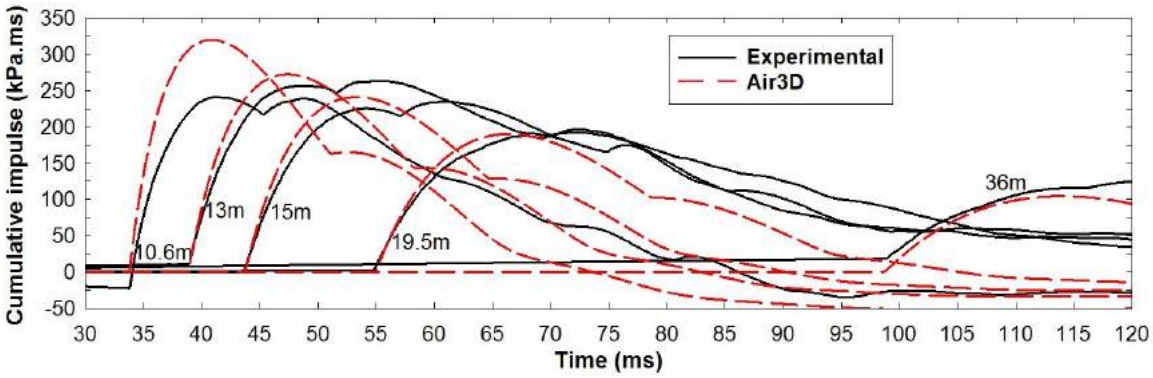

Figure 5.2: 1D Air3D static impulses compared to recorded values from the HE Windrush arena trials

Table 5.2: 1D Air3D static impulse predictions of the Windrush HE trials

$I_i(max)$ (kPa.ms)			Differences (×100%)			
Target (a)	Trial (b)	Air3D (c)	$\left(\frac{b}{a}-1\right)$	$\left(\frac{c}{a}-1\right)$	$\left(\frac{c}{a}-\frac{b}{a}\right)$	$\left(\frac{c}{b}-1\right)$
313	263.1	319.8	−15.9	+2.2	+18.1	+21.6
262	240.8	272.2	−8.1	+3.9	+12.0	+13.0
231	234.4	240.9	+1.5	+4.3	+2.8	+2.8
183	191.9	189.8	+4.7	+3.7	−1.1	−1.1
103	124.6	104.5	+21	+1.5	−19.5	−16.1

Whilst the difference in impulse between the experimental and CFD results is, in some cases almost 20%, the CFD curves were always within ±10% of the experimental curves with a closely matching waveform decay; furthermore, the peak impulse of the CFD curves closely matched the predicted values, suggesting additional trials would have shown a variety of curves all within a small range of the CFD results. As experimental blast results will never be identical, the CFD curves offer an acceptable degree of accuracy for the computational modelling.

With confidence in the static pressures, the CFD models can be expanded to investigate the reflected pressure across the surfaces of the structure. With the number of monitoring points in a CFD simulation limited only by the cell size, the reflected

pressure across the entire surface of a structure can be monitored. A model of the first structure in the HE trials, WR1A, was developed using the same input to create the previously discussed 1D curves. The model was developed to propagate the 1D blast wave to 10.5m at which point the blast was remapped into a 3D domain with extents 6m$< x <$15m, 0m$< y <$9m, 0m$< z <$4m giving the domain x,y,z dimensions 9m×9m×4m. The structure replicating WR1A was placed between 10.6m$< x <$10.72m, 4m$< y <$5m, 0m$< z <$2m, approximately in the centre of the 3D domain.

Sensitivity studies had shown 0.04m to be an ideal cell size for modelling the Windrush arena trials, in terms of precision and computational intensity. As a result, the x dimensions of the structure replicating WR1A within the CFD model were 0.12m, corresponding to three cells, compared to its actual x dimensions of 0.1m. The domain itself was defined such that the position of the structure, that is beginning on x=10.6m and z=0m and centred in the y direction would correspond to cell boundaries in all directions, thus avoiding overlap of any cells. The model was gauged using a total of 650 monitoring points spread evenly across the structure with 325 points on each face. A WRL rendering of the CFD model of WR1A is displayed in Figure 5.3, in which the red sphere represents the 41kg charge and the yellow cubes represent the cells occupied by monitoring points.

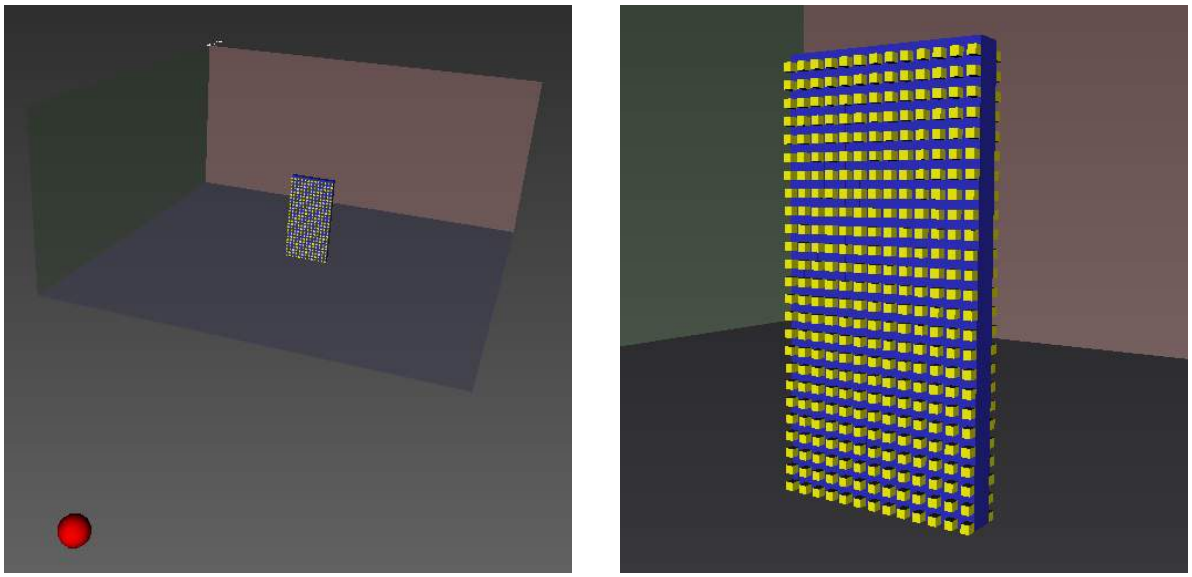

(a) Overview (b) Structure close-up

Figure 5.3: WRL image of an Air3D model of structure WR1A

As well as providing data pertaining to the loading of the structure from the blast, Air3D also illustrates the blast propagation by rending pressure regions on a specific colour scale for a given plane. The ability to visually inspect the propagation of the blast and its interaction with the structure provided additional insight into the time dependent loading of the structure, aiding the understanding of its response.

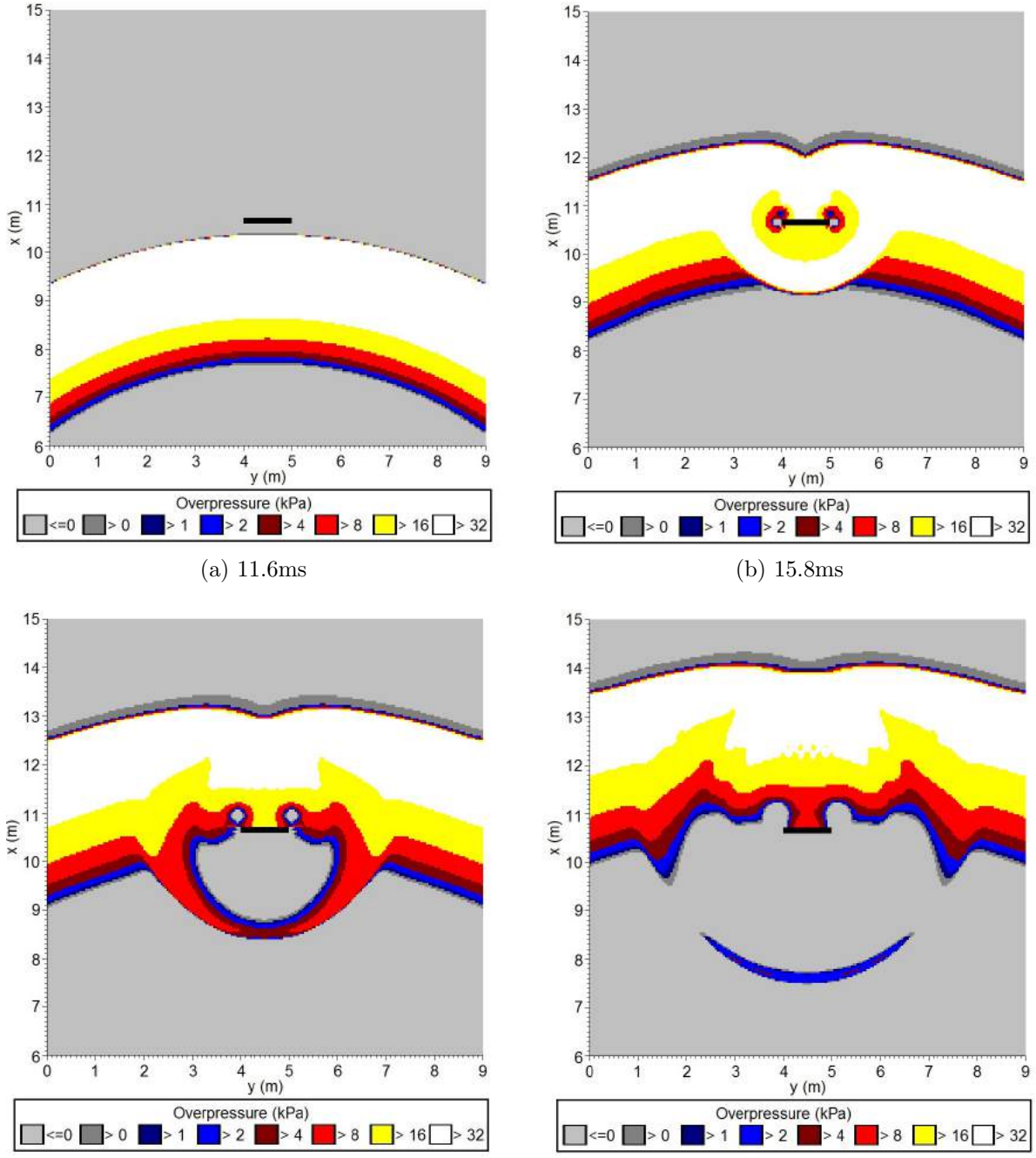

(a) 11.6ms

(b) 15.8ms

(c) 17.9ms

(d) 20.0ms

Figure 5.4: Propagation of blast wave and blast structure interaction of Air3D model of structure WR1A

Figure 5.4 shows images from the x,y plane at z=0.01m at key stages throughout the propagation of the blast. Figure 5.4a shows the ideal blast wave at 11.6ms, shortly before interacting with the structure, illustrating the curvature of the blast wave as well as the wavelength of the positive phase, approximately 3.2m. By 15.8ms, Figure 5.4b shows the structure located in the centre of the positive phase of the blast, approximately 1.5m behind the shock front.

The pressure contours also highlight the clearing of the blast wave around the structure, at 15.8ms the pressure on the rear face of the structure was higher than the front face, which the pressure contours show to be between 16-32kPa. At the sides of the structure small vortices were observed, forming as the high pressure shock front cleared the structure, filling the low pressure region at its rear. Clear reflections were observed off of the front face of the structure, propagating radial outwards in the upstream direction, with pressures higher than on the front face of the structure itself.

By 17.9ms, displayed in Figure 5.4c, the pressure across the front face of the structure had dropped below 0kPa with the reflection continuing to propagate in the upstream direction. Vortex circulation around the edges of the structure continued to force more of the blast into the centre of the rear face of the structure, resulting in higher loading, the vortices themselves propagate in the downstream direction, further decreasing the load to the rear edges of the structure. Finally by 20ms, Figure 5.4d, the blast had almost completely cleared the rear face of the structure, with the pressure dropping below 8kPa. The vortices expanded further outwards and continued to propagate in the downstream direction; however with observably lower velocities than the shock front itself, causing the vortices to fall behind the blast wave.

Using the pressure time histories from each of the monitoring points, peak pressures and impulses were acquired across the surface of the structure and plotted to interpret the application of load across the structure. Within Air3D, structures are infinitely rigid and remain fixed in place throughout the duration of the simulation. As the experimental results have shown the structures were not infinitely rigid, forming multiple crack lines and collapsing to produce debris fields, this assumption would not necessarily provide

reliable results.

As discussed in Chapter 4, the high speed video of structure WR1A (and all other structures tested in both Windrush trials) shows cracks forming approximately 5ms after the arrival of the blast; however, there is little to no observable displacement of the structure within the first 50ms of blast propagation. Furthermore, the side-on view of structure WR1A at 100ms, displayed in Figure 4.16b, shows only slight displacement of the structure about two horizontal crack lines. As the positive phase duration as predicted by the CFD models and the experimental gauge data is less than 10ms, the structures can be considered to remain fixed in place for the duration of the blast, at least in the shorter duration HE scenarios. Whilst this does not assume the structure to be infinitely rigid, the shape of the structure remains unchanged during its interaction with the blast wave, meaning the reflected pressures obtained through the CFD models can be interpreted as the load applied to the structure.

The peak reflected pressures from each monitoring point placed across the surface of the structure were plotted onto 2D surfaces using contours to represent the pressure regions across both the front and rear faces of the structure and are presented in Figures 5.5a and 5.5b respectively; the net reflected pressure, displayed in Figure 5.5c, is calculated by subtracting the maximum reflected pressure on the rear of the structure from the maximum reflected pressure on the front of the structure for each y,z position. As expected, the reflected pressure on the front face of the structure was relatively consistent at all points. The pressure at the outer extents of the structure was slightly lower due to blast clearing, the pressure was therefore highest in the centre of the structure at its base; furthermore, this pressure difference was amplified due to the slight curvature of the blast wave. The structure does not fall entirely within the Mach stem, thus the blast wave was not planar and the peak pressure at the base of the blast wave was higher.

As previously discussed, the formation of vortices around the edges of the structure caused additional loading to the centre of the rear face, leading to higher reflected pressures. Although not directly observable from Figure 5.4, which illustrates propagation through the x,y plane, clearing of the blast over the top of the structure reduced the load-

ing to the upper edges of the rear face. As the blast could not clear under the structure, the lower sections of the rear face received less loading than the upper sections. These blast clearing mechanisms resulted in the higher pressure region on the upper centre of the rear face of the structure, displayed in Figure 5.5b. Combining these two loading regions provides the net load displayed in Figure 5.5c, showing a resulting lower pressure region in the upper central section of the structure and around its edges. The loading of the centre of the rear face of the structure reduced the net load to vertical bands of high pressure near the base of the structure.

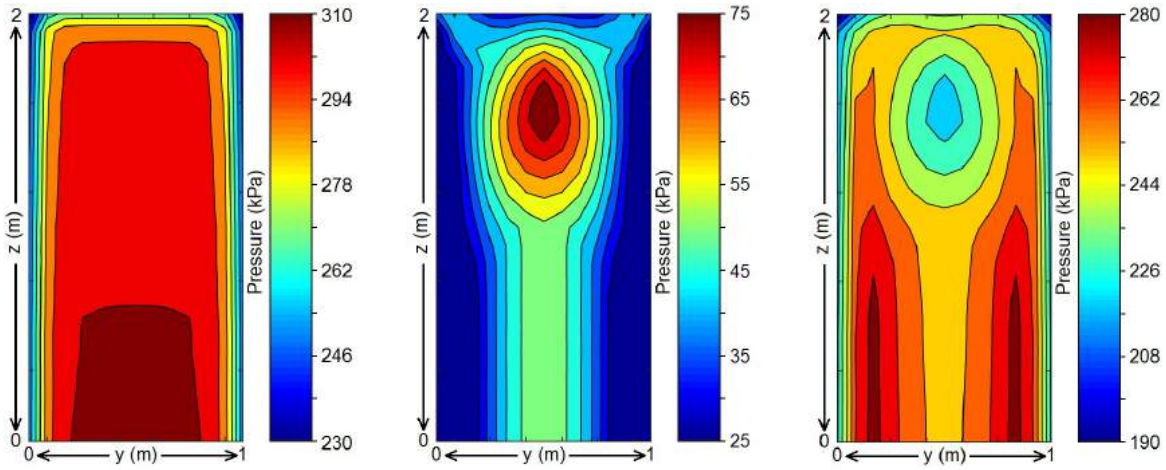

(a) Front (b) Rear (c) Net

Figure 5.5: Air3D model of structure WR1A: Maximum reflected pressure regions

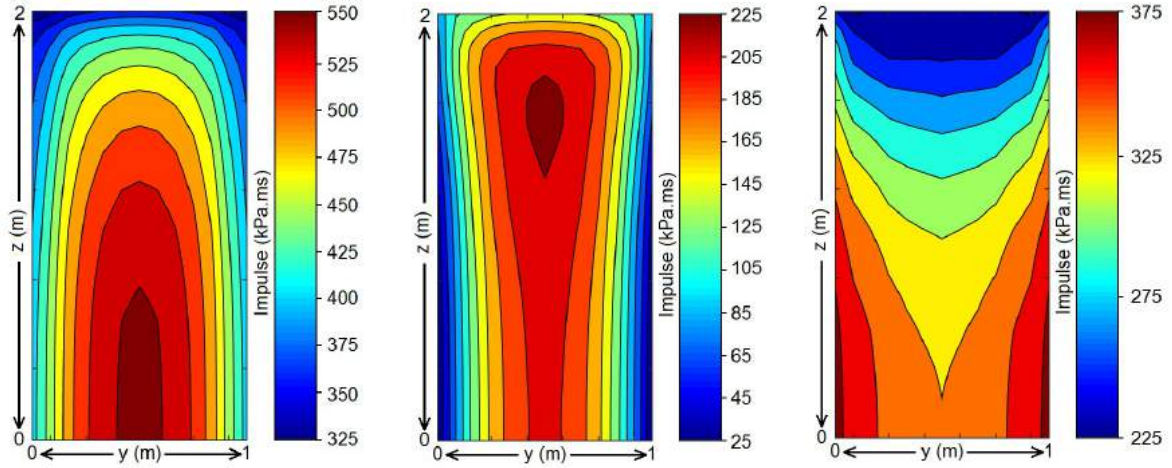

(a) Front (b) Rear (c) Net

Figure 5.6: Air3D model of structure WR1A: Maximum reflected impulse regions

Investigating the reflected pressure across the face of the structure does not illustrate the loading contours of the structure over the entire duration of the blast. The total recorded impulse for each monitoring point from the front and rear faces of the structure are plotted onto a 2D surface in Figures 5.6a and 5.6b respectively, with Figure 5.6c displaying the effective net impulse, calculated by subtracting the total impulse transmitted to the rear of the structure from the total transmitted impulse to the front face of the structure. The impulse transmitted to the front face of the structure shows a similar pattern to the maximum pressure with the highest impulse at the centre of the base of the structure, decreasing radially outwards; however the gradient of impulse was much larger than that of the reflected pressure across the front face of the structure.

The impulse contours across the rear face also show a similar pattern to the pressure regions, with much higher impulses along the central vertical axis, particularly towards the top of the structure, resulting from the vortex formation and blast clearing. Whilst the patterns of pressure and impulse on the front and rear faces are similar, the contours of net transmitted impulse and net applied pressure bare little resemblance. The ratio of values for almost every pair of monitoring points, front and rear, was much higher for the pressure than for the impulse; i.e. the impulse at any point on the rear of the structure was a higher percentage of the impulse at the front of the structure, thus having a larger effect on the effective net impulse.

Similar CFD models were developed for each of the structures in the Windrush arena series. Whilst the composition of the structure remained the same, the domain size was increased slightly for structures WR1D and WR1E to accommodate the larger blast wavelength. Inspecting the net reflected pressure and net reflected impulse contours from each of these models show a slight shift in the loading regions with the expected change in magnitude of the loading. Figure 5.7 illustrates the net reflected pressures for structures WR1B, WR1C, WR1D and WR1E, plotted over a 2D surface.

Besides the drop in maximum and minimum pressures plotted, the contours themselves also change slightly as the radial distance of the target increases. As blast waves propagates, the wavelength and hence positive phase increases, which effects both the

vortex production and clearing mechanism. Inspection of the net reflected pressure loading of structures WR1(A-E) shows both the lower pressure region in the centre of the upper section and the higher pressure regions towards the base move further towards the base. The blast wave also loses velocity as it propagates, reducing the clearing effect of the vortices, increasing the load on the rear face and effectively translating the loading regions towards the base.

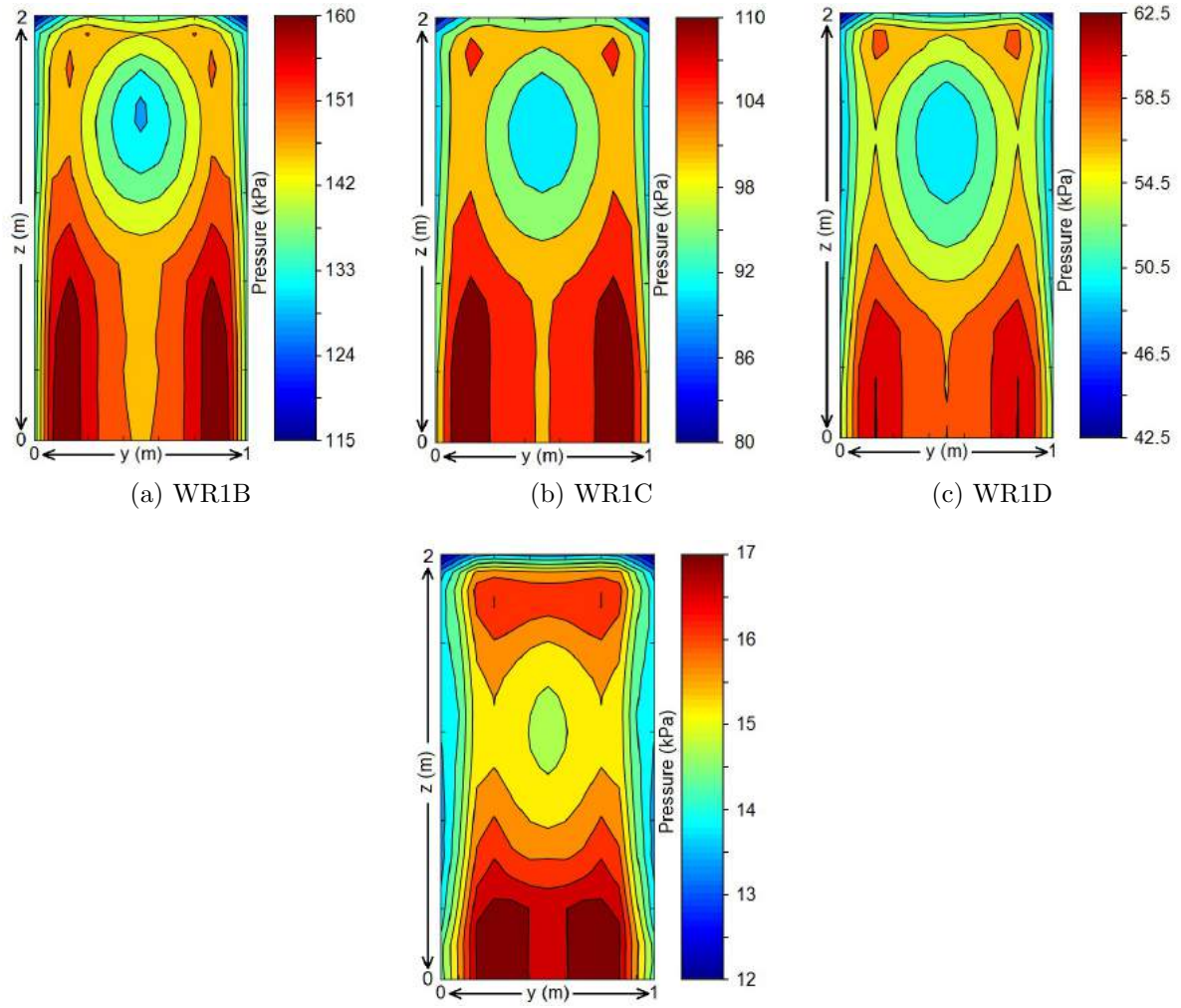

(a) WR1B (b) WR1C (c) WR1D

(d) WR1E

Figure 5.7: Air3D model of structures WR1(B-E): Maximum reflected pressure regions

The net reflected impulse measured across the surface of structures WR1B, WR1C, WR1D and WR1E were plotted over 2D surfaces and are displayed in Figure 5.8. Similarly to the net reflected pressure, the magnitude of the impulse decreases with radial distance as expected, but also the impulsive contours translate towards the base of the

structure. For each model, the highest net impulses were recorded at the edges of the structure near the base, due to the clearing effects of the blast. As the radial distance increased, a larger proportion of the rear face was loaded; however, the lower, outer edges of the structure received little impulse.

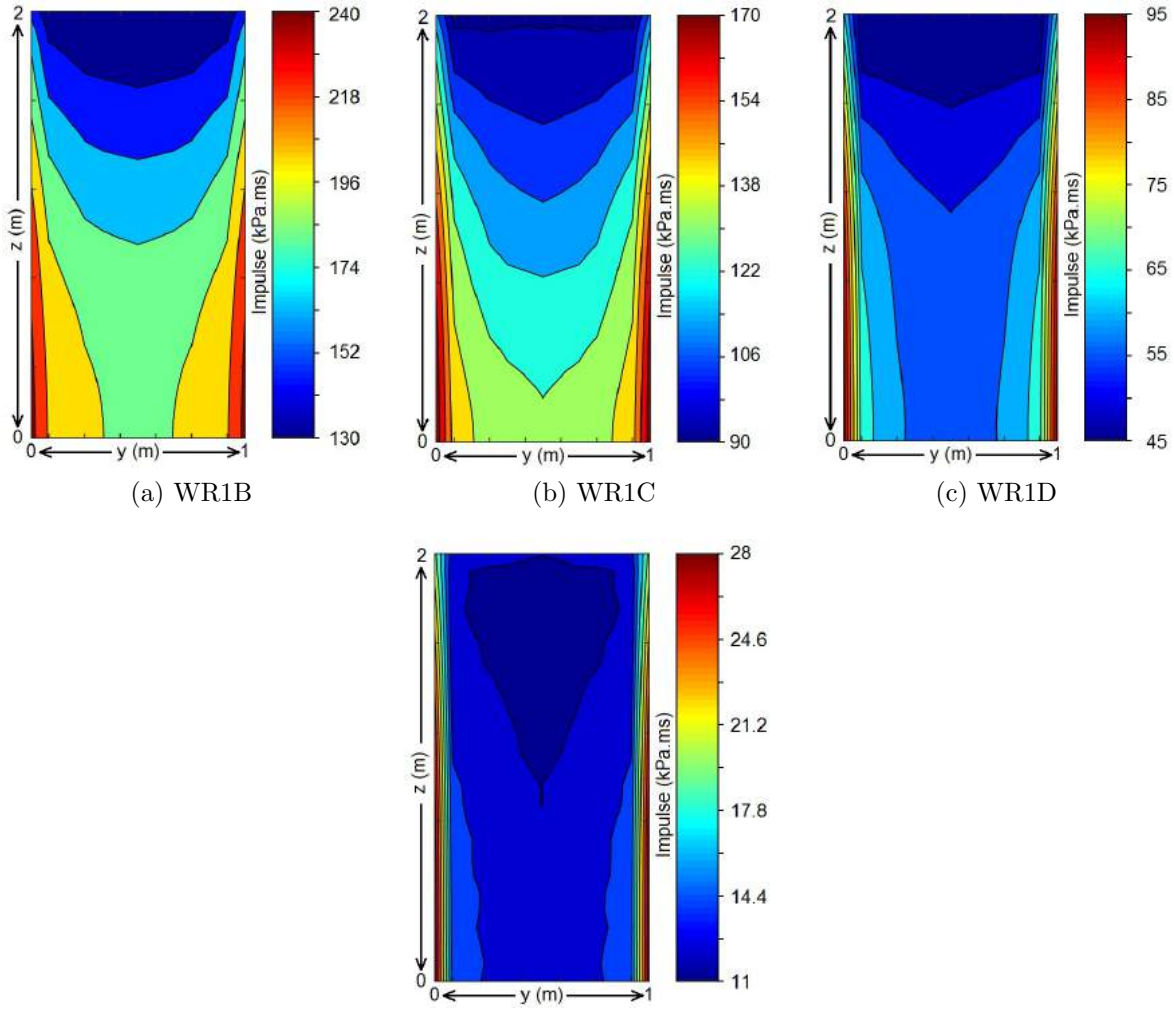

(a) WR1B (b) WR1C (c) WR1D

(d) WR1E

Figure 5.8: Air3D model of structures WR1(B-E): Maximum reflected impulse regions

Using the same methods employed to model the **A** panels of the first Windrush arena trial, the **B** and **D** panels of the second Windrush arena were modelled in Air3D to assess the interaction blast structure interactions and interpret the loading mechanisms. The same explosive charge composition was used for both of the Windrush arena trials and the second trial instrumented only three of the five radial distances used in the first trial, 10.6m, 13m and 15m. Structure WR2A, a **B** panel at the 10.6m radial, was modelled

in Air3D using the same 1D and 3D domains as structure WR1A, also at the 10.6m radial. The 1D blast was propagated to 10.5m at which point it was remapped into the 3D domain with extents 6m< x <15m, 0m< y <9m, 0m< z <4m resulting in x,y,z dimensions of 9m×9m×4m with a cell size of 0.04m and a total of 5.06×10^6 cells. The surface of the structure was covered in a total of 1200 monitoring points, 325 located on each of the outer faces and 275 on each of the inner faces. Figure 5.9 shows a WRL rendering of the CFD model in which the red sphere represents the charge location, the solid blue represents the structure and the yellow cubes represent the monitoring points.

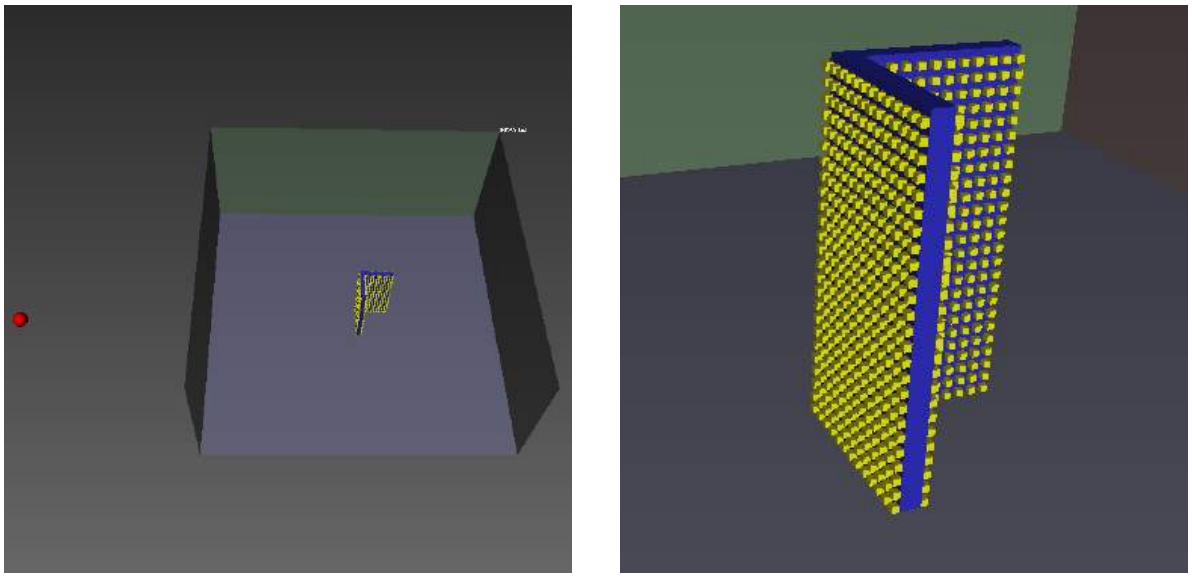

(a) Overview (b) Structure close-up

Figure 5.9: WRL image of an Air3D model of structure WR2A

Figure 5.10 illustrates the interaction of the blast with structure WR2A within the CFD model. Unlike the **A** panels from trial WR1A, the **B** panel is not symmetrical and presents a more complex interaction with the blast wave. At 15.0ms, displayed in Figure 5.10b, the blast was in the process of clearing the exposed side of the structure producing a vortex on the edge of the structure, which would be initially identical to those produced by structure WR1A. On the opposing side of the structure, the blast propagated along the side wall applying an inward force. The blast wave loaded the front face in the downstream direction and was reflected in the upstream direction, whilst the wrap around pressure loaded the rear face of the structure in the upstream direction,

although with a much lower pressure.

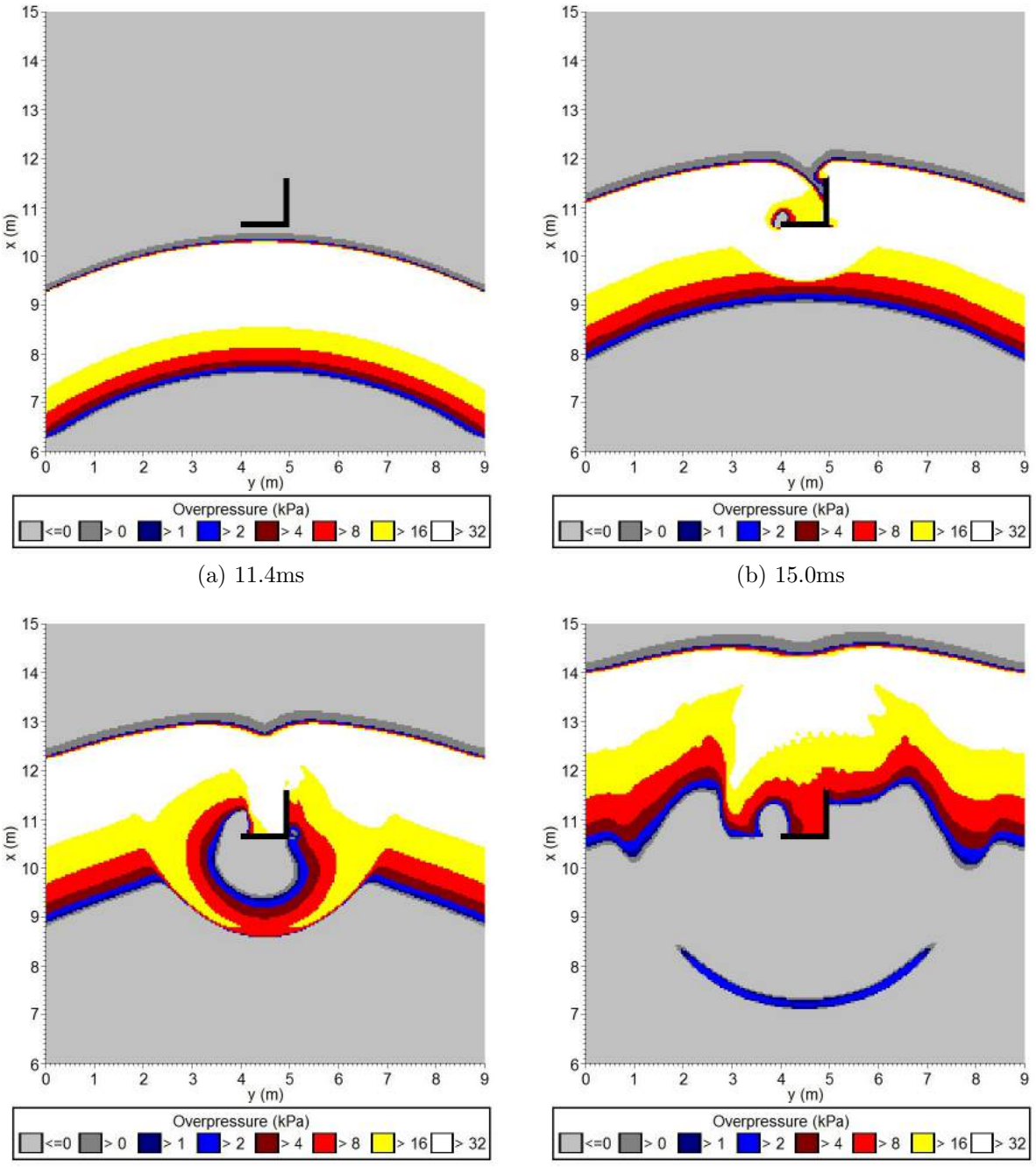

(a) 11.4ms (b) 15.0ms

(c) 17.3ms (d) 21.1ms

Figure 5.10: Propagation of blast wave and blast structure interaction of Air3D model of structure WR2A

The wrap around pressure on the inside of the structure began to reflect between the inner faces of the front and side panels, visible in Figure 5.10c which displays the propagation at 17.3ms. The pressure on the inside of the structure was clearly higher

than the front face of the front panel, which at this time was in the negative phase and on the outer face of the side panel. The reflections from the outer face of the front, blast normal panel continued to propagate in the upstream direction. At 21.1ms, shown in Figure 5.10d, the blast wave had almost entirely cleared the structure; however the reflections between both panels on the interior of the structure persisted for an additional 2ms.

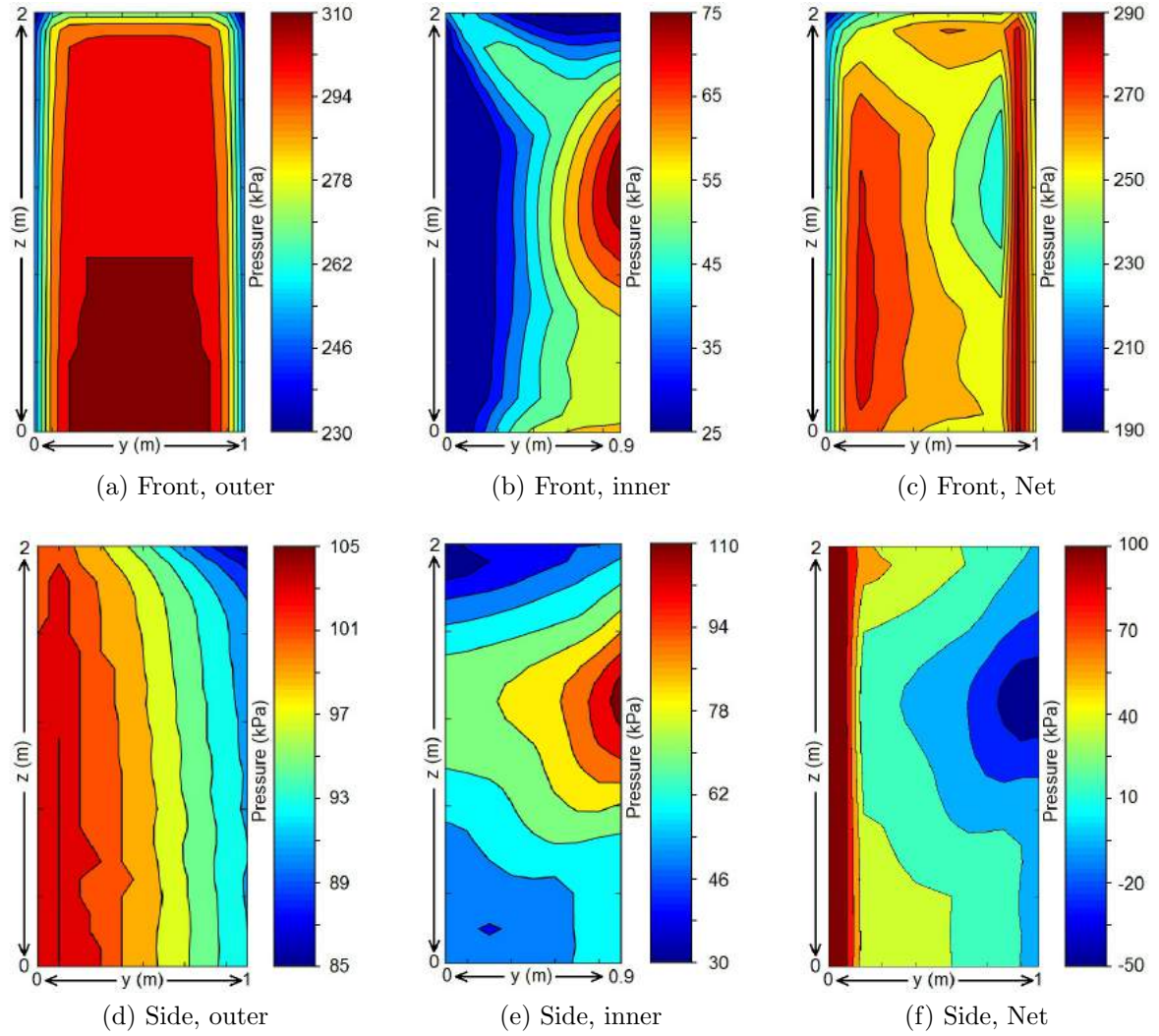

(a) Front, outer (b) Front, inner (c) Front, Net

(d) Side, outer (e) Side, inner (f) Side, Net

Figure 5.11: Air3D model of structure WR2A: Maximum reflected pressure regions

The peak pressures from each monitoring point were plotted over two 2D surface, corresponding to their respective positions on the front and side faces of the structure, displayed in Figure 5.11. The pressure on the upstream face of the front panel, displayed in Figure 5.11a, showed similar contours to the **A** panels from the first Windrush arena

trial, with higher pressure recorded in the centre of the panel towards the base. The pressure decreased towards the edges due to the clearing of the blast. The peak pressures recorded on the downstream face of the front panel, displayed in Figure 5.11b show the highest pressures recorded at approximately half height towards the side panel. The resulting net pressure, calculated by subtracting the pressure on the downstream face from the upstream face of the front panel is displayed in Figure 5.11c.

The downstream face of the front panel was monitored by 275 gauges, whilst the upstream face was monitored by 325 gauges due to the larger surface area of the upstream face. As a result, the net pressure was highest in front of the side wall where the pressure on the downstream face of the structure was effectively zero. The higher pressure region on the downstream face of the front panel results in the low pressure region in the net load. The pressure on the outer face of the side panel, displayed in Figure 5.11d shows the expected decrease of peak pressure in the downstream direction. The loading on the interior side wall, displayed in Figure 5.11e, shows the highest pressure region was located at approximately half height at the most downstream position. The resulting net load, Figure 5.11f, again shows the highest pressure corresponding to the position of the front, blast normal panel. The lowest loading region shows pressures of -50kPa, meaning the net pressure acted outwards as a result of the blast reflections on the interior face of the structure.

The maximum cumulative impulse, calculated by integrating the pressure time histories, from each monitoring point, were plotted across two 2D surfaces representing the front and side panels of the structure, similarly to the pressure and are illustrated in Figure 5.12. The impulse contours across the most upstream face of the blast normal panel, Figure 5.12a, were similar to the pressure contours, with the highest transferred impulses recorded in the centre of the structure towards the base; however the gradient of maximum impulse between the centre of the structure and its edges was much smoother than the peak pressures.

The loading of the interior, downstream face of the blast normal panel, displayed in Figure 5.12b, again shows the loading to increase towards the side panel and the base

of the structure, with the lowest regions located around the edges. The resulting net impulsive loading regions, presented in Figure 5.12c, show the expected peak region to correspond to the position of the side panel, with a relatively low net load across the face of the structure, increasing towards the base of the outer edge. The impulse on the outer face of the side panel, illustrated in Figure 5.12d, shows an inverse pattern to the peak pressure regions, with higher impulses recorded further downstream. This was due to the vortices forming around the edge of the blast normal face, reducing the pressure applied to the upstream sections of the side panel.

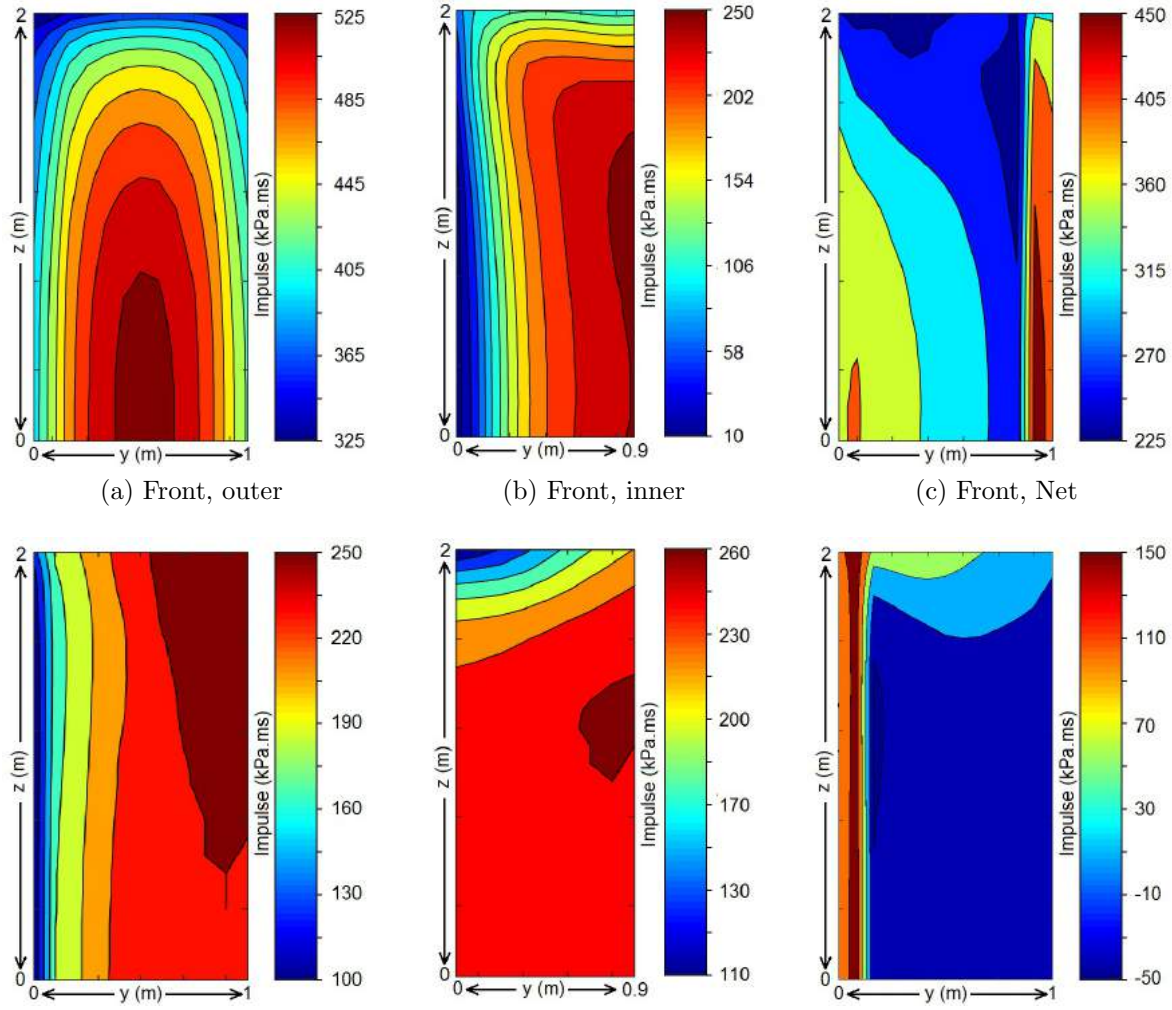

(a) Front, outer (b) Front, inner (c) Front, Net

(d) Side, outer (e) Side, inner (f) Side, Net

Figure 5.12: Air3D model of structure WR2A: Maximum reflected impulse regions

The maximum impulsive regions on the interior of the side panel, displayed in Figure 5.12e, showed a relatively even distribution of load, although slightly lower towards

the top of the structure. The resulting net impulsive loading region, displayed in Figure 5.12f, shows the highest inwards load to correspond with the position of the blast normal panel. The loading at the top of the structure is roughly zero, with the remainder of the structure showing a consistent loading of approximately −50kPa.ms, meaning the majority of the side panel experienced a net impulsive load of 50kPa.ms in the outwards direction.

Similarly to the first arena trial, the loading of the **B** panels, for both pressure and impulse, exhibited the same general regions at each of the radial stand-off distances, with minor variations. The **D** panel geometry of structure WR2B experiences a completely different interaction with the blast resulting in completely different loading regions. The Air3D model of structure WR2B used the same modelling conditions as the previous simulations, with the only differences being the geometry. Monitoring points were evenly spaced across the surface with the peak reflected pressures and peak cumulative impulses plotted onto 2D surfaces for the blast normal and side panels, displayed in Figure 5.13. The net pressure regions for structure WR2A, a **B** panel, were presented such that the net load was applied in the inward direction to both faces, thus the net load for the **D** panel is plotted such that the load is applied in the inward direction.

The net pressure on the rear, blast normal panel of the structure, displayed in Figure 5.13a is plotted in the inwards, or upstream direction. The scale shows the highest region of net pressure to be approximately -300kPa, or 300kPa in the downstream direction, across the majority of the surface of the structure, with a net pressure of approximately 0kPa at the intersection with the side panel. The net pressure acting on the side panel, displayed in Figure 5.13b, shows a peak inward pressure of 50kPa corresponding to the intersection with the rear blast normal panel. The net pressure was increasingly more negative, in the upstream direction, with a peak negative pressure of approximately -200kPa. Again, the negative pressure represents a load acting outwards, hence the peak pressure was 200kPa acting outwards. Unlike the **B** panel in which the net load was predominantly acting inwards, forcing both panels together, in the case of the **D** panel the net pressure acts outwards, pushing both panels away from each other. As the interior

of the structure is directly exposed to the blast, the build-up of reflections causes much higher peak pressures acting on the interior of both panels.

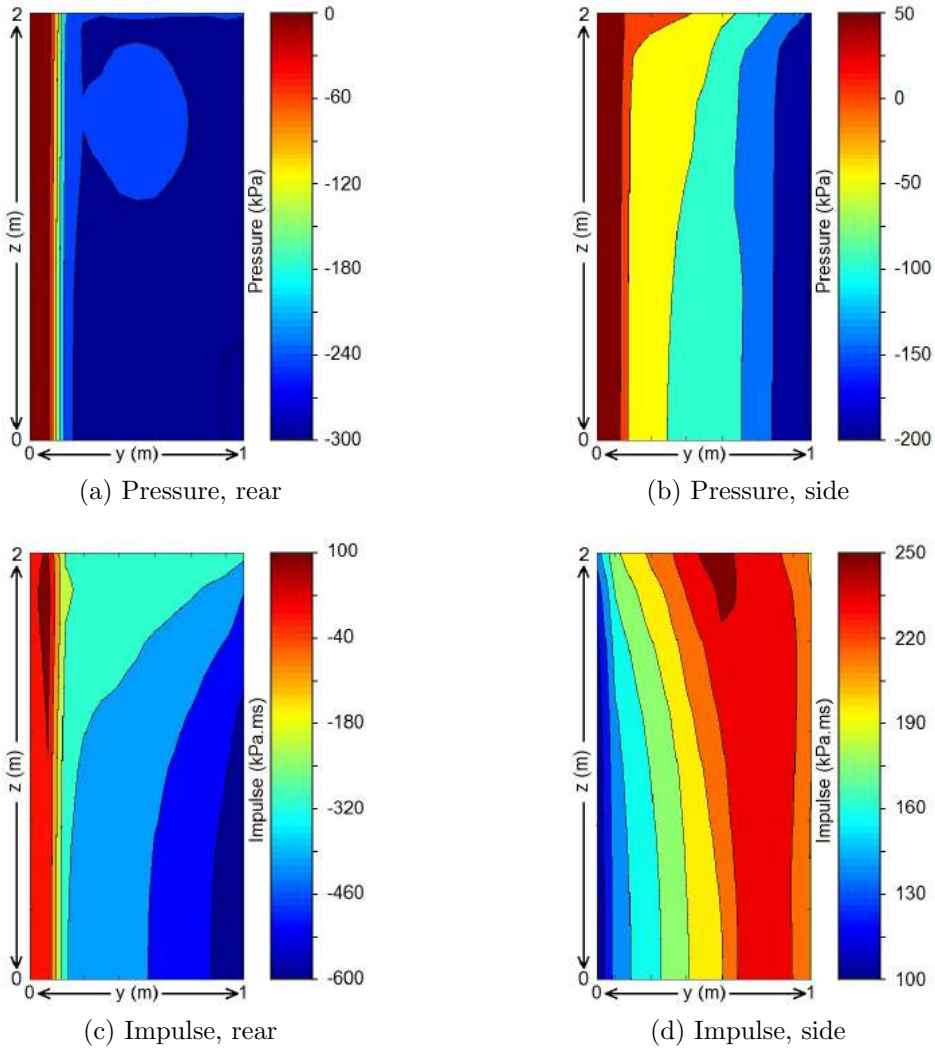

(a) Pressure, rear

(b) Pressure, side

(c) Impulse, rear

(d) Impulse, side

Figure 5.13: Air3D model of structure WR2B: Net reflected pressure and impulse

The same approximate pattern for net impulse was observed on the blast normal panel, displayed in Figure 5.13c, as the net pressure; however the net impulse of the side panel, displayed in Figure 5.13d, exhibited almost inverse net loading regions. Note that in terms of magnitude alone, the loading regions were approximately equal with the highest loading regions occurring in the most upstream positions and the lowest net loading regions located at the intersection of the blast normal panel. The loading on the outside of the side panel remains relatively unaffected by the geometry of the structure as the blast wave clears. The reflections from the interior faces of the structure provide

higher peak pressures although lower impulse, leaving the net impulsive load directed inwards.

5.1.2 Applied Element Method

The ability to assess the loading regions of any structural geometry provides key data required to iterperet the breakage mechanism and develop structural models. Furthermore, the ability to visually interpret the difference between the peak pressure and impulse loading regions identifies their effects on structural response. In the case of HE models, the structures respond long after the blast wave has passed; however in the long duration case, only a certain percentage of the impulse is transferred before the structure begins to respond. Using the structural software Extreme Loading for Structures® (*ELS*) [89] which utilises the Applied Element Method, models were run for each of the structures in both of the Windrush arena trials. The net loading regions, plotted using the gauge data from the CFD models, were used to determine where the loads should be applied to each of the structures. As reflective pressure is responsible for breakage, the load was applied in several areas based on contours of the net pressure. Within each of these regions, the pressure obtained from each individual gauge point was averaged to provide a single load curve for each of the loading regions.

The **A** panels from trial WR1 were each modelled using three loading regions. The central lower half of the structure, the outer, lower half of the structure and the upper half of the structure. The pressure profiles applied to each of the loading regions presented similar peak pressures, differing only by the waveform decay, which was primarily dictated by the rear loading. Due to the small difference between the loads in these simple cases, any additional loading regions would not increase the accuracy of the model.

As the structures tested in trial WR1 were all **A** panels with the same geometry, each structure used the same ELS model template. Figure 5.14a shows the **A** panel modelled in ELS and Figure 5.14b shows a close up of the model, detailing the element arrangement. The bricks, shown only by a wiremesh outline, were modelled as single elements as the majority of bricks, from all trials, remained undamaged. The mortar

was modelled explicitly with x,y,z dimensions 50mm×50mm×10mm along the bedding planes and as 50mm×10mm×32.5mm between bricks. Table 5.3 highlights the internal parameters of the models within ELS.

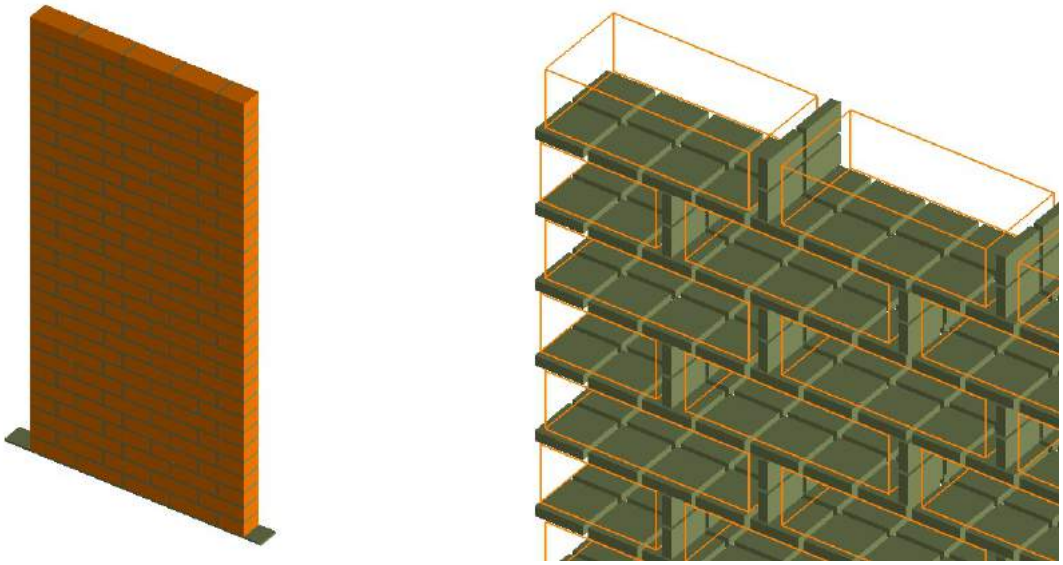

(a) Model overview (b) Structure close-up & element array

Figure 5.14: ELS / AEM Model of the **A** Panel

Table 5.3: Initial ELS internal model parameters

Parameter	Units	Brick		Mortar	
		Value	Default	Value	Default
Youngs Modulus	($kNmm^{-1}$)	19.6	✓	13.8	✓
Shear Modulus	($kNmm^{-1}$)	7.8	✓	5.5	✓
Tensile Strength	(Nmm^{-1})	1.5	✓	1.0	✓
Compressive Strength	(Nmm^{-1})	20	9.8	8	9.8
Separation Strain	(-)	0.05	0.1	0.05	0.1
Friction Coefficient	(-)	0.9	0.8	0.9	0.8
Contact Spring Unloading Stiffness Factor	(-)	9	2	9	2

The parameters shown in Table 5.3 were implemented in an attempt to closely match the specified and measured parameters of the bricks and mortar at the time of firing. The separation strain was reduced to 0.05 based on the low curing time of the mortar. The loading scenario was applied as a uniform pressure with a time step of 0.25ms for 500ms. Whilst the load was approximately 15ms due to the relatively short duration of

the blast load, this allowed ample time for the breakage patterns to form with a high resolution. An additional loading scenario was applied over a duration of 3,000ms with a time step of 5ms to allow the structure to fully collapse and form the required debris distribution. After 500ms, when the breakage has occurred, the remaining collapse of the structure is determined by pre-existing vectors and gravity, which are less variable than the formation of the crack patterns. This allows the resolution to be decreased for computational effeciency, in this case by 20×, and still maintain an accurate solution. The results of the breakage of the AEM model of structure WR1A are displayed in Figure 5.15, compared to the trial.

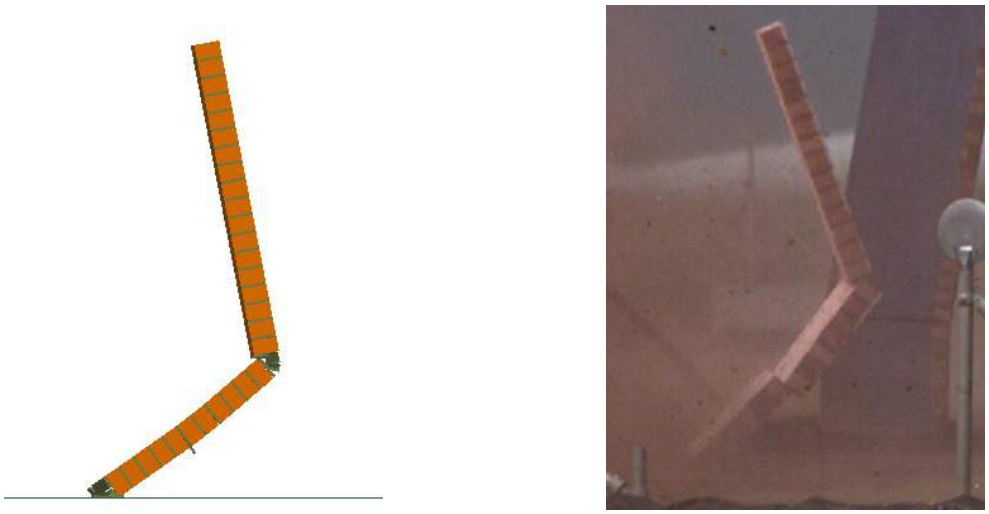

(a) AEM (b) Trial

Figure 5.15: Breakage of structure WR1A at 400ms

The breakage pattern of the AEM model was almost identical to that observed in the trial, with the AEM breakage occurring one layer of brick higher than those observed in the trial. For both the AEM model and the trial, the rotational motion of the upper and lower sections of the structure matched, with the lower section tilting in the downstream direction and the upper section tilting in the upstream direction. The resulting debris distribution of structure WR1A, from both the AEM model and the trial, are displayed in Figure 5.16.

The high density area of the debris fields, both from the AEM model and the trial cover approximately the same area, as displayed in Figures 5.16c and 5.16d, in which

the both structures were centred about (0,0). The AEM screen shot and trial debris photograph, shown in Figures 5.16a and 5.16b respectively, illustrate the key differences between the model and the trial. Whilst the breakage pattern was almost identical in both cases, the debris distribution of the AEM model is more confined. This was due to the higher fragmentation observed in the trial upon impact of the masonry with the ground, resulting in a wider overall spread of debris. The internal parameters of the AEM models primarily responsible for fragmentation and debris scatter are the separation strain and the contact spring unloading stiffness factor.

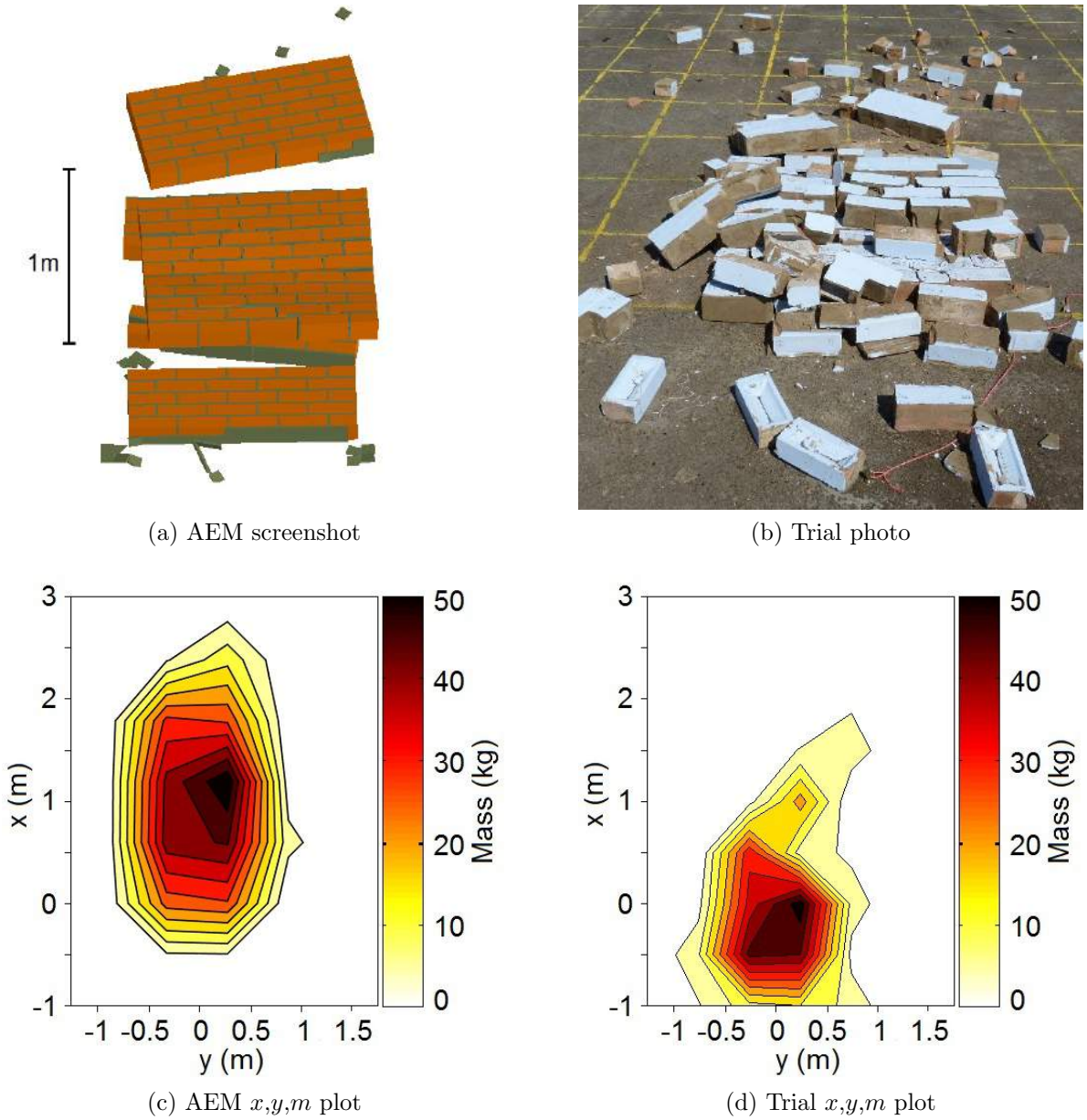

(a) AEM screenshot

(b) Trial photo

(c) AEM x,y,m plot

(d) Trial x,y,m plot

Figure 5.16: Debris distribution of structure WR1A

Through several iterations a sensitivity study, the internal parameters were adjusted such that the breakage pattern remained unchanged, whilst improving the debris distribution and ground impact fragmentation. The contact spring unloading stiffness factor was increased for the initial modelling to reduce excessive bounce and roll, which could present an issue in the long duration blast scenarios. As demonstrated by the initial model, a higher value is required to correctly model the impact of the masonry with the ground. Similarly, the coefficient of friction was reduced from 0.9 to 0.7 and the compressive strength of the mortar was further reduced to 5.8N/mm^{-2} to improve the ground impact fragmentation. The final parameter, separation strain, was also reduced by a factor of 20, from 0.05 to 0.001, resulting in the internal model parameters displayed in Table 5.4.

Table 5.4: Refined ELS internal model parameters

Parameter	Units	Brick		Mortar	
		Value	Default	Value	Default
Youngs Modulus	(kNmm^{-1})	19.6	✓	13.8	✓
Shear Modulus	(kNmm^{-1})	7.8	✓	5.5	✓
Tensile Strength	(Nmm^{-1})	1.5	✓	1.0	✓
Compressive Strength	(Nmm^{-1})	20	9.8	5.8	9.8
Separation Strain	(-)	0.001	0.1	0.001	0.1
Friction Coefficient	(-)	0.7	0.8	0.7	0.8
Contact Spring Unloading Stiffness Factor	(-)	3	2	3	2

Using the material parameters presented in Table 5.4 the AEM model of structure WR1A retained the correct breakage pattern with a more accurate debris distribution. It should be noted that a previous iteration produced the closest matching debris distribution to that of the trial. The brick and mortar parameters for this were 0.7, 0.005 and 5 for the coefficient of friction, separation strain and contact spring unloading stiffness factor respectively; however whilst the area covered by the distribution showed very good agreement with the trials, the fragmentation upon impact with the ground was much lower than the trials. The area covered by the debris distribution its density regions will most certainly vary from trial to trial, however the level of fragmentation will remain more consistent. For this reason, the previous iteration was disgarded. The debris distribution

from the final model is presented in Figure 5.17 alongside the experimental distribution.

Within a 1m^2 area centred about the origin, 51.3% of the overall debris from the experimental trial was located, compared to 35.3% in the AEM model. This was due to the mass located between -0.5m$< x <$0m in the experimental trial and not in the AEM model. Investigation of the model shows that this results from the breakage line occurring one layer of bricks lower resulting in a lower tilting moment and less upstream debris. Expanding this region to 4m^2 centred about the origin, the trial and AEM model presented 81.9% and 68.3% of the overall mass respectively. Within this region, the difference reduced from 16.5% to 13.6%. Finally the debris contained within a 9m^2 area centred about the origin was 89.1% and 97.3% of the overall mass for the trial and AEM models respectively, a difference of 8.2%.

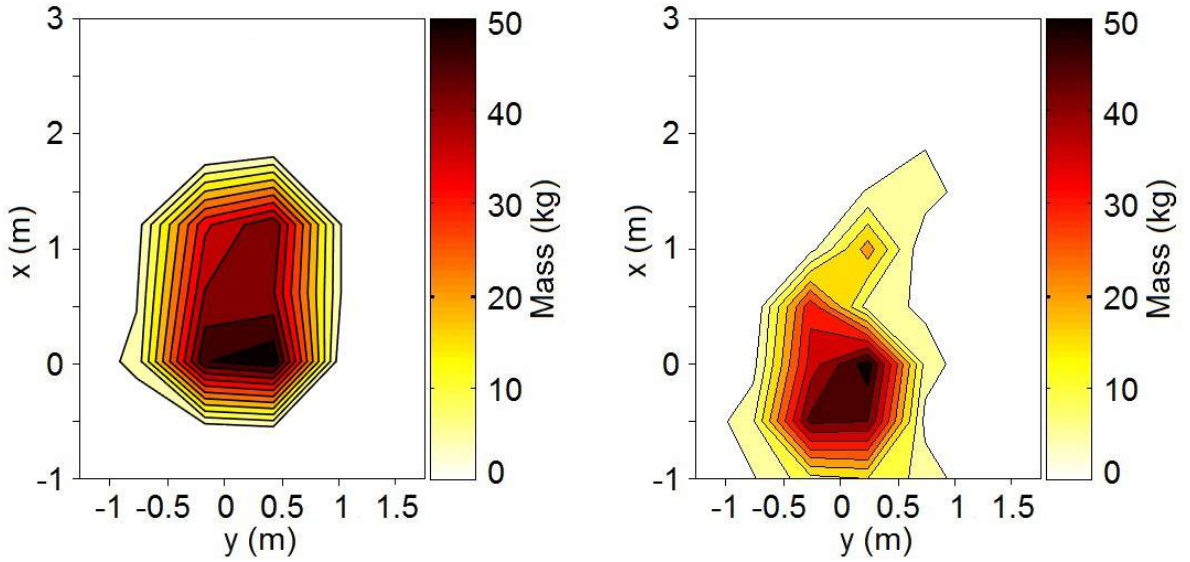

(a) AEM x,y,m plot (b) Trial x,y,m plot

Figure 5.17: Debris distribution of structure WR1A (refined AEM results)

Disregarding small mortar fragments (≈10g), the maximum longitudinal distribution for the trial was 3.5m, and 3m for the AEM model. The full longitudinal debris distributions of both the trial and the AEM model are displayed in Figure 5.18a. It is clear that the debris is confined to a smaller region for the AEM model compared to the experimental results, although the shape of the high density region is similar, which suggests the composition of the debris pile is similar. The lateral distribution, displayed in Fig-

ure 5.18b shows very good agreement with the experimental trial, both showing almost symmetrical distributions about the origin. Overall, the AEM model presents a slightly refined prediction of the debris distribution for structure WR1A. As the conditions of the experiment can never be perfectly replicated, the AEM model performed well, predicting the breakage pattern with very good agreement and the subsequent debris distribution with reasonable agreement.

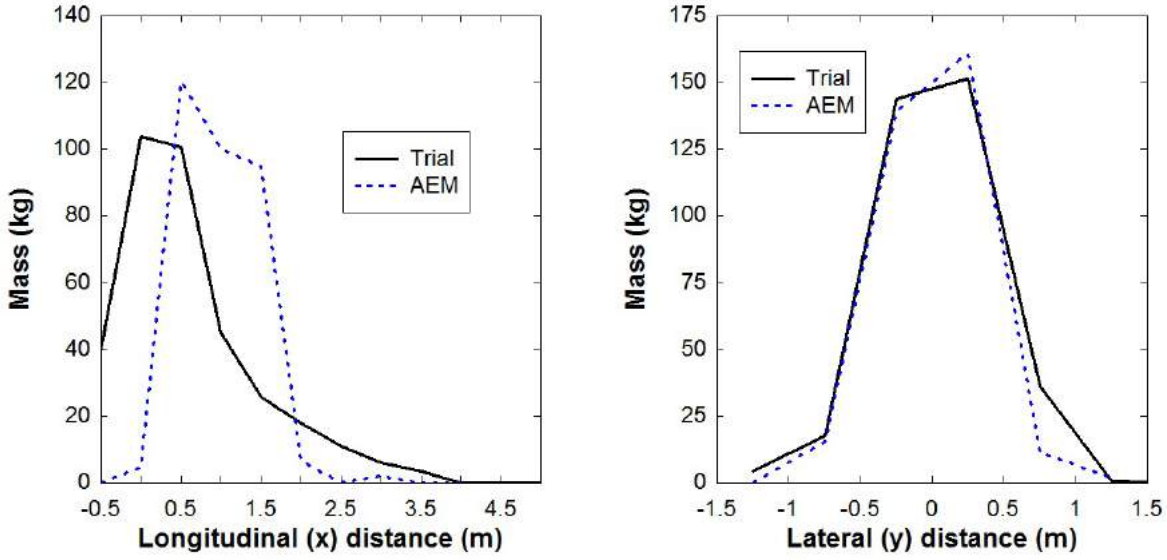

(a) Longitudinal debris distribution (b) Lateral debris distribution

Figure 5.18: WR1A AEM vs Trial debris distributions

Using the same ELS **A** panel template as displayed in Figure 5.14, an AEM model of structure WR1B was developed using the same loading regions as structure WR1A. As discussed in Section 5.1.1, the average loading regions of each structure in trial WR1 were almost identical, with only slight changes due to the blast wavelength. The loads obtained from the CFD gauge data were averaged and applied to each region. The model used the same internal parameters as displayed in Table 5.4 to ensure consistency between the models.

The breakage of the AEM model of structure WR1B was initiated by a horizontal crack forming between the 11^{th} and 12^{th} layers of brick, compared to the 7^{th} and 8^{th} observed in the experimental trial. The higher origin of the crack line caused the AEM model to tilt in the opposing direction to the trial, that is, the upper section of the

AEM model tilted in the upstream direction, compared to the upper section of the trial tilting in the downstream direction. In both cases, counter tilting of the lower section was also observed resulting in the AEM model presenting a significantly reduced debris distribution in comparison to the trial, as illustrated by Figure 5.19. Furthermore, due to the opposing tilting motion of the lower sections between the trial and AEM model, the experimental results show a significant amount of debris located between -1m< x <0m whereas the AEM model does not. The distributions presented in Figure 5.19 are scaled such the the upstream face of both structures are centred about (0,0).

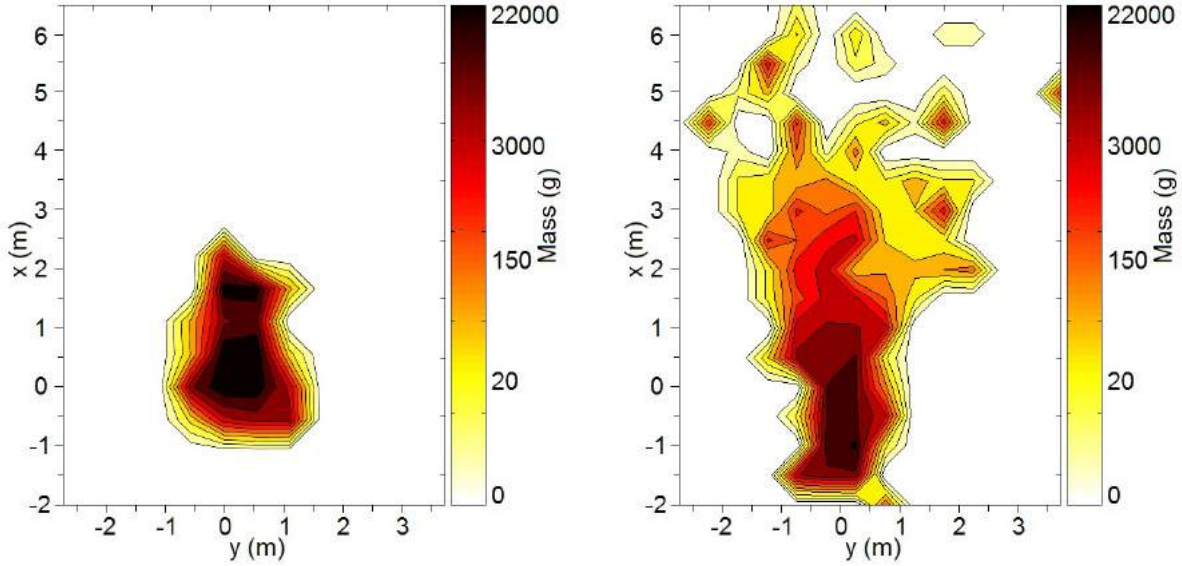

(a) AEM x,y,m plot (b) Trial x,y,m plot

Figure 5.19: Debris distribution of structure WR1B

The debris distribution of the AEM model, Figure 5.19a, was similar to that of the WR1A AEM model, with a high density distribution between 0.5m< y <0.5m and 0m< x <1.5m, whereas the experimental distribution, Figure 5.19b, shows a much larger distribution in the downstream direction. Within a 1m^2 area centred about (0,0), 26.3% and 33.9% of the overall debris from the trial and the AEM model respectively was located, giving a difference of 7.6%. This difference is reduced to 2.5%, with 69.9% and 72.4% of the overall mass of the trial and AEM model respectively, located within a 4m^2 area centred about (0,0). Finally, extending the area to 16m^2, the trial shows 92.1% of the overall debris located within this area, compared to 99.4% in the AEM model.

Despite the differences in the breakage mechanisms, the high density regions of the debris distribution were still located in approximately the same areas, highlighted by the longitudinal and lateral debris distributions, displayed in Figure 5.20. This is primarily due to the debris being confined to a relatively small area, resulting from the short duration of the blast load. The lateral distributions shows, in both cases, the debris to be confined within the region -1m< y <1m. The longitudinal distributions shows that whilst regions of high density are approximately the same magnitude, the spread was larger in the experimental trial, again due to the slight difference in breakage mechanism.

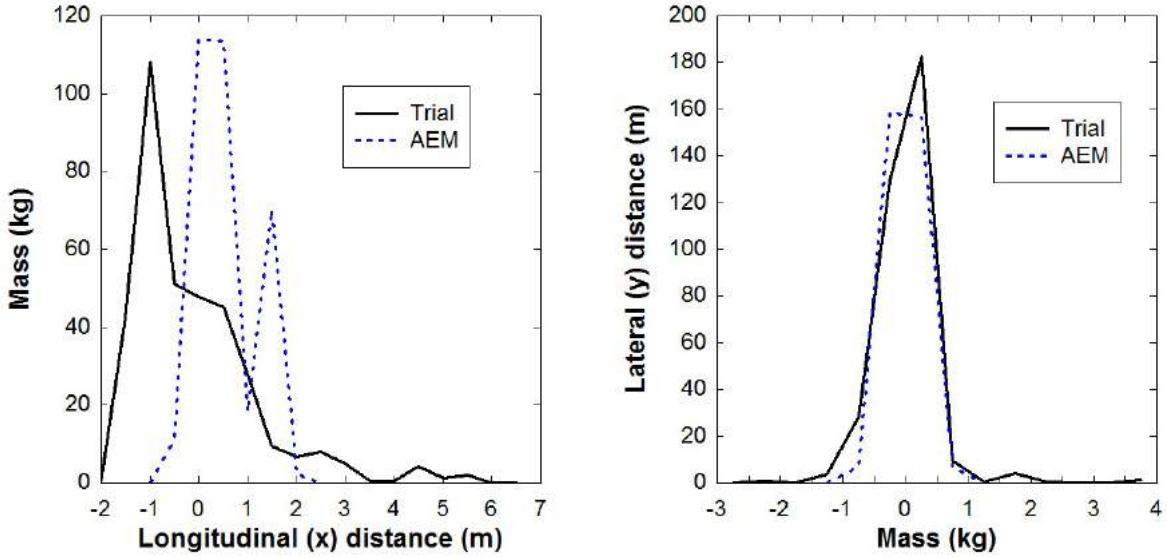

(a) Longitudinal debris distribution (b) Lateral debris distribution

Figure 5.20: WR1B AEM vs Trial debris distributions

As structure WR1C did not have the same initial conditions as the rest of the structures from trial WR1, it has not been included in the model benchmarking process. WR2C, the repeat of WR1C with the correct mortar compressive strength was instead modelled, again using the same ELS template and input parameters, as outline in Table 5.4. The loading regions were kept constant with the previous models as the CFD results showed them to be similar to both WR1A and WR1B. The experimental debris distribution of WR2C indicated that a breakage line formed approximately 0.75m above the base of the structure resulting in the upper section tilting in the downstream direction, whilst the lower section tilted in the upstream direction. The AEM model of WR2C

showed two partial horizontal breakage lines forming at approximately 0.3m and 0.7m above the base, although there was no separation, resulting in the entire structure to tilt about its base in the downstream direction. The resulting x,y,m debris distributions are displayed in Figure 5.21

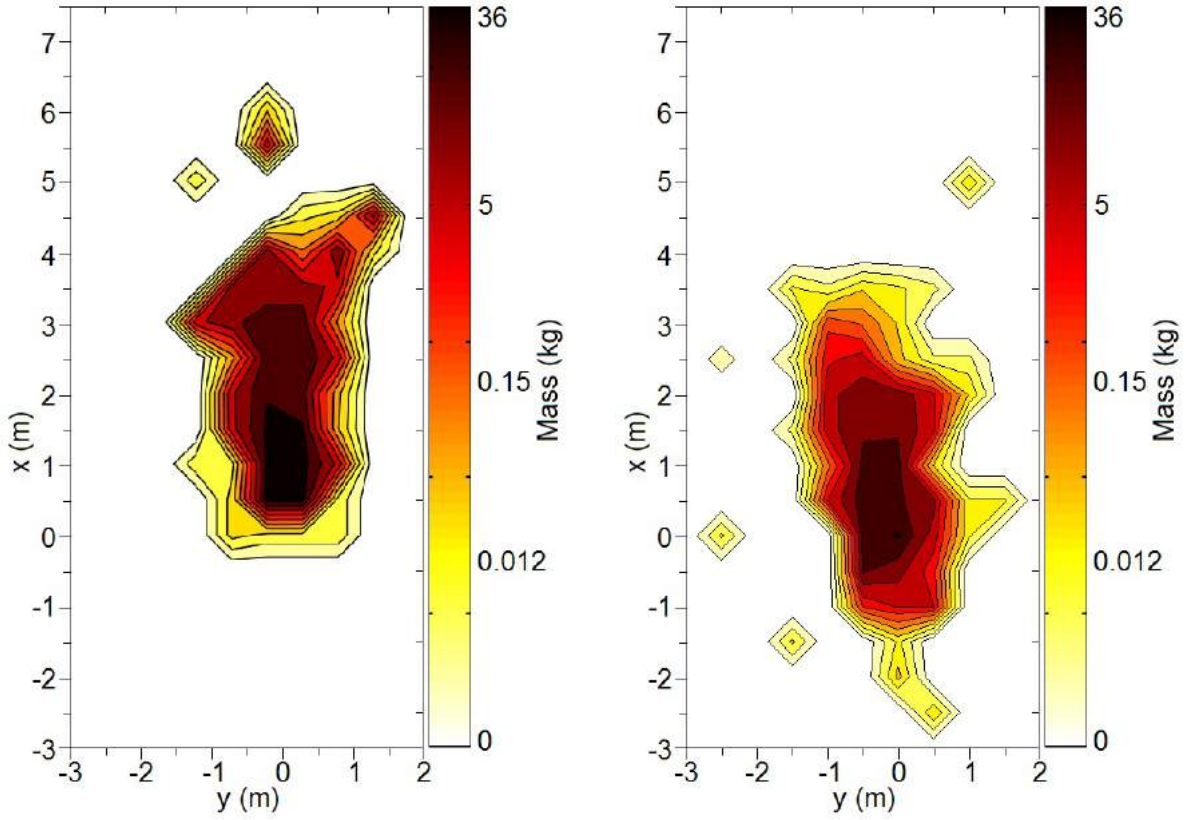

(a) AEM x,y,m plot (b) Trial x,y,m plot

Figure 5.21: Debris distribution of structure WR2C

The distribution of the AEM model is translated further upstream in the absence of any secondary tilting moments. The upstream tilting of the lower section of the structure in the experimental trials results in a higher density about the origin, with 35.0% of the overall mass located within a 1m^2 area centred about the origin, compared to 20.0% in the AEM model. This difference remains when the area is expanded to 4m^2, in which 58.6% of the overall mass from the experimental trial was located, compared to 40.1% in the AEM model. The difference between the two distribution remains between 15-20% until the area is expanded to 36m^2 to cover the increased longitudinal distribution of the AEM model.

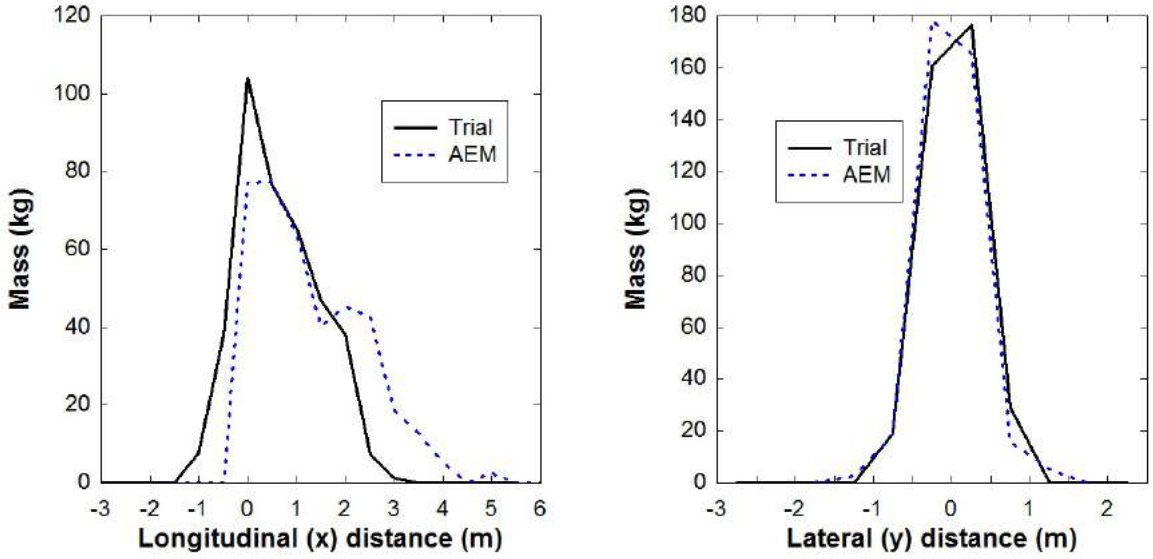

(a) Longitudinal debris distribution (b) Lateral debris distribution

Figure 5.22: WR2C AEM vs Trial debris distributions

As with all previous models, the lateral distributions, displayed in Figure 5.22b, show, in both cases, the majority of the mass constrained within -1m< y <1m and symmetrical about the origin. The longitudinal mass distributions, displayed in Figure 5.22a, show both distributions have a similar profile, with a difference of 1m between the two distributions, again resulting from the different breakage mechanisms. The longitudinal distribution of the AEM model shows a larger percentage of debris located at the upstream end of the distribution. This is a result of the increased fragmentation observed in the AEM model, due to the higher ground impact force in the absence of any tilting motion.

The loading regions for structures WR1D and WR1E were adjusted slightly based on the CFD models, highlighted by Figure 5.7, whilst the internal parameters were kept consistent with previous models, using those outlined in Table 5.4. Neither of the AEM models of WR1D or WR1E showed any response to the blast loading, matching the outcome of the experimental trials. Overall, the AEM models of the **A** panels from trial WR1 showed relatively good agreement with the experimental trials.

The models showed similar breakage patterns (formation and position of crack lines) in each model, with differences in the breakage mechanisms (primarily the direction of

rotation) leading to differences in the debris distribution. For all of the **A** panels tested in trial WR1, the AEM models showed good agreement with the expected level of fragmentation, as illustrated by Figure 5.23, which displays a screen shot of the AEM model of structure WR2C compared to a post-shot trial photograph. Both the trial and AEM distributions showed increased fragmentation in the upstream direction, resulting from ground impact forces. The lower sections of each structure also showed good agreement with decreased and similar levels of fragmentation.

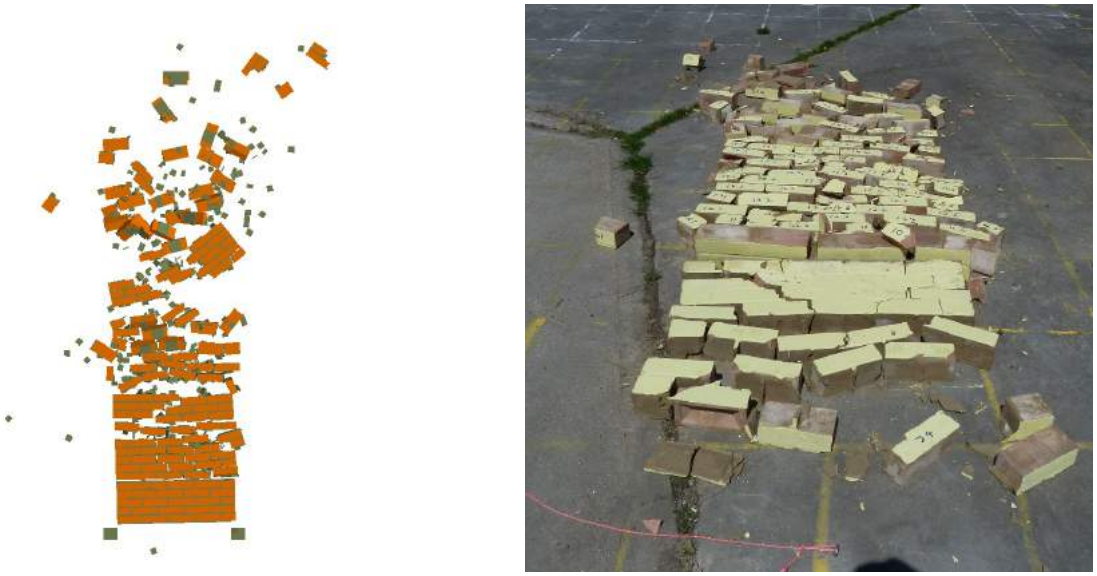

(a) AEM (b) Trial

Figure 5.23: Post-shot photograph / screenshot of WR2C illustrating fragmentation

The **B** and **D** panels instrumented in trial WR2 utilised the same ELS template, displayed in Figure 5.24, with the loading applied in different directions. The template uses the same brick and mortar sizes as the **A** panel template with the same internal parameters as described by Table 5.4. The sensitivity study, conducted to investigate the effects of the ELS internal parameters, was also conducted on the **B** panel alongside the **A** panel to ensure that the parameters had no adverse effects when applied to structures with different geometries.

The loading regions of **B** panels obtained from the CFD models were slightly more complex than those obtained from the **A** panels. Due to internal reflections of the blast wave, net pressures present on the side face of the structures resulted in larger gradients,

resulting in more sensitive loading regions. For structure WR2A, the load was applied in six regions, three on each face of the structure. The majority of the front face was covered by a single base load, with a higher load on the lower, outer edge and a lower load on the upper, inner edge. The loading on the side panel was high on its upstream edge in the absence of any rear load due to the front panel. The upper, downstream section of the side panel experienced a lower load due to internal reflections and the remainder of the side panel was reduced to a single load.

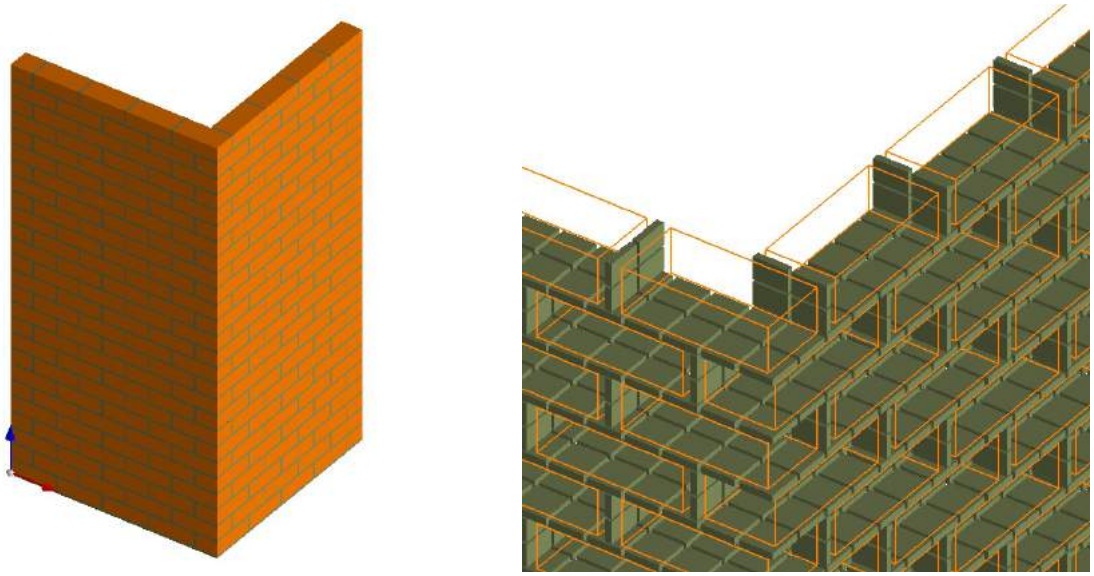

(a) Model overview (b) Structure close-up & element array

Figure 5.24: ELS / AEM Model of the **B** Panel

The x,y,m debris distribution of structure WR2A is displayed in Figure 5.25 and compares the distributions of the AEM model and experimental trial. The distribution produced by the AEM model appears to be translated by roughly 2m in both the x and y directions, resulting from the different collapse mechanisms. In the experimental trial, the side panel tilted inwards and the blast normal panel collapsed primarily outwards, whereas the AEM model showed the side panel tilt outwards and the blast normal panel collapse inwards. Although the AEM model showed the opposing collapse mechanism, the magnitude of the breakage and initial fragmentation was similar. As the **B** panel is inherently strong than the **A** panel, the loading, in both cases, was only strong enough to cause breakage. The resulting collapse mechanism was determined by a large number

of small factors, such as location, size and depth of the cracks, subsequent rotational motions about cracks and joints, structural harmonics, impurities and microfractures. The area covered by the distributions were approximately equal, with very similar levels of fragmentation.

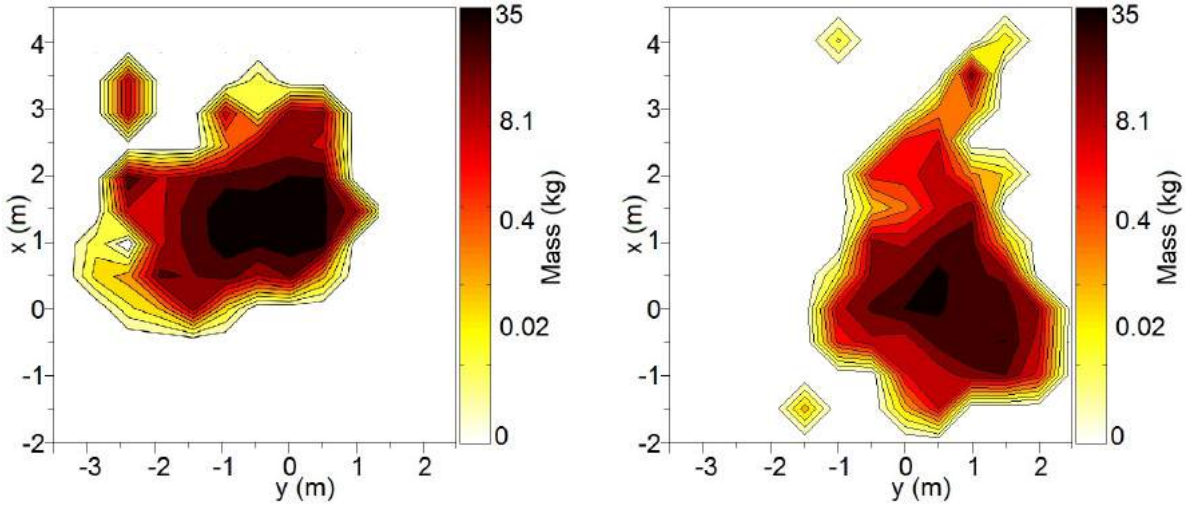

(a) AEM x,y,m plot (b) Trial x,y,m plot

Figure 5.25: Debris distribution of structure WR2A

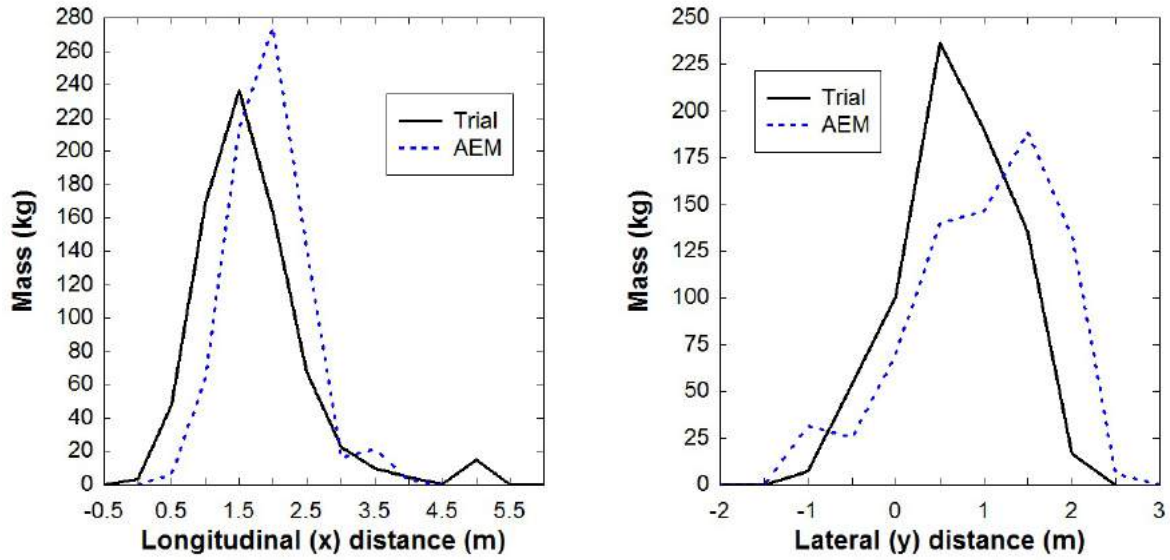

(a) Longitudinal debris distribution (b) Lateral debris distribution

Figure 5.26: WR2A AEM vs Trial debris distributions

Within a 1m^2 area centred about (0,0), the trial and AEM model presented 13.3%

and 16.4% of their overall massess respectively, with a difference of 3.1%. Increasing the squared area centred about (0,0) showed the difference in overall mass of AEM and the trial was always below 6%, with the largest difference of 5.8% present when inspecting an area of $9m^2$. This lower mass difference was primarily due to the large amount of debris located within a relatively small area.

The longitudinal debris distributions, displayed in Figure 5.26a, show good agreement with the high density region of the AEM model located 0.5m further upstream. Whilst the overall distance covered by the trial was 1.5m larger than the AEM, the amount of debris located at the extents was relatively small. The lateral distributions, displayed in Figure 5.26b, shows the debris from the AEM model to have a more even distribution, as a result of the outwards collapse of the side panel. As the side panel only accounts for 50% of the overall mass, the resulting debris distributions still show relatively good agreement, despite the difference in the collapse mechanisms.

As previously mentioned, the **D** panel has the same geometry as the **B** panel and so structure WR2B was modelled using the same ELS template as WR2A. The loading was divided into seven sections based on the CFD results, three on the rear, blast normal panel and four on the side panel. The first loading region on the blast normal panel was applied to the corner joint as the side panel negated any wrap around pressure, the second applied to the upper inner section as the internal reflections were higher resulting in a larger rear pressure, with a single, base load applied to the remainder of the blast normal panel. The loading on the side panel increased towards the rear of the structure due to the internal reflections, thus the loading was applied to four equal vertical sections.

The debris distributions of structure WR2B from both the trial and AEM model are displayed in Figure 5.27. As with WR2B, the breakage mechanisms differ slightly, despite similar crack formation, again resulting in the side panel collapsing in different directions, outwards in the trial and inwards in the AEM model. In both cases, the rear, blast normal panel collapsed outwards. Despite this difference in failure mechanism, the debris distributions cover the same approximate area. As with previous models, this is primarily due to the good agreement with fragmentation, especially that resulting from

ground impact.

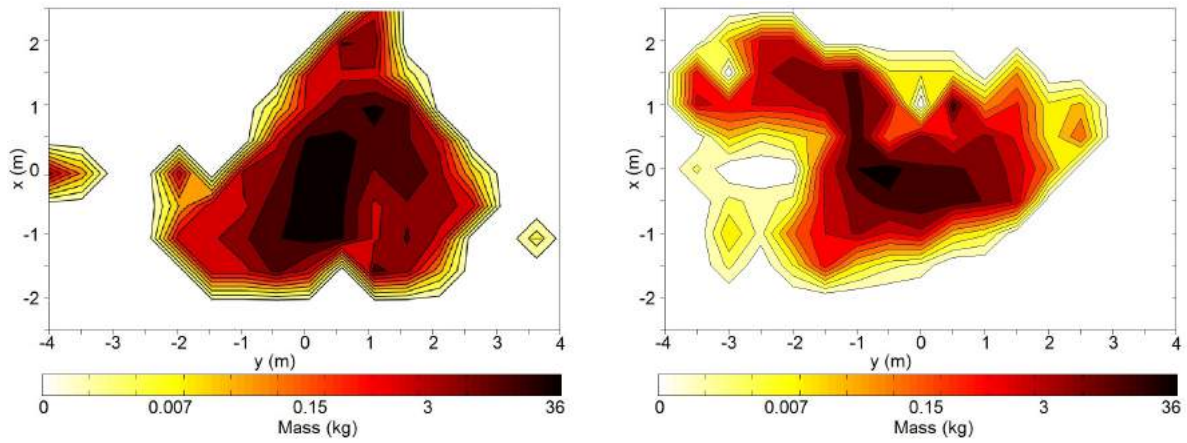

(a) AEM x,y,m plot (b) Trial x,y,m plot

Figure 5.27: Debris distribution of structure WR2B

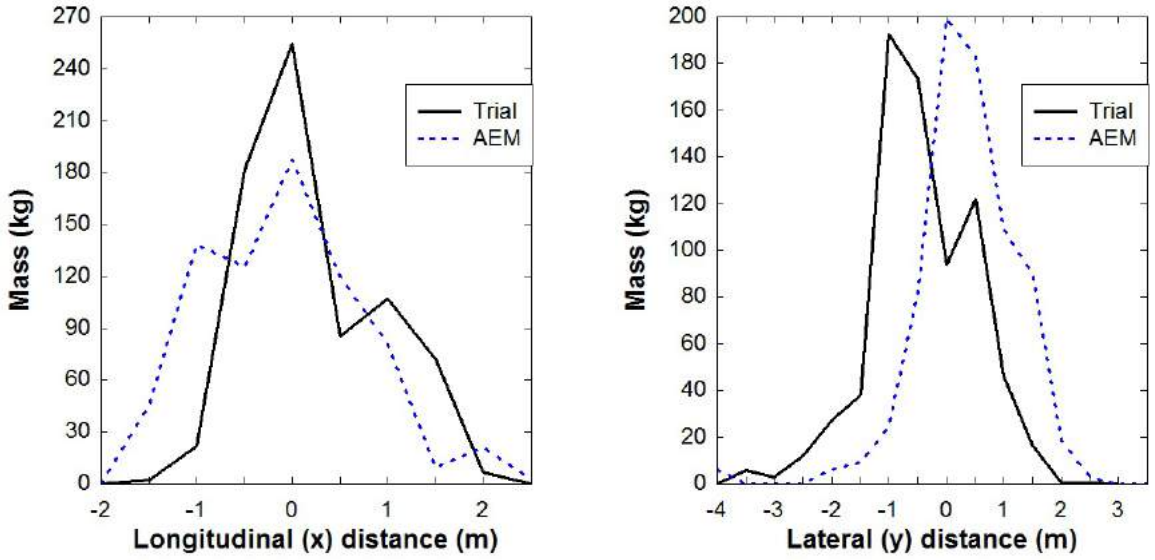

(a) Longitudinal debris distribution (b) Lateral debris distribution

Figure 5.28: WR2B AEM vs Trial debris distributions

Within a 1m^2 area located about (0,0), the trial showed 32.3% of the overall mass whereas the AEM model presented only 16.6%, resulting in a difference of 15.7%. This relatively large difference was again due to the base 4 layers from the trial remaining in their original position, thus placing presenting a high density area of debris about the origin. Extending this region to 4m^2 about (0,0), the difference further increases to

18.5%, in which 64.4% of the overall mass of the trial was located, compared to 45.9% of the AEM model. Within a 9m^2 region, the difference reduces to 10.8% presenting 85.1% of the trial debris and 74.2% of the AEM debris. Beyond $16m^2$, the difference is reduced below 1%, with the entire mass of both the model and the trial falling within a $26m^2$ rectangular area.

The longitudinal distributions, displayed in Figure 5.28a, again shows a more even distribution of the AEM model. In the experimental trial, the lower 4 layers of brick remained in their original position which was not the case in the AEM model, reducing the high density region about the origin in the AEM model. The lateral distributions, displayed in Figure 5.28b, would suggest that the side panel of the AEM model fell outwards as the distribution is weighted in the positive y direction. The majority of this debris originated from the blast normal panel, which fell outwards with a slight rotation about the corner joint, resulting in more debris in the positive y direction. In general, the lateral distribution of both the trial and the model show a very similar shape, with a 0.5m translation of the AEM reuslts. Overall, the model shows good agreement with the trial, presenting good levels of fragmentation and a similar debris distribution, which showed similar longitudinal, lateral and x,y,m scatter, including maximum extents and high density regions

The experimental trials showed structure WR2D to be the boundary case scenario, showing high levels of damage with no structural collapse, illustrated in Figure 5.29b. The structure was modelled using the same ELS template as the other two corner geometries and the loading was divided into six regions, three on each face based on the CFD results. The AEM model showed good agreement with the experimental trial, showing a similar combination of horizontal and stepped crack lines, especially in the case of the horizontal crack line present on the upper section of the side panel, highlighted by Figure 5.29a.

As bricks in the AEM models were modelled as singular elements, there was no vertical cracking present in the AEM models. This potentially contributes to the subsequent collapse of the AEM model as the force alleviated through vertical cracking is dissipated into stepped cracking across larger areas of the structure. It should be noted that it is

highly unlikely that a repeat of trial WR2D would yield the same results as the structure was highly unstable and on the verge of collapse, thus, the AEM model performed well, with good agreement in modelling the partial breakage of the boundary case scenario.

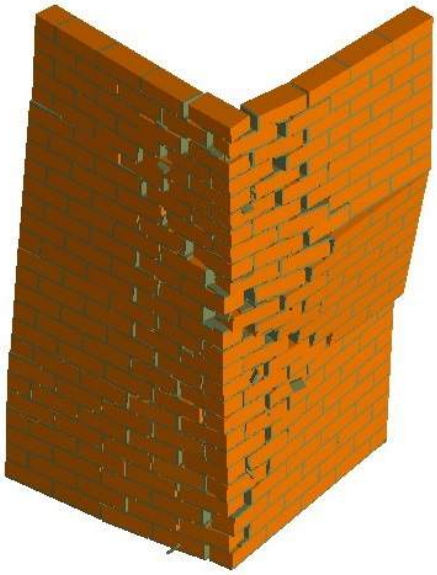

(a) AEM breakage

(b) Trial breakage

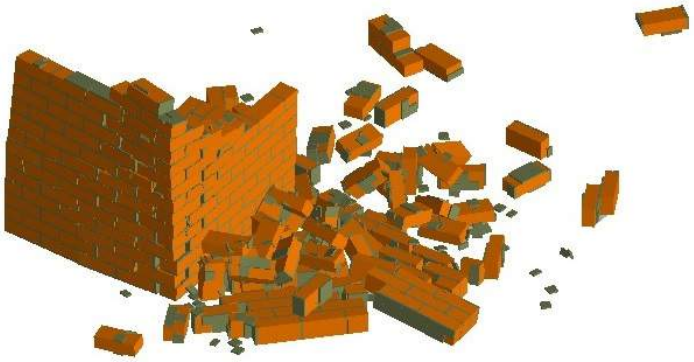

(c) AEM collapse

Figure 5.29: WR2D AEM model

The final structure WR2E showed minor cracking, with the collapse of the upper outer corner of the blast normal panel. Once again the loading was divided into three regions per panel and the same ELS template and internal parameters were used. The AEM model showed partial crack formation at the base of the structure, however the applied load was not large enough to cause any displacement about the cracks and no permanent deformation, leaving the structure standing intact.

The loads applied, both experimentally and computationally to all of the structures in trials WR1 and WR2, were small due to short positive phase duration. As a result, each of these models are, to some degree, boundary case scenarios. That is, if the experimental trials were to be repeated, the collapse mechanisms would most likely change. Ideally further trials would be required; however as both the WR1 and WR2 trials were for the purposes benchmarking AEM and gauging its appropriateness to model debris distribution, this would not be necessary. Despite the differences in debris distributions, each of the AEM models showed similar breakage patterns and correct fragmentation, due to both the initial impact of the blast wave and impact with the ground upon collapse. The exact collapse mechanisms were, in all cases, determined by a large number of small parameters as previously stated; however, in the case of long duration blast, the duration of the load is an order of magnitude larger, resulting in a distinct direction of collapse.

Based on the short duration benchmarking of AEM, the long duration models can be expected to show good agreement between breakage and fragmentation. The debris distribution when subject to long duration blast is largely determined by the in-flight ballistics, driven by the drag wind, its associated dynamic pressure and the varying drag applied to rotating airborne debris. Whilst AEM has shown promising results when modelling simple collapse, developing a robust method to apply the complex, multi-stage loading to long duration models requires an additional and lengthy benchmarking process.

5.2 Long Duration Blast

5.2.1 Computational Fluid Dynamics

By nature, the wavelength of long duration blast loads is extremely large compared to that of short duration blast loads, as the wavelength is proportional to the duration. In the case of the ABT, the wavelength of the blast is significantly larger than the strucutres being tested and as the full blast must be modelled on either side of the structure, the required domain is significantly larger than the structure itself. The large domain forces a compromise between the accuracy of the solution and the computational requirements. Although the same ratio of cell size to domain used for the short duration

case would provide accurate results, this would not allow the load applied to the structure to be monitored with the same resolution as the previous CFD models of the short duration trials. A 1D spherical blast model was run of the 4.9m section of the ABT, using modified blast parameters with a significantly higher charge density to account for the large charge mass. Results of the static overpressure from the 1D CFD model are plotted in Figure 5.30, alongside a sample static pressure time history from the 4.9m section of the ABT.

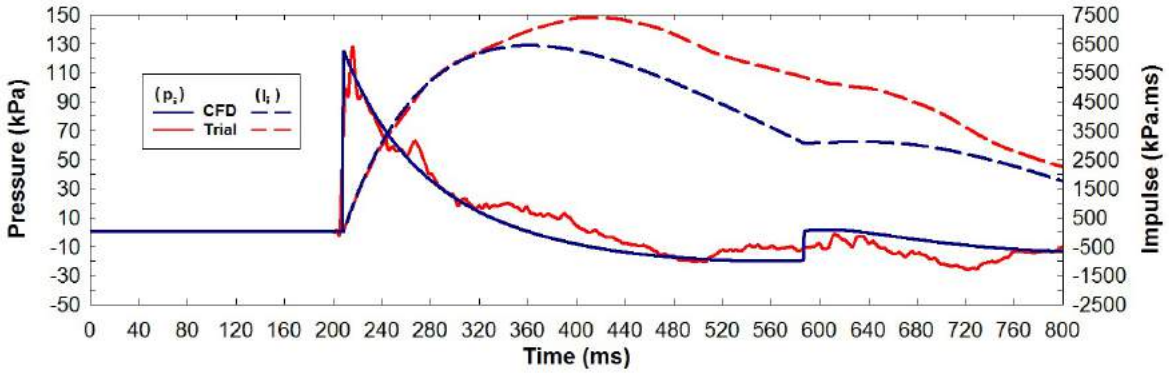

Figure 5.30: 1D Air3D and 4.9m ABT static pressure and impulse time histories

The arrival time of the experimental blast wave corresponds to the time of arrival of the blast wave after the gauge began recording, not the detonation. As the arrival time has no effect on any of the experiments or models conducted for this research, the graphs have both simply been translated such that shock discontinuities align for easy visual comparison. The static pressure time histories of the 1D CFD model and the experimental gauge data show good agreement in terms of both peak pressure and waveform decay constant. This is clearest when comparing the impulse, with the experimental results showing higher impulse. The peak pressure of the CFD model was 3% below the experimental results whereas the impulse was 13% lower. The experimental results naturally show increased noise and fluctuations in comparison to the idealised 1D CFD model. As discussed in Chapter 4, the static pressure histories recorded in the 4.9m section of the ABT always showed small peaks due to reflections of the blast from the structure.

The 1D results show the capability of CFD to model the long duration case to within an acceptable degree of accuracy. Alongside issues with size and mesh resolution, the

shape of 3D domain greatly influences the propagation of the blast, even with transmissive boundaries as the time step update of neighbouring cells produces less accurate results. A 3D CFD model was conducted in which the 1D data was remapped after 150m and the blast wave was free to propagate in 360°, the results of which are displayed in Figure 5.31, plotted against the same ABT trial results.

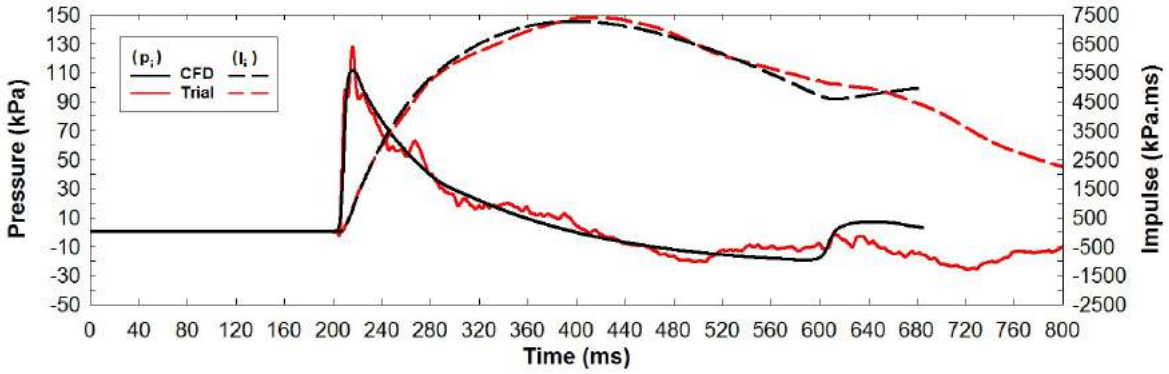

Figure 5.31: 3D, full symmetry Air3D and 4.9m ABT static pressure and impulse time histories

The peak pressure of the CFD model was 115.1kPa, 10% lower than the experimental result and 7% lower than the 1D result. Whilst this result is further from the measured data, it is closer to the predicted peak overpressure of approximately 110kPa and is thus suitably accurate. The waveform decay constant of the 3D results shows a much closer match to the experimental data than the 1D result, giving a closer approximation of the impulse which was only 2% lower than the experimental value. The results from the full symmetry model showed promise; however the domain was too large, with a cell size too high to model any of the required structures. Several additional models were conducted changing the size and shape of both the domain and cell size to assess the its effect on the blast loading. Figures 5.32a and 5.32b show a selection of static pressure and impulse time histories respectively from a variety of CFD domains, compared to the same experimental result as before, in which the domain details of curves C1-C7 are displayed in Table 5.5, relative to the charge located at (0,0,0).

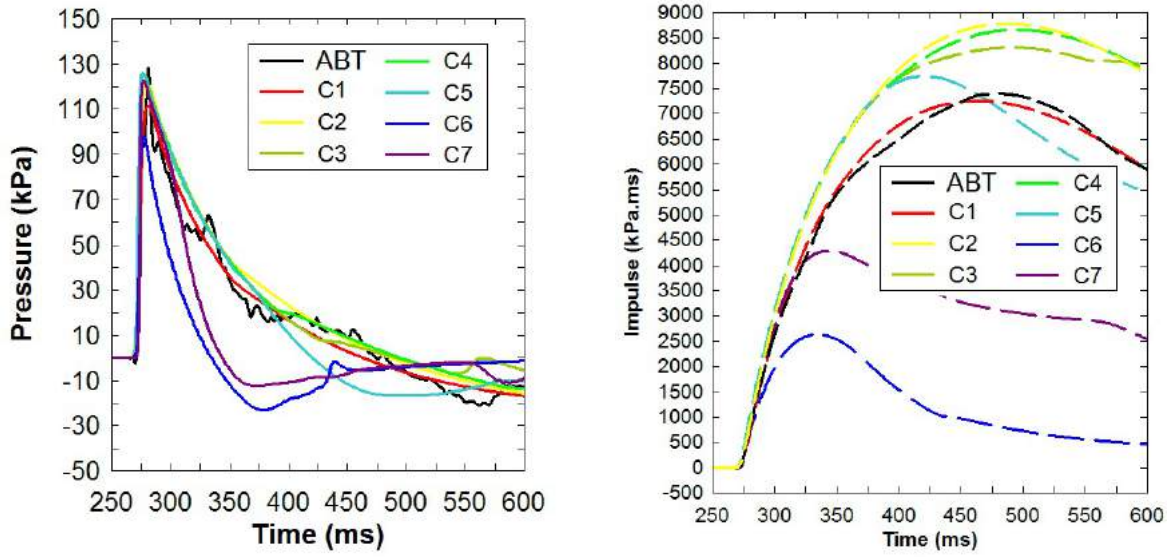

(a) Static pressure

(b) Static impulse

Figure 5.32: Air3D domain sensitivity assessment

Table 5.5: Domain extents and sizes of curves C1-C7

Curve	x (m)			y (m)			z (m)			Cell
	start	end	size	start	end	size	start	end	size	Size (m)
C1	-500	500	1000	-500	500	1000	0	60	60	1
C2	0	500	500	0	500	500	0	60	60	1
C3	100	350	250	0	80	80	0	80	80	0.7
C4	120	340	220	0	70	70	0	70	70	0.7
C5	150	330	180	0	60	60	0	60	60	0.7
C6	180	320	140	0	50	50	0	50	50	0.7
C7	200	300	100	0	40	40	0	40	40	0.5

The results from each of the domains showed peak static pressures approximately equal to the experimental data, although the waveform decay differs significantly. Curves C1 and C2 represent full symmetry and quarter symmetry models respectively and present the most accurate solutions in terms of peak pressure and waveform decay. The quarter symmetry solution however shows the highest impulse, regardless of the pressure history, potentially due to the gauge being positioned on the boundary. Curves C3, C4 and C5 all show similar results to the quarter symmetry case, with curves C6 and C7 decaying too quickly resulting in significantly less impulse. Although the domain of curve C7 was smaller than that of C6, the results were more accurate due to the finer mesh size of

0.5m compared to 0.7m. These results suggested the ideal domain size to be as small as possible with a smaller mesh size.

Further sensitivity models suggested the optimal x,y,z domain for the 4.9m section of the ABT to be approximately 180m×80m×40m, with a cell size of 0.2m. This resolution allows for 50 monitoring points per base panel per face, with a total problem size of 7.2×10^7 cells and a run time of approximately 12 hours. Images of the blast propagation, presented in Figure 5.33, illustrate the relative size of the structure, which was one cell, 0.2m in the x direction compared to the blast wave with a positive phase wavelength of approximately 70m.

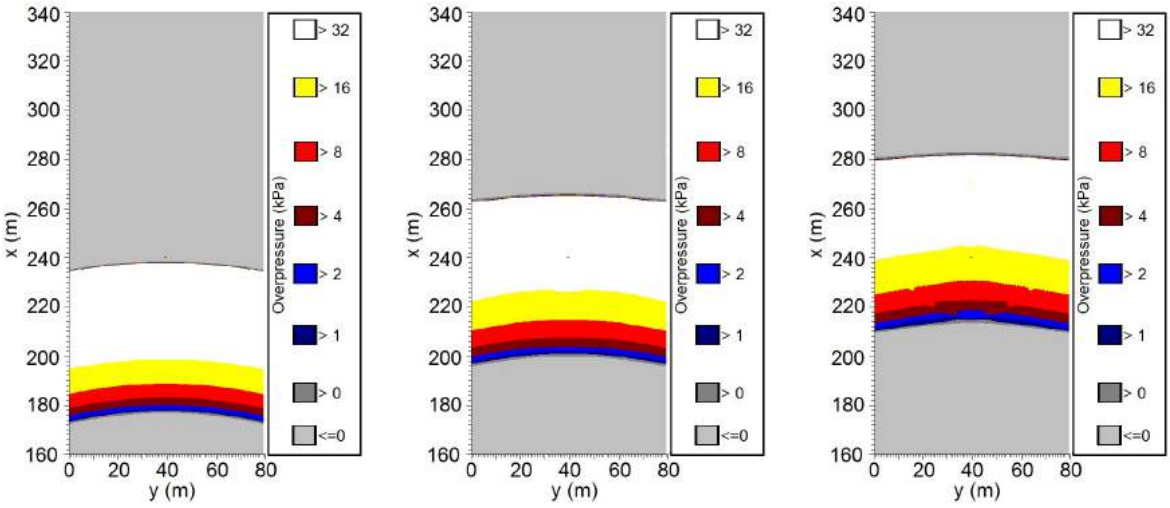

(a) 266ms (b) 324ms (c) 360ms

Figure 5.33: Air3D model of **A** panel in the 4.9m section of the ABT (MW1, MW2 & BWL1A)

The shape of the blast wave, throughout its propagation, remained accurate, with the appropriate amount of curvature; furthermore, no distortion of the blast due to the reflective or transmimsive boundaries at the domain extents was recorded around the structure, suggesting the model was both reliable and accurate. At 324ms, shown in Figure 5.33b, the structure was visible within the white region of high pressure and reflections from the structure were also visible, propagating upstream into the yellow region of lower pressure. By 360ms, Figure 5.33c, the reflection was clearly visible, as it expanded through the regions of lower pressure. Due to the size difference between

the blast wave and the structure, the blast structure interaction cannot be as clearly determined as in the short duration case, although the effects can be determined through examination of the loading points.

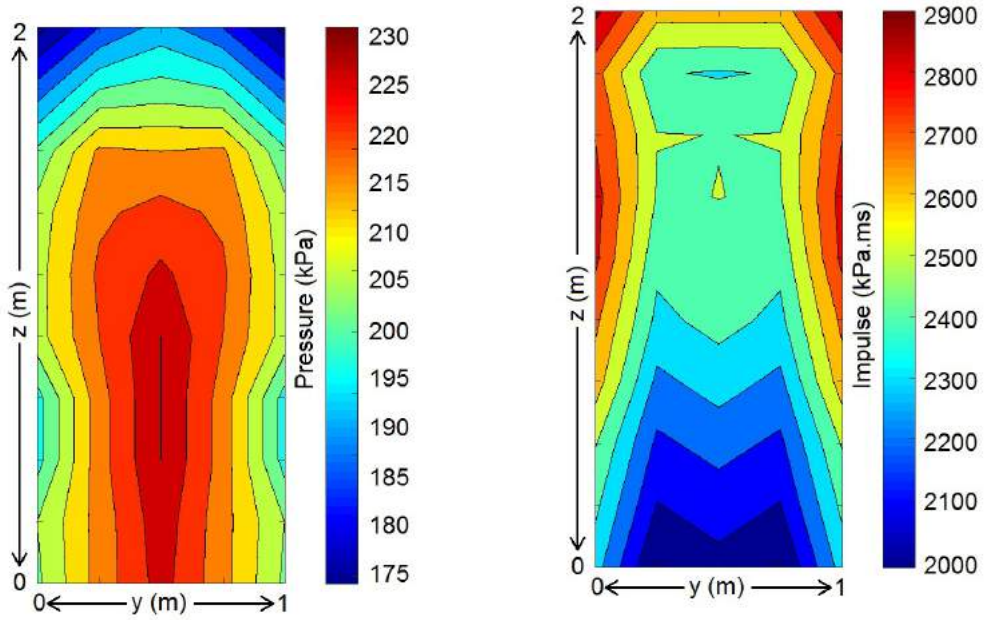

(a) Pressure (b) Impulse

Figure 5.34: Air3D net loading regions of an **A** in the 4.9m section of the ABT

Peak values of pressure and impulse were taken from each of the monitoring points across both the front and rear faces of the structure and used to calculate the net pressure and impulse in the downstream direction at each of the monitoring points. The net, peak pressure and impulse loading regions are plotted in Figures 5.34a and 5.34b respectively. In comparison to the short duration case, the net pressure contours share more similarity with the pressure regions across the front face alone. This is due to the more uniform distribution of peak pressure on the rear face of the structure as a result of increased duration of the blast wave. Contrary to the short duration case, the net impulse loading regions show the lowest impulse transmitted towards the base of the structure, increasing towards the upper, outer edges. These contours were primarily due to the loading across the rear face, with higher impulses recorded towards the base of the structure.

The impulse loading regions are less important in the long duration case, especially for individual base panels as the experimental results showed significant damage after

50ms, approximately 25% of the total loading duration in the 4.9m section of the ABT. In the case of MW1, MW2 and BWL1A, the structures had already begun to translate in addition to multiple crack formation, significantly reducing the effect of reflected pressure. As the peak values on both the front and rear faces of the structure occur within this time period, the net peak reflected pressure regions can still dictate specific crack formation across the structure.

Similar CFD models were conducted for each structure instrumented in the experimental trials, assessing the blast structure interactions and loading regions. As the structures in the 10.2m section of the ABT were on average larger and presented more complex interactions with the blast wave, the cell size was reduced to 0.1m for each model, increasing the problem size to 1.75×10^8 cells and the run time to approximately 55 hours. Additional models were conducted to investigate the effects of certain experimental parameters, including blast in-fill, structural symmetry and structure proximity.

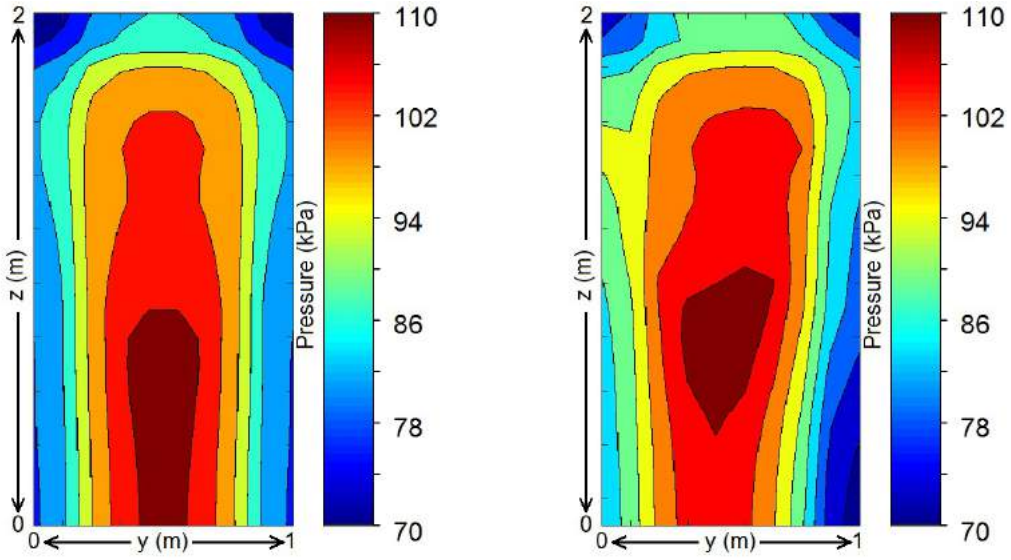

(a) Ideal (b) Experimental conditions

Figure 5.35: Air3D net peak reflective pressure region of an **A** panel in the 10.2m section of the ABT (BWL2C)

In test BWL2, structures BWL2B and BWL2C, **B** and **A** panels respectively, were separated by a relatively small lateral distance of 1m, or 1 structural dimension for each structure. As discussed in Chapter 2, the blast requires approximately 8 structural

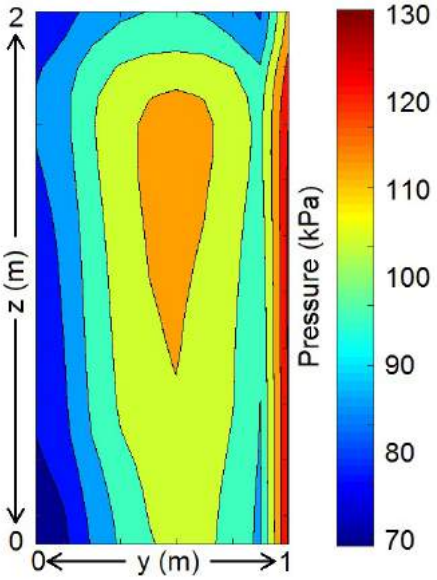

(a) Ideal (blast normal panel)

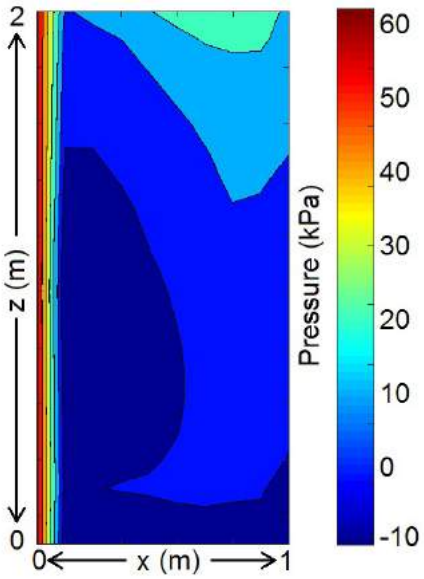

(b) Ideal (side panel)

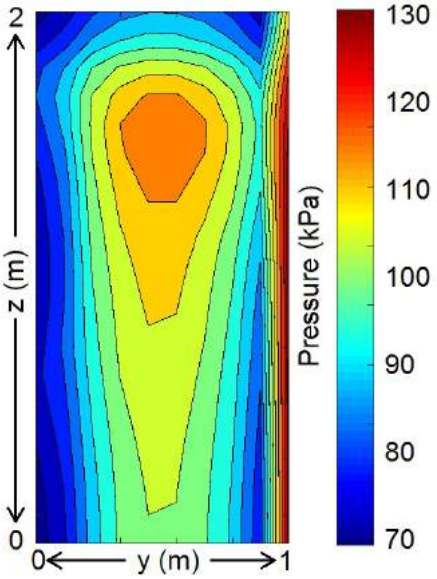

(c) Experimental conditions (blast normal panel)

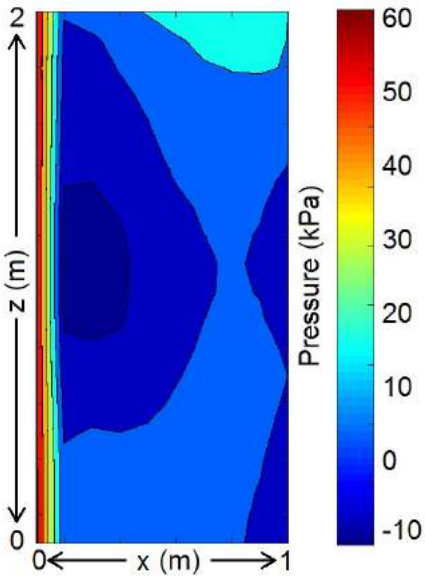

(d) Experimental conditions (side panel)

Figure 5.36: Air3D net peak reflective pressure region of a **B** panel in the 10.2m section of the ABT (BWL2B)

dimensions in the appropriate direction to return to normal flow [11]. The loading of simple CFD models of the **A** and **B** panels subjected to 200T at 250m would thus differ from the actual experimental conditions. To determine the breakage and debris distribution of each panel under ideal conditions, the benchmarking of the AEM model must be conducted with input closely matching the experimental conditions. Figure 5.35 illustrates the net peak reflected pressure loading regions of a CFD model of an **A** panel in the 10.2m section of the ABT, under ideal and experimental conditions.

The ideal case, presented in Figure 5.35a, displays the expected symmetrical distribution of load; however, under experimental conditions, with a **B** panel position 1m to the side, as illustrated in Figure 5.35b, the distribution of load is distorted. The net loading of the left side of both structures is similar as there was no interference of the blast transmitted from this direction. Lower pressures were observed towards the base of the structure on its right side in the presence of the **B** panel, most likely due to strong vortices forming between the two structure as a result of blast clearing from both sides.

Figure 5.36 shows the net peak reflected pressure regions of both the front and side panels of the **B** panel, in both the ideal case and under experimental conditions. For both the front and side panels, the loading regions are slightly distorted, due to the clearing effects of the blast and the loading of the inner faces. The loading on the downstream face of the blast normal panel increases in the presence of the neighbouring **A** panel, whilst the pressure on the inner face of the side panel decreases. As magnitude of the net load remains constant and the change in loading contours is small, the effect is most likely small.

5.2.2 Applied Element Method

Accurately modelling the interaction of long duration blast and structures is a highly complex problem, with many more variables than the short duration case. Due to scheduling of the experimental trials and the added complexity of the modelling, long duration AEM models have no been fully established; however a description of the modelling techniques are detailed in this section.

The loading of the structure can be considered as two separate loads, the breakage load and the distribution load. The breakage load is determined as the amount of impulse transmitted to the structure until no further damage occurs, that is until no further cracking occurs. The loading time for the specimens tested in the ABT was between 50-100ms, the time required for maximum cracking to occur, yet for the structures to retain their blast normal profile. During this time, the reflected pressure is the primary force acting on the structure and so this load would be applied to the structure in a similar manner to the short duration models. The loading regions would be assessed in terms of the impulse applied to the structure over the initial 50-100ms loading period and applied to the AEM models.

Once the breakage load has been applied, a seperate loading scenario must be designed to model the debris distribution. This loading scenario presents the most complex problem, as the load applied to the fragments varies based on their velocity, orientation, size and the dynamic pressure and shock density of the blast wave. The load is relative to the dynamic pressure; however the load applied to each fragment is determined by the drag coefficient and relative velocity.

5.3 Summary

The high explosive modelling routine showed good agreement with the experimental trials. The CFD models presented an average difference of 15.1% and 3.12% compared to the target static pressure and impulse respectively, with a 13.9% and 10.9% difference compared to the recorded static pressure and impulse respectively from the WR1 trial. For long duration blast the 1D CFD results presented a 3% and 13% difference to the recorded static pressure and impulse. A sensitivity study was conducted to identify the domain and mesh sizes to achieve accurate results with a reasonable solver time.

CFD results were used to investigate the blast structure interaction and assess the average loading regions across the surface of the structures. The CFD gauge data was averaged across the similar loading regions and applied to the AEM models. A sensitivity study was conducted to identify the best combination of internal material parameters

within ELS which exhibited the most accurate breakage patterns, collapse mechanisms and ground impact fragmentation, as presented in Table 5.4.

The breakage mechanisms of the AEM models showed good agreement with the experimental trials; however as the positive phase duration and impulses were low, the direction of collapse for each structure was highly unpredictable and would most likely differ with a repeat experiment. Overall the AEM models showed promising results, presenting good prediction of breakage patterns and crack formation, accurate predictions of ground impact fragmentation and good predictions of size and density regions of the resulting debris distributions.

Chapter 6

Experimental Analysis

The experimental results, presented in Chapter 4, illustrated the quantity of comparable data across all stages of structural response, including but not limited to crack formation time, crack patterns, fragmentation velocity, x,y,m debris distributions and individual brick position. The following chapter compares the results from specific structures to highlight correlations in the experimental data.

6.1 Pressure - Impulse Damage

As discussed in Chapter 1, damage predictions are often categorised using pressure-impulse curves, in which the curve typically represents structural failure. Across all of the experimental trials conducted, seven different pressure-impulse combinations were tested, one for each of the five pressure radials from the Windrush Arena trials and one for each section of the ABT. The **A** panel was the only structure tested for each of these different $P - I$ combinations and as such, the maximum longitudinal debris throw of each **A** panel is plotted in Figure 6.1a. The position of each point shows the pressure and impulse of each of the blast loads, with the size of the point representing the maximum longitudinal throw distance.

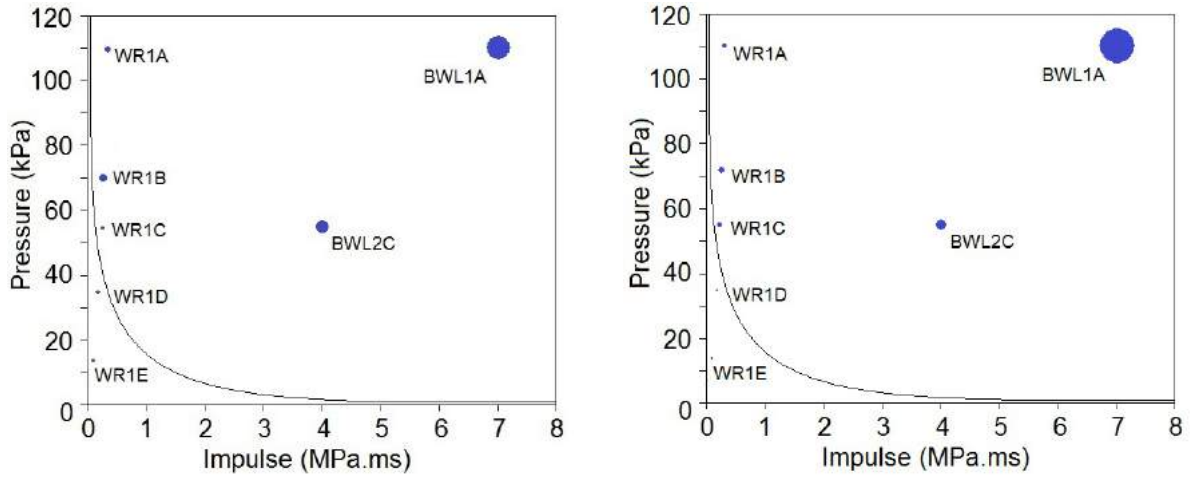

(a) Relative to maximum longitudinal (x) distance (b) Relative to maximum area

Figure 6.1: Pressure impulse ($P - I$) plot of tested **A** panels, indicating relative distribution sizes and approximated structural failure limit

The curve illustrates the approximate limit of structural failure of an **A** panel, given that structures WR1A, WR1B and WR1C all failed, whilst structures WR1D and WR1E did not. The curve has the relation

$$P = \frac{C}{I} \tag{6.1}$$

where C is an arbitrary constant which cannot be accurately determined, as the only information obtainable from the experimental results is that it must pass through the region 161.3kPa.ms$<$ I $<$234.4kPa.ms and 29.1kPa$<$ P $<$ 59.5kPa. These limits are the highest values of pressure and impulse recorded on the radial corresponding to structure WR1C and the lowest values of pressure and impulse recorded by structure WR1D. The actual size of structures WR1D and WR1E is zero, considering there was no longitudinal distribution. Structures WR1A, WR1B and WR1C are located just beyond the approximated failure curve, with their maximum longitudinal throw distances were 4m, 7m and 2.5m respectively. The distribution of structure BWL2C, located in the 10.2m section of the ABT, was 14m; however in the absence of obstructions is predicted to be 16-18m. Finally, BWL1A and MW2, both in the 4.9m section of the ABT showed maximum throw distances around 50m. As the debris is distributed in both x and y, the relative

sizes of the debris distributions increases when comparing area, an important parameter when considering any potential hazard caused by debris distribution. Figure 6.1b plots the same **A** panels on a $P - I$ diagram, illustrating their respective areas by the size of the plot point.

Structures BWL1A and MW2 were not collected with a lateral distribution, therefore the maximum rectangular area covered was estimated by comparison with BWL2C. The lateral distribution of BWL2C extended from -2m$< y <$2m, giving a total lateral distribution of 4m and a longitudinal to lateral distribution ratio of 2:7 and a total obstructed area of 56m. Using the same ratio, the maximum rectangular area covered by BWL1A would be 175m^2. It should be noted that the majority of this region would be completely empty, although within this region the debris would still pose both potential collision hazards and infrastructure obstruction.

The impulse recorded in the long duration trials was significantly more than the impulse recorded in the short duration trials, meaning on this scale the impulse applied to each structure from the arena trials was approximately equal. This results in each of the three structures which failed located just beyond the approximate failure limit. Again, compared to the area covered by the structures subjected to long duration blast loads, relative area covered by the debris of the structures subjected to short duration blast loads is approximately equal. To compare the relationship between the blast parameters and maximum area covered by the debris, Figure 6.2a parameterises the blast wave in terms of $P \times I$, a linear representation of a $P - I$ diagram.

As the area covered is calculated as a product of the maximum longitudinal and lateral extents of the debris, or final state, Figure 6.2a shows a comparison between the initial and final conditions. Although there is a limited amount of available data, restricted by the available values of $P \times I$, a linearly increasing correlation is present. As the short duration results all fall slightly above the $P - I$ failure curve, the results are clustered in the lower left hand corner of the graph. Figure 6.2b plots the blast parameters on a $\log_{10}$ scale to examine the log-linear relationship and also illustrates a correlation. Once the modelling routine has been established, the $P - I$ range can be increased and any

correlation can be robustly confirmed, for each panel type.

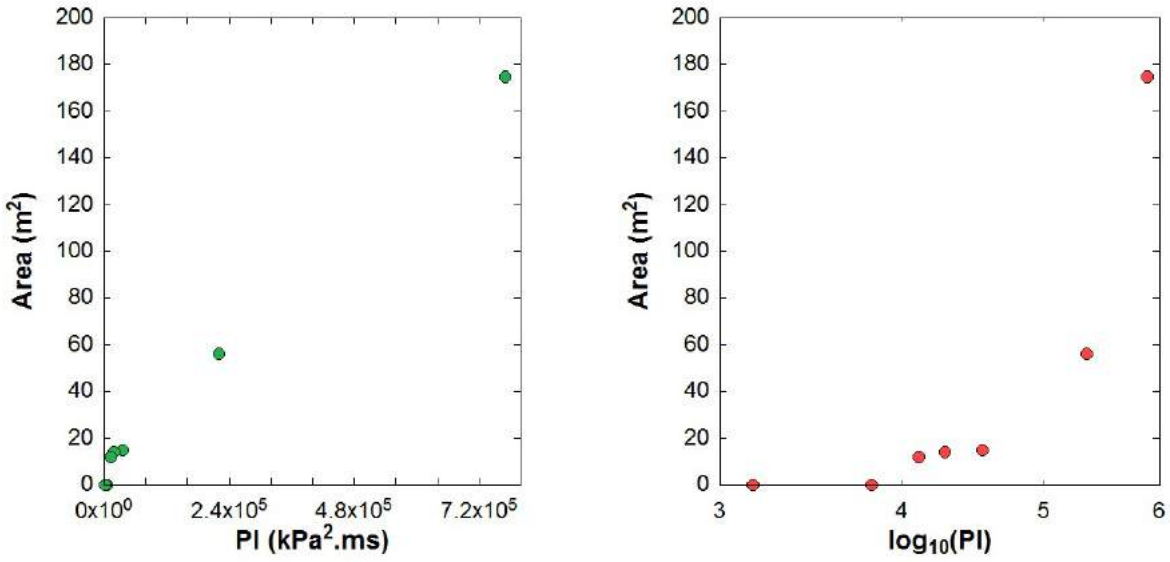

(a) Area with respect to $P \times I$

(b) Area with respect to $\log_{10}(P \times I)$

Figure 6.2: Maximum rectangular area obstructed by debris as a function of the blast load for the **A** panel

Whilst the reflective pressure is primarily responsible for the breakage mechanisms and initial fragmentation, the experimental data indicates the effect of the positive phase duration and hence impulse on initial fragmentation. Figures 6.3a and 6.3b display the number of initial fragments produced from the **A** and **B** panels respectively, when subject to the various experimental blast loads.

In both cases the initial fragmentation of structures in the ABT was significantly larger than those on the Windrush arena, due to the increased duration. For each matching pressure, the fragmentation of the **B** panel was higher than that of the **A** panel. This was potentially due to the increased mass and surface area of the structure. To examine the effect of surface area on the initial fragmentation, Figure 6.4 plots the initial fragmentation of every structure tested with respect to the number of panels from which they were constructed.

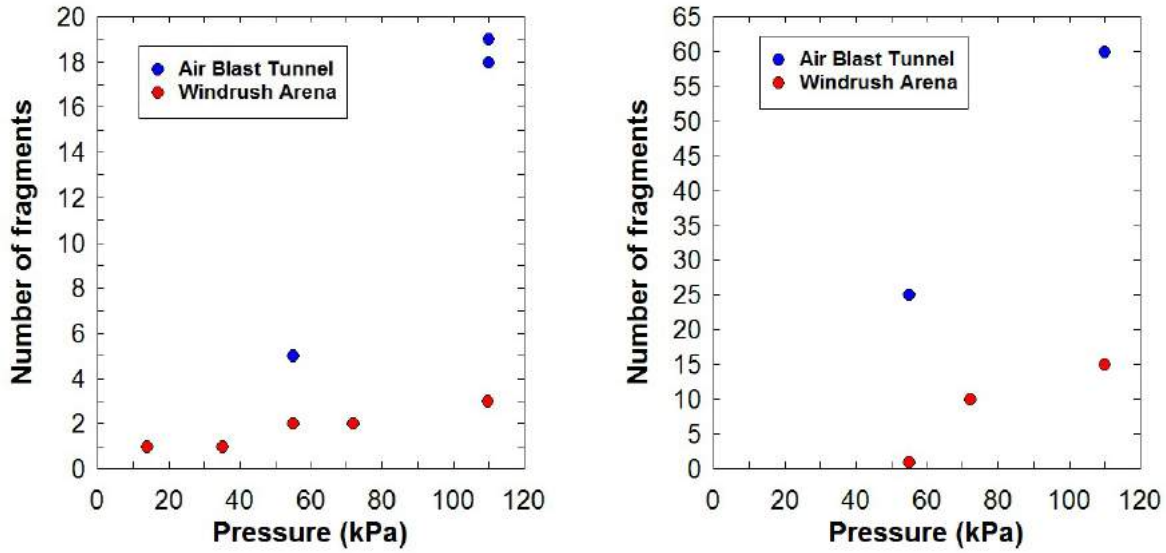

(a) **A** panels (b) **B** panels

Figure 6.3: Initial fragmentation with respect to peak static overpressure

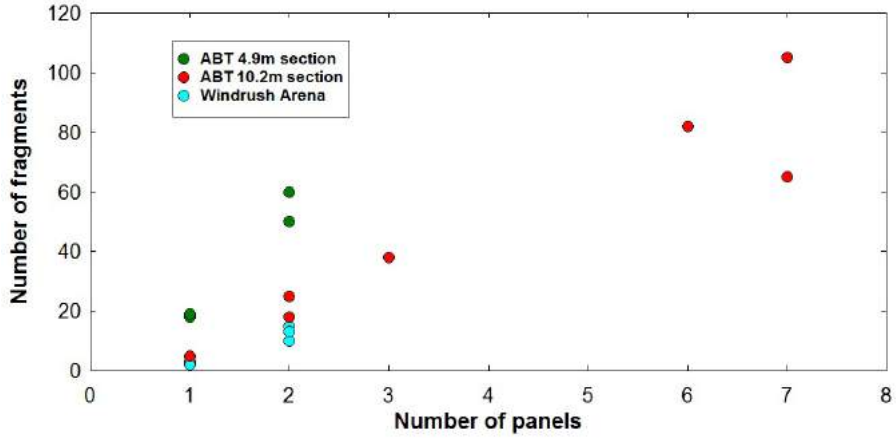

Figure 6.4: Initial fragmentation of all structures with respect to size of structure

The structures tested in the 4.9m section of the ABT and the Windrush arena only instrumented geometries of one or two panels, which was not enough to suggest any strong correlation. In the case of the 4.9m section of the ABT, the two **A** panels, MW2 and BWL1A, show almost identical initial fragmentation, whilst the **B** and **D** panels which differ in geometry show a 20% difference in the number of initial fragments. Unlike the two data sets from the ABT, the blast parameters of the Windrush arena data set vary between plot points; however, when compared in magnitude to the blast parameters

of the ABT, the Windrush parameters are all approximately equal and thus plotted as one singular group. The largest data set from the 10.2m section of the ABT shows a linearly increasing correlation between number of initial fragments and number of panels, despite the geometry of the structure. The larger enclosed structures show a big difference between two similar geometries, almost a 50% difference in fragmentation which suggests that with additional data this relation would not hold. A linear correlation is expected between structures of the same geometry, such that

$$N_f \propto n(\mathbf{P}) \tag{6.2}$$

where N_f is the number of initial fragments and $n(\mathbf{P})$ is the number of panels in panel type $\mathbf{P}$.

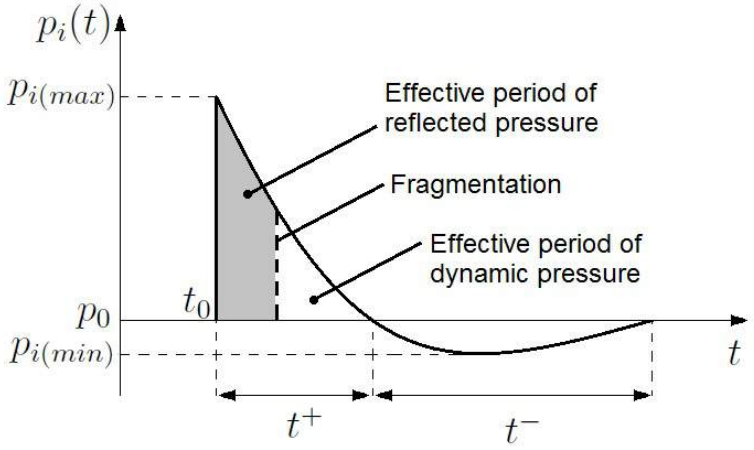

Figure 6.5: Friedlander curve representing the effective duration of the reflected pressure

Although the primary purpose of the short duration trials was to benchmark the numerical methods used for the computational analysis, the data also provided direct comparisons into the effects of blast impulse and duration. The pressure impulse diagrams plotted in Figures 6.1 illustrate the magnitude of the effect of impulse on debris distribution, yet Figure 6.3 illustrates the effects of impulse on breakage. The **A** panel tested on the arena showed 1 crack formed at 55kPa and 2 cracks formed at 110kPa, compared to 4 cracks forming at 55kPa and ≈17 forming at 110kPa in the ABT, indicating that the duration of the blast load has a significant effect on the breakage mechanism.

The duration throughout which the reflected pressure acts upon the structures is approximately equal to the time taken for the initial fragments to become unrestrained, beyond which the response is dictated primarily by the drag wind associated dynamic pressure, illustrated by Figure 6.5.

6.2 Panel Geometry & Debris Distribution

The purpose of the 'Base Panel' model as outline in Chapter 1, is to allow for fast predictions of the debris distribution of any hypothetical masonry geometry subject to given blast parameters. Within the current experimental data set, the largest number of geometries were tested in the 10.2m section of the ABT. Within the 10.2m section, the simple configurations tested were **A**, **B**, **AA** and **AB**. Due to the side wall of the ABT, the lateral debris distributions were obstructed, limiting the potential for analysis in the absence of a computational modelling routine. Using the simplified version of the base panel model, illustrated in Figure 3.3, the number of panels is reduced to two, i.e. blast normal and blast parallel. This approach increases the number of individual blast normal panels in this particular data set from four to six, allowing for some additional analysis to be conducted based on the panel configuration. Comparing the longitudinal debris data from each of these blast normal panels, the distribution patterns based on positions within the composite structure demonstrates the ability of the base panel model to predict debris distributions.

Figure 6.6 compares the longitudinal brick distributions of the outer most blast normal panels of structures BWL1B (**AB**) and BWL3B (**AA**). It should be noted that either of the blast normal panels from structure BWL3B could, under ideal circumstances, be used for this comparison. Both the distributions of 'pale' bricks from structure BWL1B and green bricks from structure BWL3B were obstructed due to the lighting array, whilst the red bricks from structure BWL3B were not. For this reason, the green bricks are used for comparative purposes due to the similar experimental conditions.

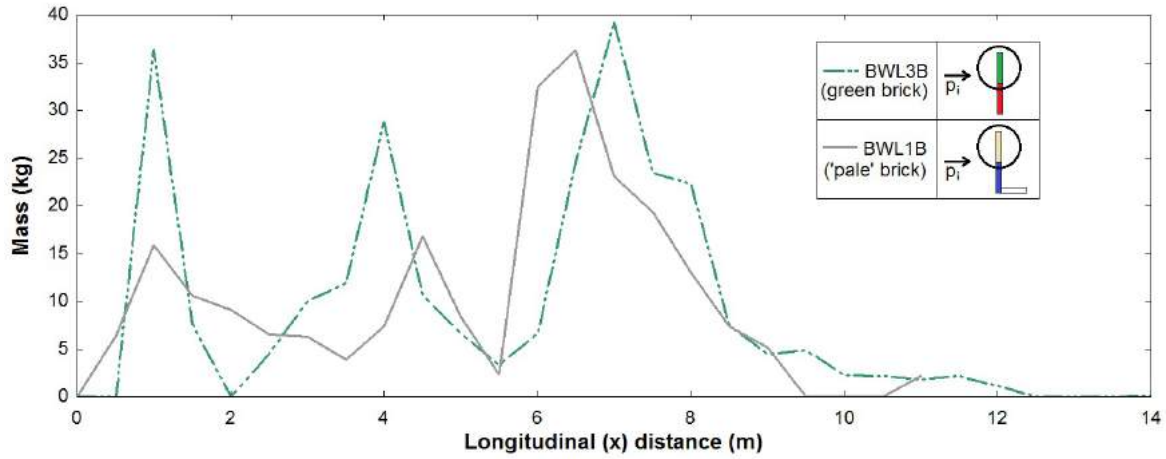

Figure 6.6: Longitudinal brick distribution of the outer blast normal panels from structures BWL1B and BWL3B

The general shape of the distributions show similarities, with areas of high density located at approximately x =1m, x =4m and between 6m< x <8m. The difference between the two distributions was larger within the first 4m, with sharper more defined peaks recorded in the distribution of green bricks from structure BWL3B. The absolute difference between the two curves ranges from 0kg to 20.5kg across the entire distribution. The difference of 0kg occurs at both extents of the distribution with 0kg recorded in each bin for each structure, whilst the peak distribution occurs at x =1m, corresponding to the larger peak of structure BWL3B. The mean bin mass across the entire distribution was 8.0kg for structure BWL1B and 9.0kg for structure BWL3B, excluding the extents of the distributions, the average bin mass increased to 10.1kg and 11.4kg respectively. The mean differences across these two ranges were 5.7kg and 6.8kg respectively, meaning that the mean difference in bin mass was approximately 65% of the mean bin mass.

Such a large mean difference between the two curves does not suggest a strong mathematical correlation; however visual inspection clearly shows strong similarities between the two distributions. Taking the median of the differences between the two sets of data points gives a value of 2.3kg, across the entire distribution and 3.9kg excluding the extents. This reduces the mean difference in bin mass to 27% across the entire distribution and 37% excluding the extents. This lower difference suggests an improved mathematical correlation, but does not account for the similar pattern between the two curves.

This particular type of analysis only compares the absolute distributions within each bin, for identical peaks separated by one bin, there would be zero correlation. To assess the similarity in the distribution patterns, Figure 6.7 displays the cumulative normalised brick mass distributions of the outer most blast normal panels of structures BWL1B and BWL3B.

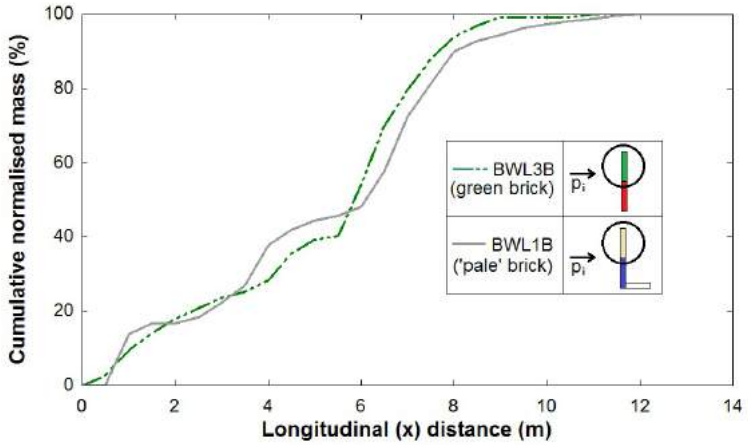

Figure 6.7: Cumulative longitudinal brick distribution of the outer blast normal panels from structures BWL1B and BWL3B

Whilst the ideal mass of each panel would be identical, the mass of bricks used to construct each of the panels was not identical due to experimental error; furthermore, during the data collection process, the mass of each fragment is rounded and some fragment types become indistinguishable, leading to a discrepancy between the total recorded post-shot masses of each of the structures. For this reason, the cumulative masses of each structure have been normalised to 100% of the overall mass, allowing for a clear comparison of the distribution patterns. Initial visual inspection shows a much closer correlation between the two curves as the separation is a function of the overall mass of the structures. The minimum and maximum differences between the two curves were 0% and 12% respectively, with the mean difference being 3%. Removing the outer extents increases this difference to 4%.

Both the actual and cumulative normalised mass distributions show a strong correlation between the two panels, suggesting that the similarities in their position within the overall structure offers a strong contribution to the shape of their distributions. The

contribution of initial position can be further examined by comparing blast normal panels connected to a corner joint. The red bricks of the blast normal panel of structure BWL2B, a **B** panel, are in a similar position to the blue bricks of structure BWL1B, a **AB** panel. The longitudinal brick mass distributions of these two panels, i.e. the red blast normal panel of structure BWL2B and the inner blue blast normal panel of structure BWL1B, are plotted in Figure 6.8.

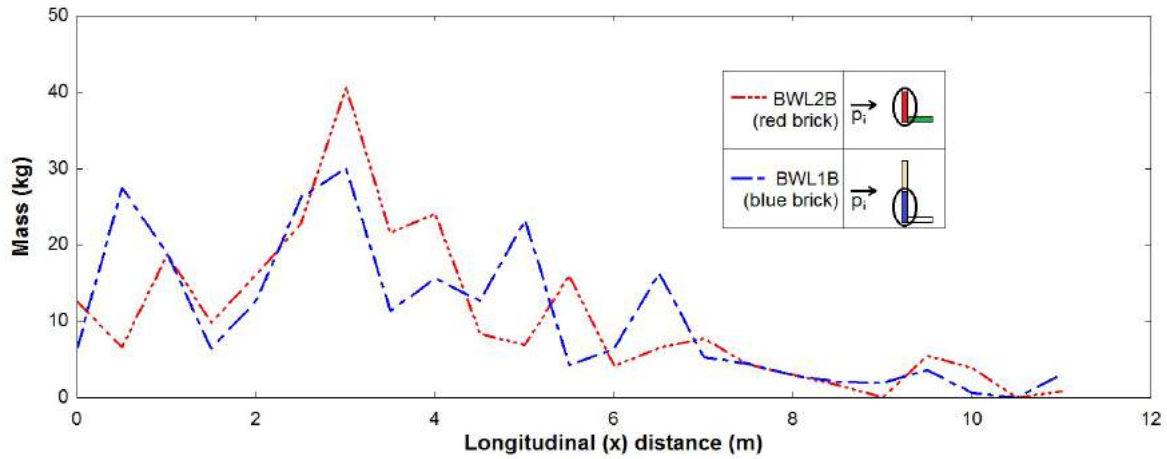

Figure 6.8: Longitudinal brick distribution of the inner blast normal panels from structures BWL1B and BWL2B

The general shape of both mass distributions show strong similarities, with an initial peak located in the first 2m, the highest density region located between 2m$< x <$4m and small peaks of similar magnitude beyond $x =$4m. Using the same statistical method applied to the previous distribution curves, the difference between the two curves ranges from 0kg to 16.3kg. Unlike the previously compared panels, the extents of both distributions contain higher quantities of mass and cannot be neglected during the analysis. The mean difference between the two distributions was 5.4kg, with both curves presenting mean bin masses of 10.5kg. This results in the mean difference in bin mass to be 51% of the overall bin mass, which, whilst lower than the previous set of curves, does not suggest a strong mathematical correlation. Taking the median difference between the two distributions, 3.4kg, the mean difference in bin mass reduces to 32%.

The cumulative normalised mass distributions of the two panels are plotted in Figure 6.9. It should be noted that whilst the cumulative masses are normalised, the absolute

recorded difference in total mass of the two structures was 70g, or 0.03%. The difference in the cumulative normalised distributions ranged between 0.02% and 7.4%, with a mean difference of 3%.

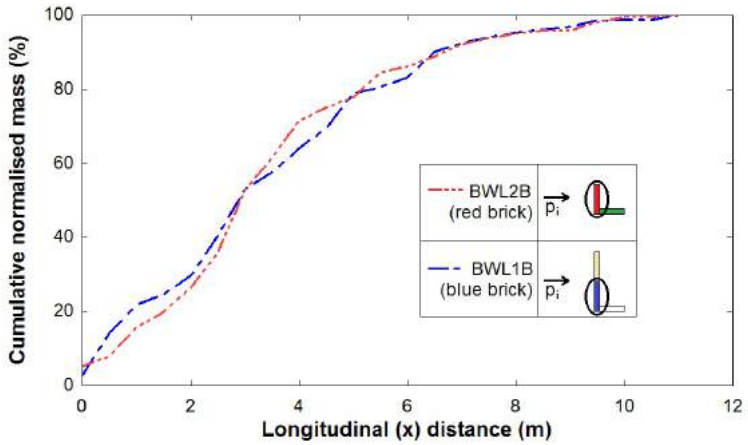

Figure 6.9: Cumulative longitudinal brick distribution of the inner blast normal panels from structures BWL1B and BWL2B

It should be noted that the inner blast normal panel from structure BWL1B was attached at both sides, whilst the blast normal panel from structure BWL2B was not. This could suggest that the behaviour of a blast normal panel is strongly determined by its proximity to a corner joint. To highlight the differences and similarities in the debris distributions of the blast normal panels, Figure 6.10 displays the cumulative normalised distributions for each of the blast normal panels of unenclosed structures in the 10.2m section of the ABT. Whilst plotting cumulative normalised distributions by nature reduces the magnitude of the difference, the difference between curves with no positional similarities is significantly larger. For example, the mean difference between BWL2C, the unrestrained **A** panel and the blast normal panel of BWL2B, a **B** panel, was 16.5%, five times larger than curves showing a correlation.

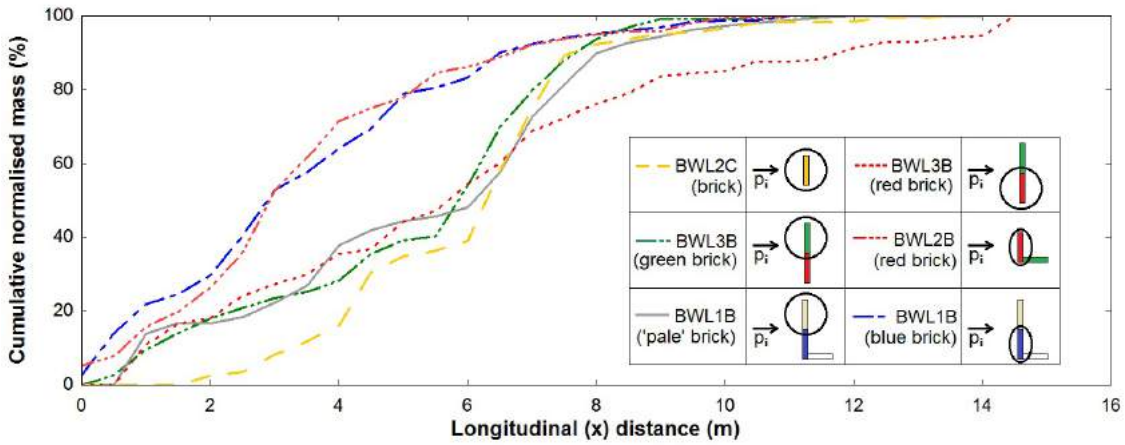

Figure 6.10: Cumulative longitudinal brick distribution all blast normal panels from the small composite panels in the 10.2m section of the ABT

The curve representing BWL2C, the unrestrained **A** panel, shows some correlation to the outer blast normal panels of structures BWL1B and BWL3B. In the absence of lateral restraint, BWL2C showed a much lower distribution within the first 2m, however after x =4m the distribution was similar to the blast normal panels connected to additional blast normal panels. Conversely, the distribution of red bricks from structure BWL3B, the **AA** panel, shows a strong correlation to the other blast normal panels in similar geometrical positions within the first 6m. Beyond 6m, the distribution becomes more uniformly distributed over a larger distance, resulting from the absence of the obstruction caused by the lighting array. These results can be used to predict the distributions of each small composite panel in the absence of the lighting. If the unrestrained **A** panel followed the same distribution pattern beyond 6m, the maximum distribution would be projected to approximately 18m.

The distance of a blast normal panel from a corner joint varies the maximum throw distance and more precisely, the regions of high density. The cumulative distributions show a strong correlation between panels with similar boundary conditions; furthermore, the cumulative normalised distributions present a range between the most restricted and unrestricted blast normal panels, suggesting the for all unenclosed blast normal panels, their cumulative normalised distributions would fall within this range. Figure 6.11 illustrates a prediction of the potential range the longitudinal cumulative normalised mass

distributions of blast normal panels can occupy.

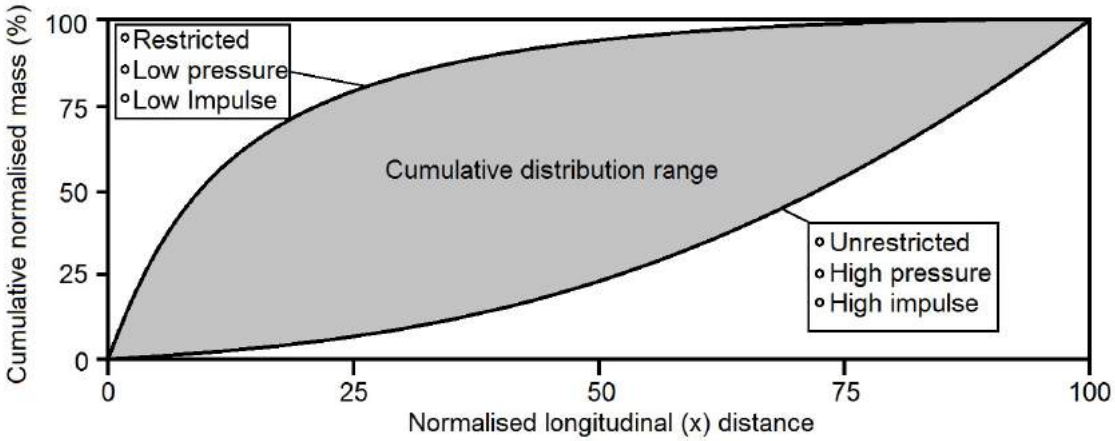

Figure 6.11: Predicted range of longitudinal cumulative normalised mass distributions of blast normal panels

Three different geometries were tested in the 4.9m section of the ABT, the **A** panel, the **B** panel and the **D** panel. The **A** and **B** panels were also tested in the 10.2m section of the ABT and the Windrush arena trials, allowing for a closer investigation of the effects of both pressure and impulse into the breakage and debris distribution mechanisms.

The longitudinal debris distributions of structures MW2, BWL1A and BWL2C, the **A** panels tested in the ABT, are displayed in Figure 6.12a, which shows no similarities between the debris distributions when subject to the different blast parameters. By normalising the distributions, plotted in Figure 6.12b, a similar distribution pattern is present between all three distributions. Each curve displays a moderate peak between 20-40% of the peak distribution, all of which correspond to a large lower fragment. The peak mass in this region was larger for structure BWL2C as the initial fragmentation was lower and hence this fragment was larger. Each of the distributions also show large peaks between 50-75% of the maximum distribution, corresponding to larger fragments created higher within the structure. It should be noted that this region also corresponds to the obstructions caused by the instrumentation columns and the lighting array. In the absence of these obstructions, the maximum distributions are all expected to be approximately 10% larger and more uniformly distributed over the latter half.

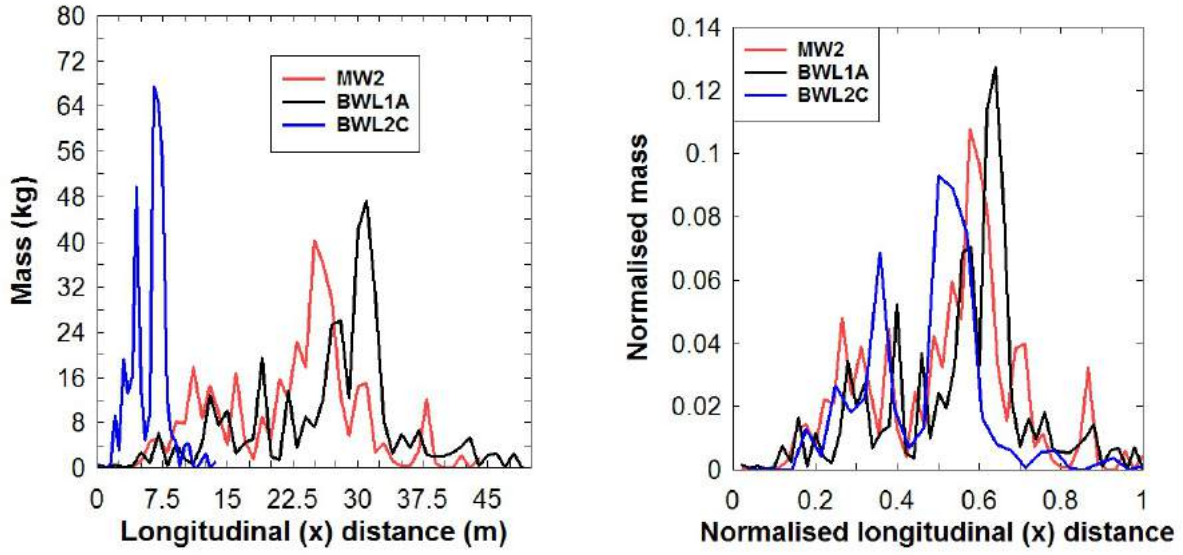

(a) Absolute distribution (b) Normalised distribution

Figure 6.12: Longitudinal (x) debris distributions of the **A** panels tested in the ABT (MW2, BWL1A and BWL2C).

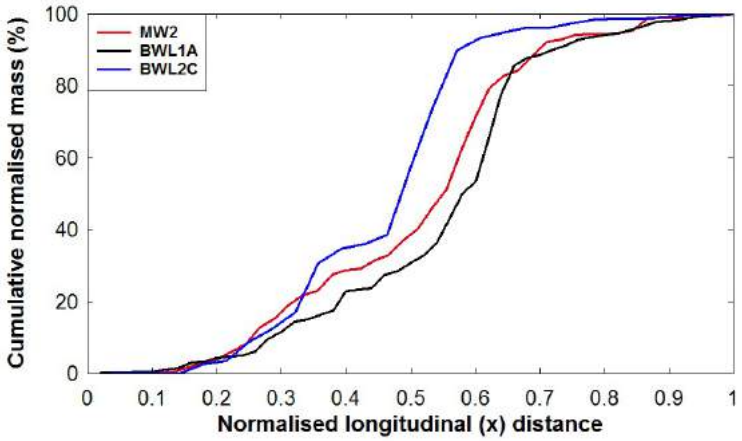

Figure 6.13: Cumulative normalised longitudinal (x) debris distributions of the **A** panels tested in the ABT (MW2, BWL1A, BWL2C).

The cumulative normalised longitudinal mass distributions of the **A** panels tested in both sections of the ABT are displayed in Figure 6.13. It should be noted that trial BWL1A is an effective repeat of trial MW2, yet the cumulative normalised distributions show as much variance as previous comparisons blast normal panels in similar geometric positions. The variance between these two trials is expected to be larger as the distance over which the mass is distributed is three times large, decreasing the probability of

finding a particular mass within any particular bin. The peak difference between MW2 and BWL1A was 18% of the overall mass with the mean difference between the two curves as 4% of the overall mass. The distribution of structure BWL2C is closer to that of structure MW2, with a peak difference of 32% and a mean difference of 6%, compared to a peak difference of 43% and a mean difference of 9% to structure BWL1A. Comparing structure BWL2C to the mean curve of MW2 and BWL1A, the peak and mean differences are 37% and 7% respectively.

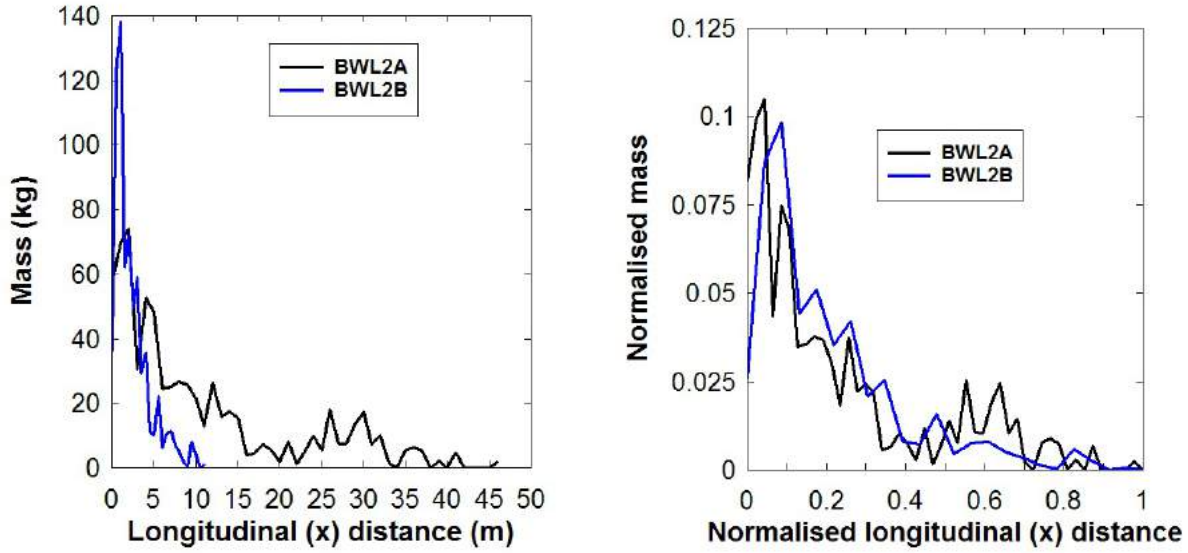

(a) Absolute distribution (b) Normalised distribution

Figure 6.14: Longitudinal (x) debris distributions of the **B** panels tested in the ABT (BWL2A and BWL2B).

The absolute distributions of BWL2A and BWL2B, the **B** panels tested in the 4.9m and 10.2m sections of the ABT respectively, are plotted in Figure 6.14a, showing no correlation between the two distributions. Figure 6.14b displays the normalised distributions of both **B** panels, showing a clearing correlation between the two curves, suggesting that the distribution pattern as a function of the maximum debris throw distance is maintained despite the blast parameters. For both distributions, the mean bin mass was 0.02, 2% of the overall mass, with a peak difference of 0.056, 5.6% of the overall bin mass and a mean difference of 0.009, 0.9% of the overall bin mass, or 43% of the mean bin mass. The cumulative normalised distribution, displayed in Figure 6.15, shows a good correlation

between the two curves, with a peak difference of 10% of the overall mass and a mean difference of 3% across the entire distribution.

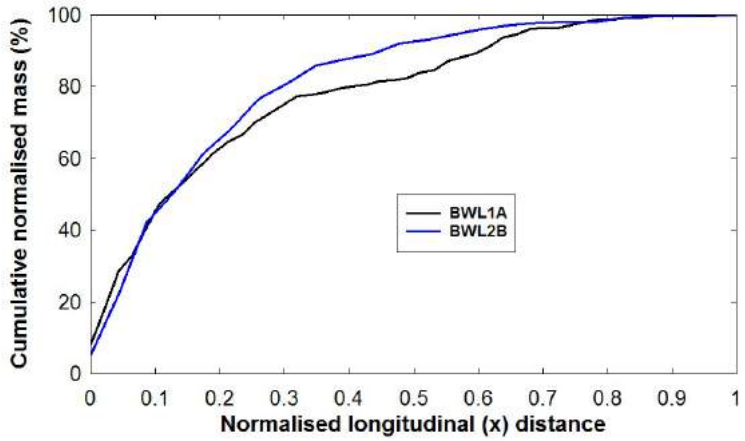

Figure 6.15: Cumulative normalised longitudinal (x) debris distributions of the **B** panels tested in the ABT (BWL2A, BWL2B).

It should be noted that the side panels of both BWL2A and BWL2B impacted the wall of the ABT, which whilst maintaining similar experimental conditions between the two structures, could potentially distort the results. Although the correlation is much clearer for the **B** panel, both the **A** and **B** panels maintain a similar distribution pattern as a function of maximum throw distance for the blast parameters of both the 10.2m and 4.9m section of the ABT.

The longitudinal distributions of all of the unenclosed structures tested in the ABT are displayed in Figure 6.16. As previously mentioned, in the absence of obstructions, the peaks at 7m in the 10.2m section and 31m in the 4.9m section are expected to be relatively uniformly distributed and the maximum distance is expected to increase. Taking the peak mass recorded at any point of any structure at all points represents the highest density distribution recorded in both sections of the ABT.

In both the 10.2m and 4.9m sections, the first 25% of the distributions present the areas of highest density, due to the corner joints and side panels. In the absence of obstructions, the density is expected to slowly decrease between 25%-100% of the overall distance. Figure 6.17 presents a prediction of the maximum distribution density indicating the relative obstruction caused by debris for unenclosed structures. The longitudinal

distribution is normalised and plotted between 0-100% as the distribution varies depending on the initial blast parameters, p_i & I_i, and the structural geometry, G. The density will be a function of both the initial mass, m and the structural geometry, G. For each of the small panels tested, the vertical height of the distribution rarely, if ever, exceeded 0.1m, the width of a brick, whilst the enclosed structures presented vertical piling up to 1m high. As expected, this suggests that larger structures with higher initial mass present higher density debris distributions.

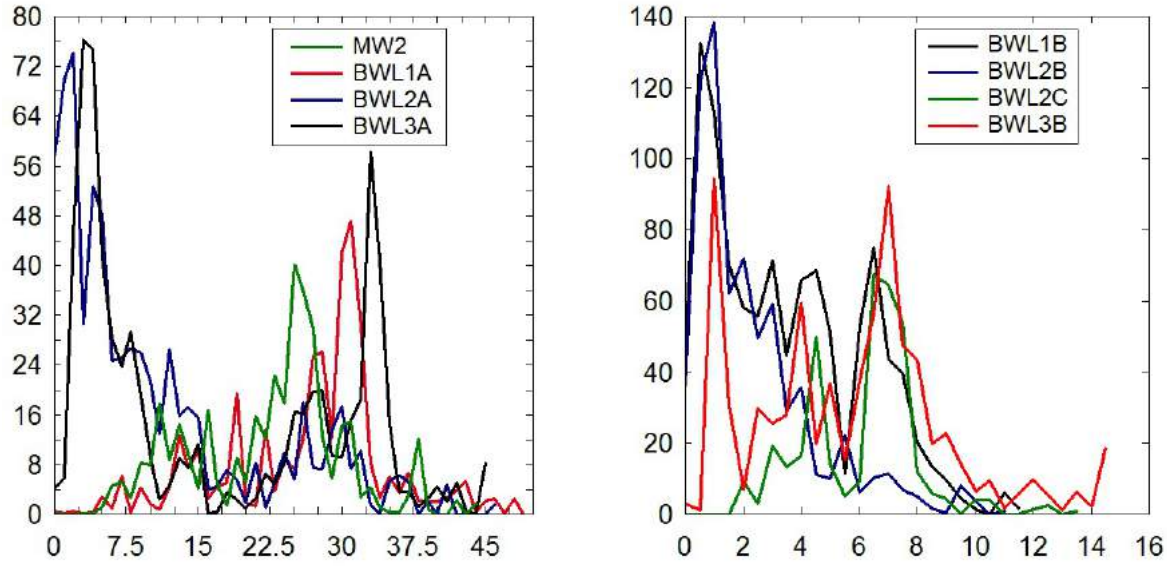

(a) 4.9m Section (b) 10.2m Section

Figure 6.16: Longitudinal debris distributions of small panels tested in the ABT

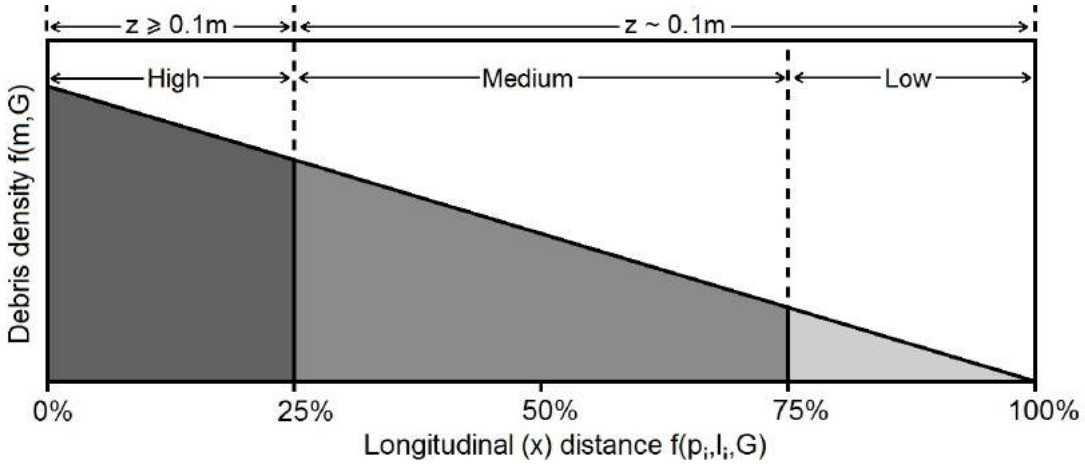

Figure 6.17: Longitudinal debris density prediction as a function of structural geometry and blast parameters

Structures such as the **A** panel do not follow the density distribution displayed in Figure 6.17 as the mass is relatively evenly distributed; however, the relative density of the debris distribution is small compared to that of a composite structure. Figure 6.17 therefore represents a conservative approximation of the areas of high density, defined as potential piling above 0.1m, with medium and low density piling with a vertical height below 0.1m. In its current form, this conservative approximation illustrates the regions in which the distribution should not exceed 0.1m in vertical height, indicating the outer extents of the distribution as the low density region.

6.3 Summary

The experimental analysis showed similar longitudinal distributions of the blast normal panels located in similar positions within the composite panels. Whilst the individual distributions presented relatively large statistical differences, the cumulative distributions showed both good visual and statistical correlations. Following this, a normalised range was proposed in which all cumulative distributions for unrestrained blast normal panels would follow.

Correlations in the distance normalised debris distributions of individual geometries were also observed for different blast parameters. This results from the similarities in the breakage patterns which lead to similar areas of high density. Comparison of all debris distributions showed that the debris distribution could be conservatively described by a linearly decreasing debris with respect to longitudinal distance.

Overall, the experimental analysis highlighted the complexity of debris distributions and the limiting resolution to which they can be predicted, i.e. regions of specific density and maximum throw distance. The results also illustrate the potential of the base panel model to predict the distribution of debris based on such limitations. By observing the differences in density and maximum throw distance with respect to the panel position within a structure, the data provided by base panel distributions could be used to approximate the debris field produced by a large, full scale structure.

Chapter 7

Conclusions

The aims, as outlined in Chapter 1 where to:

1. Investigate the effects of structural geometry on the breakage of masonry structures subject to long duration blast

2. Investigate the effects of structural geometry on the debris distribution of masonry structures subject to long duration blast

3. Investigate the effects of pressure and impulse on the breakage of masonry structures subject to long duration blast

4. Investigate the effects of pressure and impulse on the debris distribution of masonry structures subject to long duration blast

The first aim was achieved through experimental trials, highlighting the specific breakage mechanisms of the **A** and **B** panels, which showed the same basic failure modes for all of the tested blast parameters, with the level of damage increasing with both pressure and impulse. Breakage of composite **AA** and **AB** panels agreed with the base panel hy-

pothesis, demonstrating the breakage of each half of the composite structures resembling the breakage of the individual panel type.

The second aim was also achieved, with experimental results showing correlations between the normalised distributions, for both the **A** and **B** panels, regardless of blast parameters; furthermore, the debris distribution of composite panels **AA** and **AB** showed similarities to the combined distributions of their individual members. As with the first aim, this supports the base panel hypothesis and illustrates its predictive capability.

The third aim, to investigate the effects of pressure and impulse on breakage was also achieved, with data revealing the peak reflected pressure to be the key parameter regarding both crack formation and the damage severity; however, a minimum breakage time was required to achieve maximum damage for a particular overpressure. Comparison of particular geometries subjected to long and short duration blast of matching overpressures showed entirely different levels of damage. It was therefore concluded that for a given structure, a particular breakage impulse is required to cause maximum fragmentation.

The final aim, to investigate the effects of pressure and impulse on debris was also achieved in a similar manner to the third aim. The experimental data from the short duration trials revealed debris fields of particular geometries was significantly smaller than the corresponding long duration trials. That is, for a particular overpressure and structural geometry, the debris distribution was proportional to the impulse.

Additionally, from the experimental work conducted for this research project, it can be concluded that within the tested parameters:

- Pressure dictates the breakage pattern of masonry structures; however a minimum duration is required to transfer the full breakage load.
- For a given geometric shape, masonry structures will follow a particular breakage pattern, with varying severity based on the applied blast pressure and impulse.
- The characteristic normalised longitudinal debris distribution is constant for a particular geometry.

- The longitudinal debris distribution of a particular masonry panel will present a similar distribution when part of a larger structure.
- There is a uniform distribution ratio of brick and mortar for all masonry structures when subjected to blast.

The experimental trials were a success and offered new data regarding the interaction of masonry structures with long duration blast, including the breakage, fragmentation and debris dispertion for a wide range of geometries. As discussed in section 2.2, no results, experimental or otherwise, are publicly available regarding these particular mechanisms. The trials were carefully constructed, instrumented and recorded to achieve large quantities of new and useful data. The base panel method, along with the experimental data will be adopted by AWE for integration and benchmarking of various in-house fast running engineering models to assist in damage prediction.

7.1 Future Work

As the experimental data set is relatively limited due to the exclusivity of the testing facilities, the computational modelling routine is an invaluable tool in the investigation of long duration blast effects on masonry structures. The results achieved from the experimental data can be largely built upon with the assistance of computational modelling and therefore the first priority with any future research is to finish development of the computational modelling routine, which requires benchmarking of AEM for long duration blast.

Once completed, the computational modelling routine can be used to increase the data set, investigating different geometries, blast parameters and initial conditions, such as the effects of blast in-fill. A parametric study can be used to fully develop the base panel model, allowing for the development of predictive algorithms for both breakage and debris distribution. The computational modelling routine is also required to form the link between the large enclosed structures and the smaller base panels and composite panels and identify the effects of blast in-fill and restrictions on the debris distributions due to

rear walls.

As previously mentioned, masonry construction of single leaf running bonds is the simplest case, allowing for a worst case prediction. The base panel model can be further developed, investigating different masonry bonds, cavity wall insulation and other methods used in masonry construction. The base panel model can also be extended to account for the effects of panel height and axial loading, representing additional floors.

7.2 Summary

The base panel model was designed to investigate the effects of long duration blast loading on masonry and determine the effects of structural geometry on breakage and debris distributions. Both experimental trials and numerical modelling were used to assess the effects of blast on structural response, with two HE (high explosive) short duration trials and five long duration trials conducted to benchmark a computational modelling routine.

The two HE trials of 41kg TNT equivalence tested simple masonry geometries at various radial distances to both benchmark the computational routine and investigate the effects of blast impulse. The first trial placed simple panels of x,y,z dimensions 0.1m×1m×2m, **A** panels, at varying radial distances with responses observed at 110kPa, 72kPa and 55kPa presenting small debris distributions covering maximum rectangular areas up to approximately 10m^2, whilst the 35kPa and 14kPa showed no response. The second HE trial tested corner panels, (1m×1m×2m) at the 110kPa, 72kPa and 55kPa radials with 110kPa showing complete failure, 72kPa showing a high damage and 55kPa showing minor damage.

A total of five long duration trials were conducted using the Air Blast Tunnel, with two instrumentation sections of diameter 4.9m and 10.2m, creating blast overpressures of 110kPa and 55kPa with positive phase durations of approximately 200ms and 150ms respectively. Four structures with geometries utilised in the base panel model were instrumented in the 4.9m section of the ABT with average maximum longitudinal distributions of 47m, showing even distributions of both brick and mortar. Four structures with simple base panel geometries were tested in the 10.2m section of the ABT, presenting longitu-

dinal distributions of approximately 16m. A correlation was observed in the breakage patterns of specific geometries regardless of blast overpressure, with an increase in crack formation at higher pressure. Comparing the long and short duration results for masonry structures with material parameters of those tested within this research project, 100ms was identified as the approximate effective period of reflected pressure on breakage. Correlations were observed in the debris distributions of specific panels, based on their position within the larger structure, highlighting the potential of the base panel model for predicting the breakage and debris distribution of composite structures. This was also highlighted by similar patterns observed in the debris distribution of specific geometries regardless of blast overpressure. Three large enclosed structures were also instrumented in the 10.2m section of the ABT, each with a half rectangular geometry, with the blast in-fill restricted by a steel structure from the side and above.

A computational modelling routine was developed using both CFD and AEM to model masonry structures subject to long duration blast loads. The CFD modelling routine produced high resolution models of the short duration trials, with accurate load curves. For the long duration case, the CFD models produced relatively high resolution models, allowing peak loads and loading contours to be assessed; however as the structures were infinitely rigid, the results are only valid for the effective period of reflected pressure, 100ms. The AEM models provided reasonable assessments of the short duration trials, modelling the boundary cases correctly, the formation of cracks within the appropriate regions, the method of structural collapse and the area covered by the debris, all to within acceptable degrees of accuracy. Due to the scheduling of the experimental trials, AEM was not fully benchmarked against the long duration trials, requiring additional research to further develop the modelling routine.

References

[1] J. W. Reed. Anaylsis of the accidental explosion at pepcon, henderson, nevada, may 4, 1988. Technical report, Sandia National Labratories, November 1988.

[2] ARIA Development. Explosion in a fireworks storage facility, kolding, denmark. Technical report, French Ministry for Sustainable Development, April 2009.

[3] E. Burman and P. Reina. *Unplanned Explosions at Munitions Sites: Excess stockpiles as liabilities rather than assets*. Small Arms Survey, first edition, 2014.

[4] D. Cormie, G. Mays, and P. Smith. *Blast Effects on Buildings*. Thomas Telford, second edition, 2009.

[5] B. Gelfand and M. Silnikov. *Blast Effects Caused by Explosions*. European Research Office of the U.S. Army, London, England, 2004.

[6] Unified Facilities Criteria (UFC). Structures to resist the effects of accidental explosions (ufc 3-340-02). Technical report, United States Departement of Defence, December 2008.

[7] S. Glasstone and P. J. Dolan. *The Effects of Nuclear Weapons*. United States Department of Defense and the Energy Research and Development Administration, third edition, 1977.

[8] W. J. Macquorn Rankine. On the thermodynamic theory of waves of finite longitudinal disturbance. *Proceedings of the Royal Society of London*, 1869.

[9] B. M. Luccioni and D. Ambrosini. Numerical assessment of blast effects scaling procedures. *Mecnica Computacional*, Vol XXIX, 2010.

[10] W. E. Baker. Prediction and scaling of reflected impulse from strong blast waves. *International Journal of Mechanical Sciences*, 1966.

[11] C. E. Needham. *Blast Waves*. Springer, first edition, 2010.

[12] L. N. Howard and D. L. Matthews. On the vortices produced in shock diffraction. *Journal of Applied Physics*, 1956.

[13] M. Sun and K. Takayama. Vorticity production in shock diffraction. *Journal of Fluid Mechanics*, 2002.

[14] S. M. Liang and C. P. Lo. Shock/vortex interactions induced by blast waves. *American Institute of Aeronautics and Astronautics*, 2002.

[15] J. D. Anderson Jr. Governing equations of fluid dynamics. In John. F. Wendt, editor, *Computational Fluid Dynamics*. Springer Berlin Heidelberg, 2009.

[16] B. van Leer. Flux-vector splitting for the euler equations. In *8th International Conference on Numerical Methods in Fluid Dynamics*, 1982.

[17] M. S. Liou and C. J. Steffen. A new flux splitting scheme. *Journal of Computational Physics*, 107:pp. 23–39, 1993.

[18] M. S. Liou. A sequal to ausm: Ausm+. *Journal of Computational Physics*, 129:pp. 364–382, 1996.

[19] M. S. Liou and Y. Wada. An accurate and robust flux splitting scheme for shock and contact discontinuities. *Journal of Scientific Computing*, 18(3):pp. 633–657, 1997.

[20] T. A. Rose. *An Approach to the Evaluation of Blast Loads on Finite and Semi-Infinite Structures*. PhD thesis, Cranfield University, 2001.

[21] D. Ngo A. C. Scordelis. Finite element analysis of reinforced concrete beams. *Journal of the American Concrete Institute*, 1967.

[22] Y. R. Rashid. Analysis of reinforced concrete pressure vessels. *Nuclear Engineering and Design*, 1968.

[23] R. de Borst et al. Discrete vs smeared crack models for concrete fracture: Bridging the gap. *International Journal for Numerical and Analytical Methods in Geomechanics*, 1987.

[24] R. D. Cook. *Finite Element Modelling for Stress Analysis*. Wiley, first edition, 1994.

[25] K. Meguro and H. Tagel-Din. Applied element method for structural analysis: Theory and application for linear materials. *Journal of Earthquake Engineering, JSCE*, 17(1):pp. 21s–35s, 2000.

[26] Vadim I. Lishak, Vladamir I. Yagust, and David Z. Yankelevsky. 2-d orthotropic failure criteria for masonry. *Engineering Structures*, 36:360–371, 2012.

[27] M. Dhanasekar, A. W. Page, and P. W. Kleeman. The failure of brick masonry under biaxial stresses. *Proceedings of the Institute of Civil Engineers*, 79:295–313, 1985.

[28] A. W. Page. The biaxial compressive strength of brick masonry. *Proceedings of the Institute of Civil Engineers*, 71:893–906, 1981.

[29] Valerio Alecci, Mario Fagone, Tommaso Rutonno, and Mario De Stefano. Shear strength of brick masonry walls assembled with different types of mortar. *Construction and Building Materials*, 40:1038–1045, 2013.

[30] Adrian Costigan, Sara Pavía, and Oliver Kinnane. An experimental evaluation of prediction models for the mechanical behavior of unreinforced, lime-mortar masonry under compression. *Journal of Building Engineering*, 4:283–294, 2015.

[31] Jelena Milosevic, Màrio Lopes, Antònio Sousa Gago, and Rita Bento. Testing and modeling the diagonal tension strength of rubble stone masonry panels. *Engineering Structures*, 52:581–591, 2013.

[32] C. Alessandri and C. A. Brebbia. Strength of masonry walls under static horizontal loads: boundary element analysis and experimental tests. *Engineering Analysis*, 4:118–134, 1987.

[33] D. M. Herbert, D. R. Gardner, M. Harbottle, J. Thomas, and T. G. Hughes. The development of a new method for testing the lateral load capacity of small-scale masonry walls using a centrifuge and digital image correlation. *Construction and Building Materials*, 25:4465–4476, 2011.

[34] Yi Liu and Pouria Manesh. Concrete masonry infilled steel frames subjected to combined in-plane lateral and axial loading an experimental study. *Engineering Structures*, 52:331–339, 2013.

[35] Feng Yuan, Wu Xiaobin, and Zhang Shulu. Failure modes of masonry infill walls and influence on rc frame structure under earthquake. In *Tenth U.S. National Conference on Earthquake Engineering*, 2014.

[36] Alberto Mauro, Gianmarco de Felice, and Matthew J. DeJong. The relative dynamic resilience of masonry collapse mechanisms. *Engineering Structures*, 85:182–194, 2015.

[37] Adolfo Previado. Seismic vulnerability and failure modes simulation of ancient masonry towers by validated virtual finite element models. *Engineering Failure Analysis*, pages 72–87, 2015.

[38] A. Penna, M. Mandirola, M. Rota, and G. Magenes. Experimental assessment of the in-plane lateral capacity of autoclaved aerated concrete (aac) masonry walls with flat-truss bed-joint reinforcement. *Construction and Building Materials*, 82:155–166, 2015.

[39] James E. Drotleff, Coye T. Vincent, Scott A. Mullin, James D. Walker, and Bruce L. Morris. Research in close-in blast loading from high explosives. Technical report, Army Research Labratory, 1996.

[40] Robert G. S. Sewell. Blast overview and near-field effects. Technical report, Naval weapons centre, 1979.

[41] T. Micheal Baseheart. Reinforced concrete response to near field explosions. Technical report, University of Cincinnati, 1983.

[42] John W. Pastrnak, Charles E. Baker, and Larry F. Simmons. Quarter-scale close-in blast-loading experiments in support of the planned contained firing facility. Technical report, Lawrence Livermore National Laboratory, University of California, 1994.

[43] Bo Yan, Fei Liu, DianYi Song, and ZhiGang Jiang. Numerical study on damage mechanism of rc beams under close-in blast loading. *Engineering Failure Analysis*, 51:9–19, 2015.

[44] A. Dörr, N. Gebbeken, M. Larcher, M. Steyerer, Chr. Haberacker, and S. Akers. The effect of near, contact and embedded detonations on masonry structures. In *22nd Military Aspects of Blast and Shock (22nd MABS)*, Bourges, France, 2012.

[45] A. Dörr, N. Gebbeken, M. Larcher, M. Steyerer, Chr. Haberacker, and S. Akers. The effect of near-field explosions on masonry walls. In *15th International Symposium on the Interactions and Effects of Munitions and Structures (15th ISIEMS)*, Potsdam, Germany, October 2013.

[46] C. P. Pantelides, T. T. Garfield, W. D. Richins, T. K. Larson, and J. E. Blakeley. Reinforced concrete and fiber reinforced concrete panels subjected to blast detonations and post-blast static tests. *Engineering Structures*, 76:24–33, 2014.

[47] A. Ghani Razaqpur, Ahmed Tolba, and Ettore Contestabile. Blast loading response of reinforced concrete panels reinforced with externally bonded gfrp laminates. *Composites Part B*, 38:535–546, 2007.

[48] Chr. Mayrhofer. Reinforced masonry walls under blast loading. *International Journal of Mechanical Sciences*, 44:1067–1080, 2002.

[49] G. S. Urgessa and K. Maji. Dynamic response for retrofitted masonry walls for blast loading. *Journal of Engineering Mechanics*, 136:858–864, 2010.

[50] Kai Fischer, Werner Riedel, and Julia Ziehm. Full-scale validation of a blast-proof masonry wall system and assessment of coupling effects using a tdof model. In *14th International Symposium on the Interactions and Effects of Munitions and Structures (14th ISIEMS)*, September 2011.

[51] L. G. Moradi. Resistance of membrane retrofit concrete masonry walls to lateral pressure. Technical report, University of Alabama, April 2008.

[52] Lee G. Moradi, Robert J. Dinan, Bryan T. Bewick, and James S. Davidson. Resistance of concrete masonry walls with membrane cather system subject to blast loading. Technical report, Air Force Research Laboratory Materials and Manufacturing Directorate, December 2010.

[53] B. Abou-Zeid, W. El-Dakhakhni, A. Razaqpur, and S. Foo. Response of arching unreinforced concrete masonry walls to blast loading. *Journal of Structural Engineering*, 137:1205–1214, 2011.

[54] Xueying Wei and Mark G. Stewart. Model validation and parametric study on the blast response of unreinforced brick masonry walls. *International Journal of Impact Engineering*, 37:11501159, 2010.

[55] R. K. Varma, C. P. S. Tomar, and S. Parkash. Damage to brick masonry panel walls under high explosive detonations. pressure vessels and piping division. *American Society of Mechanical Engineers*, 351:207–216, 1997.

[56] C. V. B. Cunningham. The kuz-ram model for prediction of fragmentation from blasting. In *First International Symposium on Rock Fragmentation by Blasting*, pages 439–454, August 1983.

[57] Mario A. Morin and Francesco Ficarazzo. Monte carlo simulation as a tool to predict blasting fragmentation based on the kuzram model. *Computers & Geosciences*, 32:352–359, 2006.

[58] Ming Wang, Hong Hao, Yao Ding, and Zhong-Xian Li. Prediction of fragment size and ejection distance of masonry wall under blast load using homogenized masonry material properties. *International Journal of Impact Engineering*, 36:808–820, 2009.

[59] J. J. Gilvarry. Fracture of brittle solids. i. distribution function for fragment size in single fracture (theoretical). *Journal of Applied Physics*, pages 391–399, 1961.

[60] Yong Lu and Kai Xu. Prediction of debris launch velocity of vented concrete structures under internal blast. *International Journal of Impact Engineering*, 34:1753–1767, 2007.

[61] A. Dörr, K. Michael, and G. Gürke. Experimental investigations of the debris launch velocity from internally overloaded concrete structures. Technical report, Institut Kurzzeitdynamik Ernst-Mach-Institut, 2002.

[62] Kai Xu and Yong Lu. Debris velocity of concrete structures subject to explosive loading. *International Journal for Numerical and Analytical Methods in Geomechanics*, 30:917–926, 2006.

[63] M. M. van der Voort and J. Weerheijm. A statistical description of explosion produced debris dispersion. *International Journal of Impact Engineering*, 59:29–37, 2013.

[64] C. Knock, I. Horsfall, S. M. Champion, and I. C. Harrod. The bounce and roll of masonry debris. *International Journal of Impact Engineering*, 30:1–16, 2004.

[65] G. H. Reid. Misty castle series: Mill race event: Test execution report. Technical report, Defence Nuclear Agency, 1981.

[66] D. Eardley and J. Katz. Direct course and dust experiments. Technical report, Mitre Corp, April 1983.

[67] C. Maag and S. Rohrer. Project trinity 1945-1946. Technical report, JRB Associates inc, December 1982.

[68] L. Berkhouse et al. Operation greenhouse. Technical report, Defence Nuclear Agency, 1951.

[69] Steel Construction Institute. Buncefield explosion mechanism phase 1. Technical report, Steel Construction Institute, 2009.

[70] Chemical Safety Board. Preliminary findings into the west fertilizer explosion and fire. Technical report, Chemical Safety Board, June 2013.

[71] E. I. V. van den Hengel, R. J. A. Kersten, F. A. M. H. Jacobs, R. Oostdam, and N. H. A. Versloo. Ammonium nitrate behaviour in a fire. In *IChemE Symposium Series No. 153*, pages 1–5, Edinburgh, Scotland, May 2007.

[72] Olav R. Hansen and D. Michael Johnson. Improved far-field blast predictions from fast deflagrations, ddts and detonations of vapour clouds using flacs cfd. *Journal of Loss Prevention in the Process Industries*, 35:293–306, 2015.

[73] D. M. Johnson, G. B. Tomlin, and D. G. Walker. Detonations and vapour cloud explosions: Why it matters. *Journal of Loss Prevention in the Process Industries*, 36:358–364, 2015.

[74] Andrzej Pekalski, Jonathan Puttock, and Simon Chynoweth. Deflagration to detonation transition in a vapour cloud explosion in open but congested space: Large scale test. *Journal of Loss Prevention in the Process Industries*, 36:365–370, 2015.

[75] H. M. Salem and H. M. Helmy. Numerical investigation of collapse of the minnesota i-35w bridge. *Engineering Structures*, 59:635–645, 2014.

[76] Hamed Salem, Suzan Mohssen, Kenji Kosa, and Akira Hosoda. Collapse analysis of utatsu ohashi bridge damaged by tohuku tsunami using applied element method. *Journal of Advanced Concrete Technology*, 12:388–402, 2014.

[77] Huda Helmy, Hamed Hadhoud, and Sherif Mourad. Infilled masonry walls contribution in mitigating progressive collapse of multistory reinforced concrete structures according to ufc guidelines. *International Journal of Advanced Structural Engineering*, 7:233–247, 2015.

[78] Unified Facilities Criteria (UFC). Structures to resist the effects of accidental explosions (ufc 3-340-02). Technical report, United States Departement of Defence, 2009.

[79] Amy Coffield and Hojjat Adeli. Irregular steel building structures subject to blast loading. *Journal of Civil Engineering and Management*, 22:17–25, 2016.

[80] Timothy P. Kernicky, Matthew J. Whelan, David C. Weggel, and Corey D. Rice. Structural identification and damage characterization of a masonry infill wall in a full-scale building subjected to internal blast load. *Journal of Structural Engineering*, 141:D04014013–13, 2015.

[81] T. J. Kreitinger and A. K. Verma. Large blast/thermal simulator testing environment. In *18th Military Aspects of Blast and Shock*, Bad Reichenhall, Germany, September 2004.

[82] The Atomic Weapons Establisment (AWE). Discrete orion series. Technical report, Large Blast Thermal Simulator, White Sands Missile Range, New Mexico, 2005.

[83] K. O. Opalka. Large blast and thermal simulator advanced concept driver design by computational fluid dynamics. Technical report, U.S. Army Ballistics Research Labratory, 1989.

[84] R. A. Keys and S. K. Clubley. Modelling debris distribution of masonry panels subject to blast loads using experimental & applied element methods. In *15th International Symposium on the Interactions and Effects of Munitions and Structures (15th ISIEMS)*, Potsdam, Germany, October 2013.

[85] L. J. Adams et al. Simulating explosive events in the air blast tunnel. In *22nd Military Aspects of Blast and Shock (22nd MABS)*, Bourges, France, July 2012.

[86] Charles N. Kingery and Gerald Bulmash. Airblast parameters from tnt spherical air burst and hemispherical surface burst. Technical report, U.S. Army Armament Research and Development Center, Ballistic Research Laboratory, Maryland, 1984.

[87] R. A. Keys and S. K. Clubley. Experimental analysis of small masonry panels subject to long duration blast loads. In *16th International Symposium on the Interactions and Effects of Munitions and Structures (16th ISIEMS)*, Sandestin, Florida, November 2015.

[88] The British Standards Institution. *BS5628-1:2005 - Code of Practice for the use of Masonry*, 2005. Table 1.

[89] Applied Science International LLC, Applied Science International, Durham, North Carolina. *ELS Theoretical Manual*, 2010.

Appendix A

ISIEMS 15

The following pages displayed the paper written for and presented at the 15th International Symposium on the Interactions of the Effects of Munitions with Structures in Potsdamn, Germany in October 2013.

Modelling debris distribution of masonry panels subject to blast loads using experimental & applied element methods

Richard A. Keys, PhD Researcher[1], Simon K. Clubley, Lecturer in Civil Engineering[1]

[1]Infrastructure Group, Faculty of Engineering and the Environment
University of Southampton, Southampton

May 2013

Abstract

Blast loading and its interaction with structures is a complex phenomenon even in the simplest of cases and modelling its effects is a non-trivial task. This complexity is increased when dealing with long duration blast due to the drag loads associated with the dynamic pressure.

This paper establishes a scientific benchmark for the debris distribution modelling of masonry panels as the foundation of an extended in-depth research study. Experimental trials were conducted in which identical masonry walls were subjected to separate conventional high explosive and long duration blast loads for comparison. Both experiments were subsequently modelled using the Applied Element Method (*AEM*) with the computational results demonstrating good agreement. The experimental blast loads were characterised with matching overpressures for computational simplicity allowing for a direct comparison between both cases and a clear indication of the effects of impulse, dynamic pressure and entrainment on debris distribution.

Introduction

The work summarised in this paper forms a scientific basis on which a longer in-depth research projected will be conducted. This research aims to develop a set of algorithms to predict the breakage and debris distribution for a large variety of simplified masonry structures when subjected to long duration blast loads. Long duration blast loading is identified here as an explosive event in which the positive phase duration exceeds 100ms and is most commonly associated with hydrocarbon vapour cloud detonation, such as the 2005 'Buncefield Disaster' [1] and the more recent 2013 'Texas Fertilizer Plant Disaster,' or large scale explosive detonations such as the 1981 'Mill Race' Trial [2].

By nature, long duration blast waves transmit very large impulses and the non-negligible effects of drag loads associated with the dynamic pressure make its interactions and effects much more complex to model than the conventional case. To develop a modelling routine capable of accurately simulating structural response to such effects, the procedure must be applied to the conventional case to gauge its performance and appropriateness.

When modelling structural collapse the reliability of some numerical methods such as Finite Element Analysis (*FEA*) break down in the discrete phase, especially when modelling brittle materials which are susceptible to particulate breakage. It is difficult to accurately model the kinematic and ballistic interactions of the elements in this phase using nodal connections. Other numerical methods however model the element connections through alternative approaches such as the Applied Element Method (*AEM*). AEM uses face connecting springs with collision detection allowing elements to re-contact other elements during the discrete phase, thus allowing for a reliable model of the debris distribution of such failures.

The collisions between elements during the discrete phase are automatically detected and modelled by temporary shear springs and normal springs. These collisions are modelled differently depending on the type of contact made, as shown in Figure 1, which illustrates the

direction of the springs in edge-to-edge contact and the ability to model multiple element collisions [3, 4].

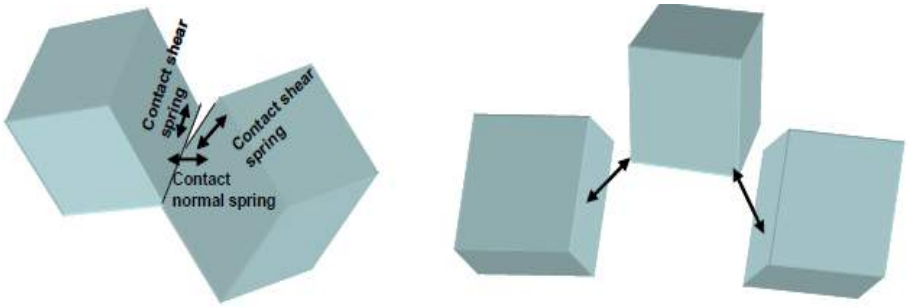

Figure 1. AEM Element Collisions [3, 4]

Methodology

This research uses conventional blast testing to develop a modeling routine using AEM to model the breakage and debris distribution of masonry. Once this routine has been established it will be adapted to incorporate long duration blast loads.

Experimental

The conventional HE tests utilised a 41kg TNT eq. charge composed of 39kg of TNT-Flake boosted by 2kg of PE-4, situated 1m above ground level resulting in an almost hemispherical blast wave. Five identical masonry walls of 2m height × 1m width were placed on radial spokes at distances designed to achieve the overpressures listed in Table 1. These radial spokes and their corresponding peak overpressures, reflected pressures, impulses, arrival times and positive phase durations as calculated using the Kingery & Bulmash Equations [5], are listed in Table 1.

r (m)	P_i (kPa)	I_i (kPa.ms)	P_r (kPa)	I_r (kPa.ms)	t_a (ms)	t^+ (ms)
10.6	110	313	310	752	12.8	10
13	73	262	186	595	18.1	11.5
15	55	231	134	505	22.9	12.3
19.5	35	183	80	378	34.2	13.7
36	14	103	30	195	78.8	16.7

Table 1. Masonry Wall Positions & Parameters for a Hemispherical Surface Burst

The walls were constructed from frogged, facing, London bricks approximately 2.1kg each with an average compressive strength of 4-6N/mm^2. The bricks were joined by a class (ii) mortar in accordance with BS:5628-1:2005 [6], with an average compressive strength of 8-10N/mm^2 (at the time of firing) and a bedding thickness of approximately 1cm. The walls were painted and each brick was numbered to determine the rough origin of the debris. Grids were sprayed around each wall with a bin resolution of 50cm × 50cm for debris collection. Endevco 8510 gauges were placed matching the radial positions of the walls to measure the static overpressure. High speed Phantom photography capturing 5000fps was used to record the breakage of the walls at the 10.6m and 13m positions from different angles.

Figure 2 illustrates a plan view of the trial arrangement and displays the exact positions of the walls. Preliminary models showed that this arrangement would not cause any significant interference between the walls.

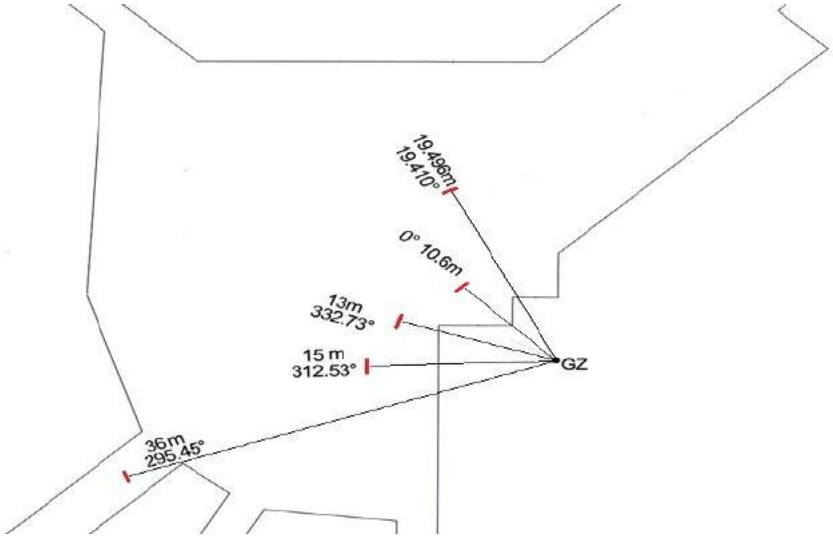

Figure 2. Schematic Diagram of Experimental Layout

The *ABT* (Air Blast Tunnel) facility at MOD Shoeburyness on Foulness Island is capable of simulating long duration blast waves replicating those of large conventional HE charges [7]. A masonry panel of the same 2m × 1m construction was placed in the ABT and subjected to a blast wave with a peak incident overpressure of $P_i \approx 110$kPa and positive phase duration $t^+ \approx 200$ms. Using the Kingery & Bulmash equations [5], this can be attributed to roughly a 500T TNT eq. burst at 250m. Free field pressure gauges were placed around the wall offset in the upstream direction by roughly 1m along with a dynamic pressure gauge. Two high speed phantom cameras capturing at 5000fps were used to record the breakage of the wall from both the upstream and side-on position.

Computational

Numerical modelling was conducted using the software Extreme Loading for Structures® (*ELS*) which utilises AEM. Preliminary computational analyses were run to resolve some of the unknown quantities and parameters. Using the Comutational Fluid Dynamics (*CFD*) code Air3D (v.9) [8], a parametric study was conducted to examine uniformly distributed gauge points on both faces of the walls.

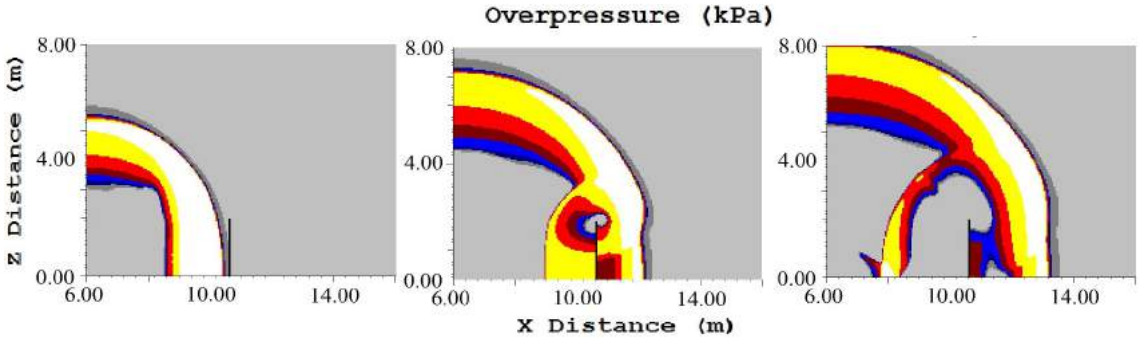

Figure 3. Air3D Model Displaying the Propagation of the Blast Wave over the Wall at 10.6m (10.8-17.6ms)

The first image in Figure 3 shows that upon reaching the 10.6m position there is still a significant curvature in the expansion of the wave with respect to the height of the wall. As a result, the wall is subjected to a non-uniform load which is accentuated by the clearing of

the blast wave and the subsequent rear loading. To accurately recreate the breakage and hence debris distribution this must be taken into account.

Using Air3D a total of 100 gauge points were uniformly placed across both faces of the walls; each gauge occupying a 20cm × 20cm area. From each gauge point the transmitted impulse is calculated and plotted. Figures 4a and 4b show the loading regions on the front and rear of the wall.

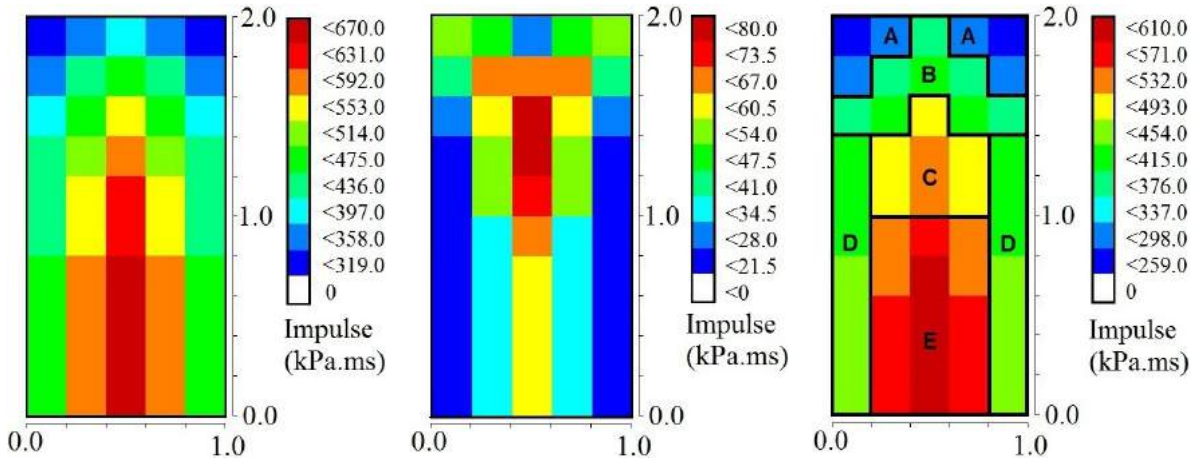

(a) Front Load **(b)** Rear Load **(c)** Net Load & Loading Regions

Figure 4. Load Distribution of the Wall at 10.6m

The impulse scale in Figure 4b shows the rear loading effect of the blast wave is between 20-80kPa.ms. This leads to a 6-25% reduction in the overall loading of the structure and is therefore vital that it is resolved. Furthermore, referring back to Figure 3, it can be seen that whilst the negative phase acts upon the front of the wall, the positive phase is still in effect on the rear of the wall, with both forces acting in the same direction. Figure 4c shows the effective net load obtained by subtracting the rear impulse from the front. The sections labelled from A to E highlight the regions to which the load will be divided within the AEM model. These regions were identified primarily based upon transmitted impulse; however, the arrival time of the blast wave at each region was also considered. This routine for identification of the loading regions is used for all models subjected to conventional blast. For this particular test all of the walls that were tested are identical; thus each simulation developed using AEM uses the same structural model with a different application of load.

Whilst this modelling routine offers promising results for the conventional case, the long duration case requires a different approach. Due to computational restrictions relating to the domain and cell size there is currently no access to a CFD model for such a high yield event. Applying the Kinergy & Bulmash equations [5] to the long duration case, it can be seen from Table 2 that for the long duration case both the incident and reflected impulses are roughly 20 times higher than for the conventional case. As a result the wall is quickly overmatched which creates difficulties in assessing the significance of the various loads.

Q (kg)	r (m)	P_i (kPa)	I_i (kPa.ms)	P_r (kPa)	I_r (kPa.ms)	t_a (ms)	t^+ (ms)
41	10.6	110	313	310	752	12.8	10
5×10^5	250	105	7052	290	16822	306.3	233.7

Table 2. Comparison of Conventional & Long duration Blast Parameters

The preliminary modelling for the long duration case will rely on the experimental gauge data which is in limited supply. The initial models apply the load instantaneously to every element of the wall as the blast wave is planar.

Results & Analysis

Experimental

Due to the circular cross section and relatively small radius of the ABT, the debris was collected in one dimensional longitudinal bins of width 1m. The one dimensional mass distribution data from each bin was extrapolated into 2D by fitting each bin to a Gaussian distribution with a mean value of $\mu = 0$ and a standard deviation of $\sigma = 1$ (standard normal distribution), as shown in Equation 1.

$$f(m, x) = m\frac{1}{\sqrt{2\pi}}e^{-\frac{x^2}{2}} \tag{1}$$

This data was then plotted as shown in Figure 5a for comparison with the conventional case shown in Figure 5b. Figure 5c shows the same data as Figure 5b, plotted on a different scale to show the localised mass distribution.

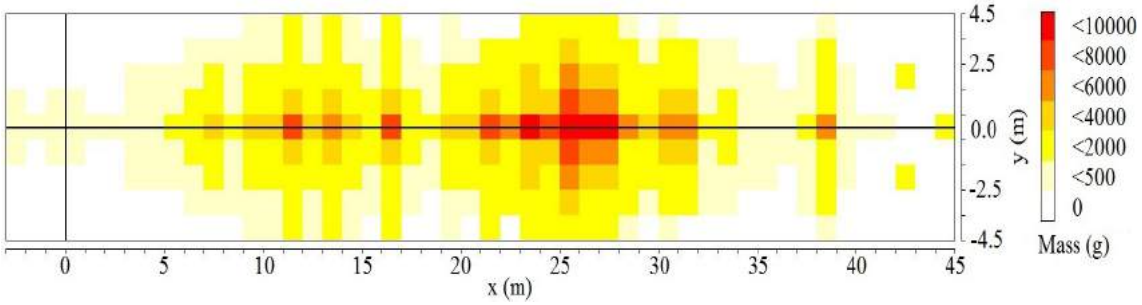

(a) 500T at 250m - Mass Normalised to 10kg

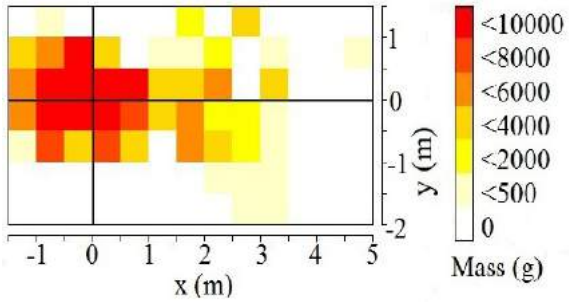

(b) 41kg at 10.6m - Mass Normalised to 10kg

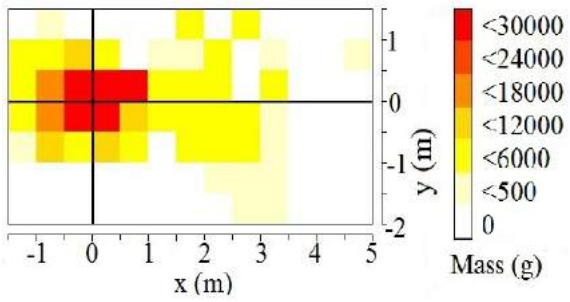

(c) 41kg at 10.6m - Mass Normalised to 30kg

Figure 5. Experimental Debris Mass Distribution Plots for $P_i \approx 110$kPa

Figure 5 demonstrates the maximum longitudinal throw distance of the debris for the long duration case is roughly 8 times that of the conventional case. The gauge data, as displayed in Figure 6, shows that the long duration event transmits over 20 times the free field impulse to that of the conventional case. Furthermore, impulse associated with the dynamic pressure in the long duration case which can interact with ballistic debris is 3 times higher than the conventional free field impulse. This illustrates the vastly increased loading potential and complexity of long duration blast.

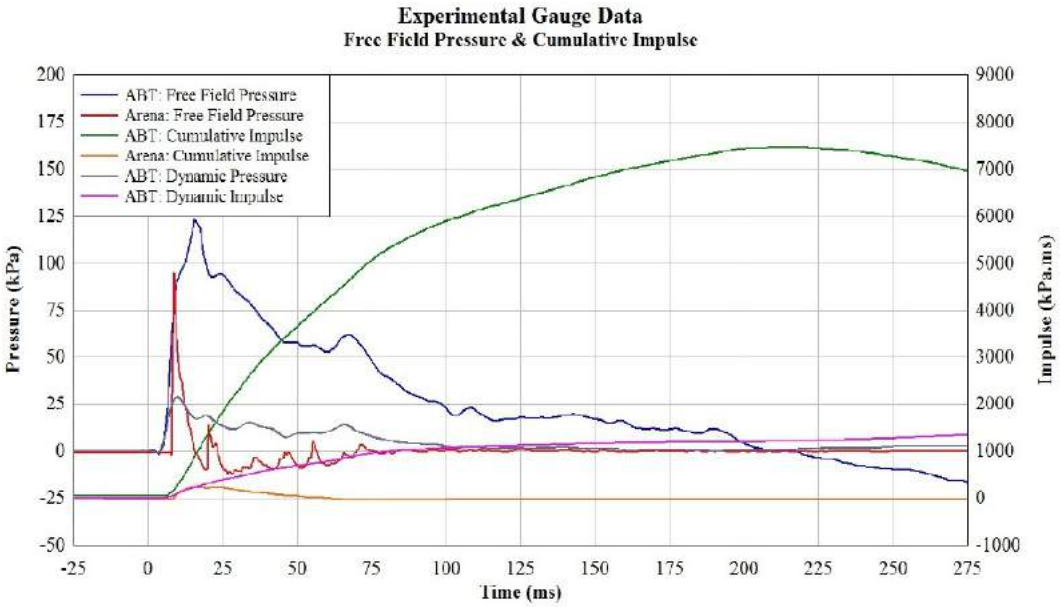

Figure 6. Experimental Free Field (& Integrated) Gauge Data

Results shown in Figure 6 are in good agreement with the predictions shown in Table 2. The results displayed in Figures 5 and 6 demonstrate the requirement for the development of a reliable relationship between the transmitted impulse, peak overpressure and spatial debris distribution for masonry.

Computational

In the early stages of this research project, time constraints have allowed for a restricted number of models. After some refinements to the modelling routine, including slight adjustments to the arrival time of the loading regions, the simulations improved drastically displaying strong correlation with the experimental results. Figure 7 compares the experimental debris field with the simulated debris field from the same viewpoint.

(a) Trial: 41kg at 10.6m **(b)** AEM: 41kg at 10.6m

Figure 7. Comparison of Experimental & Computational Final State Debris Fields

From comparison of Figures 7a and 7b it is clear that the majority of the debris has fallen within the same area. Upon comparison of the mass contained within each individual bin for both the trial and computational model the predictions show varying levels of agreement depending on the position of the bin. The largest discrepancies are seen within close proximity to the original position of the wall, in which there is a 9% difference in mass (as a percentage of the overall mass) as shown in Table 3b. However, upon decreasing proximity to the origin the mass difference per bin becomes small, with the majority of bins showing $\approx 1\%$ discrepancy. Figure 8 displays comparative spatial mass distribution plots of both the trial and AEM model.

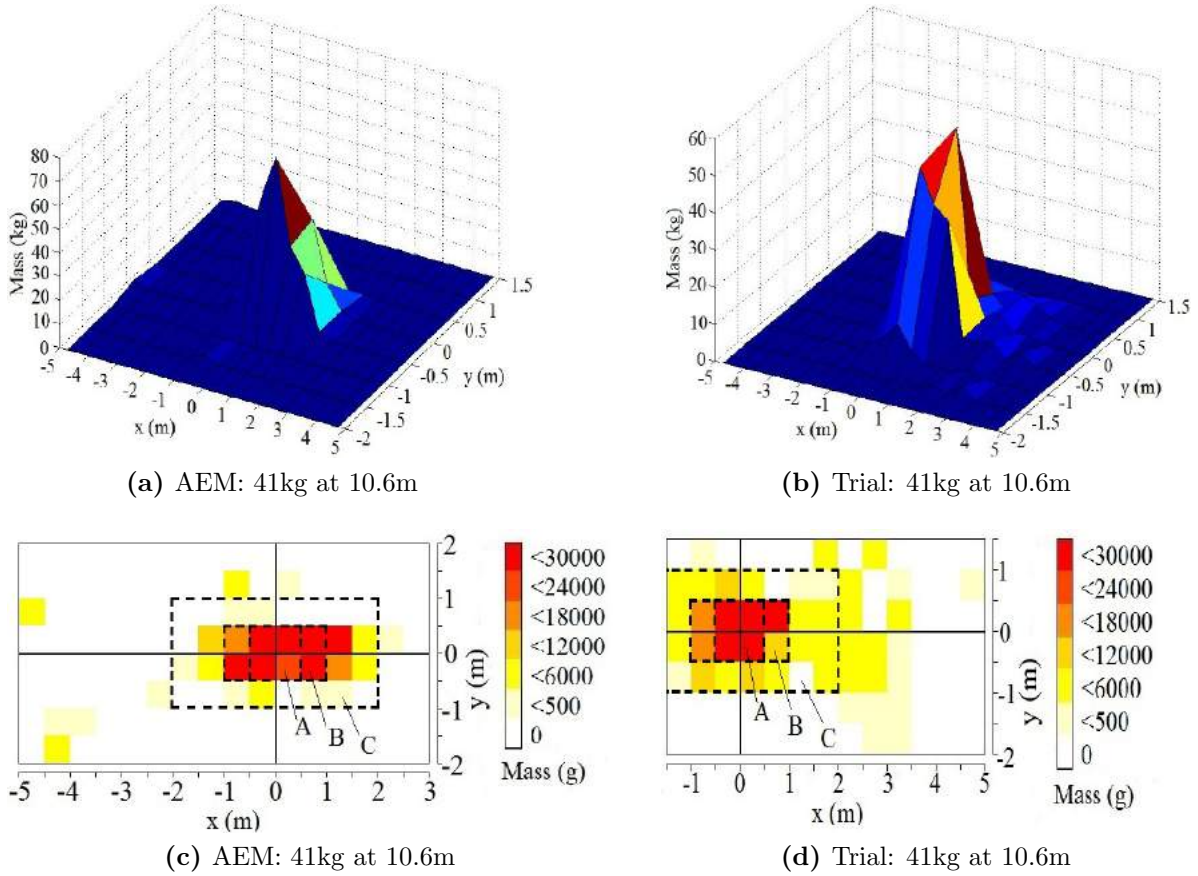

(a) AEM: 41kg at 10.6m

(b) Trial: 41kg at 10.6m

(c) AEM: 41kg at 10.6m

(d) Trial: 41kg at 10.6m

Figure 8. Debris Mass Distribution of 41kg at 10.6m (Normalised to 30kg)

After comparison of the mass contained within each individual bin, the same process can be conducted on a larger scale. Inspection of the mass within localised areas centred around the origin labelled 'A,' 'B' and 'C' as displayed in Figures 8c and 8d gives a clear indication of the difference in debris distribution. Table 3a shows the percentage of the overall mass contained within these areas. The 9% difference in bin mass fell within area A (1m $\times$ 1m); however the overall difference in area A is only 2%. Upon expanding this area to B (2m $\times$ 1m), the difference in the percentage of the overall mass increases to 9%. Finally, increasing the area to C (4m $\times$ 2m) shows a 4% difference in the overall mass.

The model shows varying levels of agreement with the trial data; however when viewed on a larger scale the results are promising. Whilst there is a 9% difference in area B, this is the equivalent to just over 1% per bin. Table 3b shows the average difference per non-zero bin as $\approx 1.4\%$. Figures 7, 8a and 8b display the debris fields of the trial and model in 3D which provides a clear view of the overall debris distribution. When viewed on this scale the potential for AEM to model such events becomes clear.

	Trial	AEM
1m×1m (A)	52%	50%
2m×1m (B)	73%	82%
4m×2m (C)	94%	98%
10m×4m	100%	100%

(a) % of Total Mass within a Localised Area

	All Bins	Bin Mass $\neq 0$
Max	9%	9%
Min	0	$< 0.1\%$
Average	0.5%	1.4%

(b) Variation of Mass per Bin (Trial vs. AEM)

Table 3. Summary Comparison of Experimental and Compuational Mass Distribution

The debris distribution of a structure is greatly dependent on the way in which it fails. Figure 9 shows the breakage patterns displayed by the structure both experimentally and computationally.

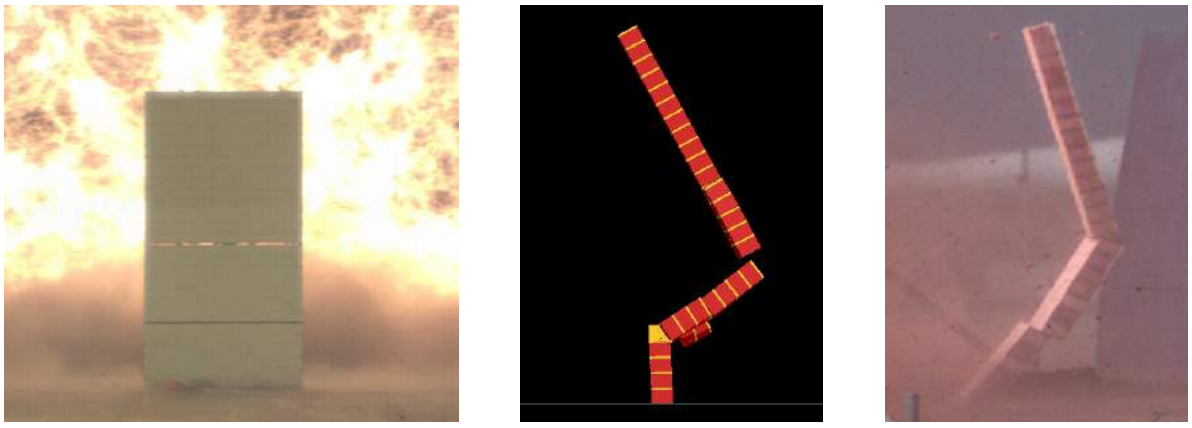

(a) 300ms (rear) **(b)** AEM at 300ms **(c)** 300ms (side)

Figure 9. Comparison of Computational & Experimental Breakage Patterns

Figures 9a, 9b and 9c demonstrate that AEM is capable of matching experimental results to a high degree of accuracy; however, whilst this breakage pattern shows good agreement with that of the experimental breakage pattern, there are small differences which explain the variation in the debris distribution. The bottom quadrant of the wall shows reduced numerical response, whereas the video footage shows the bottom section pivot and fall in the trial; this can cause a longitudinal translation of the debris field. Minor details in the breakage patterns such as this can be reduced further through measured modifications to the modelling routine.

Figure 10 indicates the debris field for the current long duration AEM model which was constructed using only experimental gauge data as represented in Figure 6.

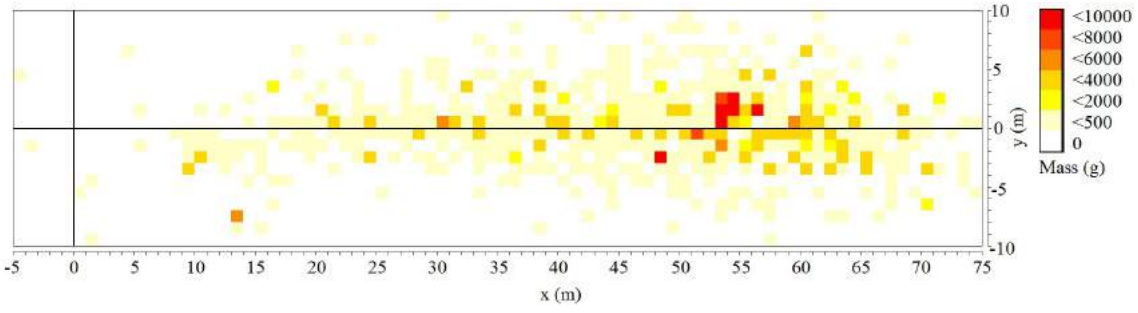

Figure 10. AEM Debris Mass Distribution of 500T at 250m (Normalised to 10kg)

A comparison of Figures 10 and 5a indicates a number of minor challenges pertaining to the absence of a properly resolved flow field. Without being able to resolve the pressure on all sides of the structure or the transferred energy before and after the structure has broken, the simulation models the upper limit of structural failure. The accuracy of the numerical model can be further improved pertaining to additional experimental results and the aid of a CFD simulation. The ability of AEM to accurately model the conventional blast case once a rigid loading routine has been established is further evidence that this is also possible for the long duration case. Adapting the loading regime at the moment of breakage to apply the dynamic pressure and negative phase over the free field pressure will reduce the kinetic energy transferred to the structure.

Summary

AEM has proven to be a powerful tool for modelling the breakage and debris distribution of masonry. The computational models developed for conventional blast, even at this early stage, have thus far shown accurate results. Whilst the model shows varying levels of agreement upon comparison of each bin, comparison of larger areas show more promising results. The debris distribution of the structure is largely determined by its failure mode; thus improvements to the modelling routine will drastically improve the debris distribution. Once a rigid modelling routine has been established for the long duration case, AEM will be used towards a parametric assessment of the breakage and debris distribution of masonry subjected to long duration blast loading.

Nomenclature

Symbols		Subscripts	
I	Impulse	a	Arrival
m	Mass	i	Incident / Free Field
P	Pressure	r	Reflected
Q	Charge Mass (TNT eq.)		
r	Radius Distance	Superscripts	
t	Time	$+$	Positive Phase
μ	Mean		
σ	Standard Deviation		

Acknowledgements

The author would like to express gratitude to the UK Ministry of Defence for providing the use of testing facilities at MoD Shoeburyness. All data hereby obtained through the use of such facilities remains the property of the UK MoD. The assistance of the Spurpark Ltd trials division is gratefully acknowledged with respect to experimental planning, instrumentation and implementation. The author would also like to thank Dr. J. Adams for his oversight and support as well as Dr. T. Rose for his assistance with CFD modelling in Air3D. Finally the author would like to express gratitude to fellow team members Mr. R. Collins and Mr. L. Clough.

References

[1] B. Burgan et al. Buncefield explosion mechanism phase 1. Technical report, Steel Construction Institute, 2009.

[2] G. H. Reid. Misty castle series: Mill race event: Test execution report. Technical report, Defence Nuclear Agency, 1981.

[3] H. Tagel-Din and N. A. Rahman. The applied element method: The ultimate analysis of progressive collapse. April 2006.

[4] Applied Science International LLC, Applied Science International, Durham, North Carolina. *ELS Theoretical Manual*, 2010.

[5] C. N. Kingery and G. Bulmash. Airblast parameters from tnt spherical air burst and hemispherical surface burst. Technical report, 1984.

[6] The British Standards Institution. *BS5628-1:2005 - Code of Practice for the use of Masonry*, 2005. Table 1, page 11.

[7] L. J. Adams et al. Simulating explosive events in the air blast tunnel. 22nd International Symposium on Military Aaspects of Blast and Shock, Bourges, France, November 2012.

[8] T. A. Rose. *An Approach to the Evaluation of Blast Loads on Finite and Infinite Structures*. PhD thesis, Cranfield University, Royal Military College of Science, 2001.

Appendix B

ISIEMS 16

The following pages show the paper written for and presented at the 16th International Symposium on the Interactions of the Effects of Munitions with Structures in Destin, Florida in November 2015.

EXPERIMENTAL ANALYSIS OF SMALL MASONRY PANELS SUBJECT TO LONG DURATION BLAST LOADING

Richard A. Keys[1*], Simon K. Clubley[2]

[1*]Infrastructure Group, Faculty of Engineering and the Environment, University of Southampton, Southampton, UK, SO17 1BJ (r.keys@soton.ac.uk)
[2] Infrastructure Group, Faculty of Engineering and the Environment, University of Southampton, Southampton, UK, SO17 1BJ (s.k.clubley@soton.ac.uk)

Abstract
Much research has been conducted towards short duration blast loading and its interaction with structures. The positive phase duration, t^+, of a typical short duration high explosive blast is often below $t^+ = 100$ms. For the purposes of this research, long duration blast is considered to be an explosive event in which $t^+ > 100$ms. This type of blast load offers added complexity when dealing with its interaction with structures due to the high impulses, drag winds and associated dynamic pressures.

As part of an extended research study to develop a set of predictive algorithms, this paper investigates the breakage patterns and debris distribution of masonry panels subject to long duration blast loads. Experimental trials were conducted using the Air Blast Tunnel at MoD Shoeburyness, a specialised facility for long duration blast, in which two masonry panels were tested. The trials displayed varying degrees of breakage followed by a substantial debris distribution in both cases.

Keywords: Long duration, Blast, Masonry, Impulse, Breakage, Debris

INTRODUCTION

Long duration blast loads by nature have a large positive phase duration in which $t^+ > 100$ms. Such blast waves are produced by detonating large quantities of high explosives, such as the 1981 'Mill Race' trial reported by Reid [1] in which 544 tonnes of ANFO were detonated, or hydrocarbon vapour cloud detonation, such as the 2005 'Buncefield Disaster' reported by Burgen et al [2].

The work presented in this paper is part of an extended research project investigating the breakage and debris distribution of masonry panels subject to long duration blast loads. Using both experimental and numerical methods, the project aims to quantify the effects of the blast load, structural geometry and material properties on the breakage and debris distribution patterns. Previous research conducted by Keys & Clubley [3] investigated the comparative debris distribution of a masonry wall subject to a short duration blast load with $p_i \approx 110$kPa and $t^+ \approx 12{:}8$ms and a long duration blast wave with $p_i \approx 110$kPa and $t^+ \approx 200$ms. This paper investigates the breakage patterns and debris distribution of both mortared and unmortared masonry panels subject to long duration blast loading.

EXPERIMENTAL CONFIGURATION

Two experimental trials were conducted at the Air Blast Tunnel (ABT) displayed in Figure 1. The ABT is a shock tube designed to replicate large explosive events as discussed by Adams & Rose [4], located at MoD Shoeburyness on Foulness Island, UK.

Figure 1. The Air Blast Tunnel (ABT)

The two experiments comprised 1m × 2m masonry walls labelled 'MW1' and 'MW2.' The MW1 trial used unmortared Class B engineering bricks (210mm × 10mm × 65mm) with a compressive strength of approximately 95Nmm^2, whilst the MW2 trial was constructed from frogged, facing, London bricks (210mm × 10mm × 65mm) with a compressive strength of approximately 40-60Nmm^2, joined by a class (ii) mortar conforming to BS:5628-1:2005 [5], with a compressive strength of approximately 60-80Nmm^2 in a 10mm bedding. Each structure was painted to improve the lighting for photography and each brick was assigned a unique number to provide insight into the individual brick distributions.

Both trials were recorded using two high speed Phantom cameras operating at 5000fps; the cameras were mounted in hardened steel boxes in the upstream and side positions with the upstream camera displayed in Figure 2(a). Endveco 8510 piezoresistive pressure transducers, shown in Figure 2(b), were used to record the static overpressures and Kulite-20D pressure transducers, shown in Figure 2(c), were used to record the dynamic pressure. Both types of gauges were placed 1m upstream from the target.

(a) **(b)** **(c)**

Figure 2. Trial Instrumentation: (a) Phantom camera support & lighting, (b) Endveco 8510 pressure transducer, (c) Kulite-20D pressure transducer

RESULTS AND DISCUSSION

The pressure histories from both the MW1 and MW2 trials, displayed in Figures 3 and 4, show a very high degree of consistency between the two ABT firings in terms of both the static overpressure and dynamic pressure profiles and peak values.

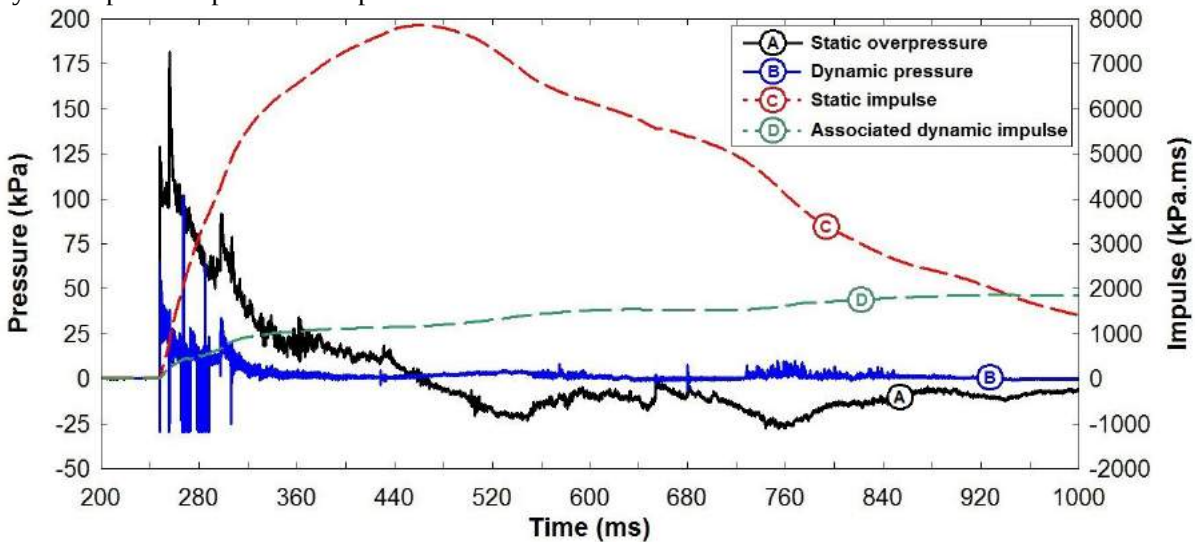

Figure 3. MW1 gauge data

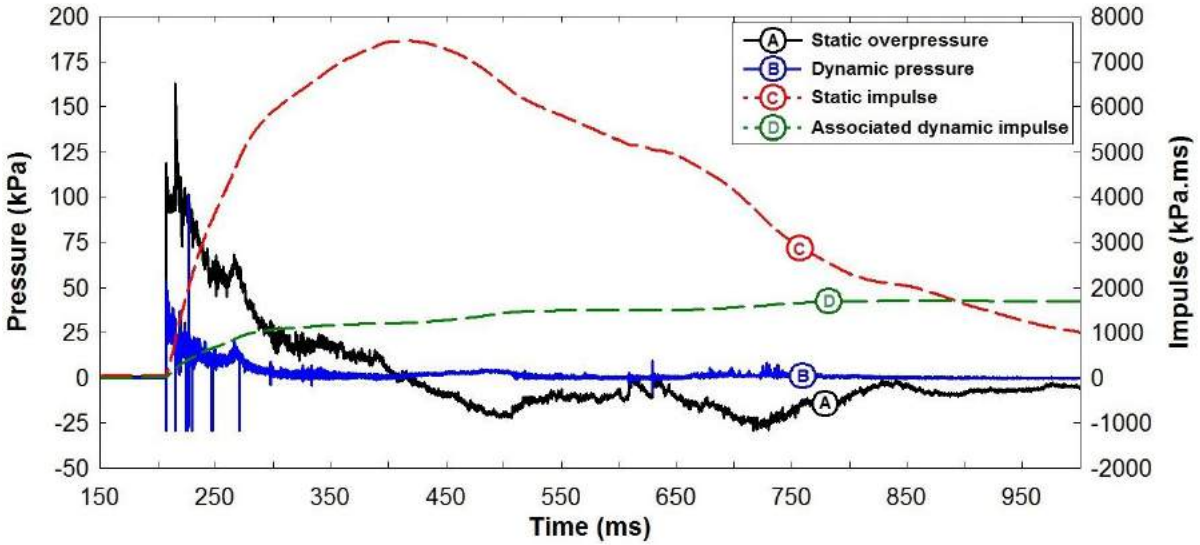

Figure 4. MW2 gauge data

The peak values recorded for the static overpressures were 181kPa for MW1 and 163kPa for MW2; a difference of 18kPa. The duration of the peak was approximately 1ms, which is negligible in terms of impulse and can potentially be due to gauge noise. The 'average peak' value for static overpressure for both trials was around 110kPa. In both cases, the positive phase duration lasted approximately 210ms, which resulted in a total transmitted impulse of 7864kPa.ms for MW1 and 7461kPa.ms for MW2. The negative phase for both trials show good consistency with a reduction in the cumulative impulse of 6437kPa.ms for MW1 and 6448kPa.ms for MW2. For both trials, the dynamic pressure readings show large fluctuations, most likely due to gauge noise. In the case of the MW1 trial, extreme fluctuations were recorded between 260ms-320ms. Notwithstanding, the total transmitted impulses due to the associated dynamic pressure from both trials offer reasonable consistency with 1886kPa.ms and 1668kPa.ms from the MW1 and MW2 trials respectively.

Both structures displayed a high level of breakage, producing extensive debris distributions. Images from the high speed photography from both MW1 and MW2 trials are shown in Figures 5 and 6 respectively.

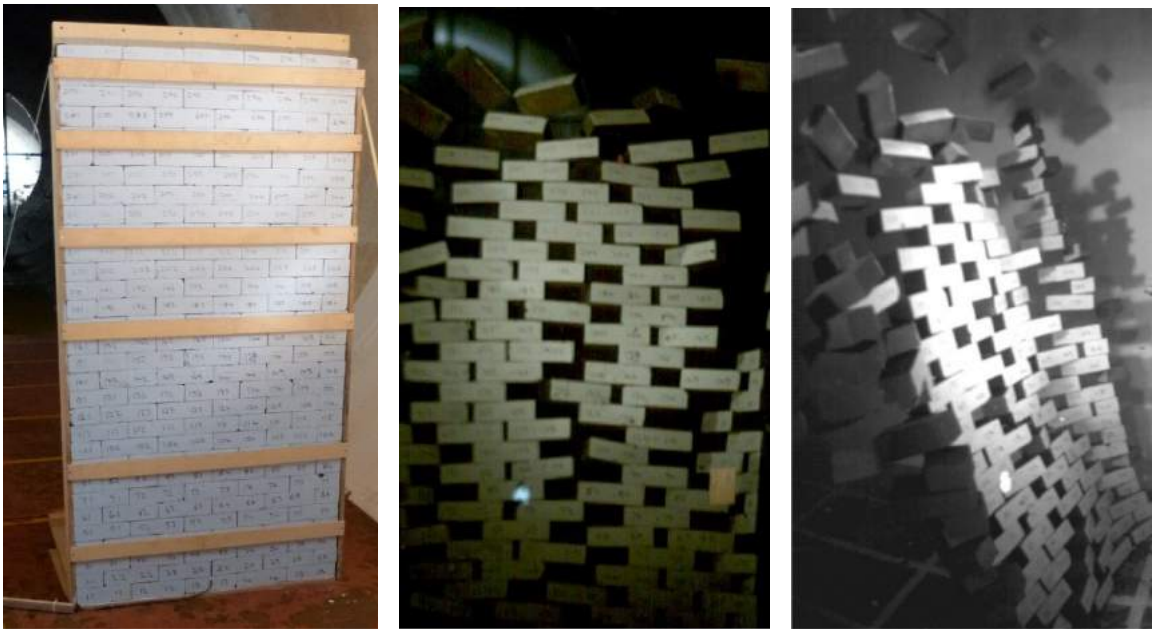

(a) **(b)** **(c)**

Figure 5. MW1 trial photography: (a) preshot - upstream perspective, (b) 100ms – upstream perspective, (c) 100ms – side perspective

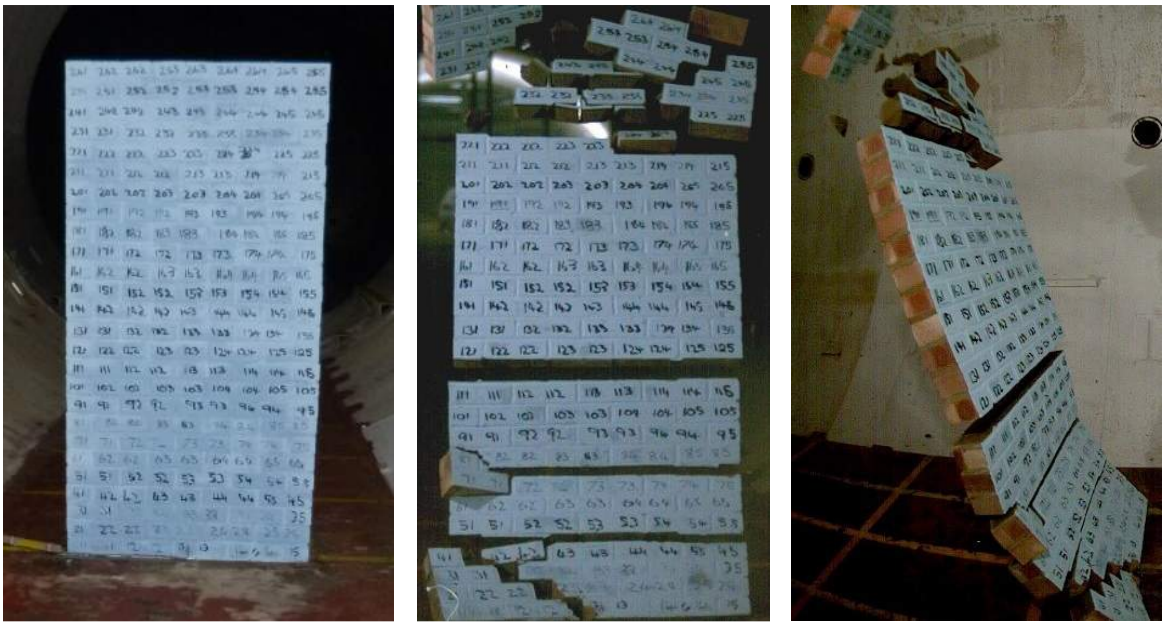

(a) **(b)** **(c)**

Figure 6. MW2 trial photography: (a) preshot - upstream perspective, (b) 100ms – upstream perspective, (c) 100ms – side perspective

Figures 5(a) and 6(a) show the MW1 and MW2 structures before firing from the upstream perspective. The wooden support framing on the MW1 structure shown in Figure 5(a) was removed before firing. The breakage pattern of the MW1 trial, displayed in Figure 5(b), shows separation of the bricks along the vertical (z) axis where the reflective pressure was highest. The reflective pressure was lowest around the edges of the structure; however, this was the weakest part of the structure, which results in increased brick separation. The breakage mechanism of the MW2 structure was simplistic by

comparison as the bedding planes of the mortar provide inherent weak points in the structure; as a result, the breakage pattern, displayed in Figure 6(b), shows four clean lines of separation along the bedding planes. Additional breakage was observed at the top of the structure where it was weakest and at the base of the structure where the reflective pressure and tilting moment were highest. Figures 5(c) and 6(c) show both structures undergo simultaneous tilting and translational movement. Analysis of the high speed photography for both trials indicate an effective velocity gradient of the initial fragments across the vertical (z) axis. Figure 7 illustrates the velocity gradients across both structures.

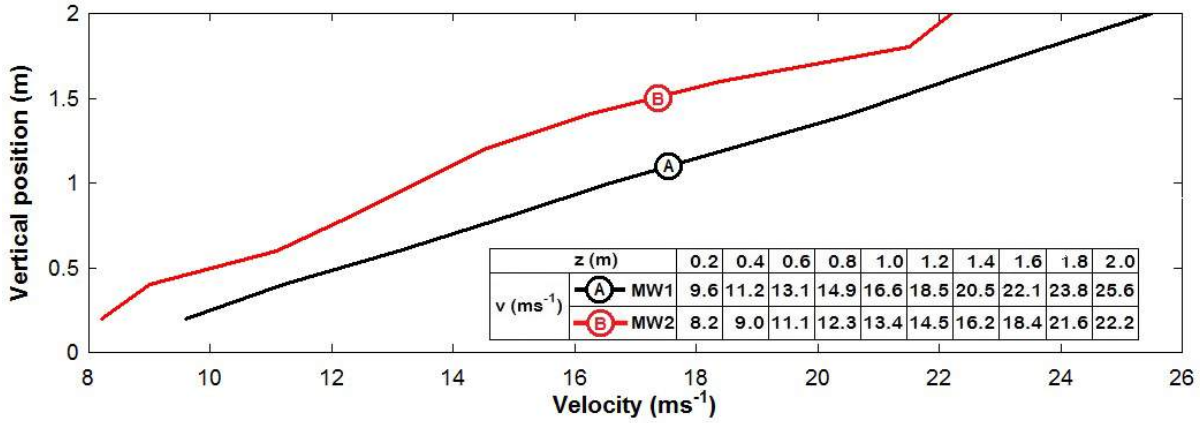

Figure 7. MW1 & MW2 initial brick velocities

The velocity gradient of MW1 was smoother than that of MW2 as the initial fragments were unrestrained, resulting in a more uniform gradient, with a total velocity range of 16ms^{-1}. The initial fragment velocities of the MW2 trial showed localised velocity gradients across the large fragments formed as a result of breakage along specific bedding planes. The range in velocities across the MW2 structure was 14ms^{-1}. The velocity gradient across the structure was a result of the increased static load from the top to the bottom of the structure, due to the increase in mass and frictional forces. The range in velocities resulted in the effective tilting of the structure which in turn dictated the point of impact with the ground and subsequent secondary breakage and debris distribution. Due to the circular cross section of the ABT, the lateral distribution of the debris was restrained for both trials; as a result, the debris data was logged in 1D longitudinal bins of length 1m along the x-axis. Figure 8 shows the longitudinal mass distribution for both MW1 and MW2. MW1 consisted of approximately 120kg of additional mass compared with MW2; for comparison between the two debris distributions, Figure 9 displays the cumulative normalised mass distribution accompanied by a summary table of the absolute cumulative distributions for both trials.

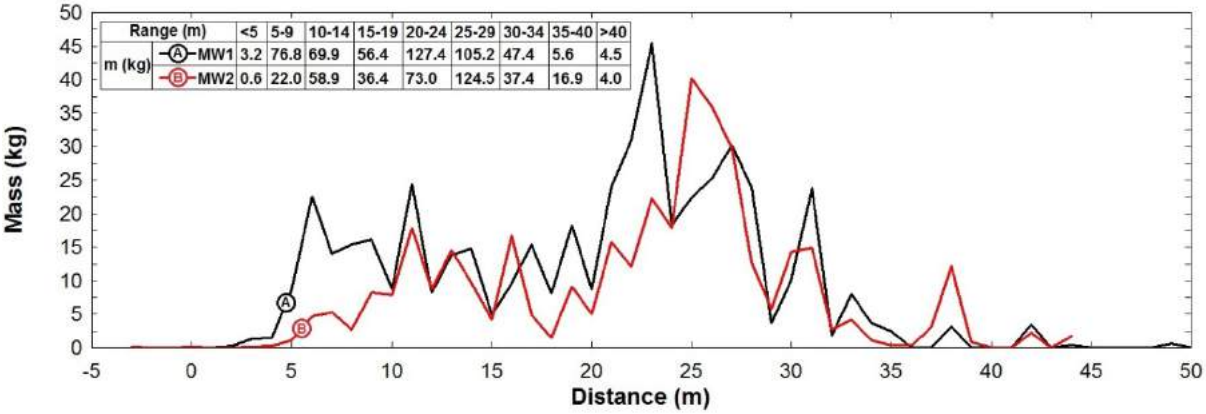

Figure 8. MW1 & MW2 longitudinal mass distribution

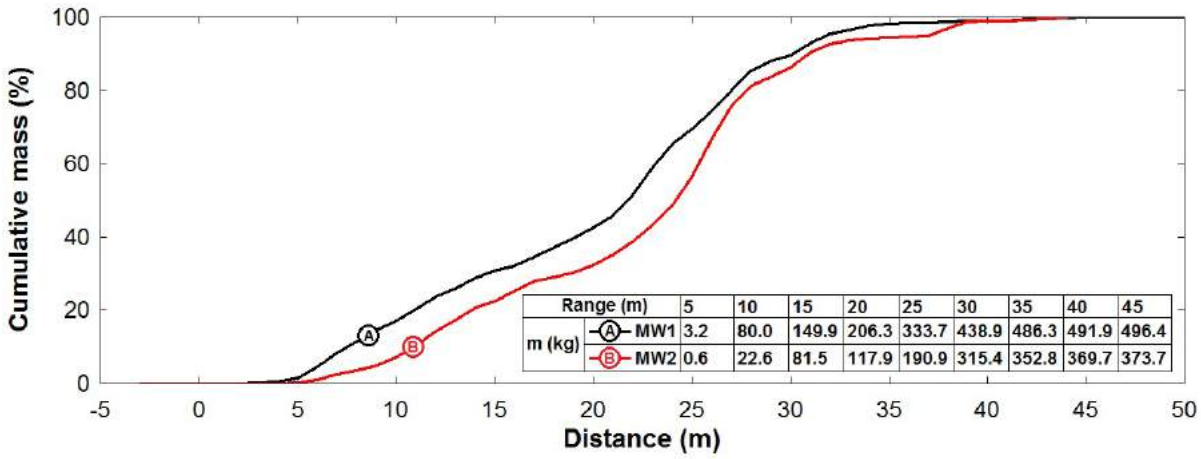

Figure 9. MW1 & MW2 longitudinal normalised cumulative mass distribution

Figure 8 shows the general shape of the debris distribution was similar in both cases, with the bulk of the mass landing within the 20m-30m range. The ABT has instrumentation columns located at approximately 31.5m from the target position; as a result of these columns, both trials showed a small peak between 30m-32m. The maximum distance was similar in both cases, with fragments located up to 44m in MW2 and up to 50m in MW1. A significantly larger portion of the mass from the MW1 trial was located between 5m-10m, which had an effect on the cumulative mass distribution, displayed in Figure 9. The shape of the cumulative distribution was similar for both trials; however, the extra mass located between 5m-10m in the case of MW1 resulted in an effective translation of the total debris distribution. Both the initial fragment velocity and the overall mass of MW1 were higher, resulting in a much higher overall momentum. This offers an explanation for the higher peak distance, but not for the reduction in the cumulative distribution. Comparison of Figures 5(b) and 6(b) show one large fragment at the base of MW2 compared to the relatively uniform breakage of MW1. The fragments from MW1 tumble and roll on impact with the ground, whereas the large fragment from MW2 slides. The launch angle from the MW2 fragment was also lower which reduces the energy dissipated to the ground and subsequent secondary fragmentation.

SUMMARY

The breakage patterns differ greatly in both trials, with MW1 showing uniform pseudo-breakage with each brick forming an individual fragment, whilst MW2 showed large initial fragments separated along bedding planes of mortar. Despite the difference in breakage patterns, initial velocities and overall mass of both structures, the debris mass distribution was similar in both cases. A detailed test specification is planned for early 2016 which will complement the MW series, specifically, the mortared MW2 trial. Utilising the same material properties of MW2, the future tests will vary the geometry and blast parameters to investigate their effects on breakage and debris distribution.

Nomenclature

Symbols		Superscripts	
I	impulse	+	positive phase
m	mass		
p	pressure		Subscripts
t	time	i	incident
v	velocity		

ACKNOWLEDGEMENTS

The authors would like to express gratitude to the UK Ministry of Defence for providing the use of testing facilities at MoD Shoeburyness. All data hereby obtained through the use of such facilities

remains the property of the UK MoD. The assistance of the Spurpark Ltd trials division is gratefully acknowledged with respect to experimental planning, instrumentation and implementation.

REFERENCES

1. Reid, G. H., “Misty castle series: Mill race event: Test execution report,” Technical report, 1981, Defence Nuclear Agency.

2. B. Burgen et. al., “Buncefield explosion mechanism phase 1,” Technical report, Steel Construction Institute, 2009.

3. Keys, R. A. and Clubley, S. K, *15th International Symposium on the Interaction of the Effects of Munitions with Structure*, Potsdam, Germany, October 2013.

4. Adams, L. J. and Rose, T. A., Simulating explosive events in the air blast tunnel, *22nd International Symposium on Military Aspects of Blast and Shock*, Bourges, France, November 2012.

5. British Standards Institution, BS5628-1:2005 - Code of Practice for the use of Masonry, 2005, Table 1, page 11.

Appendix C

Engineering Structures

The following pages display a pre-print copy of the paper submitted to Engineering Structures. At the time of writing, this paper had been submitted to the editors and was under review.

Experimental analysis of long duration blast loading and debris distribution of masonry panels

Richard A. Keys[a,*], Simon K. Clubley[a]

[a]*Advanced Structural Engineering Research, Infrastructure Group, Faculty of Engineering and the Environment, Highfield Campus, University of Southampton, Southampton, UK, SO17 1BJ*

Abstract

Blast loading of structures is a complex system dependent on a vast number of parameters from both the structure and blast wave. Even for the simplest of structures, small changes to its size and shape can have a large effect on the result when subjected to blast; additionally, small changes to the pressure or duration of the blast wave can drastically alter its interaction with a specific structure. This paper, as part of a larger in-depth research study, investigates the breakage patterns and debris distribution of masonry panels subjected to blast loads with a positive phase duration typically exceeding 100ms. Three experimental trials were conducted, in which ten masonry panels of varying geometries were subjected to blast loads with peak static overpressures of approximately 55kPa and 110kPa, with corresponding positive phase durations of 200ms and 150ms respectively. All structures underwent total structural failure, followed by significant debris distribution with the results showing structural geometry, blast overpressure and impulse to be the key parameters responsible for the breakage pattern, initial fragmentation and debris distribution respectively.

Keywords: long duration blast, masonry, debris distribution, breakage

1. Introduction

Blast and its interaction with structures is a complex system. According to Needham [1], the positive phase of a blast wave is usually characterised by overpressure and is defined as the time between shock arrival and the beginning of the negative phase of the overpressure. Integrating the overpressure with the phase duration gives the impulse transmitted by the blast wave, thus a large positive phase duration leads to a high transmitted impulse. Long duration blast is defined here as a blast wave with a positive phase duration in excess of 100ms. Examples of such explosive events include the 1981 'Mill Race trial' [2] and the 1983 'Direct Course trial' [3] in which 544 and 600 tonnes of ANFO were detonated respectively. Whilst

*Corresponding Author: Tel. +44 (0) 2380 59 2862
Email addresses: r.keys@soton.ac.uk (Richard A. Keys), s.k.clubley@soton.ac.uk (Simon K. Clubley)

such explosive events are unlikely to occur in urban environments, hydrocarbon vapour cloud detonations are capable of producing similar blast conditions and can occur at chemical storage or processing plants located within urban areas. Such examples include the 2005 'Buncfield Disaster' [4] with a predicted TNT equivalence of approximately 250 tonnes, or the 2013 'West Texas Fertilizer Disaster' [5] in which a fire lead to the combustion of 30 tonnes of ammonium nitrate, amongst other combustible materials.

Damage predictions are often made using pressure impulse (P-I) diagrams, as displayed in Figure 1, in which the ISO curves represent particular levels of damage. Whilst the multiple curves provide insight into the state of the structure and the level of damage, they offer little to no information regarding the extent of the resulting debris distribution.

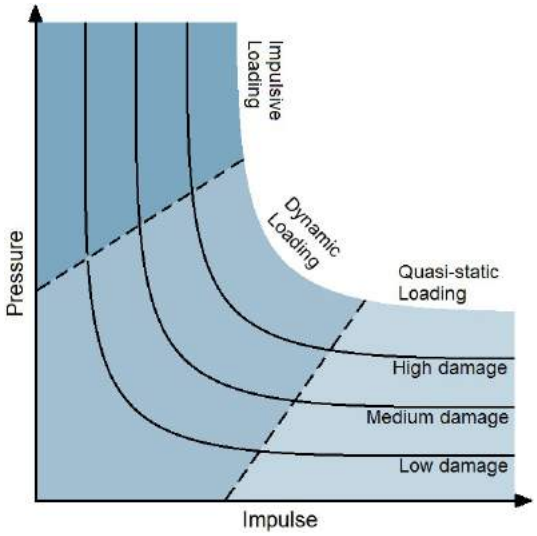

Figure 1: Representation of a P-I diagram with ISO damage curves

Much research has been conducted investigating the effects of blast loading on masonry, with primary focus on the failure mechanisms of masonry [6], [7], [8]. Many results from such research greatly improve the predictive capability of ISO curves, through both numerical and experimental results [9], [10]. Research investigating the flight paths, impact, bounce and roll of masonry debris has also been conducted, in which the final position of individual fragments are statistically predicted using source terms based on the initial conditions [11], [12]. Almost all research conducted into masonry structures and their response subject to blast loading has focused on small to medium sized charges at relatively close ranges, or in some cases, near field detonations [13]. Such detonations produce extremely high pressure blast waves, resulting in high levels of damage; however the duration of such blast events is small, rarely exceeding 50ms. Blast waves with high enough pressure to cause fragmentation and long positive phase durations continue to transfer

large amounts of energy post-breakage, resulting in substantial debris distributions, especially in the case of drag targets [14].

In the event of petro-chemical, or other large detonations in urban environments, the fragments from buildings constructed from brittle materials, such as concrete and masonry, produce a substantial debris distribution. This poses the threat of secondary damage to other structures, large scale infrastructure blockage and potentially lethal injuries. A long term goal of this research is to develop a fast running predictive model to assess the blockage of vital infrastructure and other potential damage caused by the effects of a long duration blast to one or more masonry structures. To achieve this, a combination of experimental and numerical data will assess the debris distribution produced by a wide variety of masonry geometries for various blast parameters. As an initial step, this paper analyses a set of key experimental trials which were conducted to assess the breakage and debris distribution of ten simple masonry structures when subjected to long duration blast loads.

2. Experiments

Three experimental trials, accommodating a total of ten test items, were conducted at the Air Blast Tunnel (ABT), shown in Figure 2, which is located at MoD Shoeburyness on Foulness Island in the UK. The ABT is a large shock tube designed to replicate large explosive events, with two sections for instrumentation which are 4.9m and 10.2m in diameter [15]. The ABT is also fitted with a rarefaction wave eliminator (RWE) at its exhaust to reduce unwanted reflections and complex airflow interfering with the test items. Previous trials conducted at the ABT show the maximum achievable peak static overpressure in the 4.9m and 10.2m sections to be 100-120kPa and 50-60kPa respectively with corresponding positive phase durations of approximately 200ms and 150ms [16]. Using the Kingery and Bulmash polynomials [17], the TNT equivalence of the blast wave was approximately 450 Tonnes at a stand-off distance of 250m in the 4.9m section and 200 Tonnes at 250m in the 10.2m section.

Figure 2: The Air Blast Tunnel (ABT)

With the experimental trials being the first step in a larger research project, the test items are constructed from the simplest form of masonry, single leaf running bonds. Each test item was constructed using frogged facing London bricks, with a mass of ≈2.1kg, dimensions of 210mm×100mm×65mm and a maximum compressive strength of approximately 4-6Nmm^{-2}. The bricks were joined by a class (ii) mortar conforming to BS:5628-1:2005 [18], with a tested compressive strength of approximately 8-10Nmm^{-2} in a 10mm bedding. Each test item was constrained at a vertical height of 2m corresponding to 26 layers of bricks with the base mortared to the ground; this arrangement follows the same design as previous high explosive masonry tests conducted by Keys and Clubley [19].

The primary objective of the experiments was to achieve a set of baseline results which can be used to develop damage predictions for three dimensional masonry structures. To achieve this, two categories of test items were defined; the first category employs simple geometries which represent small panels in a potential structure with the smallest panel being 1m wide. As the simple geometries involved corner panels, boundary conditions applied to the outer edges would not necessarily be consistent between structures. Therefore, for comparative purposes, the simple geometries were implemented without boundary conditions. The second category uses half rectangular structures enclosed by a steel housing designed to reduce any infill effects of the blast wave from above. The purpose of these structures is to draw comparisons between the simple base panels in isolation and as part of a larger structure without the complication of infill before breakage. To ensure there was as little infill as possible without physically connecting the masonry to the steel roof, the top layer of masonry was covered with vinyl strips, to which a layer of expanding foam was applied. This method closed the gap between the masonry and the steel, reducing any hammer effects from the roof as well as restricting the blast in-fill. This method ensures there was as little restraint on the masonry from above as reasonably possible within the confines of the ABT.

For each structure, every 1m panel was painted a different colour to allow comparisons between individual sections and every brick was assigned a unique number. To aid the post trial debris collection, 0.5m × 0.5m grids were marked on the ground in the 10.2m section; the 4.9m section however does not allow for two dimensional debris collection and so the pre-existing radial 1m bin markers were used. Both the 10.2m and 4.9m sections were instrumented with Endveco-8510 and Kulite-20D pressure transducers to monitor the static and dynamic pressures respectively. Kulite-LQ125 pressure transducers are also mounted on rigid steel surfaces to monitor reflected pressure. Each test item was recorded by two or more high speed phantom cameras mounted in protective steel cases, each recording at 2000fps. Each test item is listed in table 1 along with its unique Structure ID (SID), dimensions, target overpressure and peak recorded values from

Table 1: ABT 'BWL' series summary table

SID	Enclosed	Dimensions	Target	Recorded				
		(x, y, z)(m)	p_i (kPa)	p_i (kPa)	I (kPa.ms)	p_r (kPa)	q (kPa)	t^+ (ms)
BWL1A	-	$0.1 \times 1 \times 2$	110	100	7260	290	42	214
BWL1B	-	$1 \times 2 \times 2$	55	60	3220	129	24	150
BWL1C	✓	$4 \times 2 \times 2$	55	59	3423	129	23	168
BWL2A	-	$1 \times 1 \times 2$	110	108	7187	322	59	218
BWL2B	-	$0.1 \times 1 \times 2$	55	59	3164	131	24	160
BWL2C	-	$1 \times 1 \times 2$	55	60	3952	131	24	179
BWL2D	✓	$3 \times 1.5 \times 2$	54	60	3304	131	24	164
BLW3A	-	$1 \times 1 \times 2$	110	112	7011	320	55	219
BWL3B	-	$0.1 \times 2 \times 2$	55	57	3362	124	24	152
BWL3C	✓	$3 \times 2 \times 2$	55	57	3365	124	21	160

the closest pressure gauge.

Figures 3, 4 and 5 display plan schematic drawings of the first, second and third trials respectively for detailed reference, indicating the position of each structure with accompanying photographs and SID, positions and orientations of the phantom cameras and the position of each instrumentation arrray.

3. Results & Analysis

The pressure time histories displayed in Figures 3, 4 and 5 show that for the 10.2m section of the ABT, gauges p_i3, p_i4 and p_i5 recorded consistently higher peak pressures than gauges p_i1 and p_i2. The duration of these peak pressures are between 2-8ms and each reading appears after the arrival of the wave front, indicating that they result from reflections off of the steel enclosure. Gauges p_i1 and p_i2, located on the outer edge of the ABT, were positioned alongside each structure and thus did not record any reflections. Discarding the reflections, the mean recorded peak static overpressure in the center of the 10.2m section of the ABT across all three trials was 55kPa, with all values falling within ±3kPa of the mean and a range of 5kPa. The mean recorded peak static overpressure at the edges of the 10.2m section of the ABT across all three trials was 58kPa, with all values falling to within ±2kPa of the mean and a range of 3kPa. The overall mean recorded peak static overpressure in the 10.2m section of the ABT across all three trials was 56kPa, with all values falling to within ±4kPa of the mean and a range of 7kPa. The only static pressure gauge in the 4.9m section of the tunnel was p_i6, which was positioned upstream from the test items, also recorded small reflections from the test items. Once again, discarding the reflections, the recorded peak static overpressures in the 4.9m section of the ABT were 100kPa, 108kPa and 112kPa for trials 1, 2 and 3 respectively, giving an average peak static overpressure of 107kPa across all three trials. The recorded p_i

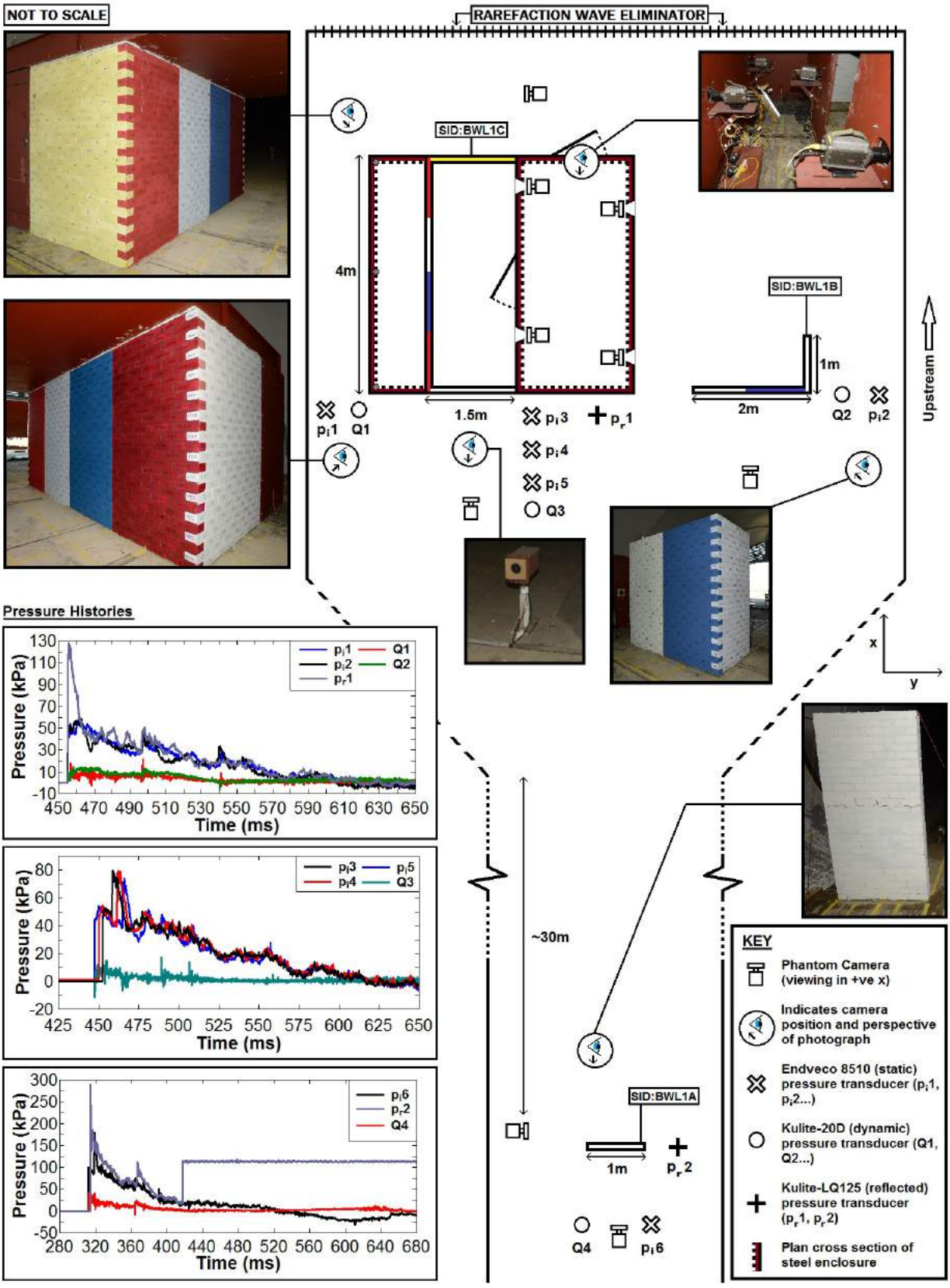

Figure 3: Plan view of ABT trial 'BWL1.' Full schematic detailing the positioning of each test item accompanied by pre-trial photographs, gauge locations and their corresponding pressure time histories with phantom camera positioning.

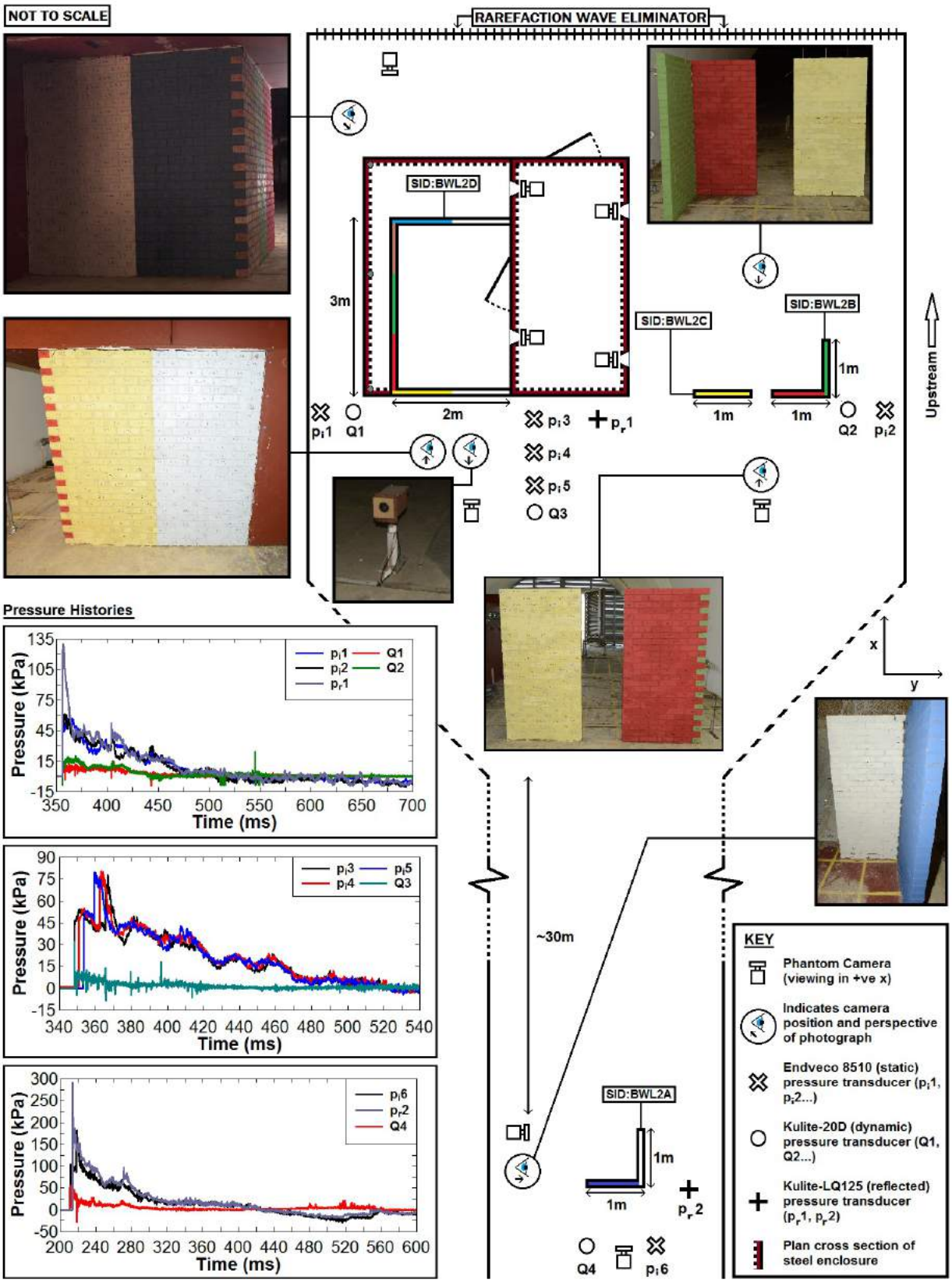

Figure 4: Plan view of ABT trial 'BWL2.' Full schematic detailing the positioning of each test item accompanied by pre-trial photographs, gauge locations and their corresponding pressure time histories with phantom camera positioning.

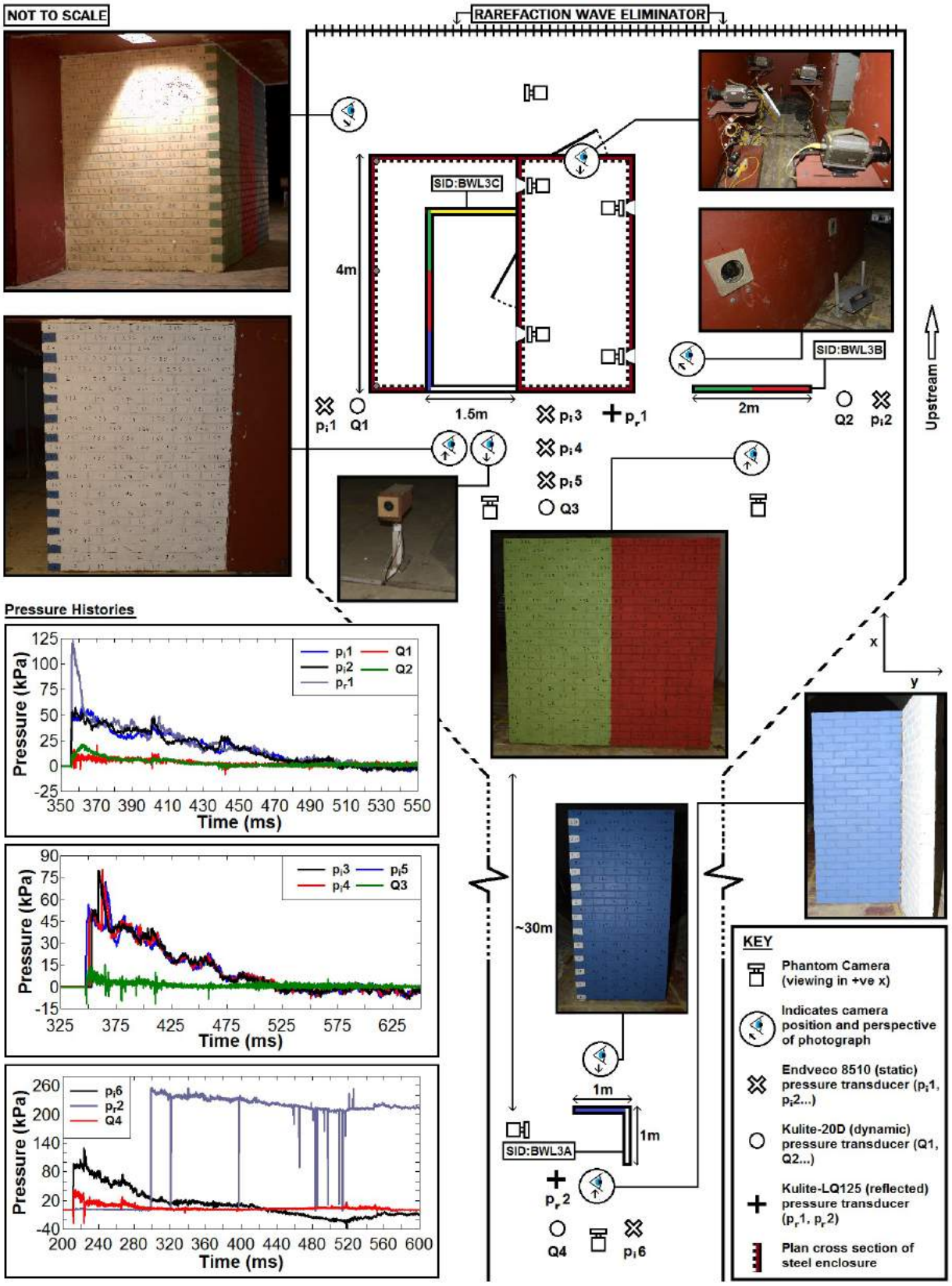

Figure 5: Plan view of ABT trial 'BWL3.' Full schematic detailing the positioning of each test item accompanied by pre-trial photographs, gauge locations and their corresponding pressure time histories with phantom camera positioning.

values displayed in Table 1 show the recorded peak static overpressures disregarding any reflections. Overall, the static overpressures were achieved to within 0-8% of the target value in the 10.2m section and 2-9% of the target value in the 4.9m section.

3.1. Breakage patterns and failure mechanisms

Figures 6 and 7 show the breakage at 50ms and 200ms respectively for each structure located in the 4.9m section of the ABT. The first visual signs of crack formation occurred between 10ms and 15ms and led to clear separation and fragmentation by 50ms. The positive phase in the 4.9m section of the ABT was approximately 200ms by which point each structure was entrained in the blast wave. The arrows shown in Figure 6 highlight the initial crack lines responsible for the breakage pattern.

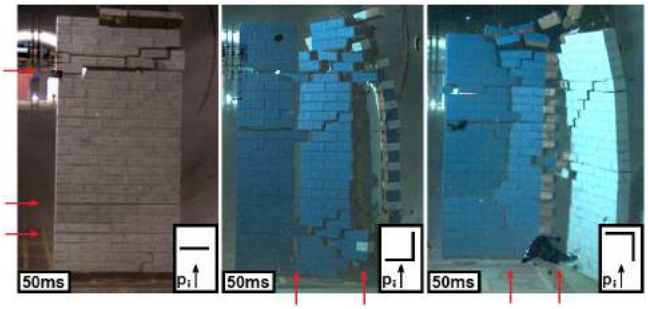

Figure 6: Breakage at 50ms (left to right: BWL1A, BWL2A, BWL3A)

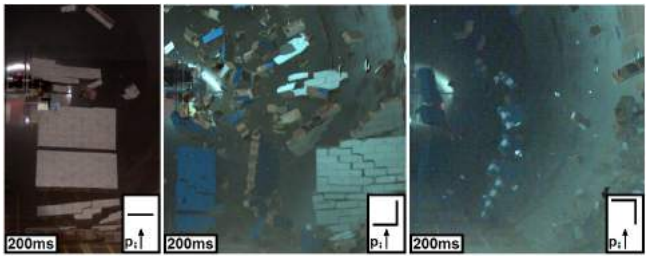

Figure 7: Breakage at 200ms (left to right: BWL1A, BWL2A, BWL3A)

The crack formation observed in structure BWL1A at 50ms are horizontal fracture lines running the width of the structure along bedding planes at approximately 0.3m, 0.5m and 1.6m from the base of the structure. At 200ms, more horizontal breakage lines were present with smaller fragments appearing at the top and bottom of the structure. The BWL1A test is a repeat of a pervious trial conducted by Keys and Clubley [20], which demonstrated an almost identical breakage pattern. Both BWL2A and BWL3A developed vertical cracks due to the added support of the corner geometry which increased resistance to

horizontal cracking. In both cases, vertical cracks form down the centre of the structure and along the corner joint which leads to rotation of the side panel about the connection, causing a larger number of initial fragments. In the case of BWL2A, the side panel did not develop any visible crack lines until the front panel was completely separated; however both the front and side panel of BWL3A begin to fail in unison. Figure 7 shows the panels normal to the blast become entrained in the blast wave by 200ms, with the corner structures both showing higher levels of initial fragmentation. The side panels of BWL2A and BWL3A are forced outwards, perpendicular to the blast wave with slight rotation from BWL3A and significantly higher rotation in BWL2A due to its initial breakage pattern.

Figures 8, 9 and 10 show the breakage at 50ms and 150ms of structures BWL1B, BWL2B&C and BWL3B respectively. These are the unenclosed, smaller structures located in the 10.2m section of the ABT, which recorded peak static overpressures of 55-65kPa with a positive phase of approximately 150ms.

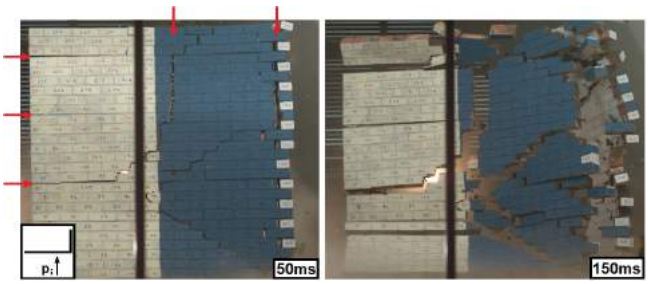

Figure 8: Breakage at 50ms (left) and 150ms (right) of BWL1B

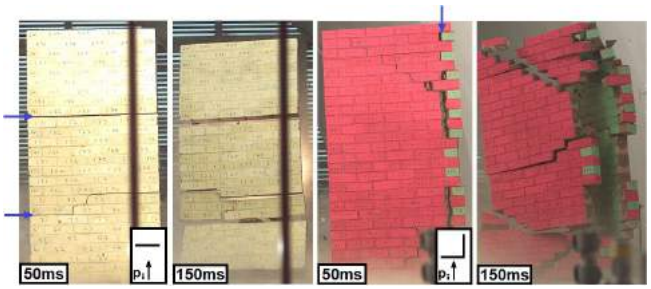

Figure 9: Breakage of (left to right) BWL2C 50ms, BWL2C 150ms, BWL2B 50ms, BWL2B 150ms

The geometry of BWL1B provides a combination of added support from the corner joint and weakness due to the larger surface area on the exposed front panel. The initial breakage pattern observed at 50ms displayed in Figure 8 shows a combination of horizontal and vertical crack lines across the exposed front panel, all of which form along bedding planes. The first cracks to form were along the corner joint, caused by the pressure across the front face which created a rotational force about the corner connection, this was

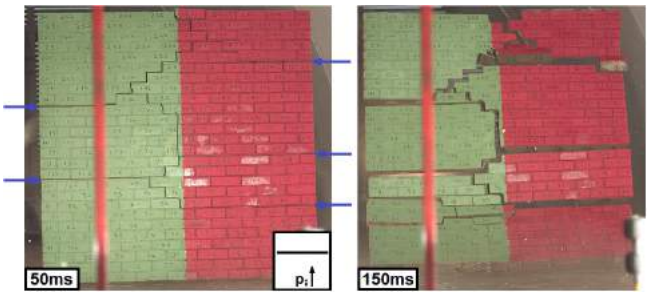

Figure 10: Breakage at 50ms (left) and 150ms (right) of BWL3B

followed shortly (≈5ms) by the detachement of the upper left quadrant. Finally, additional cracking formed in the lower right quadrant of the structure resulting from the rotational force at the joint. The side panel exhibited minimal cracking at 50ms with only small, stepped cracks forming at the top and bottom of the structure near the joint. At 150ms, the initial crack patterns caused separation, resulting in both large fragments and additional cracking, which in turn leads to a larger number of smaller fragments. Each 1m section of the structure became completely separated with the front panel split in half along the colour boundary and the side panel forced outwards with some additional rotation.

The structures BWL2C and BWL2B, shown in Figure 9, have the same geometry as structures BWL1A and BWL2A respectively but are located in the 10.2m section and thus subjected to a lower static pressure. Similar to BWL1A, at 50ms BWL2C exhibits horizontal cracking along the bedding planes at approximately 0.5m and 1.5m from the base of the structure; the crack line at 0.5m however forms across 3 bedding planes. By 150ms the lower crack extends above and below the central stepped crack resulting in the structure breaking into 5 distinct fragments. The corner structure, BWL2B, also exhibited similar breakage to its counterpart, BWL2A, with major cracking forming around the joint at 50ms; the exposed front panel however showed only minor crack lines at the top and bottom of the structure and the side panel remains completely intact. Additional horizontal cracking forms across the exposed front panel and by 150ms leads to separation into a small number of large fragments. The side panel remains mostly intact with one horizontal crack forming at approximately 1.2m above the base of the structure breaking the panel into two large fragments; as with BWL1B and BWL2A, the side panel is forced outwards towards the wall of the ABT with a rotational motion about the joint.

BWL3B, a 2m wide flat panel shown in Figure 10, forms a number of horizontal and stepped crack lines along mortar bedding planes. Horizontal cracking is expected as the linear bedding planes are the weakest parts of the structure; however as the exposed surface area is symmetric and larger than other

structures tested, a larger number of vertical and stepped crack lines are formed due to drag effects around the structure. Once the initial cracks have formed and initial fragmentation has occurred, few additional cracks are observed at the end of the positive phase at 150ms. The overall breakage mechanism was similar to a combination of the 2m wide front panel of BWL1B and the single front panel of BWL2C, with vertical and stepped cracks form along the centre of the face causing separation along its central axis and 2-3 horizontal cracks forming at similar intervals.

Breakage of the large enclosed structures in the 10.2m section of the ABT was recorded using four phantom cameras. Two cameras were positioned in the steel enclosure capturing the breakage from the inside of the structure, one was positioned upstream capturing the breakage of the front panel and one was positioned downstream capturing the breakage of the rear panel; however, the images from the rear cameras were unclear due to dust build up obscuring the camera view. Figures 11, 12 and 13 show the breakage of structures BWL1C, BWL2D and BWL3C respectively at both 50ms and 150ms from the upstream and interior perspectives.

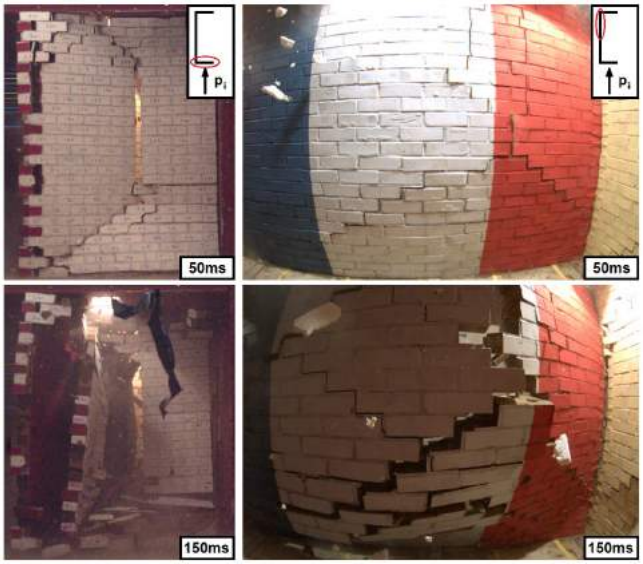

Figure 11: Breakage at 50ms (top) and 150ms (bottom) of BLW1C

Each of the large structures comprise half rectangular geometries which differ only in length and width, with measurements of 4m×1.5m, 3m×2m and 3m×1.5m for BWL1C, BWL2D and BWL3C respectively. These small changes in geometry appeared to have little effect on the overall breakage mechanisms as the camera footage shows almost identical breakage patterns at both 50ms and 150ms on all sides of the structures. At 50ms, the front panels all develop three cracks which meet at a central point. A stepped

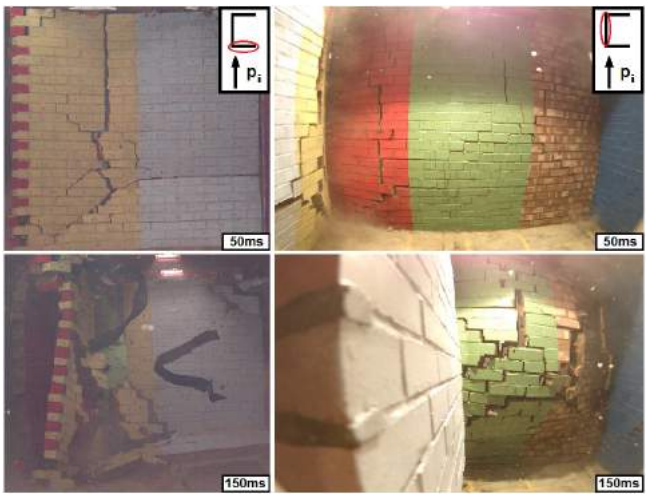

Figure 12: Breakage at 50ms (top) and 150ms (bottom) of BLW2D

crack from the base of the corner joint, rises to join a vertical crack running to the top of the structure and a horizontal crack running to the right edge, where it meets with the steel enclosure. For all three structures, the vertical crack appears between 0.8m and 1m from the corner joint, despite the front panel of BWL2D being 0.5m wider. The positioning of the horizontal crack line also appears consistently at approximately 0.7m above the base for all three structures. For each structure, a vertical crack also appears at the corner joint which spans the height of the structure. With similar crack patterns forming across the front of three structures, the resulting failure mechanisms also show high degrees of similarity. At 150ms, the initial crack patterns across the front panel of each structure cause separation into three main fragemts. The lower fragment tilts about its base and falls inwards, the fragment initially connected to the side panel rotates about the vertical crack along the corner joint and falls inwards and the final panel is forced inwards with a higher velocity and little rotation. Small differences between the number and size of additional small fragments are observed, but the overall failure mechanism of the front panel is the same in each case.

The initial breakage pattern at 50ms across the side panels are also consistent across all three structures, despite BWL1C being an additional 1m in length. In each case, stepped cracks begin to form at base of the corner joint which connects the rear and side panels. For each structure, the rising stepped crack reaches the 11^{th} row of bricks, approximately 0.8m above the ground, at roughly 1m from the connection to the rear panel where it intersects with a vertical crack running to the top of the structure and another stepped crack which runs to the base of the structure, approximately 2m from the connection to the rear panel. For each structure, a vertical crack which spans the height of the structure appears at 1m from the corner joint

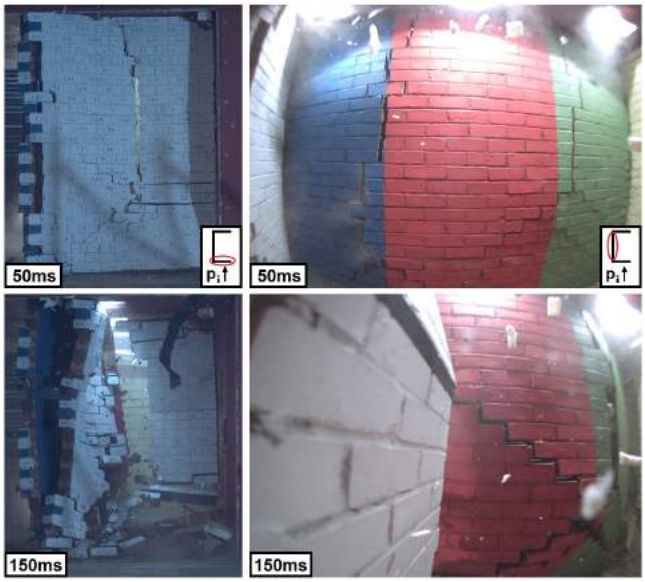

Figure 13: Breakage at 50ms (top) and 150ms (bottom) of BLW3C

connecting the front and side panels. For BWL1C and BWL3C, this vertical crack intersects stepped crack at the base of the structure; however as BWL2D is an additional 1m in length there is no intersection. By 150ms, the side panel is forced inwards primarily around the intersection of the three cracks 1m from the rear panel. A large fragment is created by the vertical crack 1m from the front panel and the corner joint connecting the front and side panels; rotation about the corner joint causes this fragment to fall outwards.

3.2. Debris distribution

To obtain an in depth analysis of the debris distributions produced by each structure, every fragment was collected and logged by mass, x-y position, material type and where applicable, brick colour and number. The higher pressures and impulses observed in the 4.9m section of the ABT resulted in much larger longitudinal debris distributions; however, due to its relatively small circular cross section, lateral displacement could not be logged. Figures 14, 15 and 16 show the longitudinal debris distributions, geometric identifier and debris statistics for structures BWL1A, BWL2A and BWL3A respectively, where the number of remaining whole bricks is shown as a percentage of the initial number of bricks, $m_f(max)$ is the mass of the largest recorded fragment, $\Sigma m(m_f > 0.1\text{kg})$ is the total mass of all recorded fragments above 0.1kg and $\Sigma m(m_f \leq 0.1\text{kg})$ is the total mass of all recorded fragments less than or equal to 0.1kg. For all distributions, x=0 refers to the point of the structure closest to the blast, i.e. in the most upstream position.

The debris distribution of structure BWL1A, shown in Figure 14, shows a series of small peaks between

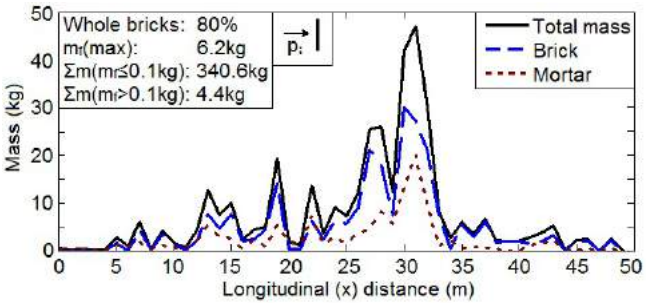

Figure 14: Longitudinal debris distribution, geometric identifier and debris statistics of BWL1A

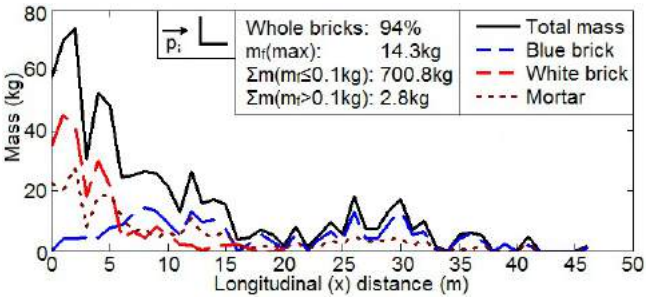

Figure 15: Longitudinal debris distribution, geometric identifier and debris statistics of BWL2A

10-25m followed by a large peak of approximately 45kg at 30m. The large peak at 30m is due to two instrumentation columns which partially obstruct the end of the 4.9m section, thus causing some debris piling. In the absence of these columns, a more uniform distribution is predicted between 30-50m with the maximum throw distance to be between 50-60m. The overall shape of the debris distribution can however be attributed to the initial crack formation and breakage pattern, with each peak corresponding to one of the initial large fragments. Approximately 80% of the bricks collected remained intact, the majority of which were found attached to varying quantities of mortar. The largest recorded fragment, with a mass of 6.2kg, was found at the 15m mark and consisted of two whole bricks mortared together, originating from the base of the structure.

The overall shape of the debris distribution of BWL2A, displayed in Figure 15, shows approximately 70% of the debris landed within 15m. This result is as expected with the white bricks, which constitute the side panel, landing within the first 5m upon impact with the wall of the ABT. The blue bricks, constituting the front panel, follow a relatively even distribution between 0-35m with a small peak of approximately 20kg at 25m and another of relatively equal magnitude coinciding with the instrumentation columns at 30m. Approximately 94% of all bricks remained intact with the largest recorded fragment, with a mass of 14.3kg,

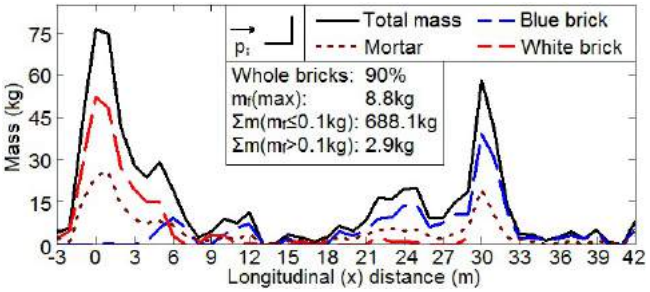

Figure 16: Longitudinal debris distribution, geometric identifier and debris statistics of BWL3A

found at 3m. The fragment consisted of 5 white bricks originating approximately 1m from the base of the side panel, close to the corner joint.

The geometry of structure BWL3A can be considered a 180° rotation of BWL2A with the panel normal to the blast located at the rear of the side panel. The debris distribution of structure BWL3A, displayed in Figure 16, shows the distribution of the white bricks, which constitute the side panel, to be very similar to that of BWL2A, the majority of which were located in the first 5m. The distribution of the blue bricks differs however, with the majority located between 20-33m. Approximately 45kg of blue bricks were located at the instrumentation columns at 30m suggesting a larger distribution between 35-50m in their absence. Similar to BWL2A, 90% of the bricks were found intact, with the largest fragment being 8.8kg. This fragment consisted of 3 whole blue bricks originating from the base of the blue panel normal to the blast.

Figures 17, 18, 19 and 16 show the longitudinal, lateral and x-y debris distributions, geometric identifier and debris statistics for structures BWL1B, BWL2B, BWL2C and BWL3A respectively, where the number of remaining whole bricks is shown as a percentage of the initial number of bricks, $m_f(max)$ is the mass of the largest recorded fragment, $\Sigma m(m_f\ 0.1\text{kg})$ is the total mass of all recorded fragments above 0.1kg and $\Sigma m(m_f \leq 0.1\text{kg})$ is the total mass of all recorded fragments less than or equal to 0.1kg. For all distributions the origin, $(x,y) = (0,0)$, refers to the centre of the front panel.

The x-y distribution of structure BWL1B, displayed in Figure 17, is cropped to show areas of high mass density. The highest density areas were located at $(x,y) = (1,2)$ followed by (7,-1). Comparison of the longitudinal and lateral debris distributions show the area of highest density at (1,2), was caused by the white bricks which constituted the side panel, which, after becoming detached from the rest of the structure, collapsed against the wall of the ABT. The second peak at (7,-1), is caused by the debris colliding with a set of lights which were used for the high speed photography. The lateral distribution shows both halves of the front panel, constructed from 'pale' and blue bricks, to comprise relatively similar distributions, with the

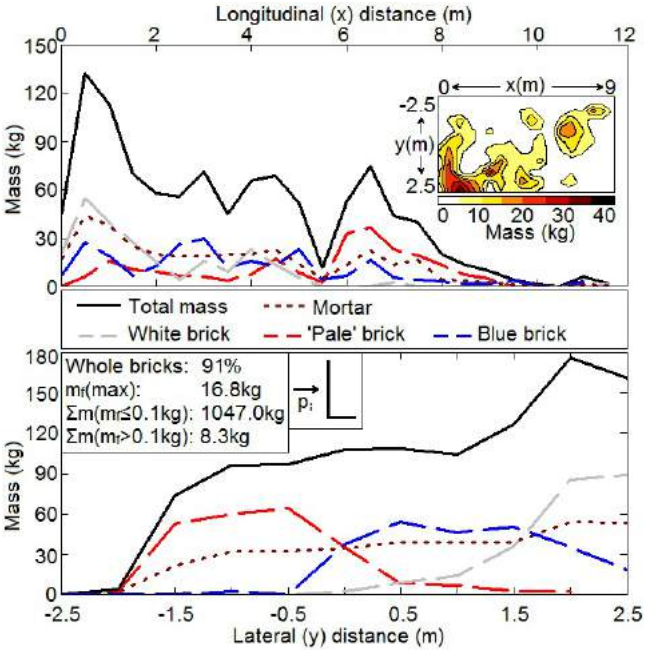

Figure 17: Longitudinal, lateral and x-y debris distribution, geometric identifier and debris statistics of BWL1B

exception of slightly more piling around the lighting at 7m for the 'pale' bricks. The lateral distributions remain unaffected by the lighting and shows an even debris distribution for both panels. The debris itself consisted of mostly large fragments, the largest of which had a mass of 16.6kg and was located in the high density regoin at (1,2). The fragment was constructed of white bricks from the base of the side panel, on its outside edge. 91% of all bricks collected remained intact with less than 1% of the debris pile consisting of small fragments less than 0.1kg.

Similarly to BWL1B, the green, side panel of BWL2B became detached and collapsed against the wall of the ABT, leaving an area of high density at (1,1.5), displayed in Figure 18. The longitudinal distribution shows the majority of the mass to have fallen within 5m of the origin with a maximum throw distance of 11m. The lateral distribution shows the red bricks from the front panel did not follow a symmetrical distribution with over 80% of the mass falling towards the wall of the ABT. This was caused by the rotation of the red panel which caused separation with the side panel. Over 95% of the bricks remained intact and many large fragments were found in the debris pile, 8 of which had a mass exceeding 10kg and the three largest fragments had masses of 23.4kg, 24.7kg and 26.7kg. The largest fragment was located at (0.5,1) and consisted of 6 red bricks and 2 green bricks from the base of the corner joint. The other two large fragments were located in the high density area surrounding (1,1.5) and were both made up from green

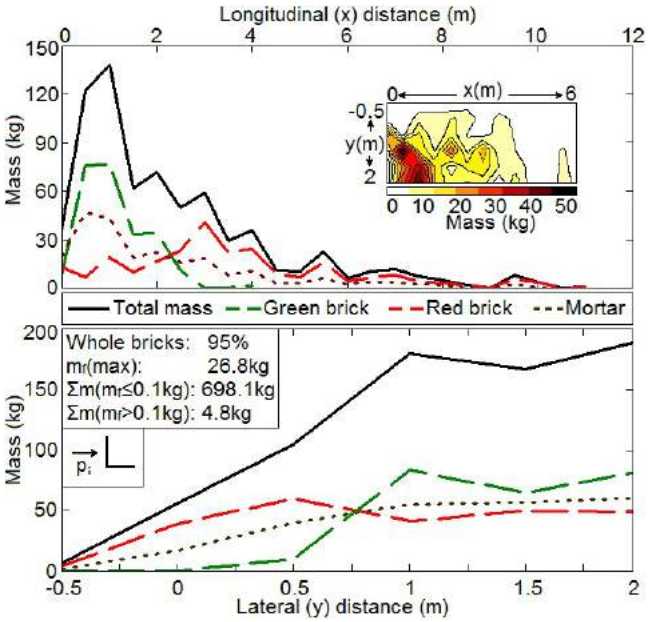

Figure 18: Longitudinal, lateral and x-y debris distribution, geometric identifier and debris statistics of BWL2B

bricks originating middle and the top of the side panel.

The x-y debris distribution of structure BWL2C, displayed in Figure 19, shows two regions of high density, located at (5,0) and (7,0) with magnitudes of approximately 50kg and 75kg respectively, the latter resulting from the lighting obstruction. The initial breakage, caused by horizontal crack formation, segmented the structure into 4 distinct, large fragments with the peak at (5,0) being caused by the impact of the lowest fragment with the ground. The lateral distribution is symmetric about the origin for both the individual brick and mortar distributions. The largest fragment with a mass of 26.0kg was located in the first high density region at (5,0) and was constructed of 10 bricks originating from the lower outside edge of the structure. In the absence of the lighting obstruction, the overall longitudinal distribution is expected to have a larger maximum throw distance with the high density region at 7m to be distributed between 6-12m.

BWL3B shared a very similar debris distribution, both longitudinally and laterally to that of BWL2C. The longitudinal distribution, displayed in Figure 20, shows even distributions of both red and green bricks. Three distinct peaks were observed of approximately 95kg at 1m, followed by 60kg at 4m and 95kg at 7m. The first two peaks were caused by the initial breakage pattern, specifically large fragments from the lower section of the structure and the final peak at 7m was again caused by impact with the lighting array. Similarly to BWL2C, in the absence of the lighting, the peak at 7m is predicted to be distributed between 6-12m. The lateral distribution shows both symmetrical distributions of the individual red and green panels

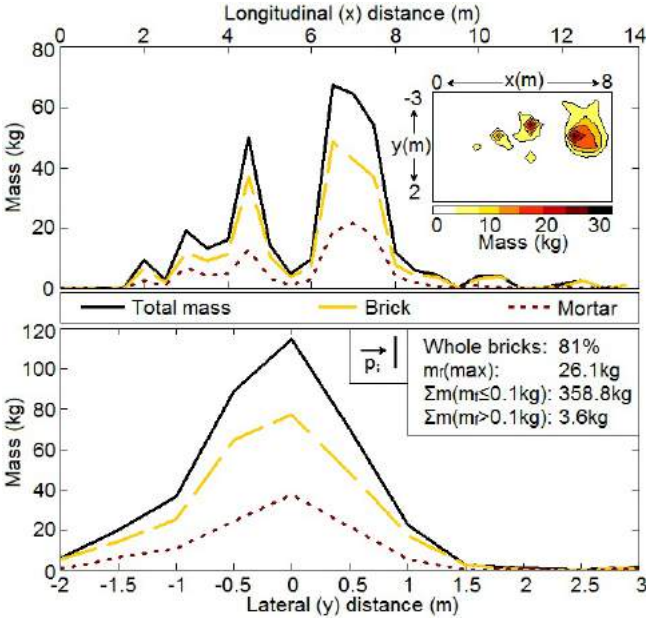

Figure 19: Longitudinal, lateral and x-y debris distribution, geometric identifier and debris statistics of BWL2C

and thus the corresponding overall lateral distribution. The largest fragment recorded from any of the unenclosed structures, with a mass of 27.5kg, was located at (0.5,0.5) and consisted of 6 red bricks and 3 green bricks, originating from the centre of the base of the structure.

Due to extremely high density debris distribution of the large enclosed structures, accurately collecting and measuring the debris was not readily possible; furthermore, safety issues due to the unstable nature of the debris made any manual measurements both impractical and dangerous. The large enclosed structures were recorded safely with extensive photography and are displayed in Figures 21, 22 and 23, which show the debris distributions of BWL1C, BWL2D and BWL3C respectively, accompanied by an outline sketch of the debris pile which indicates the original position of the structure.

The debris distribution of BWL1C, displayed in Figure 21, shows the rear and rear side panels constrained between the floor and the roof of the steel enclosure. This shows the enclosure has successfully stopped blast infill from above as it clears the structure, meaning the rear panel is only exposed to the wrap around pressure from the opposing direction. The static pressure acting on the side and rear of the structure force both panels inwards, creating a rotational motion about the corner joint, wedging the rear panel in place. Blocked by the rear panel, the debris produced by the front panel collects against the rear panel and the steel container, forming the highest point of the debris pile at approximately 1m high. The base of this high density area is formed by white and red bricks from the rear side panels which are covered by white bricks from the front

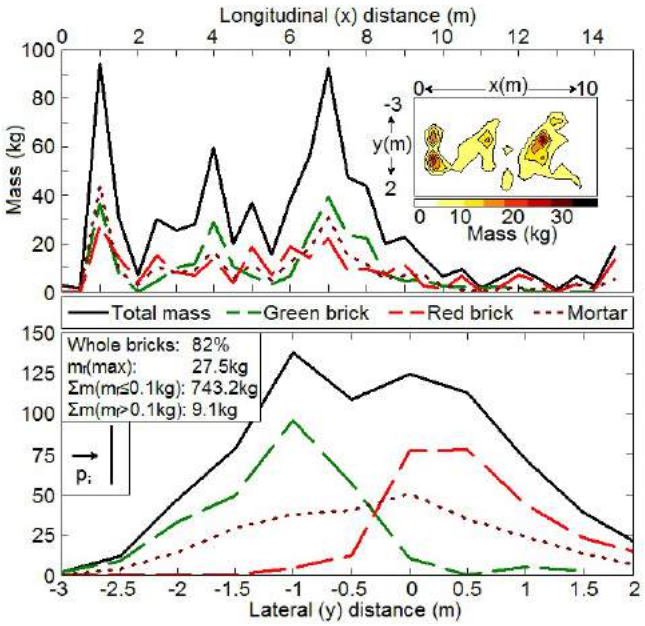

Figure 20: Longitudinal, lateral and x-y debris distribution, geometric identifier and debris statistics of BWL3B

panel. Once the front panel is breached, the infill effect of the blast forces the front, red section of the side wall outwards, resulting in the additional 2m lateral distribution. The total area covered by the debris was approximately $10m^2$.

Covering approximately $12.5m^2$, structure BWL2D produced a similar debris distribution and is displayed in Figure 22. As with BWL1C, the rear panel is constrained against the roof of the steel enclosure; however, there was increased breakage to the rear panel, resulting in 0.5m of the rear panel closest to the steel enclosure to become detached and collapse. The rear panel of BWL2D was much more delicately wedged in place with a large number of lose bricks hanging from the edge of the structure. The front and rear panels of BWL2D were 2m across, 0.5m wider than the other two enclosed structures giving it a larger, weaker cross section; once the front panel was breached, a larger volume of compressed air entered the structure, resulting in a higher pressure acting on the inside of the front section of the side wall, causing a larger lateral distribution. Most of the debris was located at the rear of the structure reaching approximately 0.6m high and consisted of green bricks from the centre side panel, covered by white and yellow bricks from the front panels.

The smallest of the three enclosed structures, BWL3C, produced the largest debris pile covering an approximate area of $16m^2$, shown in Figure 23. Unlike the other two enclosed structures, the rear wall was not restricted by the roof of the steel enclosure. This followed as a result of the front panel impacting

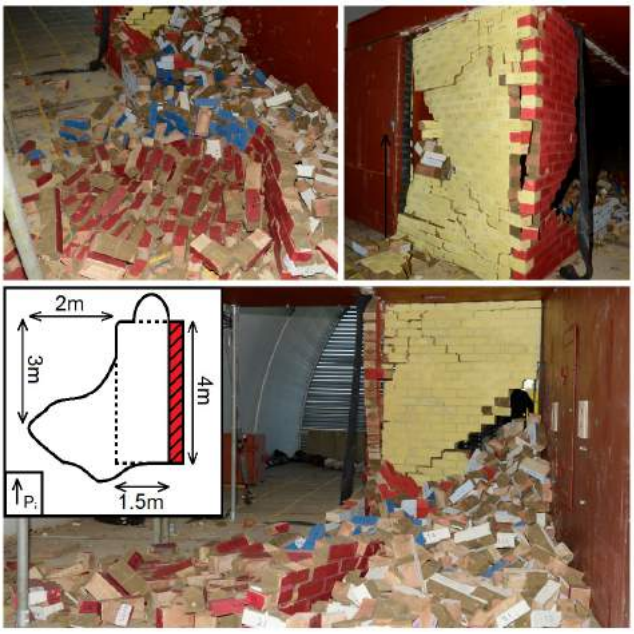

Figure 21: Debris distribution of structure BWL1C

the rear, significantly weakening the lower half of the rear wall and causing it to collapse. The increased rotational force on the rear corner joint, resulting from the collapse of the rear panel, caused the rear, green side panel to become delicately wedged against the roof of the steel enclosure. The white bricks, originating from the front panel, were evenly spread across the interior at the bottom of the debris pile. Towards the rear, the yellow bricks from the rear wall cover the white bricks, forming the top layer of the debris pile with a peak height of approximately 0.6m. The red bricks from the centre panel of the side wall cover the white bricks in the middle section of the interior, with the blue bricks from the front of the side wall forming the entire lateral distribution at the front of the structure.

4. Conclusions

Initial comparisons of all test items show a number of similarities in terms of both breakage and debris distribution. Structures BWL1A and BWL2C, which both share the same 1m wide geometry, both form the same set of horizontal cracks by 50ms; however BWL1C, which was subjected to 110kPa displayed a much larger number of initial fragments. Previous experiments conducted by Keys and Clubley [19] which subjected the same 1m wide panel to a 110kPa for 10ms also showed the same initial breakage patterns, suggesting peak static overpressure to be the key parameter influencing breakage patterns. This was also observed in other geometries, structures BWL2A and BWL2B, which share the same 1m×1m

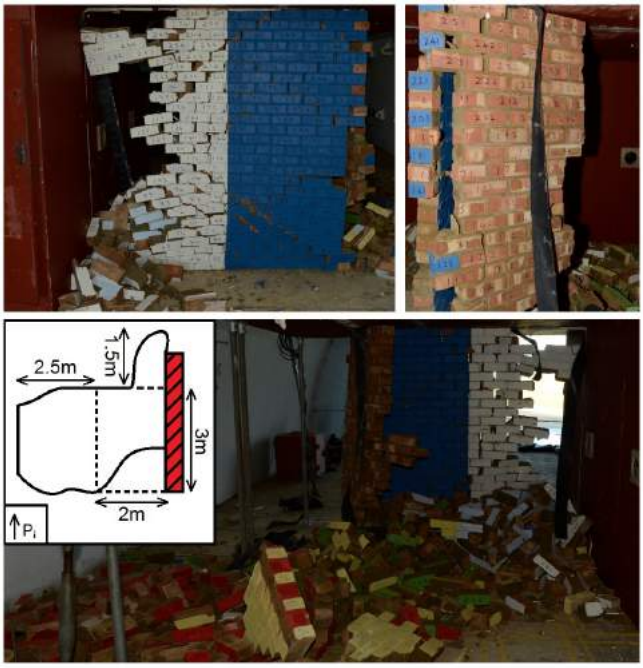

Figure 22: Debris distribution of structure BWL2D

corner geometry, also develop the same basic crack patterns along the corner joints, yet BWL2A which was subjected to 110kPa shows a much higher number of initial fragments.

The similarities in crack formation are also apparent when comparing individual panels within the overall geometry. Structure BWL1B, which had a 2m wide front panel and a 1m side panel, is a supposition of structures BWL2B and BWL2C. At both 50ms and 150ms, the breakage of the corner section of BWL1B shows similar crack formation to BWL2B and the outside panel of BWL1B also shows the same initial crack pattern as BWL2C. Although the larger structure, BWL1B, showed the same basic crack pattern in each panel, the overall number of initial fragments was much higher. Structure BWL3B, a 2m wide panel, shares the geometry of two BWL2C panels. The left, green panel of BWL3B shows very similar breakage as BWL2C at 50ms with two horizontal cracks dividing the structure into three approximately equal sized fragments. The right, red panel also forms horizontal cracks; however in slightly different positions, connected at the centre of the structure by stepped cracks. In both comparisons the overall breakage pattern is very similar; however the structure with the larger incident surface area develops more initial fragments.

The same basic patterns in the debris distribution occur based on the geometry of the structure. Every structure which had both front and side panels show the side panels forced outwards, followed by the front panel entrained in the blast wave with the farthest fragment always originating from the top three layers

Figure 23: Debris distribution of structure BWL3C

of the front panel. In the 4.9m section of the ABT, the maximum longitudinal throw distance ranges from 42-50m, a difference of 16% and 12-14m in the 10.2m section, a difference of 15%.

The debris distributions of the large enclosed structures all followed the same basic breakage patterns, differing only slightly with geometry. This led to all three debris distributions comprising the same basic shape, with slight differences resulting from the breakage pattern and thus geometry. Comparing the front panels of the enclosed structures with the unenclosed structures shows the additional fragmentation caused by drag and clearing effects. All of the large enclosed structures show minimal breakage on the front panel close to the steel enclosure, with each one developing only one low horizontal crack. In the absence of the steel wall, the clearing of the outer edge causes additional breakage on the unenclosed structures. The rear panels of the enclosed structures, which are shielded from infill, reduce the longitudinal distribution by absorbing the momentum of the front panels. In the absence of the steel enclosure, the blast infill from above is expected to cause failure in the rear panels and an outwards force on the side panels; without a rear wall absorb the momentum of the front panels, in combination with an equalised force on the side panels, a much larger longitudinal and lateral distribution is expected.

The initial crack lines and fractures formed within the first 25ms greatly influence the initial fragmentation and the overall debris distribution. Cracking forms along the weakest parts of the structure and each test showed the cracks forming almost exclusively along bedding planes, with a total of 89% of bricks

from all unenclosed structures remaining intact after testing. Breakage patterns can also be influenced by inherent weaknesses or inconsistencies within the structures; although this did not have too much of an effect within these experimental trials as similar structures follow similar failure mechanisms. A numerical modelling platform is currently under development to run a thorough analysis of the blast structure interactions, failure mechanisms and debris distribution patterns of each structure.

5. Acknowledgements

Funding for analytical/experimental research provided by EPSRC Grant: EP/M009254/1. The authors would like to express gratitude to the UK Ministry of Defence for providing the use of testing facilities at MoD Shoeburyness. All data hereby obtained through the use of such facilities remains the property of the UK MoD. The assistance of the Spurpark Ltd trials division is gratefully acknowledged with respect to experimental planning, instrumentation and implementation.

References

[1] C. Needham, Blast Waves, Springer, 2010.

[2] G. H. Reid, Misty castle series: Mill race event: Test execution report, Tech. rep., Defence Nuclear Agency (1981).

[3] D. Eardley, J. Katz, Direct course and dust experiments, Tech. rep., Mitre Corp (April 1983).

[4] B. Burgan, et al., Buncefield explosion mechanism phase 1, Tech. rep., Steel Construction Institute (2009).

[5] Chemical Safety Board, Preliminary findings into the west fertilizer explosion and fire, Tech. rep., Chemical Safety Board (June 2013).

[6] G. S. Urgessa, K. Maji, Dynamic response for retrofitted masonry walls for blast loading, Journal of Engineering Mechanics.

[7] C. Mayrhofer, Reinforced masonry walls under blast loading, International Journal of Mechanical Sciences 44 (6) (2002) 1067 – 1080, seventh International Symposium on Structural Failure and Plasticity.

[8] M. Badr, et al., Response of arching unreinforced concrete masonry walls to blast loading, Journal of Structural Engineering 137 (2011) 1205 – 1214.

[9] X. Wei, M. G. Stewart, Model validation and parametric dtudy on the blast response of unreinforced brick masonry walls, International Journal of Impact Engineering 37 (11) (2010) 1150 – 1159.

[10] A. Mutalib, et al., Deivation of empirical formulae to predict pressure and impulse asymptotes for p-i diagrams of one-way rc panels, Journal of Civil, Environmental, Structural, Construction and Architectural Engineering 7 (8) (2013) 585 – 588.

[11] J. W. M. M. van der Voort, A statistical description of explosion produced debris dispersion, International Journal of Impact Engineering 59 (2013) 29 – 37.

[12] C. Knock, et al., The bounce and roll of masonry debris, The International Journal of Impact Engineering 30 (2004) 1 – 16.

[13] A. Doerr, et al., The effect of near-field explosions on masonry walls, in: 15th International Symposium on the Interactions and Effects of Munitions and Structures (15th ISIEMS), Potsdam, Germany, 2013, pp. P043, 1–12.

[14] S. Glasstone, P. J. Dolan, The Effect of Nuclear Weapons, United States Department of Defence, 1977.

[15] L. J. Adams, T. A. Rose, Simulating explosive events in the air blast tunnel, in: 22nd International Symposium on Military Aaspects of Blast and Shock, Bourges, France, 2012, pp. P58, 1–14.

[16] S. K. Clubley, Long duration blast loading of cylindrical shell structures with variable fill level, Thin Structures 85 (2014) 234–239.

[17] C. N. Kingery, G. Bulmash, Airblast parameters from tnt spherical air burst and hemispherical surface burst, Tech. rep., U.S. Army Armament Research and Development Center, Ballistic Research Laboratory, Maryland (1984).

[18] The British Standards Institution, BS5628-1:2005 - Code of Practice for the use of Masonry, table 1, page 11 (2005).

[19] R. A. Keys, S. K. Clubley, Modelling debris distribution of masonry panels subject to blast loads using experimental & applied element methods, in: 15th International Symposium on Interaction of the Effects of Munitions with Structures, Potsdam, Germany, 2013, pp. P069, 1–10.

[20] R. A. Keys, S. K. Clubley, Experimental analysis of small masonry panels subject to long duration blast loading, in: 16th International Symposium on Interaction of the Effects of Munitions with Structures, Sandestin, Florida, 2015, pp. 1–7.